Theoretical and Experimental Investigations on Different Triangular Shaped Radiators

Thesis submitted by

Sudipta Maity

Doctor of Philosophy (Engineering)

Department of Electronics and Telecommunication Engineering
Faculty Council of Engineering & Technology
Jadavpur University
Kolkata, India

2016

JADAVPUR UNIVERSITY
KOLKATA – 700 032, INDIA

INDEX NO. 59/12/E

1. **Title of the thesis:** Theoretical and Experimental Investigations on Different Triangular Shaped Radiators

2. **Name, Designation & Institution of the Supervisor:**

Professor Bhaskar Gupta
Professor, Electronics and Telecommunication Engineering Department
Jadavpur University, Kolkata – 700 032, West Bengal, India

3. **List of Publications:**

[1] **Sudipta Maity** and Bhaskar Gupta, "Cavity Model Analysis of 30°–60°–90° Triangular Microstrip Antenna," *International Journal of Electronics and Communications (AEÜ),* vol. 69, pp. 923-932, 2015.

[2] **Sudipta Maity** and Bhaskar Gupta, "Closed Form Expressions to Find Radiation Patterns of Rectangular Dielectric Resonator Antennas for Various Modes," *IEEE Trans. on Antennas and Propagation*, vol. 62, no. 12, pp. 6524-6527, Dec. 2014

[3] **Sudipta Maity** and Bhaskar Gupta, "Simplified Analysis for 30°–60°–90° Triangular Microstrip Antenna," *Journal of Electromagnetic Waves and Applications*, vol. 28, issue: 01, pp. 91 – 101, Nov. 2013

[4] **Sudipta Maity** and Bhaskar Gupta, "Accurate Resonant Frequency of Isosceles Right Angled Triangular Patch Antenna," *Microwave and Optical Technology Letters*, vol. 55, no. 6, pp. 1306-1308, June 2013

[5] **Sudipta Maity** and Bhaskar Gupta, "Comments on 'A Triangular Dielectric Resonator Antenna Excited by a Coaxial Probe'," *Microwave and Optical Technology Letters*, vol. 54, no. 6, pp. 1548, June 2012

Journals under Review/Revision Stage:

[1] **Sudipta Maity** and Bhaskar Gupta, "Theoretical Investigations on Equilateral Triangular Dielectric Resonator Antenna," communicated to ***IET Microwaves, Antennas & Propagation*** (1st Revision submitted)

[2] "Experimental Investigations on Wideband Triangular Dielectric Resonator Antenna," communicated to ***IEEE Transaction on Antennas and Propagation*** (1st Revision submitted)

[3] **Sudipta Maity** and Bhaskar Gupta, "Analysis of Horizontally Inhomogeneous Rectangular Dielectric Resonator Antenna," communicated to ***International Journal of Electronics and Communications (AEÜ)*** (Under Review)

[4] **Sudipta Maity** and Bhaskar Gupta, "Simple Procedure to Evaluate Singularity Free Expressions for Radiation Patterns of an Antenna with Rectilinear Symmetry," communicated to ***Waves in Random and Complex Media*** (Under Review)

[5] **Sudipta Maity** and Bhaskar Gupta, "Theoretical Investigations on 45°-45°-90° Triangular Microstrip Antenna," communicated to ***IETE Journal of Research*** (Under Review)

[6] **Sudipta Maity** and Bhaskar Gupta, "Theoretical investigation on 30°–60°–90° triangular dielectric resonator antenna," communicated to ***IEEE Antennas and Wireless Propagation Letters*** (Under Review)

[7] **Sudipta Maity** and Bhaskar Gupta, "Approximate Investigations on Isosceles Triangular Microstrip Antenna in Fundamental Mode," communicated to ***IEEE Transaction on Antennas and Propagation*** (Under Review)

[8] **Sudipta Maity** and Bhaskar Gupta, "Calculation of resonant frequency for isosceles triangular dielectric resonators," communicated to ***IET Electronics Letters*** (Under Review)

4. List of Patents: Nil

5. List of Presentations at National / International Conference:

[1] **Sudipta Maity** and Bhaskar Gupta**,** "Resonant Frequency of Isosceles Right Angled Triangular Dielectric Resonator Antenna," *URSI Regional Conference in Radio Science (RCRS) 2014*, Pune, India, Jan 2014

[2] **Sudipta Maity** and Bhaskar Gupta, "Input Impedance of Probe Fed Rectangular Dielectric Resonator Antenna," *URSI Regional Conference in Radio Science (RCRS) 2014*, Pune, India, Jan 2014

[3] **Sudipta Maity**, "Approximate Solution for Fundamental Mode of 45°–45°–90° Triangular Microstrip Antenna," 4th *IEEE Applied Electromagnetic Conference (AEMC) 2013*, Bhubaneswar, India, Dec 2013

[4] **Sudipta Maity**, Sanghamitra Dasgupta and Bhaskar Gupta, "Resonant Frequency and Field Solution of Isosceles Triangular Dielectric Resonator Antenna," 31st *Progress In Electromagnetics Research* Symposium (PIERS) -2012, ISBN: 978-1-934142-20-2, Kuala Lumpur, Malaysia, pp. 1113 – 1115, March 2012

[5] **Sudipta Maity**, Sanghamitra Dasgupta and Bhaskar Gupta, "Wideband Isosceles 75°-30°-75° Triangular Dielectric Resonator Antenna," 31st *Progress In Electromagnetics Research* Symposium (PIERS) -2012, ISBN: 978-1-934142-20-2, Kuala Lumpur, Malaysia, pp. 1109 – 1112, March 2012

[6] **Sudipta Maity**, Sanghamitra Dasgupta and Bhaskar Gupta, "Fast Adaptive Least Mean Square Algorithm," 31st *Progress In Electromagnetics Research* Symposium (PIERS) -2012, ISBN: 978-1-934142-20-2, Kuala Lumpur, Malaysia, pp. 1666 – 1669, March 2012

[7] **Sudipta Maity**, "Hybrid Triangular Dielectric Resonator Antenna (DRA) for WLAN/ISM Application," *IEEE Indian Antenna Week (IAW) 2011*, Kolkata, India, paper ID: SPC – 1052, Dec 2011

[8] **Sudipta Maity**, Sanghamitra Dasgupta and Bhaskar Gupta, "On the Solution of Isosceles 120^0 Triangular Dielectric Resonator Antenna," *7th International Conference on microwaves, Antenna, Propagation and Remote Sensing*, ICMARS-2011, Jodhpur, India, abstract pp. 34-35, Dec 2011

[9] **Sudipta Maity**, Sanghamitra Dasgupta and Bhaskar Gupta, "More Accurate Resonant Frequency Evaluation of Triangular Isosceles 120^0 Patch Antenna," *7th International Conference on microwaves, Antenna, Propagation and Remote Sensing*, ICMARS-2011, Jodhpur, India, abstract pp. 96-97, Dec 2011

6. Awards:

[1] Received **2nd Prize** in Young Scientist Award paper competition for the paper titled **"Input Impedance of Probe Fed Rectangular Dielectric Resonator Antenna,"** URSI Regional Conference in Radio Science (RCRS) 2014, Pune, India, Jan 2014

[2] Awarded **2nd prize** in the Student Paper Contest (SPC) for the paper titled **"Approximate Solution for Fundamental Mode of 45°–45°–90° Triangular Microstrip Antenna,"** 4th IEEE Applied Electromagnetic Conference (AEMC) 2013, Bhubaneswar, India, Dec 2013

[3] Awarded **1st prize** in the Student Paper Contest (SPC) for the paper titled **"Hybrid Triangular Dielectric Resonator Antenna (DRA) for WLAN/ISM Application,"** *IEEE Indian Antenna Week (IAW)-2011*, Kolkata, India, Dec 2011

[4] Received 1st prize for oral presentation in the technical session on Antenna Analysis, Synthesis and Measurement for the paper titled **"On the Solution of Isosceles 120° Triangular Dielectric Resonator Antenna,"** *7th International Conference on microwaves, Antenna, Propagation and Remote Sensing*, ICMARS-2011, Jodhpur, India, Dec 2011

[5] Received 2nd prize for poster presentation in the technical session on Antenna Analysis, Synthesis and Measurement for the paper titled **"More Accurate Resonant Frequency Evaluation of Triangular Isosceles 120° Patch Antenna,"** *7th International Conference on microwaves, Antenna, Propagation and Remote Sensing*, ICMARS-2011, Jodhpur, India, Dec 2011

CERTIFICATE FROM THE SUPERVISOR/S

This is to certify that the thesis entitled **"*Theoretical and Experimental Investigations on Different Triangular Shaped Radiators*"** submitted by **Sri Sudipta Maity,** who got his name registered on **5th September, 2012** for the award of Ph.D. (Engg.) degree of Jadavpur University is absolutely based upon his own work under the supervision of **Prof. Bhaskar Gupta,** Department of Electronics and Telecommunication Engineering, Jadavpur University, Kolkata, India and that neither his thesis nor any part of the thesis has been submitted for any degree/diploma or any other academic award anywhere before.

_____

Signature of Supervisor
and Date with Official Seal

ACKNOWLEDGEMENTS

First and foremost, I must acknowledge the great influence of my guide Prof. Bhaskar Gupta which brought me back from my corporate service to the academic environment and finally resulted in my Ph.D. dissertation. During this work, I have received immense help from him. His continuous support, encouragement and positive thinking have changed my way of thinking which has helped me not only to work on something new but also my outlook toward society.

I am grateful to all the faculty members of the Department of Electronics and Telecommunication Engineering, Jadavpur University, Kolkata, India who have given me valuable suggestions throughout the duration of my work. I enjoyed discussing and receiving advice from Prof. Amit Konar, Prof. Chandan Kumar Sarkar, Prof. Chayanika Bose, Prof. Salil Kumar Sanyal to name a few. I am indebted to Dr. Sudhabindu Ray, Dr. Manotosh Biswas and Dr. Sayan Chatterjee who guided me along the correct path to solve a particular problem. I have received immense help from Dr. Sudhabindu Ray in practical measurements. I am also grateful to all official staffs of Electronics & Telecommunication Engineering Department.

My entire research work was carried out at the Microstrip Circuits and Components Laboratory of the Electronics and Telecommunication Engineering (ETCE) Department, Jadavpur University, Kolkata, India. Hence, I take the opportunity to acknowledge the DST-PURSE Programme, Govt. of India (Ref. No. P-1/RS/161/2011, Dated 27th May, 2011) for monetary support from 30th May, 2011 to 30th March, 2013 and CSIR, Govt. of India (ACK. No.: 143174/2K12/1 and File No.-09/096(767)/2013-EMR-I) for providing the fund from 1st April, 2013 to 31st May, 2015.

Proceeding chronologically from the time I started my Ph.D. I would like to acknowledge Dr. Samik Chakraborty, Mrs. Ayona Chakraborty, Dr. S. Sankaralingam, Dr. Rajeev Wakodkar, Dr. Rajendra Prosad Ghosh, Dr.

Sanghamitra Dasgupta, Dr. Sriparna Bhattacharya, Mr. Sharanbasappa Belamgi, Dr. Amrita Chakraborty, Dr. Arindam Deb, Mr. Sumit Mitra, Mr. Buddhadev Pradhan, Mrs. Balaka Biswas, Mr. Ardhendu Kundu, Mrs. Rinki Ghosal, Mr. Prosenjit Das, Mr. Mishor Biswas, Mr. Arka Bhattacharya, Mr. Suman Pradhan and Ms. Sriparna De. Mere thanks will not be enough to justify the help I have received from Dr. Sayantan Dhar and Mr. Kaushik Patra. They helped me a lot by giving new ideas, techniques during my work. Special gratitude is due to Mr. Kaushik Patra for his cooperation in antenna fabrication and experiment.

I would like to acknowledge the help I received for fabricating my antennas. I would to thank Mr. Dhiraj Chatterjee of Micron India for fabricating some microstrip antennas. Mere thanks will not be enough to express the help I have received from my brother-in-law (elder), Mr. Goutam Kr. Maji and his entire team in cutting the Dielectric Resonator Antennas (DRAs) and metallic plate.

I would also like to express my special gratitude to all staffs of our 'Central Library (CL)' and 'Departmental Library (DL)' for providing valuable books immediately for my research.

I am grateful to Mr. Riddhasattam Basu, Ph.D. student, University of Illinois, Urbana and Mr. Suman Bhunia, Ph.D. student, Dept. of Computer Science, University of Nevada, Reno, USA for their help in finding research article. I am also grateful to my childhood friends Late Vikram Saha who died on 6th April, 2014 and Mr. Sandip Samajdar for their support and encouragement.

Finally, this acknowledgement will not be complete without recognizing the support I have received from my family. They have put up with my strange hours of work and terribly non social practices. Finally, I would like to dedicate this thesis to my beloved father who is no more with me now. Without the blessings of my parents, I could not have been what I am now.

Sudipta Maity

ABSTRACT

In this doctoral dissertation, theoretical and experimental investigations on various triangular shaped Microstrip Antennas (MAs) and Dielectric Resonator Antennas (DRAs) are presented in a systematic way irrespective of their applications if any. For theoretical investigation, the antenna is modeled here as a "Cavity". Wave equation is solved within the cavity (here, antenna) for a given boundary conditions first to find the approximate solution of the eigenfunction. Internal electric $(\vec{E})$ and magnetic $(\vec{H})$ fields are plotted using conventional 'slope method' (or gradient method) to identify various modes. Radiation characteristics of a particular mode are then investigated. Input impedance, far-field patterns, total Q-factor, radiated power, gain, bandwidth, radiation efficiency etc. are investigated. Closed form expressions are given here to predict the input impedance and far-field radiation patterns for different modes.

Literature survey shows that Rectangular DRA (RDRA) has been investigated at fundamental TE^{y}_{111} mode only using magnetic dipole moment. The untouched areas (i.e. input impedance, far-field patterns, total Q-factor, radiated power, gain, bandwidth, radiation efficiency etc.) on RDRA are also investigated here for different TE^{y}_{mnp} modes.

In this doctoral dissertation, radiation characteristics are presented for:

- Equilateral Triangular Microstrip Antenna (ETMA)
- 30°–60°–90° Triangular Microstrip Antenna (TMA)
- 45°–45°–90° TMA
- Isosceles TMA.
- Rectangular DRA (RDRA)
- Equilateral Triangular Dielectric Resonator Antenna (ETDRA)
- 30°–60°–90° Triangular Dielectric Resonator Antenna (TDRA)
- 45°–45°–90° TDRA.

- Isosceles TDRA.
- Inhomogeneous RDRA.

A simple, novel and time efficient procedure is developed to compute singularity free expressions for computing far-field radiation patterns of any antenna with rectilinear symmetry. This technique is also extended here to compute stored energy, dielectric loss, conductor loss etc.

It is found that our analytical solutions can predict the results orders faster than numerical EM simulators. Typical results are shown in Table 1 with respect to rectangular and triangular shaped antennas. For this comparison, a personal computer having Core 2 duo Intel processor and 3GB RAM is used.

Table 1
Comparison of Time between Analytical Solution and EM Simulators

SL No	Antenna	Mode	Time (seconds)			
			Numerical EM Simulator			Analytical Theory (our)
			IE3D	HFSS	CST	
1	Rectangular MA	TM_{11}^{z}	156	189	169	2.86
		TM_{20}^{z}	162	194	208	1.89
2	Equilateral TMA	TM_{10}^{z}	194	284	302	2.45
		TM_{30}^{z}	211	327	311	2.66
3	Rectangular DRA	TE_{111}^{y}	-	246	352	2.72
		TE_{313}^{y}	-	277	324	2.81
4	Equilateral TDRA	TM_{10}^{z}	-	338	355	2.89
		TM_{20}^{z}	-	341	379	2.82

Our analytical solutions can efficiently be utilized as entire domain full-wave MoM analysis. Further, the results of these theoretical investigations can easily be extended to the cases of triangular shaped waveguides, filters, oscillators, cavities etc.

Dedicated

To My Father

and

My childhood friend

Late Vikram Saha

(21st Jan, 1986 – 6th April, 2014)

Contents

List of Figures

List of Tables

List of Tables

Part I

Introduction

Chapter

1. **Introduction**
2. **Literature Survey**

Chapter I

Introduction

1.1 Introduction

The design and development of modern communication systems are highly dependent on the performance of an antenna. Metallic dipole, waveguide aperture, horn, Microstrip Antenna (MA) etc are widely used for different applications starting from radio frequency to microwave frequencies. As the frequency goes upward to 100-300GHz or higher, metallic losses may limit the use of the antenna. Obviously an antenna without any metallic surface can be used to avoid the metallic loss at higher frequency. Dielectric Resonator Antenna (DRA) made up of low-loss dielectric material is a suitable candidate for high frequency application [1].

It is well known that the size of an antenna varies inversely with operating frequency. An antenna operating in the fundamental mode will have small size at high frequency and the small size of the antenna may not be suitable with other circuitry and feeding mechanism. Higher-order modes of the same antenna may solve this problem if the corresponding mode satisfies all the required specification. Therefore, it is very important to have a proper knowledge on the characteristics of various higher order modes of an antenna [2]. Obviously, antennas having high degrees of freedom will give more flexibility to choose the fundamental as well as higher order modes of an antenna.

1.2 Choice of Topic

Literature survey shows that the researchers have focused on hemispherical, cylindrical and parallelepiped shaped 3-dimensional antennas. The above mentioned shapes have one (radius), two (radius and height) and

three (length, width and height) dimensional degrees of freedom respectively [3, 4]. Scalene triangular cylindrical shaped antennas have four degrees of freedom (3 unequal sides and height) and will give more flexibility compared to conventional rectangular shaped antennas.

Elliptic, parabolic, bipolar, etc. co-ordinate systems [3] are also available where the wave equation can be solved, but those geometries are not practically suitable for making an antenna due to complicated geometry. Even the customized small sizes of 3D hemispherical and circular cylindrical antennas are also not easy to fabricate due to their curvature surface. A small error may lead to exciting an unexpected mode. Whereas, rectangular shaped antennas have planar surfaces which are very easy to make from a practical point of view. Therefore, antennas having planar surfaces such as rectangular, triangular, pentagonal, hexagonal, octagonal etc. shaped geometries should get preference to design an antenna. But researchers have focused on rectangular shaped antennas only. The wave equation can easily be solved within a rectangular geometry, whereas there are no straight ways to solve the wave equation for other geometries in Cartesian coordinate system. The inclined nature of arm(s) restricts us to apply the boundary conditions directly. Time consuming trial-error method using either fabrication and measurement or 3D full-wave EM simulation can solve this problem for a particular geometry. Due to that reason, triangular, pentagonal, hexagonal, octagonal etc. shaped geometries did not get much attention. Out of these, triangular geometry is the simplest one and is considered here to design an antenna in this doctoral dissertation.

A triangular shaped antenna has got several advantages such as:

- A scalene triangle (three unequal sides) has more degrees of freedom than rectangular (length and width) or circular (radius only) shaped geometry which will give more flexibility to design an antenna, cavity resonator, waveguide etc.

- It can store more energy than rectangular or circular cylindrical or spherical shaped antennas.
- For a given resonant frequency, it takes smaller area. For example, when the relative permittivity of DRA is equal to 100, thickness of the DRA is 1mm and the resonant frequency is 8.50 GHz, the Rectangular DRA (RDRA) and Cylindrical DRA (CDRA) occupy the area 50mm^2 and 15.2mm^2 respectively whereas the Equilateral Triangular DRA (ETDRA) will occupy 10.8mm^2. Hence, the more compact antenna can be made using triangular geometry [5].
- The compactness of antenna can further be improved by replacing an equilateral triangular geometry by 30°–60°–90° triangular geometry. For a given resonant frequency, 30°–60°–90° triangular shaped MA (or DRA) takes just half the area compared to that of equilateral shaped MA (or DRA) as shown in this dissertation.
- Equilateral Triangular Microstrip Antenna (ETMA) supports various radiation characteristics [6].
- One can excite six equilateral triangular antennas parasitically whereas maximum four antennas are possible for rectangular geometry.
- Due to high quality factor, Triangular Microstrip Antenna (TMA) is a narrowband antenna. This property can easily be utilized to design a narrow band antenna for receiving signals in noisy environments
- The property of smaller size with respect to rectangular and circular cylindrical geometry can be utilized to design circulator, filter etc.
- Multiband antennas can easily be made using triangular shaped antennas. For example, equilateral TMA can excite three broadside modes for a single coaxial probe excitation [6].
- It is possible to excite five broadside radiating modes (30°–60°–90° TMA) using a single coaxial probe to create a penta-band antenna.
- It is possible to suppress the fundamental mode of 45°–45°–90° TMA without any extra circuitry.

Literature survey shows that the researchers have focused on equilateral TMA only. The detailed literature survey is presented in Chapter II. We have extended the analysis of different triangular shaped radiators both for Microstrip Antenna (MA) and Dielectric Resonator Antenna (DRA) version. Most of the advantages as mentioned above are fruitful results of this theoretical investigation.

It is important to investigate new shaped antenna geometry always. After this investigation, the advantages or disadvantages of the investigated object will come out as fruitful results. If it is found after rigorous investigation that the new investigated geometry do not show any advantages, the future researchers will not waste their valuable time on that geometry. Obviously, it will help the researchers. Further, if the limitations of the antenna geometry are known beforehand, it will always help the future researchers to achieve their requirement using that geometry by overcoming those limitations.

Theoretical investigations always have potential in terms of application. We have to utilize the pros and cons of any theory for a specific application. Sometimes, it might be looked apparent that there is (or will be) no practical application with respect to an observer. For example, after the invention of Fourier series in terms of trigonometric series by J. B. J. Fourier, it was rejected by J. L. Lagrange for publication in 1807 [7, pp. 165]. Now-a-days, Fourier series is being applied almost in every domain.

Therefore, in this doctoral dissertation, the main objective is to investigate the properties of various triangular shaped antennas (both, 2-dimensional and 3-dimensional cases) irrespective of their applications if any. Analytical solutions are given to predict the results. It is found that our analytical solutions can predict the results orders faster than numerical EM simulators [8-10]. Typical results are shown in Table 1.1 with respect to rectangular and triangular shaped antennas. For this comparison, a personal computer having Core 2 duo Intel processor and 3GB RAM is used.

Further, the results of these theoretical investigations can easily be extended to the cases of triangular shaped waveguides, filters, cavities etc.

Table 1.1
Comparison of time between analytical solution and EM simulators

SL No	Antenna	Mode	Time (seconds)			
			Numerical EM Simulator			Analytical Theory
			IE3D [8]	HFSS [9]	CST [10]	
1	Rectangular MA	TM_{11}^{z}	156	189	169	2.86
		TM_{20}^{z}	162	194	208	1.89
2	Equilateral TMA	TM_{10}^{z}	194	284	302	2.45
		TM_{30}^{z}	211	327	311	2.66
3	Rectangular DRA	TE_{111}^{y}	-	246	352	2.72
		TE_{313}^{y}	-	277	324	2.81
4	Equilateral TDRA	TM_{10}^{z}	-	338	355	2.89
		TM_{20}^{z}	-	341	379	2.82

1.3 Scope of Work and Motivation

Literature survey shows that the Microstrip Antennas (MA) and Dielectric Resonator Antennas (DRA) are two strong candidates at microwave frequency. DRA shows superiority over the MA at millimeter wave application due to the absence of conductor loss. Conventional cavity model [11-15] is generally adopted to investigate the microstrip antennas. According to cavity model, the microstrip antenna has constant field variation along the thickness of the substrate which results in the tangential components $\vec{E}_x(\propto \partial/\partial z)$ and $\vec{E}_y(\propto \partial\partial z$ (please see Fig. 1.1) being equal to zero. Therefore, only *Ez* component is utilized to investigate the MA according to cavity model. Rectangular and circular shaped MAs have been widely investigated using this cavity model. Resonant frequency, input impedance, radiation patterns, quality factor, gain, bandwidth, etc. have been widely investigated and reported.

In case of DRA, only cylindrical DRA (CDRA) has been investigated analytically by S. A. Long *et al* in 1983 [1]. In [1], the CDRA has been modeled

as a cavity bounded by Perfect Magnetic Conductors (PMC). Approximate solution for the eigenfunction has also been given therein for TE and TM modes. "Equivalence Principle" [4, 16] has been used to predict the far field radiation patterns with close form compact expressions for the fundamental TM_{101}^{z} mode. Input impedance of CDRA has also been reported by them in 1986 [17]. Resonant frequency and far-field radiation patterns of hemispherical and rectangular shaped DRAs have also been investigated by S. A. Long *et al* [18-19]. The internal fields for the fundamental TM_{101}^{z} mode have been reported for Hemispherical DRA (HDRA) in [18] whereas results on Rectangular DRA (RDRA) have been reported in [19] without any explicit mathematical relation to the internal fields. Further, resonant frequencies for various TE and TM modes have been reported by R. K. Mongia in 1992 [20]. In 1997, eigenfunction, radiation Q-factor, stored energy etc have been investigated for the fundamental TE_{111}^{z} mode by R. K. Mongia *et al* [21]. Therefore, theoretical analysis on RDRA is still under nascent stage.

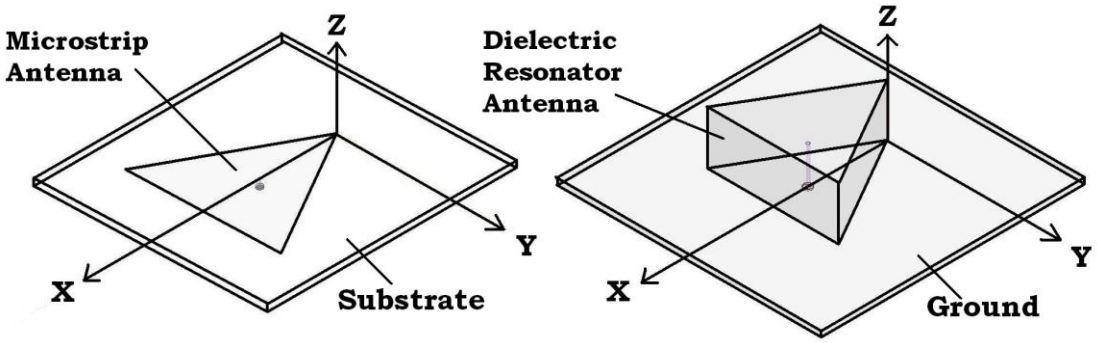

Fig. 1.1 3D geometry of equilateral triangular shaped MA (left) and DRA (right)

Full-wave analyses such as Method of Moment (MoM), Finite element Method (FEM), Finite Difference Time Domain (FDTD) etc. are time consuming process. Huge computational time and large memory are required to solve a particular problem. Such types of process are run in the background of commercially available 3D EM simulators. Numerical 3D EM simulators are easy to understand and are able to handle arbitrary geometry within few minutes. But the user does not get any information which is running in the

back-end. Therefore, the working principle of an electromagnetic object still remains hidden to the user. Beside, the numerical 3D EM simulator can determine the resonant frequency, radiation patterns, etc. but takes a long time (minimum 4-5 minutes for one structure) whereas the analytical solutions give the results within 2-3 seconds as shown throughout this dissertation. Analytical solutions are user friendly both from understanding and application point of view. Once the problem is solved analytically, the closed form results can efficiently be utilized for different application. Further, the analytical solutions are efficiently utilized for entire domain full-wave MoM analysis [22-23]. Therefore, it is very important to have analytical results on ETDRA.

It should be pointed here that the triangular and rectangular shaped radiators both are analyzed in the rectangular coordinate system (x, y, z). For example, the eigenfunctions for equilateral triangular and rectangular geometries as shown in Fig. 1.2 with Neumann boundary conditions can be expressed as:

$$\psi(x,y) = cos\frac{2\pi l}{\sqrt{3}a}(x+R)\,cos\left(\frac{2\pi(m-n)}{3a}y\right) + cos\frac{2\pi m}{\sqrt{3}a}(x+R)\,cos\left(\frac{2\pi(n-l)}{3a}y\right) + cos\frac{2\pi}{\sqrt{3}a}(x+R)\,cos\left(\frac{2\pi(l-m)}{3a}y\right) \quad ; \text{ for equilateral triangle} \tag{1.1}$$

and

$$\psi(x,y) = cos\left(\frac{m\pi}{a}x\right)cos\left(\frac{n\pi}{b}y\right) \quad ; \text{ for rectangle} \tag{1.2}$$

where all terms are carrying their usual meaning. Hence, the mathematical analysis of a single equilateral triangular geometry with PMC boundary conditions is equivalent to the analysis of simultaneous three rectangular geometries. Therefore, the theoretical results are first verified with measured data for rectangular shaped radiators.

In this dissertation, triangular shaped Microstrip Antennas (MA) and Dielectric Resonator Antennas (DRA) are investigated analytically by considering the antenna as a “Cavity”. Characteristics of different triangular

shaped MA and DRAs are presented in a systematic way. Advantages, disadvantages, limitation, etc. all are discussed whenever necessary. Theoretical results are verified with measured data as found in the published literature or by own experimental data.

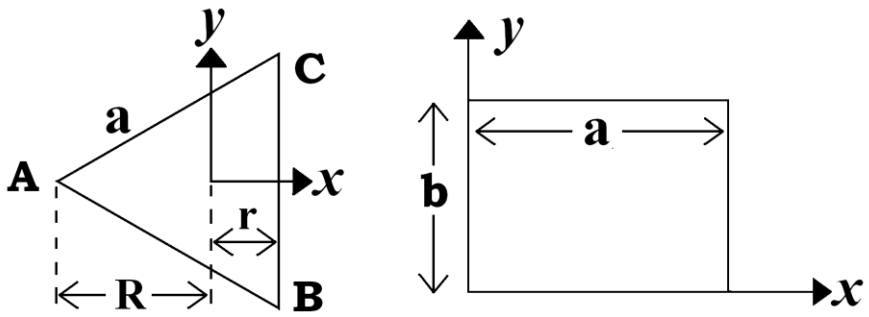

Fig. 1.2 Geometry of equilateral triangle (left) and rectangle (right)

1.4 Procedure for Theoretical Investigations

In this dissertation, different triangular shaped MAs and DRAs are investigated theoretically. The antenna is first assumed as a "Cavity". The wave equation is solved within the cavity (here, antenna) for a given boundary conditions first to find the approximate solution of the eigenfunction. Internal electric $(\vec{E})$ and magnetic $(\vec{H})$ fields are plotted using conventional 'slope method' (or gradient method) to identify various modes. Standard mode nomenclature [3-4, 16, 24] is used to identify various modes. Radiation characteristics of a particular mode are then investigated. Input impedance, far-field patterns, total Q-factor, radiated power, gain, bandwidth, radiation efficiency etc. are investigated. Finally, these are presented in respective chapters systematically.

1.5 Organization of Dissertation

Before starting any mathematical analysis on triangular shaped radiators, it is very important to have a brief idea on previous works. After that, it will be very helpful to summarize the theoretical analysis during this period.

Therefore, this doctoral dissertation is divided into five parts. In Part I, introduction and literature survey are discussed. In Part II, different types of Triangular Microstrip Antennas (TMA) are investigated. In the Part III section, Triangular Dielectric Resonator Antennas (TDRA) are analyzed. In the last section, Part IV, numerically efficient techniques are described which are developed during this work. In Part V, brief conclusions and scope of future works are given. A brief overview of the organization of the chapters is as:

Part I:

- **Chapter I** **:** Theoretical background and scope of work is presented in this chapter briefly.
- **Chapter II** **:** A brief literature survey on different triangular shaped radiators is presented.

Part II:

- **Chapter III** **:** In this chapter, Equilateral Triangular Microstrip Antennas (ETMA) is presented. Eigenfunction, resonant frequency, internal field components, input impedance, radiation patterns, etc. are investigated.
- **Chapter IV** **:** The characteristics of 30°–60°–90° Triangular Microstrip Antenna (TMA) is discussed using the cavity model.
- **Chapter V** **:** 45°–45°–90° TMA is investigated. Eigenfunction, input impedance, radiation characteristics, etc. are presented.
- **Chapter VI** **:** Tri-linear transformation is modified to investigate certain isosceles TMA.

Part III:

- **Chapter VII** **:** Radiation characteristics of Rectangular Dielectric Resonator Antenna (RDRA) are presented for arbitrary TE^{y}_{mnp} modes. Approximate solution of eigenfunction, resonant frequency, internal field variation, far-field radiation patterns etc. are presented.

- **Chapter VIII** **:** In this chapter, the radiation characteristics of an Equilateral Triangular Dielectric Resonator Antenna (ETDRA) are presented.

- **Chapter IX** **:** 30°–60°–90° Triangular Dielectric Resonator Antenna (TDRA) is discussed in detail.

- **Chapter X** **:** 45°–45°–90° TDRA is presented in this chapter. Eigenfunction, resonant frequency, radiation patterns, quality factor, etc. are discussed.

- **Chapter XI** **:** Some theoretical investigations on different isosceles triangular dielectric resonator antenna are presented.

Part IV:

- **Chapter XII** **:** Inhomogeneous rectangular dielectric resonator antenna is also investigated here theoretically.

- **Chapter XIII** **:** A simple procedure is demonstrated for computing singularity free far-field radiation patterns of any antenna having rectilinear symmetry.

Part V:

- **Chapter XIV** **:** In this chapter, conclusions are drawn of this theoretical investigation. Scope of future works is also suggested.

Chapter II

Literature Survey

2.1 Introduction

Literature survey plays an important role in the field of research to find the scope of work. It is important to have a proper knowledge of previous works if any, to avoid the repetition of any work. As our main objective is to investigate the different triangular shaped radiators, a brief, concise literature survey is presented here on different triangular shaped geometries.

2.2 60°–60°–60° Triangular Shaped Radiators

The explicit solution of Helmholtz wave equation for an equilateral triangular metallic waveguide has been summarized by S. A. Schelkunoff in his book 'Electromagnetic Waves' in 1943 [24]. The eigenfunctions (ψ) and eigenvalues are given for both TE and TM modes of propagation in Cartesian coordinate system. Tri-linear transformation has been adopted to obtain the solution. A suitable choice of tri-linear transformation is also given there. Graphical field distributions for first few modes are also given.

Operational modes of a waveguide Y-circulator using demagnetized triangular ferrite post has been investigated both theoretically and experimentally by Y. Akaiwa in 1970s [25-26]. Duality theorem [4] has been applied to obtain the eigenfunctions of a demagnetized triangular ferrite post. The solutions of the wave equation for TE and TM modes with Dirichlet's boundary condition ($\psi = 0$) are dual for TM and TE modes with Neumann boundary condition ($\partial\psi/\partial n = 0$) respectively. Theoretical resonant frequencies have been compared with experimental data for fundamental TM^z_{101} mode. The rotational property of the eigenfunctions of the equilateral triangular ferrite post has been investigated in [26].

An extensive theoretical and experimental work on planar triangular microstrip resonators have been carried out by J. Helszajn in 1978 [27-28]. For theoretical investigation, the fields within the equilateral triangular resonator have been assumed as invariant along the thickness of the substrate which was very small compared to the operating wavelength. Distribution of electric field (in dB) along the edges, stored energy, radiation quality factor (Q_r) etc have been investigated. Various properties of the eigenfunctions of an equilateral triangular resonator have been investigated to construct the circulator [29-34]. In [29], admittance of complex gyrator contour has been investigated using a contour integral formulation. E-plane circulator using single equilateral triangular shaped resonator has been investigated in [30]. The fictitious magnetic wall has been considered to excite the odd modes only. The transverse resonance technique has been applied to predict the propagation constant. In [31], conventional geometry of circulator has also been perturbed by magnetic wall ridges to improve its tunability. Three magnetic ridges have been used along the structural symmetric line of the equilateral triangular resonator. An extensive mode charts has been given therein for different dimensions of magnetic ridges with experimental validations. Perturbation technique has been applied to compute loaded Q-factor. In [32], the theory of an equilateral triangular resonator has also been extended to obtain the cutoff wave numbers and working principle of a regular hexagon.

Radiation characteristics of an equilateral triangular microstrip resonator have been investigated analytically by M. Cuhaci in 1977 [35] and the details can be found in his Master of Applied Science dissertation [36]. Radiation patterns and radiation Q-factor (Q_r) both have been investigated for fundamental TM^z_{101} mode. Radiation properties have been investigated from electric surface current distribution ($\vec{J_s}$). Closed form compact expressions for far-field radiation patterns have also been given there. Various losses on the microstrip resonators have been investigated. Different procedures to excite the

triangular microstrip resonator have been described by equivalent circuit parameters. An extensive comparison between theoretical results with experimental data has also been included in his thesis.

In 1980, the working principle of an equilateral Triangular Microstrip Antenna (TMA) from magnetic surface current ($\overrightarrow{M_s}$) has been reported for the first time by I. J. Bahl and P. Bhartia in their book 'Microstrip Antennas' [15]. A detailed procedure to evaluate the far-field radiation patterns from magnetic surface current can be found in that book. The concepts on effective permittivity (ε_{eff}) and effective length (a_e) [27, 37] have been utilized to account the fringing effect. Far-field radiation patterns, stored energy (W_T), radiated power (P_r), radiation Q-factor (Q_r) etc have been investigated with closed form expressions for fundamental TM^z_{101} mode only in [15].

In [37], the transverse resonance technique has been used to investigate different microstrip resonators. For theoretical simplicity, original microstrip resonator has been sub-divided into several rectangular strips and each strip has been replaced by equivalent waveguide transmission line model. The discontinuity between any two successive strips has been modeled as lumped element. Theoretical results have been verified with magnetic wall approximation and experimental data.

Segmentation technique [38-39] has also been reported to investigate the planar microstrip structure. First, one complicated microstrip structure has been segmented into several rectangular shaped resonators. The Green's function of rectangular geometry with proper boundary condition (either electric or magnetic) has been utilized to find the characteristics of the original problem. The S-matrix has been utilized for theoretical investigation. Originally, the segmentation technique was limited to a structure which could be decomposed into several rectangular ones. The development of Green's function for different triangular geometries (45°–45°–90°, 60°–60°–60° and 30°–60°–90°) by R. Chadha *et al* in 1980 [40] has accelerated the utilization of segmentation technique. To evaluate the Green's function for 45°–45°–90°, 60°–

60°–60° and 30°–60°–90° shaped triangular geometries, simple image source method has been utilized. Due to small thickness of substrate along *z*-direction (please see Fig. 1.1), the Green's function was evaluated for *x*-*y* plane only. 2D Fourier series expansion method has been applied to obtain the required Green's function. Development of Green's function can be found in detail in [41-42].

Full wave analysis has also been reported on isosceles triangular shaped microstrip antennas by A. K. Sharma *et al* in 1982 [43]. The problem has been solved in the spectral domain. Wave equation was solved in spectral domain by considering *TE* and *TM* modes. Method of moment was applied to convert the integral equations into linear equations. Galerkin technique has been applied to determine the transverse charge density on the patch. Theoretical results on resonant frequency for 45°–45°–90° and 60°–60°–60° TMAs have been verified with experimental data for fundamental mode only. In [44], entire domain basis functions have been utilized to predict the resonant frequency of an equilateral TMA. Extensive experimental data have been compared with theoretical results to show the effectiveness of the entire domain basis function.

Field theory approach has also been applied to investigate triangular waveguide [45], triangular ferrite post [46] etc. In [45], the internal fields have been expressed first as an infinite sum of mode voltage and mode current by considering both *TE* and *TM* modes. By considering 'N' terms for *TM* mode and 'M' terms for *TE* mode, the generalized telegraphist's equations have been transformed into the algebraic eigenvalue equation. After solving this eigenvalue equation, the phase constant has been evaluated. Attenuation constant, stored energy, power distribution, etc. have also been investigated therein. Equilateral triangular dielectric waveguide and 'Y' dielectric waveguide have been investigated using this procedure. In [46], H-plane waveguide junction with three-sided ferrite prism has been investigated using the infinite summation of cylindrical circular modes. The point-matching technique has been applied to find the fields at ferrite-air interface. A finite system of

inhomogeneous equation has been solved to obtain the exact field distribution. Theoretical results have been verified for waveguide junction circulator with cylindrical ferrite post.

Geometrical Optics (GO) have also been reported to investigate the un-fed triangular microstrip resonators by E. F. Keuster *et al* in 1983 [47]. Different geometries such as 45°–45°–90°, 60°–60°–60° and 30°–60°–90° triangles have been investigated. This approach was based on the solution of complex reflection co-efficient for a plane-wave incident at an angle φ on a straight edge. The patch has been assumed as a cavity formed and the eigenvalue problem has been solved using plane-wave reflection under the patch. The total electric field was expressed as a sum of reflected waves and perturbation technique was applied to solve this problem. Simple formulas have been given for radiation Q-factor, but these are limited to TM^z_{m0} and TM^z_{mm} modes for Equilateral TMA (ETMA). However, the accuracy of the theory is limited due to non-consideration of various losses.

Y. Tu has used a similar approach in his masters' thesis in 1983 [48]. Reflection of plane waves has been adopted to obtain the characteristic equation and the resonant frequency as well as the quality factor for 45°–45°–90°, 60°–60°–60° and 30°–60°–90° TMAs. A simple procedure has been demonstrated therein to obtain the Q-factor from Smith chart as found in [49]. Comparison between measured and calculated resonant frequency and quality factor has been tabulated. No comparative study between theoretical and experimental input impedance has been performed.

Superposition of plane-waves along with Snell's Law has been investigated by P. L. Overfelt *et al* in 1983 [50]. Complete solutions for Transverse Electric (TE) and Transverse Magnetic (TM) modes have been given for four metallic hollow triangular waveguides (45°–45°–90°, 60°–60°–60°, 30°–60°–90° and 30°–30°–120°) in 1986 [51]. Simple magnetic wall boundary conditions have been applied for theoretical investigations. The existence of odd mode solutions for an equilateral triangular metallic waveguide has been

pointed therein. But, it was already pointed by F. E. Borgnis and C. H. Papas long ago, in 1958 with closed form expressions [52].

Field solutions for *TE* and *TM* modes have been derived therein for different shaped metallic waveguides. Recently, the mode function of an equilateral triangle has been reported by B. J. McCartin for Dirichlet [53], Neumann [54] or mixed [55] boundary conditions. Details can also be found in [56-57] also. In [53-55], tri-linear coordinate system has been utilized for theoretical investigation. Due to inclined sides of an equilateral triangle, new local coordinate system has been generated inside the triangle using triangular coordinate system (u, v, w). Wave equation has been solved using triangular coordinate system which was finally converted to the original coordinate system (x, y). Superposition of shifted plane waves has been used to find the exact solution for an equilateral triangle with proper boundary conditions (Dirichlet [53], Neumann [54] or mixed [55] boundary conditions). Finally, mathematical identities have been utilized to find the wave numbers.

Modal analysis of an equilateral TMA has been reported by K. F. Lee *et al* in 1988 [6]. Cavity model [11-12] has been used to analyze the characteristics of a probe fed equilateral TMA for different TM_{mn}^{z} modes. Input impedance, far-field radiation patterns, Q-factor etc have been investigated. Conventional magnetic surface current model has been utilized for far-field calculation. Theoretical results have been compared with experimental data as found in the open literature [15, 58]. It should be pointed here that the errors in the expressions of far-field radiation patterns have been corrected by K. F. Lee *et al* in 1988 [6].

Several CAD models [59-75] have also been reported to define the effective length (a_e) and effective permittivity (ε_e) of the ETMA for predicting the resonant frequencies of different TM_{mn}^{z} modes more accurately. Other techniques such as neuro-fuzzy approach [76], artificial neural network [77], Tabu search method [78] etc. have also been applied to predict its resonant frequency. In [76], five layer Adaptive Neuro-Fuzzy Inference System (ANFIS)

has been utilized to find the resonant frequency. First order Sugeno fuzzy model with back-propagation (BP) algorithm and Least Square Method (LSM) have been used to compute unknowns. On the other hand, adaptive multilayer perceptron has been used in [77] to calculate the resonant frequency for different modes. Learning rate (η) and momentum coefficient (α) both have been utilized to accelerate the learning process. In [78], the Artificial Neural Networks (ANNs) have been trained using a parallel tabu search algorithm to find the resonant frequencies. Theoretical results have been compared with experimental data for rectangular, circular, and equilateral triangular shaped microstrip antennas.

Once the property of an antenna is known, we can easily use it for different applications. For example, ETMA has been widely investigated for broadband [79-84] and ultra-wideband [85-88] applications. Simple L-shaped probe has been used to excite the triangular microstrip antenna to obtain wide bandwidth (42% in [79] and 61% in [83]) whereas folded shorting wall along with shorting pin has been demonstrated to obtain 28.1% bandwidth [81]. In [82], V-shaped slot on equilateral TMA whose apex was shorted to ground has been reported for wideband application (25% bandwidth) covering UMTS and ISM band. In [86], simple microstrip fed triangular monopole antenna with tapered ground plane has been reported covering 2.9 GHz to 12 GHz band.

Besides, ETMA has also been reported for circularly polarized [89-91], dual frequency [92] and multiband [93] application and operation in array configuration [94-95]. To obtain circular polarization, three 30°–30°–120° shaped (approximately) triangular slots have been cut on equilateral triangular resonator in [90] whereas simple narrow slots and cross-slot have been demonstrated for circular polarization in [91]. In [93], tunable equilateral triangular microstrip antenna has been reported for multiband operation. To obtain the multiband operation (1.95 GHz – 2.16 GHz), varactor diodes and F-shaped slits have been used therein. By changing the bias voltage, the switching between one frequency to another has been obtained. The designed

antenna has return loss better than 20 dB with gain between 2.87dBi to 3.1dBi. In [94], cross-slot has been applied on an equilateral triangular microstrip antenna for circular polarization. This basic antenna geometry has been utilized to design sequentially rotated antenna array using two elements for wide (40MHz) axial ratio bandwidth application. In [95], antenna arrays using an equilateral triangular microstrip antenna have been reported to improve the radiation characteristics (gain, directivity and beam width).

Equilateral triangular geometry has also been used for filters [96-99] and Substrate Integrated Waveguide (SIW) [100] applications. In [96], dual mode operation of the triangular patch resonator has been demonstrated using Wheeler's cavity mode theory. The rotational property of equilateral triangular geometry has been utilized to explain the operation of dual mode band pass filters. Equilateral triangular microstrip patch resonator has also been investigated using slots and parasitic elements for dual-mode band pass operation [97]. A triangular ring shaped resonator has been demonstrated for band stop filter application in [98]. Higher order modes of the resonator have been excited for this purpose. On the other hand, in [99], a compact metal–insulator–metal (MIM) waveguide with a triangular-annular channel has been reported to the plasmonic filter application.

The performance of an ETMA has been enhanced by modifying the ground plane [101-102]. Two symmetrical corrugations beside the triangular patch radiator and a U-shaped ground plane has been reported in [101] for wideband application (114%) covering 0.66 GHz to 2.41 GHz. On the other hand, folded-line-shaped defected ground structure (DGS) has been demonstrated with improved skirt rejection in [102]. A good literature survey of the various shapes DGS and uses of DGS can be found in [103]. The procedure has also been demonstrated to reduce the cross-pol level of an ETMA [104]. In [104], dual L-strip lines have been utilized to excite the equilateral triangular microstrip antenna with thick air substrate. These two L-strip lines have been placed face-to-face with a 180°-phase shift. Due to the use of air-substrate, the

impedance bandwidth has been improved whereas the use of dual L-strip lines reduced the cross-pol level compared to single L-strip line.

The size reduction procedure has also been reported to make compact antenna [105]. Simple F-shaped probe has been used therein to excite the equilateral triangular microstrip antenna covering 3.1 GHz to 5.0 GHz (approx. 47%). The F-shaped probe has been placed along the symmetric line near to the apex to excite the antenna.

On the other hand, triangular shaped Dielectric Resonator Antenna (DRA) has been investigated experimentally by A. Ittipiboon *et al* in 1993 [106]. In [106], the non-availability of theory on triangular DRA has been clearly mentioned. A triangular shaped DRA has been obtained by cutting a rectangular DRA diagonally. Experimental results on resonant frequency and far-field radiation patterns have been discussed. It has been pointed out therein that the radiation patterns are similar to a horizontal magnetic dipole placed on a conducting ground plane.

Literature survey shows that some experimental works have been reported on the performance of thin equilateral Triangular DRA (TDRA) for the fundamental TM_{101}^{z} mode [107-111]. Several feeding mechanisms such as aperture on the ground plane [107], slot line [108], conformal strip [109], rectangular waveguide aperture [110], disk loaded coaxial aperture [111] etc. have been utilized to excite the low profile Equilateral TDRA (ETDRA). In [107], a thin ETDRA having relative permittivity ε_r equal to 82 has been excited using a slot. Approximate expression as reported in [25] on demagnetized equilateral triangular shaped ferrite post has been applied in [107] to predict the resonant frequency of an ETDRA for fundamental TM_{101}^{z} mode using magnetic wall model. A standing wave solution along the triangular cross section has been explicitly given therein whereas the same along the height of the ETDRA has not been reported. The offset position of the ETDRA has been adjusted for optimal performance. In [109], conformal strip has been used along the median of the ETDRA to excite the ETDRA. With reference to this configuration, an

improved impedance bandwidth of 5.5% has been obtained which was 1.8 times wider than that of the aperture-coupled configuration [107]. Experimental investigations on slot coupled thin ETDRA has been reported in [108] where slot position with respect to ETDRA has been adjusted for optimal performance.

In [110], the ETDRA has been excited using waveguide aperture. In [110], the ETDRA has been placed on a large ground plane and the slot was kept on the open-end of a rectangular waveguide. With this feed mechanism, the thin ETDRA has been demonstrated for 11.4% impedance bandwidth. An extremely useful excitation procedure has been demonstrated for thin ETDRA in [111]. Circular shaped conducting disk has been placed on the top of the coaxial probe for better impedance matching between the ETDRA and feed. From experimental far-field patterns of [107-111], it is found the ETDRA can efficiently be utilized as a broadside radiator with lower cross-pol level.

The ETDRA has also been investigated analytically using the simple waveguide model and the mode matching technique to predict the resonant frequency by A. A. Kishk in 2001 [112]. A transcendental equation has been given therein to compute the wave number along the height (z-direction, say) of the ETDRA. It is found that this transcendental equation is in error. This is explained in detail with mathematical proof in this dissertation. Further, explicit solution for the field variation along the height of the ETDRA has not been provided in [100-112].

ETDRA has also been demonstrated for wideband application [113] and antenna array application [114]. In [113], the ETDRA has been excited using coaxial probe. Input impedance$(Z_{in} = R + jX)$, far-field radiation patterns, etc have been investigated therein using the numerical EM simulator. In case of array application [114], three ETDRAs have been excited using a single coaxial probe placed near apex of each ETDRA. A comparative study can be found therein on a single element and three element array as well as for single element dual segment (stack configuration) and three elements dual segments.

ETDRA has also been investigated using an EM simulator for WLAN applications in [115]. In [116], a brief historical review and current state of art on DRA have been presented in detail.

It should be noted here that numerical techniques have also been reported in a general sense to analyze arbitrary shaped waveguides [117-120]. For example, in [117], boundary value problem in waveguides has been solved using Kirchhoff's integral formulation of the electromagnetic field and the solution can handle conventional air filled waveguide as well as partially dielectric filled waveguides and triangular waveguides, whereas generalized mesh-free approximation has been reported in [120]. The surface integral equation has been reported to compute the cutoff wave numbers for arbitrary shaped waveguides [121]. Both TE and TM modes have been investigated using surface integral equation which was solved using an iterative process. Due to absence of charge in case of TM modes, the computation of TM mode cut-off frequency was faster than the TE cases.

In [122], 2D electromagnetic boundary value problems (including trapezoidal and triangular waveguides) have been solved iteratively using Schwarz's procedure by M. F. Iskander. Full-wave method of moments in spectral domain analysis has also been reported for equilateral microstrip antenna and equilateral waveguide antenna [123-125]. Recently, different antennas including microstrip and dielectric resonator antennas have been investigated using characteristic modes [126]. In [126], the electric field integral equation has been solved using method of moment to investigate the antenna using characteristic modes. Mode tracking technique has been applied to obtain the correct mode accurately. Although the process can handle arbitrary shaped antenna in general, theoretical investigations have been reported in [126] for equilateral TMA and equilateral TDRA only.

It should be pointed here that equilateral triangular shaped monopole antenna has also been widely investigated using commercially available software and the results have been verified experimentally [127-131]. In [127],

a small and simple triangular-ring-shaped printed monopole antenna has been reported for wideband application covering 4.2 GHz to 9.8 GHz. In [128], a Co Planar Waveguide (CPW) fed planar triangular shaped monopole antenna has been reported for DCS1800 and the IEEE 802.11a 5.2/5.8 GHz WLAN application with high gain (4-6 dBi) throughout the operating band. Parametric study has been performed therein for different flare angles to optimize the antenna. In [129], fractal geometry has been applied to triangular monopole antenna with truncated and notched ground for the Ultra Wide Band (UWB) application covering 2.6 GHz to 14.26 GHz band. The ground plane of the triangular monopole antenna has been modified in [130] to obtain ultra wide band (2.5 GHz – 10.8 GHz) characteristics. Wideband (1.42 GHz – 2.7 GHz) circular polarization using a triangular monopole antenna has been demonstrated in [131]. Asymmetric feed configuration has been utilized to obtain wide (62%) axial-ratio bandwidth in [131].

Further, theoretical investigation has also been reported on equilateral triangular semiconductor laser [132-134]. In [132-134], the equilateral triangular semiconductor has been modeled as optical micro-cavity first and then wave equation has been solved for TE and/or TM cases. Theoretical results for resonant frequency and quality factors [132-133] have been verified using the FDTD technique. The effect of metal layers on different modes has also been reported in [132].

Although the practical applications of triangular shaped geometry in microwave field have started in the 1970s following the works of A. Yoshihiko [25], it is interesting to note that triangular shape had already been applied in rotating missile problem in 1959 [135]. Extensive experimental results have been reported therein. Further, the triangular shaped geometry is also an attractive object in the field of elasticity. Stress has been investigated on equilateral and isosceles right triangular geometry by I. S. Sokolnikoff in 1946 [136]. Triangular geometry has also been investigated in the domain of fluid dynamics [137-139], heat transfer [140], vibration [141] etc.

2.3 45°–45°–90° Triangular Shaped Radiators

Another triangular shaped radiator, more precisely 45°–45°–90° Triangular Microstrip Antenna (TMA) has been focused on after equilateral TMA. But the explicit solution for eigenfunctions, input impedance, radiation characteristics for different modes etc. are still under research.

Field distribution for the first few modes of 45°–45°–90° Triangular Wave Guide (TWG) has been shown by S. A. Schelkunoff in his Book, 'Electromagnetic Waves' [24]. Corresponding eigenfunctions for a particular mode has also been given therein, but the general solution of 45°–45°–90° TWG has not been mentioned explicitly. The general expression for eigenvalues k_{mn} (i.e. in other term, the resonant frequency, $f_r = k_{mn}c/(2\pi\sqrt{\varepsilon_r})$ where all terms are carrying their usual meaning) of a 45°–45°–90° TMA for arbitrary TM_{mn}^{z} modes have been expressed of I. J. Bahl and P. Bhartia in [142] as:

$$k_{mn} = \left(\frac{\pi}{a}\right)\sqrt{m^2 + mn + 2n^2} \tag{2.1}$$

where m, n are modal indices and a is the length of the isosceles triangle's sides. At the dominant mode ($m = 0$ and $n = 1$) the resonance wave number is given by [142-143]:

$$k_{01} = \sqrt{2}\pi/a \tag{2.2}$$

Analytical solution of a 45°–45°–90° triangular membrane for Dirichlet's boundary condition ($\psi = 0$) has been given by P. M. Morse and H. Feshbach in 1953 [144] and the corresponding eigenvalues has been given therein by:

$$k_{mn} = (\pi/a)\sqrt{m^2 + 2mn + 2n^2} \tag{2.3}$$

To obtain the eigenfunctions for *TE* mode, superposition theorem has been applied therein. Modal distribution for few modes in the triangular membrane

can be found therein. According to [144], fundamental mode occurs for $m = 1$ and $n = 1$. Therefore, the resonance wave number of the dominant mode ($m = 1$ and $n = 1$) is given by $k_{01} = \sqrt{5}\pi/a$.

Comparing equations (2.1) and (2.3), eigenvalues take different expressions for TE mode of metallic waveguide or using duality, TM mode of dielectric waveguide/ microstrip antenna bounded by magnetic conductor. Further, according to P. L. Overfelt *et al* [51], the eigenvalues of metallic waveguide for TE mode should be $k_{mn} = (\pi/a)\sqrt{m^2 + n^2}$. Thus, three different expressions for eigenvalues are reported in literature without any general validation for all possible modes. In this dissertation, we have investigated 45°–45°–90° triangular shaped microstrip antenna and dielectric resonator antenna. Correct expression for eigenvalues, is given here for microstrip antenna and dielectric resonator antenna with experimental validation for different modes.

In [47-48], 45°–45°–90° triangular microstrip resonator has been investigated using Geometrical Optics (GO). Radiation Q-factor and resonant frequency have also been discussed there for few modes. Similar procedure has also been reported in [145] to investigate the 45°–45°–90° TMA. The performance of 45°–45°–90° TMA has been predicted therein using eight reflected waves. The coefficients of those reflected waves have been determined using complex contour integration. Input impedance, radiation Q-factor and resonant frequency have been discussed therein for fundamental (dominant) mode only.

The use of segmentation technique [38-39] to investigate the planar microstrip structure is similar to equilateral TMA, but limited to fundamental mode of operation [146-147]. It should be noted here that the Green's functions are available for 45°–45°–90°, 60°–60°–60° and 30°–60°–90° triangular geometry for different mode [40], but the investigation of higher order modes of a planar microstrip structure using that Green's function has not been reported yet. In [148], segmentation and desegmentation techniques have been

utilized to investigate different 45°–45°–90° TMA. To determine the input impedance, the coupling matrices have been evaluated in a general multiport sense. Accelerated techniques have been utilized in [148] for faster convergence of infinite summation. Finally, this technique has been applied to design an antenna for circular polarization.

The eigenvalues of 45°–45°–90° triangular metallic waveguide [51] have efficiently been utilized for predicting the resonant frequency for different modes of a 45°–45°–90° TMA [149]. One antenna has also been fabricated for experimental validation of resonant frequency for first four modes. Far-field radiation patterns have also been given there showing the broad side radiating nature of the 45°–45°–90° TMA without any closed form expressions for predicting far-field patterns. Further, input impedance, Q-factors, etc. have also not been investigated therein.

In [150], eigenfunctions of 45°–45°–90° triangular geometry for different boundary conditions has been reported by P. L. Overfelt in 1989. The eigenfunctions have been derived by modeling one side wall as Perfect Electric Conductor (PEC) and rest two walls as Perfect Magnetic Conductor (PMC) and vice versa. This analysis has also been extended to investigate four sided uniform waveguide. Contour plots of the first two modes for different waveguides have also been given therein.

2.4 30°–60°–90° Triangular Shaped Radiators

30^o-60^o-90^o triangular shaped radiator is a most compact antenna element reported so far among rectangular, circular, annular and equilateral triangular shaped antenna [151]. At fundamental mode of operation around 2.6 GHz, the rectangular, circular, semi-circular, annular ring and equilateral triangular MAs take almost 3.6, 3.2, 1.6, 2.5 and 2 times area compared to 30°–60°–90° TMA respectively where all antennas have been excited using a coaxial - probe [151, Table 2.13]. Therefore, 30^o-60^o-90^o triangular shape is an important geometry.

30^o-60^o-90^o triangular microstrip resonator has also been investigated using Geometrical Optics (GO) [47-48] or by superposition of plane-waves [51] like equilateral triangular geometry. Resonant frequency (f_r) and radiation quality factor (Q_r) have been discussed only in [47-48] whereas input impedance has been investigated in [152]. Complex contour integration has been applied as applied for 45°–45°–90° TMA in [145]. In case of 30°–60°–90° TMA, the electric field under the patch has been expressed as a sum of twelve plane waves whereas the same was eight for 45°–45°–90° TMA. Due to the large numbers of plane waves, computation complexity has been increased in case of 30°–60°–90° TMA. After solving the complex coefficients of the plane waves, the conventional EMF method has been used to predict the input impedance of the 30°–60°–90° TMA. Theoretical results of input impedance and Q-factor both have been compared with experimental data. It should be pointed here that only the fundamental mode of 30°–60°–90° [152] and 45°–45°–90° [145] shaped TMA have been investigated only by G. A. Kyriacou *et al* [145, 152].

The comment paper by Zhang and Fu on [153] in 1991 revealed that the pioneering work on 30^o-60^o-90^o triangular waveguide has been done by Prof. Weigen Lin in 1979 [153-154]. As already mentioned earlier, the eigenfunctions for *TE* and *TM* modes of a 30^o-60^o-90^o metallic triangular waveguide have been reported long ago, in 1958 by F. E. Borgnis and C. H. Papas [52].

Literature survey shows that researchers have used the result on eigenvalues only to calculate the resonant frequency for 30^o-60^o-90^o TMA [155]. Three different TMAs (60^o-60^o-60^o, 30^o-60^o-90^o and 30^o-30^o-120^o shaped TMA) have been investigated using the IE3D EM simulator [8]. Based on EM simulator, an expression for accounting the fringing effect has also been given therein. The characteristics of 30^o-60^o-90^o TMA and 30^o-30^o-120^o TMA have not been explored therein (60^o-60^o-60^o TMA has been reported by K. F. Lee *et al* in 1988 [6]).

A simulation based comparative study between 30^o-60^o-90^o TMA and 15^o-75^o-90^o TMA on effective size, bandwidth, gain, etc. have also been reported

by Olaimat *et al* in 2011 [156]. One prototype has been fabricated for comparison purpose. No theoretical development is observed. In [157], 30^o-60^o-90^o TMA has been investigated using an EM simulator. Resonant frequency, beam width, bandwidth and far-field patterns have been investigated in [157]. Comparative study between 30^o-60^o-90^o TMA and 15^o-75^o-90^o TMA on effective size, bandwidth, gain etc. have also been reported therein.

2.5 Isosceles Triangular Shaped Radiators

Literature survey shows that shielded isosceles triangular microstrip resonator has been investigated using spectral domain method of moments by A. K. Sharma *et al* in 1982 [43]. Fourier transformation has been applied for theoretical investigation. Fundamental mode has been investigated only. Theoretical results are verified with experimental data for different isosceles triangular microstrip resonators.

The transmission line model has also been utilized to investigate different isosceles TMAs by K. Kathiravan *et al* in 1989 [158] for fundamental mode. The isosceles TMA has been approximated as a circular segment whose two sides coincide with the two iso-sides of the isosceles TMA. To account for the fringing effect, the curved side has been expressed as effective length (a_e) of the isosceles TMA and all calculations have been performed using a_e . The transmission line model has been applied to compute the modal current and voltage for TM_α mode only. In [158], α has been considered only as modal index instead of two modal indices 'mn' as found in rectangular, equilateral etc. shaped microstrip antennas. Resonant frequency (f_r), radiation Q-factor (Q_r) and maximum value of the real part of input impedance (R_m) have been reported therein in tabular form for different apex angle. It has been found that as the apex angle decreases it is found from [158] that f_r decreases, Q_r and R_m increases. We have also found similar observation in case of isosceles TMA using cavity model as presented in this dissertation.

In [159-160], isosceles 46^o-46^o-84^o TMA has been reported for ultra wideband application. The idea to obtain the desired results is similar to [105] as explained earlier and is not repeated here for brevity. Recently, isosceles (and equilateral) TMA has been investigated as electrically small reconfigurable antenna in 2011 [161]. To construct electrically small antenna, blocking capacitors has been utilized. The DC bias has been varied from 2V to 20V. Far-field radiation patterns, efficiency and gain have been investigated therein.

2.6 Conclusion

Literature survey on different triangular shaped antennas is presented in a systematic way to understand the current state of art. In summary, we can conclude that:

- Radiation characteristics of an equilateral TMA have been reported for different TM_{mn}^{z} modes using modal analysis.
- Resonant frequency of 45°–45°–90° and 30°–60°–90° TMAs for different TM_{mn}^{z} modes have been reported only.
- Input impedance and quality factor of a 45°–45°–90° TMA has been reported for fundamental TM_{10}^{z} mode only.
- The resonant frequency of an equilateral TDRA has been reported only for different TM_{mn}^{z} modes.

Therefore, there is plenty of scope to work on triangular shaped radiators. In this dissertation, theoretical investigations are performed on different TMAs and TDRAs as given below:

- Cavity model analysis is performed on 45°–45°–90°, 30°–60°–90° and isosceles TMAs
- Radiation characteristics of 60°–60°–60°, 30°–60°–90°, 45°–45°–90° and isosceles TDRAs are presented by treating the TDRAs as a cavity.

Part II

Microstrip Antenna (MA)

Chapter

3. **Equilateral Triangular MA (ETMA)**
4. **30°–60°–90° Triangular MA (TMA)**
5. **45°–45°–90° TMA**
6. **Isosceles TMA**

Chapter III

Equilateral Triangular Microstrip Antenna

3.1 Introduction

Equilateral Triangular Microstrip Antenna (ETMA) as shown in Fig. 3.1 has been investigated by K. F. Lee *et al* in 1988 [6] using conventional cavity model [11-15]. According to the cavity model, the internal field components are independent of z-direction. On substituting $\partial/\partial z = 0$, one can easily find that $E_x = 0 = E_y$ because $E_x \propto \partial/\partial z$ and $E_y \propto \partial/\partial z$. Therefore, the radiation characteristics of an ETMA are dependent on E_z components only. Still, evaluation of far-field patterns of an ETMA is quite complex compared to rectangular Microstrip Antenna (MA) because of the inclined sides. It is important to obtain a detailed description for evaluating the far-field patterns of an ETMA. It will be helpful to solve the problem not only with Equilateral Triangular Dielectric Resonator Antenna (ETDRA), where all the internal field components are functions of x-y-z coordinates but other triangular shaped radiator also.

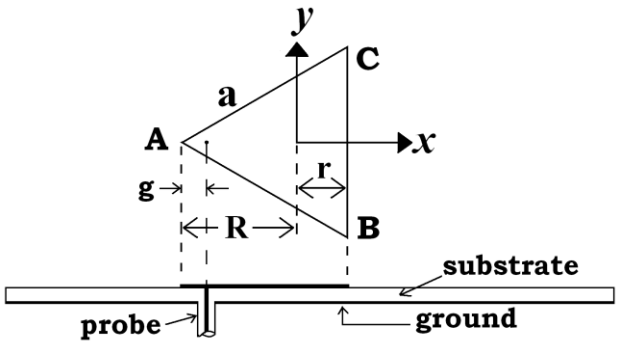

Fig. 3.1 Geometry and feed configuration of antenna

Although the theoretical results are summarized in [6], we have derived all expressions showing every step in detail. The analysis of equilateral TMA is very important to know its characteristics. The theory on ETMA can easily be extended to investigate other triangular shaped resonators, oscillators, filters etc.

The inherent structural symmetry of ETMA leads to flexibility in the choice of feed. It is found that:

- Equilateral TMA shows more number of broadside radiating modes compared to rectangular MA. ETMA shows three broadside radiation modes among the first five modes.
- For moderate value of input resistance, ETMA can efficiently be utilized as a triple band antenna using a single coaxial probe feed.
- ETMA can be used for multiband application.
- ETMA shows high Q-factor compared to rectangular MA. Therefore, ETMA is a narrow band structure. This property can efficiently be utilized to make equilateral triangular shaped filters.
- ETMA can store high energy compared to rectangular MA.

3.2 Theory

In this section, an equilateral TMA is investigated analytically using conventional cavity model [11-15]. The antenna geometry of an ETMA having side length a is shown in Fig. 3.1 where the standard Cartesian coordinate system is adopted. The antenna is placed on a substrate having thickness d and relative permittivity ε_r. Coaxial probe is placed at (x_o, y_o) point to excite the antenna. Eigenfunctions, eigenvalues, far-field radiation patterns, input impedance, radiated power (P_r in %), total Q-factor (Q_t), gain (G), bandwidth (BW), efficiency (e) are investigated.

3.2.1 Eigenfunctions

To evaluate the eigenfunctions (ψ_{mn}) for TM^z mode, the ETMA is modeled as a cavity. The ground plane is removed first by applying image theory which results an equilateral triangular cavity having $h = 2d$. The side walls of the ETMA are modeled as Perfect Magnetic Conductor (PMC) whereas the top and bottom surfaces are modeled as Perfect Electric Conductor (PEC). Conventional cavity model [11-15] is applied to evaluate the eigenfunctions (ψ_{mn}) of an ETMA. According to cavity model, the eigenction (ψ_{mn}) is independent of z-

coordinate, because the thickness of the patch (h) is much smaller than the operating wavelength. Mathematically, this can be written as $\partial/\partial z = 0$. Therefore, the eigenfunctions (ψ_{mn}) is a function of x-y coordinates only. Tri-linear transformation is used as defined in [24] to generate the local coordinate system inside the equilateral triangular section. The equilateral triangular section is symmetric with respect to x-axis as shown in Fig. 3.1. But after applying tri-linear transformation, the symmetry gets shifted to y-axis. Following [53], one can easily obtain the ψ_{mn} function both for even and odd modes. The solutions of ψ_{mn} for even (ψ^e_{mn}) and odd (ψ^o_{mn}) modes are given by [24, 51, 53]:

$$\psi^e_{mn} = cos\frac{2\pi l}{\sqrt{3}a}(x+R)\,cos\left(\frac{2\pi(m-n)}{3a}y\right) + cos\frac{2\pi m}{\sqrt{3}a}(x+R)\,cos\left(\frac{2\pi(n-l)}{3a}y\right) + cos\frac{2\pi n}{\sqrt{3}a}(x+R)\,cos\left(\frac{2\pi(l-m)}{3a}y\right) \quad (3.1a)$$

and

$$\psi^o_{mn} = cos\frac{2\pi l}{\sqrt{3}a}(x+R)\,sin\left(\frac{2\pi(m-n)}{3a}y\right) + cos\frac{2\pi m}{\sqrt{3}a}(x+R)\,sin\left(\frac{2\pi(n-l)}{3a}y\right) + cos\frac{2\pi}{\sqrt{3}a}(x+R)\,sin\left(\frac{2\pi(l-m)}{3a}y\right) \quad (3.1b)$$

where m, n, l are integers such that $l = -(m+n), R = a/\sqrt{3}$ and other terms are carrying their usual meaning.

Some properties of even and odd mode solutions along the triangular section of an isolated ETMA are shown in Fig. 3.2 for some modes. The 'even' and 'odd' mode solutions of ψ_{mn} are clearly evident from Fig. 3.2.

The internal field components for TM^z mode due to probe excitation ($\vec{J}$) are given by:

$$E_z = D_{mn}\psi_{mn}(x,y)$$
$$H_x = -\frac{j}{\omega\mu\varepsilon}\frac{dE_z}{dy}$$

$$H_y = \frac{j}{\omega\mu\varepsilon}\frac{dE_z}{dx}$$
$$E_x = E_y = H_z = 0 \qquad (3.2a)$$

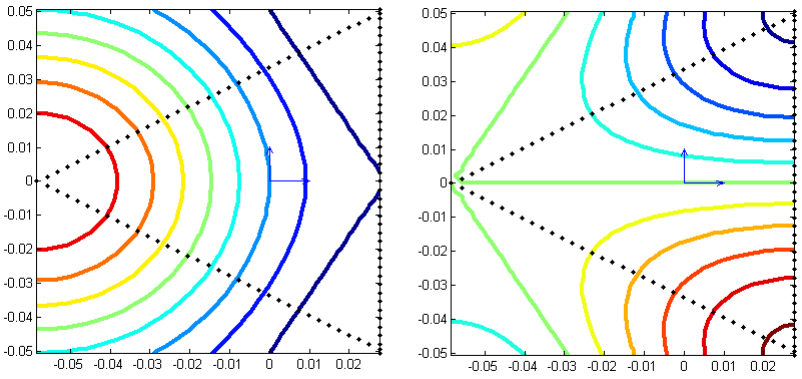

(a) Even (left) and odd (right) mode for TM_{10}^{z} mode

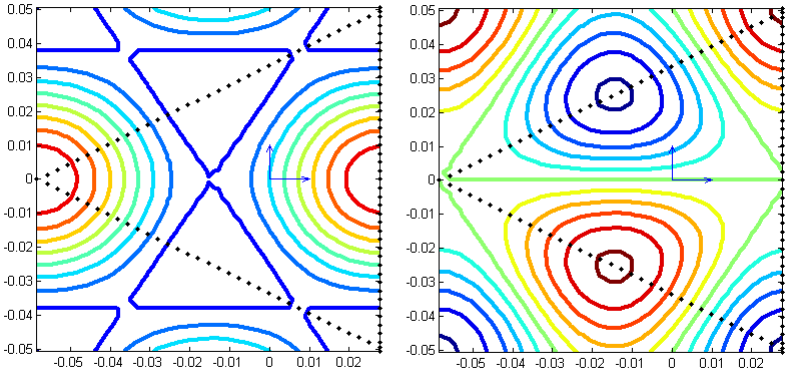

(b) Even (left) and odd (right) mode for TM_{20}^{z} mode

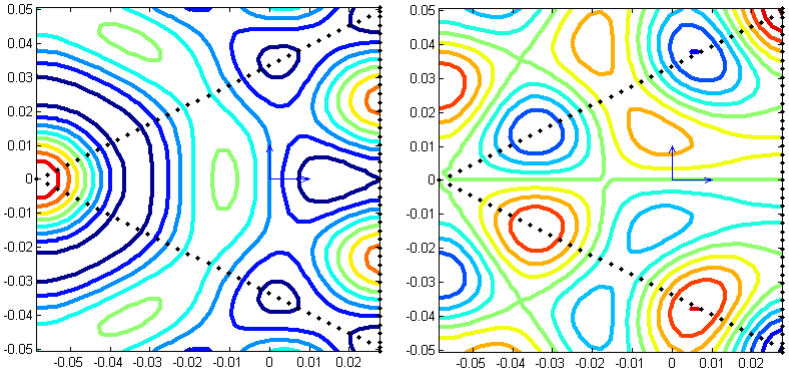

(c) Even (left) and odd (right) mode for TM_{31}^{z} mode

Fig. 3.2 Even (left) and odd (right) mode property of the eigenfunctions

where

$$D_{mn} = j\omega\mu \sum_{m=0}^{\infty}\sum_{n=0}^{\infty} \frac{1}{(k^2 - k_{mn}^2)} \frac{< J\psi_{mn} >}{< \psi_{mn}\psi_{mn} >} \qquad (3.2b)$$

Theoretical magnetic field lines for even mode within the ETMA are shown in Fig. 3.3 for first four modes.

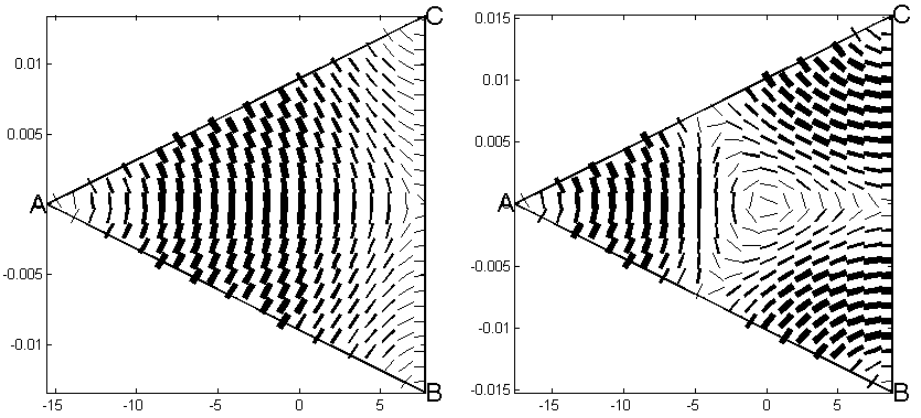

(a) Magnetic field lines for TM_{10}^z (left) and TM_{11}^z (right) mode

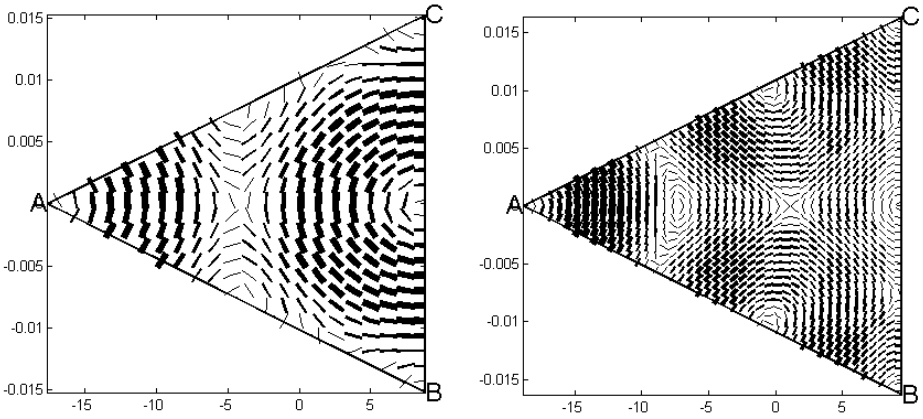

(b) Magnetic field lines for TM_{20}^z (left) and TM_{21}^z (right) mode

Fig. 3.3 Magnetic field patterns within the ETMA at $z = 0$ surface for different modes

To investigate the even (ψ_{mn}^e) and odd (ψ_{mn}^o) mode solutions, a probe fed ETMA is simulated using Finite Element Method (FEM) based commercial 3D numerical full-wave EM Simulator HFSS [9]. Different combinations of dimensions and relative permittivity are also investigated. Different feeding techniques are also applied such as aperture, strip, microtsrip line, etc. But we

did not observe any 'odd' mode field distribution (please see Fig. 3.3) along the triangular cross-section. Therefore, we discuss here the 'even' mode solution only. Far-field radiation patterns, radiated power, Quality factor (Q-factor), bandwidth etc. are investigated.

It should be pointed here that to excite the 'odd' mode, we have to introduce a null along its median which is only possible by using extra circuitry such as shorting pin. Therefore, the original geometry of the antenna must be perturbed to exite the 'odd' mode using conventional feeding structures. In that case, perturbation must be accounted to predict the actual radiation characteristics of the ETMA.

3.2.2 Resonant Frequency

The eigenvalues for an ETMA are given by [24]:

$$k^2 = \left(\frac{4\pi}{3a}\right)^2 (m^2 + mn + n^2) \qquad (3.4a)$$

The resonant frequency can be found using

$$f_r = \frac{kc}{2\pi(\varepsilon_r)^{1/2}} \qquad (3.4b)$$

where c is the velocity of light in free space and ε_r is the relative permittivity of substrate. For fixed values of a and ε_r, the resonant frequencies of the first 20 modes are shown in Table 3.1.

To account the effect of fringing, several CAD models have been reported for efficient evaluation of effective side length (a_e). In this dissertation, a_e is evaluated as [12-15]:

$$a_e = a + h/(\varepsilon_r)^{0.05} \qquad (3.4c)$$

It is assumed that the effect of permittivity is inherently included in the effective side length (a_e) here as found in the case of circular MA [14].

Table 3.1

Resonant frequencies for first 20 modes of an ETMA

($a = 100mm, \varepsilon_r = 2.32$)

Sl No	Mode	Resonant Frequency (GHz)		Sl No	Mode	Resonant Frequency (GHz)
1	TM^z_{10}	1.3125		11	TM^z_{50}	6.5625
2	TM^z_{11}	2.2733		12	TM^z_{33}	6.8200
3	TM^z_{20}	2.6250		13	TM^z_{42}	6.9451
4	TM^z_{21}	3.4726		14	TM^z_{51}	7.3077
5	TM^z_{30}	3.9375		15	TM^z_{43}	7.9836
6	TM^z_{22}	4.5466		16	TM^z_{52}	8.1966
7	TM^z_{31}	4.7323		17	TM^z_{44}	9.0933
8	TM^z_{40}	5.2500		18	TM^z_{53}	9.1875
9	TM^z_{32}	5.7211		19	TM^z_{54}	10.251
10	TM^z_{41}	6.0146		20	TM^z_{55}	11.367

3.2.3 Far-Field Radiation Patterns

"Equivalence Principle" [4, 16] is used to evaluate the far-zone electric field. For theoretical simplicity, the apex (A) of the triangle ABC is shifted to the origin. Substituting $x = x' - R$ in equation (3.1a), we get:

$$\psi_{mn} = cos\left(\frac{2\pi l}{\sqrt{3}a}x\right)cos\left(\frac{2\pi(m-n)}{3a}y\right) + cos\left(\frac{2\pi m}{\sqrt{3}a}x\right)cos\left(\frac{2\pi(n-l)}{3a}y\right) + cos\left(\frac{2\pi n}{\sqrt{3}a}x\right)cos\left(\frac{2\pi(l-m)}{3a}y\right)$$

$$= \sum_{i=1}^{3} cos(\alpha_i x)\, cos(\beta_i y) \qquad (3.5a)$$

where

$$\alpha_1 = \frac{2\pi l}{\sqrt{3}a} \quad , \quad \alpha_2 = \frac{2\pi m}{\sqrt{3}a} \quad , \quad \alpha_3 = \frac{2\pi n}{\sqrt{3}a}$$

$$\beta_1 = \frac{2\pi(m-n)}{3a} \quad , \quad \beta_2 = \frac{2\pi(n-l)}{3a} \quad , \quad \beta_3 = \frac{2\pi(l-m)}{3a} \qquad (3.5b)$$

The effect of shifting along the x-axis will be reflected as a multiplying factor $exp(jV_1R)$ with the modal amplitude where $V_1 = k_o\, sin(\theta)\, cos(\varphi)$. Magnetic surface current $(\vec{M}_s)$ model [12-15, 162] is used here to investigate the ETMA. A closed form analytical expressions are given here.

Magnetic Surface Current $(\vec{M}_s)$ Model

To utilize this model, AC, BC and AB sides having a rectangular cross-section are modeled as Perfect Magnetic Conductors (PMC).

Surface Current along AC Surface (PMC)

$$M_s^{AC} = \vec{E} \times \hat{n} = [0\hat{x} + 0\hat{y} + E_z\hat{z}] \times \left(\hat{y}cos(\alpha) - \hat{x}sin(\alpha)\right); \quad \alpha = \pi/6$$
$$= 0 - \hat{x}E_z cos(\alpha) + 0 - \hat{y}E_z sin(\alpha)$$
$$= -\hat{x}E_z cos(\alpha) - \hat{y}E_z sin(\alpha) \qquad (3.6a)$$

Surface Current along AB Surface (PMC)

$$M_s^{AB} = \vec{E} \times \hat{n} = [0\hat{x} + 0\hat{y} + E_z\hat{z}] \times \left(-\hat{y}cos(\alpha) - \hat{x}sin(\alpha)\right); \quad \alpha = \pi/6$$
$$= 0 + \hat{x}E_z cos(\alpha) + 0 - \hat{y}E_z sin(\alpha)$$
$$= \hat{x}E_z cos(\alpha) - \hat{y}E_z sin(\alpha) \qquad (3.6b)$$

Surface Current along BC Surface (PMC)

$$M_s^{BC} = \vec{E} \times \hat{n} = [0\hat{x} + 0\hat{y} + E_z\hat{z}] \times \hat{x} = 0 + \hat{y}E_z = \hat{y}E_z \qquad (3.6c)$$

Fields along AC Surface (PMC)

The magnetic surface current along the AC surface is evaluated from equation (3.6a) as:

$$M_s^{AC} = -\hat{x}E_z cos(\alpha) - \hat{y}E_z sin(\alpha) = \hat{x}M_{sx}^{AC} + \hat{y}M_{sy}^{AC} \qquad (3.6a)$$

- **$\hat{x}$-component $\vec{F}$ due to M_s^{AC} surface current**

$$F_x^{AC} = C_{xy} \times \int_l \int_{z=-d}^{d} [M_{sx}^{AC}] \times e^{j(V_1x + V_2y + V_3z)} dldz\, aty = \eta x \qquad (3.7a)$$

$$= C_{xy} \times [-E_3] \times (\chi^2) \times (I_{AC}^{x1} \times I_s^z) \tag{3.7b}$$

where

$$I^z = \int_{z=-d}^{d} e^{jV_3 z} dz = 2d\,sinc(dV_3) \tag{3.7c}$$

$$I_{AC}^{x1} = C_{xy} \times \int_{l} [M_{sx}^{AC}] \times e^{j(V_1 x + V_2 y)} dl\, aty = \eta x \tag{3.7d}$$

which can be expressed as:

$$I_{AC}^{x1} = \frac{1}{4}\sum_{i=1}^{3}\left(\frac{1}{jC_i^{x1}}\left(e^{jC_i^{x1}M} - 1\right) + \frac{1}{jD_i^{x1}}\left(e^{jD_i^{x1}M} - 1\right) + \frac{1}{jE_i^{x1}}\left(e^{jE_i^{x1}M} - 1\right) + \frac{1}{jF_i^{x1}}\left(e^{jF_i^{x1}M} - 1\right)\right) \tag{3.7e}$$

where

$$\begin{cases} C_i^{x1} = \alpha_i + \beta_i\eta + \chi_1 \\ D_i^{x1} = -\alpha_i + \beta_i\eta + \chi_1 \\ E_i^{x1} = \alpha_i - \beta_i\eta + \chi_1 \\ F_i^{x1} = -\alpha_i - \beta_i\eta + \chi_1 \\ \chi_1 = k_o \sin(\theta)\,(\cos(\Phi) + \eta \sin(\Phi)) \\ \eta = tan\left(\frac{\Omega}{2}\right) = tan\left(\frac{\pi}{6}\right) = \frac{1}{\sqrt{3}} \end{cases} \tag{3.7f}$$

To evaluate the value of I_{AC}^{x1}, we need the find the values of $C_i^{x1}, D_i^{x1}, E_i^{x1}$ and F_i^{x1} and these are given be:

$C_1^{x1} = -b(n-l) + \chi_1$ $\quad$ $E_1^{x1} = b(l-m) + \chi_1$

$C_2^{x1} = -b(l-m) + \chi_1$ $\quad$ $E_2^{x1} = b(m-n) + \chi_1$

$C_3^{x1} = -b(m-n) + \chi_1$ $\quad$ $E_3^{x1} = b(n-l) + \chi_1$

$D_1^{x1} = -b(l-m) + \chi_1$ $\quad$ $F_1^{x1} = b(n-l) + \chi_1$

$D_2^{x1} = -b(m-n) + \chi_1$ $\quad$ $F_2^{x1} = b(l-m) + \chi_1$

$D_3^{x1} = -b(n-l) + \chi_1$ $\quad$ $F_3^{x1} = b(m-n) + \chi_1$

On separation of $(n-l)$ terms, one can get the expression $\left(FF_{x1}^{(n-l)}\right)$ having $C_1^{x1}, D_3^{x1}, E_3^{x1}, F_1^{x1}$terms only.

$$FF_{x1}^{(n-l)} = \frac{1}{4}\sum_{i=1}^{3}\left(\frac{1}{jC_i^{x1}}\left(e^{jC_i^{x1}M}-1\right)+\frac{1}{jD_i^{x1}}\left(e^{jD_i^{x1}M}-1\right)+\frac{1}{jE_i^{x1}}\left(e^{jE_i^{x1}M}-1\right)\right.$$
$$\left.+\frac{1}{jF_i^{x1}}\left(e^{jF_i^{x1}M}-1\right)\right)$$
$$= \frac{-j}{((n-l)^2b^2-\chi_1^2)} \times \left[e^{j\chi_1 M}\{jb(n-l)\sin(b(n-l)M)-\chi_1\cos(b(n-l)M)\}+\chi_1\right] \quad (3.7g)$$

Similarly, on separation of $(l-m)$ and $(m-n)$ terms, one can write:

$$FF_{x1}^{(l-m)} = \frac{-j}{((l-m)^2b^2-\chi_1^2)}$$
$$\times \left[e^{j\chi_1 M}\{jb(l-m)\sin(b(l-m)M)-\chi_1\cos(b(l-m)M)\}+\chi_1\right] \quad (3.7h)$$
$$FF_{x1}^{(m-n)} = \frac{-j}{((m-n)^2b^2-\chi_1^2)}$$
$$\times \left[e^{j\chi_1 M}\{jb(m-n)\sin(b(m-n)M)-\chi_1\cos(b(m-n)M)\}+\chi_1\right] \quad (3.7i)$$

It should be pointed here that the expressions for $FF_{x1}^{(n-l)}, FF_{x1}^{(l-m)}$ and $FF_{x1}^{(m-n)}$ are exactly same as reported in [6]. For example, $FF_{x1}^{(n-l)}$ can be expressed as:

$$FF_{x1}^{(n-l)} = \frac{-j}{((n-l)^2b^2-\chi_1^2)} \times \left[e^{j\chi_1 M}\{jb(n-l)\sin(b(n-l)M)-\chi_1\cos(b(n-l)M)\}+\chi_1\right]$$
$$= \frac{j}{((n-l)^2b^2-\chi_1^2)}$$
$$\times \left[e^{j\chi_1 M}\left\{\frac{jb(n-l)}{-1}\sin(b(n-l)M)+\chi_1\cos(b(n-l)M)\right\}-\chi_1\right]$$
$$= \frac{j\chi_1}{((n-l)^2b^2-\chi_1^2)} \times \left[e^{j\chi_1 M}\left\{\frac{jb(n-l)}{j^2\chi_1}\sin(b(n-l)M)+\cos(b(n-l)M)\right\}-1\right]$$
$$= \frac{j\chi_1}{((n-l)^2b^2-\chi_1^2)} \times \left[e^{j\chi_1 M}\left\{\frac{b(n-l)}{j\chi_1}sin(b(n-l)M)+cos(b(n-l)M)\right\}-1\right]$$

which is exactly similar to [6] except the (−) sign. The (−) sign of $[-E_z]$ is included to calculate the $FF_{x1}^{(n-l)}$ term. Therefore, we can write:

$$I_{AC}^{x1} = \frac{-j}{((n-l)^2b^2-\chi_1^2)} \times \left[e^{j\chi_1 M}\{jb(n-l)\,sin(b(n-l)M)-\chi_1\,cos(b(n-l)M)\}+\chi_1\right]$$

$$+\frac{-j}{((l-m)^2b^2-\chi_1^2)}\times\left[e^{j\chi_1 M}\{jb(l-m)\,sin(b(l-m)M)-\chi_1\,cos(b(l-m)M)\}+\chi_1\right]$$
$$+\frac{-j}{((m-n)^2b^2-\chi_1^2)}\times\left[e^{j\chi_1 M}\{jb(m-n)\,sin(b(m-n)M)-\chi_1\,cos(b(m-n)M)\}+\chi_1\right] \quad (3.8)$$

- **$\hat{y}$-component of due to $\mathbf{M_s^{AC}}$ surface current**

$$F_y^{AC}=C_{xy}\times\int_l\int_{z=-d}^{d}\left[M_{sy}^{AC}\right]\times e^{j(V_1x+V_2y+V_3z)}dldz \qquad at \quad x=y/\eta \quad (3.9a)$$

where

$$I^z=\int_{z=-d}^{d}e^{jV_3z}dz=2dsinc(dV_3) \quad (3.9b)$$

$$I_{AC}^{y1}=C_{xy}\times\int_l\left[M_{sy}^{AC}\right]\times e^{j(V_1x+V_2y)}dl \quad at \quad x=y/\eta \quad (3.9c)$$

which can be expressed as:

$$I_{AC}^{y1}=\frac{1}{4}\sum_{i=1}^{3}\left(\frac{1}{jC_i^{y1}}\left(e^{jC_i^{y1}B/2}-1\right)+\frac{1}{jD_i^{y1}}\left(e^{jD_i^{y1}B/2}-1\right)+\frac{1}{jE_i^{y1}}\left(e^{jE_i^{y1}B/2}-1\right)+\frac{1}{jF_i^{y1}}\left(e^{jF_i^{y1}B/2}-1\right)\right) \quad (3.9d)$$

where

$$\begin{cases} C_i^{y1}=\alpha_i/\eta+\beta_i+\sqrt{3}\chi_1 \\ D_i^{y1}=-\alpha_i/\eta+\beta_i+\sqrt{3}\chi_1 \\ E_i^{y1}=\alpha_i/\eta-\beta_i+\sqrt{3}\chi_1 \\ F_i^{y1}=-\alpha_i/\eta-\beta_i+\sqrt{3}\chi_1 \\ \chi_1=k_o\sin(\theta)\,(\cos(\Phi)+\eta\sin(\Phi)) \\ \eta=tan\left(\frac{\Omega}{2}\right)=tan\left(\frac{\pi}{6}\right)=\frac{1}{\sqrt{3}} \end{cases} \quad (3.9e)$$

$C_i^{y1}, D_i^{y1}, E_i^{y1}$ and F_i^{y1} are evaluated first and they are given by:

$$C_1^{y1} = \sqrt{3}[-b(n-l)+\chi_1] \qquad E_1^{y1} = \sqrt{3}[b(l-m)+\chi_1]$$
$$C_2^{y1} = \sqrt{3}[-b(l-m)+\chi_1] \qquad E_2^{y1} = \sqrt{3}[b(m-n)+\chi_1]$$
$$C_3^{y1} = \sqrt{3}[-b(m-n)+\chi_1] \qquad E_3^{y1} = \sqrt{3}[b(n-l)+\chi_1]$$
$$D_1^{y1} = \sqrt{3}[-b(l-m)+\chi_1] \qquad F_1^{y1} = \sqrt{3}[b(n-l)+\chi_1]$$
$$D_2^{y1} = \sqrt{3}[-b(m-n)+\chi_1] \qquad F_2^{y1} = \sqrt{3}[b(l-m)+\chi_1]$$
$$D_3^{y1} = \sqrt{3}[-b(n-l)+\chi_1] \qquad F_3^{y1} = \sqrt{3}[b(m-n)+\chi_1]$$

On separation of$(n-l)$ terms, one can get the expression for $FF_{y1}^{(n-l)}$ having $C_1^{y1}, D_3^{y1}, E_3^{y1}, F_1^{y1}$ terms only. Therefore, we can write:

$$FF_{x1}^{(n-l)} = \frac{1}{4}\sum_{i=1}^{3}\left(\frac{1}{jC_i^{y1}}\left(e^{jC_i^{y1}B/2}-1\right)+\frac{1}{jD_i^{y1}}\left(e^{jD_i^{y1}B/2}-1\right)+\frac{1}{jE_i^{y1}}\left(e^{jE_i^{y1}B/2}-1\right)\right.$$
$$\left.+\frac{1}{jF_i^{y1}}\left(e^{jF_i^{y1}B/2}-1\right)\right)$$

$$= \frac{1}{4}\left[-\frac{1}{j\sqrt{3}\{b(n-l)-\chi_1\}}\left(e^{\frac{j\{-b(n-l)+\chi_1\}\sqrt{3}B}{2}}-1\right)\right.$$
$$-\frac{1}{j\sqrt{3}\{b(n-l)-\chi_1\}}\left(e^{\frac{j\{-b(n-l)+\chi_1\}\sqrt{3}B}{2}}-1\right)$$
$$+\frac{1}{j\sqrt{3}\{b(n-l)+\chi_1\}}\left(e^{\frac{j\{b(n-l)+\chi_1\}\sqrt{3}B}{2}}-1\right)$$
$$\left.+\frac{1}{j\sqrt{3}\{b(n-l)+\chi_1\}}\left(e^{\frac{j\{b(n-l)+\chi_1\}\sqrt{3}B}{2}}-1\right)\right]$$

$$= \frac{-j}{\sqrt{3}((n-l)^2b^2-\chi_1^2)} \times \left[e^{j\chi_1 M}\{jb(n-l)\sin(b(n-l)M)-\chi_1\cos(b(n-l)M)\}+\chi_1\right]$$

Similarly, on separation of $(l-m)$ and $(m-n)$ terms, one can write:

$$FF_{y1}^{(l-m)} = \frac{-j}{\sqrt{3}((l-m)^2b^2-\chi_1^2)}$$
$$\times \left[e^{j\chi_1 M}\{jb(l-m)\sin(b(l-m)M)-\chi_1\cos(b(l-m)M)\}+\chi_1\right]$$

$$FF_{y1}^{(m-n)} = \frac{-j}{\sqrt{3}((m-n)^2b^2-\chi_1^2)} \times \left[e^{j\chi_1 M}\{jb(m-n)\sin(b(m-n)M) - \chi_1\cos(b(m-n)M)\} + \chi_1\right]$$

Hence, we can write:

$$I_{AC}^{y1} = \frac{-j}{\sqrt{3}((n-l)^2b^2-\chi_1^2)} \times \left[e^{j\chi_1 M}\{jb(n-l)\sin(b(n-l)M) - \chi_1\cos(b(n-l)M)\} + \chi_1\right]$$
$$+\frac{-j}{\sqrt{3}((l-m)^2b^2-\chi_1^2)} \times \left[e^{j\chi_1 M}\{jb(l-m)\sin(b(l-m)M) - \chi_1\cos(b(l-m)M)\} + \chi_1\right]$$
$$+\frac{-j}{\sqrt{3}((m-n)^2b^2-\chi_1^2)} \times \left[e^{j\chi_1 M}\{jb(m-n)\sin(b(m-n)M) - \chi_1\cos(b(m-n)M)\} + \chi_1\right] \quad (3.10)$$

Fields along AB Surface (PMC)

Magnetic surface current along the AB surface is evaluated from equation (3.6b) as:

$$M_s^{AB} = \hat{x}E_z cos(\alpha) - \hat{y}E_z sin(\alpha) = \hat{x}M_{sx}^{AB} + \hat{y}M_{sy}^{AB} \qquad (3.6b)$$

- **$\hat{x}$-component $\vec{F}$ due to M_s^{AB} surface current**

$$F_x^{AB} = C_{xy} \times \int_l \int_{z=-h}^{h} [M_{sx}^{AB}] \times e^{j(V_1x+V_2y+V_3z)} dldz \quad at \quad y = -\eta x \qquad (3.11a)$$

$$= C_{xy} \times [E_3] \times (\chi^2) \times (I_{AC}^{x2} \times I^z) \qquad (3.11b)$$

where

$$I_{AC}^{x2} = \int_{x=0}^{M} \left(\sum_{i=1}^{3} \cos(\alpha_i x)\cos(-\beta_i \eta x)\right) \times e^{jx\chi_2} dx \quad ; \quad \chi_2 = V_1 - \eta V_2 \qquad (3.11c)$$

$$= \int_{x=0}^{M} \left(\sum_{i=1}^{3} \cos(\alpha_i x)\cos(\beta_i \eta x)\right) \times e^{jx\chi_2} dx$$

$$= I_{AC}^{x1}|_{\chi_1=\chi_2} \qquad (3.11d)$$

- **$\hat{y}$-component $\vec{F}$ due to M_s^{AB} surface current**

$$F_y^{AB} = C_{xy} \times \int_l \int_{z=-h}^{h} \left[M_{sy}^{AB}\right] \times e^{j(V_1 x + V_2 y + V_3 z)} dy dz \quad at\ x = -\frac{y}{\eta} \tag{3.12a}$$

$$= C_{xy} \times [-E_3] \times (\chi^2) \times \left(I_{AB}^{y2} \times I^z\right) (3.12.b)$$

where

$$I_{AB}^{y2} = \int_{y=-\frac{B}{2}}^{0} \left(\sum_{i=1}^{3} \cos(\alpha_i x) \cos(\beta_i y)\right) \times e^{j(V_1 x + V_2 y)} dy \quad at \quad x = -\frac{y}{\eta} \tag{3.12c}$$

$$= \int_{y=-\frac{B}{2}}^{0} \left(\sum_{i=1}^{3} \cos(-\alpha_i y/\eta) \cos(\beta_i y)\right) \times e^{-jy\sqrt{3}\chi_2} dy$$

$$\left[V_1 x + V_2 y = \frac{-1}{\eta} \times k_o \sin(\theta) (\cos(\varphi) - \eta \sin(\varphi)) = \frac{-1}{\eta} \times \chi_2 = -\sqrt{3}\chi_2\right]$$

Performing similar calculation as down in case of F_y^{AC}, we can write:

$C_1^{y2} = \sqrt{3}[-b(n-l) - \chi_2]$ $\quad$ $E_1^{y2} = \sqrt{3}[b(l-m) - \chi_2]$

$C_2^{y2} = \sqrt{3}[-b(l-m) - \chi_2]$ $\quad$ $E_2^{y2} = \sqrt{3}[b(m-n) - \chi_2]$

$C_3^{y2} = \sqrt{3}[-b(m-n) - \chi_2]$ $\quad$ $E_3^{y2} = \sqrt{3}[b(n-l) - \chi_2]$

$D_1^{y2} = \sqrt{3}[-b(l-m) - \chi_2]$ $\quad$ $F_1^{y2} = \sqrt{3}[b(n-l) - \chi_2]$

$D_2^{y2} = \sqrt{3}[-b(m-n) - \chi_2]$ $\quad$ $F_2^{y2} = \sqrt{3}[b(l-m) - \chi_2]$

$D_3^{y2} = \sqrt{3}[-b(n-l) - \chi_2]$ $\quad$ $F_3^{y2} = \sqrt{3}[b(m-n) - \chi_2]$

and separating $(n-l)$ terms, one can get the expression $\left(FF_{y2}^{(n-l)}\right)$ having $C_1^{y1}, D_3^{y1}, E_3^{y1}, F_1^{y1}$terms only as:

$$FF_{y2}^{(n-l)} = \frac{1}{4} \sum_{i=1}^{3} \left(\frac{1}{jC_i^{y2}} \left(1 - e^{-jC_i^{y2} B/2}\right) + \frac{1}{jD_i^{y2}} \left(1 - e^{-jD_i^{y2} B/2}\right) + \frac{1}{jE_i^{y2}} \left(1 - e^{-jE_i^{y2} B/2}\right) + \frac{1}{jF_i^{y2}} \left(1 - e^{-jF_i^{y2} B/2}\right) \right)$$

$$= \frac{1}{4}\left[\frac{1}{j\sqrt{3}\{-b(n-l)-\chi_2\}}\left(1-e^{\frac{-j\{-b(n-l)-\chi_2\}\sqrt{3}B}{2}}\right)\right.$$
$$+\frac{1}{j\sqrt{3}\{-b(n-l)-\chi_2\}}\left(1-e^{\frac{-j\{-b(n-l)-\chi_2\}\sqrt{3}B}{2}}\right)$$
$$+\frac{1}{j\sqrt{3}\{b(n-l)-\chi_2\}}\left(1-e^{\frac{-j\{b(n-l)-\chi_2\}\sqrt{3}B}{2}}\right)$$
$$\left.+\frac{1}{j\sqrt{3}\{b(n-l)-\chi_2\}}\left(1-e^{\frac{-j\{b(n-l)-\chi_2\}\sqrt{3}B}{2}}\right)\right]$$

$$= \frac{1}{4}\left[-\frac{2}{j\sqrt{3}\{b(n-l)-\chi_2\}}\left(e^{j\{-b(n-l)+\chi_2\}M}-1\right)\right.$$
$$\left.+\frac{2}{j\sqrt{3}\{b(n-l)+\chi_2\}}\left(e^{j\{b(n-l)+\chi_2\}M}-1\right)\right] \quad ; \; M=\sqrt{3}a/2$$

which is exactly same as found for I_{AC}^{y1} where $\chi_1 = \chi_2$. Hence,

$$FF_{y2}^{(n-l)} = \frac{-j}{\sqrt{3}((n-l)^2b^2-\chi_2^2)} \times \left[e^{j\chi_2 M}\{jb(n-l)\sin(b(n-l)M)-\chi_2\cos(b(n-l)M)\}+\chi_2\right] \quad (3.12d)$$

Similarly, on separation of$(l-m)$and $(m-n)$ terms, one can write:

$$FF_{y2}^{(l-m)} = \frac{-j}{\sqrt{3}((l-m)^2b^2-\chi_2^2)} \times \left[e^{j\chi_2 M}\{jb(l-m)\sin(b(l-m)M)-\chi_2\cos(b(l-m)M)\}+\chi_2\right]$$

$$FF_{y2}^{(m-n)} = \frac{-j}{\sqrt{3}((m-n)^2b^2-\chi_2^2)} \times \left[e^{j\chi_2 M}\{jb(m-n)\sin(b(m-n)M)-\chi_2\cos(b(m-n)M)\}+\chi_2\right]$$

$$I_{AB}^{y2} = \frac{-j}{\sqrt{3}((n-l)^2b^2-\chi_2^2)} \times \left[e^{j\chi_2 M}\{jb(n-l)\sin(b(n-l)M)-\chi_2\cos(b(n-l)M)\}+\chi_2\right]$$
$$+\frac{-j}{\sqrt{3}((l-m)^2b^2-\chi_2^2)} \times \left[e^{j\chi_2 M}\{jb(l-m)\sin(b(l-m)M)-\chi_2\cos(b(l-m)M)\}+\chi_2\right]$$
$$+\frac{-j}{\sqrt{3}((m-n)^2b^2-\chi_2^2)} \times \left[e^{j\chi_2 M}\{jb(m-n)\sin(b(m-n)M)-\chi_2\cos(b(m-n)M)\}+\chi_2\right] \quad (3.13)$$

Fields along BC Surface (PMC)

The magnetic surface current along the BC surface is evaluated from equation (3.6c) as:

$$M_s^{BC} = \hat{y}E_z \tag{3.6c}$$

- **$\hat{y}$-component $\vec{F}$ due to M_s^{BC} surface current**

$$F_y^{BC} = C_{xy} \times \int_{y=-B/2}^{B/2} \int_{z=-d}^{d} [E_z] \times e^{j(V_1x+V_2y+V_3z)} dydz \quad at\ x = M \tag{3.14a}$$

$$= C_{xy} \times e^{jV_1M} \times \int_{y=-\frac{B}{2}}^{\frac{B}{2}} \int_{z=-d}^{d} E_3(\chi^2) \left(\sum_{i=1}^{3} \cos(\alpha_i M) \cos(\beta_i y) \right) \times e^{j(V_1x+V_2y+V_3z)} dydz$$

$$= C_{xy} \times (E_3\chi^2) \times e^{jV_1M} \times \left(\sum_{i=1}^{3} \cos(\alpha_i M) \times \int_{y=-\frac{B}{2}}^{\frac{B}{2}} \cos(\beta_i y) \times e^{jV_2y}\, dy \right) \times \int_{z=-d}^{d} e^{jV_3z} dz$$

$$F_y^{BC} = C_{xy} \times [E_3] \times (\chi^2) \times e^{jV_1M} \times I_{BC}^{y1} \times I^z \tag{3.14b}$$

where

$$I_{BC}^{y1} = \sum_{i=1}^{3} \cos(\alpha_i M) \times \int_{y=-\frac{B}{2}}^{\frac{B}{2}} \cos(\beta_i y) \times e^{jV_2y}\, dy \tag{3.14c}$$

$$= \sum_{i=1}^{3} \cos(\alpha_i M) \times \frac{1}{2} \times \int_{y=-\frac{a}{2}}^{\frac{a}{2}} \left(e^{j(\beta_i+V_2)y} + e^{j(-\beta_i+V_2)y} \right) \times e^{jV_2y}\, dy \quad ;\ B = a$$

For $i = 1, \beta_i = \beta_1 = \frac{2\pi(m-n)}{3a}$;

$$FF_{y3}^{(m-n)} = \frac{1}{2} \times cos(\alpha_1 M) \times \left[\frac{1}{j(\beta_1 + V_2)} \left(e^{j(\beta_1+V_2)\frac{a}{2}} - e^{-j(\beta_1+V_2)\frac{a}{2}} \right) + \frac{1}{j(-\beta_1 + V_2)} \left(e^{j(-\beta_1+V_2)\frac{a}{2}} - e^{-j(-\beta_1+V_2)\frac{a}{2}} \right) \right]$$

$$= \frac{1}{2} \times cos(\pi l) \times \left(\frac{2sin\left(\frac{(\beta_1+V_2)a}{2}\right)}{(\beta_1+V_2)} - \frac{2sin\left(\frac{(-\beta_1+V_2)a}{2}\right)}{(\beta_1-V_2)} \right)$$

$$= \frac{cos(\pi l)}{\left(\frac{2\pi}{3a}\right)^2((m-n)^2-v^2)} \times \frac{4\pi}{3a}$$

$$\times \left[(m-n)\, sin\left(\frac{\pi(m-n)}{3}\right) cos\left(\frac{V_2 a}{2}\right) - 2V_2 . \frac{3a}{4\pi} cos\left(\frac{\pi(m-n)}{3}\right) sin\left(\frac{V_2 a}{2}\right) \right]$$

$$FF_{y3}^{(m-n)} = \frac{3a\, cos(\pi l)}{\pi[(m-n)^2-v^2]}$$

$$\times \left[(m-n)\, sin\left(\frac{\pi(m-n)}{3}\right) cos\left(\frac{\pi v}{3}\right) - v\, cos\left(\frac{\pi(m-n)}{3}\right) sin\left(\frac{\pi v}{3}\right) \right] \qquad (3.14d)$$

$$v = \frac{3aV_2}{2\pi} = \frac{3ak_o sin(\theta)\, sin(\varphi)}{2\pi} \quad ; \quad \frac{V_2 a}{2} = \frac{\pi v}{3}$$

Similarly,

$$FF_{y3}^{(n-l)} = \frac{3a\cos(\pi m)}{\pi[(n-l)^2-v^2]} \times \left[(n-l)\sin\left(\frac{\pi(n-l)}{3}\right)\cos\left(\frac{\pi v}{3}\right) - v\cos\left(\frac{\pi(n-l)}{3}\right)\sin\left(\frac{\pi v}{3}\right) \right]$$

$$FF_{y3}^{(l-m)} = \frac{3a\cos(\pi n)}{\pi[(l-m)^2-v^2]}$$

$$\times \left[(l-m)\sin\left(\frac{\pi(l-m)}{3}\right)\cos\left(\frac{\pi v}{3}\right) - v\cos\left(\frac{\pi(l-m)}{3}\right)\sin\left(\frac{\pi v}{3}\right) \right]$$

Hence,

$$I_{BC}^{y1} = \frac{3a\cos(\pi m)}{\pi[(n-l)^2-v^2]} \times \left[(n-l)\sin\left(\frac{\pi(n-l)}{3}\right)\cos\left(\frac{\pi v}{3}\right) - v\cos\left(\frac{\pi(n-l)}{3}\right)\sin\left(\frac{\pi v}{3}\right) \right]$$

$$+ \frac{3a\cos(\pi n)}{\pi[(l-m)^2-v^2]} \times \left[(l-m)\sin\left(\frac{\pi(l-m)}{3}\right)\cos\left(\frac{\pi v}{3}\right) - v\cos\left(\frac{\pi(l-m)}{3}\right)\sin\left(\frac{\pi v}{3}\right) \right]$$

$$+ \frac{3a\cos(\pi l)}{\pi[(m-n)^2-v^2]} \times \left[(m-n)\sin\left(\frac{\pi(m-n)}{3}\right)\cos\left(\frac{\pi v}{3}\right) - v\cos\left(\frac{\pi(m-n)}{3}\right)\sin\left(\frac{\pi v}{3}\right) \right] \qquad (3.15)$$

Summary:

The components for far-zone electric fields are summarized here as:

$$F_x = F_x^{AC} + F_x^{AB}$$
$$F_y = F_y^{AC} + F_y^{AB} + F_y^{BC}$$
$$F_z = 0 \tag{3.16}$$

where

$$F_x^{AC} = C_{xy} \times [-E_3] \times (\chi^2) \times (I_{AC}^{x1} \times I^z)$$
$$F_y^{AC} = C_{xy} \times [-E_3] \times (\chi^2) \times (I_{AC}^{Y1} \times I^z)$$

$$F_x^{AB} = C_{xy} \times [E_3] \times (\chi^2) \times (I_{AB}^{x4} \times I^z)$$
$$F_y^{AB} = C_{xy} \times [-E_3] \times (\chi^2) \times (I_{AB}^{y2} \times I^z)$$

$$F_y^{BC} = C_{xy} \times [E_3] \times (\chi^2) \times e^{jV_1M} \times I_{BC}^{y1} \times I^z$$
$$I^z = 2d \times sinc(dV_3)$$

$$I_{AC}^{x1} = \frac{-j}{((n-l)^2b^2 - \chi_1^2)} \times \left[e^{j\chi_1 M}\{jb(n-l)\sin(b(n-l)M) - \chi_1\cos(b(n-l)M)\} + \chi_1\right]$$
$$+\frac{-j}{((l-m)^2b^2 - \chi_1^2)} \times \left[e^{j\chi_1 M}\{jb(l-m)\sin(b(l-m)M) - \chi_1\cos(b(l-m)M)\} + \chi_1\right]$$
$$+\frac{-j}{((m-n)^2b^2 - \chi_1^2)} \times \left[e^{j\chi_1 M}\{jb(m-n)\sin(b(m-n)M) - \chi_1\cos(b(m-n)M)\} + \chi_1\right]$$

$$I_{AC}^{y1} = \frac{-j}{\sqrt{3}((n-l)^2b^2 - \chi_1^2)} \times \left[e^{j\chi_1 M}\{jb(n-l)\sin(b(n-l)M) - \chi_1\cos(b(n-l)M)\} + \chi_1\right]$$
$$+\frac{-j}{\sqrt{3}((l-m)^2b^2 - \chi_1^2)} \times \left[e^{j\chi_1 M}\{jb(l-m)\sin(b(l-m)M) - \chi_1\cos(b(l-m)M)\} + \chi_1\right]$$
$$+\frac{-j}{\sqrt{3}((m-n)^2b^2 - \chi_1^2)} \times \left[e^{j\chi_1 M}\{jb(m-n)\sin(b(m-n)M) - \chi_1\cos(b(m-n)M)\} + \chi_1\right]$$

$$I_{AB}^{x2} = I_{AC}^{x1}|_{\chi_1=\chi_2}$$

$$I_{AB}^{y2} = \frac{-j}{\sqrt{3}((n-l)^2b^2 - \chi_2^2)} \times \left[e^{j\chi_2 M}\{jb(n-l)\sin(b(n-l)M) - \chi_2\cos(b(n-l)M)\} + \chi_2\right]$$
$$+\frac{-j}{\sqrt{3}((l-m)^2b^2 - \chi_2^2)} \times \left[e^{j\chi_2 M}\{jb(l-m)\sin(b(l-m)M) - \chi_2\cos(b(l-m)M)\} + \chi_2\right]$$

$$+\frac{-j}{\sqrt{3}((m-n)^2b^2-\chi_2^2)}\times\left[e^{j\chi_2 M}\{jb(m-n)\sin(b(m-n)M)-\chi_2\cos(b(m-n)M)\}+\chi_2\right]$$

$$I_{BC}^{y1}=\frac{3a\cos(\pi m)}{\pi[(n-l)^2-v^2]}\times\left[(n-l)\sin\left(\frac{\pi(n-l)}{3}\right)\cos\left(\frac{\pi v}{3}\right)-v\cos\left(\frac{\pi(n-l)}{3}\right)\sin\left(\frac{\pi v}{3}\right)\right]$$
$$+\frac{3a\cos(\pi n)}{\pi[(l-m)^2-v^2]}\times\left[(l-m)\sin\left(\frac{\pi(l-m)}{3}\right)\cos\left(\frac{\pi v}{3}\right)-v\cos\left(\frac{\pi(l-m)}{3}\right)\sin\left(\frac{\pi v}{3}\right)\right]$$
$$+\frac{3a\cos(\pi l)}{\pi[(m-n)^2-v^2]}\times\left[(m-n)\sin\left(\frac{\pi(m-n)}{3}\right)\cos\left(\frac{\pi v}{3}\right)-v\cos\left(\frac{\pi(m-n)}{3}\right)\sin\left(\frac{\pi v}{3}\right)\right]$$

$$V_1=k_o\,sin(\theta)\,cos(\varphi)\;\;;\;\;V_2=k_o\,sin(\theta)\,sin(\varphi)\;\;;\;\;V_3=k_o\,cos(\theta)\;\;;\;v=\frac{3aV_2}{2\pi}$$

$$\chi_1=\left(V_1+V_2/\sqrt{3}\right)\;\;;\;\chi_2=\left(V_1-V_2/\sqrt{3}\right)\;\;;\;b=\frac{4\pi}{3\sqrt{3}a}\;\;;\;sinc(x)=\frac{sin(x)}{x}$$

Here, C_{xy} is constant and other terms are carrying their usual meaning. Therefore, the far-zone electric field at point $P(r,\theta,\varphi)$ can be expressed as [16]:

$$E_\theta=-\frac{jk_o\exp(-jk_or_d)}{4\pi r}\times exp(-jV_1R)\times\left[L_\varphi\right] \quad (3.17a)$$

$$E_\varphi=\frac{jk_o\exp(-jk_or_d)}{4\pi r}\times exp(-jV_1R)\times\left[L_\theta\right] \quad (3.17b)$$

where

$$L_\theta=F_xcos(\theta)cos(\varphi)+F_ycos(\theta)sin(\varphi)-F_zsin(\theta) \quad (3.18a)$$

$$L_\varphi=-F_xsin(\varphi)+F_ycos(\varphi) \quad (3.18b)$$

Here, all terms are carrying their usual meaning.

3.2.4 Input Impedance

The conventional concept of 'filamentary current model' is used here to evaluate the input impedance of a probe fed ETMA. The current is modeled as a one dimensional uniform current ribbon having effective width w_x along x axis as:

$$\vec{J} = \hat{z}J(x)\delta(y) \tag{3.19}$$

where

$$J(x) = \begin{cases} \frac{I_o}{w_x}, & x_o - \frac{w_x}{2} \le x \le x_o + \frac{w_x}{2} \\ 0, & \text{elsewhere} \end{cases} \quad ; \quad X_o = -a/\sqrt{3} + g \tag{3.20}$$

The RF voltage $V_{in}(= -E_z(x_o, y_o)d)$ is evaluated at the feed point (x_o, y_o) and the input impedance is then calculated as [13]:

$$Z_{in} = R + jX = \frac{V_{in}}{I_o} = -j\omega\mu\frac{d}{I_o}\sum_{m=0}^{\infty}\sum_{n=m}^{\infty}\frac{A_{mn}\psi_{mn}(x_o, y_o)}{\left[k_o^2\varepsilon_r\left(1 - j\delta_{eff}\right) - k_{mn}^2\right]} \tag{3.21}$$

where $k^2 = k_o^2\varepsilon_r\left(1 - j\delta_{eff}\right)$ and $\delta_{eff}(= 1/Q_t)$ is effective loss tangent where Q_t is total quality factor.

3.2.5 Radiated Power, Quality factor, Efficiency and Gain

For efficient evaluation of the input impedance of an ETMA, we have to evaluate the quality factor (Q-factor) accurately. The total Q-factor (Q_t) is evaluated as [12-15]:

$$Q_t = \frac{\omega_r W_t}{P_c + P_d + P_r} \tag{3.22}$$

where W_t is the total energy stored in the patch at resonance ω_r, P_c and P_d are conductor loss and dielectric loss respectively and P_r is radiated power. These quantities are evaluated using standard procedures as [12-15]:

$$P_d = \frac{\omega\varepsilon_o\varepsilon_r tan\delta}{2}\iiint |E|^2 dv \tag{3.23}$$

$$P_c = 2 \times \frac{R_s}{2}\iint |H_s|^2 ds \tag{3.24}$$

$$P_r = \frac{1}{2\eta_o} \int_{\varphi=0}^{2\pi} \int_{\theta=0}^{\pi/2} \left(|E_\theta|^2 + |E_\varphi|^2 \right) r^2 sin\theta d\theta d\varphi \quad (3.25)$$

$$W_t = \frac{\varepsilon_o \varepsilon_r}{2} \iiint |E|^2 dv \quad (3.26)$$

$$BW = \frac{1}{Q_t \sqrt{2}} \times 100\% \quad (3.27)$$

$$e = \frac{P_r}{P_c + P_d + P_r} \times 100\% \quad (3.28)$$

$$D = \frac{4\pi U_{max}}{P_r} \quad (3.29)$$

$$G = eD \quad (3.30)$$

$$U_{max} = \frac{r^2}{2\eta_o} \times \left[|E_\theta|^2 + |E_\varphi|^2 \right]_{max} \quad (3.31)$$

Here e, R_s, ω_r and $tan\delta$ are efficiency, surface resistivity, resonant frequency and loss tangent of the substrate respectively and other symbols are carrying their usual meaning. The effect of surface wave ($f_c^{TM} = nc/\left(2d\sqrt{\varepsilon_r - 1}\right)$, $n =$ 0,1,2 ... and $f_c^{TE} = (2n-1)c/\left(4d\sqrt{\varepsilon_r - 1}\right)$, $n =$ 1,2,3 ... [163]) is neglected here as the 1st higher order mode i.e. TE_1 mode shows much higher frequency than our investigated operating frequency range.

3.3 Results

In this section, theoretical results on resonant frequency, far-field patterns, input impedance, etc. are discussed for various TM_{mn}^z modes. Theoretical results are verified against experimental data as reported in [6, 15, 58]. MATLAB™ [164] routines are written for numerical implementation.

3.3.1 Resonant Frequency

The resonant frequency is calculated using effective length (a_e) of the ETMA as shown in Table 3.2. Slight modification in the effective length (a_e) is able to predict the resonant frequency with an error of 1.5% only.

Table 3.2

Experimental validation of resonant frequency

($a = 100mm, \varepsilon_r = 2.32$)

Sl No	Mode	Resonant Frequency (GHz)			Error (%)	
		Mea. [6]	Theory [6]	Our	Theory [6]	Our
1	TM_{10}^z	1.280	1.2989	1.2928	1.4799	0.99954
2	TM_{11}^z	2.242	2.2498	2.2392	0.34949	-0.12555
3	TM_{20}^z	2.550	2.5979	2.5856	1.8779	1.3956
4	TM_{21}^z	3.400	3.4367	3.4204	1.0788	0.60035
5	TM_{30}^z	3.824	3.8968	3.8784	1.9045	1.4221

3.3.2 Input Impedance

The knowledge of input impedance is very important for designing an antenna. The coaxial probe is modeled here as uniform current ribbon of effective width w_x along x axis. The value of w_x is considered equal to 6mm as found in [6].

It is important to discuss the effect of total Q-factor (Q_t) on the input impedance characteristics. Accurate computation of Q_t plays an important role to predict the input impedance accurately. If Q_t changes for fixed value of a and ε_r, the magnitude of the input impedance changes. Typical results are shown for TM_{10}^z mode in Fig. 3.4. This type of variation is found in all other modes also.

The experimental values of Q_t for TM_{10}, TM_{20} and TM_{21} modes are 122, 72 and 99 respectively for $a = 100mm, d = 1.59mm$ and $\varepsilon_r = 2.32$ at the resonant frequency [6]. Theoretical values for the same are 128.95, 74.097 and 99.969 respectively. Theoretical and experimental [58] input impedance variations with frequency of an ETMA having $a = 100mm, d = 1.59mm, g = 3mm$ and $\varepsilon_r = 2.32$ are shown in Fig. 3.5 for first five modes.

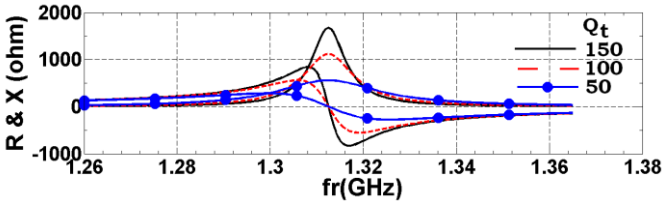

Fig. 3.4 Effect of Q-factor (Q_t) on the input impedance characteristics at TM_{10}^z mode ($a = 100\text{mm}, d = 1.59\text{mm}, \varepsilon_r = 2.32, g = 13mm$)

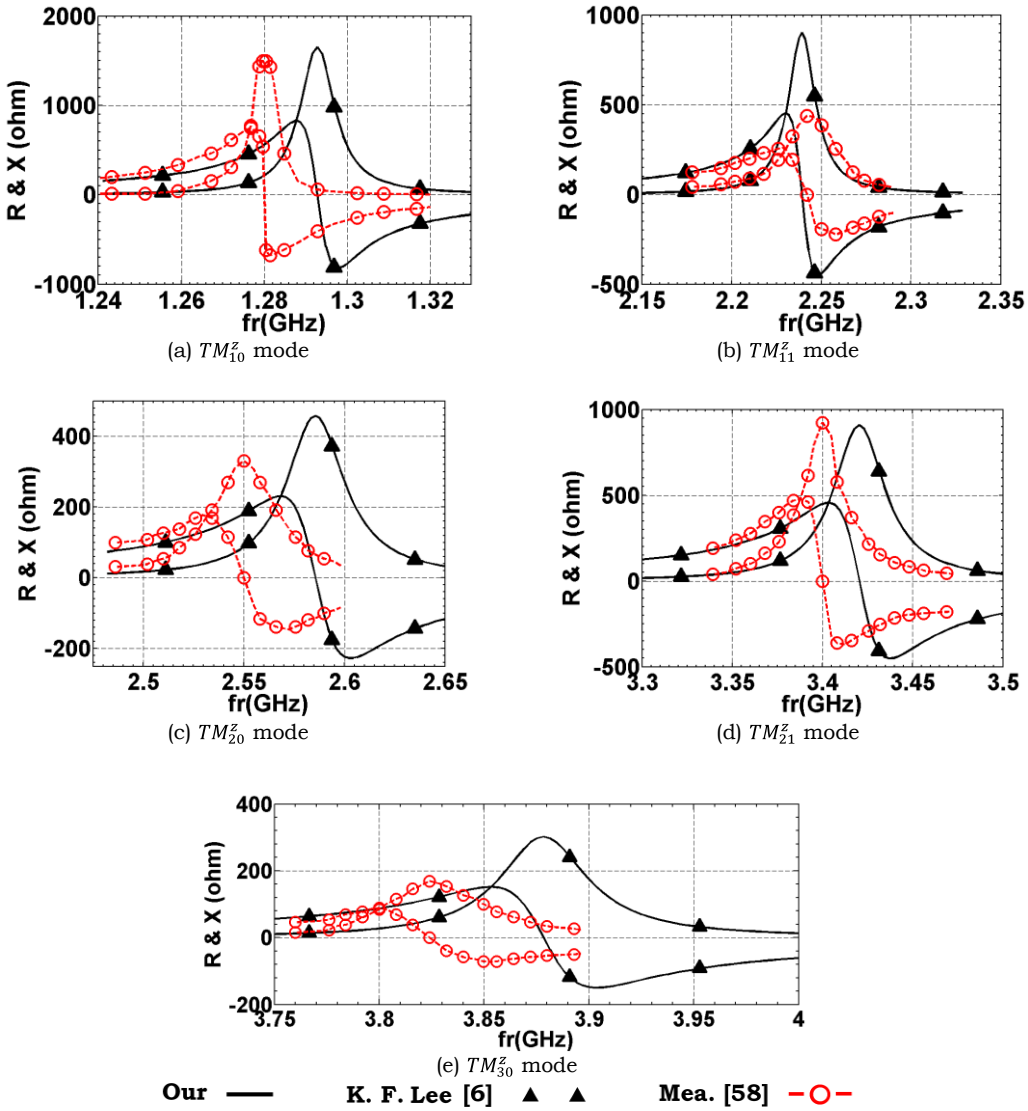

Fig. 3.5 Comparison of input impedance with experimental data for different modes ($a = 100mm, h = 1.59mm, g = 3mm, \varepsilon_r = 2.32$)

From Fig. 3.5, it is found that the variation of the input impedance with frequency for $g = 3mm$ is in close agreement for TM_{10}^z and TM_{21}^z modes.

Although the theoretical and experimental Q_t for TM_{20} mode are close to each other, but a significant error is observed in the real part of the input impedance. This type of discrepancy is also reported in [6].

The theory developed here using cavity model is exactly the same as reported in [6]. Therefore, our theoretical results are similar to [6]. One interesting point is observed during this work. In [6], variation of input impedance with frequency for TM_{11}^z and TM_{30}^z modes had not been reported. From Fig. 3.5(b) and 3.5(d), it is found that the theoretical input impedance is almost doubled with respect to the experimental data. It is worth mentioning here that these two modes (TM_{11}^z and TM_{30}^z modes) produce a null in the broadside direction as will be seen in the next section.

3.3.3 Radiation Patterns

A detailed description of normalized far-field radiation patterns have been reported in [6]. Therefore, the theoretical results on the far-field patterns are plotted here using the absolute value of gain (in dB) as shown in Figs. 3.6. From Fig. 3.6, it found that TM_{10}^z, TM_{20}^z and TM_{21}^z modes are radiating in the broadside direction, whereas TM_{11}^z and TM_{30}^z modes show a null in the broadside direction.

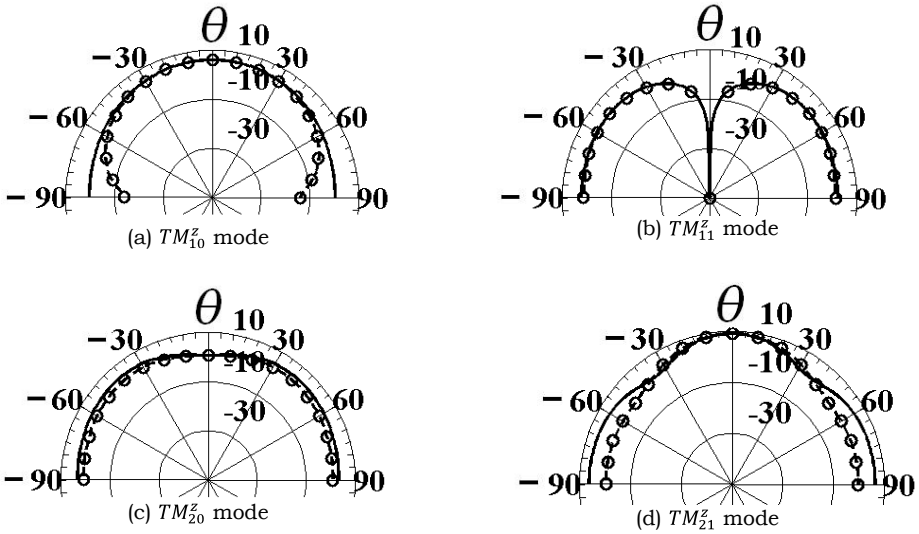

(a) TM_{10}^z mode (b) TM_{11}^z mode

(c) TM_{20}^z mode (d) TM_{21}^z mode

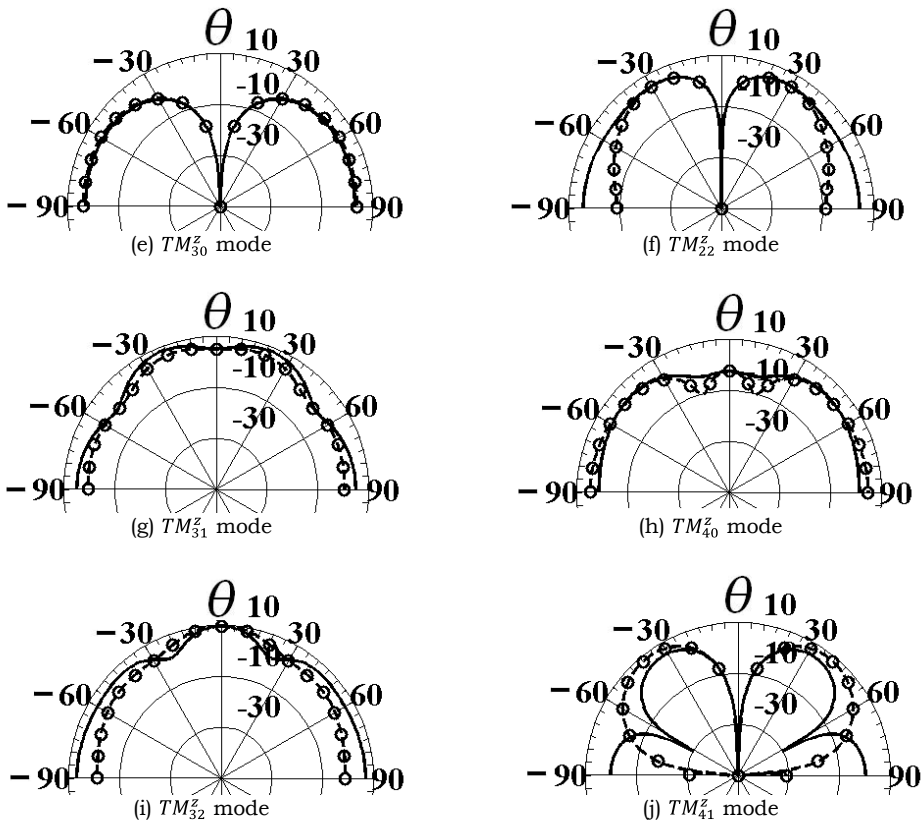

Fig. 3.6 Far-field E-plane (solid line) and H-plane (dashed line with circle) power patterns of an ETMA for different modes (a = 100mm, d = 1.59mm, ε_r = 2.32)

Theoretical far-field radiation patterns are also compared with experimental data [15] for dominant TM_{10} mode. It is found that the far-field power patterns are in good agreement with experimental data as shown in Fig. 3.7.

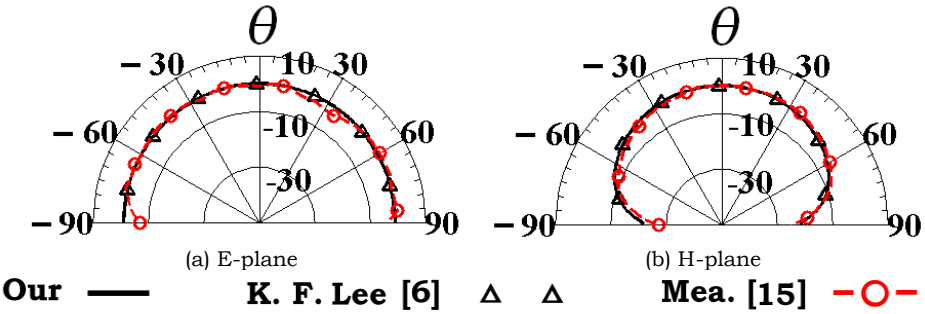

Fig. 3.7 Experimental validation of far-field power patterns of an ETMA for TM^z_{10} mode (d = 1.27, ε_r = 10 at 9.6GHz)

3.3.4 Radiated Power, Quality factor, Efficiency and Gain

Radiated power in percentage P_r (in %), defined as $(2\pi/Q_r) \times 100$ where Q_r is radiation Q-factor, total Q-factor (Q_t), gain, bandwidth (BW), efficiency (e) etc. are also calculated using this theory. These are shown for the first five modes in Fig. 3.8. In Fig. 3.8, the antenna specification of the ETMA ($a = 100\text{mm}, h = 1.59\text{mm}$ and $\varepsilon_r = 2.32$) is kept here same as reported in [6] to show the correctness of our computation. It is found from Fig. 3.8 that the radiated power (P_r in %), gain (G) and radiation efficiency (e in %) are directly to proportional to the resonant frequency and increases with frequency as shown in Fig. 3.8(a), 3.8(c) and 3.8(e) respectively. Total Q-factor is increasing up to a certain value of frequency and after that it is decreasing with frequency for a particular mode as shown in Fig. 3.8(b). From Fig. 3.8 (d), it is found that the BW is decreasing up to a certain value of frequency and after that it is increasing with frequency as expected because BW is just inversely related to the total Q - factor.

In Table 3.3, radiation characteristics of first few modes are shown for $a = 100mm, h = 1.59mm, \varepsilon_r = 2.32$ and $tan\delta = 0.0005$. Radiated power (P_r in %), radiation Q-factor (Q_r), total Q-factor (Q_t), BW (in %), gain (in dB), radiation efficiency (e) are shown. From Table 3.3, it is found that most of the higher order modes produce a higher gain compared to fundamental TM_{10}^z mode.

It should be pointed here that our theoretical Q-factors, Q_r and Q_t as shown in Table 3.3 are little bit higher compared to the theoretical data as reported in [6]. This is due to slight modification in the calculation of effective length (a_e) of the ETMA. This small change can predict the resonant frequency with an error of 1.5%, whereas the maximum error as reported in [6] is 2% (for TM_{30}^z mode).

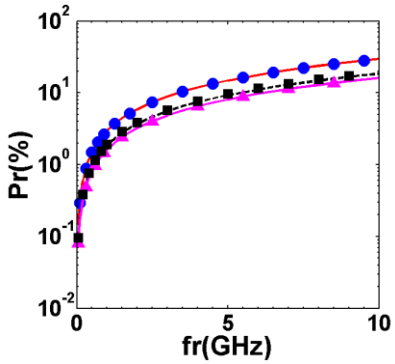

(a) Variation of P_r (in %) with frequency

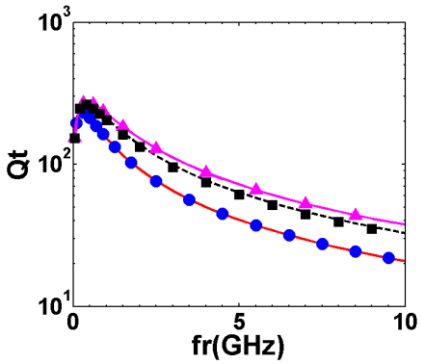

(b) Variation Q_t with frequency

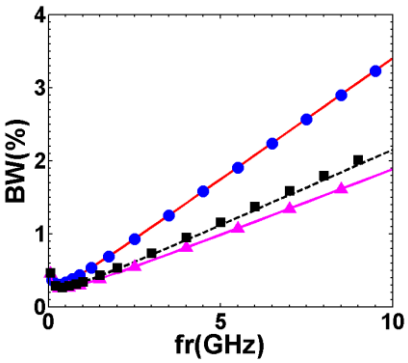

(c) Variation of BW with frequency

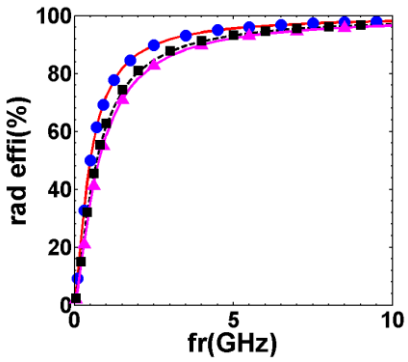

(d) Variation of $e(\%)$ with frequency

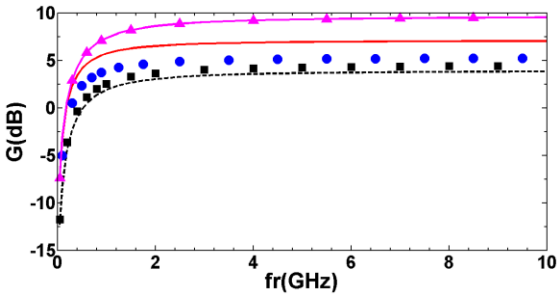

(e) Variation of G with frequency

TM_{10}^z TM_{11}^z TM_{20}^z TM_{21}^z TM_{30}^z

Fig. 3.8 Radiation characteristics of an ETMA for different modes ($d = 1.59\text{mm}, \varepsilon_r = 2.32$)

Table 3.3

Radiation characteristics of first few modes of an ETMA

($a = 100mm, d = 1.59mm, \varepsilon_r = 2.32, tan\delta = 0.0005$)

Sl No	Mode	f_r (GHz)	$P_r(\%)$	Q_r	Q_t	BW (%)	Gain (dB)	$e(\%)$
1	TM_{10}^z	1.293	3.832	164	129	0.5483	6.083	78.64
2	TM_{11}^z	2.239	4.148	151.5	125.3	0.5643	3.146	82.73
3	TM_{20}^z	2.586	7.652	82.11	74.1	0.9543	4.882	90.24
4	TM_{21}^z	3.42	5.525	113.7	99.96	0.7074	9.115	87.9
5	TM_{30}^z	3.878	7.459	84.24	76.69	0.922	4.155	91.05
6	TM_{22}^z	4.478	7.609	82.57	75.57	0.9356	5.281	91.53
7	TM_{31}^z	4.661	5.268	119.3	105.3	0.6713	8.296	88.32
8	TM_{40}^z	5.171	8.07	77.86	71.83	0.9844	5.441	92.26
9	TM_{32}^z	5.635	7.742	81.15	74.76	0.9458	9.752	92.12
10	TM_{41}^z	5.924	3.29	191	159.3	0.4438	8.267	83.43
11	TM_{50}^z	6.464	7.71	81.49	75.25	0.9396	6.728	92.35
12	TM_{33}^z	6.718	8.067	77.88	72.22	0.9791	7.125	92.73
13	TM_{42}^z	6.841	7.538	83.36	76.93	0.9192	8.208	92.29
14	TM_{51}^z	7.198	6.71	93.64	85.69	0.8252	7.317	91.52
15	TM_{60}^z	7.757	7.477	84.04	77.69	0.9101	6.278	92.45

3.4 Conclusion

In this chapter, Equilateral Triangular Microstrip Antenna (ETMA) is investigated using the cavity model. Although the investigations on ETMA have been reported three decades earlier (in 1988) by K. F. Lee *et al* [6], we have derived it analytically. It will help us to investigate the other triangular shaped radiators viz. Triangular Microstrip Antenna (TMA) or Triangular Dielectric Resonator Antenna (TDRA).

From this investigation, it is found that:

- TM_{10}, TM_{20} and TM_{21} modes produce a peak in the broadside direction
- TM_{11} and TM_{30} modes produce a null in the broadside direction
- Input impedance characteristics are in good agreement with experimental data for TM_{10}, TM_{20} and TM_{21} modes

- The theoretical magnitude of the input impedance is almost double compared to experimental data for TM_{11} and TM_{30} modes. These two modes produce null in the broadside direction.
- Most of the higher order modes produce a higher gain compared to fundamental TM_{10}^{z} mode.

Chapter IV

30°–60°–90° Triangular Microstrip Antenna

4.1 Introduction

In Chapter III, Equilateral Triangular Microstrip Antenna (ETMA) is investigated. If we divide the ETMA along its median, we will get two identical 30°–60°–90° Triangular Microstrip Antennas (TMA). Literature survey shows that researchers have focused to compute the resonant frequencies for different modes of a 30°–60°–90° TMA [155]. Input impedance of 30°–60°–90° TMA has also been reported for fundamental mode only [152]. Radiation characteristics of a 30°–60°–90° TMA has not been reported so far.

In this chapter, 30°–60°–90° TMA is investigated analytically using cavity model [12-15]. Modal analysis is performed for TM_{mn}^{z} mode of a probe fed 30°–60°–90° TMA. For theoretical investigation, the coaxial probe is modeled in three different ways:

I. One dimensional (1D) uniform ribbon along $\hat{x}$ direction
II. One dimensional (1D) uniform ribbon along $\hat{y}$ direction
III. Two dimensional (2D) rectangular shaped sheet.

Closed form expressions are given here for predicting the far-field radiation patterns of a 30°–60°–90° TMA. Input impedance, Q-factor, radiated powers (in %), Gain (G), Band Width (BW) etc. are investigated. Theoretical results are verified with experimental data.

The study of 30°–60°–90° TMA is very important to design a compact antenna with respect to conventional regular shaped MAs. At fundamental mode of operation around 2.6GHz, the rectangular, circular, annular ring, semi-circular and equilateral triangular MAs take almost 3.6, 3.2, 2.5, 1.6 and 2 times area compared to 30°–60°–90° TMA respectively where all antennas

have been excited using a 50Ω coaxial-probe [151, Table 2.13]. Further, Study of 30°–60°–90° TMA is very important compared to the above mentioned MAs from far-field radiation point of view. It is found that the first 9 modes of the 30°–60°–90° TMA shows a peak in the broadside direction as discussed in this chapter.

It should be pointed here that we have reported most of this works in [165-166] during our dissertational research. First five modes are discussed in those papers. Therefore, in this chapter, we will discuss the radiation characteristics of first 10 modes for TM_{mn}^{z} mode of a probe fed 30°–60°–90° TMA.

4.2 Theory

In this section, 30°–60°–90° TMA is investigated analytically using conventional cavity model [12-15]. In Fig. 4.1, the antenna geometry is shown in the standard Cartesian coordinate system. Base (AB) length of the 30°–60°–90° TMA is a and the probe is placed at (x_o, y_o) point. The antenna is placed on a grounded substrate whose thickness (d) is small compared to the operating wavelength. Eigenfunctions, eigenvalues, far-field radiation patterns, input impedance, Q-factor, gain, bandwidth etc. are investigated. One antenna prototype is fabricated for experimental validation.

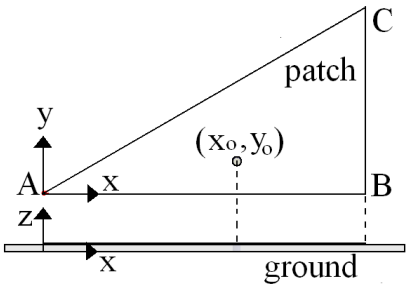

Fig. 4.1 Geometry of 30°–60°–90°TMA

4.2.1 Eigenfunctions

The conventional cavity model is used to investigate the 30°–60°–90° TMA which support TM_{mn}^{z} mode only. Assuming no variation along $\hat{z}$ direction (thin substrate i.e. thickness of substrate d is much less than operating wavelength) as shown in Fig. 4.1, the eigenfunctions ψ_{mn} will be a function of x-

y coordinate only. To predict the approximate solution for eigenfunctions (ψ_{mn}) of 30°–60°–90° TMA for TM^z mode, the concept of duality is applied as found for equilateral triangular resonator in [25, 27]. The eigenfunctions (ψ) for TE^z mode with electric boundary condition i.e. Dirichlet boundary condition ($\psi = 0$) is equivalent to the eigenfunctions for TM^z mode with magnetic boundary condition i.e. Neumann boundary condition ($d\psi/dn = 0$). For, example [4, 16, 24], a waveguide (metallic or dielectric) is placed in the *x-y-z* coordinate system such that $0 \leq x \leq a,\ 0 \leq y \leq b$ and it is infinitely long along the *z*-direction. If the waveguide is bounded in the *x-y* direction by metals, the boundary conditions will be a Dirichlet boundary condition ($\psi = 0$). Applying this condition for TE^z mode, one can easily obtain

$$\psi_{TE^z_{mn}}(x,y) = cos\left(\frac{m\pi x}{a}\right) cos\left(\frac{n\pi y}{b}\right) \tag{4.2a}$$

Here, all terms are carrying their usual meaning. In case of dielectric waveguide, the boundary conditions will be a Neumann boundary condition ($d\psi/dn = 0$). Applying this condition for TM^z mode, we obtain

$$\psi_{TM^z_{mn}}(x,y) = cos\left(\frac{m\pi x}{a}\right) cos\left(\frac{n\pi y}{b}\right) \tag{4.2b}$$

Hence, the eigenfunctions (ψ_{mn}) of 30°–60°–90° triangular resonator having Perfect Magnetic Conductor (PMC) for TM^z mode can be found by duality from TE^z mode of 30°–60°–90° triangular waveguide with the Perfect Electric Conductor (PEC) and is given by [52, 153-154]:

$$\psi_{mn}(x,y) = \cos\frac{\pi l x}{a}\cos\left(\frac{\pi(m-n)}{\sqrt{3}a}y\right) + \cos\frac{\pi m x}{a}\cos\left(\frac{\pi(n-l)}{\sqrt{3}a}y\right) + \cos\frac{\pi n x}{a}\cos\left(\frac{\pi(l-m)}{\sqrt{3}a}y\right) \tag{4.3}$$

where m, n, l are mode indices such that $l + m + n = 0$. Hence, the internal field for TM^Z mode due to probe excitation ($\vec{J}$) is given by:

$$E_z = \sum_{m=0}^{\infty}\sum_{n=0}^{\infty} A_{mn}\psi_{mn}(x,y) \quad ; \quad A_{mn} = \frac{j\omega\mu}{(k^2 - k_{mn}^2)} \frac{< J\psi_{mn} >}{< \psi_{mn}\psi_{mn} >} \tag{4.4}$$

The complete internal field configuration is

$$E_z = A_{mn}\left[\cos\left(\frac{l\pi x}{a}\right)\cos\left\{\frac{(m-n)\pi y}{\sqrt{3}a}\right\} + \cos\left(\frac{m\pi x}{a}\right)\cos\left\{\frac{(n-l)\pi y}{\sqrt{3}a}\right\} + \cos\left(\frac{n\pi x}{a}\right)\cos\left\{\frac{(l-m)\pi y}{\sqrt{3}a}\right\}\right]$$

$$H_x = \frac{jA_{mn}}{\omega\mu\varepsilon}\left[\frac{(m-n)\pi}{\sqrt{3}a}\cos\left(\frac{l\pi x}{a}\right)\sin\left\{\frac{(m-n)\pi y}{\sqrt{3}a}\right\} + \frac{(n-l)\pi}{\sqrt{3}a}\cos\left(\frac{m\pi x}{a}\right)\sin\left\{\frac{(n-l)\pi y}{\sqrt{3}a}\right\} + \frac{(l-m)\pi}{\sqrt{3}a}\cos\left(\frac{n\pi x}{a}\right)\sin\left\{\frac{(l-m)\pi y}{\sqrt{3}a}\right\}\right]$$

$$H_y = -\frac{jA_{mn}}{\omega\mu\varepsilon}\left[\frac{l\pi}{a}\sin\left(\frac{l\pi x}{a}\right)\cos\left\{\frac{(m-n)\pi y}{\sqrt{3}a}\right\} + \frac{m\pi}{a}\sin\left(\frac{m\pi x}{a}\right)\cos\left\{\frac{(n-l)\pi y}{\sqrt{3}a}\right\} + \frac{n\pi}{a}\sin\left(\frac{n\pi x}{a}\right)\cos\left\{\frac{(l-m)\pi y}{\sqrt{3}a}\right\}\right]$$

$$H_z = E_x = E_y = 0 \tag{4.5}$$

The contour of electric field on the antenna surface is shown in Fig. 4.2 for first 10 modes of a 30°–60°–90° TMA having $a = 100mm, d = 0.762mm$ and $\varepsilon_r = 2.5$ at their modal frequency. The same antenna is simulated using 3D EM simulator HFSS [9]. Coaxial probe is placed in different positions to excite the 30°–60°–90° TMA. Simulated magnitudes of the total electric field on the antenna surface are also shown in Fig. 4.2. It is found that the magnitude distribution of the electric field on the patch surface is not dependent on the probe position but that alone determines the mode of operation. It is clear from Fig. 4.2 that the approximate solution for the eigenfunctions $\psi_{mn}(x,y)$ as given by equation (4.3) is the required eigenfunctions of the 30°–60°–90° TMA with magnetic wall for TM^z modes.

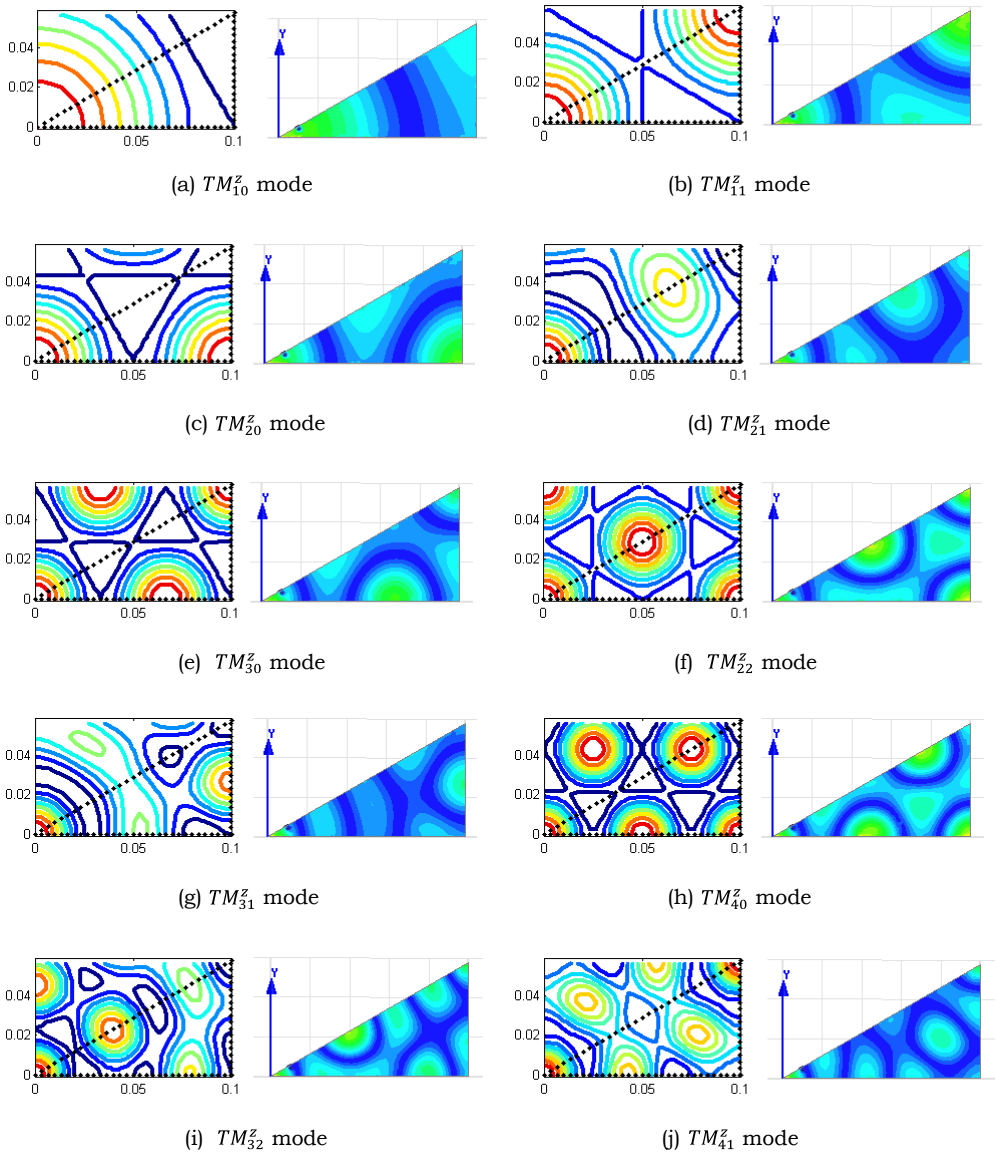

(a) TM_{10}^{z} mode (b) TM_{11}^{z} mode

(c) TM_{20}^{z} mode (d) TM_{21}^{z} mode

(e) TM_{30}^{z} mode (f) TM_{22}^{z} mode

(g) TM_{31}^{z} mode (h) TM_{40}^{z} mode

(i) TM_{32}^{z} mode (j) TM_{41}^{z} mode

Fig. 4.2 Normalized field for different TM_{mn}^{z} modes
Right : Plot of magnitude of the electric field on the patch surface using HFSS
Left : contour plot of eigenfunctions

4.2.2 Resonant Frequency

The eigenvalues for a 30°–60°–90° TMA are given by [52, 153-154]:

$$k^2 = \left(\frac{2\pi}{\sqrt{3}a}\right)^2 (m^2 + mn + n^2) \tag{4.6}$$

The resonant frequency can be found using

$$fr_{mn} = \frac{kc}{2\pi(\varepsilon_r)^{1/2}} \tag{4.7}$$

where c is the velocity of light in free space and ε_r is the relative permittivity of substrate. For fixed values of a, the eigenvalues for the first 20 modes of 30°–60°–90° TMA are shown in Table 4.1.

Table 4.1

Resonant frequencies for first 20 modes of a 30°–60°–90° TMA

($a = 100mm, \varepsilon_r = 2.32$)

Sl No	Mode	Resonant Frequency (GHz)		Sl No	Mode	Resonant Frequency (GHz)
1	TM^z_{10}	1.0950		11	TM^z_{50}	5.4749
2	TM^z_{11}	1.8966		12	TM^z_{33}	5.6897
3	TM^z_{20}	2.1900		13	TM^z_{42}	5.7941
4	TM^z_{21}	2.8970		14	TM^z_{51}	6.0966
5	TM^z_{30}	3.2849		15	TM^z_{43}	6.6605
6	TM^z_{22}	3.7931		16	TM^z_{52}	6.8381
7	TM^z_{31}	3.9480		17	TM^z_{44}	7.5862
8	TM^z_{40}	4.3799		18	TM^z_{53}	7.6648
9	TM^z_{32}	4.7729		19	TM^z_{54}	8.5520
10	TM^z_{41}	5.0178		20	TM^z_{55}	9.4828

To account the effect of fringing, the effective side length (a_e) of the 30°–60°–90° TMA is [27]:

$$a_e = a + 0.25 \times h/(\varepsilon_r)^{1/2} \tag{4.8}$$

4.2.3 Feed Model

Proper feed modeling plays an important role to predict the input impedance characteristics of an antenna. Literature survey shows that the coaxial probe feed has been modelled as either 1D uniform current ribbon [6] or 2D rectangular shaped strip [13]. There is no comparative study between the effects of 1D and 2D feed modeling. In this work, feed ($\vec{J}$) is modeled in three

different ways:

I. Uniform current ribbon of effective width w_x along $\hat{x}$ direction $(\vec{J}_x)$ [6],

II. Uniform current ribbon of effective width w_y along $\hat{y}$ direction $(\vec{J}_y)$ and

III. Two dimensional rectangular shaped strip $(\vec{J}_{xy})$ of effective area $w_x \times w_y$ [13]

These three definitions for the feed can be expressed as:

I. $\vec{J}_x = \hat{z}J(x)\delta(y - y_o)$

$$J(x) = \begin{cases} I_o/w_x, & x_o - w_x/2 \le x \le x_o + w_x/2 \\ 0, & \text{elsewhere} \end{cases} \quad (4.9a)$$

II. $\vec{J}_y = \hat{z}\delta(x - x_o)J(y)$

$$J(y) = \begin{cases} I_o/w_y, & y_o - w_y/2 \le y \le y_o + w_y/2 \\ 0, & \text{elsewhere} \end{cases} \quad (4.9b)$$

III. $\vec{J}_{xy} = \hat{z}J(x, y)$

$$J(x,y) = \begin{cases} I_o/(w_x w_y), x_o - w_x/2 \le x \le x_o + w_x/2 \\ y_o - w_y/2 \le y \le y_o + w_y/2 \\ 0, \quad \text{elsewhere} \end{cases} \quad (4.9c)$$

A comparative study is performed here for the first time between all three types of feed modeling to understand the effect of different definitions.

4.2.4 Far-Field Radiation Patterns

To predict the far-field radiation patterns of a 30°–60°–90° TMA, magnetic surface current $(\vec{M}_s)$ model is used [6, 12-15,162]. Magnetic surface current $(\vec{M}_s)$ is evaluated along its periphery AC, BC and AB sides as

$$\vec{M}_s = 2\vec{E} \times \hat{n} \quad (4.10)$$

The evaluation of far-zone electric fields is exactly similar to as shown for equilateral TMA in Chapter III and is not repeated here for the sake of brevity. The far-zone electric fields at point $P(r,\theta,\varphi)$ can be expressed as:

$$E_\theta = -\frac{jk_o \exp(-jk_o r_d)}{4\pi r} \times exp(jV_1 R) \times \left[L_\varphi\right] \tag{4.11a}$$

$$E_\varphi = \frac{jk_o \exp(-jk_o r_d)}{4\pi r} \times exp(jV_1 R) \times [L_\theta] \tag{4.11b}$$

where

$$L_\theta = F_x cos(\theta)cos(\varphi) + F_y cos(\theta)sin(\varphi) - F_z sin(\theta) \tag{4.12a}$$

$$L_\varphi = -F_x sin(\varphi) + F_y cos(\varphi) \tag{4.12b}$$

$$F_x = 2C_{xy} \times A_{mn} \times (-F_{x1} + F_{x2}) \tag{4.13a}$$

$$F_y = 2C_{xy} \times A_{mn} \times \left(-F_{y1} + e^{jaV_1} \times F_{y2}\right) \tag{4.13b}$$

$$F_{x1} = \frac{-j}{((n-l)^2 b^2 - \chi_1^2)} \times \left[e^{j\chi_1 a}\{jb(n-l)sin(b(n-l)a) - \chi_1 cos(b(n-l)a)\} + \chi_1\right]$$
$$+\frac{-j}{((l-m)^2 b^2 - \chi_1^2)} \times \left[e^{j\chi_1 a}\{jb(l-m)sin(b(l-m)a) - \chi_1 cos(b(l-m)a)\} + \chi_1\right]$$
$$+\frac{-j}{((m-n)^2 b^2 - \chi_1^2)} \times \left[e^{j\chi_1 a}\{jb(m-n)sin(b(m-n)a) - \chi_1 cos(b(m-n)a)\} + \chi_1\right]$$

$$F_{x2} = \frac{a}{\pi[l^2 - \chi_2^2]} \times \left[e^{jV_1 a}\{lsin(l\pi) + j\chi_2 cos(l\pi)\} - j\chi_2\right]$$
$$+ \frac{a}{\pi[m^2 - \chi_2^2]} \times \left[e^{jV_1 a}\{msin(m\pi) + j\chi_2 cos(m\pi)\} - j\chi_2\right]$$
$$+ \frac{a}{\pi[n^2 - \chi_2^2]} \times \left[e^{jV_1 a}\{nsin(n\pi) + j\chi_2 cos(n\pi)\} - j\chi_2\right]$$

$$F_{y1} = \frac{-j}{\sqrt{3}((n-l)^2 b^2 - \chi_1^2)} \times \left[e^{j\chi_1 a}\{jb(n-l)sin(b(n-l)a) - \chi_1 cos(b(n-l)a)\} + \chi_1\right]$$
$$+\frac{-j}{\sqrt{3}((l-m)^2 b^2 - \chi_1^2)} \times \left[e^{j\chi_1 a}\{jb(l-m)sin(b(l-m)a) - \chi_1 cos(b(l-m)a)\} + \chi_1\right]$$
$$+\frac{-j}{\sqrt{3}((m-n)^2 b^2 - \chi_1^2)} \times \left[e^{j\chi_1 a}\{jb(m-n)sin(b(m-n)a) - \chi_1 cos(b(m-n)a)\} + \chi_1\right]$$

$$F_{y2} = \frac{\sqrt{3}a\cos(l\pi)}{\pi[(m-n)^2-\chi_3^2]} \times \left[e^{j\chi_3\pi/3}\left((m-n)sin(\pi(m-n)/3) + j\chi_3\cos(\pi(m-n)/3)\right) - j\chi_3\right] + \frac{\sqrt{3}a\cos(l\pi)}{\pi[(n-l)^2-\chi_3^2]} \times \left[e^{j\chi_3\pi/3}\left((n-l)sin(\pi(n-l)/3) + j\chi_3\cos(\pi(n-l)/3)\right) - j\chi_3\right] + \frac{\sqrt{3}a\cos(l\pi)}{\pi[(l-m)^2-\chi_3^2]} \times \left[e^{j\chi_3\pi/3}\left((l-m)sin(\pi(l-m)/3) + j\chi_3\cos(\pi(l-m)/3)\right) - j\chi_3\right] \quad (4.14)$$

$$C_{xy} = \frac{\varepsilon_o\, d}{4\pi}.\frac{e^{-jk_o r}}{r} \quad ; \quad \eta = \frac{1}{\sqrt{3}} \quad ; \quad b = \frac{2\pi}{3a}$$

$$V_1 = k_o\, sin(\theta)\, cos(\varphi) \quad ; \quad V_2 = k_o\, sin(\theta)\, sin(\varphi)$$

$$\chi_1 = V_1 + \eta V_2 \quad ; \quad \chi_2 = V_1 a/\pi \quad ; \quad \chi_3 = \sqrt{3}aV_2/\pi \quad (4.15)$$

Here, A_{mn} is modal amplitude of a particular mode and other terms are carrying their usual meaning.

4.2.5 Input Impedance

Evaluation of the input impedance (Z_{in}) is straight forward as given in [13]. The RF voltage (V_{in}) at the feed point (x_o, y_o) is evaluated as:

$$V_{in} = -E_z(x_o, y_o)d \quad (4.16)$$

Therefore, the input impedance becomes:

$$Z_{in} = \frac{V_{in}}{I_o} = R + jX = -\frac{d}{I_o}\sum_{m=0}^{\infty}\sum_{n=0}^{\infty} A_{mn}\,\psi_{mn}(x_o, y_o) \quad (4.17)$$

Here, $k^2 = k_o^2\varepsilon_r\left(1 - j\delta_{eff}\right)$, and $\delta_{eff}(= 1/Q_t)$ is effective loss tangent, Q_t is total quality factor. Therefore, accurate evaluation of $A_{mn}\left(= \frac{j\omega\mu}{(k^2-k_{mn}^2)}\,\frac{<J\psi_{mn}>}{<\psi_{mn}\psi_{mn}>}\right)$ will play a vital role to predict the input impedance.

In this dissertation, the feed $(\vec{J})$ is modeled in three different ways as $\vec{J}_x, \vec{J}_y$ and $\vec{J}_{xy}$ as given by equations (4.11a) - (4.11c). The inner product $(< J\psi_{mn} >)$

between the feed ($\vec{J}$) and the eigenfunctions (ψ_{mn}) can be expressed as:

Case I: $\vec{J} = \vec{J}_x = \hat{z}J(x)\delta(y - y_o)$

$$< J\psi_{mn} >= I_o \cos\left(\frac{\pi(m-n)}{\sqrt{3}a} y_o\right) \times \cos\left(\frac{\pi l}{a} x_o\right) \operatorname{sinc}\left(\frac{\pi l}{a}\frac{w_x}{2}\right) + I_o \cos\left(\frac{\pi(n-l)}{\sqrt{3}a} y_o\right) \times \cos\left(\frac{\pi m}{a} x_o\right) \operatorname{sinc}\left(\frac{\pi m}{a}\frac{w_x}{2}\right) + I_o \cos\left(\frac{\pi(l-m)}{\sqrt{3}a} y_o\right) \times \cos\left(\frac{\pi n}{a} x_o\right) \operatorname{sinc}\left(\frac{\pi n}{a}\frac{w_x}{2}\right) \quad (4.18a)$$

Case II: $\vec{J} = \vec{J}_y = \hat{z}\delta(x - x_o)J(y)$

$$< J\psi_{mn} >= I_o \cos\left(\frac{\pi(m-n)}{\sqrt{3}a} y_o\right) \times \cos\left(\frac{\pi l}{a} x_o\right) \operatorname{sinc}\left(\frac{\pi(m-n)}{\sqrt{3}a}\frac{w_y}{2}\right) + I_o \cos\left(\frac{\pi(n-l)}{\sqrt{3}a} y_o\right) \times \cos\left(\frac{\pi m}{a} x_o\right) \operatorname{sinc}\left(\frac{\pi(n-l)}{\sqrt{3}a}\frac{w_y}{2}\right) + I_o \cos\left(\frac{\pi(l-m)}{\sqrt{3}a} y_o\right) \times \cos\left(\frac{\pi n}{a} x_o\right) \operatorname{sinc}\left(\frac{\pi(l-m)}{\sqrt{3}a}\frac{w_y}{2}\right) \quad (4.18b)$$

Case III: $\vec{J} = \vec{J}_{xy} = \hat{z}J(xy)$

$$< J\psi_{mn} >= I_o \cos\left(\frac{\pi l}{a} x_o\right) \operatorname{sinc}\left(\frac{\pi l}{a}\frac{w_x}{2}\right) \times \cos\left(\frac{\pi(m-n)}{\sqrt{3}a} y_o\right) \operatorname{sinc}\left(\frac{\pi(m-n)}{\sqrt{3}a}\frac{w_y}{2}\right) + I_o \cos\left(\frac{\pi m}{a} x_o\right) \operatorname{sinc}\left(\frac{\pi m}{a}\frac{w_x}{2}\right) \times \cos\left(\frac{\pi(n-l)}{\sqrt{3}a} y_o\right) \operatorname{sinc}\left(\frac{\pi(n-l)}{\sqrt{3}a}\frac{w_y}{2}\right) + I_o \cos\left(\frac{\pi n}{a} x_o\right) \operatorname{sinc}\left(\frac{\pi n}{a}\frac{w_x}{2}\right) \times \cos\left(\frac{\pi(l-m)}{\sqrt{3}a} y_o\right) \operatorname{sinc}\left(\frac{\pi(l-m)}{\sqrt{3}a}\frac{w_y}{2}\right) \quad (4.18c)$$

where $\operatorname{sinc}(x) = \sin(x)/x$

4.2.6 Radiated Power, Quality factor, Efficiency and Gain

Radiated power in percentage $P_r(\%)$ which is defined as $(2\pi/Q_r) \times 100$ where Q_r is the radiation quality factor, dielectric loss (P_d), conductor loss (P_c),

radiation loss (P_r), total stored energy (W_t), bandwidth (BW), efficiency (e), directivity (D), gain (G) etc. are also calculated using standard procedure as found [12-15] or as calculated for equilateral TMA in Chapter III. The effect of surface wave loss is neglected here. Therefore, the total quality factor (Q_t) is defined as:

$$Q_t = \frac{\omega_r W_t}{P_c + P_d + P_r} \tag{4.19}$$

4.3 Results

In this section, theoretical results on resonant frequency, far-field patterns, input impedance, etc. are discussed for various TM^z_{mn} modes. One antenna prototype having $a = 100mm, d = 0.762mm, \varepsilon_r = 2.5$ and $tan\,\delta = 0.0035$ is fabricated in our laboratory for experimental validation as shown in Fig. 4.3.

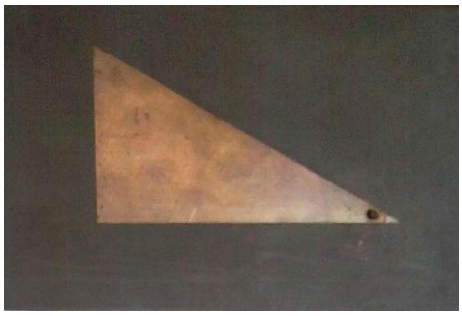

Fig. 4.3 Photograph of fabricated antenna

The antenna is excited using standard 50Ω co-axial probe whose inner conductor radius is 0.63mm. The same is also simulated using FEM based numerical EM simulator HFSS [9] or MoM based commercial software IE3D [8]. The results are verified with experimental data and/or data obtained using an EM simulator.

4.3.1 Resonant Frequency

In this section, theoretical resonant frequencies are compared with our own experimental data. Some experimental data are also collected from [48]. In [48], five antenna geometries have been excited at their fundamental TM^z_{10} mode. In our case, we have successfully excited fist five modes as shown in Table 4.2. It is found that our experimental data show excellent agreement with theoretically computed resonant frequency compared to [48]. This may be due

to manual collection of experimental data from earlier network analyzer in 1983. From Table 4.2, it is found that the maximum absolute error between the theoretical (f_r^t) and our measured (f_r^m) resonant frequency is 0.37%.

Table 4.2

Experimental validation of resonant frequency for TM_{mn}^z modes

Antenna	a (mm)	Mode (TM_{mn}^z)	Res. Freq. (GHz)		Error (%)
			f_r^m	f_r^t	
d = 0.76mm, ε_r = 2.34, $\tan\delta$=0.0018 [48]	62.354	TM_{10}^z	1.722	1.811	5.19
	60.622	TM_{10}^z	1.765	1.863	5.56
	56.292	TM_{10}^z	1.882	2.006	6.59
	51.962	TM_{10}^z	2.046	2.173	6.20
	47.631	TM_{10}^z	2.204	2.37	7.53
d = 0.762mm, ε_r = 2.5, $\tan\delta$=0.0035 (our)	100	TM_{10}^z	1.093	1.094	0.06
	100	TM_{11}^z	1.891	1.894	0.17
	100	TM_{20}^z	2.181	2.187	0.29
	100	TM_{21}^z	2.904	2.894	-0.36
	100	TM_{30}^z	3.269	3.281	0.37

4.3.2 Radiation Patterns

Power patterns for various modes are calculated for different feed modeling ($w_x = w_y = 6mm$). For a particular mode, it is found that J_x, J_y and J_{xy} give non-distinguishable power patterns. For example, typical radiation patterns with gain (dB) for TM_{10} and TM_{21} modes are shown in Figs. 4.4. Therefore, the nature of radiation patterns for various modes is discussed for J_x excitation only.

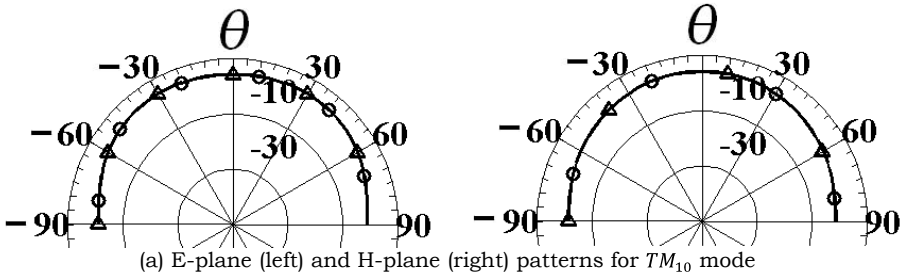

(a) E-plane (left) and H-plane (right) patterns for TM_{10} mode

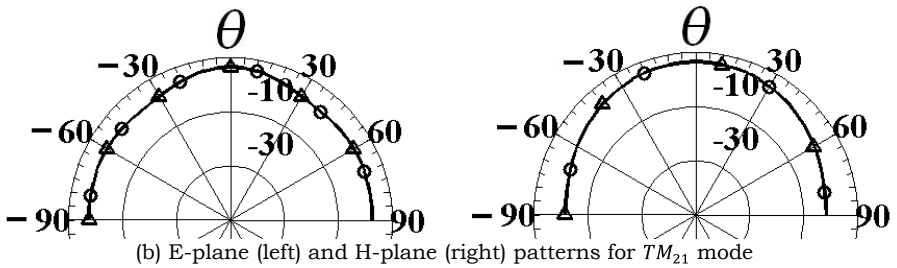

(b) E-plane (left) and H-plane (right) patterns for TM_{21} mode

Fig. 4.4 Comparison of far-field power patterns for different feed: J_x (solid line), J_y (triangle) and J_{xy} (circle) ($a = 100mm, d = 1.59mm, \varepsilon_r = 2.32, tan\,\delta = 0.0005$)

It should be pointed here that the comparison between J_x, J_y and J_{xy} on far-field radiation patterns are shown in our paper [166] for TM_{20} mode which is published as TM_{21} mode. This is a typographical error for which erratum has been communicated to the publishers.

Far-field E-plane ($\varphi = 0^o$) and H-plane ($\varphi = 90^o$) power patterns of a 30°–60°–90° TMA having $a = 86.603mm, d = 1.59mm, \varepsilon_r = 2.32, tan\,\delta = 0.0005$ are shown in Fig. 4.5 with absolute gain for first 10 modes. Antenna parameters are kept similar to equilateral TMA (side length = 100mm) for comparison purpose. It is found from Fig. 4.5 that first nine modes of a 30°–60°–90° TMA shows a peak in the broadside direction. Slight dip is observed in the broadside direction for TM_{31} mode. TM_{41} mode is the first mode which shows null in the broadside direction. Therefore, 30°–60°–90° TMA shows more number of broadside modes than equilateral TMA.

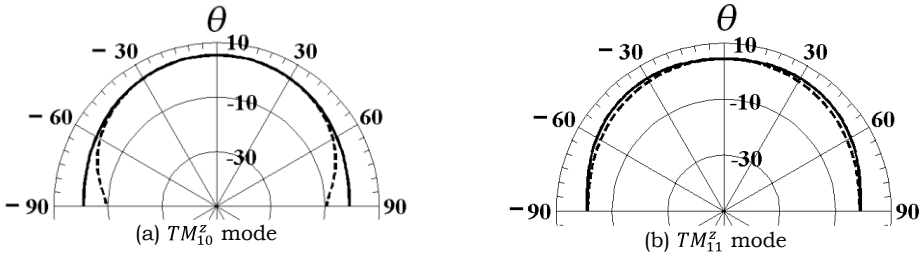

(a) TM_{10}^z mode (b) TM_{11}^z mode

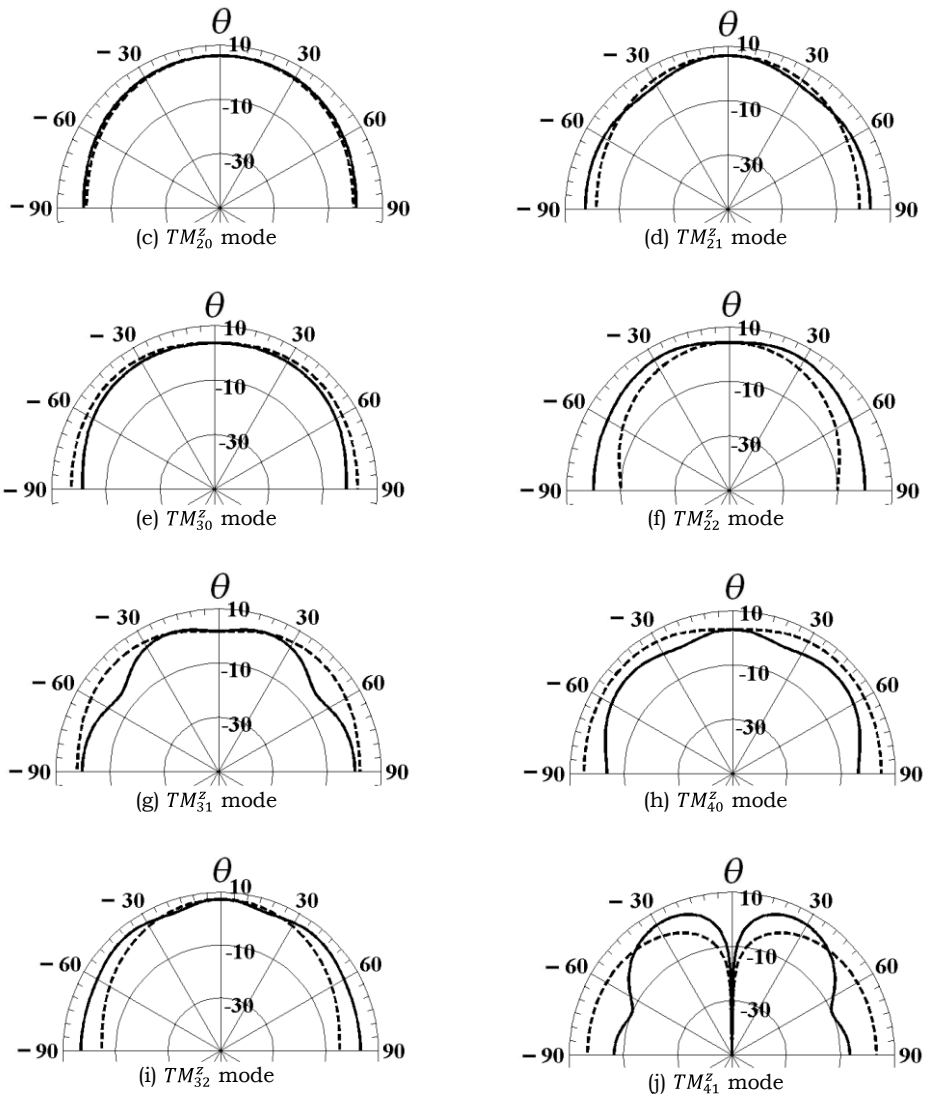

Fig. 4.5 Theoretical E-plane (solid line) and H-plane (dashed line) power patterns for various TM^z_{mn} modes (a = 86.603mm, h = 1.59mm, ε_r = 2.32 and $\tan\delta$=0.0005)

For experimental validation, theoretical results are compared with experimental data as shown in Fig. 4.6. In Fig. 4.6, Numerical Integration (NI) using the inbuilt functions (*syms, matlabFunction, quad2d* etc.) of MATLAB™ is also performed to evaluate far-zone electric field to show the correctness of our theory. Data obtained using EM simulator HFSS [9] and IE3D [8] are also shown in Fig. 4.6. It is found that our theoretical results on far-field radiation patterns are in close agreement with experimental data and/or data obtained using an EM simulator.

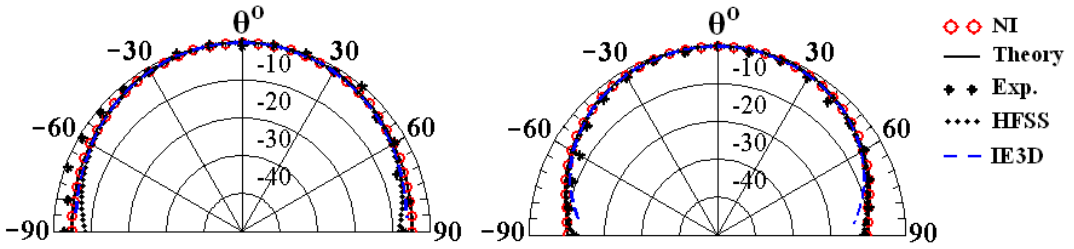

(a) E-plane (left) and H-plane (right) power patterns for TM_{10} mode

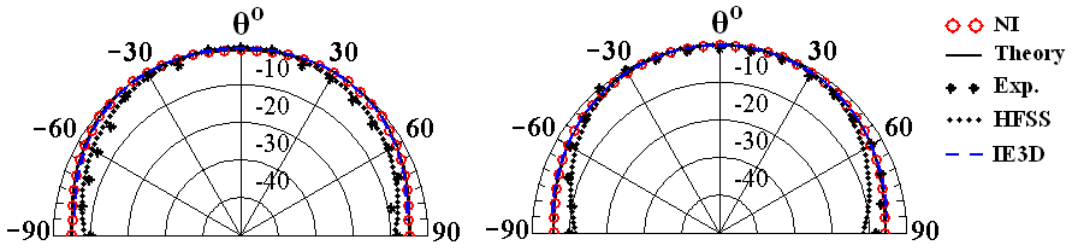

(b) E-plane (left) and H-plane (right) power patterns for TM_{11} mode

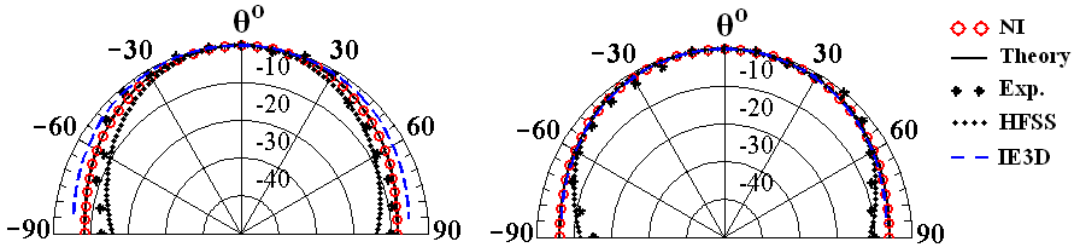

(c) E-plane (left) and H-plane (right) power patterns for TM_{20} mode

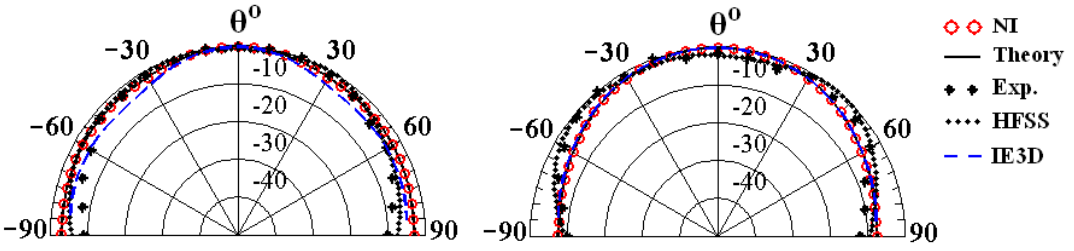

(d) E-plane (left) and H-plane (right) power patterns for TM_{21} mode

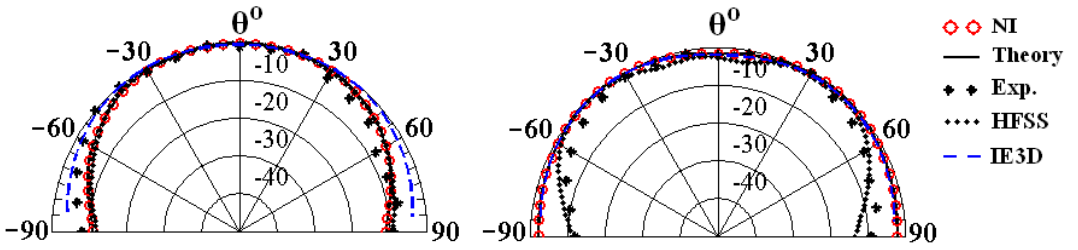

(e) E-plane (left) and H-plane (right) power patterns for TM_{30} mode

Fig. 4.6 Experimental validation of power patterns for various TM_{mn}^{z} modes ($a = 100mm, h = 0.762mm, \varepsilon_r = 2.5, tan\,\delta = 0.0035$)

4.3.3 Input Impedance

Input impedance (Z_{in}) characteristics for three different types of feed modeling are depicted in Fig. 4.7. It is found from Fig. 4.7 that all types of feed modeling show almost same Z_{in} with reasonable value of w_x and/or w_y for a particular mode. In [6], it is clearly mentioned that the effective length of uniform current ribbon has been considered equal to 6mm to get agreement with experimental data. But, it is found that the effect of w_x and/or w_y on the input impedance profile is negligible and it is very difficult to differentiate those curves from each other. J_x, J_y and J_{xy} show almost same results as shown in Fig. 4.8. One can choose w_x and/or w_y as small as 0.1mm or as high as 10mm. Hence it is concluded that cavity model analysis of 30°–60°–90° TMA will give same results both for one dimensional and/or two dimensional feed modeling. It should be pointed here that for some impractical values of w_x and/or w_y say for example 30mm, there is a possibility to have little differences of input impedance computed for different feed modeling. In such cases, the effective length of feed width will be comparable to patch dimensions and will not be considered.

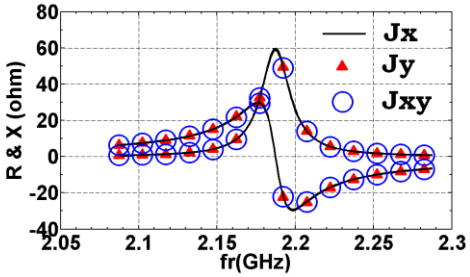

Fig 4.7 Input impedance of TM_{20} mode for different feed ($a = 100mm, h = 0.762mm, \varepsilon_r = 2.5, x_o = 50mm, y_o = 4mm, w_x = 6mm, w_y = 6mm$)

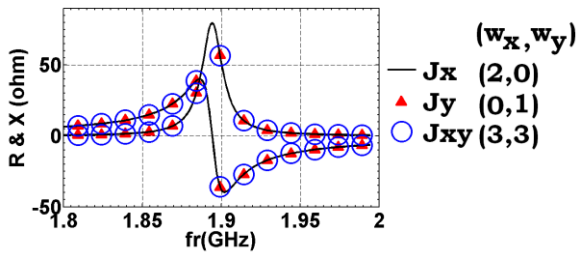

Fig 4.8 Variation of input impedance with different feed dimensions at TM_{11} mode ($a = 100mm, h = 0.762mm, \varepsilon_r = 2.5, x_o = 50mm, y_o = 4mm$): w_x, w_y are in mm.

Theoretical results on input impedance are compared with experimental data for first five broadside modes are shown in Fig. 4.9 for $a = 100mm, h = 0.762mm, \varepsilon_r = 2.5, x_o = 10mm, y_o = 4mm$ and $w_x = w_y = 6mm$. Measured quality factor (Q_t^m) as discussed in next sub-section is used to calculate the input impedance for various modes. For better clarity and resolution, results are

shown only for $\vec{J}_{xy}$. It is found that theoretical results are in good agreement with experimental data. It is quite obvious to have a little discrepancy between theoretical and experimental results because many factors are not considered in cavity model analysis. This type of discrepancy in input impedance of an equilateral TMA is also noticeable for TM_{10}, TM_{20} and TM_{21} modes [6, Figs. 12-13].

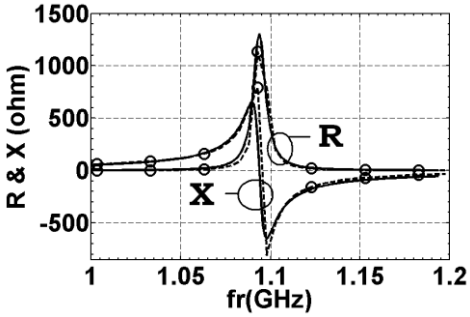

(a) Input impedance for TM_{10} mode ($f_r^t = 1.094GHz, f_r^m = 1.093GHz$, error = 0.06%)

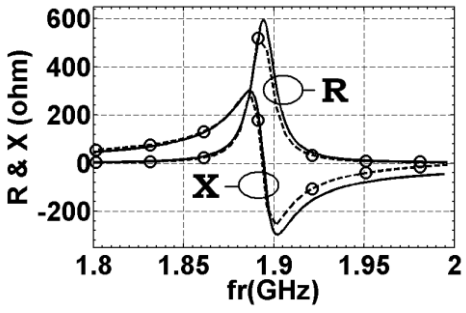

(b) Input impedance for TM_{11} mode ($f_r^t = 1.094GHz, f_r^m = 1.093GHz$, error = 0.06%)

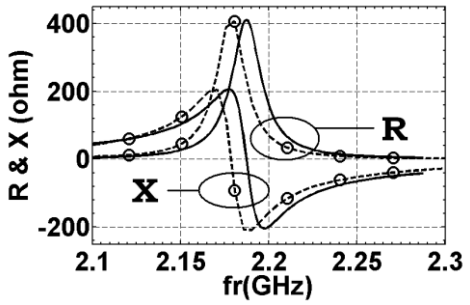

(c) Input impedance for TM_{20} mode ($f_r^t = 1.094GHz, f_r^m = 1.093GHz$, error = 0.06%)

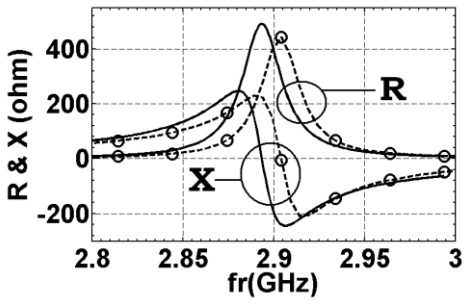

(d) Input impedance for TM_{21} mode ($f_r^t = 1.094GHz, f_r^m = 1.093GHz$, error = 0.06%)

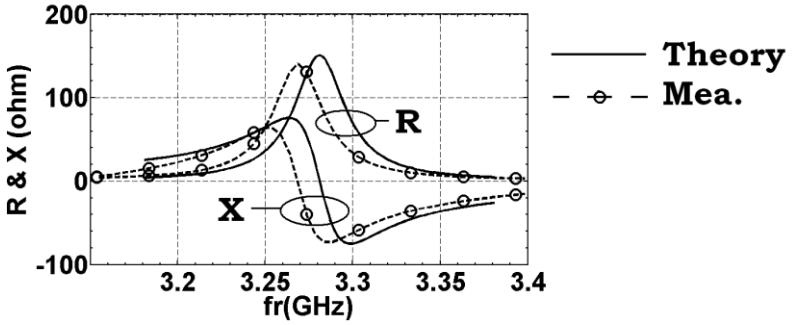

(e) Input impedance for TM_{30} mode ($f_r^t = 3.281GHz, f_r^m = 3.269GHz$, error = 0.36%)

Fig. 4.9 Experimental validation of input impedance for different TM_{mn}^z modes ($a = 100mm, h = 0.762mm, \varepsilon_r = 2.5, x_o = 45mm, y_o = 10mm$)

Variation of input resistance (max) with feed location is of interest to excite single or multiple modes. A typical point D (x_d, y_d) is assumed on AC (please see Fig. 4.1) and the variations of input resistance with different feed positions along DB path for first five broadside modes are investigated. Typical plot is shown in Fig. 4.10 for $a = 100mm, d = 0.762mm, \varepsilon_r = 2.5$.

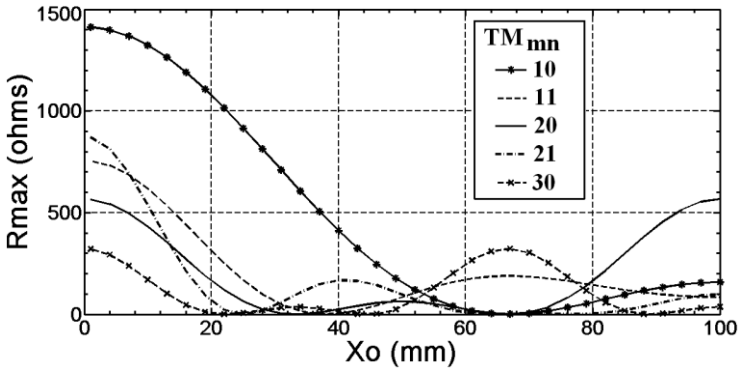

Fig 4.10 Variation of maximum input resistance with feed location ($a = 100mm, d = 0.762mm, \varepsilon_r = 2.5$ and $x_d = 1mm$)

From Fig. 4.10, one can easily find a probe location to excite all five modes. For example, if the feed is placed at $(x_o = 52mm, y_o)$ on DB line (x_d = 1mm) we obtain R = 100, 105, 57, 73 and 69 Ω for TM_{10}, TM_{11}, TM_{20}, TM_{21} and TM_{30} modes respectively. It should be noted here that equilateral TMA shows three broadside radiating modes (TM_{10}, TM_{20} and TM_{21}) among first five modes with reasonable input resistance (50-100Ω) [6]. This broadside radiation characteristic can make 30°–60°–90° TMA more attractive compared to equilateral TMA.

4.3.4 Radiated Power, Quality factor, Efficiency and Gain

In this section, radiated power in percentage P_r (%) which is evaluated as $= 2\pi/Q_r \times 100\%$ where Q_r is radiation Q-factor, total Q-factor (Q_t), bandwidth (BW), gain (G) etc. are discussed. It is important to have a knowledge on total quality factor (Q_t) and P_r(%) to design an antenna as an efficient radiator. Due to different excitations, modal amplitudes differ for a particular mode. It is found that the intermediate data such as W_t, P_c, P_d etc may vary but the

concerned final results i.e. $P_r(\%), Q_r(=\omega_r W_t/P_r)$, Q_t, G etc are not distinguishable as expected. Typical results are shown in Table 4.3 for TM_{11} and TM_{30} modes. A closer look reveals that the final quantities (please see equations 3.31 – 3.40 in Chapter III) are independent of modal amplitudes. The final quantities are obtained after normalization with respect to modal amplitude of E_z because other two components of electric field i.e. E_x and E_y are equal to zero in cavity model analysis [12-15]. Further, the effect of feed position on Q-factor is also very small [6].

Table 4.3

Comparison of various quantities for different feed modeling

$(a = 86.603mm, d = 1.59mm, \varepsilon_r = 2.32, tan\,\delta = 0.0005)$

Mode	J	Intermediate Parameter				Final Parameter					
		W_t	P_r	P_c	P_d	P_r (%)	e(%)	Q_r	Q_t	BW	G (dB)
TM_{11}^z	J_x	0.000423	4.39E+04	5259	3011	4.576	84.13	137.3	115.5	0.6121	4.982
	J_y	0.000426	4.42E+04	5300	3035	4.576	84.13	137.3	115.5	0.6121	4.982
	J_{xy}	0.000421	4.37E+04	5238	2999	4.576	84.13	137.3	115.5	0.6121	4.982
TM_{30}^z	J_x	0.000354	1.49E+05	5795	4367	10.69	93.6	58.75	54.99	1.286	5.834
	J_y	0.000352	1.48E+05	5764	4343	10.69	93.6	58.75	54.99	1.286	5.834
	J_{xy}	0.000345	1.45E+05	5644	4253	10.69	93.6	58.75	54.99	1.286	5.834

In Table 4.4, theoretical results on total Q-factor (Q_t^t) are compared with measured data (Q_t^m). As regards the experimental data presented in [48, Table 4] too, agreement with our theory is better than that the theory presented therein. From Table 4.4, it is clear that the theoretical total Q-factors (Q_t^t) are in excellent agreement with our measurements (Q_t^m) whereas significant error is observed while comparing with measured data as presented in [48, Table 4]. This may be due to manual collection of data (possibly, from analog system) in 1983 [48].

Variations of $P_r(\%), Q_r, Q_t, BW, e$ and G with resonant frequency for first five modes are shown in Figs. 4.11 for J_{xy} only. In Table 4.5, radiation characteristics of first 15 modes are shown for $a = 86.603mm, h = 1.59mm, \varepsilon_r = 2.32$ and $tan\delta = 0.0005$. The base length of the 30°–60°–90° TMA is kept equal

to the median of an equilateral TMA having side length 100mm for comparison purpose. From Table 4.5, it is found that suitable higher order modes can produce higher gain compared to fundamental TM_{10}^{z} mode.

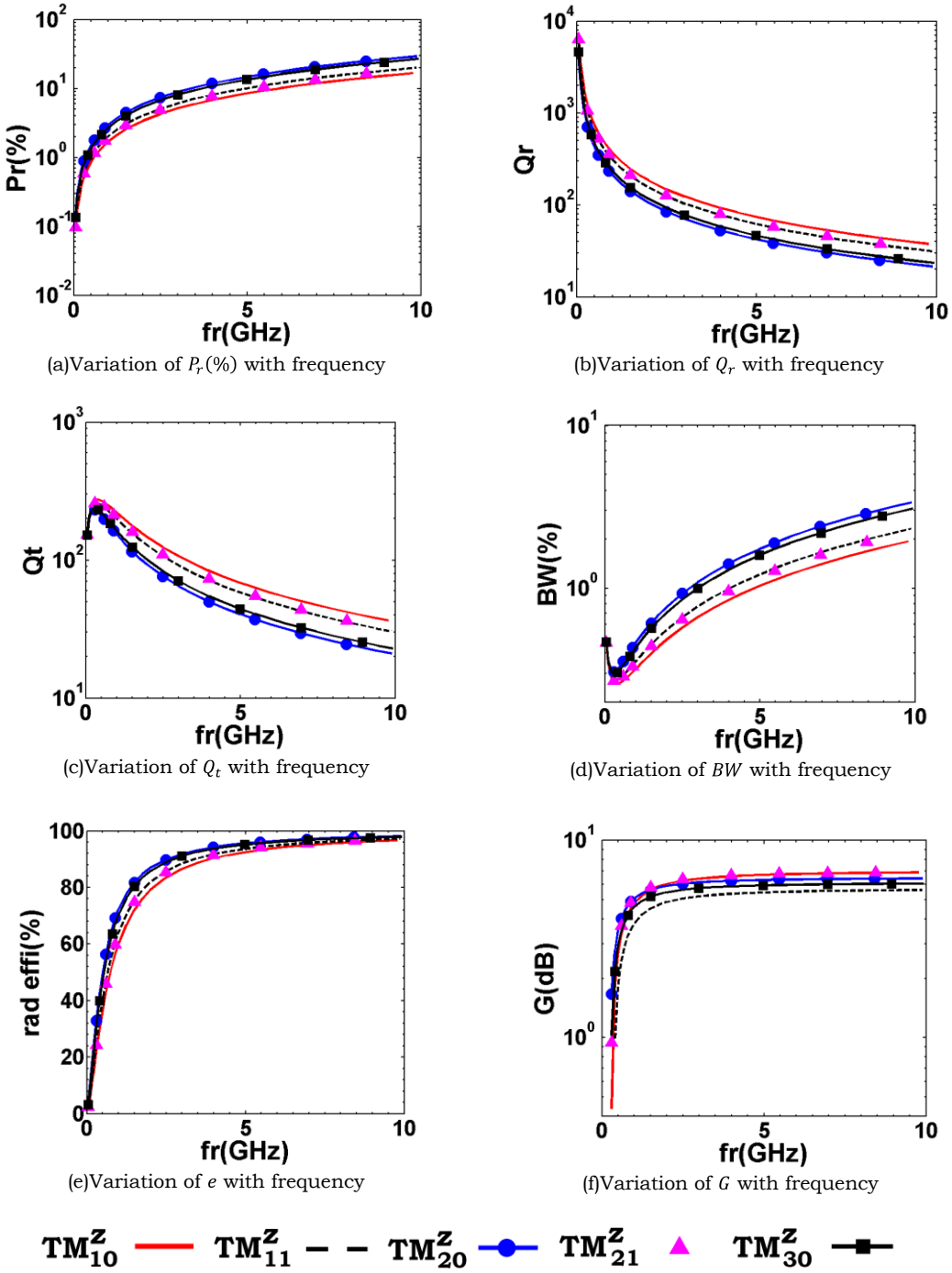

(a)Variation of $P_r(\%)$ with frequency

(b)Variation of Q_r with frequency

(c)Variation of Q_t with frequency

(d)Variation of BW with frequency

(e)Variation of e with frequency

(f)Variation of G with frequency

Fig. 4.11 Radiation characteristics of 30°–60°–90° TMA ($d = 1.59mm, \varepsilon_r = 2.32, tan\delta = 0.0005$)

Table 4.4

Comparison of total Q-factor for TM_{mn}^{z} modes

Antenna	a (mm)	Mode	Mea. Q_t	Theo. Q_t	Error (%)
d = 0.76mm, ε_r = 2.34, $\tan\delta$=0.0018 [48]	62.354	TM_{10}^{z}	133.2	172	29.1
	60.622	TM_{10}^{z}	126.07	171	35.6
	56.292	TM_{10}^{z}	125.47	169	34.7
	51.962	TM_{10}^{z}	120.35	166	37.9
	47.631	TM_{10}^{z}	116	162	39.6
d = 0.762mm, ε_r = 2.5, $\tan\delta$=0.0035 (our)	100	TM_{10}^{z}	136	137.8	1.32
	100	TM_{11}^{z}	126	124.9	-0.009
	100	TM_{20}^{z}	109	110.9	1.74
	100	TM_{21}^{z}	111.7	112.9	1.07
	100	TM_{30}^{z}	93.4	92.7	-0.007

Table 4.5

Characteristics of first 15 modes of a 30°–60°–90° TMA

$(a = 100mm, d = 1.59mm, \varepsilon_r = 2.32, tan\delta = 0.0005)$

Sl No	Mode	f_r (GHz)	$P_r(\%)$	Q_r	Q_t	$BW(\%)$	G (dB)	$e(\%)$
1	TM_{10}^{z}	1.134	1.929	325.8	208.1	0.3397	5.093	63.89
2	TM_{11}^{z}	1.964	3.98	157.9	128.6	0.5496	4.85	81.5
3	TM_{20}^{z}	2.267	6.733	93.32	82.72	0.8548	5.983	88.64
4	TM_{21}^{z}	2.999	5.883	106.8	94.15	0.751	6.524	88.15
5	TM_{30}^{z}	3.401	9.197	68.32	63.09	1.121	5.795	92.35
6	TM_{22}^{z}	3.927	9.16	68.59	63.52	1.113	7.009	92.61
7	TM_{31}^{z}	4.088	7.089	88.63	80.43	0.8792	5.854	90.75
8	TM_{40}^{z}	4.535	11.1	56.61	53.24	1.328	6.903	94.05
9	TM_{32}^{z}	4.942	8.11	77.47	71.43	0.9899	7.223	92.2
10	TM_{41}^{z}	5.195	7.651	82.13	75.45	0.9371	6.85	91.88
11	TM_{50}^{z}	5.669	12.13	51.78	49.1	1.44	7.579	94.83
12	TM_{33}^{z}	5.891	11.61	54.14	51.25	1.38	8.332	94.66
13	TM_{42}^{z}	5.999	8.551	73.48	68.28	1.036	7.912	92.92
14	TM_{51}^{z}	6.312	8.747	71.83	66.91	1.057	7.811	93.15
15	TM_{60}^{z}	6.802	11.49	54.69	51.84	1.364	8.187	94.79

4.4 Conclusion

In this chapter, theoretical investigations on 30°–60°–90° Triangular Microstrip Antenna (TMA) is presented using the cavity model. Modal analysis

is performed for TM_{mn}^{z} mode of a probe fed 30°–60°–90° TMA. Coaxial probe is modeled here in three different ways to study its input impedance characteristics. It is found that all three definitions for feed modeling are able to predict almost indistinguishable characteristics. From this theoretical investigation, it is found that:

- For a given resonant frequency, 30°–60°–90° TMA takes half area compared to equilateral TMA
- First 9 modes produce a peak in the broadside direction
- TM_{41} mode is the first mode which produces a null in the broadside direction
- It is possible to excite first five modes for a reasonable value of input impedance using single coaxial probe. This feature can efficiently be utilized to design a penta-band antenna using 30°–60°–90° TMA.

Chapter V

45°–45°–90° Triangular Microstrip Antenna

5.1 Introduction

Theoretical investigations on Equilateral Triangular Microstrip Antenna (ETMA) and 30°–60°–90° Triangular Microstrip Antennas (TMA) are presented in the last two chapters using 'Cavity Model'. Besides these two triangular shaped antennas, isosceles 45°–45°–90° triangular shaped Microstrip Antenna (MA) has also been reported in which only resonant frequency has been computed for various modes only [149]. The Green's function of the isosceles 45°–45°–90° TMA has been reported for segmentation technique [40]. Input impedance has been calculated for fundamental TM_{10}^{z} mode only [145]. Modal analysis of isosceles 45°–45°–90° TMA has not been reported so far. Therefore, we take this opportunity to investigate the isosceles 45°–45°–90° TMA using the cavity model.

It is found that the isosceles 45°–45°–90° TMA takes just half area compared to square MA for a given resonant frequency. Further, isosceles 45°–45°–90° TMA can be used as a triple band antenna as shown in section 5.3.

In this chapter, characteristics of 45°–45°–90° Triangular Microstrip Antenna (TMA) is presented. Modal analysis is performed for TM_{mn}^{z} modes of a probe fed 45°–45°–90° TMA using cavity model [12-15] for the first time. As the thickness of the substrate (say, along $\hat{z}$ direction) is much less than the operating wavelength, the standing wave field variation can be assumed constant along the thickness of the substrate (i.e. $\partial/\partial z = 0$). This physical phenomenon is proved in this chapter mathematically. Approximate solution for the eigenfunctions $\psi_{mnp}(x, y, z)$ is given here. Closed form expressions for far-field radiation patterns are given here for isosceles 45°–45°–90° TMA. Input impedance, Q-factor, radiated power, gain, bandwidth, etc. are investigated and

are presented in a systematic way. Theoretical results are verified with experimental data.

5.2 Theory

In this section, isosceles 45°–45°–90° TMA is investigated analytically using conventional cavity model [12-15]. In Fig. 5.1, the antenna geometry of the isosceles 45°–45°–90° TMA is shown in the rectangular coordinate system where the antenna is placed along the *x*-*y* surface. The antenna is aligned along the *z*-axis. Base (AB) length of the isosceles 45°–45°–90° TMA is a and the probe is placed at (x_o, y_o) point. Eigenfunctions, eigenvalues, far-field radiation patterns, input impedance etc. are investigated.

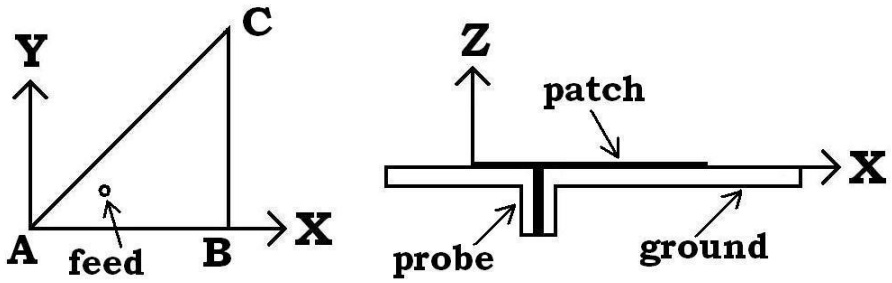

Fig. 5.1 Geometry of isosceles 45°–45°–90° TMA

5.2.1 Eigenfunctions

The conventional cavity model is used to investigate the isosceles 45°–45°–90° TMA. To predict the approximate solution for eigenfunctions (ψ) of isosceles 45°–45°–90° TMA for TM^z_{mn} modes, the antenna is assumed as a cavity whose rectangular side walls (AC, AB and BC) are Perfect Magnetic Conductors (PMC) and the top and bottom surfaces are Perfect Electric Conductors (PEC). Due to the existence of one inclined plane (AC side as shown in Fig. 5.1), the eigenfunction is expressed first as:

$$\psi = F(x, y) \times H(z) \tag{5.1}$$

where

$$H(z) = \left[Ae^{jk_z z} + Be^{-jk_z z}\right] \tag{5.2}$$

To obtain the $F(x,y)$ function, we follow the procedure here given by W. R. Smythe in 1939 [168]. According to W. R. Smyth, the superposition of two square wave-guide fields will produce the field of an isosceles right-triangular guide with the same cutoff frequency. Therefore, we can write:

$$F(x,y) = A \times \psi_{mn} + B \times \psi_{nm} \quad \text{where} \quad \psi_{pq} = \cos\left(\frac{p\pi x}{a}\right)\cos\left(\frac{q\pi y}{b}\right) \quad \text{and} \quad b = a$$

$$= A \times \cos\left(\frac{m\pi x}{a}\right)\cos\left(\frac{n\pi y}{a}\right) + B \times \cos\left(\frac{n\pi x}{a}\right)\cos\left(\frac{m\pi y}{a}\right) \qquad \text{as} \quad b = a \tag{5.3}$$

Now, PMC is applied along the periphery of the isosceles right TMA. It is found that:

$$\boldsymbol{H_x = \frac{1}{\mu}\frac{\partial \psi}{\partial y} = 0 \ \text{ at } y = 0} \quad \text{and} \quad \boldsymbol{H_y = \frac{-1}{\mu}\frac{\partial \psi}{\partial x} = 0 \ \text{ at } x = a}$$

To satisfy the remaining boundary conditions $\left(\frac{\partial f(x,y)}{\partial n} = 0\right)$ along $y = x$ plane, we decompose the normal components $(\hat{n})$ into x and y components as:

$$\left[\frac{\partial F(x,y)}{\partial n}\right]_{y=x} = \frac{1}{\sqrt{2}} \times \left[-\frac{\partial F(x,y)}{\partial x} + \frac{\partial F(x,y)}{\partial y}\right]_{y=x} \tag{5.4}$$

$$= \frac{1}{\sqrt{2}} \times (A - B) \times \left[+\frac{m\pi}{a} \times \sin\left(\frac{m\pi x}{a}\right)\cos\left(\frac{n\pi x}{a}\right) - \frac{n\pi}{a} \times \sin\left(\frac{n\pi x}{a}\right)\cos\left(\frac{m\pi x}{a}\right)\right] = 0$$

$$\Rightarrow (A - B) = 0 \qquad \Rightarrow A = B \tag{5.5}$$

Hence,

$$F(x,y) = A \times \left[\cos\left(\frac{m\pi x}{a}\right)\cos\left(\frac{n\pi y}{a}\right) + \cos\left(\frac{n\pi x}{a}\right)\cos\left(\frac{m\pi y}{a}\right)\right] \tag{5.6}$$

Computing k_z

$$\boldsymbol{E_x = \frac{-j}{\omega\mu\epsilon}\frac{\partial^2 \psi}{\partial x \partial z} = 0 \ \text{at } z = d}$$

$$\Rightarrow \frac{-j}{\omega\mu_2\varepsilon_2} \times F_x(x,y) \times jk_z \times \left[Ae^{jk_z z} - Be^{-jk_z z}\right] = 0 \quad \text{at } z = d$$

$$\Rightarrow B = Ae^{j2k_z d} \tag{5.7}$$

Hence,

$$\psi = A \times \left[\cos\left(\frac{m\pi x}{a}\right)\cos\left(\frac{n\pi y}{a}\right) + \cos\left(\frac{n\pi x}{a}\right)\cos\left(\frac{m\pi y}{a}\right)\right] \times e^{jk_z d} \times \cos(k_z(z-d)) \tag{5.8}$$

Now,

$$\boldsymbol{E_x = \frac{-j}{\omega\mu\epsilon}\frac{\partial^2\psi}{\partial x \partial z} = 0 \text{ at } z = -d}$$

$$\Rightarrow \frac{-j}{\omega\mu_2\varepsilon_2} \times F_x(x,y) \times (-k_z) \times A \times e^{jk_z d} \times \sin\big(k_z(z-d)\big) = 0 \quad \text{at } z = d$$

$$\Rightarrow \sin(k_z 2d) = 0 = \sin(p\pi) \qquad \Rightarrow k_z = \frac{p\pi}{2d} \tag{5.9}$$

Therefore, ψ can be expressed as:

$$\psi = \left[\sum_{i=1}^{2} \cos(\alpha_i x)\cos(\beta_i y)\right] \times \cos(k_z(z-d)) \tag{5.10}$$

where $\alpha_1 = m\pi/a,\ \ \alpha_2 = n\pi/a,\ \ \beta_1 = n\pi/a,\ \ \beta_2 = m\pi/a\ ,\ \ k_z = p\pi/2d$ (5.11)

Now, the antenna is excited using a $\hat{z}$-directed coaxial probe. The $\vec{E}_z$ component will satisfy the inhomogeneous wave equation whose solution can be expressed as:

$$E_z = j\omega\mu \sum_{m=0}^{\infty}\sum_{n=0}^{\infty} \frac{1}{(k^2 - k_{mn}^2)} \frac{< J\psi_{mnp} >}{< \psi_{mnp}\psi_{mnp} >} \psi_{mnp}(x,y,z) \tag{5.12}$$

In next sub-section, it is shown that the third modal index p takes the value equal to 1 for very high order modes (357^{th} mode for $a = 100mm, d = 1.59mm, \varepsilon_r = 2.32$) which may not be excited practically using conventional feeding mechanism for thin substrate. Therefore, we will discuss the TM_{mnp}^{z} modes with $p = 0$ which means that there is no variation of fields along the

height of the substrate. This is equivalent to assume $\partial/\partial z = 0$ for thin substrate as reported earlier by Y. T. Lo *et al* [11]. The eigenfunctions with $p = 0$ can be written as:

$$\psi_{mnp}(x, y, z) \cong \psi_{mn}(x, y) = F(x, y) \tag{5.13}$$

The complete internal field configuration is

$$E_z = A_{mn}[cos(\alpha_1 x)\, cos(\beta_1 y) + cos(\alpha_2 x)\, cos(\beta_2 y)]$$
$$H_x = \frac{jA_{mn}}{\omega\mu\varepsilon}[\beta_1\, cos(\alpha_1 x)\, sin(\beta_1 y) + \beta_2\, cos(\alpha_2 x)\, sin(\beta_2 y)]$$
$$H_y = -\frac{jA_{mn}}{\omega\mu\varepsilon}[\alpha_1\, sin(\alpha_1 x)\, cos(\beta_1 y) + \alpha_2\, sin(\alpha_2 x)\, cos(\beta_2 y)]$$
$$H_z = E_x = E_y = 0 \tag{5.14}$$

Here, A_{mn} is modal amplitude and other terms are carrying their usual meaning. In Fig. 5.2, internal magnetic field distributions are shown for some modes. Three sides *AC*, *AB* and *BC* are also shown to define the triangular region. The magnitude of the magnetic field is first normalized and then is calculated in dB.

5.2.2 Resonant Frequency

The resonant frequencies for arbitrary TM^z_{mnp} modes of the 45°–45°–90° TMA can easily be evaluated from separation equation $\left(\chi^2 + k_z^2 = \varepsilon_r k_0^2\right.$ where $\chi = (\pi/a)(m^2 + n^2)^{1/2}$) as:

$$f_r = \frac{c}{2\pi\sqrt{\varepsilon_r}} \times \left[\left(\frac{\pi}{a}\right)^2 (m^2 + n^2) + k_z^2\right]^{1/2} \tag{5.15}$$

where c is the velocity of light in free space and ε_r is the relative permittivity of substrate. For fixed values of a, the resonant frequencies are computed for various modes as shown in Table 5.1. It should be pointed here that χ takes same expression for square MA as found for 45°–45°–90° TMA. Therefore, 45°–

45°–90° TMA takes just half area compared to square MA for a given resonant frequency.

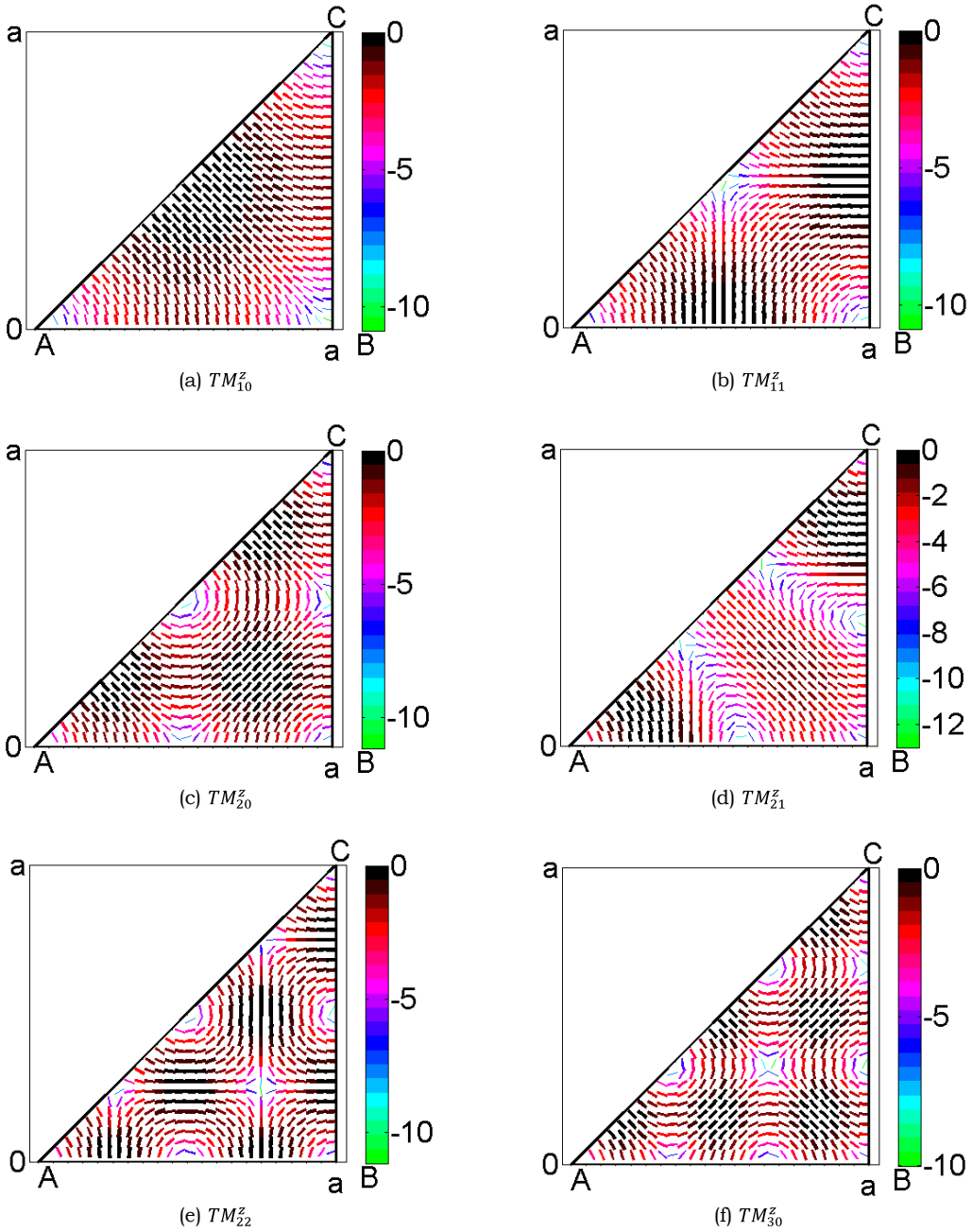

(a) TM_{10}^z (b) TM_{11}^z

(c) TM_{20}^z (d) TM_{21}^z

(e) TM_{22}^z (f) TM_{30}^z

Fig. 5.2 Internal magnetic field distribution (in dB) for some modes ($a = 100mm, d = 1.59mm, \varepsilon_r = 2.32$)

In Table 5.1, resonant frequency for first 25 modes are shown for $a = 100mm, d = 1.59mm, \varepsilon_r = 2.32$. It is found that the third modal index p takes a value equal to 1 first for the 357th mode. Practical excitation of such super

high order mode is quite impossible using conventional thin substrate. Thicker substrates may be used to excite modes with $p = 1$. In that case, the antenna will act as a metal loaded Dielectric Resonator Antenna (DRA). Investigations on DRA (rectangular and triangular shaped DRAs) are presented in Chapters VII to XI. Therefore, we will focus here on various modes with $p = 0$ of microstrip patch antennas. It is also found that use of thinner substrate will shift that mode (with $p = 1$) to upward direction. For example, an isosceles 45°–45°–90° TMA having $a = 100mm, d = 0.762mm, \varepsilon_r = 2.32$ will produce the first mode with $p = 1$ at 1100th position ($f_r^{TM^z_{42,50,0}} = 64.276GHz$, $f_r^{TM^z_{101}} = 64.599GHz$, $f_r^{TM^z_{111}} = 64.607\ GHz$). As the excitation of higher order modes with $p = 1$ is quite impossible in practice for Microstrip Antenna (MA), the mode will be termed as TM^z_{mn} instead of TM^z_{mnp}. If not mentioned, it is assumed that the third modal index p is equal to zero.

Table 5.1

Resonant frequencies for various modes of a 45°–45°–90° TMA

($a = 100mm, d = 1.59mm, \varepsilon_r = 2.32$)

Sl No	Mode	Resonant Frequency (GHz)		Sl No	Mode	Resonant Frequency (GHz)
1	TM^z_{100}	0.9844		16	TM^z_{250}	5.3010
2	TM^z_{110}	1.3921		17	TM^z_{440}	5.5685
3	TM^z_{200}	1.9688		18	TM^z_{350}	5.7399
4	TM^z_{120}	2.2011		19	TM^z_{600}	5.9063
5	TM^z_{220}	2.7842		20	TM^z_{160}	5.9877
6	TM^z_{300}	2.9531		21	TM^z_{260}	6.2257
7	TM^z_{130}	3.1129		22	TM^z_{540}	6.3031
8	TM^z_{230}	3.5492		23	TM^z_{230}	6.6034
9	TM^z_{400}	3.9375		24	TM^z_{700}	6.8906
10	TM^z_{140}	4.0587		25	TM^z_{550}	6.9606
11	TM^z_{330}	4.1764		**Modes having $p \geq 1$**		
12	TM^z_{240}	4.4023		355	$TM^z_{29,12,0}$	30.894
13	TM^z_{500}	4.9219		356	$TM^z_{5,31,0}$	30.910
14	TM^z_{430}	4.9219		357	TM^z_{101}	30.971
15	TM^z_{150}	5.0194		358	TM^z_{111}	30.987

It should be pointed here that Prof. C. A. Balanis has investigated the rectangular MA using 3D cavity model in [162]. But, image theory has not been applied to remove the ground plane. Therefore, the half wave number along the height of the patch antenna will be double compared to our theory. As the investigated mode has a third modal index equal to zero ($p = 0$), the half wave number along the height does not play any role in the prediction of antenna characteristics. Further, no comment is made there on the occurrence of higher order mode with $p = 1$. In this dissertation, the physical phenomenon of microstrip patch antenna (i.e. $\partial/\partial z = 0$) is explained with mathematical proof.

To account the effect of fringing, the effective side length (a_e) of the isosceles 45°–45°–90° TMA [12, 14, 27] is expressed as:

$$a_e = a + 1.25 \times d \times \varepsilon_r^{-0.25} \tag{5.16}$$

5.2.3 Feed Model

Proper feed modeling plays an important role to predict the input impedance characteristics of an antenna. In case of 30°–60°–90° TMA (please see Chapter IV), we have presented an extensive investigations on feed modeling for cavity model analysis of a microstrip antenna. In case of isosceles 45°–45°–90° TMA, feed ($\vec{J}$) is modeled in four different ways:

I. Uniform current ribbon of effective width w_x along $\hat{x}$ direction ($\vec{J}_x$) [6],
II. Uniform current ribbon of effective width w_y along $\hat{y}$ direction ($\vec{J}_y$) and
III. Two dimensional rectangular shaped strip ($\vec{J}_{xy}$) of effective area $w_x \times w_y$ [13]
IV. Delta function along *x*-*y* coordinates ($\vec{J}_d$)

These four definitions are expressed as:

I. $\vec{J}_x = \hat{z}J(x)\delta(y - y_o)P(z)$

$$J(x) = \begin{cases} I_o/w_x, & x_o - w_x/2 \le x \le x_o + w_x/2 \\ 0, & \text{elsewhere} \end{cases} \quad (5.17a)$$

II. $\vec{J}_y = \hat{z}\delta(x - x_o)J(y)P(z)$

$$J(y) = \begin{cases} I_o/w_y, & y_o - w_y/2 \le y \le y_o + w_y/2 \\ 0, & \text{elsewhere} \end{cases} \quad (5.17b)$$

III. $\vec{J}_{xy} = \hat{z}J(x,y)P(z)$

$$J(x,y) = \begin{cases} I_o/(w_x w_y), & x_o - w_x/2 \le x \le x_o + w_x/2 \\ & y_o - w_y/2 \le y \le y_o + w_y/2 \\ 0, & \text{elsewhere} \end{cases} \quad (5.17c)$$

IV. $\vec{J}_d = \hat{z}\delta(x - x_o)\delta(y - y_o)P(z)$ (5.17d)

where I_o is magnitude of current and $P(z) = 1$ for $-d \le z \le d$. A comparative study is performed here for these four types of feed modeling to understand the effect of feed on the performance of a TMA.

5.2.4 Far-Field Radiation Patterns

To predict the far-field radiation patterns of an isosceles 45°–45°–90° TMA, magnetic surface current $(\vec{M}_s = 2\vec{E} \times \hat{n})$ model is used [6, 11-15, 162]. Magnetic surface current $(\vec{M}_s)$ is evaluated along its periphery AC, BC and AB sides. The steps are similar to those as done for equilateral and 30°–60°–90° TMA. Therefore, we will not present the time consuming steps for brevity. The far-zone electric field at point $P(r, \theta, \varphi)$ can be expressed as:

$$E_\theta = -\frac{jk_o \exp(-jk_o r)}{4\pi r} \times [L_\varphi] \quad (5.18a)$$

$$E_\varphi = \frac{jk_o \exp(-jk_o r)}{4\pi r} \times [L_\theta] \quad (5.18b)$$

where

$$L_\theta = F_x cos(\theta)cos(\varphi) + F_y cos(\theta)sin(\varphi) - F_z sin(\theta) \quad (5.19a)$$

$$L_\varphi = -F_x sin(\varphi) + F_y cos(\varphi) \tag{5.19b}$$

$$F_x = F_x^{AC} + F_x^{AB}$$

$$F_y = F_y^{AC} + F_y^{BC}$$

$$F_z = 0$$

$$F_x^{AC} = C_{xy} \times [-E_3] \times \left(k_x^2 + k_y^2\right) \times I_{AC}^{x1}$$

$$F_y^{AC} = C_{xy} \times [-E_3] \times \left(k_x^2 + k_y^2\right) \times I_{AC}^{y1}$$

$$F_x^{AB} = C_{xy} \times [E_3] \times F_{x2}$$

$$F_y^{BC} = C_{xy} \times [E_3] \times e^{jaV_1} \times F_{y2} \tag{5.20}$$

$$I_{AC}^{x1} = \frac{j\chi_1}{((m+n)^2 b^2 - \chi_1^2)} \times \left[e^{j\chi_1 a} \times \cos\big((m+n)\pi\big) - 1\right] + \frac{j\chi_1}{((m-n)^2 b^2 - \chi_1^2)} \times \left[e^{j\chi_1 a} \times \cos\big((m-n)\pi\big) - 1\right] = I_{AC}^{y1}$$

$$F_{x2} = \frac{ja\chi_2}{\pi[m^2 - \chi_2^2]} \times \left[e^{jV_1 a} cos(m\pi) - 1\right] + \frac{ja\chi_2}{\pi[n^2 - \chi_2^2]} \times \left[e^{jV_1 a} cos(n\pi) - 1\right]$$

$$F_{y2} = \frac{ja\chi_3 \cos(m\pi)}{\pi[n^2 - \chi_3^2]} \times \left[e^{jV_2 a} \cos(n\pi) - 1\right] + \frac{ja\chi_3 \cos(n\pi)}{\pi[m^2 - \chi_3^2]} \times \left[e^{jV_2 a} \cos(m\pi) - 1\right] \tag{5.21}$$

$$C_{xy} = \frac{A_{mn} 2h\varepsilon_o}{4\pi} . \frac{e^{-jk_o r}}{r} \quad ; \quad \eta = tan(\pi/4) = 1 \quad ; \quad b = \pi/a$$

$$V_1 = k_o \, sin(\theta) \, cos(\varphi) \quad ; \quad V_2 = k_o \, sin(\theta) \, sin(\varphi)$$

$$\chi_1 = (V_1 + V_2) \quad ; \quad \chi_2 = V_1 a/\pi \quad ; \quad \chi_3 = aV_2/\pi \tag{5.22}$$

Here, A_{mn} is modal amplitude of a particular mode and other terms are carrying their usual meaning.

5.2.5 Input Impedance

To find the input impedance, the RF voltage (V_{in}) at the feed point (x_o, y_o) is evaluated as [13]:

$$V_{in} = -E_z(x_o, y_o)d \tag{5.23}$$

Therefore, the input impedance becomes:

$$Z_{in} = \frac{V_{in}}{I_o} = R + jX = -j\omega\mu \frac{d}{I_o} \sum_{m=0}^{\infty} \sum_{n=0}^{\infty} \frac{A_{mn}}{(k^2 - k_{mn}^2)} \psi_{mn}(x_o, y_o) \tag{5.24}$$

where

$$k^2 = k_o^2 \varepsilon_r \left(1 - j\delta_{eff}\right) \tag{5.25}$$

and δ_{eff} is effective loss tangent, defined as $\delta_{eff} = 1/Q_t$. Here Q_t is total quality factor.

5.2.6 Radiated Power, Quality factor, Efficiency and Gain

Evaluation of radiated power in percentage $P_r(\%)$ which is defined as $(2\pi/Q_r) \times 100$ where Q_r is the radiation quality factor [15], conductor loss (P_c), dielectric loss (P_d), radiation loss (P_r), total stored energy (W_t), directivity (D), efficiency (e), gain (G), bandwidth (BW) are evaluated using standard procedure as found in [12-15] or as calculated for equilateral TMA in Chapter III to find the radiation characteristics of the isosceles 45°–45°–90° TMA. The effect of surface wave loss is neglected here. Therefore, the total quality factor (Q_t) is defined as:

$$Q_t = \omega_r W_t / (P_c + P_d + P_r) \tag{5.26}$$

5.3 Results

In this section, theoretical results on resonant frequency, far-field patterns, input impedance, etc. are discussed for various TM_{mn}^z modes. One antenna prototype having $a = 70mm, d = 0.762mm, \varepsilon_r = 2.5$ and $tan\,\delta = 0.0035$ is fabricated in our laboratory for experimental validation. The conducting patch is cut manually and is pasted on the substrate using gum as shown in Fig. 5.3. This process is very cost effective as we can save the cost of the chemicals to fabricate a microstrip antenna using the etching procedure. The

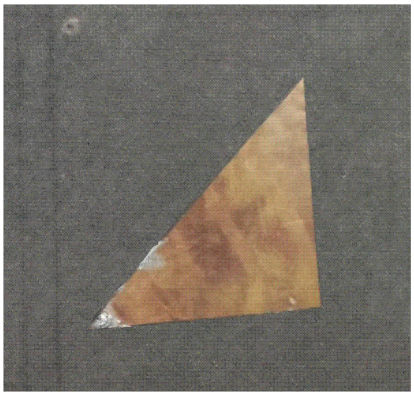

Fig. 5.3 Photograph of fabricated antenna ($a = 70mm, d = 0.762mm, \varepsilon_r = 2.5, tan\,\delta = 0.0035$)

same substrate can be re-utilized to make another microstrip antenna. Further, we can make an antenna prototype within few minutes manually. The antenna is excited using standard 50Ω co-axial probe whose inner conductor radius is 0.63mm. The same is also simulated using commercially available FEM based numerical 3D EM simulator, HFSS [9]. The results are verified with experimental data and/or data obtained using an EM simulator.

5.3.1 Resonant Frequency

In this section, theoretical resonant frequencies are compared with our own experimental data. We have successfully excited fist seven modes. Different modes are identified by observing their internal field distribution. The resonant frequencies are computed using (a, ε_r) and (a_e, ε_r) as shown in Table 5.2. It is found from Table 5.2, that our theory can predict the resonant frequency with an accuracy of less than 1%.

5.3.2 Radiation Patterns

For theoretical investigations on 45°–45°–90° TMA, we have modeled the feed current in four different ways. For a particular mode, it is found that J_x, J_y,J_{xy} and J_d give exactly same far-field radiation patterns and these are non-distinguishable from each other ($w_x = w_y = 6mm$). For example, typical radiation patterns with gain (dB) for TM_{12}^z and TM_{40}^z modes are shown in Fig. 5.4. Therefore, the far-field radiation patterns for various modes are discussed for J_d excitation only as it does not process any single or double integration in the evaluation of $< J\psi_{mn} >$. In case of other simple definitions $(\vec{J}_x, \vec{J}_y$ and $\vec{J}_{xy})$, far-

field radiation patterns do not vary with w_x and/or w_y as found earlier for 30°–60°–90° TMA. This is shown in shown in Fig. 5.5 for TM_{32}^z modes.

Table 5.2

Experimental validation of resonant frequency for TM_{mn}^z modes

($a = 70mm, d = 0.762mm, \varepsilon_r = 2.5, \tan\delta = 0.0035$)

Mode	Resonant Freq. (GHz)			Error (%)	
	Exp.	f_{r1}^{theo} (a, ε_r)	f_{r2}^{theo} (a_e, ε_r)	(a, ε_r)	(a_e, ε_r)
TM_{10}^z	1.329	1.3547	1.3402	1.9324	0.8412
TM_{11}^z	1.893	1.9158	1.8953	1.205	0.1215
TM_{20}^z	2.683	2.7094	2.6804	0.9826	-0.0984
TM_{21}^z	2.971	3.0292	2.9967	1.9576	0.8661
TM_{22}^z	3.769	3.8316	3.7906	1.6614	0.5731
TM_{30}^z	3.984	4.064	4.0205	2.0092	0.9171
TM_{31}^z	4.221	4.2839	4.238	1.4897	0.4032

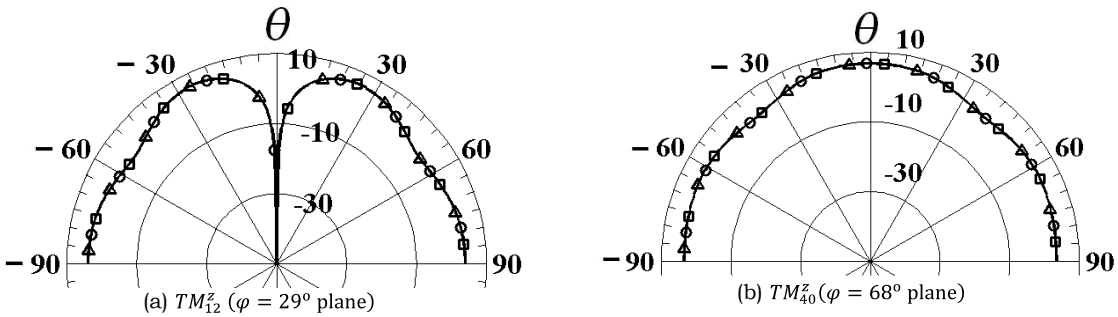

Fig. 5.4 Far-field power patterns with absolute gain (dB) for different feed modeling: J_x (in solid line), J_y (in triangle), J_{xy} (in circle) and J_d (in square) ($a = 100mm, d = 1.59mm, \varepsilon_r = 2.32, tan\,\delta = 0.0005$)

Far-field radiation patterns of a 45°–45°–90° TMA having $a = 100mm, d = 1.59mm, \varepsilon_r = 2.32$ and $tan\,\delta = 0.0005$ are calculated using our analytical closed form expressions. It is found that the far-field power patterns at $\varphi = 0^o$ is exactly the same as found for $\varphi = 90^o$ plane. Therefore, it is important to investigate the field patterns at $\varphi = 0^o, 45^o, 90^o$ and 135^o planes as the polarization of an antenna is mainly investigated at those four planes. In Fig. 5.6, normalized field strengths are shown for first few modes. Form Fig.

5.6, it is found that E_θ and E_φ both components are present at $\varphi = 0^o, 45^o$ and 90^o planes whereas only one component i.e. either E_θ or E_φ is present at $\varphi = 135^o$ plane. Further, E_θ and E_φ both components take an exact same value at $\varphi = 0^o$ and 90^o planes. For further investigation, magnitude and angle of E_θ and E_φ components are calculated at $\theta = 0^o$ as shown in Table 5.3. The angular difference (D_θ) between E_θ and E_φ is also shown for reference. The angular difference (D_θ) is either 0° or 180°. Similar observation is also found for other broadside radiating modes.

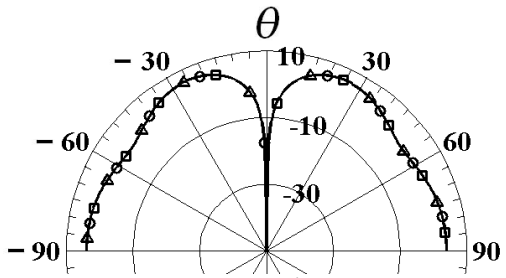

(a) TM_{32}^z ($\varphi = 53^0$ plane)

Fig. 5.5 Far-field power patterns with absolute gain (dB) for different dimensions of w_x and/or w_y: J_x (in solid line), J_y (in star), J_{xy} (in circle) ($a = 100mm, d = 1.59mm, \varepsilon_r = 2.32, tan\,\delta = 0.0005$)

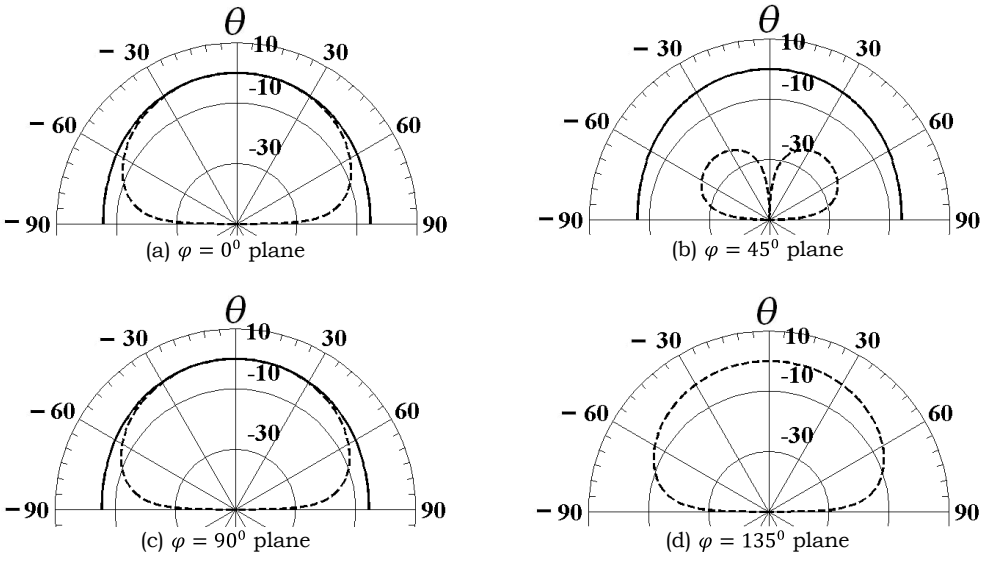

(a) $\varphi = 0^0$ plane (b) $\varphi = 45^0$ plane

(c) $\varphi = 90^0$ plane (d) $\varphi = 135^0$ plane

(i) Plot of normalized E_θ (in solid line) and E_φ (in dashed line) for TM_{10}^z mode

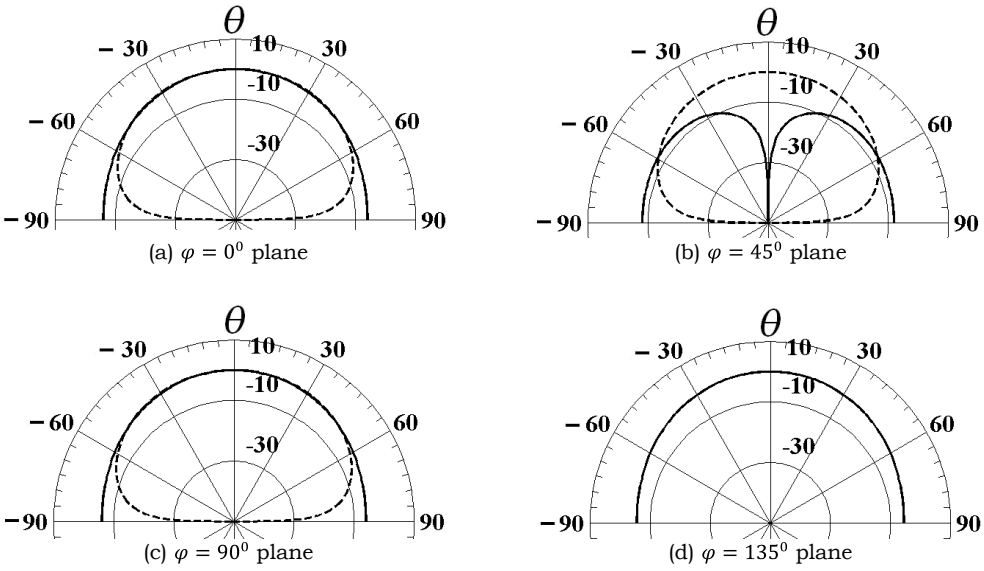

(a) $\varphi = 0^0$ plane (b) $\varphi = 45^0$ plane

(c) $\varphi = 90^0$ plane (d) $\varphi = 135^0$ plane

(ii) Plot of normalized E_θ (in solid line) and E_φ (in dashed line) for TM_{11}^z mode

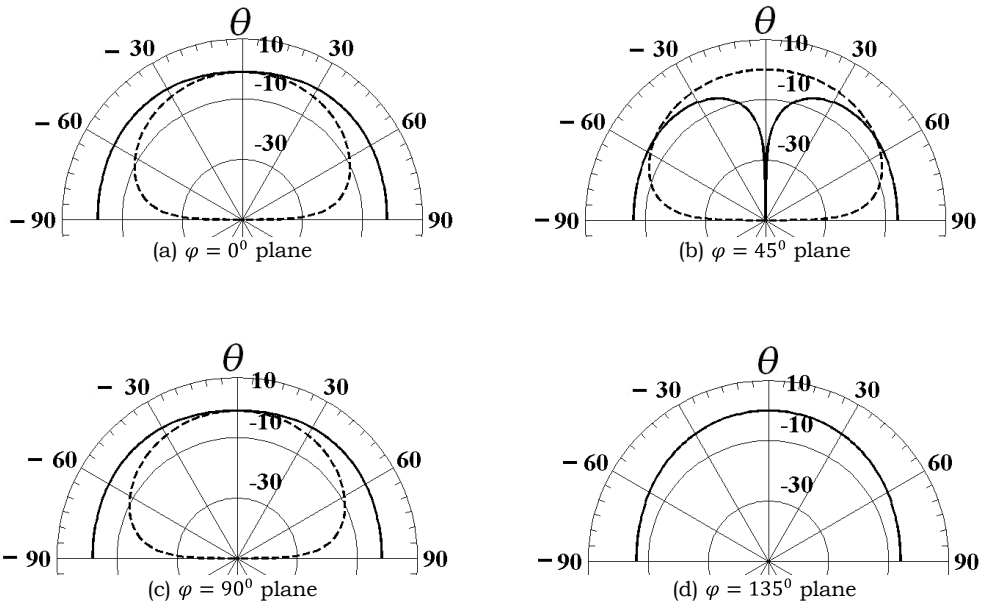

(a) $\varphi = 0^0$ plane (b) $\varphi = 45^0$ plane

(c) $\varphi = 90^0$ plane (d) $\varphi = 135^0$ plane

(iii) Plot of normalized E_θ (in solid line) and E_φ (in dashed line) for TM_{20}^z mode

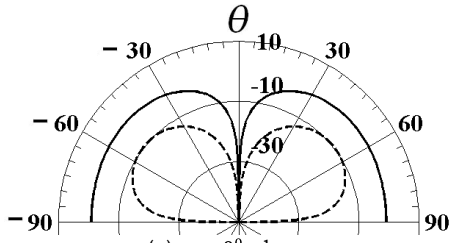

(a) $\varphi = 0^0$ plane

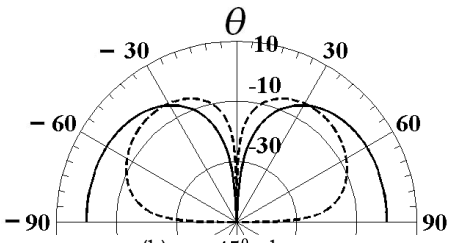

(b) $\varphi = 45^0$ plane

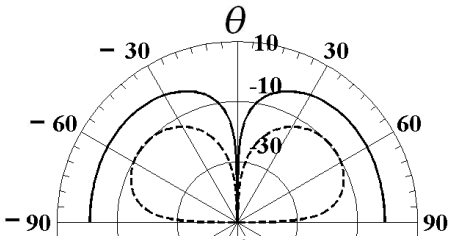

(c) $\varphi = 90^0$ plane

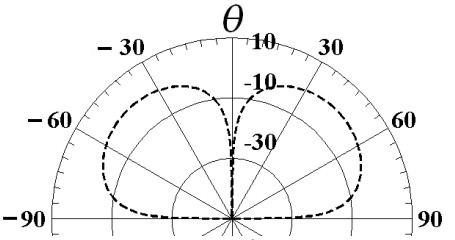

(d) $\varphi = 135^0$ plane

(iv) Plot of normalized E_θ (in solid line) and E_φ (in dashed line) for TM_{21}^z mode

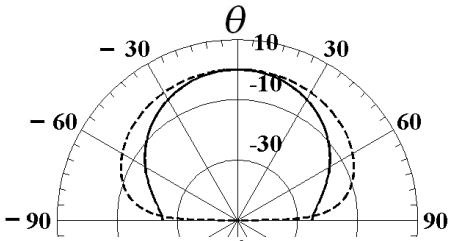

(a) $\varphi = 0^0$ plane

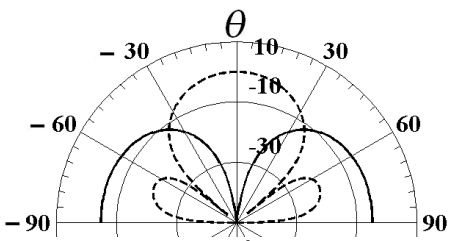

(b) $\varphi = 45^0$ plane

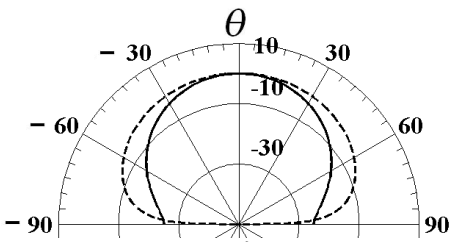

(c) $\varphi = 90^0$ plane

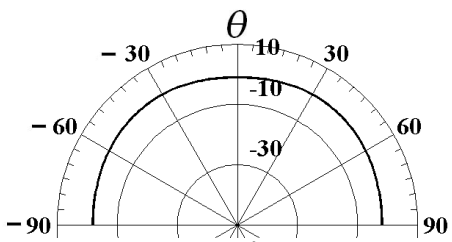

(d) $\varphi = 135^0$ plane

(v) Plot of normalized E_θ (in solid line) and E_φ (in dashed line) for TM_{22}^z mode

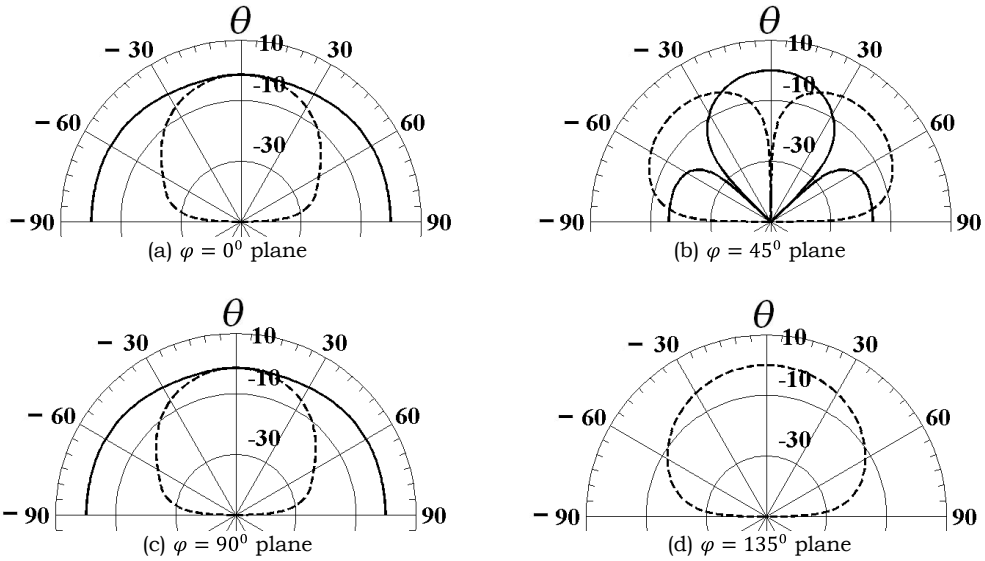

(vi) Plot of normalized E_θ (in solid line) and E_φ (in dashed line) for TM_{30}^z mode
Fig. 5.6 Plot of normalized far-zone field strength for various TM_{mn}^z modes
($a = 100mm, d = 1.59mm, \varepsilon_r = 2.32, tan\,\delta = 0.0005$)

It should be pointed here that principle planes ($\varphi = 0^o$ and 90^o planes) contain either E_θ or E_φ in case of rectangular and circular shaped microstrip antennas whereas 45°–45°–90° TMA contains both E_θ and E_φ at $\varphi = 0^o$ and 90^o planes.

Table 5.3

Comparative study between E_θ or E_φ for TM_{mn}^z modes at $\theta = 0^o$

($a = 100mm, d = 1.59mm, \varepsilon_r = 2.32, \tan\delta = 0.0005$)

Mode	φ (degree)	E_{Total} (dB)	Magnitude (dB)		Angle (degree)		D_θ (degree)
			E_θ	E_φ	E_θ	E_φ	
TM_{10}^z	0	84.7	81.7	81.7	74.9	74.9	0
	45	84.7	84.7	-240.4	74.9	-105.1	180
	90	84.7	81.7	81.7	74.9	-105.1	180
	135	84.7	-240.4	84.7	-105.1	-105.1	0
TM_{22}^z	0	102.8	99.7	99.7	129.9	-50.1	180
	45	102.8	-219.3	102.8	129.9	-50.1	180
	90	102.8	99.7	99.7	-50.1	-50.1	0
	135	102.8	102.8	-219.3	-50.1	-50.1	0

For experimental validation, theoretical results are compared with experimental data [149, 167] as shown in Fig. 5.7. It is found that our theoretical results on far-field radiation patterns are in close agreement with experimental data.

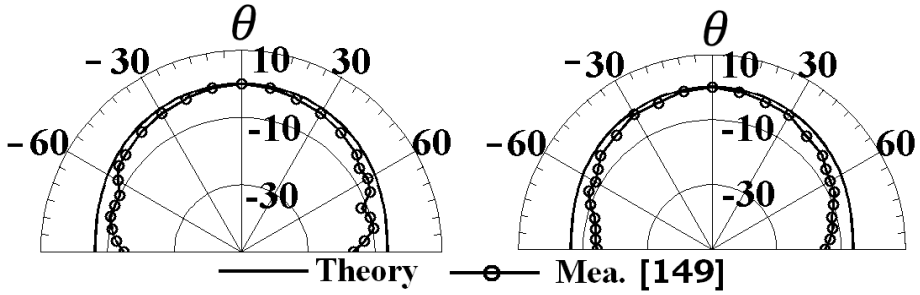

(a) E-plane ($\varphi = 0^o$) (b) H-plane ($\varphi = 90^o$)

(i) TM_{10}^z Mode: ($a = 25.4mm, \varepsilon_r = 4.4$) [149]

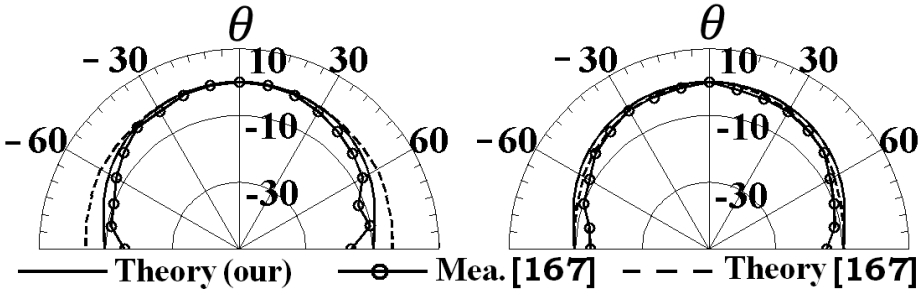

(a) E-plane ($\varphi = 0^o$) (b) H-plane ($\varphi = 90^o$)

(ii) TM_{11}^z Mode ($a = 30mm, \varepsilon_r = 2.55$) [167]

Fig. 5.7 Experimental validation of far-field power patterns for different TM_{mn}^z modes

5.3.3 Input Impedance

For efficient excitation of a particular mode, the knowledge on input impedance (Z_{in}) and its variation with feed location are very important. For theoretical investigations, coaxial probe is modeled here in four different ways. The effect of different definitions of probe excitation on input impedance is investigated first. Typical results are shown for TM_{12}^z mode in Fig. 5.8. It is found that they all produce the same result. It is also found that the input impedance do not vary with w_x and/or w_y for a particular mode. This is shown in shown in Fig. 5.9 for TM_{32}^z mode. Hence it is concluded that cavity model

analysis of microstrip antenna gives the same results for one dimensional or two dimensional or delta function of feed modeling. Further, any reasonable feed dimension can be used for $\vec{J}_x, \vec{J}_y$ and $\vec{J}_{xy}$. For better clarity and resolution, theoretical results are shown only for $\vec{J}_d$ only. Therefore, it is concluded to use $\vec{J}_d$ to investigate the microstrip antenna using the simple cavity model as it does not process any single or double integration in the evaluation of $< J\psi_{mn} >$.

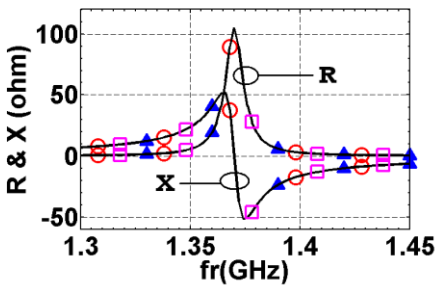

Fig. 5.8 Effect of different feed modeling on input impedance for TM_{11}^z mode: J_x (in solid line), J_y (in star), J_{xy} (in circle) and J_d (in square) ($a = 100mm, d = 1.59mm, \varepsilon_r = 2.32$, $tan\,\delta = 0.0005, w_x = w_y = 3mm, x_o = 40mm$, $y_o = 5mm$): w_x and w_y are in mm

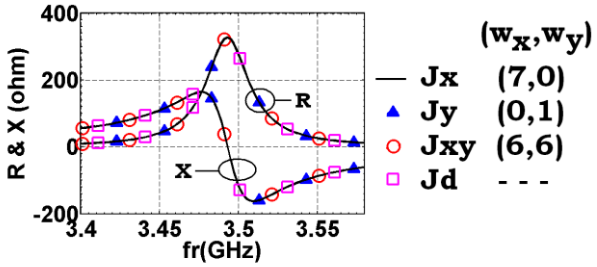

Fig. 5.9 Effect of feed dimensions w_x and/or w_y on input impedance for TM_{32}^z mode: J_x (in solid line), J_y (in triangle), J_{xy} (in circle) and J_d (in square) ($a = 100mm, d = 1.59mm, \varepsilon_r = 2.32$, $tan\,\delta = 0.0005, x_o = 40mm, y_o = 5mm$) : w_x and w_y are in mm

Therefore, theoretical results on input impedance ($Z_{in} = R + jX$) are verified with experimental data with the help of $\vec{J}_d$ only as shown in Fig. 5.10 for first four broadside radiating modes. It is found that our theoretical results are in good agreement with experimental data. Little discrepancy is found in the measured X at TM_{20}^z mode as shown in Fig. 5.10(c). This may be due to small air gap between the conducting patch and substrate, inevitable for our fabrication technique.

Further, it is quite obvious to have a little discrepancy between theoretical and experimental results because many factors are not considered in cavity model analysis, such as thickness of conducting patch, the finite size of the substrate and ground plane, etc. This type of discrepancy in input impedance of an equilateral TMA is also noticeable for TM_{10}^z mode [6, Fig. 12] and TM_{20}^z and TM_{21}^z modes [6, Fig. 13].

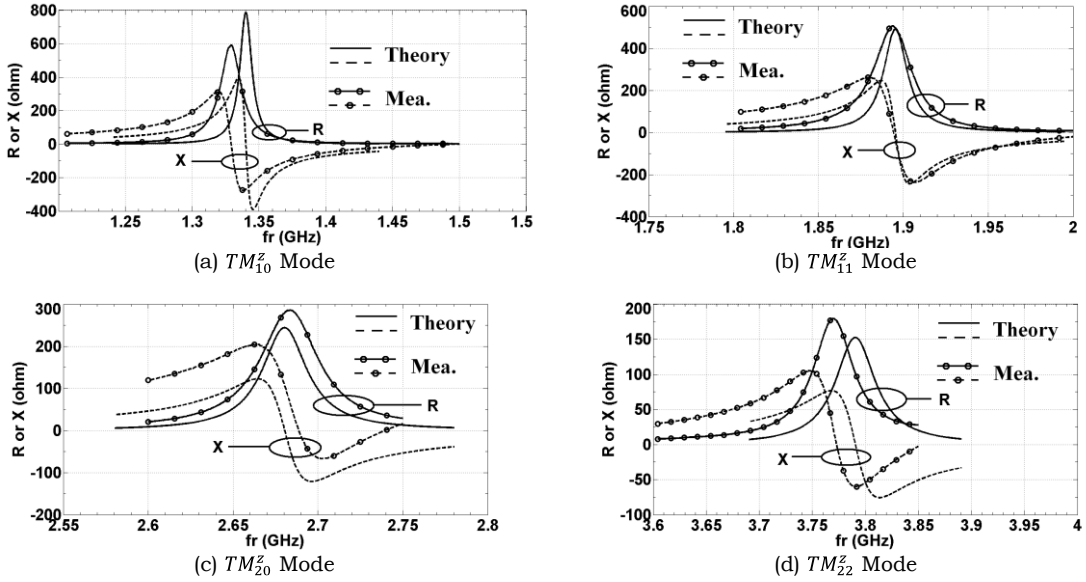

(a) TM_{10}^{z} Mode (b) TM_{11}^{z} Mode

(c) TM_{20}^{z} Mode (d) TM_{22}^{z} Mode

Fig. 5.10 Experimental validation of input impedance for different modes ($a = 70mm, d = 0.762mm, \varepsilon_r = 2.5,\ tan\,\delta = 0.0035, x_o = 5mm, y_o = 2mm$)

Variation of Z_{in} with feed position is also important to excite one or more than one broadside radiating modes. If we have a prior knowledge, we can easily avoid trial and error method. A closer look reveals that eigenfunctions ψ_{mn} of an isosceles 45°–45°–90° TMA is a superposition of eigenfunctions of rectangular MA for TM_{mn} and TM_{nm} modes. Therefore, it is easy to excite two broadside modes. It is found that one can excite three broadside radiating modes by choosing a proper field position. A typical point $D\ (x_d, y_d)$ is selected on AC sides and the probe is traversed from D to B. Typical results are shown in Fig. 5.11 for TM_{10}, TM_{11} and TM_{22} modes which produce 71, 72 and 80Ω maximum input resistance respectively at $x_o = 66mm$. Therefore, isosceles 45°–45°–90° TMA can also be utilized as a triple band antenna like equilateral TMA. From Fig. 5.11, it is clear that the TM_{20} mode will not be excited for $62mm < x_o < 66.5mm$ as it produces almost zero input resistance in that region. Therefore, mode suppression is possible without any extra circuitry (i.e. shorting pin). In a similar way, we can suppress other higher order modes also by selecting proper feed position.

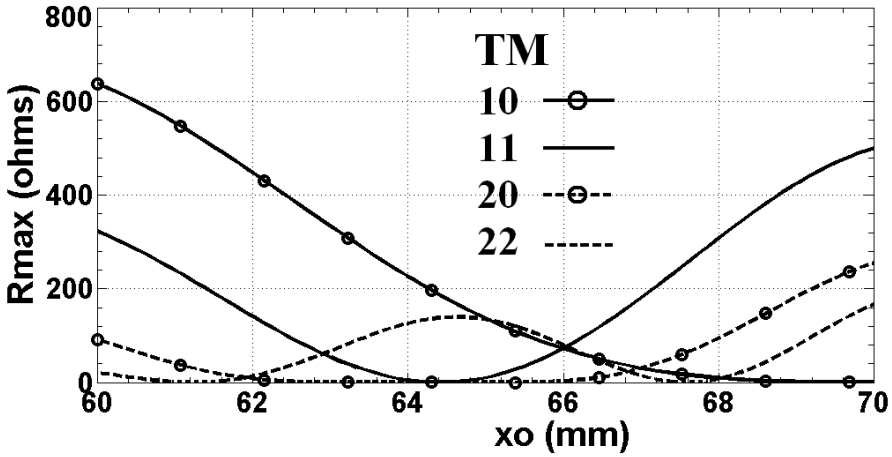

Fig. 5.11 Variation of maximum input resistance for different modes ($a = 70mm, d = 0.762mm, \varepsilon_r = 2.5, tan\,\delta = 0.0035, x_d = 60mm$)

It is very interesting to note that we can easily suppress the fundamental TM_{10}^z mode of an isosceles 45°–45°–90° TMA without any shorting pin or any other extra circuitry. If we choose the feed position near to corners A or C, all modes are always excited. In case of feed position near to corner B, the fundamental TM_{10}^z mode is being suppressed and the TM_{11}^z mode becomes the first excited mode. This is shown in Fig. 5.12.

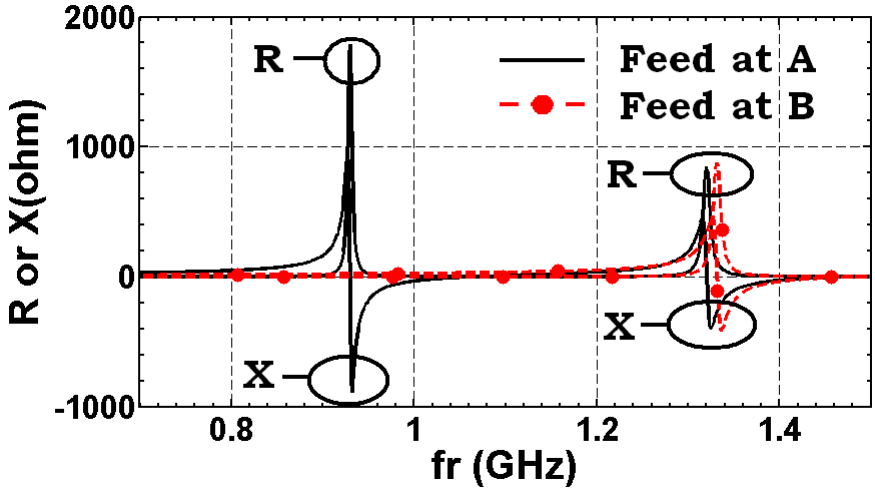

Fig. 5.12 Suppression of fundamental TM_{10}^z mode: feed at A ($x_o = 10mm, y_o = 5mm$) and B ($x_o = 90mm, y_o = 10mm$) : ($a = 70mm, d = 0.762mm, \varepsilon_r = 2.5,\ tan\,\delta = 0.0035$)

5.3.4 Radiated Power, Quality factor, Efficiency and Gain

In this section, radiated power (P_r in %), Q-factor, bandwidth (BW), gain (G), efficiency (e) etc. are discussed. It is important to have a prior knowledge on total quality factor (Q_t) and radiated power $P_r(\%)$ to design an antenna as an efficient radiator. Due to different excitations, modal amplitudes differ for a particular mode. It is found that the intermediate data such as W_t, P_c, P_d etc may vary, but the concerned final results i.e. $P_r(\%), Q_r(=\omega_r W_t/P_r)$, Q_t, G etc are not distinguishable as expected. Typical results are shown in Table 5.4 for TM_{21} and TM_{40} modes. A closer look reveals that these final quantities are independent of modal amplitudes. Basically, the far-zone electric field of a microstrip antenna is mainly dependent on the magnitude of $\vec{E}_z$ and independent of other field components according to cavity model analysis [12-15]. Therefore the magnitude of $\vec{E}_z$ is cancelled from numerator and denominator. Similar observation is also found for 30°–60°–90° TMA in Chapter IV. Further, the effect of feed position on Q-factor is also very small [6].

Table 5.4

Comparison of various quantities for different feed modeling

$(a = 100mm, d = 1.59mm, \varepsilon_r = 2.32, tan\,\delta = 0.0005)$

Mode	J	Intermediate Parameter				Final Parameter					
		W_t	P_r	P_c	P_d	P_r (%)	Q_r	Q_t	e(%)	BW	G (dB)
TM_{21}^z	J_x	4.64E+09	3.64E+17	5.69E+16	3.21E+16	3.6	176.5	141.8	80.3	0.5	5.1
	J_y	4.64E+09	3.64E+17	5.69E+16	3.21E+16	3.6	176.5	141.8	80.3	0.5	5.1
	J_{xy}	4.63E+09	3.63E+17	5.68E+16	3.20E+16	3.6	176.5	141.8	80.3	0.5	5.1
	J_d	4.65E+09	3.64E+17	5.70E+16	3.22E+16	3.6	176.5	141.8	80.3	0.5	5.1
TM_{40}^z	J_x	2.05E+09	6.91E+17	3.34E+16	2.50E+16	8.687	72.33	66.69	92.21	1.06	6.74
	J_y	2.04E+09	6.86E+17	3.31E+16	2.48E+16	8.687	72.33	66.69	92.21	1.06	6.74
	J_{xy}	2.03E+09	6.84E+17	3.31E+16	2.48E+16	8.687	72.33	66.69	92.21	1.06	6.74
	J_d	2.06E+09	6.92E+17	3.34E+16	2.50E+16	8.687	72.33	66.69	92.21	1.06	6.74

Variations of $P_r(\%)$, Q_r, Q_t, BW, e and G with resonant frequency for first five modes are shown in Fig. 4.13 for J_d only.

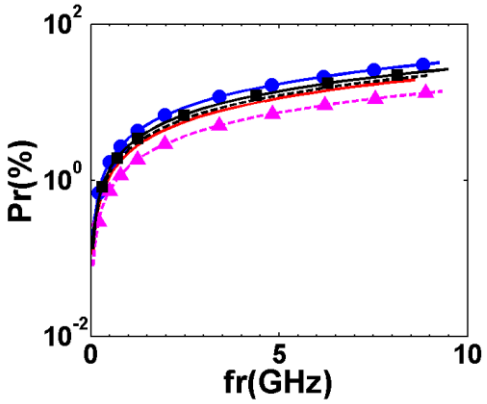

(a)Variation of $P_r(\%)$ with frequency

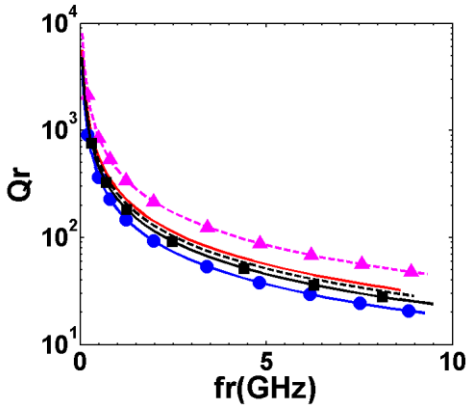

(b)Variation of Q_r with frequency

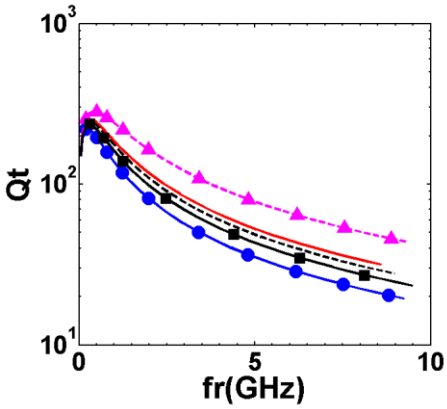

(c)Variation of Q_t with frequency

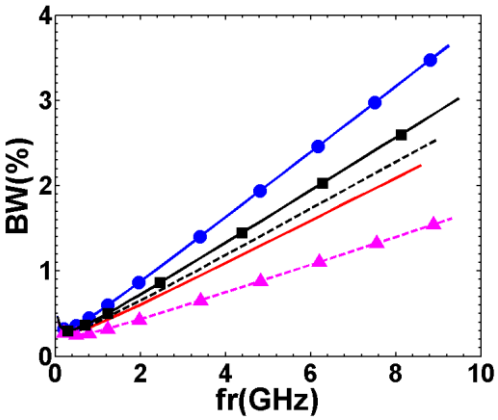

(d)Variation of BW with frequency

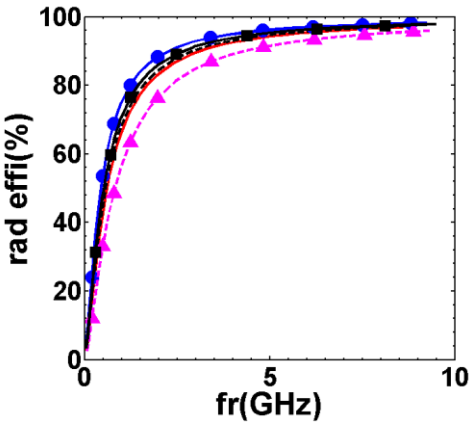

(e)Variation of e with frequency

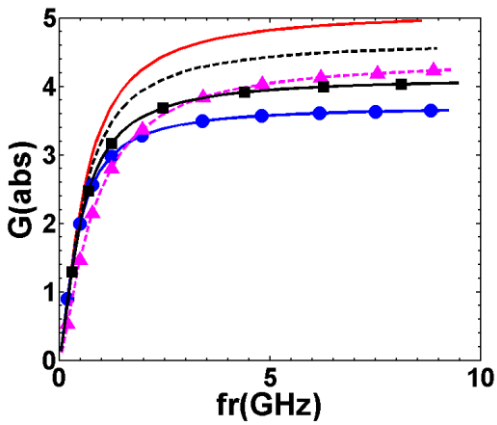

(f)Variation of G with frequency

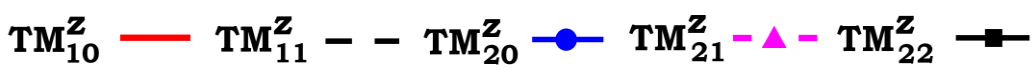

Fig. 5.13 Radiation characteristics of 45°–45°–90° TMA ($d = 1.59mm, \varepsilon_r = 2.32, tan\delta = 0.0005$)

In Table 5.5, radiation characteristics of first few modes are shown for $a = 100mm, h = 1.59mm, \varepsilon_r = 2.32$ and $tan\delta = 0.0005$. The base length of the 30°–

60°–90° TMA is kept equal to the median of an equilateral TMA having side length 100mm. Radiated power in percentage (P_r in %), radiation Q-factor (Q_r), total Q-factor (Q_t), BW (in %), gain (in dB), radiation efficiency (e) are shown. From Table 5.5, it is found that suitable higher order modes can produce higher gain compared to fundamental TM_{10}^z mode.

Table 5.5

Characteristics of first 15 modes of a 45°–45°–90° TMA

($a = 100mm, d = 1.59mm, \varepsilon_r = 2.32$ and $tan\delta = 0.0005$)

Sl No	Mode	f_r (GHz)	$P_r(\%)$	Q_r	Q_t	BW (%)	Gain (dB)	$e(\%)$
1	TM_{10}^z	0.9688	2.174	289	188.8	0.3745	5.24	65.34
2	TM_{11}^z	1.37	3.362	186.9	143.4	0.4932	5.55	76.73
3	TM_{20}^z	1.938	6.663	94.3	82.99	0.852	5.15	88.01
4	TM_{12}^z	2.166	3.199	196.4	154.2	0.4585	5.41	78.51
5	TM_{22}^z	2.74	7.034	89.32	80.07	0.8832	7.04	89.64
6	TM_{30}^z	2.906	8.054	78.01	70.97	0.9963	5.76	90.98
7	TM_{13}^z	3.064	5.075	123.8	107.2	0.6597	5.21	86.59
8	TM_{23}^z	3.493	5.175	121.4	105.9	0.6675	6.30	87.25
9	TM_{40}^z	3.875	8.687	72.33	66.69	1.06	6.74	92.21
10	TM_{14}^z	3.994	5.71	110	97.6	0.7245	6.40	88.7
11	TM_{33}^z	4.11	7.772	80.85	73.98	0.9558	8.87	91.5
12	TM_{24}^z	4.332	6.621	94.9	85.7	0.8251	6.57	90.3
13	TM_{34}^z	4.844	5.891	106.7	95.49	0.7405	7.42	89.52
14	TM_{15}^z	4.94	6.325	99.33	89.62	0.789	8.42	90.22
15	TM_{25}^z	5.217	8.082	77.75	71.75	0.9856	6.04	92.28

5.4 Conclusion

In this chapter, theoretical investigations on isosceles 45°–45°–90° Triangular Microstrip Antenna (TMA) is presented using the cavity model. Physical explanation of the 3D cavity model is provided for the first time indicating how it reduces to the standard 2D case for small values of substrate heights. Modal analysis is performed for different TM_{mn}^z modes of a probe fed 45°–45°–90° TMA. Feed (coaxial probe) is modeled here in four different ways to study its input impedance characteristics and far-field radiation patterns. It is

found that all four definitions for feed modeling are able to predict almost indistinguishable characteristics. From this theoretical investigation, it is found that:

- For a given resonant frequency, 45°–45°–90° TMA takes half area compared to the square microstrip antenna
- It is better to use $\vec{J}_d$ to investigate the microstrip antenna using simple cavity model as it does not process any single or double integration in the evaluation of $< J\psi_{mn} >$.
- Excitation of higher TM^z_{mnp} modes with third modal index p equal to 1 is quite impossible using conventional feeding mechanism for thin substrate. Therefore, the 3D eigenfunctions $\psi_{mnp}(x,y,z)$ becomes 2D eigenfunctions $\psi_{mn}(x,y)$ because $H(z)$ becomes equal to unity (i.e. constant) with third modal index $p = 0$.
- Four modes ($TM^z_{10}, TM^z_{11}, TM^z_{20}$ and TM^z_{22}) out of first five mode produce a peak in the broadside direction
- It is possible to excite three modes for a reasonable maximum value of input resistance (R) using a single coaxial probe. Therefore, 45°–45°–90° TMA can be used as a triple band antenna.
- Fundamental TM^z_{10} mode can easily be suppressed without any shorting pin or any other extra circuitry.

Chapter VI

Isosceles Triangular Microstrip Antenna

6.1 Introduction

In the last three chapters, theoretical investigations on Equilateral Triangular Microstrip Antenna (ETMA), 30°–60°–90° Triangular Microstrip Antennas (TMA) and isosceles 45°–45°–90° TMAs are presented using 'Cavity Model'. A mathematical explanation of having a third modal index equal to zero for the small thickness of substrate height is given here for the first time. Characteristics of different modes are presented in a systematic way so that one can utilize it to design an antenna efficiently.

Besides these three triangular shapes, eigenfunctions for a given set of boundary conditions is not available for other triangular shaped geometries. An arbitrary shaped triangle is characterized by three unequal angles. Evaluation of eigenfunctions for such type of triangular geometries is very difficult and has not been reported yet. An attempt is made to find the solution for an isosceles triangular geometry by Damle *et al* [169] using tri-linear transformation as defined in [53-55]. As the tri-linear transformation found in literature [53-55] is applicable only for equilateral triangular geometry, the attempt by Damle *et al* [169] is not valid for arbitrary shaped isosceles triangular geometry. Further, it is clearly mentioned in [169] that the general solution of an isosceles triangle is not possible using tri-linear transformation.

But, it is found that the approximate solution of an arbitrary shaped isosceles triangular microstrip antenna can be obtained using tri-linear transformation for fundamental TM_{10}^{z} mode. In case of higher order modes, the solution for eigenfunctions and eigenvalues both do not satisfy the wave equation simultaneously. We tried to define a CAD model to obtain an approximate solution of eigenfunctions for higher order modes, but this CAD

model produces large error (50-60% or more, sometimes 150%) in the prediction of resonant frequency. If we try to predict the resonant frequency using CAD model, we did not get proper internal field distribution. Therefore, we will restrict our investigation on fundamental TM_{10}^{z} mode only.

In this chapter, theoretical investigation on arbitrary shaped isosceles Triangular Microstrip Antenna (TMA) is presented for fundamental TM_{10}^{z} mode only. Approximate solutions for eigenfunctions and eigenvalues are obtained using tri-linear transformation as defined by S. A. Schelkunoff [24]. Radiation characteristics, input impedance, radiated powers, total Q-factors, gain, etc. are discussed in detail for different isosceles TMA. Limitation of our theory is also described. Two antenna prototypes are fabricated and measured in our laboratory. Theoretical results are verified with experimental data.

6.2 Theory

In this section, theoretical investigations on arbitrary shaped isosceles TMA are presented using the concept of 3D cavity model as introduced in Chapter V. Antenna geometry of an isosceles TMA is shown in Fig. 6.1 where the antenna is placed along *x*-*y* surface of the rectangular coordinate system. The antenna is bounded by AC, AB and BC sides along the *x*-*y* surface. The antenna is aligned along the *z*-axis. The length of equal sides (AC and AB) is a and the equal angles θ_{iso} are adjacent to the BC side as shown in Fig. 6.1. The antenna is excited using 50Ω coaxial probe which is placed at (x_o, y_o) point. Eigenfunctions, eigenvalues, far-field radiation patterns, input impedance, Q-factors etc. are investigated.

6.2.1 Eigenfunctions

To evaluate the eigenfunctions $\psi_{mnp}(x, y, z)$ of an isosceles TMA, the antenna is assumed as cavity whose side walls are Perfect Magnetic Conductor (PMC) and top and bottom walls are Perfect Electric Conductor (PEC).

Therefore, the cavity is basically a 3D structure whose eigenfunctions is expressed as:

$$\psi = F(x,y) \times H(z) \tag{6.1}$$

where $H(z) = \left[Ae^{jk_z z} + Be^{-jk_z z}\right]$ (6.2)

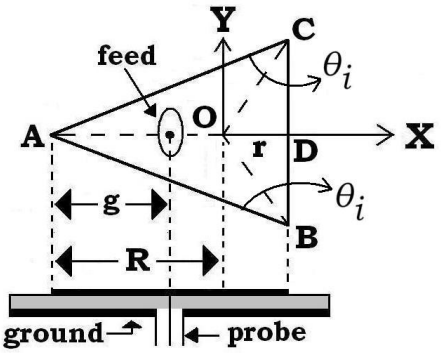

Fig. 6.1 Geometry of isosceles TMA

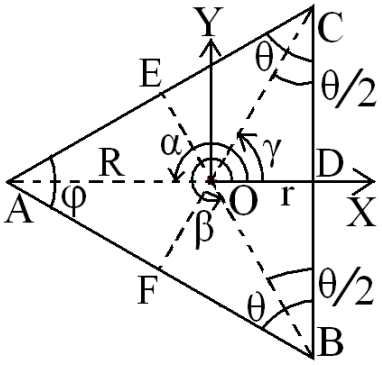

Fig. 6.2 Coordinate for trilinear transformation

To obtain the $F(x,y)$ function, we use the tri-linear coordinate system as equilateral triangle is a special case of an isosceles triangle. Further, we follow the procedure as reported by B. McCartin [53] for theoretical derivation. The geometry of the isosceles triangle with tri-linear coordinate system is shown in Fig. 6.2 where with $AB = AC = a, BC = b, \angle ACB = \angle ABC = \theta, \angle CAB = \varphi, OD = r$ and $AO = R$. The coordinates of any point P within the isosceles triangle can be expressed in terms of tri-linear coordinate system (u,v,w) as:

$$u = (x\cos\alpha + y\sin\alpha)$$
$$v = (x\cos\beta + y\sin\beta)$$
$$w = (x\cos\gamma + y\sin\gamma) \tag{6.3}$$

such that

$$u + v + w = 0 \tag{6.4}$$

From Fig. 6.2, it is easily observed that $\alpha = \pi, \beta = 2\pi - \gamma, \gamma = \pi/2 - \varphi/2$. With this definition of (u,v,w), we can write

$$u = x\cos(\alpha) + y\sin(\alpha) = -x \tag{6.5a}$$

$$w = x\cos(\gamma) + y\sin(\gamma) = px + qy \quad \text{where} \quad p = \sin(\theta/2)\,, q = \cos(\theta/2) \tag{6.5b}$$

$$v = x\cos(\beta) + y\sin(\beta) = px - qy \tag{6.5c}$$

To satisfy the basic property of trilinear co-ordinate system, i.e. $u + v + w = 0$, we have modify it using $(\mathbb{U}, \mathbb{V}, \mathbb{W})$ such that

$$\mathbb{U} = 2pu = gu \quad ; \quad g = 2p$$

$$\mathbb{V} = v$$

$$\mathbb{W} = w \tag{6.6}$$

The two dimensional Helmholtz equation is given by

$$\frac{d^2F}{dx^2} + \frac{d^2F}{dy^2} + \chi^2 F = 0 \qquad \text{where} \quad F \equiv F(x, y) \tag{6.7}$$

Following [53], the complete solution can be expressed as:

$$F(x, y) = \sum_{i=1}^{3} \cos\left[\alpha_i \left(x + \frac{R}{T_1}\right)\right] \cos\left(\beta_i y\right) \tag{6.8}$$

$$\alpha_1 = \frac{\pi l T_1}{H}, \qquad \alpha_2 = \frac{\pi m T_1}{H}, \qquad \alpha_3 = \frac{\pi n T_1}{H} \tag{6.9}$$

$$\beta_1 = \frac{\pi}{2}\left[J(m - l) + \frac{(m + l)}{G}\right] T_2 \tag{6.10a}$$

$$\beta_2 = \frac{\pi}{2}\left[J(n - m) + \frac{(n + m)}{G}\right] T_2 \tag{6.10b}$$

$$\beta_3 = \frac{\pi}{2}\left[J(l - n) + \frac{(n + l)}{G}\right] T_2 \tag{6.10c}$$

$$\chi_{mn}^2 = \frac{2}{3}\,\pi^2 \left[\frac{S}{H^2} + \frac{Q}{4}\left(3J^2 + \frac{1}{G^2}\right)\right](m^2 + mn + n^2) \tag{6.11}$$

$$l + m + n = 0 \quad ; \quad \{l, m, n\} = 0, \pm 1, \pm 2, \pm 3 \cdots \tag{6.12}$$

$$t = \sin\left(\frac{\varphi}{2}\right), \qquad G = (r + 2tR), \qquad H = (r + R), \qquad J = \frac{SG}{H^2 Q} \tag{6.13}$$

$$r = (b/2)\,tan(\theta/2)\ ;\ p = sin(\theta/2)\ ;\ q = cos(\theta/2)\ ;\ T_1 = 2p\ ;\ T_2 = 2q \tag{6.14}$$

The evaluation of $H(z)$ is straight forward as shown for 45°–45°–90° TMA in Chapter V and is not repeated here for brevity. Therefore, we can write the eigenfunctions (ψ) as:

$$\psi = F(x,y) \times H(z)$$
$$= \left(\sum_{i=1}^{3} \cos[\alpha_i(x+R)]\cos[\beta_i y]\right) \times \cos(k_z(z-d)) \; ; \; k_z = \frac{p\pi}{2d} \;\; , \quad p = 0,1,2,3,\cdots \quad (6.15)$$

Excitation of higher order modes with $p \geq 1$ is impossible for thin substrate as explained in detail in Chapter V and is not repeated here for the sake of brevity. Therefore, the eigenfunctions $\psi_{mnp}(x,y,z)$ can be expressed as $\psi_{mn}(x,y)$.

Now, the antenna is excited using a $\hat{z}$-directed coaxial probe. The $\vec{E}_z$ component will satisfy the inhomogeneous wave equation whose solution can be expressed as:

$$E_z = j\omega\mu \sum_{m=0}^{\infty}\sum_{n=0}^{\infty} \frac{1}{(k^2 - k_{mnp}^2)} \frac{< J\psi_{mnp} >}{< \psi_{mnp}\psi_{mnp} >} \psi_{mnp}(x,y,z) \;\; ; \;\; k_{mnp}^2 = \chi_{mn}^2 + k_z^2 \quad (6.16)$$

$$= j\omega\mu \sum_{m=0}^{\infty}\sum_{n=0}^{\infty} \frac{1}{(k^2 - k_{mn}^2)} \frac{< J\psi_{mn} >}{< \psi_{mn}\psi_{mn} >} \psi_{mn}(x,y) \qquad ; \qquad p = 0$$

$$= j\omega\mu \sum_{m=0}^{\infty}\sum_{n=0}^{\infty} \frac{A_{mn}}{(k^2 - k_{mn}^2)} \psi_{mn}(x,y) \qquad ; \qquad A_{mn} = \frac{< J\psi_{mn} >}{< \psi_{mn}\psi_{mn} >} \quad (6.17)$$

Limitation

It should be pointed here that the tri-linear transformation is valid for equilateral triangle only, not for any arbitrary shaped triangle as per its definition [24]. In [169], it is clearly mentioned that general solutions for isosceles triangle are not possible to obtain using tri-linear transformation as defined in [53-55]. Mathematical proof is also given there to justify the basis of our analysis. In case of our analysis, the solution of an arbitrary shaped isosceles triangle is obtained using tri-linear transformation as defined in [24]. It is found that the solutions on eigenfunctions and eigenvalues of an isosceles

$\theta_i - \theta_i - \varphi_i$ TMA having $\theta_i \geq 60°$ are valid for fundamental mode ($m = 1, n = 0, p = 0$) only. In case of higher order mode, the solution of eigenfunctions and eigenvalues both do not satisfy the wave equation simultaneously. Several CAD models are tried to obtain the general solution with the existing solutions as derived here on eigenfunctions and eigenvalues but we did not get proper results. For a particular CAD model, the solutions (eigenfunctions and eigenvalues) for different isosceles triangle are compared with the solutions of an equilateral triangle as equilateral triangle is a special case of an isosceles triangle. We did not get a suitable CAD model which is valid for all isosceles triangles including an equilateral triangle for all higher order modes. Similar observation is also found for the isosceles $\theta_i - \theta_i - \varphi_i$ TMA having $\theta_i < 60°$. Further, as the angle θ_i decreases from 60° of an isosceles $\theta_i - \theta_i - \varphi_i$ TMA, say for example $\theta_i = 30°$, it is found that the theoretical field patterns do not match with data obtained using 3D EM simulator HFSS [9] at fundamental TM_{10}^z mode. Therefore, we will discuss the fundamental TM_{10}^z mode of an isosceles $\theta_i - \theta_i - \varphi_i$ TMA having $\theta_i \geq 60°$. The properties of different isosceles TMA at fundamental TM_{10}^z mode are also presented next few sections.

In Fig. 6.3, internal magnetic field distributions for some isosceles TMA are shown for fundamental TM_{100}^z mode only. Three sides *AC*, *AB* and *BC* are also shown to define the triangular region. The normalized magnitude of magnetic field (in dB) is used to express the internal fields for different isosceles TMA.

6.2.2 Resonant Frequency

To compute the resonant frequency (f_r), separation equation ($\chi^2 + k_z^2 = \varepsilon_r k_0^2$) is used. Therefore, we can write:

$$f_r = \frac{c}{2\pi\sqrt{\varepsilon_r}} \times [\chi^2 + k_z^2]^{1/2} \tag{6.18}$$

where c is the velocity of light in free space and ε_r is the relative permittivity of substrate.

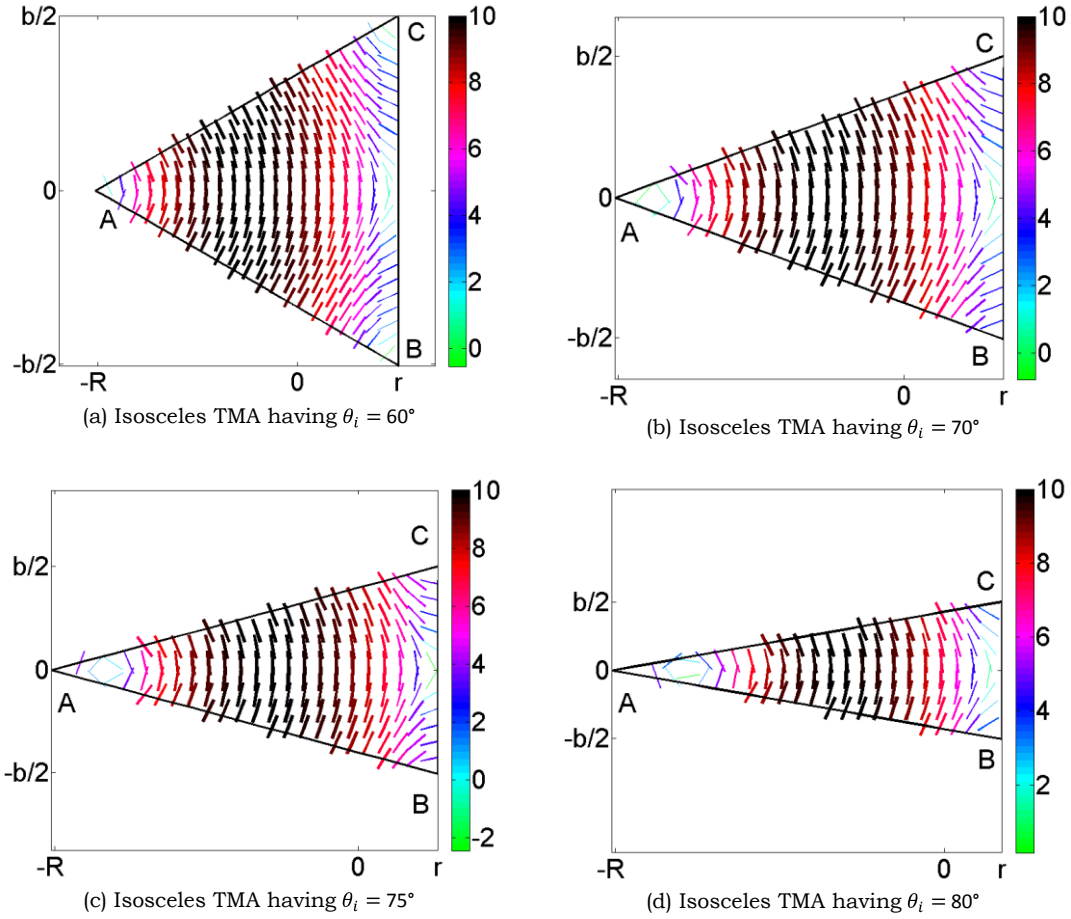

(a) Isosceles TMA having $\theta_i = 60°$

(b) Isosceles TMA having $\theta_i = 70°$

(c) Isosceles TMA having $\theta_i = 75°$

(d) Isosceles TMA having $\theta_i = 80°$

Fig. 6.3 Approximate internal magnetic field distribution (in dB) for some isosceles TMA at fundamental TM_{10}^z mode (a = 100mm, d = 1.59mm, ε_r = 2.32

To account the effect of fringing, several isosceles $\theta_i - \theta_i - \varphi_i$ TMAs are simulated in 3D EM simulator HFSS [9]. It is found that as the angle θ_i increases from 60° to 90°, resonant frequency decreases. Typical results are shown in Fig. 6.4. It is interesting to note that the physical area of an isosceles 65°–65°–50° TMA is greater than the those for isosceles 80°–80°–20° TMA as shown in Fig. 6.5. For example, the area of $\Delta AB'C'$ is smaller than the area of ΔABC. Similarly, the area of $\Delta AB''C''$ is smaller than the area of $\Delta AB'C'$.

Therefore, the resonant frequency decreases as the physical area of isosceles $\theta_i - \theta_i - \varphi_i$ TMA decreases.

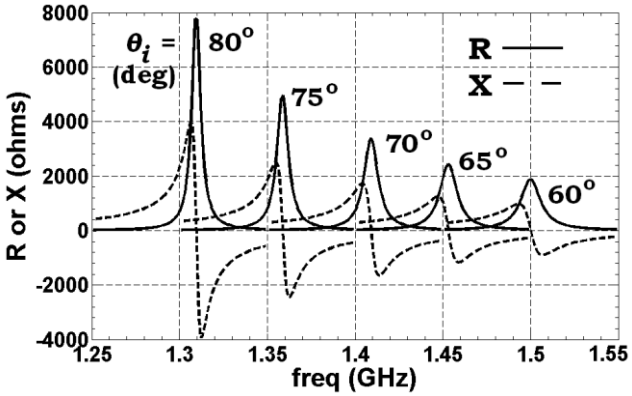

Fig. 6.4 Variation of simulated input impedance for different isosceles TMAs ($a = 80mm, d = 1.59mm, \varepsilon_r = 2.32, \tan\delta = 0.0005, g = 5mm$)

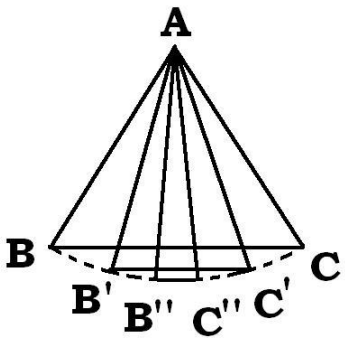

Fig.6.5 Geometry of different isosceles triangle

Based on data obtained from the 3D EM simulator, a curve fitted expression for the effective side length (a_e) of the isosceles $\theta_i - \theta_i - \varphi_i$ TMA [12-15] is expressed as:

$$a_e = R_1 \times R_2 \times [a + d \times (\varepsilon_r)^{-0.25}] \tag{6.19a}$$

where

$$R_1 = \begin{cases} 0.97, & \theta_i = 60^o \\ 1.05, & \theta_i > 60^o \end{cases} \tag{6.19b}$$

$$R_2 = 0.6692 \times {\varepsilon_r}^{0.007584 \times \theta_i} + \frac{5.207}{10^{10}} \times {\varepsilon_r}^{0.2507 \times \theta_i} \tag{6.19c}$$

Here, the angle θ_i is in degrees.

6.2.3 Feed Model

In Chapter V, feed ($\vec{J}$) is modeled in four different ways to investigate the input impedance characteristics of an isosceles 45°–45°–90° TMA as:

I. Uniform current ribbon of effective width w_x along $\hat{x}$ direction ($\vec{J}_x$) [6],

II. Uniform current ribbon of effective width w_y along $\hat{y}$ direction $(\vec{J}_y)$ and

III. Two dimensional rectangular shaped strip $(\vec{J}_{xy})$ of effective area $w_x \times w_y$ [13]

IV. Delta function $(\vec{J}_d)$ along x-y coordinates

Comparative study is also presented between all four definitions of feed modeling to understand the effect of feed on the performance of a TMA. It is found that they all produce same results. Therefore, for theoretical simplicity, we define the feed $(\vec{J})$ here as

$$\vec{J}_d = \hat{z}\delta(x - x_o)\delta(y - y_o) \tag{6.20}$$

6.2.4 Far-Field Radiation Patterns

To predict the far-field radiation patterns of any isosceles TMA, magnetic surface current model is applied [6, 12-15, 162]. Magnetic surface currents $\left(\vec{M}_s = 2\vec{E} \times \hat{n}\right)$ are evaluated along its periphery AC, BC and AB sides using the 'Equivalence Principle' [4, 16]. The steps are similar to those for equilateral, 30°–60°–90° or 45°–45°–90° TMA and are time consuming. A very simple, time efficient and computationally efficient technique is applied to evaluate the far-field radiation patterns of any isosceles TMA. This process is general and is applied to different planar (aperture or microstrip antennas) and non-planar (dielectric resonator antenna) antennas as presented in Chapter XIII. Therefore, the steps are not repeated here for brevity. The far-zone electric field at point $P(r, \theta, \varphi)$ can be expressed as [16]:

$$E_\theta = -\frac{jk_o \exp(-jk_o r)}{4\pi r} \times \left[L_\varphi\right] \tag{6.21a}$$

$$E_\varphi = \frac{jk_o \exp(-jk_o r)}{4\pi r} \times [L_\theta] \tag{6.21b}$$

$$L_\theta = F_x cos(\theta)cos(\varphi) + F_y cos(\theta)sin(\varphi) - F_z sin(\theta) \tag{6.22a}$$

$$L_\varphi = -F_x sin(\varphi) + F_y cos(\varphi) \tag{6.22b}$$

where all terms are carrying their usual meaning and F_x, F_y, F_z are evaluated using the process presented in Chapter XIII.

6.2.5 Input Impedance

To evaluate the input impedance (Z_{in}) at the feed point (x_o, y_o), the RF voltage (V_{in}) is calculated at (x_o, y_o) as [13]:

$$V_{in} = -E_z(x_o, y_o)h \tag{6.23}$$

Therefore, the input impedance can be expressed as:

$$Z_{in} = \frac{V_{in}}{I_o} = R + jX = -j\omega\mu \frac{h}{I_o} \sum_{m=0}^{\infty} \sum_{n=0}^{\infty} \frac{A_{mn}}{(k^2 - k_{mn}^2)} \psi_{mn}(x_o, y_o) \tag{6.24}$$

where $k^2 = k_o^2 \varepsilon_r (1 - j\delta_{eff})$. Here δ_{eff} is the effective loss tangent, defined as $\delta_{eff} = 1/Q_t$ where Q_t is total quality factor.

6.2.6 Radiated Power, Quality factor, Efficiency and Gain

Neglecting the effect of surface wave loss, radiated power $P_r(\%)$, radiation loss (P_r), conductor loss (P_c), dielectric loss (P_d), total stored energy (W_t), efficiency (e), gain (G), directivity (D), Bandwidth (BW) etc. are evaluated using standard procedure as found in [12-16] or as calculated for equilateral TMA in Chapter III. Therefore, the total quality factor (Q_t) is defined as:

$$Q_t = \frac{\omega_r W_t}{P_c + P_d + P_r} \tag{6.25}$$

6.3 Results

In this section, theoretical results on resonant frequency, far-field patterns, input impedance, etc. are discussed for various isosceles TMA at fundamental TM_{10}^z mode. Two antennas are fabricated in our laboratory for experimental validation as shown in Fig. 6.6. These two antennas are excited

using standard 50Ω co-axial probe whose inner conductor radius is 0.63mm. The same are also simulated using FEM based numerical 3D EM simulator, HFSS [9]. Theoretical results are compared with experimental data and/or data obtained using 3D EM simulator HFSS to show the accuracy of our theory.

Fig. 6.6 Photograph of fabricated isosceles TMAs: left θ_i = 77° and right θ_i = 68°

6.3.1 Resonant Frequency

Theoretical resonant frequencies are compared with experimental data as shown in Table 6.1. It is found, our theoretical results are in close agreement with measured (f_r^m) resonant frequency with accuracy of 1.5%.

Table 6.1

Experimental Validation of Resonant Frequency

θ_i (deg)	a (mm)	d (mm)	ε_r	Frequency (GHZ)		Error (%)
				Theory	Mea.	
60	100	1.59	2.32	1.2643	1.28 [6]	-1.224
68	50	0.762	2.5	2.1456	2.132	0.639
77	50	0.762	2.5	2.0684	2.046	1.096

5.3.2 Radiation Patterns

In this section, theoretical results on far-field radiation patterns for different isosceles TMA are investigated for fundamental TM_{10}^z mode. Normalized electric field strength at $\varphi = 0^o$ and $\varphi = 90^o$ plane are shown Fig. 6.7 for some isosceles TMA.

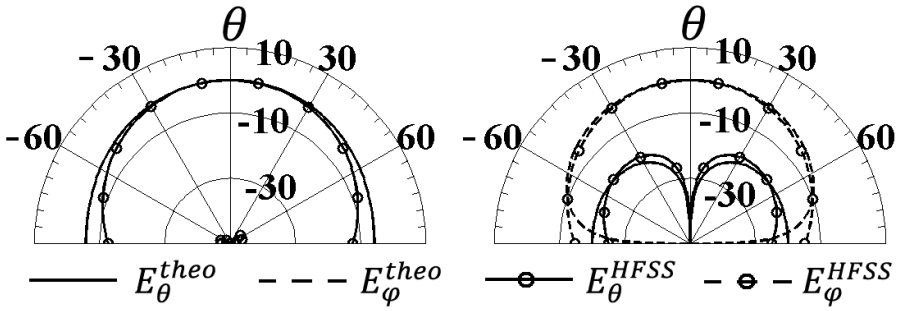

(a) φ = 0° plane (b) φ = 90° plane

(i) Normalized far-zone field patterns for θ_i= 60°

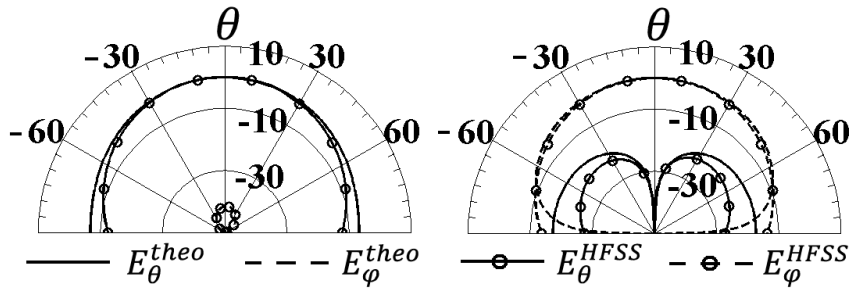

(a) φ = 0° plane (b) φ = 90° plane

(ii) Normalized far-zone field patterns for θ_i= 65°

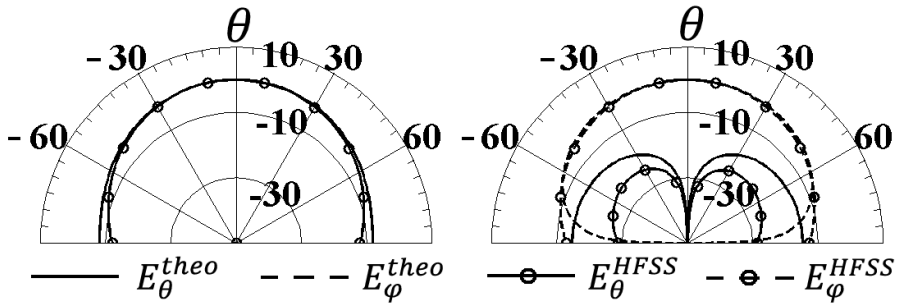

(a) φ = 0° plane (b) φ = 90° plane

(iii) Normalized far-zone field patterns for θ_i= 70°

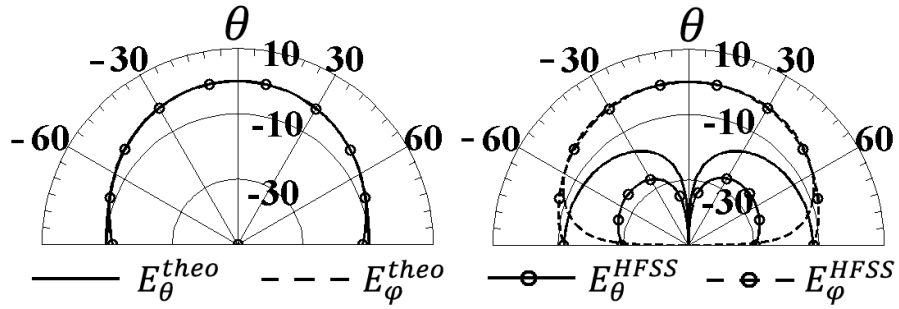

(a) φ = 0° plane (b) φ = 90° plane

(iv) Normalized far-zone field patterns for θ_i= 75°

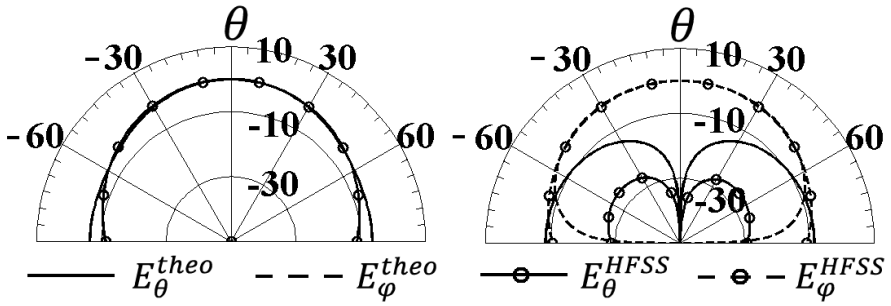

(a) φ = 0° plane (b) φ = 90° plane

(v) Normalized far-zone field patterns for θ_i= 80°

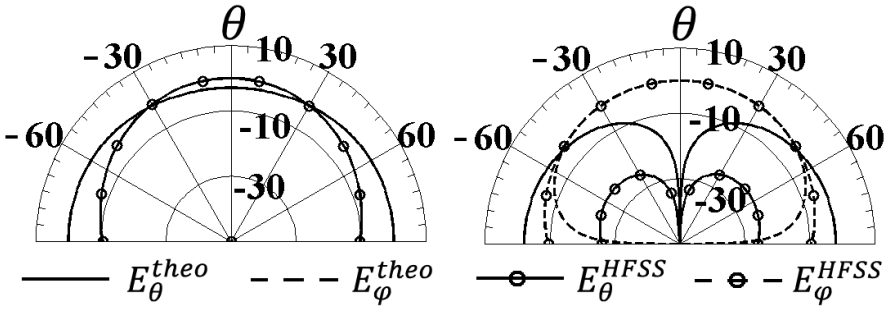

(a) φ = 0° plane (b) φ = 90° plane

(vi) Normalized far-zone field patterns for θ_i= 85°

Fig. 6.7 Plot of normalized far-zone field strength for various isosceles TMA ($a = 100mm, d = 1.59mm, \varepsilon_r = 2.32, tan\,\delta = 0.0005$)

Form Fig. 6.7, it is found that our theoretical results are in good agreement with data obtained from 3D EM simulator HFSS [9]. Further, it is also found from Fig. 6.7 that theoretical E_θ component is present only at $\varphi = 0^o$ plane whereas both E_θ and E_φ components are present at $\varphi = 90^o$ plane. Further, the magnitude of simulated E_φ component is quite small compared to E_θ at $\varphi = 0^o$ plane. Therefore, the radiation at $\varphi = 0^o$ plane is basically due to E_θ component. It is also clear from Figs. 6.7 that the fundamental TM_{10}^z mode of all isosceles TMA produces a peak in the broadside direction.

For experimental validation, our theoretical results on E-plane ($\varphi = 0^o$ plane) and H-plane ($\varphi = 90^o$ plane) are compared with experimental data for some isosceles TMA having θ_i= 60°, 68° and 77° as shown in Figs. 6.8. It is found that our theory is in good agreement with experimental data. Little discrepancy is found which is due to the finite size of ground plane.

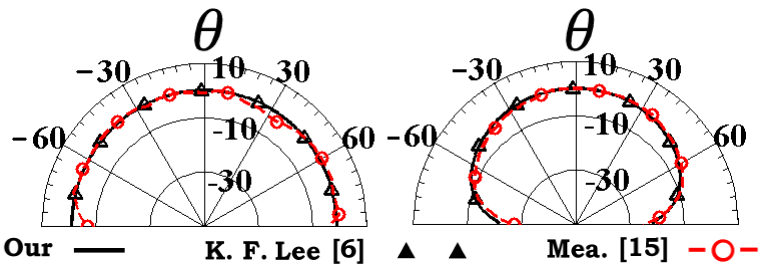

(a) $\varphi = 0^o$ plane (b) $\varphi = 90^o$ plane

(i) Theoretical and experimental power patterns for θ_i= 60° ($\varepsilon_r = 10, d = 1.27mm, f_r = 10\text{GHz}$) [15]

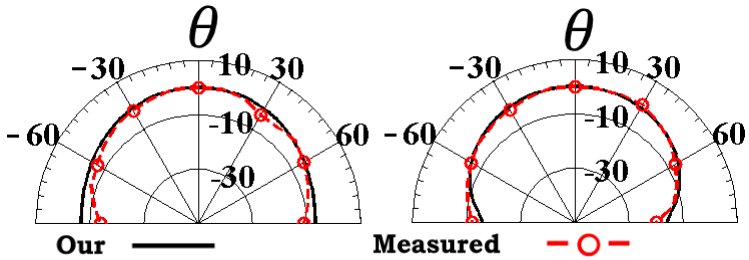

(a) $\varphi = 0^o$ plane (b) $\varphi = 90^o$ plane

(ii) Theoretical and experimental power patterns for θ_i= 68° ($a = 50mm, d = 0.762mm, \varepsilon_r = 2.5$)

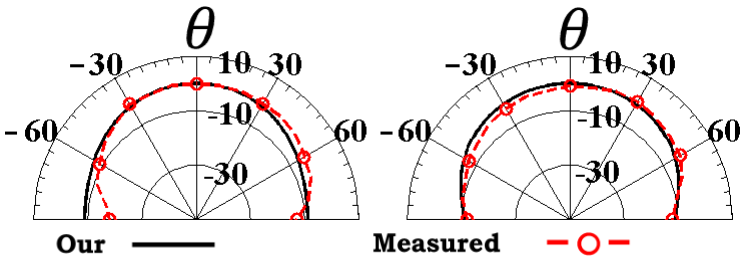

(a) $\varphi = 0^o$ plane (b) $\varphi = 90^o$ plane

(iii) Theoretical and experimental power patterns for θ_i= 77° ($a = 50mm, d = 0.762mm, \varepsilon_r = 2.5$)

Fig. 6.8 Experimental validation of far-field power patterns for different isosceles TMAs

6.3.3 Input Impedance

Variation of input impedance with frequency for different isosceles TMA in fundamental TM_{10}^z mode are shown in Fig. 6.9 for $a = 80mm, h = 1.59mm, \varepsilon_r = 2.32, tan\delta = 0.0005$ and $g = 5mm$. In Fig. 6.9, comparison of input impedance ($Z_{in} = R + jX$) between our theory and data obtained using 3D EM simulator HFSS [9] are shown for different isosceles TMA. It is found that our theoretical results on input impedance show close agreement with data obtained from 3D EM simulator HFSS. Little discrepancy is found in R. This may be due to our simplified theory which does not account for the finite size of ground plane. It is worth mentioning here that this type of discrepancy is also found in

equilateral TMA [6, 12-14].

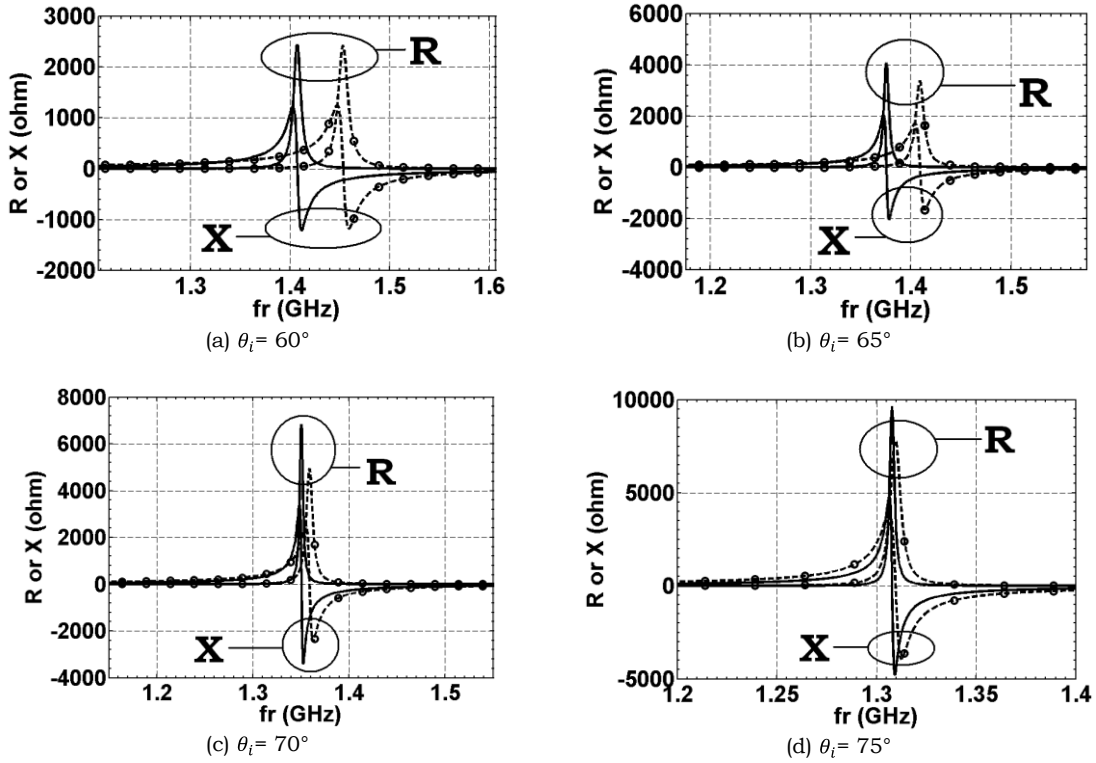

(a) θ_i= 60° (b) θ_i= 65°

(c) θ_i= 70° (d) θ_i= 75°

Fig. 6.9 Comparison of input impedance with data obtained using 3D EM simulator HFSS for different isosceles TMA ($a = 80mm, d = 1.59mm, \varepsilon_r = 2.32, tan\,\delta = 0.0005, g = 5mm$)

In Fig. 6.10, theoretical results on Z_{in} are compared with experimental data for different isosceles TMA. It is found that our theory is in good agreement with experimental data.

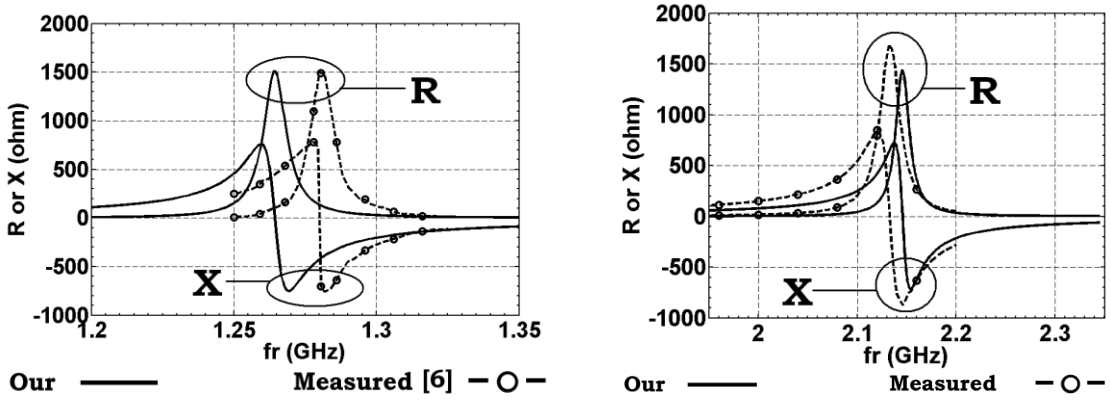

(a) θ_i= 60° ($a = 100mm, d = 1.59mm, \varepsilon_r = 2.32, tan\,\delta = 0.0005, g = 3mm$) [6]

(b) θ_i= 68° ($a = 50mm, d = 0.762mm, \varepsilon_r = 2.5, tan\,\delta = 0.0035, g = 5mm$)

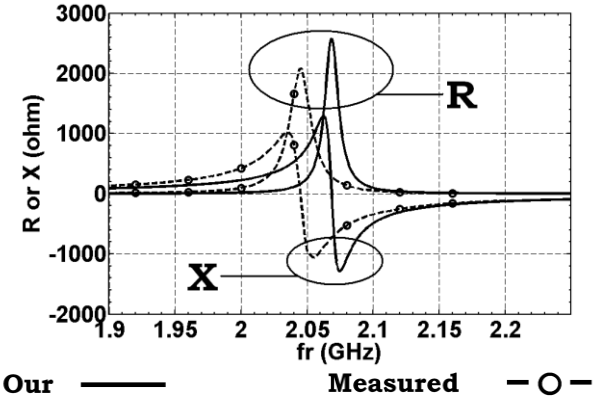

(c) θ_i= 77° ($a = 50mm, d = 0.762mm, \varepsilon_r = 2.5, tan\,\delta = 0.0035, g = 5mm$)

Fig. 6.10 Experimental validation of input impedance for different isosceles TMA

6.3.4 Radiated Power, Quality factor, Efficiency and Gain

In this section, radiated power, Q-factor, bandwidth (BW), gain (G) etc. are discussed. It is important to have a knowledge on total quality factor (Q_t) and radiated power $P_r(\%)$ to design an antenna as an efficient radiator. In Table 6.2, radiation characteristics of different isosceles TMAs are shown for $a = 100mm, d = 1.59mm, \varepsilon_r = 2.32$ and $tan\delta = 0.0005$. It is found that Q-factors increase with θ_i.

Table 6.2

Radiation Characteristics of different Isosceles TMAs

($a = 100mm, d = 1.59mm, \varepsilon_r = 2.32, tan\delta = 0.0005$)

Sl No	θ_i (deg)	fr (GHz)	$P_r(\%)$	Q_r	Q_t	BW (%)	Gain (abs)	$e(\%)$
1	60	1.171	3.47	181.1	138.2	0.5118	3.938	76.31
2	65	1.132	2.239	280.7	188.7	0.3747	3.609	67.24
3	70	1.107	1.269	495.1	265.3	0.2665	3.047	53.58
4	75	1.086	0.5925	1060	369.8	0.1912	2.137	34.87
5	80	1.052	0.2229	2819	468.1	0.1511	0.9762	16.61
6	85	1.051	0.1554	4044	492.7	0.1435	0.3565	12.18

Variations of $P_r(\%)$, Q_t, e and G with resonant frequency for first five modes are shown in Fig. 6.11. From Fig. 6.11, it is found that it is possible to achieve higher gain compared to 60°-60°-60° TMA.

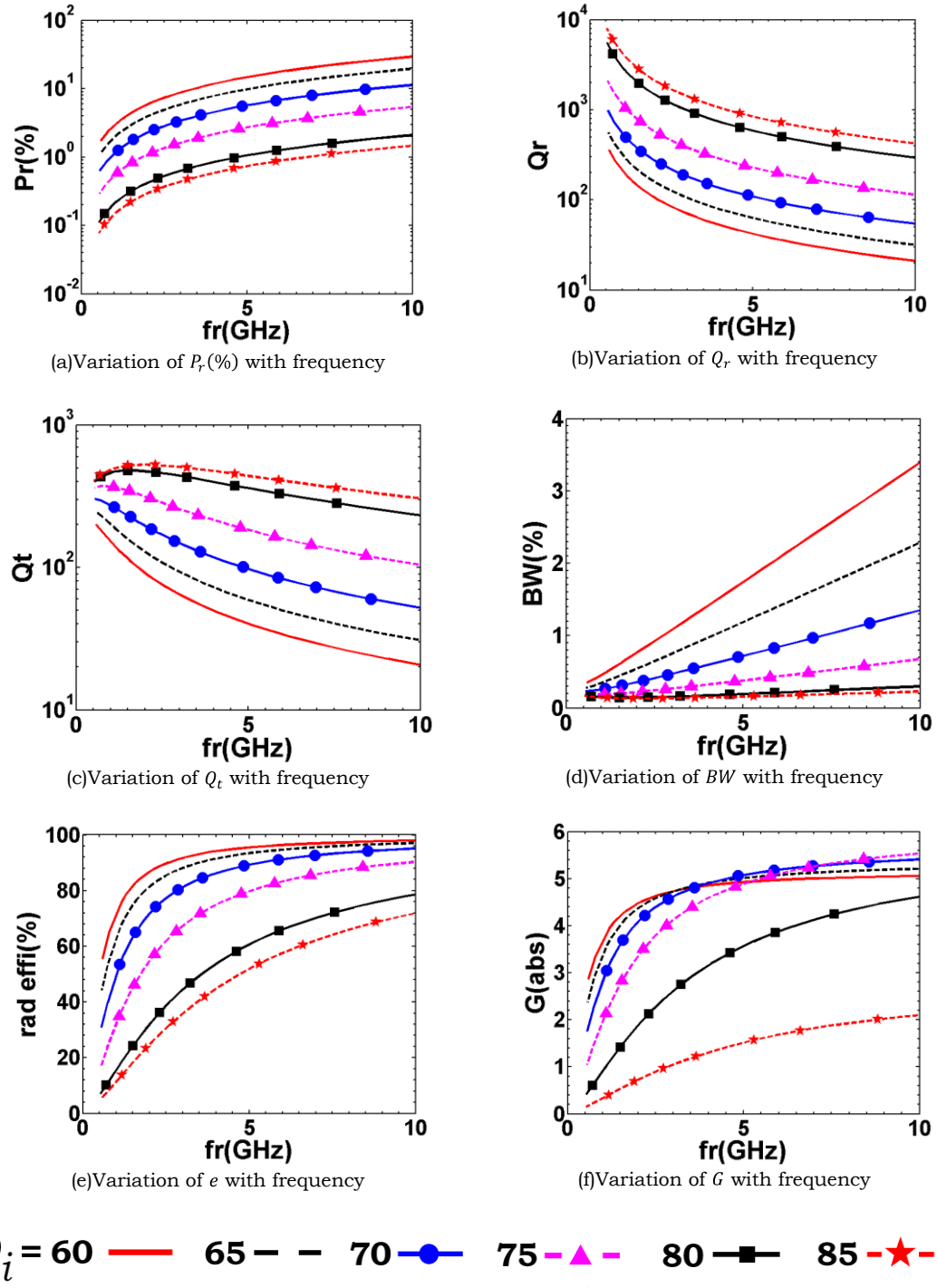

(a)Variation of $P_r(\%)$ with frequency

(b)Variation of Q_r with frequency

(c)Variation of Q_t with frequency

(d)Variation of BW with frequency

(e)Variation of e with frequency

(f)Variation of G with frequency

Fig. 6.11 Radiation characteristics of different isosceles TMAs ($d = 1.59mm, \varepsilon_r = 2.32, tan\delta = 0.0005$)

6.4 Conclusion

In this chapter, details of theoretical investigations on isosceles Triangular Microstrip Antenna (TMA) with, results are presented using the cavity model. Trilinear transformation [24] is modified to obtain the approximate solutions on eigenfunctions and eigenvalues. As the trilinear transformation is applicable for equilateral triangle only, it is found that our theory is only for fundamental TM_{10}^{z} mode of isosceles $\theta_i - \theta_i - \varphi_i$ TMA having $\theta_i \geq 60°$. Resonant frequency, input impedance, far-field patterns, Q-factors etc. are investigated. Theoretical results are verified with experimental data and data obtained using 3D EM simulator HFSS [9] to show the accuracy of our theory. From this theoretical investigation, it is found that:

- Fundamental TM_{10}^{z} mode of isosceles $\theta_i - \theta_i - \varphi_i$ TMA produces a peak in the broadside direction.
- Resonant frequency decreases as θ_i increases from 60° to 90°. Therefore, our theory can efficiently be utilized to make compact antenna.
- Our theory is valid for isosceles $\theta_i - \theta_i - \varphi_i$ TMA having $\theta_i \geq 60°$.

Part III

Dielectric Resonator Antenna (DRA)

Chapter

Introduction

We have discussed so far different triangular shaped microstrip patch antennas such as equilateral Triangular Microstrip Antenna (TMA), 30°–60°–90° TMA, 45°–45°–90° TMA and isosceles TMA for TM^z mode of operation. Cavity model [12-15] is adopted here to investigate the characteristics of those triangular shaped microstrip antennas. The analysis is presented for Microstrip Antennas (MA) having no variation along the thickness (or height, say $\hat{z}$-direction) of the substrate (i.e. $\partial/\partial z = 0$). Therefore, the $\hat{z}$-directed electric field component $\vec{E}_z$ has been used to derive the far-zone radiation patterns only, because the other two tangential components $\vec{E}_x(\propto \partial/\partial z)$ and $\vec{E}_y(\propto \partial/\partial z)$ are equal to zero according to cavity model. In case of Dielectric Resonator Antenna (DRA), $\vec{E}_x$ and $\vec{E}_y$ components are not zero and their effects must be accounted for accurate prediction of far-field radiation patterns and other characteristics. Typical geometry of Equilateral Triangular MA (ETMA) and Equilateral Triangular DRA (ETDRA) are shown in Chapter I (please see Fig. 1.1).

A closer look of the eigenfunctions $\left(\psi(x,y)\right)$ for rectangular ($0 \le x \le a$ and $0 \le y \le b$) and equilateral triangular geometry (as shown in Fig. 3.1 in Chapter III) for magnetic boundary wall condition ($d\psi/dn = 0$) can be written as:

- **For Rectangular Geometry**

$$\psi_R(x,y) = cos\left(\frac{m\pi}{a}x\right) cos\left(\frac{n\pi}{b}y\right) \qquad (P.1)$$

- **For Equilateral Geometry**

$$\psi_T(x,y) = cos\frac{2\pi l}{\sqrt{3}a}(x+R)\, cos\left(\frac{2\pi(m-n)}{3a}y\right) + cos\frac{2\pi m}{\sqrt{3}a}(x+R)\, cos\left(\frac{2\pi(n-l)}{3a}y\right) + cos\frac{2\pi}{\sqrt{3}a}(x+R)\, cos\left(\frac{2\pi(l-m)}{3a}y\right) \qquad (P.2)$$

The eigenfunction $\psi_T(x,y)$ can be expressed with respect to $\psi_R(x,y)$ as:

$$[\psi_T(x,y)]_{x'=x+R} = \sum_{i=1}^{3} cos(\alpha_i x')\, cos(\beta_i y) = \sum_{i=1}^{3} \psi_R(x',y) \qquad (P.3)$$

Therefore, theoretical investigations on an equilateral triangular geometry are equivalent to investigate three rectangular geometries simultaneously.

Further, as mentioned in Chapter III that the evaluation of far-field radiation patterns from 'Equivalence Principle' [4, 16] for an ETMA is a much more complex and lengthier process compared to that for Rectangular MA (RMA) due to the inclined planes (or surfaces) of the ETMA. This is due to the complex expressions for the $\hat{z}$ -directed electric field component $\vec{E}_z$ (or eigenfunction). In case of Triangular Dielectric Resonator Antenna (TDRA), all internal field components are functions of *x-y-z* coordinates. Hence, the mathematical treatment of TDRA will be a little bit more complex compared to ETMA. Cartesian coordinate system is suitable to investigate the triangular shaped DRAs. Therefore, it is important to develop a theory on Rectangular DRA (RDRA) for theoretical simplicity first as the three sides of the RDRA are either parallel of perpendicular to *x-y-z* axis in the Cartesian coordinate system. After that, this theory will be extended to investigate different triangular shaped DRAs.

Literature survey shows that the Rectangular DRA (RDRA) has been investigated for fundamental TE^{y}_{111} mode only. Analytical solution for arbitrary TE^{y}_{mnp} modes has not been reported. Even, the explicit solution (approximate) for the eigenfunction of a RDRA for TE^{y}_{mnp} modes has not been reported so far. Therefore, the investigations on RDRA will help us in two aspects:

- The unfocused analytical aspects on the RDRA will be investigated here for arbitrary TE^{y}_{mnp} modes
- The investigations on RDRA will help us to analyze the triangular shaped DRAs.

In the next chapter (Chapter VII), theoretical investigations on RDRA are

presented. A brief literature survey on RDRA is also given to know the current state of art. In Chapters VIII – XI, different triangular shaped DRAs are investigated analytically.

Chapter VII

Rectangular Dielectric Resonator Antenna

7.1 Introduction

Dielectric Resonator Antenna (DRA) made up with low-loss dielectric material is very attractive due to high gain and inherent wideband nature. Hemispherical, cylindrical and rectangular shaped DRAs have been investigated widely. Rectangular DRA (RDRA) gives better flexibility to design an antenna in terms of frequency and bandwidth for its two aspect ratios (length/height and width/height) over hemispherical and cylindrical DRAs. The radiation property of a RDRA is similar to that of a magnetic dipole and its fundamental TE^{y}_{111} mode has been investigated only [21]. Radiation Q-factor (Q_r) has also been investigated therein using the concept of magnetic dipole moment.

Far-field radiation patterns of a RDRA have been reported by S. A. Long *et al.* in 1983 [19] for fundamental mode only. No closed form expressions have been reported therein. An attempt has also been made to investigate the radiation characteristics of a RDRA for fundamental TE^{y}_{111} mode by A. S. Zoubi in his Ph.D. dissertation in 2008 [170]. Closed form expressions to predict the far-field radiation patterns have been given there for TE^{y}_{111} mode.

Radiation characteristics of the RDRA for higher order $TE^{x}_{\delta mn}$ modes have been investigated theoretically using the concept of magnetic dipole and array factor and experimentally verified by Aldo Petosa *et al* in 2011 [171]. In [171], a full-wave simulator has been utilized to find the area of maximum field confinement to design the RDRA. The spacing (s) between any two modes (or array element) has been estimated as 0.4λ for calculating far-field patterns. Moreover, no compact expression is available to find the radiation pattern for a given mode. Besides, in [171], it has been claimed that the $TE^{x}_{\delta m1}$ mode for

$m > 1$ produces a null in the broadside direction. This observation is not correct as shown in this chapter.

In this section, theoretical investigations on RDRA are presented. Conventional Dielectric Waveguide Model (DWM) is used to investigate the RDRA for arbitrary TE^{y}_{mnp} modes where m, n and p are modal indices along the x, y and z-direction respectively. Approximate solution for the eigenfunction is given here. Closed form expressions are given here to predict the far-zone electric field for arbitrary TE^{y}_{mnp} modes. Radiation characteristics for different modes are also investigated here. The theory on "probes in the waveguide" is used here to predict the input impedance of a probe inserted RDRA. Closed form expressions are given here to predict the input impedance of a RDRA for different TE^{y}_{mnp} modes. Theoretical results are verified with published experimental data.

It should be mentioned here that the theory developed during this dissertational period is partially reported in [172-173].

7.2 Theory

In this section, theoretical investigations on source free RDRA having dimensions $a \times b \times d$ and relative permittivity ε_r is presented. In Fig. 7.1, antenna geometry is shown in the standard Cartesian coordinate system. The antenna is placed on a metallic ground, whose size is sufficiently large compare to the RDRA. Rectangular dielectric resonator shows both TE and TM modes [20] but the practical existence of TM mode in case of RDRA is in doubt [21]. Therefore, we will discuss the TE modes only. Eigenfunctions, eigenvalues, far-field radiation patterns, input impedance, Q-factor etc. are investigated. One antenna prototype is fabricated for experimental validation.

7.2.1 Eigenfunctions and Eigenvalues

In Fig. 7.1, the antenna geometry is shown where a rectangular DRA

having dimensions $a \times b \times d$ and relative permittivity ε_r is placed on a ground plane at $z = 0$. The origin is placed at the center of the base of the RDRA. By applying the image theory, the ground plane is removed first and the process results an source free isolated RDRA having dimensions of $a \times b \times h$ where $h = 2d$. Conventional simple boundary conditions [21] are applied to investigate different TE^{y}_{mnp} modes of the source free isolated RDRA. Perfect Magnetic Conductors (PMC) are applied at $x = \pm a/2$ and $z = \pm h/2$ surfaces, whereas Imperfect Magnetic Conductors (IPMC) are applied along $y = \pm b/2$ surfaces.

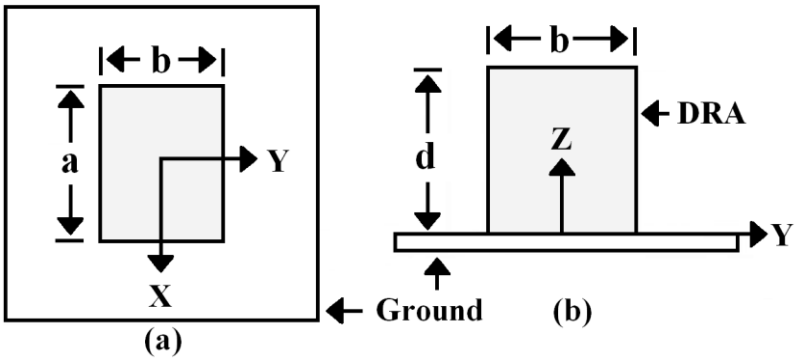

Fig 7.1 Geometry of the antenna (a) top view and (b) side view

After solving the wave function inside the RDRA, one can find the eigenfunctions (ψ_{mnp}) for TE^{y}_{mnp} modes as:

$$\psi_{mnp} = sin\left[k_x\left(x + \frac{a}{2}\right)\right] cos(k_y y)\, sin\left[k_z\left(z + \frac{h}{2}\right)\right] \tag{7.1}$$

where $k_x = m\pi/a$, $k_z = p\pi/h$ and the third wave number k_y can be found after solving the transcendental equation:

$$k_y \tan\left(k_y b/2\right) = \sqrt{(\varepsilon_r - 1)k_o^2 - k_y^2} \tag{7.2}$$

The resonant frequency is found from separation equation and is given by:

$$k_x^2 + k_y^2 + k_z^2 = \varepsilon_r k_o^2 \tag{7.3}$$

For fundamental TE^{y}_{111} mode of operation, substituting $m = 1, n = 1$ and $p = 1$,

the eigenfunction becomes

$$\psi_{111} = cos(k_x x)\, cos(k_y y)\, cos(k_z z) \tag{7.4}$$

which is exactly same as reported in [21].

The electric and magnetic fields inside the RDRA can be expressed for TE^{y}_{mnp} modes as:

$$E_x = \left(\frac{Ak_z}{\varepsilon}\right) sin\left[k_x\left(x+\frac{a}{2}\right)\right] cos(k_y y)\, cos\left[k_z\left(z+\frac{h}{2}\right)\right]$$

$$E_y = 0$$

$$E_z = \left(\frac{-Ak_x}{\varepsilon}\right) cos\left[k_x\left(x+\frac{a}{2}\right)\right] cos(k_y y)\, sin\left[k_z\left(z+\frac{h}{2}\right)\right]$$

$$H_x = \left(\frac{jAk_x k_y}{\omega\mu\varepsilon}\right) cos\left[k_x\left(x+\frac{a}{2}\right)\right] sin(k_y y)\, sin\left[k_z\left(z+\frac{h}{2}\right)\right]$$

$$H_y = \left(\frac{-jA}{\omega\mu\varepsilon}\right)(k_x^2+k_z^2)\, sin\left[k_x\left(x+\frac{a}{2}\right)\right] cos(k_y y)\, sin\left[k_z\left(z+\frac{h}{2}\right)\right]$$

$$H_z = \left(\frac{jAk_y k_z}{\omega\mu\varepsilon}\right) sin\left[k_x\left(x+\frac{a}{2}\right)\right] sin(k_y y)\, cos\left[k_z\left(z+\frac{h}{2}\right)\right] \tag{7.5}$$

where A is a constant and other notations are denoting the usual meaning. Internal field distribution for some modes are shown in Fig. 7.2.

7.2.2 Far-Field Radiation Patterns

To find the radiation characteristics, 'Equivalence Principle' [4, 16] is applied. It is known [21] that the RDRA shows non-confined modes and does not satisfy $\hat{n} \times \vec{H} = 0$ on all surfaces. For theoretical investigations, $x = \pm a/2$ and $z = \pm h/2$ surfaces are modeled as Perfect Magnetic Conductors (PMC) whereas the $y = \pm b/2$ surfaces are modeled as Imperfect Magnetic Conductor (IPMC). Therefore, the magnetic surface currents $\left(\vec{M}_s = \vec{E} \times \hat{n}\right)$ and electric surface currents $\left(\vec{J}_s = \hat{n} \times \vec{H}\right)$ on the surfaces of the RDRA both are to be evaluated depending on the boundary conditions.

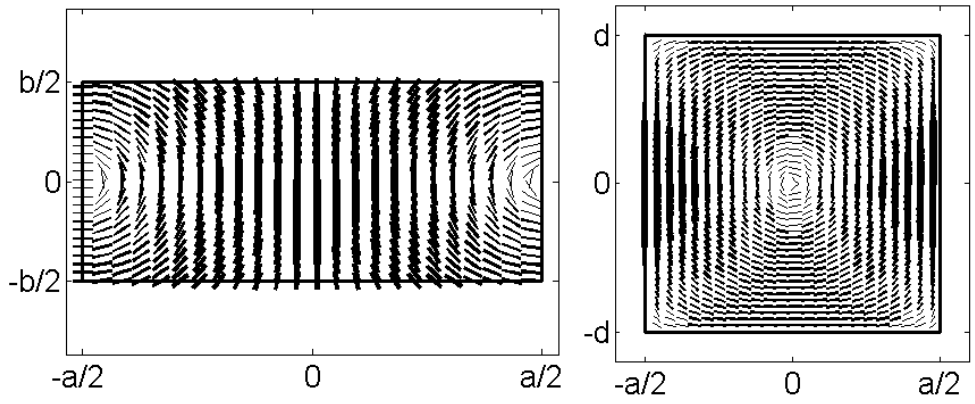

(a) Plot of magnetic (left) and electric (right) field for TE^{y}_{111} mode

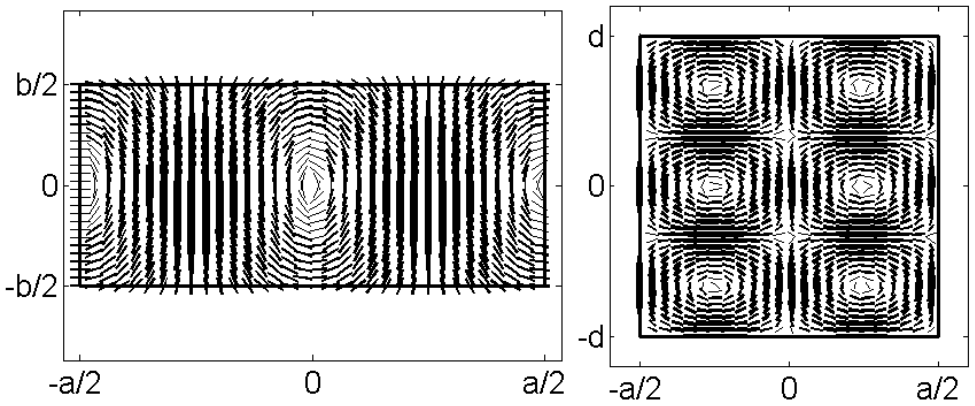

(b) Plot of magnetic (left) and electric (right) field for TE^{y}_{213} mode

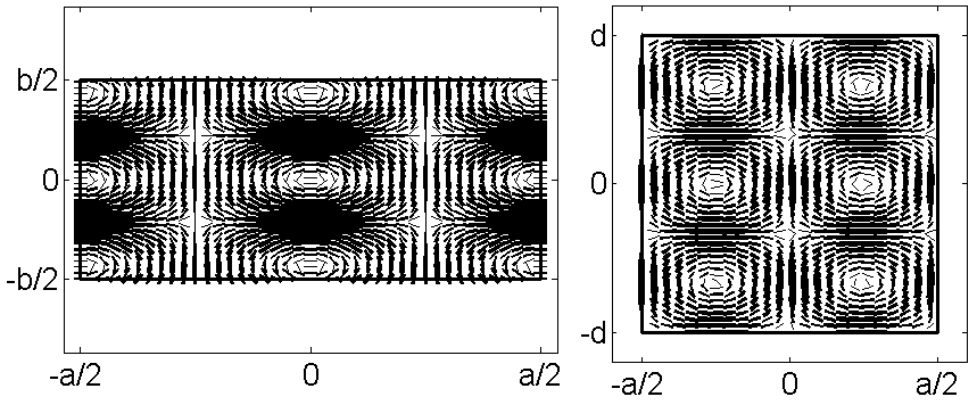

(c) Plot of magnetic (left) and electric (right) field for TE^{y}_{233} mode

Fig. 7.2 Magnetic field patterns along x-y surface at $z = 0$ (left) and electric field patterns along x-z surface at $y = 0$ (right) patterns for various modes ($a = d = 9.31mm, b = 4.6mm, \varepsilon_r = 80$)

The magnetic surface currents $(\vec{M}_s)$ and electric surface currents $(\vec{J}_s)$ will be evaluated from the internal field distribution of the RDRA. Therefore, all the integrals related to far-zone electric, can be expressed as:

$$I = \int_{x=-\frac{P}{2}}^{\frac{P}{2}} \left\{ \begin{matrix} sin\left[U\left(x+\frac{Q}{2}\right)\right] \\ \text{or} \\ cos\left[U\left(x+\frac{Q}{2}\right)\right] \end{matrix} \right\} \times e^{jVx} dx = f_x(P,Q,R,S,U,V)$$

$$= \int_{x=-P/2}^{P/2} \left[\frac{e^{jU\left(x+\frac{Q}{2}\right)} + R \times e^{-jU\left(x+\frac{Q}{2}\right)}}{S} \right] \times e^{jVx} dx$$

$$= \left\{ \frac{P}{S} \times e^{\frac{jUQ}{2}} \times sinc\left[\frac{(V+U)P}{2}\right] \right\} + \left\{ \frac{RP}{S} \times e^{-\frac{jUQ}{2}} \times sinc\left[\frac{(V-U)P}{2}\right] \right\} \quad (7.6)$$

where P, Q, U and V are known for a given function and $sinc = sin(x)/x$. Two constant terms R and S are introduced to deal with either $sin(\ )$ or $cos(\ )$ term. This function will be utilized to evaluate the closed form expressions for far-field radiation patterns of a RDRA.

For theoretical investigations, it is assumed that E_1, E_2, E_3, H_1, H_2 and H_3 are the field strength of E_x, E_y, E_z, H_x, H_y and H_z components respectively. Magnetic surface current $(\vec{M}_s)$, electric surface current $(\vec{J}_s)$ and the corresponding fields along each surface are evaluated as:

A. Fields along AB surface $(y = -b/2)$

$$\vec{J}_s^{AB} = \hat{n} \times \vec{H} = (-\hat{y}) \times \left[H_x\hat{x} + H_y\hat{y} + H_z\hat{z}\right] = [H_x\hat{z} - H_z\hat{x}] \quad (7.7a)$$

$$\vec{M}_s^{AB} = \vec{E} \times \hat{n} = [E_x\hat{x} + 0 + E_z\hat{z}] \times (-\hat{y}) = [-E_x\hat{z} + E_z\hat{x}] \quad (7.7b)$$

$$F_x^{AB} = A \times E_3 \times cos\left(-\frac{k_y b}{2}\right) \times f_x\begin{pmatrix} P=a, Q=a, R=1, S=2 \\ U=k_x, V=k_o sin(\theta) cos(\varphi) \end{pmatrix}$$

$$\times f_z\begin{pmatrix} P=h, Q=d, R=-1, S=2j \\ U=k_z, V=k_o cos(\theta) \end{pmatrix} \times exp\left(-jk_o\left(\frac{b}{2}\right) sin(\theta) sin(\varphi)\right)$$

$$F_y^{AB} = 0$$

$$F_z^{AB} = A \times (-E_1) \times cos\left(-\frac{k_y b}{2}\right) \times f_x\begin{pmatrix} P=a, Q=a, R=-1, S=2j \\ U=k_x, V=k_o sin(\theta) cos(\varphi) \end{pmatrix}$$

$$\times f_z\begin{pmatrix} P=h, Q=d, R=1, S=2 \\ U=k_z, V=k_o cos(\theta) \end{pmatrix} \times exp\left(-jk_o\left(\frac{b}{2}\right) sin(\theta) sin(\varphi)\right)$$

$$A_x^{AB} = A \times (-H_3) \times sin\left(-\frac{k_y b}{2}\right) \times f_x\begin{pmatrix} P = a, Q = a, R = -1, S = 2i \\ U = k_x, V = k_o sin\,(\theta) cos\,(\varphi) \end{pmatrix}$$

$$\times f_z\begin{pmatrix} P = h, Q = d, R = 1, S = 2 \\ U = k_z, V = k_o cos\,(\theta) \end{pmatrix} \times exp\left(-jk_o\left(\frac{b}{2}\right) sin(\theta) sin(\varphi)\right)$$

$$A_y^{AB} = 0$$

$$A_z^{AB} = A \times H_1 \times sin\left(-\frac{k_y b}{2}\right) \times f_x\begin{pmatrix} P = a, Q = a, R = 1, S = 2 \\ U = k_x, V = k_o \sin(\theta) \cos(\varphi) \end{pmatrix}$$

$$\times f_z\begin{pmatrix} P = h, Q = d, R = -1, S = 2i \\ U = k_z, V = k_o cos\,(\theta) \end{pmatrix} \times exp\left(-jk_o\left(\frac{b}{2}\right) sin(\theta) sin(\varphi)\right) \quad (7.8)$$

B. Fields along BC surface $(x = +a/2)$

$$\vec{M}_s^{BC} = \vec{E} \times \hat{n} = [E_x\hat{x} + 0 + E_z\hat{z}] \times (\hat{x}) = [E_z\hat{y}] \quad (7.9)$$

$$F_x^{BC} = 0$$

$$F_y^{BC} = A \times E_3 \times (-1)^m \times f_y\begin{pmatrix} P = b, Q = 0, R = 1, S = 2 \\ U = k_y, V = k_o sin\,(\theta) sin(\varphi) \end{pmatrix}$$

$$\times f_z\begin{pmatrix} P = h, Q = d, R = -1, S = 2j \\ U = k_z, V = k_o cos(\theta) \end{pmatrix} \times exp\left(jk_o\left(\frac{a}{2}\right) si\,n(\theta)\, cos(\varphi)\right)$$

$$F_z^{BC} = 0 \quad (7.10)$$

C. Fields along DC surface $(y = +b/2)$

$$\vec{J}_s^{DC} = \hat{n} \times \vec{H} = (\hat{y}) \times \left[H_x\hat{x} + H_y\hat{y} + H_z\hat{z}\right] = [-H_x\hat{z} + H_z\hat{x}] \quad (7.11a)$$

$$\vec{M}_s^{DC} = \vec{E} \times \hat{n} = [E_x\hat{x} + 0 + E_z\hat{z}] \times (\hat{y}) = [E_x\hat{z} - E_z\hat{x}] \quad (7.11b)$$

$$F_x^{DC} = A \times (-E_3) \times cos\left(\frac{k_y b}{2}\right) \times f_x\begin{pmatrix} P = a, Q = a, R = 1, S = 2 \\ U = k_x, V = k_o sin\,(\theta) cos\,(\varphi) \end{pmatrix}$$

$$\times f_z\begin{pmatrix} P = h, Q = d, R = -1, S = 2j \\ U = k_z, V = k_o cos\,(\theta) \end{pmatrix} \times exp\left(jk_o\left(\frac{b}{2}\right) sin(\theta) si\,n(\varphi)\right)$$

$$F_y^{DC} = 0$$

$$F_z^{DC} = A \times E_1 \times cos\left(\frac{k_y b}{2}\right) \times f_x\begin{pmatrix} P = a, Q = a, R = -1, S = 2j \\ U = k_x, V = k_o sin\,(\theta) cos\,(\varphi) \end{pmatrix}$$

$$\times f_z\begin{pmatrix} P = h, Q = d, R = 1, S = 2 \\ U = k_z, V = k_o cos\,(\theta) \end{pmatrix} \times exp\left(jk_o\left(\frac{b}{2}\right) si\,n(\theta)\, si\,n(\varphi)\right)$$

$$A_x^{DC} = A \times H_3 \times sin\left(\frac{k_y b}{2}\right) \times f_x\begin{pmatrix} P=a, Q=a, R=-1, S=2i \\ U=k_x, V=k_o sin\,(\theta) cos\,(\varphi)\end{pmatrix}$$
$$\times f_z\begin{pmatrix} P=h, Q=d, R=1, S=2 \\ U=k_z, V=k_o cos\,(\theta)\end{pmatrix} \times exp\left(jk_o\left(\frac{b}{2}\right) si\,n(\theta)\, si\,n(\varphi)\right)$$

$$A_y^{DC} = 0$$

$$A_z^{DC} = A \times (-H_1) \times sin\left(\frac{k_y b}{2}\right) \times f_x\begin{pmatrix} P=a, Q=a, R=1, S=2 \\ U=k_x, V=k_o \sin(\theta)\cos(\varphi)\end{pmatrix}$$
$$\times f_z\begin{pmatrix} P=h, Q=d, R=-1, S=2i \\ U=k_z, V=k_o cos\,(\theta)\end{pmatrix} \times exp\left(jk_o\left(\frac{b}{2}\right) si\,n(\theta)\, si\,n(\varphi)\right) \quad (7.12)$$

D. Fields along AD surface $(x = -a/2)$

$$\vec{M}_s^{AD} = \vec{E} \times \hat{n} = [E_x\hat{x} + 0 + E_z\hat{z}] \times (-\hat{x}) = [-E_z\hat{y}] \quad (7.13)$$

$$F_x^{AD} = 0$$

$$F_y^{AD} = A \times (-E_3) \times f_y\begin{pmatrix} P=b, Q=0, R=1, S=2 \\ U=k_y, V=k_o sin\,(\theta) sin(\varphi)\end{pmatrix} \times f_z\begin{pmatrix} P=h, Q=d, R=-1, S=2j \\ U=k_z, V=k_o cos(\theta)\end{pmatrix}$$
$$\times exp\left(-jk_o\left(\frac{a}{2}\right) si\,n(\theta)\, cos(\varphi)\right)$$

$$F_z^{AD} = 0 \quad (7.14)$$

E. Fields along TOP surface $(z = +h/2)$

$$\vec{M}_s^{TOP} = \vec{E} \times \hat{n} = [E_x\hat{x} + 0 + E_z\hat{z}] \times (\hat{z}) = [-E_x\hat{y}] \quad (7.15)$$

$$F_x^{TOP} = 0$$

$$F_y^{TOP} = A \times (-E_1) \times (-1)^p \times f_x\begin{pmatrix} P=a, Q=a, R=-1, S=2j \\ U=k_x, V=k_o sin(\theta) cos(\varphi)\end{pmatrix}$$
$$\times f_y\begin{pmatrix} P=b, Q=0, R=1, S=2 \\ U=k_y, V=k_o sin(\theta) sin(\varphi)\end{pmatrix} \times exp\left(jk_o\left(\frac{d}{2}\right) cos(\theta)\right)$$

$$F_z^{TOP} = 0 \quad (7.16)$$

F. Fields along BOTTOM surface $(z = -h/2)$

$$\vec{M}_s^{BOTTOM} = \vec{E} \times \hat{n} = [E_x\hat{x} + 0 + E_z\hat{z}] \times (-\hat{z}) = [E_x\hat{y}] \quad (7.17)$$

$$F_x^{BOTTOM} = 0$$

$$F_y^{BOTTOM} = A \times E_1 \times (-1)^p \times f_x\begin{pmatrix} P=a, Q=a, R=-1, S=2j \\ U=k_x, V=k_o sin(\theta)cos(\varphi) \end{pmatrix} \times f_y\begin{pmatrix} P=b, Q=0, R=1, S=2 \\ U=k_y, V=k_o sin(\theta)sin(\varphi) \end{pmatrix} \times exp\left(-jk_o\left(\frac{d}{2}\right)cos(\theta)\right)$$

$$F_z^{BOTTOM} = 0 \tag{7.18}$$

where E_1, E_3, H_1, H_2 and H_3 are the field strength of E_x, E_z, H_x, H_y and H_z respectively and $f_{i=x,y,z}(P, Q, R, S, U, V)$ function is defined by equation (7.6).

The total far-zone electric field at point $P(r, \theta, \varphi)$ is evaluated as [16]:

$$E_\theta = -\frac{jk_o \exp(-jk_o r)}{4\pi r} \times \left[L_\varphi + \eta_0 N_\theta\right] \tag{7.19a}$$

$$E_\varphi = \frac{jk_o \exp(-jk_o r)}{4\pi r} \times \left[L_\theta - \eta_0 N_\varphi\right] \tag{7.19b}$$

where,

$$N_\theta = A_x cos(\theta)cos(\varphi) + A_y cos(\theta)sin(\varphi) - A_z sin(\theta)$$
$$N_\varphi = -A_x sin(\varphi) + A_y cos(\varphi)$$

$$L_\theta = F_x cos(\theta)cos(\varphi) + F_y cos(\theta)sin(\varphi) - F_z sin(\theta)$$
$$L_\varphi = -F_x sin(\varphi) + F_y cos(\varphi) \tag{7.20}$$

$$F_x = F_x^{AB} + F_x^{DC}$$
$$F_y = F_y^{BC} + F_y^{AD} + F_y^{TOP} + F_y^{BOTTOM}$$
$$F_z = F_z^{AB} + F_z^{DC}$$
$$A_x = A_x^{AB} + A_x^{DC}$$
$$A_y = 0$$
$$A_z = A_z^{AB} + A_z^{DC} \tag{7.21}$$

The expressions for F_x, F_y, F_z, A_x, A_y and A_z can be put together to obtain a closed form expression. We have reported the final closed form expressions to compute the far-field radiation patterns of a RDRA for various TE_{mnp}^y modes in [172] and are not repeated here for the sake of brevity.

7.2.3 Input Impedance

Evaluation of the input impedance of a RDRA is based on "Probes in Cavities" as found in [4]. This theory has been applied to find the input impedance of a Cylindrical DRA (CDRA) for fundamental TM_{110}^{z} mode by S. A. Long *et al.* in 1986 [17]. This theory is applied here to find the input impedance of RDRA for fundamental TE_{111}^{y} mode whose dimensions are $a \times b \times d$ and relative permittivity is ε_r. Input impedance for fundamental TE_{111}^{y} mode can be written as [4]:

$$Z_{in} = \frac{-j\omega(a_o/I_o)^2}{\omega^2 - \omega_o^2\left(1 + \frac{j}{Q_t}\right)} \tag{7.22}$$

where

$$a_o = \iiint \vec{E}_o \cdot \vec{J}\, dv \tag{7.23}$$

Here, $\vec{E}_o$ Is electric field inside RDRA for $TE_{111}^{y?}$ mode, $\vec{J}$ is probe current density, I_o is the magnitude of current, ω is operating frequency, ω_o is resonant frequency and Q_t is total quality factor. Electric field inside the RDRA must be normalized such that

$$\varepsilon \iiint \vec{E}_o \cdot \vec{E}_o^{*}\, dv = \varepsilon \iiint \left|\vec{E}_o\right|^2 dv = 1 \tag{7.24}$$

where $\varepsilon = \varepsilon_r \varepsilon_o$. The normalized electric fields inside the RDRA can be expressed as:

$$E_x = \left(\frac{-k_z}{B\varepsilon}\right)\cos(k_x x)\cos(k_y y)\sin(k_z z)$$

$$E_y = 0$$

$$E_z = \left(\frac{k_x}{B\varepsilon}\right)\sin(k_x x)\cos(k_y y)\cos(k_z z) \tag{7.25}$$

where B is normalization factor and evaluated according to equation (7.24) as:

$$B^2 = \varepsilon \iiint \left|\vec{E}_o\right|^2 dv$$

$$= \varepsilon \int_{x=-a/2}^{a/2} \int_{y=-b/2}^{b/2} \int_{z=0}^{d} [|E_x|^2 + 0 + |E_z|^2]\, dxdydz$$

$$= \varepsilon \int_v \left[\left(\frac{-k_z}{\varepsilon}\right)^2 \cos^2(k_x x)\cos^2(k_y y)\sin^2(k_z z) + \left(\frac{k_x}{\varepsilon}\right)^2 \sin^2(k_x x)\cos^2(k_y y)\cos^2(k_z z)\right] dv$$

$$= \frac{1}{\varepsilon}[k_z^2 \times I_1 + k_x^2 \times I_2 \tag{7.26}$$

where

$$I_1 = \int_v \cos^2(k_x x)\cos^2(k_y y)\sin^2(k_z z)\, dv = \frac{abd}{8}\left[1 + sinc(k_y b)\right] \tag{7.27}$$

$$I_2 = \int_v \sin^2(k_x x)\cos^2(k_y y)\cos^2(k_z z)\, dv = \frac{abd}{8}\left[1 + sinc(k_y b)\right] \tag{7.28}$$

Therefore, we can write:

$$B^2 = \frac{1}{\varepsilon}[k_z^2 \times I_1 + k_x^2 \times I_2 = \frac{1}{\varepsilon} \times \frac{abd}{8} \times \left[1 + sinc(k_y b)\right][k_z^2 + k_x^2] \tag{7.29}$$

Probe current density $(\vec{J})$ is modeled here as one dimensional $\hat{z}$ directed current as [4]:

$$\vec{J} = \begin{cases} \hat{z} I_o \dfrac{\sin[k(l-z)]}{\sin(kl)} \delta(x - x_o)\delta(y - y_o), & z \le l \\ 0 \quad , & z > l \end{cases} \tag{7.30}$$

where k is wave number inside the RDRA, l is probe length and (x_o, y_o) is probe location. This approximation will be valid when $l/r \gg 1$ where r is the radius of the coaxial probe.

The last unknown quantity a_o, as defined by equation (7.23) is evaluated as:

$$a_o = \iiint \vec{E}_o . \vec{J}\, dv$$

$$= \iiint [E_x \hat{x} + E_y \hat{y} + E_z \hat{z}] . [J_x \hat{x} + J_y \hat{y} + J_z \hat{z}]\, dv$$

$$= \iiint_{Probe} E_z J_z \, dv$$

$$= I_o \left(\frac{k_x}{B\varepsilon}\right)\left[\frac{sin(k_x x_o)cos(k_y y_o)}{sin(kl)}\right][cos(k_z l) - cos(kl)]\left[\frac{k}{k^2 - k_z^2}\right]$$

$$\frac{a_o}{I_o} = \left(\frac{k_x}{B\varepsilon}\right)\left[\frac{sin(k_x x_o)cos(k_y y_o)}{sin(kl)}\right][cos(k_z l) - cos(kl)]\left[\frac{k}{k^2 - k_z^2}\right] \quad (7.31)$$

Summary for TE_{111}^{y} mode:

The Input impedance of the probe inserted RDRA for TE_{111}^{y} mode can be evaluated as:

$$Z_{in} = \frac{-j\omega(a_o/I_o)^2}{\omega^2 - \omega_o^2\left(1 + \frac{j}{Q_t}\right)} \quad (7.32a)$$

$$\frac{a_o}{I_o} = \left(\frac{k_x}{B\varepsilon}\right)\left[\frac{sin(k_x x_o)cos(k_y y_o)}{sin(kl)}\right][cos(k_z l) - cos(kl)]\left[\frac{k}{k^2 - k_z^2}\right] \quad (7.32b)$$

$$B^2 = \frac{1}{\varepsilon} \times \frac{abd}{8} \times \left[1 + sinc(k_y b)\right][k_z^2 + k_x^2] \quad ; \quad \varepsilon = \varepsilon_r \varepsilon_o \quad (7.32c)$$

Summary for TE_{mnp}^{y} mode:

In case of TE_{mnp}^{y} modes, the final closed form expressions to evaluate the input impedance of the probe inserted RDRA are:

$$Z_{in} = \frac{-j\omega(a_o/I_o)^2}{\omega^2 - \omega_o^2\left(1 + \frac{j}{Q_t}\right)} \quad (7.33a)$$

$$\frac{a_o}{I_o} = \left(\frac{-k_x}{B\varepsilon}\right)\left[\frac{cos\left(k_x\left(x_o + \frac{a}{2}\right)\right)cos(k_y y_o)}{sin(kl)}\right] \times \left[\frac{k\, sin\{k_z(l+d)\} - k_z\, sin\{kl - k_z d\}}{k_z^2 - k^2}\right] \quad (7.33b)$$

$$B^2 = \frac{1}{\varepsilon} \times \frac{abd}{8} \times \left[1 + sinc\left(k_y b\right)\right]\left[k_z^2 + k_x^2\right] \quad ; \quad \varepsilon = \varepsilon_r \varepsilon_o \tag{7.33c}$$

7.2.4 Radiated Power, Quality factor, Efficiency and Gain

An isolated DRA does not contain any conductor. But, to use the dielectric block as an antenna, a metallic ground plane is required to support the feed structure. Therefore, the conductor loss due to the conducting ground plane must be accounted to predict its radiation characteristics, but the amount of conductor loss will be small compared to microstrip antenna as the DRA does not contain any metallic patch on it. Radiated power in percentage may be evaluated as [15] $P_r(\%) = (2\pi/Q_r) \times 100$ where Q_r is the radiation quality factor, conductor loss (P_c), dielectric loss (P_d), radiation loss (P_r), total stored energy (W_t), Bandwidth (BW), efficiency (e), directivity (D), gain (G) are also calculated using standard procedure as found in [12-16] or as calculated in Chapter III. Due to the absence of surface wave [5, 174], the effect of surface wave loss is neglected here. Therefore, the total quality factor (Q_t) is evaluated as:

$$Q_t = \frac{\omega_r W_t}{P_c + P_d + P_r} \tag{7.34}$$

It should be pointed here that IPMC is applied along $y = \pm b/2$ surfaces to compute the eigenfunctions of the RDRA. If the stored electric and magnetic energy within the RDRA are W_e and W_m respectively, it is found that $W_e \neq W_m$. These are also evaluated using numerical integration. We found the same results. For further investigation, we have derived the W_e and W_m for rectangular waveguide (PEC boundary) and rectangular microstrip antenna (PMC boundary) and it is found that that $W_e = W_m$. Therefore, to compute the Q-factors, we have to find separately W_e and W_m to compute the total stored energy W_t. This observation ($W_e \neq W_m$ for imperfect boundary wall) is also found for equilateral triangular DRA as shown in the next chapter.

In case of RDRA, W_e is evaluated as:

$$W_e = (\varepsilon/4)\iiint \left|\vec{E}\right|^2 dv \qquad \text{where} \qquad \varepsilon = \varepsilon_r\varepsilon_o$$

$$= (\varepsilon/4) \times |A/\varepsilon|^2 \times \int_{x=-a/2}^{a/2}\int_{y=-b/2}^{b/2}\int_{z=0}^{d} [|E_x|^2 + 0 + |E_z|^2]\, dxdydz$$

$$= (\varepsilon/4) \times |A/\varepsilon|^2 \times \int_v \left[\left(\frac{-k_z}{\varepsilon}\right)^2 sin^2\left(k_x\left(x+\frac{a}{2}\right)\right) cos^2(k_y y) cos^2(k_z(z+d)) + \left(\frac{k_x}{\varepsilon}\right)^2 cos^2\left(k_x\left(x+\frac{a}{2}\right)\right) cos^2(k_y y) sin^2(k_z(z+d))\right] dv$$

$$= (\varepsilon/4) \times |A/\varepsilon|^2 \times [k_z^2 \times I_1 + k_x^2 \times I_2] \qquad (7.35a)$$

where

$$I_1 = \int_v sin^2\left(k_x\left(x+\frac{a}{2}\right)\right) cos^2(k_y y) cos^2(k_z(z+d))\, dv$$

$$= \left[x - \frac{sin\left(2k_x\left(x+\frac{a}{2}\right)\right)}{(2k_x)}\right]_{x=0}^{a/2} \times \left[y + \frac{sin(2k_y y)}{(2k_y)}\right]_{y=0}^{b/2} \times \frac{1}{2} \times \left[z + \frac{sin(2k_z(z+d))}{(2k_z)}\right]_{z=0}^{d}$$

$$= \left[\frac{a}{2} - \frac{sin(2k_x a)}{(2k_x)}\right] \times \frac{b}{2}\left[1 + sinc(k_y b)\right] \times \frac{1}{2}\left[d - \frac{sin(2k_z d)}{(2k_z)}\right]$$

$$I_1 = \frac{abd}{8}\left[1 + sinc(k_y b)\right] \quad ; \quad 2k_x a = 2m\pi\,, \quad 2k_z d = 2p\pi \qquad (7.35b)$$

Similarly,

$$I_2 = \int_v cos^2\left(k_x\left(x+\frac{a}{2}\right)\right) cos^2(k_y y) sin^2(k_z(z+d))\, dv$$

$$= \frac{abd}{8}\left[1 + sinc(k_y b)\right] \qquad (7.35c)$$

Hence,

$$W_e = (\varepsilon/4) \times |A/\varepsilon|^2 \times [k_z^2 \times I_1 + k_x^2 \times I_2 \quad ; \quad \varepsilon = \varepsilon_r\varepsilon_o$$

$$= (\varepsilon/4) \times |A/\varepsilon|^2 \times \frac{abd}{8} \times (k_x^2 + k_z^2)\left[1 + sinc\left(k_y b\right)\right] \tag{7.36}$$

Similarly, the magnetic stored energy W_m is evaluated as:

$$W_m = (\mu/4) \times \iiint \left|\vec{H}\right|^2 dv$$

$$= (\mu/4) \times \int_{x=-a/2}^{a/2} \int_{y=-b/2}^{b/2} \int_{z=0}^{d} \left[|H_x|^2 + \left|H_y\right|^2 + |H_z|^2\right] dxdydz$$

$$= \left(\frac{\mu}{4}\right) \times \left|\frac{A}{\omega\mu\varepsilon}\right|^2 \times (k_x^2 + k_z^2) \times \frac{abd}{8}$$

$$\times \left\{k_y^2\left[1 - sinc\left(k_y b\right)\right] + (k_x^2 + k_z^2)\left[1 + sinc\left(k_y b\right)\right]\right\} \tag{7.37}$$

Therefore, the total stored energy within the RDRA can be evaluated as:

$$W_t = W_e + W_m \tag{7.38}$$

where

$$W_e = (\varepsilon/4) \times |A/\varepsilon|^2 \times \frac{abd}{8} \times (k_x^2 + k_z^2)\left[1 + sinc\left(k_y b\right)\right] \quad ; \quad \varepsilon = \varepsilon_r \varepsilon_o$$

$$W_m = \left(\frac{\mu}{4}\right) \times \left|\frac{A}{\omega\mu\varepsilon}\right|^2 \times (k_x^2 + k_z^2) \times \frac{abd}{8} \times \left\{k_y^2\left[1 - sinc\left(k_y b\right)\right] + (k_x^2 + k_z^2)\left[1 + sinc\left(k_y b\right)\right]\right\}$$

It should be pointed here that the expression for W_e appears to be half of that reported in [5, 21, 174]. This difference is presumably due to non-consideration of the ground plane for supporting the feed.

7.3 Results

In this section, theoretical results on resonant frequency, far-field patterns, input impedance etc. are discussed. Radiation characteristics for various TE_{mnp}^{y} modes are discussed. From rigorous 3D EM simulation using HFSS [9], we do not observe any mode along the y-direction having $n > 1$. Therefore, we discuss here TE_{m1p}^{y} modes. One antenna having $a = d =$

$9.31mm, b = 4.6mm, \varepsilon_r = 80$ and $tan\,\delta = 0.0005$ is simulated using HFSS. The antenna is excited using standard 50Ω co-axial probe whose inner conductor radius is 0.63mm. Theoretical results are verified with experimental data and/or data obtained using an EM simulator.

7.3.1 Resonant Frequency

Three transcendental equations have been reported by R. K. Mongia in 1992 [20] using Marcatili's waveguide model [175] to predict the resonant frequency for various TE^y_{mnp} modes. In this work, we have applied simple boundary conditions [21] (PMC at $x = \pm a/2$ and $z = \pm h/2$ and IPMC at $y = \pm b/2$) are applied, which results a single transcendental equation for predicting the resonant frequency. Simultaneous solution of three transcendental equations is a little bit more complex than solving one transcendental equation. In Table 7.1, comparison between theoretical and experimental resonant frequencies for different modes is shown. Theoretical resonant frequencies are also compared with data obtained using 3D EM simulator HFSS for some higher order modes as shown in Table 7.2. In Table 7.3, theoretical results on resonant frequencies for first 20 modes are shown for a RDRA having $a = d = 9.31mm, b = 4.6mm, \varepsilon_r = 80$.

Table 7.1

Comparison of resonant frequencies with experimental data

Sl. No	Ref.	a (mm)	b (mm)	d (mm)	ε_r	Mode	Reso. Freq. (GHz)	
							Theory	Experiment
1	[176]	20.8	10.5	18.5	10	TE^y_{111}	3.483	3.40
2	[176]	20.8	10.5	18.5	10	TE^y_{113}	5.276	5.18
3	[177]	10	10	6.1	10	TE^y_{115}	24.435	23.86
4	[177]	10	10	6.1	10	TE^y_{119}	24.465	23.87

Table 7.2

Comparison of resonant frequencies with simulated data

($a = d = 9.31mm, b = 4.6mm, \varepsilon_r = 80$)

Sl. No	Mode	Reso. Freq. (GHz)	
		Theory	HFSS [9]
1	TE^{y}_{211}	4.38	4.39
2	TE^{y}_{213}	5.13	5.21
3	TE^{y}_{311}	6.06	6.17
4	TE^{y}_{313}	6.60	6.67

Table 7.3

Resonant frequencies for first 20 modes of a RDRA

($a = d = 9.31mm, b = 4.6mm, \varepsilon_r = 80$)

Sl No	Mode	Reso. Freq. (GHz)		Sl No	Mode	Reso. Freq. (GHz)
1	TE^{y}_{111}	2.7577		11	TE^{y}_{411}	7.7753
2	TE^{y}_{113}	3.9411		12	TE^{y}_{217}	7.7753
3	TE^{y}_{211}	4.3843		13	TE^{y}_{413}	8.1937
4	TE^{y}_{213}	5.1352		14	TE^{y}_{317}	8.7816
5	TE^{y}_{115}	5.4655		15	TE^{y}_{415}	8.9685
6	TE^{y}_{311}	6.0649		16	TE^{y}_{511}	9.5061
7	TE^{y}_{215}	6.3408		17	TE^{y}_{513}	9.8474
8	TE^{y}_{313}	6.6038		18	TE^{y}_{417}	10.014
9	TE^{y}_{117}	7.0978		19	TE^{y}_{515}	10.496
10	TE^{y}_{315}	7.5568		20	TE^{y}_{611}	11.251

7.3.2 Far-Field Radiation Patterns

In this section, theoretical results on far-field radiation patterns are presented for various TE^{y}_{mnp} modes. Modes with even values of p will not be excited for a RDRA placed on a metallic ground plane [5, 177] as electric field for these modes will be short circuited. Therefore, theoretical results are

presented for odd values of p only. Far-field power are computed at $\varphi = 0^o$ (E-plane) and $\varphi = 90^o$ (H-plane) planes. The maximum values (in dB) at these two planes are stored in E_{max} and H_{max} variables respectively. The magnitudes of E_{max} and H_{max} variables are comparable for modes having odd values of m (i.e. $TE^y_{1np}, TE^y_{3np}, TE^y_{5np}$ etc. modes) whereas a large difference is found for modes having even values of m (i.e. $TE^y_{2np}, TE^y_{4np}, TE^y_{4np}$ etc. modes). Typical results are shown for few modes in Table 7.4 for $a = d = 9.31mm, b = 4.6mm, \varepsilon_r = 80$ and $tan\,\delta = 0.0005$.

Table 7.4

Comparison of gain at $\varphi = 0^o$ and $\varphi = 90^o$ Plane

($a = d = 9.31mm, b = 4.6mm, \varepsilon_r = 80, tan\,\delta = 0.0005$)

Sl No	Modes (TE^y_{mnp})	Resonant Frequency (GHz)	E_{max} (in dB) ($\varphi = 0^o$ plane)	H_{max} (in dB) ($\varphi = 90^o$ plane)
1	TE^y_{111}	2.76	4.57	4.39
2	TE^y_{211}	4.38	5.46	-299.27
3	TE^y_{413}	8.19	3.51	-307.58
4	TE^y_{515}	10.45	-2.22	-2.85
5	TE^y_{811}	14.77	8.56	-308.96

This type of discrepancies in the far-field power patterns for the modes having even values of m at $\varphi = 90^o$ (H-plane) plane is not observed in the 3D EM simulator. To find the reason of such type of discrepancies, the internal fields are observed. One antenna having $a = d = 9.31mm, b = 4.6mm, \varepsilon_r = 80$ and $tan\,\delta = 0.0005$ is simulated using HFSS [9]. Simulated internal field patterns for TE^y_{213} mode are shown in Figs. 7.3 at the resonant frequency (5.203GHz). Due to the presence of the ground plane at $z = 0$, electric field distribution is shown for $z = 0$ to $z = d$. Theoretical field patterns for TE^y_{213} mode are shown in Fig. 7.2(b) which is exactly similar to Fig. 7.3. Therefore, it is a TE^y_{213} mode. The eigenfunctions, obtained from source free analysis of an

isolated RDRA, is able to predict the internal fields, but unable to predict the far-field power patterns of modes having even values of m (i.e. TE^{y}_{2np} , TE^{y}_{4np}, TE^{y}_{4np} etc. modes) at $\varphi = 90^{o}$ plane. This may be due to the application of simple boundary conditions [21] (PMC at $x = \pm a/2$ and $z = \pm h/2$ and IPMC at $y = \pm b/2$).

For, further investigation, a Rectangular Microstrip Antenna (RMA) is investigated using cavity model [12-15]. Closed form expressions for far-field radiation patterns are given in [14, Chap. 4]. These expressions are used to compute the far-field radiation patterns. Similar observation is also found for RMA as found for RDRA. Typical results are shown for a RMA having $a = 114.3mm, b = 76.2mm, \varepsilon_r = 2.32, tan\,\delta = 0.0005$ and $h_{sub} = 1.59mm$ at TM^{z}_{21} mode. The magnitudes of E_{max} (at $\varphi = 0^{o}$ plane) and H_{max} (at $\varphi = 90^{o}$ plane) are 2.49dB and -311.51dB respectively. We have also derived the closed form expressions for far-zone electric field E_θ and E_φ. In case of our theory, we found exactly the same results. This type of discrepancy is not found from data obtained using 3D EM simulator HFSS. This may be due to the limited analysis on TM mode with PMC boundary conditions. The use of both TE and TM modes with imperfect walls can give the proper solution. Mode matching techniques must be used to solve this problem. It is very surprising that the RMA has been investigated extensively using the cavity model. But this type of discrepancy has not been pointed out in the literature.

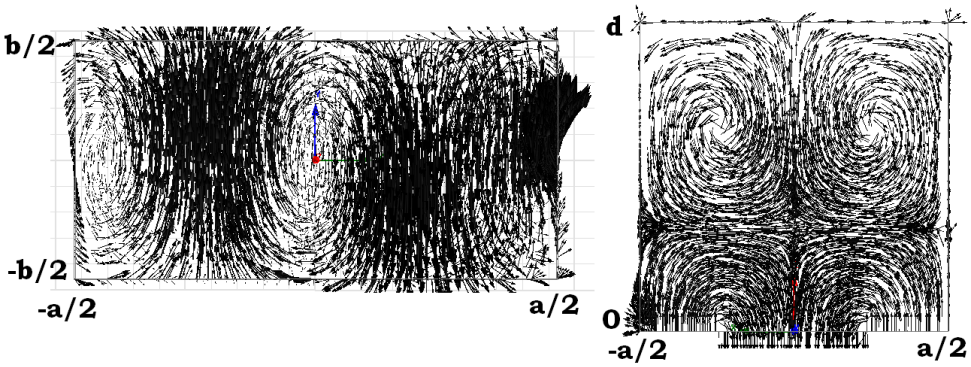

Fig. 7.3 Simulated magnetic field patterns along x-y surface at $z = 0$ (left) and electric field patterns along x-z surface at $y = 0$ (right) patterns for TE^{y}_{213} mode ($a = d = 9.31mm, b = 4.6mm, \varepsilon_r = 80$)

In case of rectangular DRA, a similar phenomenon is also found. RDRA is investigated here for TE mode only using simple boundary conditions. We are trying to investigate the RDRA using both TE and TM modes simultaneously for imperfect boundary walls in all six surfaces. Due to the large number of unknowns, it is very difficult to solve the problem in the space domain. For example, following Marcatili's method [175], we will have 6 unknowns for the fields inside the RDRA and 6 unknowns for the fields outside the RDRA for TE mode only. Similarly, 12 numbers of unknowns will be there for TM mode. Therefore, we have to solve the problem on RDRA for 24 numbers of unknowns.

The fruitful outcome of this investigation is that the single mode (TE mode for RDRA and TM mode RMA) solution with simple boundary conditions is unable to predict the far-field radiation patterns with an absolute gain for all modes which produce a null in the broadside direction in a general sense. The problem is identified on rectangular geometry (rectangular microstrip antenna and rectangular DRA).

In case of our analysis of RDRA for TE^{y}_{mnp} modes, the discrepancy in the prediction of far-field radiation patterns for even values of m at $\varphi = 90^{o}$ plane is overcome by:

- Obtaining the normalized far-field power patterns at $\varphi = 90^{o}$ plane and then
- Adding the overall gain (G) with the normalized power patterns at $\varphi = 90^{o}$ plane

The first step, increases the power patterns from a low value (-300dB approximately) to 0dB. In the second step, addition of overall gain (G) with the normalized power pattern at $\varphi = 90^{o}$ plane makes the patter compared to the E-plane ($\varphi = 0^{o}$) power pattern. Theoretical far-field power patterns at $\varphi = 0^{o}$ (E-plan) and $\varphi = 90^{o}$ planes (H-plane) are shown in Figs. 7.4 for first 10 modes of a RDRA having $a = d = 9.31mm, b = 4.6mm, \varepsilon_r = 80$ and $tan\,\delta = 0.0005$.

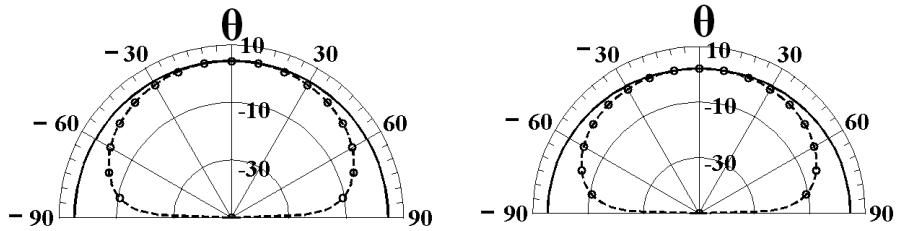

(a) Far-zone E-plane (solid line) and H-plane (circle with dashed line) power patterns with absolute gain (in dB) for TE^{y}_{111} (left) and TE^{y}_{113} (right) modes

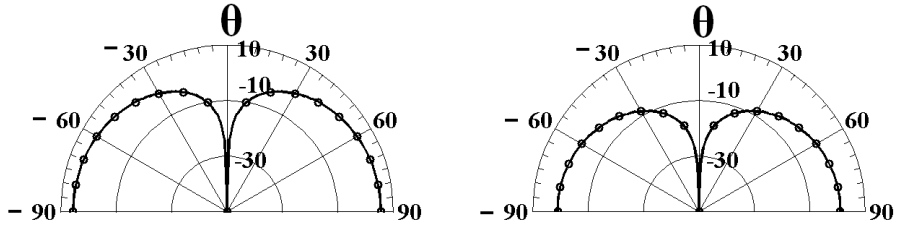

(b) Far-zone E-plane (solid line) and H-plane (circle with dashed line) power patterns with absolute gain (in dB) for TE^{y}_{211} (left) and TE^{y}_{213} (right) modes

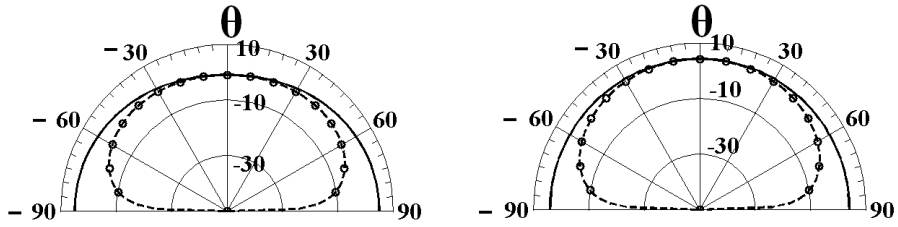

(c) Far-zone E-plane (solid line) and H-plane (circle with dashed line) power patterns with absolute gain (in dB) for TE^{y}_{115} (left) and TE^{y}_{311} (right) modes

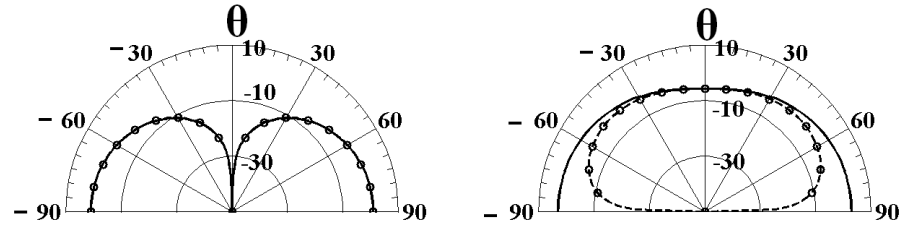

(d) Far-zone E-plane (solid line) and H-plane (circle with dashed line) power patterns with absolute gain (in dB) for TE^{y}_{215} (left) and TE^{y}_{313} (right) modes

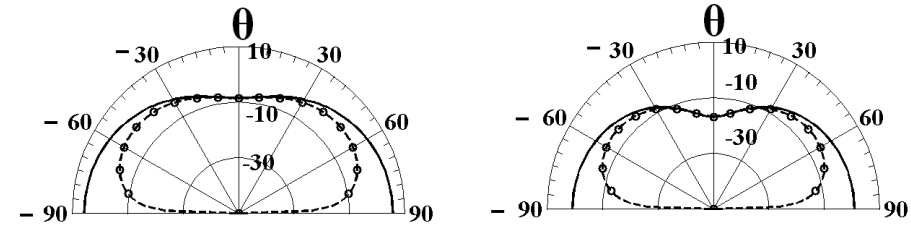

(e) Far-zone E-plane (solid line) and H-plane (circle with dashed line) power patterns with absolute gain (in dB) for TE^{y}_{117} (left) and TE^{y}_{315} (right) modes

Fig. 7.4 Plot of far-zone power patterns with absolute gain (in dB) for various TE^{y}_{mnp} modes ($a = d = 9.31mm, b = 4.6mm, \varepsilon_r = 80, tan\,\delta = 0.0005$)

From Fig. 7.4, it is found that modes with even values of m (here $TE^{y}_{211}, TE^{y}_{213}$ and TE^{y}_{215} modes) show a null in the broadside direction. Some modes such as $TE^{y}_{117}, TE^{y}_{315}$ modes show a dip in the broadside direction. This is due to the improper choice of dimensions for the excitement of a particular mode at their corresponding resonant frequency. For example, wire antenna [178] having length equal to 0.5λ shows a peak in the broadside direction whereas a wire antenna having length equal to 1.5λ shows beam splitting and dip in the broadside direction. Improper choice of dimensions produces a large dip in the broadside direction. For further verification, typical results are shown in Fig. 7.5 for pure TE^{y}_{111} and TE^{y}_{311} modes. If d is changed as in Fig. 7.5, mode purity is preserved from theoretical point for TE^{y}_{111} mode but the magnitude of field distribution along the surfaces of RDRA differs significantly. This changes the theoretical contributions of F_y and A_x drastically and results in a broadside dip (or null). Similar behavior is also found for TE^{y}_{311} mode. The same observation had already been reported by McAllister *et al* [19, Fig. 4] in 1983 for TE^{y}_{111} mode only without any explicit mathematical relation. In this work, closed form expressions are given to predict the radiation characteristics of RDRA for various TE^{y}_{mnp} modes.

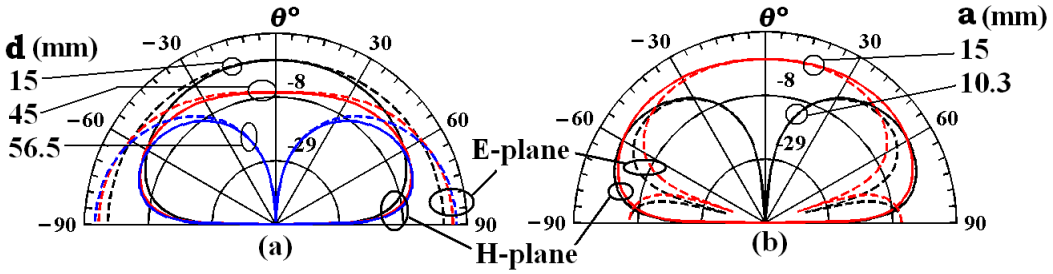

Fig. 7.5 Effect of dimensions on E-plane (dashed) and H-plane (solid) power patterns for (a) TE^{y}_{111} mode (a = b = 15mm) (b) TE^{y}_{311} mode (b = d = 15mm); (ε_r = 8.9, $tan\delta$ = 0.0005)

Further, it is clear from Fig. 7.4 that TE^{y}_{113} mode (Fig. 7.4(c)) produces more gain in the broadside direction compared to TE^{y}_{313} mode (Fig. 7.4(d)). This observation is correct for the RDRA having $a = d = 9.31mm, b = 4.6mm, \varepsilon_r = 80$ and $tan\,\delta = 0.0005$. TE^{y}_{313} mode can produce more gain in the broadside direction compared to TE^{y}_{113} mode by selecting proper dimensions and

permittivity of the RDRA. This is shown in Fig. 7.6 for a = 10mm, b = 6mm, d = 7mm, ε_r = 10, $tan\delta$ = 0.0005.

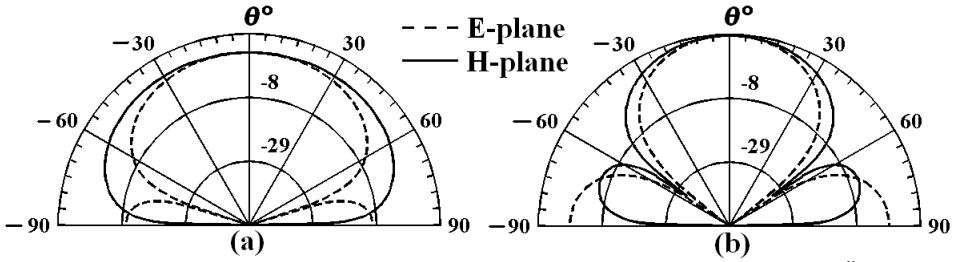

Fig. 7.6 Gain enhancement by selecting proper dimensions and permittivity (a) for TE^{y}_{311} mode (b) for TE^{y}_{313} mode (a = 10mm, b = 6mm, d = 7mm, ε_r = 10, $tan\delta$ = 0.0005)

For experimental validation, far-field E-plane and H-plane power patterns are computed for TE^{y}_{111}, TE^{y}_{113} and TE^{y}_{115} modes as shown in Fig. 7.7. Experimental data are collected from published literature [21, 171]. Theoretical results for TE^{y}_{111} mode is normalized with respect to -50dB as found in [21] whereas the results for TE^{y}_{113} and TE^{y}_{115} modes are normalized with respect to -35dB as found in [171]. It is found that our theoretical results are in close agreement with experimental data.

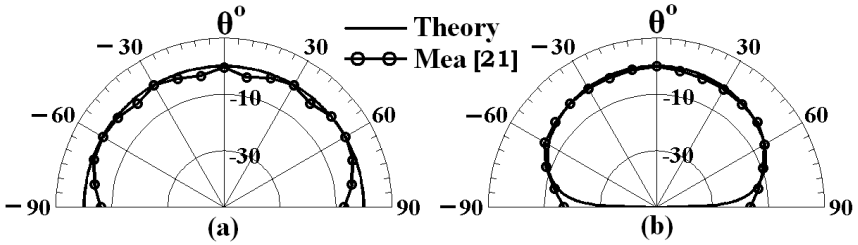

(i) Normalized power patterns for TE^{y}_{111} mode (a) E-plane (b) H-plane (a = h=9.31mm, b = 4.6mm, ε_r = 37.84) [21]

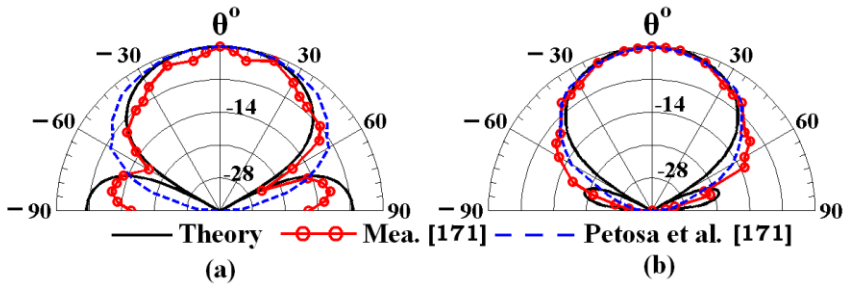

(ii) Normalized power patterns for TE^{y}_{113} mode (a) E-plane (b) H-plane ($a = b = 6mm, h = 15mm, \varepsilon_r = 10$) [171]

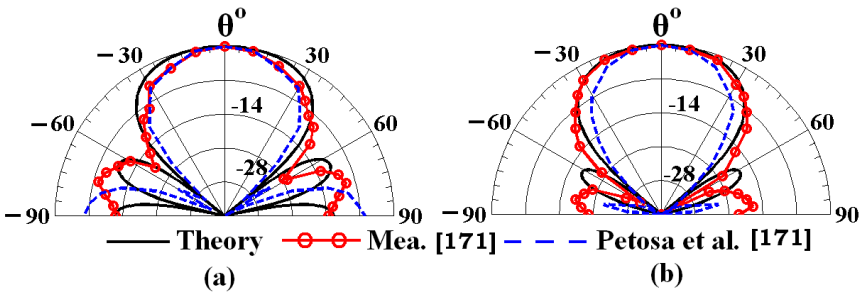

(iii) Normalized power patterns for TE_{115}^{y} mode (a) E-plane (b) H-plane ($a = b = 5mm, h = 30mm, \varepsilon_r = 10$) [171]

Fig. 7.7 Experimental validation of far-field power patterns for different modes

Normalized field patterns for $TE_{211}^{y}, TE_{213}^{y}, TE_{311}^{y}$ and TE_{313}^{y} modes of a RDRA having $a = h = 9.31\,mm, b = 4.6\,mm$ and $\varepsilon_r = 80$ are shown in Fig. 7.8. It is clear that theoretical results are in good agreement with normalized measured data or data obtained using 3D EM simulator HFSS [9].

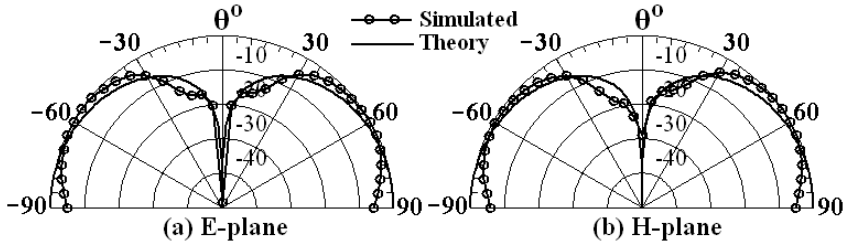

(a) Power patterns for TE_{211}^{y} mode: theory (4.38GHz), simulated (4.39GHz)

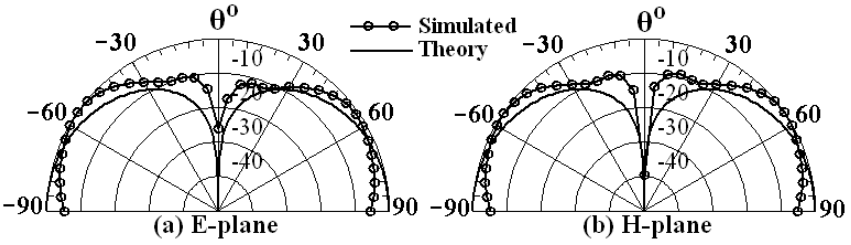

(b) Power patterns for TE_{213}^{y} mode: theory (5.13GHz), simulated (5.21GHz)

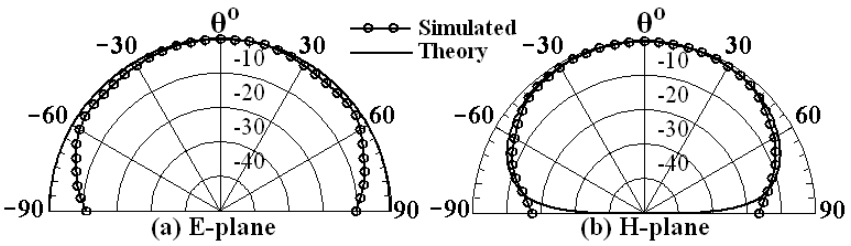

(c) Power patterns for TE_{311}^{y} mode: theory (6.06GHz), simulated (6.17GHz)

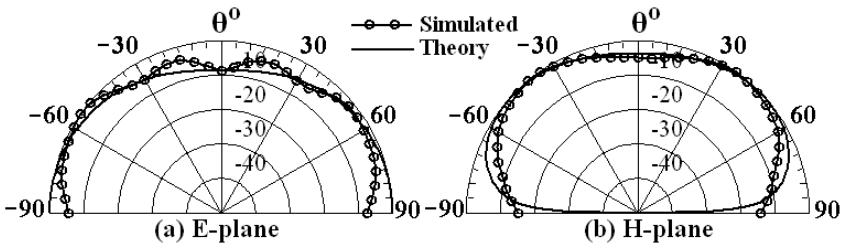

(d) Power patterns for TE^{y}_{313} mode: theory (6.60GHz), simulated (6.66GHz)

Fig. 7.8 Comparison of normalized theoretical far-field power patterns with data obtained using 3D EM simulator HFSS for TE^{y}_{211}, TE^{y}_{213}, TE^{y}_{311} and TE^{y}_{313} modes ($a = d = 9.31mm, b = 4.6mm, \varepsilon_r = 80, tan\,\delta = 0.0005$)

7.3.3 Input Impedance

In this section, the theoretical result on input impedance is presented. Probe fed RDRA has been reported by S. A. Long *et al.* in 1983 [19]. In that communication, rectangular DRA having $a = 30mm, b = h = 15mm, \varepsilon_r = 8.9$ has been excited using a coaxial probe whose length (l) is 10.3mm as shown in Fig 7.1. The coaxial Probe has been placed inside the DRA along x-axis and near to the edge of the RDRA [19, 179]. But in [19], no information about the exact probe position is available. Besides that, the probe radius (r) has also not been mentioned there. Rigorous 3D EM simulation is performed using FEM based commercial software HFSS [9] for $r = 0.63mm$. As the probe position $(x_p, 0)$ is not available in [19], a parametric study is performed for various values of x_p and it is found that $x_p = 9$ mm gives reasonable results as reported in [19, Fig. 2]. Our theory (with measured Q_t) is applied to calculate the input impedance of probe inserted RDRA for $x_p = 9mm$. Theoretical, simulated and measured [19] results are shown in Fig. 7.9. It is found that our theoretical results are in agreement with measured and/or simulated data. Little discrepancies are there as our model does not account for probe radius. Further, our theory does not account the field outside the RDRA in the evaluation of a_o.

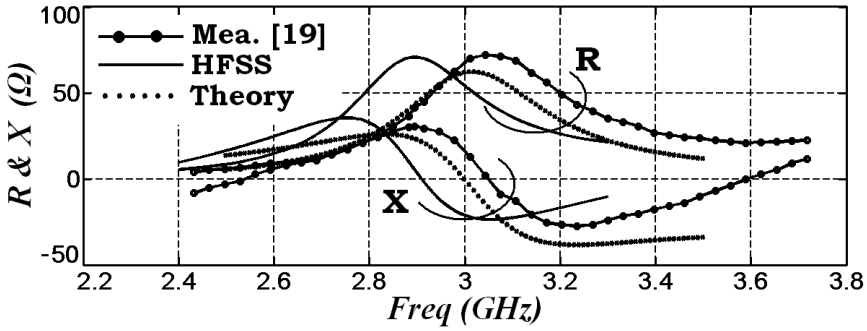

Fig. 7.9 Experimental validation of input impedance for TE_{111}^{y} mode ($a = 30mm, b = d = 15mm, \varepsilon_r = 8.9, l = 10.3mm, x_p = 9mm, r = 0.63mm$) [19]

7.3.4 Radiated Power, Quality factor, Efficiency and Gain

In this analysis, the effect of feed mechanism is not considered. Stored energy, different types of losses, etc. is calculated using the source free theory. Bandwidth (BW), efficiency (e), gain (G) etc are also calculated. A general MATLAB® [164] code is written to obtain various quantities for different modes.

In [21], radiation Q-factor (Q_r) has been evaluated from magnetic dipole moment for TE_{111}^{y} mode as:

$$\vec{P}_m = \frac{1}{2}\int_v \left(\vec{R} \times \vec{J}_p\right) dv \tag{7.41}$$

where $\vec{R}$ is vector from origin, v is volume of RDRA and $\vec{J}_p \left(= j\omega\varepsilon_o(\varepsilon_r - 1)\vec{E}\right)$ is volume polarization current density. Closed form expression has been reported there for evaluating Q_r as $Q_r = 2\omega_o W_e / P_{rad}$ where ω_o is resonant frequency, W_e is stored electric energy and $P_{rad}\left(= 10k_o^2\left|\vec{P}_m\right|^2\right)$ is the radiated power from the magnetic dipole of moment $\vec{P}_m$. In Fig. 7.10, variation of normalized radiation Q-factor ($= Q_r/\sqrt[3]{\varepsilon_r}$) with (d/b) ratio for $a = b = 10mm$ is shown for TE_{111}^{y} mode. Theoretical results on normalized radiation Q-factor as reported in [21] is also shown in that graph. From Fig. 7.10, it is found that the nature of the graphs is almost similar for a certain value of (d/b) ratio (here, approximately equal to 2). Beyond that, as the ratio of (d/b) is increasing for fixed value of a and b,

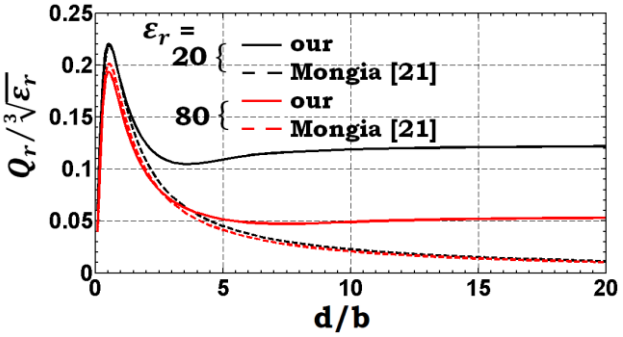

Fig. 7.10 Variation of normalized radiation Q-factor with (d/b) ratio for TE_{111}^{y} mode $(a = b = 10mm)$

normalized Q_r increases whereas the same is decreasing according to [21]. This may be due to the approximate (or equivalent) theory for computing Q_r in [21] whereas our theory is based on standard procedure as found in [12-16] or as calculated for Equilateral Triangular Microstrip Antenna (ETMA) in Chapter III. In Table 7.5, our theory is compared with magnetic dipole theory for computing the radiation Q-factor. Measured data [21] is also shown there. It is found that our theory gives the same results as reported in [21]. But most of the cases, our theory is a little bit closer to experimental data compared to the theory based on magnetic dipole moment. The discrepancy between the theory and experimental data may be due to non-consideration of feed mechanism.

Table 7.5

Comparison of Rad. Q-factor for TE_{111}^{y} mode with measured data [21]

Sl No	a (mm)	b (mm)	d (mm)	ε_r	Radiation Q-factor (Q_r)		
					Mongia [21]	Our	Exp [21]
1	7.45	2.98	7.45	79.46	128.7	74.2	95
2	8.6	2.58	8.6	37.84	37.9	20.85	28.5
3	8.77	3.51	8.77	37.84	44	26.416	31.5
4	15.24	3.1	7.62	10.8	5.8	5.1185	5.9
5	10.16	10.16	7.11	20	18.9	18.971	15.4
6	10.16	7.11	10.16	20	15.9	15.39	14.3
7	9.31	9.31	4.6	37.84	48.1	47.249	32.3
8	15.24	7.62	7.62	37.84	47.6	42.52	34.1
9	7.62	7.62	15.24	37.84	23.5	24.455	18.9
10	8.77	3.51	8.77	37.84	31.3	26.416	24.1
11	8.77	8.77	3.51	37.84	45.5	45.226	31.3
12	9.31	4.6	9.31	37.84	34.8	30.468	22.4
13	12.7	2.54	2.54	79.46	86.8	73.898	45.4
14	12.7	6.35	6.35	79.46	139.6	122.48	73.6
15	7.7	7.7	7.7	79.46	117.6	111.3	56.4

It should be pointed here that in [21], stored electric energy (W_e) has been computed for isolated RDRA ($a \times b \times 2d$), not for RDRA ($a \times b \times d$) placed on a metallic ground plane as discussed earlier in the previous section. Therefore, the theoretical results on radiation Q-factor Q_r ($= 2\omega W_e/P_r$) will be half as reported in [21]. Further, image theory has to be applied to remove the ground plane, which will produce a magnetic dipole having twice strength $(2\vec{P}_m)$ as reported in [171]. The radiation Q-factor will further be reduced.

Some experimental results on radiation Q-factor (Q_r) have been reported in [180] without proper mode identifications. Rigorous 3D simulations are performed to identify various TE modes by observing their field patterns near the measured resonant frequency (f_r^M). Some unknown modes for RDRA are also observed, which are not yet reported in literature. These modes are discarded for the time being as we are interested in TE_{mnp}^{y} modes only. It is also found that our theory gives much higher value of Q_r compared to measured and/or simulated ones for degenerate modes, possibly due to coupling of modes and consequent reduction of Q-factor. Table 7.6 shows a comparison between theoretical (Q_r^T), measured (Q_r^M) [180] and simulated (Q_r^S) values of Q_r for various TE modes only without any mode degeneracy. An Isolated RDRA having dimensions of $a \times b \times h$ is modeled here as a probe fed RDRA whose dimensions are $a \times b \times d$ where $d = h/2$ above the ground plane according to image theory. This might be one of the reasons for inconsistency between measured, simulated and theoretical data.

Our theoretical (superscript 'T') model is also applied to find the gain and BW for various modes and compared with measured data (superscript 'M'). Some typical results are shown in Table 7.7. (From the plot of measured $|S_{11}|$ ([171], Fig. 7) it is easily seen that multiple modes have been excited in RDRA1 (1st sample of Table 7.7). For this reason, measured BW (BW_M) is not compared to this sample in Table 7.7). It is found that our results are in agreement with measured values. Slight discrepancies are there as our model does not account for feed.

Table 7.6

Comparison of radiation Q factor with [180]

Ref [180]		f_r (GHz)			Mode		Q_r		
Table	Sample	f_r^M	f_r^S	f_r^T	Mode no as in [180]	HFSS	Q_r^M	Q_r^S	Q_r^T
II	A	4.67	4.65	4.34	1	TE_{111}^y	90	74.6	131.3
II	B	5.68	5.65	5.33	1	TE_{111}^y	31.5	35.5	45.8
II	C	6.32	6.27	5.93	1	TE_{111}^y	28.5	31.2	39.7
III	A	6.59	6.57	6.35	1	TE_{111}^y	58	65	77.5
III	A	7.78	7.78	7.47	3	TE_{211}^y	700	1262	1458
III	B	7.99	7.92	7.81	1	TE_{111}^y	22.5	29.3	27.2
III	B	9.47	9.47	9.19	3	TE_{211}^y	241	217.2	246.2
III	C	11.48	11.47	11.3	2	TE_{211}^y	144	131	139

Table 7.7

Comparison gain and BW for various modes ($tan\delta = 0.0005$)

Ref	ε_r	Dimension (mm)			Mode	Gain (dBi)		BW (%)	
		a	b	D		G_M	G_T	BW_M	BW_T
[171]	10	7	7	10	TE_{111}^y	5.5	5.64	-	10.65
	10	5	5	30	TE_{115}^y	10.2	10.93	7.26	9.2
[5]	10	52	52	25.4	TE_{111}^y	-	4.81	8.2	8.17
	12	27.5	27.5	28.5	TE_{111}^y	-	5.14	10.2	7.59
	20	47	47	12.8	TE_{111}^y	-	5.00	5.1	4.57
	25	25.4	25.4	20	TE_{111}^y	-	4.81	3.6	2.69
	40	21.1	21.1	14.7	TE_{111}^y	-	4.68	1.9	1.38
	100	12	12	15	TE_{111}^y	-	4.48	1.0	0.53
[176]	10	31.9	26.1	15.9	TE_{111}^y	4.04	4.75	9.09	7.8
[181]	10	21	18	5	TE_{111}^y	-	5.35	11.21	10.9

Typical theoretical results on Q_r, G and BW for higher order modes with odd values of m and p of a RDRA having a = 15.24mm, b = 7.62mm, h = 3.1mm and ε_r = 10.8 are shown in Table 7.8. From Table 7.8, it is found that, by selecting the proper material and dimensions of RDRA, a higher order mode may give an enhanced gain over TE_{111}^y mode.

Table 7.8

Radiation characteristics of various TE^{y}_{mnp} modes

$(a = 25mm, b = 15mm, d = 30mm, \varepsilon_r = 10, tan\delta = 0.0005)$

Sl No	Mode	f_r (GHz)	P_r (%)	e (%)	Q_r	Q_t	BW (%)	Gain (dB)	W_e	W_m
1	TE^{y}_{111}	2.658	104.0	99.63	6.04	6.02	11.75	5.46	1.17E+08	8.21E+07
2	TE^{y}_{113}	3.605	10.01	96.47	62.75	60.54	1.17	8.51	2.38E+08	1.93E+08
3	TE^{y}_{211}	4.408	37.07	99.05	16.95	16.79	4.21	9.76	3.71E+08	3.21E+08
4	TE^{y}_{115}	4.894	11.48	97.04	54.72	53.10	1.33	8.86	4.63E+08	4.12E+08
5	TE^{y}_{213}	4.981	5.33	93.84	118.0	110.7	0.64	10.57	4.80E+08	4.30E+08
6	TE^{y}_{215}	5.945	3.96	92.04	158.5	145.9	0.48	10.41	6.93E+08	6.42E+08
7	TE^{y}_{311}	6.202	9.25	96.43	67.93	65.51	1.08	5.90	7.56E+08	7.04E+08
8	TE^{y}_{117}	6.302	11.77	97.19	53.41	51.90	1.36	7.25	7.81E+08	7.29E+08
9	TE^{y}_{313}	6.607	19.05	98.25	32.98	32.40	2.18	11.06	8.59E+08	8.08E+08
10	TE^{y}_{217}	7.132	4.31	92.74	145.7	135.1	0.52	10.19	1.00E+09	9.52E+08
11	TE^{y}_{315}	7.344	1.54	82.02	408.4	335.0	0.21	8.83	1.06E+09	1.01E+09
12	TE^{y}_{119}	7.765	7.55	95.74	83.26	79.72	0.89	7.81	1.19E+09	1.14E+09
13	TE^{y}_{411}	8.024	34.95	99.05	17.98	17.81	3.97	10.00	1.27E+09	1.22E+09
14	TE^{y}_{317}	8.323	0.63	65.15	1005.	654.8	0.11	9.18	1.36E+09	1.32E+09
15	TE^{y}_{413}	8.335	26.06	98.73	24.11	23.80	2.97	10.14	1.37E+09	1.32E+09
16	TE^{y}_{219}	8.444	4.61	93.25	136.2	127.0	0.56	10.35	1.40E+09	1.36E+09
17	TE^{y}_{415}	8.924	3.05	90.13	206.4	186.0	0.38	9.68	1.56E+09	1.52E+09
18	TE^{y}_{319}	9.465	1.05	75.98	598.1	454.5	0.16	10.91	1.76E+09	1.71E+09
19	TE^{y}_{417}	9.739	1.62	83.02	387.4	321.6	0.22	8.49	1.86E+09	1.81E+09
20	TE^{y}_{511}	9.863	15.24	97.87	41.22	40.35	1.75	13.90	1.91E+09	1.86E+09

It is interesting to note that for fixed aspect ratios (a/d and b/d ratios), variation of $P_r(\%)$, Q_r, Q_t, BW, e and G with respect to d (or resonant frequency) are almost constant for different TE^{y}_{mnp} modes. Typical results are shown in Fig. 7.11 with respect to d.

Variations of $P_r(\%), Q_r, Q_t, BW, e$ and G with (a/d) ratio are shown in Fig. 7.12 for some modes. $P_r(\%)$ and Q_r are calculated from magnetic dipole moment theory as reported in [21] are also shown (in dotted black line) therein for comparison purpose.

In Fig. 7.13, variations of $P_r(\%), Q_r, Q_t, BW, e$ and G with (b/d) ratio are shown for some modes. It is found from Figs. 7.12 and 7.13, by selecting proper mode for given dimensions and permittivity of the RDRA, we can achieve both high gain and BW.

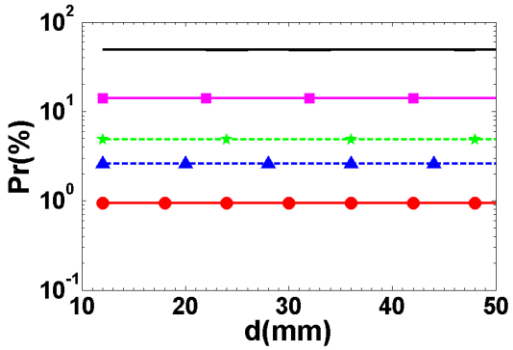

(a) Variation of $P_r(\%)$ with d

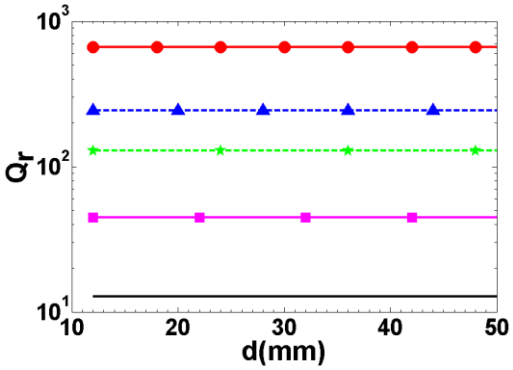

(b) Variation of Q_r with d

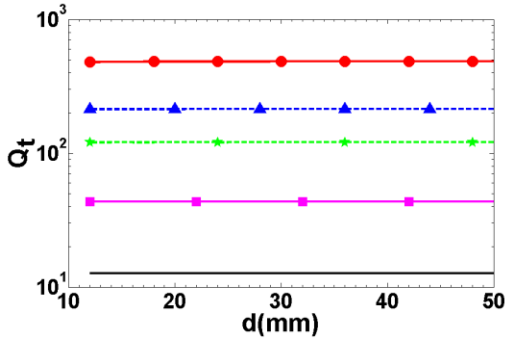

(c) Variation of Q_t with d

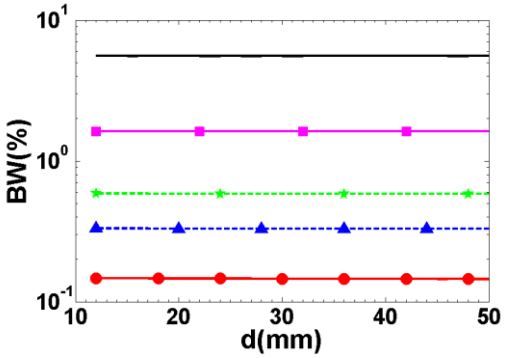

(d) Variation of BW with d

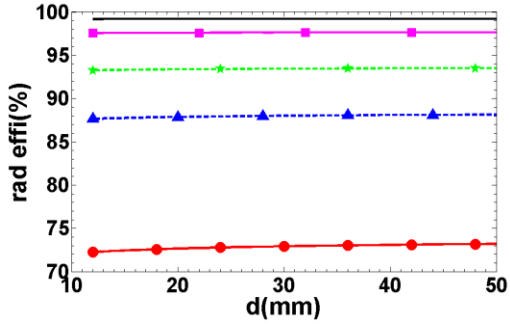

(e) Variation of rad. efficiency with d

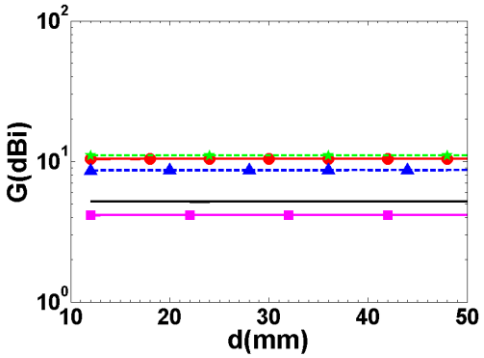

(f) Variation of G(dB) with d

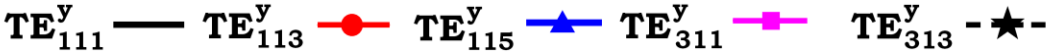

Fig 7.11 Radiation characteristics of RDRA for different TE^{y}_{mnp} modes for fixed a/d and b/d : ($a/d = 0.75, b/d = 0.5, \varepsilon_r = 20, \tan\delta = 0.0005$)

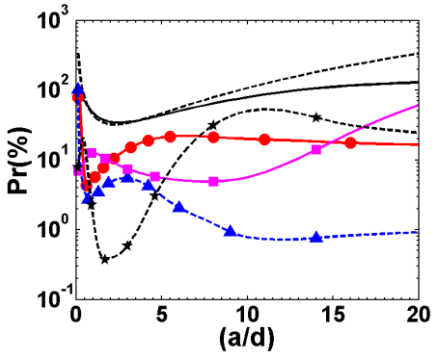

(a) Variation of $P_r(\%)$ with (a/d) ratio

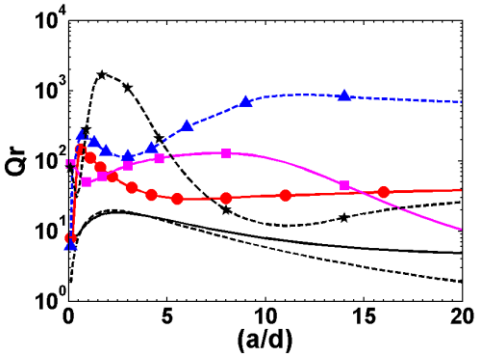

(b) Variation of Q_r with (a/d) ratio

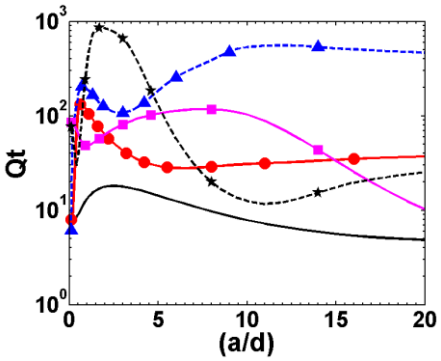

(c) Variation of Q_t with (a/d) ratio

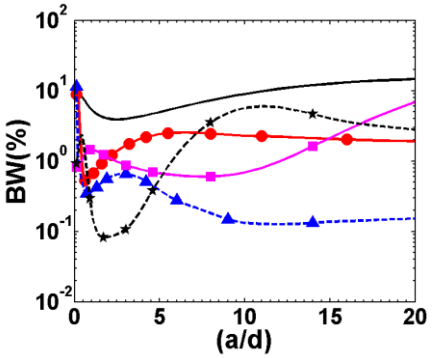

(d) Variation of BW with (a/d) ratio

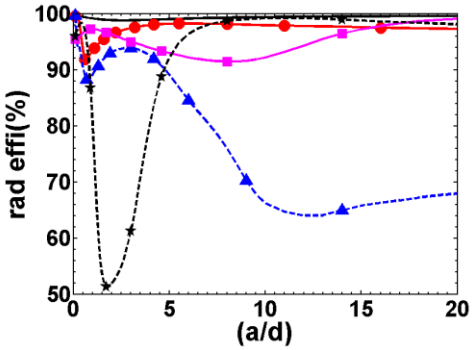

(e) Variation of rad. efficiency with (a/d) ratio

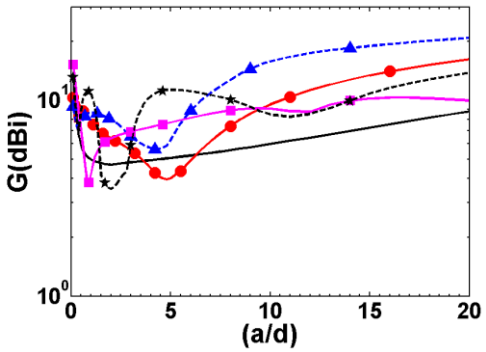

(f) Variation of $G(\mathrm{dB})$ with (a/d) ratio

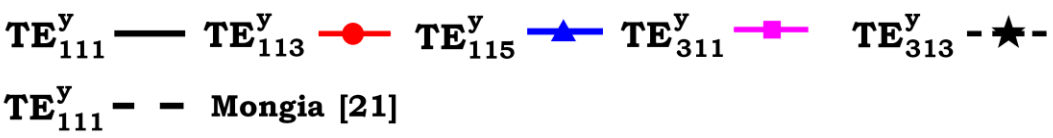

Fig 7.12 Radiation characteristics of RDRA for different TE^{y}_{mnp} modes with (a/d) ratio: $(a = 30mm, b = 15mm, \varepsilon_r = 20, \tan\delta = 0.0005)$

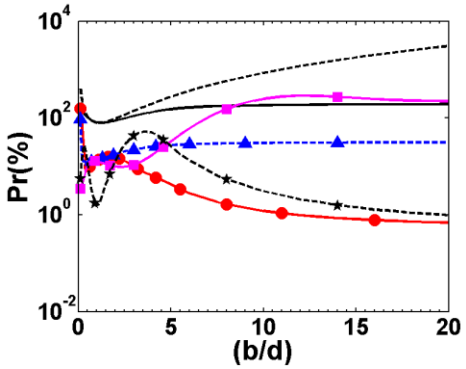

(a) Variation of $P_r(\%)$ with (b/d) ratio

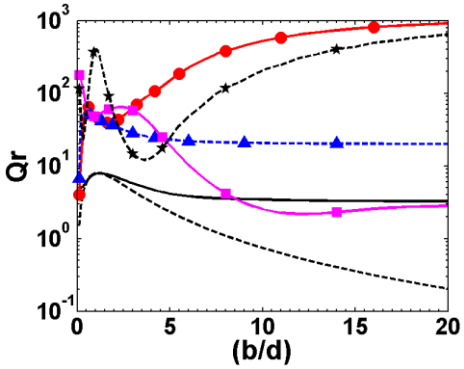

(b) Variation of Q_r with (b/d) ratio

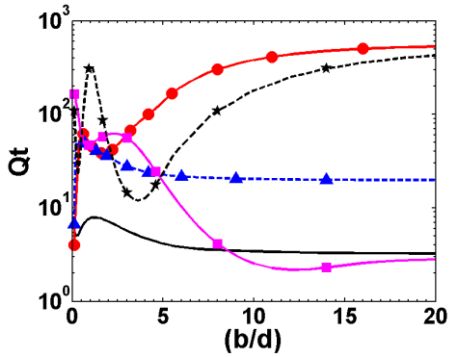

(c) Variation of Q_t with (b/d) ratio

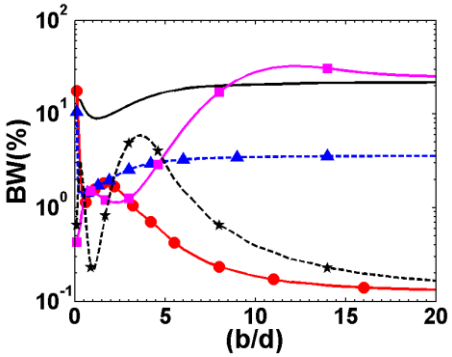

(d) Variation of BW with (b/d) ratio

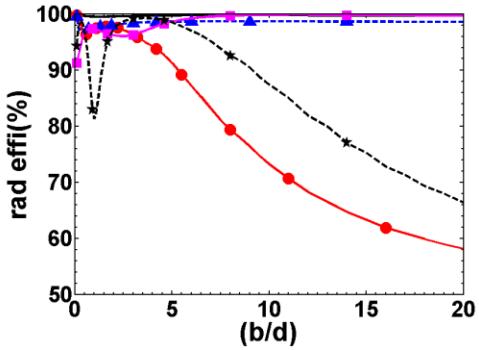

(e) Variation of rad. efficiency with (b/d) ratio

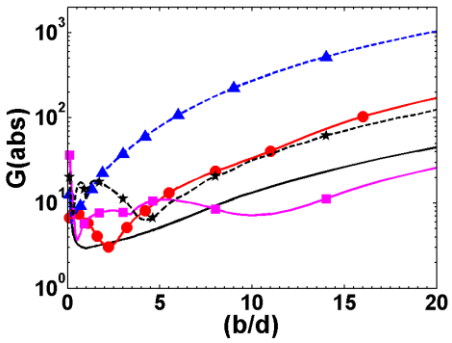

(f) Variation of $G(\mathrm{dB})$ with (b/d) ratio

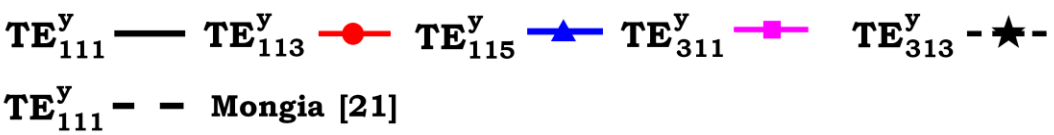

Fig 7.13 Radiation characteristics of RDRA for different TE^{y}_{mnp} modes with (b/d) ratio: $(a = 30mm, b = 15mm, \varepsilon_r = 10, \tan\delta = 0.0005)$

7.4 Conclusion

In this chapter, theoretical investigation on Rectangular Dielectric Resonator Antenna (RDRA) is presented for TE^{y}_{mnp} modes. The RDRA is modeled here as source free cavity for theoretical investigations. Approximate solution for the eigenfunction is given here. Closed form analytic expressions are given here to predict the far-zone electric field and the input impedance of a probe inserted RDRA. Radiation characteristics of the RDRA are also presented. Radiated power $P_r(\%)$, radiation Q-factor (Q_r), total stored energy (W_t), bandwidth (BW), efficiency (e), gain (G) etc. are also discussed here. From this theoretical investigation, it is found that:

- All TE^{y}_{mnp} modes with odd values of m and p, produce a peak in the broadside direction.
- RDRA supports different far-field radiation patterns.
- Due to the existence of imperfect wall at $y = \pm b/2$, stored magnetic energy (W_m) and electric energy (W_e) are not equal.
- By selecting proper dimensions and relative permittivity of the RDRA, higher order modes can produce higher gain compared to fundamental TE^{y}_{111} mode.
- For a given mode, radiated power $P_r(\%)$, total Q-factor (Q_t), efficiency (e), gain (G) etc become almost same for fixed values of aspect ratios $(a/d$ and $b/d)$.

Chapter VIII

Equilateral Triangular Dielectric Resonator Antenna

8.1 Introduction

Dielectric Resonator Antenna (DRA) made up of low loss dielectric material is a potential element for modern communication system. Theoretical and experimental investigations have been reported extensively on hemispherical and cylindrical DRAs [5, 174]. In the previous chapter, theoretical investigations on rectangular DRAs (RDRA) are presented analytically for arbitrary TE^{y}_{mnp} modes. Radiation characteristics for different TE^{y}_{mnp} modes of a RDRA are presented in a systematic way to understand its working principle properly. We have also reported this analytical work [172] partially in 2014 although the RDRA has been investigated by several researchers since 1983.

On the other hand, Equilateral Triangular DRA (ETDRA) did not receive much attention. Conventional source-free ETDRA having side length a, height d and relative permittivity ε_r on a metallic ground plane is shown Fig. 8.1. Literature survey shows that some experimental works have been reported on the performance of thin ETDRA for fundamental TM^{z}_{101} mode [107-111]. Several feeding mechanisms such as aperture on the ground plane [107], slot line [108], conformal strip [109], rectangular waveguide aperture [110], disk loaded coaxial aperture [111] etc had also been utilized by K. W. Leung *et al* to excite the ETDRA. A qualitative comparison can be made from those experimental investigations as reported in [107-111] but it will be limited to thin (or low-profile i.e. $d \ll a$) ETDRA and fundamental TM^{z}_{101} mode only. It is important to have some theoretical investigations to understand the working principle of an ETDRA for arbitrary dimensions (a, d) and relative permittivity ε_r for different

TM^z_{mnp} modes.

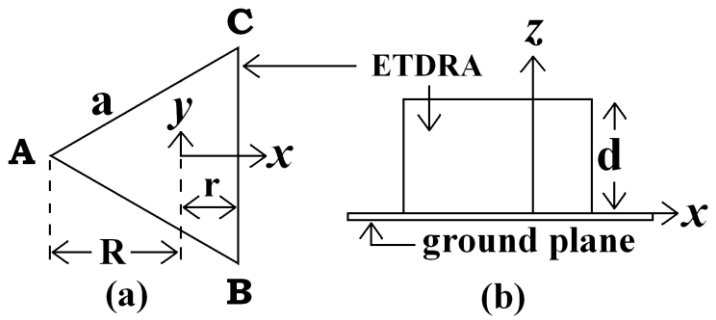

Fig. 8.1 Conventional antenna configuration (a) top view (b) side view

The first paper on ETDRA [107] has been reported by K. W. Leung *et al* where the closed form solutions for the eigenfunctions and eigenvalues have given for an ETDRA. Going through [107], one can encounter some confusion on eigenfunctions and eigenvalues from theoretical point. The expressions for eigenfunctions and eigenvalues as reported in [107] are not simultaneously applicable to a single electromagnetic object. For theoretical investigation, approximate solution for eigenfunction of the ETDRA has been expressed in [107] as:

$$\psi = F(x,y) \times H(z) \tag{8.1}$$

where

$$F(x,y) = cos\frac{2\pi l}{\sqrt{3}a}(x+R)\,cos\left(\frac{2\pi(m-n)}{3a}y\right) + cos\frac{2\pi m}{\sqrt{3}a}(x+R)\,cos\left(\frac{2\pi(n-l)}{3a}y\right) + cos\frac{2\pi}{\sqrt{3}a}(x+R)\,cos\left(\frac{2\pi(l-m)}{3a}y\right) \tag{8.2}$$

$$H(z) = e^{jk_z z} \tag{8.3}$$

Here m, n, l, p are integers such that $l = -(m+n), R = a/\sqrt{3}$ and other terms are carrying their usual meanings. It is clear that the field variation along the finite height (or length) of the ETDRA has been expressed as a (−ve) z-directed travelling wave ($e^{jk_z z}$). To predict the resonant frequency (f_r), k_z has been assumed equal to $\pi/2d$ for fundamental TM^z_{101} mode [25, 107] while the other

two wave numbers are obtained following the procedure suggested by S. A. Schelkunoff [24]. It has been clearly mentioned in [107] that the resonant frequency is determined predominantly by the height of ETDRA when $a \gg d$. Therefore, the field variation along the height of ETDRA must be a standing wave, instead of travelling wave. Otherwise, the resonant frequency must be independent of the height of ETDRA as found in conventional cavity model analysis of microstrip antenna [6, 11-15]. Therefore, the eigenfunctions have been reported for equilateral triangular dielectric waveguide whereas the eigenvalues have been given for equilateral triangular dielectric cavity.

In [112], the triangular surfaces on the top and bottom of an isolated ETDRA are modeled as Imperfect Magnetic Conductors (IPMC), whereas the side walls having rectangular cross-section are modeled as Perfect Magnetic Conductors (PMC) to investigate the TM^z mode of an ETDRA. The mode matching technique has been utilized therein to predict the third wave number (k_z) along the height of the ETDRA as given below [112]:

$$k_z \tan(k_z d - \pi/2) = \sqrt{(\varepsilon_r - 1)k_o^2 - k_z^2} \tag{8.4}$$

Mathematical steps for obtaining equation (8.4) have not been given there. It is found that equation (8.4) is in error. Equation (8.4) should contain the ε_r factor as a multiplication constant to the right sight for TM^z mode of analysis [4, 16, 182]. This is explained in detail with proper mathematical theory in the theory section. Explicit solution for the standing wave field variation along the height (say, $H(z)$ function) of the ETDRA has also not been provided in [112].

The standing wave field variation along the height of the ETDRA can be assumed as either

$$H(z) = \begin{Bmatrix} sin \\ cos \end{Bmatrix} (k_z z) \tag{8.5a}$$

or

$$H(z) = \begin{Bmatrix} sin \\ cos \end{Bmatrix} [k_z (z + \alpha)] \tag{8.5b}$$

where α is the phase constant for a particular mode. It is evident that equation (8.5b) will take the same form as defined by equation (8.5a) for $\alpha = n\pi/2$ where $n = 0,1,2,3,4,\ldots$. Both forms as given in equations (8.5a) and (8.5b) satisfy the separation equation [4, 16] i.e. $\chi^2 + k_z^2 = \varepsilon_r k_0^2$ where χ is the composite wave number along the x-y direction [24] and k_0 is the free-space wave number after multiplication by $F(x, y)$ as given in equation (8.2). A complete standing wave field pattern inside the dielectric resonator antenna may be obtained for which the eigenvalues are same in all cases. But the field variation may not be same along the height of the ETDRA. To justify this matter, k_z is computed from the equation (8.4) as reported in [112] for the time being and different expressions for $H(z)$ as defined by equations (8.5a) and (8.5b) are used to plot the internal electric field variation along the height ($-d \leq z \leq d$) of an isolated ETDRA for the fundamental TM_{101}^z mode at $y = 0$ plane (ABCD surface, say). This is shown in Fig. 8.2.

It is clear from Fig. 8.2 that the internal field distributions along the height of ETDRA ($y = 0$ plane) for different cases are not same. But the theoretical resonant frequencies are equal (here, 1.5GHz) in all cases. For TM_{101}^z mode, there must be only one half cycle along the height of the isolated ETDRA. But Figs. 8.2(a) and 8.2(d) both contain almost two half cycles along the height of the isolated ETDRA for TM_{101}^z mode. Such types of internal field distribution cannot be excited for DRA placed over a metallic ground plane [5, 174, 177] as the mode will be short circuited. In Fig. 8.2(c), partial introduction of another half cycle with one complete half cycle is produced at the upper portion of the isolated ETDRA. Hence, Figs. 8.2(a), 8.2(c) and 8.2(d) are not correct field distributions along the height of an isolated ETDRA. Fig. 8.2(b) contains one full cycle (at the middle portion) but the partial introduction of other two half cycles are found. Hence, Fig. 8.2(b) cannot be accepted as correct electric field distribution along the height of an isolated ETDRA. It should be pointed here that a trial-error method can be used for different values of α to achieve only one half cycle along the height of an isolated

ETDRA. Obviously, it will be a time consuming process for different values of a, d and ε_r. Exact internal field distribution of a cavity (here, ETDRA) is essential to investigate its other electromagnetic properties such as stored energy, quality factor etc.

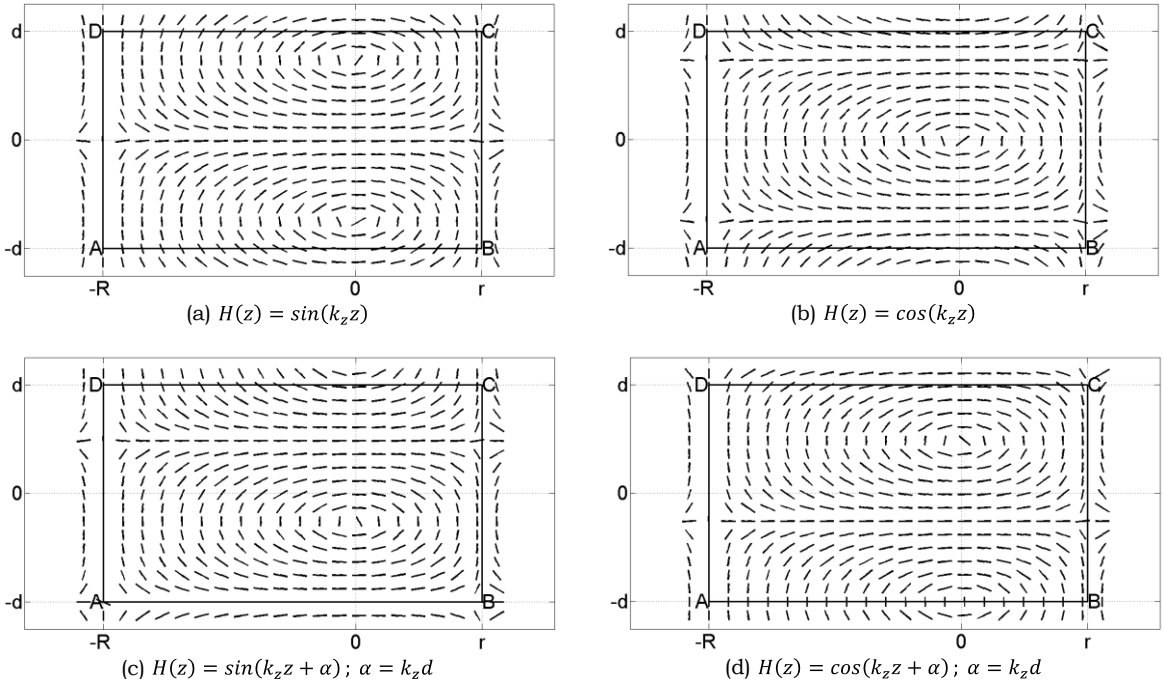

(a) $H(z) = sin(k_z z)$ (b) $H(z) = cos(k_z z)$

(c) $H(z) = sin(k_z z + \alpha)\,;\ \alpha = k_z d$ (d) $H(z) = cos(k_z z + \alpha)\,;\ \alpha = k_z d$

Fig. 8.2 Electric field variation along the height an isolated ETDRA along y=0 plane (a = 66mm, d = 24mm, ε_r = 12)

The formula for predicting the resonant frequency for different TM^z_{mnp} modes produces a large error for arbitrary dimensions and permittivity of the ETDRA. With the help of correct transcendental equation for computing k_z as explained later in this dissertation, one will get almost 16% error in the prediction of resonant frequency for an ETDRA having a = 66mm, d = 24mm, ε_r = 12 as reported in [112]. This is also shown with proper theoretical proof.

Further, literature survey shows that Equilateral Triangular Microstrip Antenna (ETMA) [6, 11-15, 35-36] has been investigated theoretically but the ETDRA has not been analyzed theoretically so far. Closed form expressions for far-field radiation patterns of different TM^z_{mn} modes of ETMA have been reported in [6]. There is no formula for predicting the far-field radiation

patterns of an ETDRA. In summary, the characteristics of an ETDRA have not been reported so far. Therefore, there is a wide area to work on ETDRA.

In this chapter, equilateral triangular dielectric resonator antenna is investigated theoretically. Approximate solution for the eigenfunction of an ETDRA is given for TM^z mode using simple waveguide model. For theoretical investigation, the triangular surfaces on the top and bottom of the source free isolated ETDRA are modeled either as Perfect Magnetic Conductors (PMC) or Imperfect Magnetic Conductors (IPMC), whereas the side walls of rectangular cross-section are modeled as PMC only. Both cases are considered separately to investigate the ETDRA. Field variation along the triangular section (i.e. x-y plane) of an ETDRA with PMC boundary condition is obtained from the TE^z mode of an equilateral triangular metallic waveguide [24] by applying duality as found in [25, 27], or as detailed in generalized form in [52-53]. Explicit solutions of field variation along the height of an ETDRA are given here using PMC and IPMC models for the first time. Two different general approaches are applied to find the third wave number k_z for IPMC boundary conditions along the height of the ETDRA. Both solutions give the same results as expected. But we did not obtain equation (8.4) as reported in [112]. This is explained here with theoretical proof. It is found that the resonant frequencies computed using a magnetic wall model (all surfaces are PMC) and mixed magnetic wall model (PMC and IPMC) are almost equal for different modes. However, without introduction of the concept of effective area, as suggested by us, both models lead to considerable error in the predicting of resonant frequency. The concept of reduction in effective area due to magnetic field lines which avoid the corners is accounted here by defining the effective dimension of ETDRA to predict the resonant frequencies for different TM^z_{mnp} modes. Our curve fitted expressions for effective dimensions can predict the resonant frequency with an accuracy of 4%. Close form expressions for far-field radiation patterns of the fundamental TM^z_{101} mode are given here using 'Equivalence Principle' [4, 16] for both models (PMC and IPMC). Theoretical results on resonant frequencies and far-field

radiation patterns are compared with experimental data as found in the published literature [107-113] to show the accuracy of our theory for different dimensions and relative permittivity of ETDRA. One prototype is also fabricated for further experimental verification.

The study on ETDRA is very important from computational time. If we have a closed form analytical solution, we can easily predict the radiation characteristics of an ETDRA quickly compared to 3D numerical full wave EM simulator. To justify this fact, a personal computer having Core 2 duo Intel processor (clock frequency = 2.2 GHz) and 3GB RAM is used to investigate the characteristics of some ETDRAs using commercially available numerical 3D EM simulators, HFSS and CST. The same are also evaluated using our analytic solutions as given in this dissertation. A comparison of time is shown in Table 8.1. It is clear from Table 8.1 that analytical solution can predict the far-field radiation patterns of an antenna much faster than numerical EM simulators.

Table 8.1

Comparison of time between analytical solution and EM simulators

Sl No	Antenna Parameters			Time (seconds)		
	a (mm)	d (mm)	ε_r	HFSS	CST	Analytical
1	66	24	12	288	317	2.97
2	36	21	10	311	308	2.72
3	24	15	38.74	291	344	3.15
4	10	5	82	307	305	2.88
5	20	12	25	346	312	3.03

Further, the analytical solutions are efficiently utilized for entire domain full-wave MoM analysis of an antenna [23]. Therefore, it is very important to have analytical results on ETDRA.

8.2 Theory

In this section, theoretical investigations on source free ETDRA having side length a, height d and relative permittivity ε_r is presented. In Fig. 8.1, antenna geometry is shown in the standard Cartesian coordinate system. The

antenna is placed on a metallic ground, whose size is sufficiently large compare to the ETDRA. TM^z mode of the ETDRA is discussed here. Eigenfunctions, eigenvalues, far-field radiation patterns, radiated power, gain, Q-factor etc. are investigated. One antenna prototype is fabricated for experimental validation.

8.2.1 Eigenfunctions

In Fig. 8.1, the antenna geometry is shown where an equilateral triangular DRA having side length a, height d and relative permittivity ε_r is placed on a ground plane at $z = 0$ surface. The origin is placed at the in-center (or orthocenter) of the triangular geometry. By applying the image theory, the ground plane is removed first and the process results an source free isolated ETDRA having side length a, height h where $h = 2d$. The simple waveguide model is applied here to find the approximate solution of eigenfunctions ($\psi = F(x,y) \times H(z)$) for arbitrary TM^z_{mnp} modes. Here, $F(x,y)$ is the standing wave solution along the x-y direction, whereas $H(z)$ is the standing wave solution along the z-direction.

8.2.1.1 Evaluation of $F(x,y)$ Function

To evaluate the standing wave field variation $F(x,y)$ along the x-y direction, the side walls having rectangular cross-section of the ETDRA are modeled as PMC. Tri-linear transformation is used as defined in [24] to generate local co-ordinate system inside the equilateral triangular section. The equilateral triangular section is symmetric with respect to x-axis as shown in Fig. 8.1. But after applying tri-linear transformation, the symmetry gets shifted to y-axis. Following [53], one can easily obtain the $F(x,y)$ function both for even and odd modes. The solution of $F(x,y)$ function for even mode is defined by equation (8.2) whereas the solution for odd mode is given by [53]:

$$F(x,y) = cos\frac{2\pi l}{\sqrt{3}a}(x+R)\,sin\left(\frac{2\pi(m-n)}{3a}y\right) + cos\frac{2\pi m}{\sqrt{3}a}(x+R)\,sin\left(\frac{2\pi(n-l)}{3a}y\right)$$

$$+ \cos\frac{2\pi}{\sqrt{3}a}(x+R)\sin\left(\frac{2\pi(l-m)}{3a}y\right) \tag{8.6}$$

where R, m, n, l are as defined earlier. Even and odd properties of the eigenfunctions for some TM^z modes are shown in Chapter III for equilateral Triangular Microstrip Antenna (ETMA) (please see Fig. 3.2) and is not repeated here for the sake of brevity.

If we want to plot the internal electric $\vec{E}$ and magnetic $\vec{H}$ field distribution along the x-y plane at z = constant surface, we do not have to have any knowledge about $H(z)$ function. For a fixed value of z, $H(z)$ function will take constant value and this constant value can be clumped up with the modal magnitude. Therefore, we can easily plot the $\vec{E}$ or $\vec{H}$ field within the ETDRA along the x-y plane as done for microstrip patch antenna. Typical results are shown in Fig. 8.3 for 'even' and 'odd' mode solution.

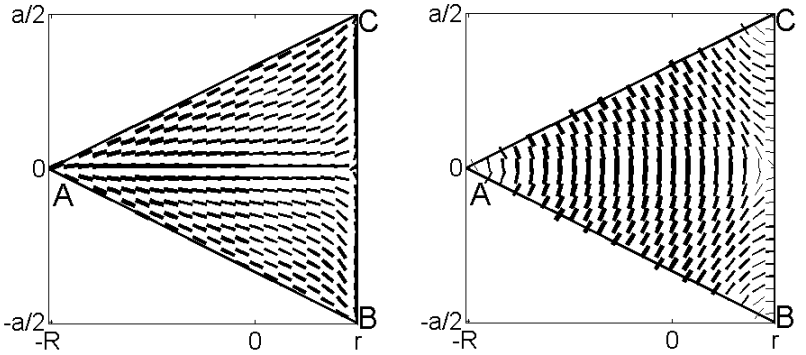

(a) Internal electric (left) and magnetic (right) field distribution for 'even' TM^z_{101} mode

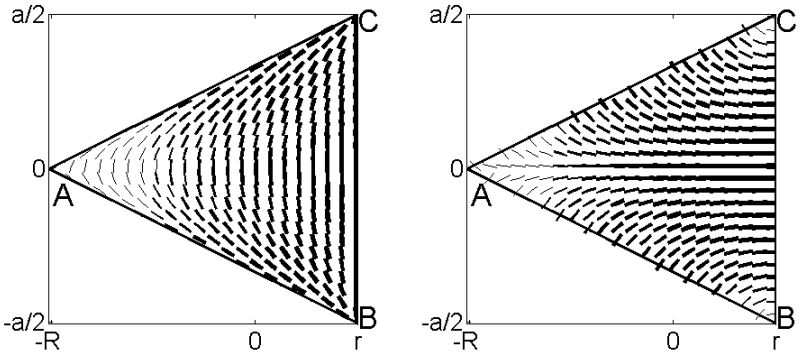

(b) Internal electric (left) and magnetic (right) field distribution for 'odd' TM^z_{101} mode

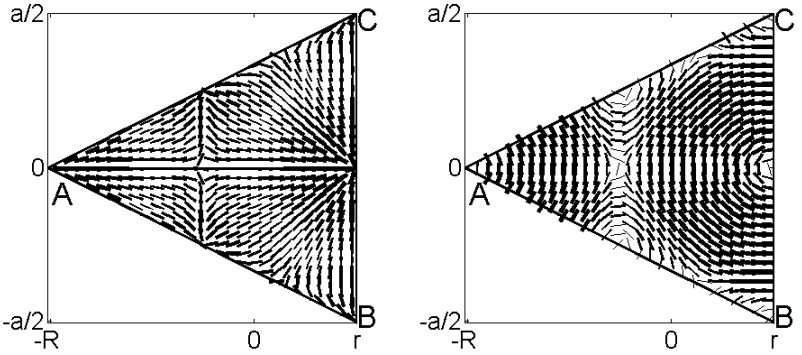

(c) Internal electric (left) and magnetic (right) field distribution for 'even' TM^z_{201} mode

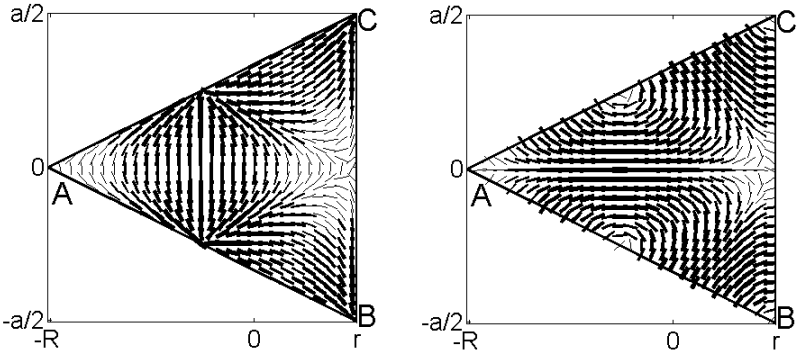

(d) Internal electric (left) and magnetic (right) field distribution for 'odd' TM^z_{201} mode

Fig. 8.3 Internal electric $(\vec{E})$ and magnetic $(\vec{H})$ field distribution for 'even' and 'odd' mode (a = 66mm, d = 24mm, ε_r = 12)

To investigate the even (ψ^e) and odd (ψ^o) mode solutions, a probe fed ETDRA is simulated using FEM based numerical full-wave 3D EM Simulator HFSS [9]. Different combinations of dimensions (a, d) and relative permittivity (ε_r) are also used. Different feeding techniques are also applied such as aperture on the ground plane, strip, microtsrip line etc. Internal electric $\vec{E}$ and magnetic $\vec{H}$ field distribution along the x-y plane at $z = d/2$ surface are observed to identify various modes. It is found that all modes are 'even' TM^z modes. We did not observe any 'odd' mode field distribution (please see Fig. 8.3) along the triangular cross-section. Similar observation is also found for equilateral triangular microstrip antennas due to plausible reason already discussed. Therefore, we discuss here 'even' modes of ETDRA only.

8.2.1.2 Evaluation of $H(z)$ Function

Literature survey shows that the standing wave filed solution along the height of the ETDRA ($H(z)$ function) is not reported so far explicitly. Simple waveguide model is applied to find the approximate solution for $H(z)$ function. Two cases for the boundary conditions are considered separately. First, it is assumed that the source free isolated ETDRA is bounded by Perfect Magnetic Conductor (PMC) along its height also. This model is termed as 'PMC model'. The $H(z)$ function is assumed as:

$$H(z) = (A\cos(k_z z) + B\sin(k_z z)), \qquad |z| \le d \tag{8.7}$$

After applying PMC at $z = \pm d$, we obtain:

$$H(z) = \left[\frac{A}{\sin(k_z d)}\right] \times \sin\big(k_z(d-z)\big); \quad k_z = p\pi/(2d) \;;\; p = 1,2,3,4 \ldots \tag{8.8}$$

The constant terms $A/\sin(k_z d)$ can easily be clumped up with the modal amplitude. At fundamental mode ($p = 1$), k_z is equal to $\pi/(2d)$ which is exactly the same as reported in [25, 107]. In [25, 107], the origin of k_z has not been reported explicitly. An intuitive method has been used to predict the value of k_z at fundamental mode. Here, we derived the expressions for predicting k_z at different TM^z_{mnp} modes using 'PMC model'.

In the second case, it is assumed that most of the field lines are confined within the source free isolated ETDRA and the fields outside the isolated ETDRA are decaying exponentially along the z-direction. This model is termed as 'IPMC model'. Thus, following Marcatili's method [175], the $H(z)$ function can be expressed as:

$$H(z) = \begin{cases} A_3 e^{\gamma_z(z+d)}, & z \le -d \\ A_1\cos(k_z z) + A_2\sin(k_z z), & |z| \le d \\ A_4 e^{-\gamma_z(z-d)}, & z \ge d \end{cases} \tag{8.9}$$

where $d = h/2$, $\chi^2 + k_z^2 = \varepsilon_r k_0^2$ and $\chi^2 - \gamma_z^2 = k_0^2$. Here, k_0 is the free-space wave number, χ is the composite wave number along the *x-y* direction [24] and given by:

$$\chi = \left(\frac{4\pi}{3a}\right)(m^2 + mn + n^2)^{1/2} \tag{8.10}$$

and other terms are carrying their usual meaning. Tangential components of both electric and magnetic fields must be continuous at $z = \pm d$ surface. This process leads to a complex transcendental equation as:

$$[k_z\, tan(k_z\, h/2) - \varepsilon_r \gamma_z][\varepsilon_r \gamma_z\, tan(k_z\, h/2) + k_z] = 0 \tag{8.11}$$

$$\gamma_z^2 = (\varepsilon_r - 1)k_0^2 - k_z^2 \tag{8.12}$$

The second factor of the equation (8.11) can be rearranged as:

$$\varepsilon_r \times \gamma_z = -k_z\, cot(k_z\, h/2) = -k_z\, tan(\pi/2 - k_z\, h/2)$$
$$\Rightarrow k_z\, tan(k_z\, h/2 - \pi/2) = \varepsilon_r \times \sqrt{(\varepsilon_r - 1)k_o^2 - k_z^2} \tag{8.13}$$

After matching the tangential electric and magnetic fields at $z = \pm d$, the $H(z)$ function can be simplified as:

$$H(z) = \begin{cases} cos(k_z z), & k_z\, tan(k_z\, h/2) - \varepsilon_r \gamma_z = 0 \quad (8.14) \\ sin(k_z z), & \varepsilon_r \gamma_z\, tan(k_z\, h/2) + k_z = 0 \quad (8.15) \end{cases}$$

The multiplication of $F(x, y)$ and $H(z)$ functions will give the final approximate solution for the eigenfunctions $(\psi(x, y, z))$.

In comparing equation (8.13) with equation (8.4), it is evident that both equations are same except for the ε_r factor. Equation (8.4) satisfies all the data in the Table 1 of [112] as already pointed by us in [183]. Now, if we assume that the ε_r factor is a typographical error in [112], then the field variation along the height of the ETDRA will be $sin(k_z z)$ (according to equation (8.15)) which will produce a zero electric field at $z = 0$ (please see Fig. 8.2(a)). But the odd mode solution, i.e. $H(z) = sin(k_z z)$ along the height of the DRA, placed on a

metallic ground plane, is not possible as electric field for these odd modes will be short circuited [5, 177] because $H(z) = 0$ at $z = 0$. Hence, the final expression for $H(z)$ function is

$$H(z) = cos(k_z z) \tag{8.16}$$

where k_z is the solution of transcendental equation

$$k_z \, tan(k_z \, h/2) - \varepsilon_r \gamma_z = 0 \tag{8.17}$$

For further investigation, the $H(z)$ function along the height of the isolated ETDRA is assumed as [175]:

$$H(z) = \begin{cases} A_3 e^{\gamma_z (z+d)}, & z \le -d \\ A \, cos(k_z z + \beta), & |z| \le d \\ A_4 e^{-\gamma_z (z-d)}, & z \ge d \end{cases} \tag{8.18}$$

Obviously, equation (8.18) is different form of equation (8.9). Tangential electric and magnetic field components are matched at $z = \pm d$, leading to:

$$k_z h = (p-1)\pi + 2\tan^{-1}\left(\varepsilon_r \times \frac{\gamma_z}{k_z}\right) \;\; ; \quad p = 1,2,3,4 \ldots. \tag{8.19}$$

$\gamma_z = \sqrt{(\varepsilon_r - 1)k_0^2 - k_z^2}$ and $\beta = (p-1)\pi/2$.

It should be pointed here that individual analysis of even and odd mode solutions for TM modes of a dielectric waveguide using the mode matching technique will always contain ε_r as a multiplication factor to γ_z whereas μ_r will come as a multiplication factor to γ_z for TE modes [4, 16, 182] where μ_r is the relative permeability of the dielectric waveguide. In the present work, two different general solutions for field variation along the height of the isolated ETDRA as shown by equations (8.9) and (8.18) are applied for the TM^z mode of analysis. In both cases, ε_r results as a multiplication factor to γ_z. Hence, equation (8.4) as reported in [112] should contain ε_r as a multiplication factor to γ_z. This may be a typographical error. Further, equation (8.4) with ε_r factor is the characteristic equation for the odd mode solution of an isolated dielectric

waveguide as obtained in equation (8.15) and this odd mode solution will produce a zero electric field at $z = 0$ (please see Fig. 8.2(a)). A DRA placed on a metallic ground plane does not support odd mode solution along its height (here, z-direction) [5, 174,177]. Hence, the explicit solution for the field variation along the height of an isolated ETDRA must be an even mode solution as obtained by equations (8.16) or (8.18).

If equation (8.4) is correct and does not carry any ε_r factor with γ_z as explained above, the correctness of equation (8.4) is questionable. Further, equation (8.4) does not support the field variation along the height of an isolated ETDRA where the partial introduction of another half cycle is observed as shown in Fig. 8.2.

Different constant of equation (8.18) i.e. A, A_3 and A_4 must be evaluated to find the final expression for $H(z)$ function. After evaluating those constant, one can easily express the $H(z)$ function as:

$$H(z) = A \times \begin{cases} \frac{1}{\mu_r} \times cos(k_z d + \beta) \times e^{-\gamma_z (z - h/2)}, & z > d \\ cos(k_z z + \beta) \quad , & |z| \leq d \\ \frac{1}{\mu_r} \times cos(k_z d - \beta) \times e^{\gamma_z (z + h/2)} \, , & z < d \end{cases} \tag{8.20}$$

In Fig. 8.4, the different expressions of $H(z)$ as obtained by equations (8.8), (8.16) and (8.18) are used with 'even' mode solution of $F(x, y)$ as defined by equation (8.2) to plot the internal electric field along the height of the isolated ETDRA for the fundamental TM_{101}^{z} mode. From Fig. 8.4, it is found that all three types of expressions for $H(z)$ are giving similar electric field distribution. The partial introduction of another half cycle as shown in Fig. 8.2 is not observed according to [174, 184]. Further, it is found from Fig. 8.4 that the centre of electric field variation along the height is at origin as expected, not at the centre of the surface (here ABCD). It should be pointed here that the theoretical center of the electric field distribution along the height for cylindrical and rectangular shaped DRAs is at the origin as well as at the centre of the surface. This is because of the placement of cylindrical and

rectangular shaped DRAs are symmetrical about the origin for theoretical investigation. In case of ETDRA, the origin is placed at the in-centre (or orthocenter).

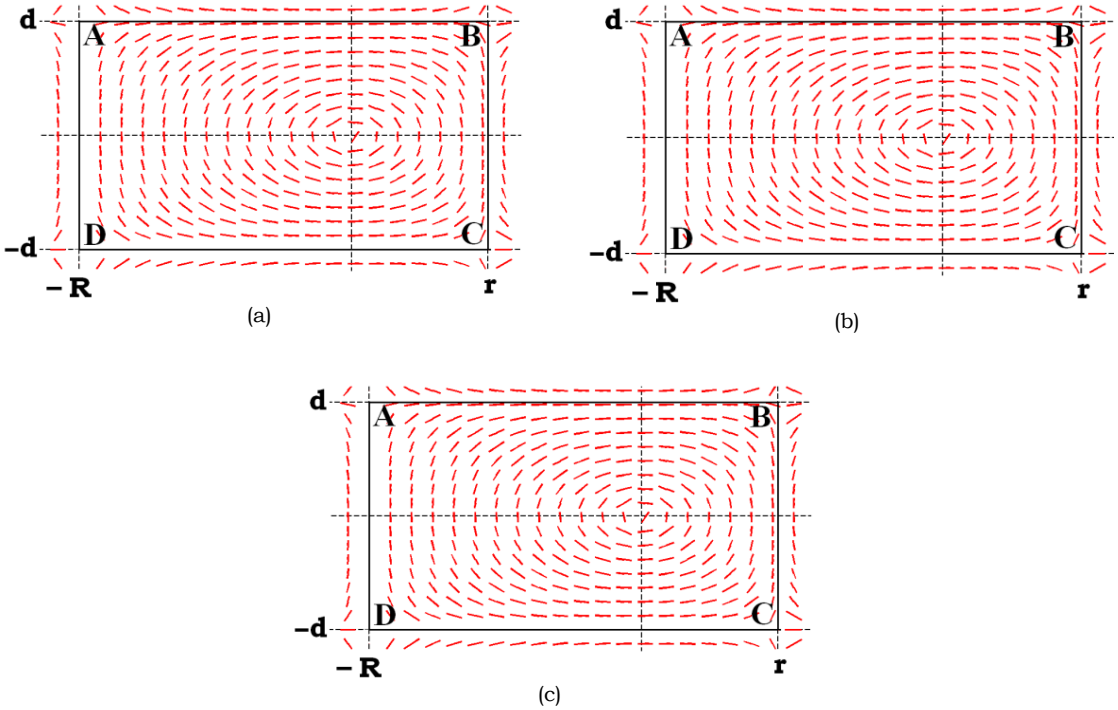

Fig. 8.4 Electric field variation along the height (y = 0 plane) an isolated ETDRA for TM^z_{101} mode (a = 40mm, d = 20mm, ε_r = 37.84)
(a) $H(z) = sin(k_z(h/2 - z))$ where k_z is defined by equation (8.8)
(b) $H(z) = cos(k_z z)$ where k_z is defined by equation (8.17)
(c) $H(z) = cos(k_z z + \beta)$ where k_z is defined by equation (8.19)

Following equation (8.18) for 'IPMC model', the approximate solution for the eigenfunctions (ψ^e) of an isolated ETDRA is given by:

$$\psi^e_{mnp} = \left[cos\frac{2\pi l}{\sqrt{3}a}(x+R)\,cos\left(\frac{2\pi(m-n)}{3a}y\right) + cos\frac{2\pi m}{\sqrt{3}a}(x+R)\,cos\left(\frac{2\pi(n-l)}{3a}y\right) + cos\frac{2\pi}{\sqrt{3}a}(x+R)\,cos\left(\frac{2\pi(l-m)}{3a}y\right)\right] \times \begin{cases} sin[k_z(d-z)] \text{for} PMC \\ cos(k_z z + \beta) \text{ for} IPMC \end{cases} \quad (8.21)$$

The complete electric and magnetic fields inside the ETDRA can be expressed for TM^z_{mnp} modes as:

$$E_x = \left(\frac{-jA}{\omega\mu\varepsilon}\right)\left(\sum_{i=1}^{3} -\alpha_i \sin[\alpha_i(x+R)]\cos(\beta_i y)\right)\begin{cases}(-k_z)\,cos[k_z(d-z)] & PMC\\ (-k_z)\,sin[k_z z+\beta] & IPMC\end{cases}$$

$$E_y = \left(\frac{-jA}{\omega\mu\varepsilon}\right)\left(\sum_{i=1}^{3} -\beta_i \cos[\alpha_i(x+R)]\sin(\beta_i y)\right)\begin{cases}(-k_z)\,cos[k_z(d-z)] & PMC\\ (-k_z)\,sin[k_z z+\beta] & IPMC\end{cases}$$

$$E_z = \left(\frac{-jA}{\omega\mu\varepsilon}\right)(\chi^2)\left(\sum_{i=1}^{3} cos[\alpha_i(x+R)]\,cos(\beta_i y)\right)\begin{cases}sin[k_z(d-z)] & PMC\\ cos[k_z z+\beta] & IPMC\end{cases}$$

$$H_x = \left(\frac{A}{\mu}\right)\left(\sum_{i=1}^{3} -\beta_i \cos[\alpha_i(x+R)]\sin(\beta_i y)\right)\begin{cases}sin[k_z(d-z)] & PMC\\ cos[k_z z+\beta] & IPMC\end{cases}$$

$$H_y = \left(\frac{-A}{\mu}\right)\left(\sum_{i=1}^{3} -\alpha_i \sin[\alpha_i(x+R)]\cos(\beta_i y)\right)\begin{cases}sin[k_z(d-z)] & PMC\\ cos[k_z z+\beta] & IPMC\end{cases}$$

$$H_z = 0 \qquad (8.22)$$

where A is a constant and other notations are denoting their usual meaning. It is important to have some knowledge on graphical internal electric and magnetic field patterns for different modes. Typical results are already shown in Fig. 8.3 for some lower order modes. In Figs. 8.5 -8.6, internal field distribution for some higher order modes are shown.

8.2.2 Resonant Frequency

The resonant frequency of an isolated source free ETDRA for arbitrary TM^z_{mnp} mode is evaluated from separation equation $\left(\chi^2 + k_z^2 = \varepsilon_r k_0^2 \text{ where } \chi = (4\pi/3a)(m^2+mn+n^2)^{1/2}\right)$ as:

$$f_r = \frac{c}{2\pi\sqrt{\varepsilon_r}} \times \left[\left(\frac{4\pi}{3a}\right)^2 (m^2+mn+n^2) + k_z^2\right]^{1/2} \qquad (8.23)$$

where c is the velocity of light in free space.

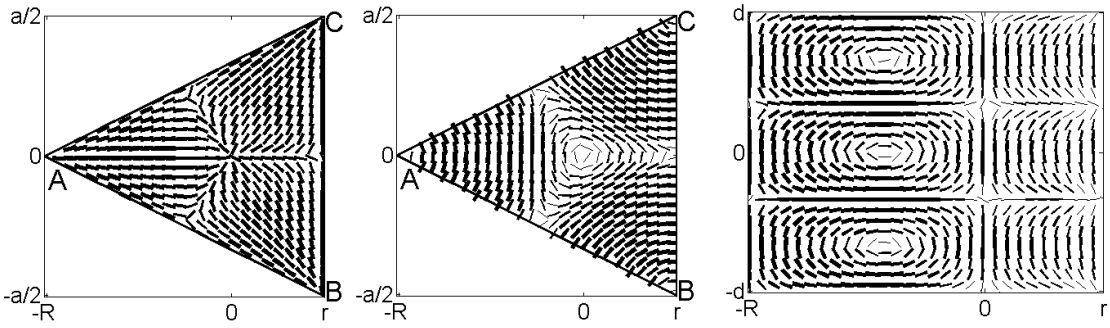

(a) (b) (c)

Fig. 8.5 Internal field distribution for TM^z_{113} modes (a = 66mm, d = 24mm, ε_r = 12)
(a) $\vec{E}$-field patterns at $z = d/2$ plane (b) $\vec{H}$-field patterns at $z = d/2$ plane
(c) $\vec{E}$field patterns at $y = 0$ plane

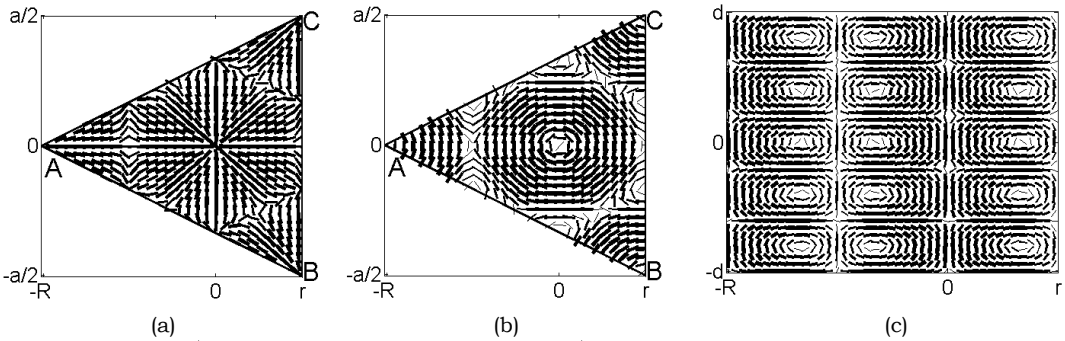

(a) (b) (c)

(a) $\vec{E}$-field patterns at $z = d/2$ plane (b) $\vec{H}$-field patterns at $z = d/2$ plane
(c) $\vec{E}$field patterns at $y = 0$ plane

Fig. 8.6 Internal field distribution for TM^z_{305} modes (a = 66mm, d = 24mm, ε_r = 12)

In Table 8.2, k_z computed using equations (8.8), (8.17) and (8.19) to find the resonant frequencies are shown for different TM^z_{mnp}modes of an isolated source free ETDRA having $a = 66mm, d = 24mm$ and $\varepsilon_r = 12$ [112]. From Table 8.2, it is clear that both equations (8.17) and (8.19) give exactly the same results for different modes as expected. The error is maximum (19% aprox.) for the fundamental TM^z_{101} mode and the error is decreasing for higher order modes.

Equation (8.8) for computing k_z is able to predict the resonant frequency with 3-5% error for low-profile ETDRA ($a = 20mm, d \approx 1mm, \varepsilon_r = 82$) [107-111]. Theoretical results are verified with experimental data. In case of arbitrary dimensions of ETDRA (not low-profile ETDRA), k_z produces almost 16% error in the prediction of f_r of an ETDRA having $a = 66mm, d = 24mm$ and $\varepsilon_r = 12$ [112]

as shown in Table 8.2. The transcendental equation for computing k_z as reported in [112] is in error. We have successfully demonstrated this fact with proper mathematical derivation. Our transcendental equations (8.17) and (8.19) for computing k_z are also produce 19% error as shown in Table 8.2. Similar observation had already been reported by A. Yoshihiko in 1974 for demagnetized equilateral triangular shaped ferrite posts [25]. In [25], it is clearly mentioned that the theoretical resonant frequency of such type of triangular ferrite posts can be smaller than experimental data by 20% at higher frequencies. This type of error is due to non-consideration of feed mechanism and the size of finite ground plane in the prediction of resonant frequency [21].

Table 8.2

Comparison of resonant frequency for different expressions of k_z

($a = 66mm, d = 24mm, \varepsilon_r = 12$)[112]

Mode	Resonant Frequency (GHz)				Error (%)		
	equ. (8.8)	equ. (8.17)	equ. (8.19)	[112]	equ. (8.8)	equ. (8.17)	equ. (8.19)
TM^z_{101}	1.256	1.220	1.220	1.5	16.3	18.7	18.7
TM^z_{201}	1.968	1.956	1.956	2.2	10.6	11.1	11.1
TM^z_{211}	2.483	2.476	2.476	2.8	11.3	11.6	11.6
TM^z_{221}	3.160	3.156	3.156	3.3	4.2	4.4	4.4
TM^z_{311}	3.279	3.275	3.275	3.6	8.9	9.0	9.0
TM^z_{411}	4.107	4.105	4.105	4.4	6.7	6.7	6.7
TM^z_{421}	4.714	4.712	4.712	4.8	1.8	1.8	1.8

The concept of fringing effect is well established for microstrip antennas [6, 11-15]. But, the effect of fringing in DRA has not been reported explicitly [5, 174]. Hence, it is expected to have a third factor for making the experimental (or simulated) resonant frequencies higher than the theoretical values. The reduction in effective area can be explained with the help of electric field lines which avoid the corners (if any) as explained by S. A. Schekunoff in [24] for waveguides bounded by Perfect Electric Conductors (PEC) and applying 'Principle of Duality' for our case bounded by Perfect Magnetic Conductors (PMC). To justify this fact, S. A. Schekunoff had given an excellent example in

[24]. The ratio of cutoff frequency between circular and semi-circular metallic waveguides (i.e. bounded by Perfect Electric Conductor (PEC)) having same radius is approximately equal to $\sqrt{2}$ i.e. 1.4. In practice, the same is found equal to 1.6. The magnetic field lines tend to avoid the corners in semi-circular metallic waveguide which results in reduction of effective area and as a consequence, the cutoff frequency of the semi-circular metallic waveguide increases. In our case, the ETDR bounded by PMC contains three acute angles. Due to three acute angles, electric field lines will avoid all corners and this process will result a smaller effective size than its actual physical size. Typical results of simulated internal electric field are shown in Fig. 8.7.

It should be pointed here that our source free theory does not include the effect of excitation. The avoidance of electric field from three corners due to PMC boundary condition is also not reflected by our theory as shown in Fig. 8.8. The theoretical contour of field lines is matching with data obtained from 3D EM simulator HFSS but the magnitude differs. This type of discrepancy is not found in equilateral Triangular Microstrip Antenna (TMA).

For a first order approximation, curve-fitted formula for computing the effective length (a_e) of ETDRA is defined for various TM^z_{mnp} modes as:

$$a_e = a \times (1.003 \times e^{-0.0001747t} - 0.4172 \times e^{-0.4967t}) - 0.01 \times (d/a) \times \varepsilon_r^{-1.75} \qquad (8.24)$$

Here, $t = |m| + |n|$. The effective height (d_e) of the ETDRA is expressed as [185]:

$$d_e = d \times (1 - 1.0 \times \varepsilon_r^{-1}) \qquad (8.25)$$

It is worth mentioning here that the use of equations (8.24) and (8.25) for effective dimensions (a_e, d_e) are consistent with the internal field distribution as shown in Figs. 8.3 – 8.6 respectively.

To have an idea on modal indices for different modes, the resonant frequencies are computed for first few modes using both 'PMC' and 'IPMC' model. This is shown in Table 8.3. It is found from Table 8.3 that mode degeneracy occurs for $m \neq n \neq 0$.

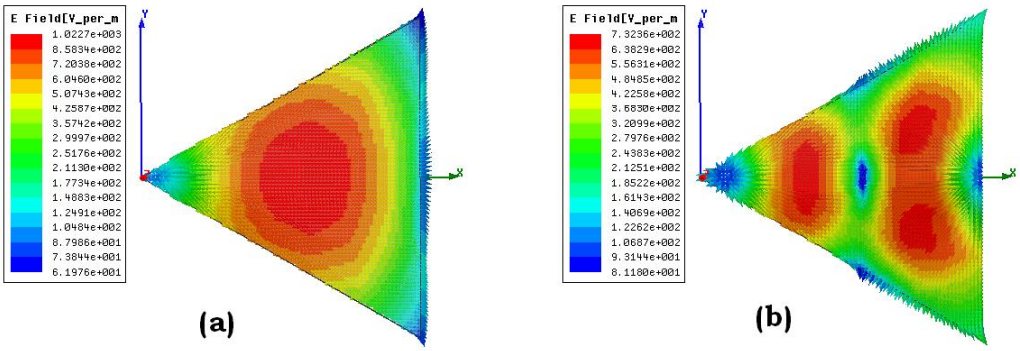

Fig. 8.7 Confinement of $\vec{E}$-field which avoid the corners within the ETDRA bounded by PMC for different modes (a = 66mm, d = 24mm, ε_r = 12) (a) TM^z_{101} mode (b) TM^z_{201} mode

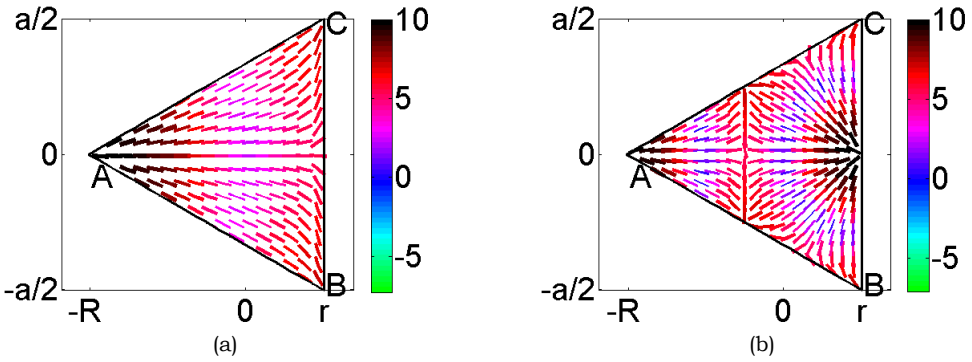

Fig. 8.8 Theoretical (source free theory) Internal $\vec{E}$-field distribution (in dB) for different modes of an ETDRA (a = 66mm, d = 24mm, ε_r = 12) (a) TM^z_{101} mode (b) TM^z_{201} mode

Table 8.3

Resonant frequencies (f_r) for first few modes of an ETDRA

($a = 66mm, d = 24mm, \varepsilon_r = 12$)

Sl No	Mode	f_r (GHz)		Sl No	Mode	f_r (GHz)	
		equ. (8.8)	equ. (8.19)			equ. (8.8)	equ. (8.19)
1	TM^z_{101}	1.2561	1.2201	11	TM^z_{131}	3.2791	3.2753
2	TM^z_{111}	1.7626	1.7479	12	TM^z_{311}	3.2791	3.2753
3	TM^z_{201}	1.9676	1.9561	13	TM^z_{213}	3.5595	3.5136
4	TM^z_{121}	2.483	2.4761	14	TM^z_{123}	3.5595	3.5136
5	TM^z_{211}	2.483	2.4761	15	TM^z_{401}	3.612	3.6088
6	TM^z_{301}	2.7739	2.6083	16	TM^z_{303}	3.7682	3.7304
7	TM^z_{103}	2.843	2.7684	17	TM^z_{321}	3.9166	3.914
8	TM^z_{113}	3.1003	3.0138	18	TM^z_{231}	3.9166	3.914
9	TM^z_{221}	3.1604	3.1515	19	TM^z_{223}	4.0611	4.031
10	TM^z_{203}	3.2212	3.1562	20	TM^z_{141}	4.1072	4.1048

8.2.3 Far-Field Radiation Patterns

Far-field radiation patterns of an equilateral triangular microstrip antenna have been reported in 1988 by K. F. Lee *et al* [6] using conventional cavity model [6, 11-15] where $\vec{E}_z$ component has been utilized only, because the tangential components ($\propto \partial/\partial z$) $\vec{E}_x$ and $\vec{E}_y$ are equal to zero according to cavity model ($H(z) = \text{constant}$) [6, 11-15]. Mathematical explanation for obtaining $\vec{E}_x = \vec{E}_y = 0$ for microstrip patch antenna is already given in Chapter V. In case of ETDRA, $\vec{E}_x$ and $\vec{E}_y$ components are not zero and their effects must be accounted for accurate prediction of the far-field radiation patterns.

To find the far field radiation patterns of an ETDRA for arbitrary TM^z_{mnp} modes, 'Equivalence Principle' [4, 16] is applied by the author for the first time. For theoretical investigation, the triangular surfaces on the top and bottom of the source free isolated ETDRA are modeled either as Perfect Magnetic Conductors (PMC) or Imperfect Magnetic Conductors (IPMC), whereas the side walls of rectangular cross-section are modeled as PMC only. Therefore, the magnetic surface currents $(\vec{M}_s = \vec{E} \times \hat{n})$ and electric surface currents $(\vec{J}_s = \hat{n} \times \vec{H})$ on the surfaces of the ETDRA both are to be evaluated depending on the boundary conditions (PMC or IPMC).

To make the calculation simple, we place the apex of triangle ABC at origin. Hence, the eigenfunctions $\psi_{mnl}(x, y, z)$ can be written as:

$$\psi_{mnl} = A_{mnl}\left(\sum_{i=1}^{3} cos(\alpha_i x)\, cos(\beta_i y)\right)\begin{cases} sin[k_z(d-z)] & PMC \\ cos[k_z z + \beta] & IPMC \end{cases} \tag{8.26}$$

This effect of shifting will be accounted in the final expressions for far-field radiation patterns. Further, the slope of AC and AB surfaces (please see Fig. 8.1) are defined as $+\eta$ and $-\eta$ respectively where $\eta = 1/\sqrt{3}$. Further, for theoretical calculation, it is assumed that

$$f(x, y, z) = xk_o sin(\theta)\cos(\varphi) + yk_o sin(\theta)\sin(\varphi) + zk_o cos(\theta) = xV_1 + yV_2 + zV_3$$

where $V_1 = k_o sin(\theta)\cos(\varphi)$; $V_2 = k_o sin(\theta)\sin(\varphi)$; $V_3 = k_o cos(\theta)$

Surface Current along AC Surface (PMC)

$$M_s^{AC} = \vec{E} \times \hat{n} = \left[E_x\hat{x} + E_y\hat{y} + E_z\hat{z}\right] \times \left(\hat{y}cos(\alpha) - \hat{x}sin(\alpha)\right); \quad \alpha = \pi/6$$

$$= -\hat{x}E_z cos(\alpha) - \hat{y}E_z sin(\alpha) + \hat{z}\left(E_x cos(\alpha) + E_y sin(\alpha)\right) \quad (8.27a)$$

Surface Current along AB Surface (PMC)

$$M_s^{AB} = \vec{E} \times \hat{n} = \left[E_x\hat{x} + E_y\hat{y} + E_z\hat{z}\right] \times \left(-\hat{y}cos(\alpha) - \hat{x}sin(\alpha)\right); \quad \alpha = \pi/6$$

$$= \hat{x}E_z cos(\alpha) - \hat{y}E_z sin(\alpha) + \hat{z}\left(-E_x cos(\alpha) + E_y sin(\alpha)\right) \quad (8.27b)$$

Surface Current along BC Surface (PMC)

$$M_s^{BC} = \vec{E} \times \hat{n} = \left[E_x\hat{x} + E_y\hat{y} + E_z\hat{z}\right] \times \hat{x} = -\hat{z}E_y + \hat{y}E_z = \hat{y}E_z - \hat{z}E_y \quad (8.27c)$$

Surface Current along TOP Surface ($z = +d$) (PMC)

$$M_s^{Top} = \vec{E} \times \hat{n} = \left[E_x\hat{x} + E_y\hat{y} + E_z\hat{z}\right] \times (\hat{z}) = \left[-\hat{y}E_x + \hat{x}E_y\right] = \hat{x}E_y - \hat{y}E_x \quad (8.27d)$$

$$J_s^{Top} = \hat{n} \times \vec{H} = (\hat{z}) \times \left[H_x\hat{x} + H_y\hat{y} + H_z\hat{z}\right] = \left[\hat{y}H_x - \hat{x}H_y\right] = -\hat{x}H_y + \hat{y}H_x \quad (8.27e)$$

Surface Current along BOTTOM Surface ($z = -d$) (IMPC)

$$M_s^{Bottom} = \vec{E} \times \hat{n} = \left[E_x\hat{x} + E_y\hat{y} + E_z\hat{z}\right] \times (-\hat{z}) = \left[\hat{y}E_x - \hat{x}E_y\right] = -\hat{x}E_y + \hat{y}E_x \quad (8.27f)$$

$$J_s^{Bottom} = \hat{n} \times \vec{H} = (-\hat{z}) \times \left[H_x\hat{x} + H_y\hat{y} + H_z\hat{z}\right] = \left[-\hat{y}H_x + \hat{x}H_y\right] \quad (8.27g)$$

Evaluation of I_z for PMC and IPMC Model:

Closer look reveals that $H(z)$ function is changed due to different boundary conditions. Therefore, the contribution of the height (I_z)of the ETDRA on far-field radiation patterns is evaluated separately. The final results of two important integrals as defined below will be used for this calculation.

$$\int e^{ax}\cos(bx)\,dx = \frac{e^{ax}}{(b^2 + a^2)} \times (a\cos(bx) + b\sin(bx)) \quad (8.28a)$$

$$\int e^{ax}\sin(bx)\,dx = \frac{e^{ax}}{(b^2 + a^2)} \times (a\sin(bx) - b\cos(bx)) \quad (8.28b)$$

- **For PMC Model:**

$$I_s^z = \int_{z=-d}^{d} \sin[k_z(d-z)] \times e^{jk_o z\cos(\theta)} dz$$

$$= \int_{z=-d}^{d} \sin[k_z(d-z)] \times e^{jzV_3} dz \qquad ; \quad V_3 = k_o cos(\theta)$$

$$= -j \times d \times \left[e^{jk_z d} \times sinc\big((v_3 - k_z)d\big) - e^{-jk_z d} \times sinc\big((v_3 + k_z)d\big)\right] \qquad (8.29a)$$

and

$$I_c^z = \int_{z=-d}^{d} \cos[k_z(d-z)] \times e^{jk_o z\cos(\theta)} dz \qquad ; \; k_z = \frac{p\pi}{2d}$$

$$= \int_{z=-d}^{d} \cos[k_z(d-z)] \times e^{jzV_3} dz \qquad ; \quad V_3 = k_o cos(\theta)$$

$$= d \times \left[e^{jk_z d} \times sinc\big((v_3 - k_z)d\big) + e^{-jk_z d} \times sinc\big((v_3 + k_z)d\big)\right] \qquad (8.29b)$$

- **For IPMC:**

$$I_s^z = \int_{z=-d}^{d} \sin[k_z z + \beta] \times e^{jk_o z\cos(\theta)} dz$$

$$= \int_{z=-d}^{d} \sin[k_z z + \beta] \times e^{jzV_3} dz \qquad ; \quad V_3 = k_o cos(\theta)$$

$$= \frac{2jV_3}{(k_z^2 - V_3^2)} [\sin(k_z d)\cos(\beta)\, cos(dV_3) + j\cos(k_z d)\sin(\beta)\, sin(dV_3)]$$

$$- \frac{2k_z}{(k_z^2 - V_3^2)} [j\cos(k_z d)\cos(\beta)\, sin(dV_3) - \sin(k_z d)\sin(\beta)\, cos(dV_3)] \qquad (8.29c)$$

and

$$I_c^z = \int_{z=-d}^{d} cos[k_z z + \beta] \times e^{jk_o z\cos(\theta)} dz$$

$$= \int_{z=-d}^{d} cos[k_z z + \beta] \times e^{jzV_3} dz \qquad ; \quad V_3 = k_o cos(\theta)$$

$$= \frac{2jV_3}{(k_z^2 - V_3^2)}[j\cos(k_z d)\cos(\beta)\, sin(dV_3) - \sin(k_z d)\sin(\beta)\, cos(dV_3)]$$

$$+ \frac{2k_z}{(k_z^2 - V_3^2)}[\sin(k_z d)\cos(\beta)\, cos(dV_3) + j\cos(k_z d)\sin(\beta)\, sin(dV_3)] \quad (8.29d)$$

The contributions of the x and y coordinate values on the far-field radiation patterns are quite similar to equilateral triangular microstrip antenna (ETMA). Therefore, the final results are given here.

Fields along AC Surface (PMC)

$$M_s^{AC} = -\hat{x}E_z cos(\alpha) - \hat{y}E_z sin(\alpha) + \hat{z}\left(E_x cos(\alpha) + E_y sin(\alpha)\right)$$

- **$\hat{x}$-component $\vec{F}$ due to M_s^{AC} surface current**

$$M_s^{AC} = -\hat{x}E_z cos(\alpha) - \hat{y}E_z sin(\alpha) + \hat{z}\left(E_x cos(\alpha) + E_y sin(\alpha)\right)$$

$$F_x^{AC} = C_{xy} \times \int_l \int_{z=-d}^{d} [-E_z cos(\alpha)] \times e^{j\times f(x,y,z)} dl dz \quad at\ y = \eta x \quad ;\ \eta = 1/\sqrt{3} \qquad (8.30a)$$

$$= C_{xy} \times [-E_3] \times (\chi^2) \times I_{AC}^{x} \times \begin{cases} I_{zS}^{PMC} & PMC \\ I_{zC}^{IPMC} & IPMC \end{cases}$$

where

$$I_z = \int_{z=-d}^{d} \begin{cases} sin[k_z(d-z)] & PMC \\ cos[k_z z + \beta] & IPMC \end{cases} \times e^{jV_3 z} dz = \begin{cases} I_{zS}^{PMC} & PMC \\ I_{zC}^{IPMC} & IPMC \end{cases} \qquad (8.30b)$$

$$I_{AC}^{x} = \int_{x=0}^{M} \left(\sum_{i=1}^{3} \cos(\alpha_i x)\cos(\beta_i y) \right) \times e^{j\times(xV_1 + yV_2)} dx \text{ at } \ y = \eta x \ ; \ \ \chi_1 = V_1 + V_2/\sqrt{3}$$

$$= \frac{-j}{((n-l)^2 b^2 - \chi_1^2)} \times \left[e^{j\chi_1 M}\{jb(n-l)\sin(b(n-l)M) - \chi_1 \cos(b(n-l)M)\} + \chi_1 \right]$$

$$+ \frac{-j}{((l-m)^2 b^2 - \chi_1^2)} \times \left[e^{j\chi_1 M}\{jb(l-m)\sin(b(l-m)M) - \chi_1 \cos(b(l-m)M)\} + \chi_1 \right]$$

$$+ \frac{-j}{((m-n)^2 b^2 - \chi_1^2)}$$

$$\times \left[e^{j\chi_1 M}\{jb(m-n)\sin(b(m-n)M) - \chi_1 \cos(b(m-n)M)\} + \chi_1 \right] \quad (8.30c)$$

and $b = 4\pi/\left(3\sqrt{3}a\right)$

- **$\hat{y}$-component $\vec{F}$ due to M_s^{AC} surface current**

$$M_s^{AC} = -\hat{x}E_z cos(\alpha) - \hat{y}E_z sin(\alpha) + \hat{z}\left(E_x cos(\alpha) + E_y sin(\alpha)\right)$$

$$F_y^{AC} = C_{xy} \times \int_l \int_{z=-h}^{h} [-E_z sin(\alpha)] \times e^{j\times f(x,y,z)} dldz \quad at\ x = \frac{y}{\eta} \quad ;\ \eta = 1/\sqrt{3} \tag{8.31a}$$

$$= C_{xy} \times [-E_3] \times (\chi^2) \times I_{AC}^{y} \times \begin{cases} I_{zS}^{PMC} & PMC \\ I_{zC}^{IPMC} & IPMC \end{cases}$$

where

$$I_{AC}^{y} = \int_{x=0}^{a/2} \left(\sum_{i=1}^{3} \cos(\alpha_i x) \cos(\beta_i y) \right) \times e^{j\times(xV_1 + yV_2)} dy\ at \quad x = y/\eta$$

$$= \frac{-j}{\sqrt{3}((n-l)^2 b^2 - \chi_1^2)} \times \left[e^{j\chi_1 M} \{ jb(n-l) \sin(b(n-l)M) - \chi_1 \cos(b(n-l)M) \} + \chi_1 \right]$$

$$+ \frac{-j}{\sqrt{3}((l-m)^2 b^2 - \chi_1^2)} \times \left[e^{j\chi_1 M} \{ jb(l-m) \sin(b(l-m)M) - \chi_1 \cos(b(l-m)M) \} + \chi_1 \right]$$

$$+ \frac{-j}{\sqrt{3}((m-n)^2 b^2 - \chi_1^2)} \times \left[e^{j\chi_1 M} \{ jb(m-n) \sin(b(m-n)M) - \chi_1 \cos(b(m-n)M) \} + \chi_1 \right] \tag{8.31b}$$

- **$\hat{z}$-component $\vec{F}$ due to M_s^{AC} surface current**

$$M_s^{AC} = -\hat{x}E_z cos(\alpha) - \hat{y}E_z sin(\alpha) + \hat{z}\left(E_x cos(\alpha) + E_y sin(\alpha)\right)$$

$$F_z^{AC} = C_{xy} \times \int_l \int_{z=-d}^{d} \left[E_x cos(\alpha) + E_y sin(\alpha)\right] \times e^{j\times f(x,y,z)} dldz \quad at\ y = \eta x \tag{8.32a}$$

$$= C_{xy} \times [E_1 \times I_{AC}^{zx1} + E_2 \times (1/\sqrt{3}) \times I_{AC}^{zx2}] \times \begin{cases} (-k_z) \times I_{zC}^{PMC} & PMC \\ (-k_z) \times I_{zS}^{IPMC} & IPMC \end{cases}$$

where

$$I_z = \int_{z=-d}^{d} \begin{cases} (-k_z)\cos[k_z(d-z)] & PMC \\ (-k_z)\sin[k_z z+\beta] & IPMC \end{cases} \times e^{jV_3 z} dz = \begin{cases} (-k_z) \times I_{zC}^{PMC} & PMC \\ (-k_z) \times I_{zS}^{IPMC} & IPMC \end{cases} \quad (8.32b)$$

$$I_{AC}^{zx1} = \int_{x=0}^{M} \left(\sum_{i=1}^{3} -\alpha_i \sin(\alpha_i x)\cos(\beta_i y) \right) \times e^{j\times(xV_1 + yV_2)} dx \; at \quad y = \eta x$$

$$= \frac{e(n-l)}{((n-l)^2 b^2 - \chi_1^2)} \times \left[e^{j\chi_1 M} \{ b(n-l)\cos(b(n-l)M) - j\chi_1 \sin(b(n-l)M) \} - b(n-l) \right]$$

$$+ \frac{e(l-m)}{((l-m)^2 b^2 - \chi_1^2)}$$

$$\times \left[e^{j\chi_1 M} \{ b(l-m)\cos(b(l-m)M) - j\chi_1 \sin(b(l-m)M) \} - b(l-m) \right]$$

$$+ \frac{e(m-n)}{((m-n)^2 b^2 - \chi_1^2)}$$

$$\times \left[e^{j\chi_1 M} \{ b(m-n)\cos(b(m-n)M) - j\chi_1 \sin(b(m-n)M) \} - b(m-n) \right] \quad (8.32c)$$

where $b = 4\pi/\left(3\sqrt{3}a\right)$, $e = \pi/\left(\sqrt{3}a\right)$

and

$$I_{AC}^{zx2} = \int_{x=0}^{M} \left(\sum_{i=1}^{3} -\beta_i \cos(\alpha_i x)\sin(\beta_i y) \right) \times e^{j\times(xV_1 + yV_2)} dx \; at \quad y = \eta x$$

$$= \frac{e(n-l)}{\sqrt{3}[(n-l)^2 b^2 - \chi_1^2]} \times \left[e^{j\chi_1 M} \{ b(n-l)\cos(b(n-l)M) - j\chi_1 \sin(b(n-l)M) \} - b(n-l) \right]$$

$$+ \frac{e(l-m)}{\sqrt{3}[(l-m)^2 b^2 - \chi_1^2]}$$

$$\times \left[e^{j\chi_1 M} \{ b(l-m)\cos(b(l-m)M) - j\chi_1 \sin(b(l-m)M) \} - b(l-m) \right]$$

$$+ \frac{e(m-n)}{\sqrt{3}[(m-n)^2 b^2 - \chi_1^2]}$$

$$\times \left[e^{j\chi_1 M} \{ b(m-n)\cos(b(m-n)M) - j\chi_1 \sin(b(m-n)M) \} - b(m-n) \right]$$

$$= \frac{1}{\sqrt{3}} \times I_{AC}^{zx1} \quad (8.32d)$$

Hence,

$$F_z^{AC} = C_{xy} \times [E_1 \times I_{AC}^{zx1} + E_2 \times (1/\sqrt{3}) \times I_{AC}^{zx2}] \times \begin{cases} (-k_z) \times I_{zC}^{PMC} & PMC \\ (-k_z) \times I_{zS}^{IPMC} & IPMC \end{cases}$$

$$= C_{xy} \times \left[E_1 \times I_{AC}^{zx1} + E_2 \times (1/\sqrt{3}) \times \left(\frac{I_{AC}^{zx1}}{\sqrt{3}}\right)\right] \times \begin{cases} (-k_z) \times I_{zC}^{PMC} & PMC \\ (-k_z) \times I_{zS}^{IPMC} & IPMC \end{cases}$$

$$= C_{xy} \times I_{AC}^{zx1} \times \left[E_1 + \frac{E_2}{3}\right] \times \begin{cases} (-k_z) \times I_{zC}^{PMC} & PMC \\ (-k_z) \times I_{zS}^{IPMC} & IPMC \end{cases} \quad (8.32e)$$

Fields along AB Surface (PMC)

$$M_s^{AB} = \hat{x}E_z cos(\alpha) - \hat{y}E_z sin(\alpha) + \hat{z}\left(-E_x cos(\alpha) + E_y sin(\alpha)\right)$$

- **$\hat{x}$-component $\vec{F}$ due to M_s^{AB} surface current**

$$M_s^{AB} = \hat{x}E_z cos(\alpha) - \hat{y}E_z sin(\alpha) + \hat{z}\left(-E_x cos(\alpha) + E_y sin(\alpha)\right)$$

$$F_x^{AB} = C_{xy} \times \int_l \int_{z=-d}^{d} [E_z cos(\alpha)] \times e^{j \times f(x,y,z)} dl dz \quad at\ y = -\eta x$$

$$= C_{xy} \times E_3 \times (\chi^2) \times I_{AB}^{x} \times \begin{cases} I_{zS}^{PMC} & PMC \\ I_{zC}^{IPMC} & IPMC \end{cases}$$

where

$$I_{AB}^{x} = \int_{x=0}^{M} \left(\sum_{i=1}^{3} \cos(\alpha_i x) \cos(-\beta_i \eta x)\right) \times e^{jx\chi_2} dx\,; \qquad \chi_2 = V_1 - V_2/\sqrt{3}$$

$$= \int_{x=0}^{M} \left(\sum_{i=1}^{3} \cos(\alpha_i x) \cos(\beta_i \eta x)\right) \times e^{jx\chi_2} dx$$

$$= I_{AC}^{x}|_{\chi_1 = \chi_2} \quad (8.33)$$

- **$\hat{y}$-component $\vec{F}$ due to M_s^{AB} surface current**

$$M_s^{AB} = \hat{x}E_z cos(\alpha) - \hat{y}E_z sin(\alpha) + \hat{z}\left(-E_x cos(\alpha) + E_y sin(\alpha)\right)$$

$$F_y^{AB} = C_{xy} \times \int_l \int_{z=-d}^{d} [-E_z sin(\alpha)] \times e^{j \times f(x,y,z)} dl dz \quad at\ x = -\frac{y}{\eta} \quad (8.34a)$$

$$= C_{xy} \times [-E_3] \times (\chi^2) \times I_{AB}^{y} \times \begin{cases} I_{zS}^{PMC} & PMC \\ I_{zC}^{IPMC} & IPMC \end{cases}$$

where

$$I_{AB}^{y} = \int_{y=-a/2}^{0} \left(\sum_{i=1}^{3} \cos(\alpha_i x)\cos(\beta_i y) \right) \times e^{j\times(xV_1 + yV_2)} dy \; at \quad x = -y/\eta$$

$$= \frac{-j}{\sqrt{3}((n-l)^2 b^2 - \chi_2^2)} \times \left[e^{j\chi_2 M} \{ jb(n-l)\sin(b(n-l)M) - \chi_2 \cos(b(n-l)M) \} + \chi_2 \right]$$

$$+ \frac{-j}{\sqrt{3}((l-m)^2 b^2 - \chi_2^2)} \times \left[e^{j\chi_2 M} \{ jb(l-m)\sin(b(l-m)M) - \chi_2 \cos(b(l-m)M) \} + \chi_2 \right]$$

$$+ \frac{-j}{\sqrt{3}((m-n)^2 b^2 - \chi_2^2)} \times \left[e^{j\chi_2 M} \{ jb(m-n)\sin(b(m-n)M) - \chi_2 \cos(b(m-n)M) \} + \chi_2 \right] \quad (8.34b)$$

- **$\hat{z}$-component $\vec{F}$ due to M_s^{AB} surface current**

$$M_s^{AB} = \hat{x}E_z cos(\alpha) - \hat{y}E_z sin(\alpha) + \hat{z}\left(-E_x cos(\alpha) + E_y sin(\alpha) \right)$$

$$F_z^{AB} = C_{xy} \times \int_{l} \int_{z=-d}^{d} \left[-E_x cos(\alpha) + E_y sin(\alpha) \right] \times e^{j\times f(x,y,z)} dl dz \qquad at\ y = -\eta x \quad (8.35a)$$

$$= C_{xy} \times [-E_1] \times \left(I_{AC}^{zx1}|_{\chi_1=\chi_2} \times \begin{cases} (-k_z) \times I_{zC}^{PMC} & PMC \\ (-k_z) \times I_{zS}^{IPMC} & IPMC \end{cases} \right)$$

$$- C_{xy} \times [E_2 \times (1/\sqrt{3})] \times \left(I_{AC}^{zx2}|_{\chi_1=\chi_2} \times \begin{cases} (-k_z) \times I_{zC}^{PMC} & PMC \\ (-k_z) \times I_{zS}^{IPMC} & IPMC \end{cases} \right)$$

$$= [-1] \times C_{xy} \times I_{AB}^{zx} \times [E_1 + (E_2/3)] \times \begin{cases} (-k_z) \times I_{zC}^{PMC} & PMC \\ (-k_z) \times I_{zS}^{IPMC} & IPMC \end{cases} \quad (8.35b)$$

where

$$I_{AB}^{zx} = I_{AC}^{zx1}|_{\chi_1=\chi_2} = I_{AC}^{zx}|_{\chi_1=\chi_2} \quad (8.35c)$$

Fields along BC Surface (PMC)

$$M_s^{BC} = \vec{E} \times \hat{n} = \left[E_x\hat{x} + E_y\hat{y} + E_z\hat{z} \right] \times \hat{x} = -\hat{z}E_y + \hat{y}E_z = \hat{y}E_z - \hat{z}E_y$$

- **$\hat{y}$-component $\vec{F}$ due to M_s^{BC} surface current**

$$M_s^{BC} = \vec{E} \times \hat{n} = \left[E_x\hat{x} + E_y\hat{y} + E_z\hat{z} \right] \times \hat{x} = -\hat{z}E_y + \hat{y}E_z = \hat{y}E_z - \hat{z}E_y$$

$$F_y^{BC} = C_{xy} \times \int_l \int_{z=-d}^{d} [E_z] \times e^{j \times f(x,y,z)} dl dz \quad at\ x = M = \frac{\sqrt{3}a}{2} \tag{8.36a}$$

$$= C_{xy} \times [E_3] \times (\chi^2) \times e^{jV_1 M} \times I_{BC}^{y} \times \begin{cases} I_{zS}^{PMC} & PMC \\ I_{zC}^{IPMC} & IPMC \end{cases}$$

where

$$I_{BC}^{y} = \int_l \left(\sum_{i=1}^{3} \cos(\alpha_i x) \cos(\beta_i y) \right) \times e^{j \times (yV_2)} dl \text{ at } x = M = \frac{\sqrt{3}a}{2}$$

$$= \sum_{i=1}^{3} \cos(\alpha_i M) \times \int_{y=-a/2}^{a/2} \cos(\beta_i y) \times e^{jV_2 y}\, dy$$

$$= \frac{3a\cos(\pi m)}{\pi[(n-l)^2 - v^2]} \times \left[(n-l) \sin\left(\frac{\pi(n-l)}{3}\right) \cos\left(\frac{\pi v}{3}\right) - v \cos\left(\frac{\pi(n-l)}{3}\right) \sin\left(\frac{\pi v}{3}\right) \right]$$

$$+ \frac{3a\cos(\pi n)}{\pi[(l-m)^2 - v^2]} \times \left[(l-m) \sin\left(\frac{\pi(l-m)}{3}\right) \cos\left(\frac{\pi v}{3}\right) - v \cos\left(\frac{\pi(l-m)}{3}\right) \sin\left(\frac{\pi v}{3}\right) \right]$$

$$+ \frac{3a\cos(\pi l)}{\pi[(m-n)^2 - v^2]} \times \left[(m-n) \sin\left(\frac{\pi(m-n)}{3}\right) \cos\left(\frac{\pi v}{3}\right) - v \cos\left(\frac{\pi(m-n)}{3}\right) \sin\left(\frac{\pi v}{3}\right) \right]$$

$$; \quad v = \frac{3aV_2}{2\pi} = \frac{3ak_o sin(\theta) \sin(\varphi)}{2\pi} \tag{8.36b}$$

- **$\hat{z}$-component $\vec{F}$ due to M_s^{BC} surface current**

$$M_s^{BC} = \vec{E} \times \hat{n} = \left[E_x \hat{x} + E_y \hat{y} + E_z \hat{z}\right] \times \hat{x} = -\hat{z}E_y + \hat{y}E_z = \hat{y}E_z - \hat{z}E_y$$

$$F_z^{BC} = C_{xy} \times \int_{y=-B/2}^{B/2} \int_{z=-d}^{d} \left[-E_y\right] \times e^{j \times f(x,y,z)} dy dz \text{ at } x = M = \frac{\sqrt{3}a}{2} \tag{8.37a}$$

$$= C_{xy} \times [-E_2] \times e^{jV_1 M} \times I_{BC}^{z} \times \begin{cases} (-k_z) \times I_{zC}^{PMC} & PMC \\ (-k_z) \times I_{zS}^{IPMC} & IPMC \end{cases}$$

where

$$I_{BC}^{z} = \int_l \left(\sum_{i=1}^{3} -\beta_i \cos(\alpha_i x) \sin(\beta_i y) \right) \times e^{j \times (yV_2)} dl \text{ at } x = M = \frac{\sqrt{3}a}{2}$$

$$= \sum_{i=1}^{3} \cos(\alpha_i M) \times \int_{y=-a/2}^{a/2} -\beta_i \sin(\beta_i y) \times e^{jV_2 y}\, dy$$

$$= \frac{2j(n-l)\cos(\pi m)}{[(n-l)^2 - v^2]} \times \left[(n-l)\cos\left(\frac{\pi(n-l)}{3}\right)\sin\left(\frac{\pi v}{3}\right) - v\sin\left(\frac{\pi(n-l)}{3}\right)\cos\left(\frac{\pi v}{3}\right)\right]$$
$$+ \frac{2j(l-m)\cos(\pi n)}{[(l-m)^2 - v^2]} \times \left[(l-m)\cos\left(\frac{\pi(l-m)}{3}\right)\sin\left(\frac{\pi v}{3}\right) - v\sin\left(\frac{\pi(l-m)}{3}\right)\cos\left(\frac{\pi v}{3}\right)\right]$$
$$+ \frac{2j(m-n)\cos(\pi l)}{[(m-n)^2 - v^2]}$$
$$\times \left[(m-n)\cos\left(\frac{\pi(m-n)}{3}\right)\sin\left(\frac{\pi v}{3}\right) - v\sin\left(\frac{\pi(m-n)}{3}\right)\cos\left(\frac{\pi v}{3}\right)\right] \quad (8.37b)$$

Fields along TOP Surface $(z = +d)$

$$M_s^{Top} = \vec{E} \times \hat{n} = \left[E_x\hat{x} + E_y\hat{y} + E_z\hat{z}\right] \times (\hat{z}) = \left[-\hat{y}E_x + \hat{x}E_y\right] = \hat{x}E_y - \hat{y}E_x$$

$$J_s^{Top} = \hat{n} \times \vec{H} = (\hat{z}) \times \left[H_x\hat{x} + H_y\hat{y} + H_z\hat{z}\right] = \left[\hat{y}H_x - \hat{x}H_y\right] = -\hat{x}H_y + \hat{y}H_x$$

- **$\hat{x}$-component $\vec{F}$ due to M_s^{Top} surface current**

$$M_s^{Top} = \vec{E} \times \hat{n} = \left[E_x\hat{x} + E_y\hat{y} + E_z\hat{z}\right] \times (\hat{z}) = \left[-\hat{y}E_x + \hat{x}E_y\right] = \hat{x}E_y - \hat{y}E_x$$

$$F_x^{Top} = C_{xy} \times \int_{x=0}^{M} \int_{y=-\eta x}^{\eta x} \left[E_y\right] \times e^{j \times f(x,y,z)} dxdy \quad at\ z = d \quad (8.38a)$$

$$= C_{xy} \times [E_2] \times I_{cs} \times e^{jdV_3} \times \begin{cases} (-k_z)\cos[k_z(d-z)] & PMC \ ; z = d \\ (-k_z)\sin[k_z z + \beta] & IPMC \ ; z = d \end{cases}$$

where

$$I_{cs} = \int_{x=0}^{M} \int_{y=-\eta x}^{\eta x} \left(\sum_{i=1}^{3} -\beta_i \cos(\alpha_i x)\sin(\beta_i y)\right) \times e^{j \times (xV_1 + yV_2)} dxdy \quad (8.38b)$$

- **$\hat{x}$-component $\vec{A}$ due to J_s^{Top} surface current**

$$J_s^{Top} = \hat{n} \times \vec{H} = (\hat{z}) \times \left[H_x\hat{x} + H_y\hat{y} + H_z\hat{z}\right] = \left[\hat{y}H_x - \hat{x}H_y\right] = -\hat{x}H_y + \hat{y}H_x$$

$$A_x^{Top} = C_{xy} \times \int_{x=0}^{M} \int_{y=-\eta x}^{\eta x} \left[-H_y\right] \times e^{j \times f(x,y,z)} dxdy \quad at\ z = d \quad (8.39a)$$

$$= C_{xy} \times [-H_2] \times I_{sc} \times e^{jdV_3} \times \begin{cases} \sin[k_z(d-z)] & PMC \ ; z = d \\ \cos[k_z z + \beta] & IPMC \ ; z = d \end{cases}$$

where

$$I_{sc} = \int_{x=0}^{M} \int_{y=-\eta x}^{\eta x} \left(\sum_{i=1}^{3} -\alpha_i \sin(\alpha_i x) \cos(\beta_i y) \right) \times e^{j\times(xV_1 + yV_2)} dxdy \qquad (8.39b)$$

- **$\hat{y}$-component $\vec{F}$ due to M_s^{Top} surface current**

$$M_s^{Top} = \vec{E} \times \hat{n} = \left[E_x\hat{x} + E_y\hat{y} + E_z\hat{z}\right] \times (\hat{z}) = \left[-\hat{y}E_x + \hat{x}E_y\right] = \hat{x}E_y - \hat{y}E_x$$

$$F_y^{Top} = C_{xy} \times \int_{x=0}^{M} \int_{y=-\eta x}^{\eta x} [-E_x] \times e^{j\times f(x,y,z)} dxdy \quad at\ z = d$$

$$= C_{xy} \times [-E_1] \times I_{sc} \times e^{jdV_3} \times \begin{cases} (-k_z)\cos[k_z(d-z)] & PMC \ ; z = d \\ (-k_z)\sin[k_z z + \beta] & IPMC \ ; z = d \end{cases} \qquad (8.40)$$

- **$\hat{y}$-component $\vec{A}$ due to J_s^{Top} surface current**

$$J_s^{Top} = \hat{n} \times \vec{H} = (\hat{z}) \times \left[H_x\hat{x} + H_y\hat{y} + H_z\hat{z}\right] = \left[\hat{y}H_x - \hat{x}H_y\right] = -\hat{x}H_y + \hat{y}H_x$$

$$A_y^{Top} = C_{xy} \times \int_{x=0}^{M} \int_{y=-\eta x}^{\eta x} [H_x] \times e^{j\times f(x,y,z)} dxdy \quad at\ z = d$$

$$= C_{xy} \times [H_1] \times I_{cs} \times e^{jdV_3} \times \begin{cases} \sin[k_z(d-z)] & PMC \ ; z = d \\ \cos[k_z z + \beta] & IPMC \ ; z = d \end{cases} \qquad (8.41)$$

Fields along BOTTOM Surface ($z = -d$)

$$M_s^{Bottom} = \vec{E} \times \hat{n} = \left[E_x\hat{x} + E_y\hat{y} + E_z\hat{z}\right] \times (-\hat{z}) = \left[\hat{y}E_x - \hat{x}E_y\right] = -\hat{x}E_y + \hat{y}E_x$$

$$J_s^{Bottom} = \hat{n} \times \vec{H} = (-\hat{z}) \times \left[H_x\hat{x} + H_y\hat{y} + H_z\hat{z}\right] = \left[-\hat{y}H_x + \hat{x}H_y\right]$$

- **$\hat{x}$-component $\vec{F}$ due to M_s^{Bottom} surface current**

$$M_s^{Bottom} = \vec{E} \times \hat{n} = \left[E_x\hat{x} + E_y\hat{y} + E_z\hat{z}\right] \times (-\hat{z}) = \left[\hat{y}E_x - \hat{x}E_y\right] = -\hat{x}E_y + \hat{y}E_x$$

$$F_x^{Bottom} = C_{xy} \times \int_{x=0}^{M} \int_{y=-\eta x}^{\eta x} \left[-E_y\right] \times e^{j\times f(x,y,z)} dxdy \quad at\ z = -d$$

$$= C_{xy} \times [-E_2] \times I_{cs} \times e^{-jdV_3} \times \begin{cases} (-k_z)\cos[k_z(d-z)] & PMC \ ; z = -d \\ (-k_z)\sin[k_z z + \beta] & IPMC \ ; z = -d \end{cases} \qquad (8.42)$$

- **$\hat{x}$-component $\vec{A}$ due to J_s^{Bottom} surface current**

$$J_s^{Bottom} = \hat{n} \times \vec{H} = (-\hat{z}) \times \left[H_x\hat{x} + H_y\hat{y} + H_z\hat{z}\right] = \left[-\hat{y}H_x + \hat{x}H_y\right]$$

$$A_x^{Bottom} = C_{xy} \times \int_{x=0}^{M} \int_{y=-\eta x}^{\eta x} [H_y] \times e^{j \times f(x,y,z)} dxdy \quad at\ z = d$$

$$= C_{xy} \times [H_2] \times I_{sc} \times e^{-jdV_3} \times \begin{cases} sin[k_z(d-z)] & PMC \ ; z = -d \\ cos[k_z z + \beta] & IPMC \ ; z = -d \end{cases} \tag{8.43}$$

- **$\hat{y}$-component $\vec{F}$ due to M_s^{Bottom} surface current**

$$M_s^{Bottom} = \vec{E} \times \hat{n} = \left[E_x\hat{x} + E_y\hat{y} + E_z\hat{z}\right] \times (-\hat{z}) = \left[\hat{y}E_x - \hat{x}E_y\right] = -\hat{x}E_y + \hat{y}E_x$$

$$F_y^{Bottom} = C_{xy} \times \int_{x=0}^{M} \int_{y=-\eta x}^{\eta x} [E_x] \times e^{j \times f(x,y,z)} dxdy \quad at\ z = -d$$

$$= C_{xy} \times [E_1] \times I_{sc} \times e^{-jdV_3} \times \begin{cases} (-k_z)\, cos[k_z(d-z)] & PMC \ ; z = -d \\ (-k_z)\, sin[k_z z + \beta] & IPMC \ ; z = -d \end{cases} \tag{8.44}$$

- **$\hat{y}$-component $\vec{A}$ due to J_s^{Bottom} surface current**

$$J_s^{Bottom} = \hat{n} \times \vec{H} = (-\hat{z}) \times \left[H_x\hat{x} + H_y\hat{y} + H_z\hat{z}\right] = \left[-\hat{y}H_x + \hat{x}H_y\right]$$

$$A_y^{Bottom} = C_{xy} \times \int_{x=0}^{M} \int_{y=-\eta x}^{\eta x} [-H_x] \times e^{j \times f(x,y,z)} dxdy \quad at\ z = d$$

$$= C_{xy} \times [-H_1] \times I_{cs} \times e^{-jdV_3} \times \begin{cases} sin[k_z(d-z)] & PMC \ ; z = -d \\ cos[k_z z + \beta] & IPMC \ ; z = -d \end{cases} \tag{8.45}$$

Here, E_1, E_2, E_3, H_1, H_2 and H_3 are the field strength of E_x, E_y, E_z, H_x, H_y and H_z components respectively, C_{xy} is constant and other terms are carrying their usual meaning. The far-zone electric field at point $P(r, \theta, \varphi)$ is evaluated as [10]:

$$E_\theta = -\frac{jk_o \exp(-jk_o r)}{4\pi r} \times exp(-jV_1 R) \times \left[L_\varphi + \eta_0 N_\theta\right] \tag{8.46a}$$

$$E_\varphi = \frac{jk_o \exp(-jk_o r)}{4\pi r} \times exp(-jV_1 R) \times \left[L_\theta - \eta_0 N_\varphi\right] \tag{8.46b}$$

where,

$$N_\theta = A_x cos(\theta) cos(\varphi) + A_y cos(\theta) sin(\varphi) - A_z sin(\theta)$$

$$N_\varphi = -A_x sin(\varphi) + A_y cos(\varphi)$$

$$L_\theta = F_x cos(\theta)cos(\varphi) + F_y cos(\theta)sin(\varphi) - F_z sin(\theta)$$
$$L_\varphi = -F_x sin(\varphi) + F_y cos(\varphi) \quad (8.47)$$

$$F_x = F_x^{AC} + F_x^{AB} + F_x^{Top} + F_x^{Bottom}$$
$$F_y = F_y^{AC} + F_y^{AB} + F_y^{BC} + F_y^{Top} + F_y^{Bottom}$$
$$F_z = F_z^{AC} + F_z^{AB} + F_z^{BC} \quad (8.48a)$$

$$A_x = A_x^{Top} + A_x^{Bottom}$$
$$A_y = A_y^{Top} + A_y^{Bottom}$$
$$A_z = 0 \quad (8.48b)$$

Here, all terms are carrying their usual meaning. Various constant as defined during the evaluation of far-field radiation patterns are summarized here for reference purpose.

$$V_1 = sin(\theta)\cos(\varphi) \quad ; \quad V_2 = sin(\theta)\sin(\varphi) \quad ; \quad V_3 = cos(\theta) \quad (8.49a)$$
$$\chi_1 = k_o sin(\theta)(\cos(\varphi) + \eta \sin(\varphi)) = (V_1 + \eta V_2) \quad ; \quad \eta = 1/\sqrt{3}$$
$$\chi_2 = k_o\, sin(\theta)\,(cos(\Phi) - \eta\, sin(\Phi)) = (V_1 - \eta V_2) \quad (8.49b)$$

$$v = \frac{3aV_2}{2\pi} = \frac{3ak_o sin(\theta)\sin(\varphi)}{2\pi} \quad ; \quad b = \frac{4\pi}{3\sqrt{3}a} \quad ; \quad e = \frac{\pi}{\sqrt{3}a} \quad (8.49c)$$

8.2.4 Radiated Power, Quality factor, Efficiency and Gain

Radiated power in percent may be computed as [15] $P_r(\%) = (2\pi/Q_r) \times 100$ where Q_r is the radiation quality factor, conductor loss (P_c), dielectric loss (P_d), radiation loss (P_r), total stored energy (W_t), Bandwidth (BW), efficiency (e), directivity (D), gain (G) are also calculated using standard procedure as found in [12-16] or as calculated for equilateral TMA in Chapter III. Due to the absence of surface wave [5, 174], the effect of surface wave loss is neglected here. Therefore, the total quality factor (Q_t) is evaluated as:

$$Q_t = \frac{\omega_r W_t}{P_c + P_d + P_r} \quad (8.50)$$

It should be pointed here that in case of IPMC model, IPMC is applied along $z = \pm d$ surfaces to compute the eqigenfunction of the source free ETDRA. It is found that the stored electric energy (W_e) is not equal to stored magnetic energy (W_m). In case of PMC model, it is found that $W_e = W_m$. The total stored energy within the ETDRA is then evaluated as:

$$W_t = W_e + W_m \tag{8.51}$$

8.2.5 Input Impedance

Prediction of input impedance (Z_{in}) is also important for an antenna. The input impedance is evaluated in a similar process as demonstrated for rectangular DRA in Chapter VII as [4]:

$$Z_{in} = \frac{-j\omega(a_o/I_o)^2}{\omega^2 - \omega_o^2\left(1 + \frac{j}{Q_t}\right)} \tag{8.52}$$

where

$$a_o = \iiint \vec{E}_o \cdot \vec{J}\, dv \tag{8.53}$$

Here, $\vec{E}_o$ is electric field inside the ETDRA for a particular mode, $\vec{J}$ is probe current density, I_o is the magnitude of current, ω is operating frequency, ω_o is resonant frequency and Q_t is total quality factor. Electric field inside the ETDRA is normalized such that

$$\varepsilon \iiint \vec{E}_o \cdot \vec{E}_o^*\, dv = \varepsilon \iiint \left|\vec{E}_o\right|^2 dv = 1 \tag{8.54}$$

where $\varepsilon = \varepsilon_r \varepsilon_o$. Probe current density ($\vec{J}$) is modeled here as one dimensional $\hat{z}$ directed current as [4]:

$$\vec{J} = \begin{cases} \hat{z} I_o \dfrac{\sin[k_d(l-z)]}{\sin(k_d l)} \delta(x - x_o)\delta(y - y_o), & z \le l \\ 0 \quad , & z > l \end{cases} \tag{8.55}$$

where $k_d = p\pi/(2l)$, l is probe length and (x_o, y_o) is the probe location. This approximation will be valid when $l/r \gg 1$ where r is the radius of the coaxial probe. The reason for defining $k_d = p\pi/(2l)$ instead of wave number ($k_d = k_o\sqrt{\varepsilon_r}$) within the ETDRA is demonstrate in the next section.

8.3 Results

In this section, theoretical results on resonant frequency, far-field patterns, Q-factor, etc. are discussed for various modes. It is found that the electric field gets confined in the middle portion of the ETDRA due to three corners (having acute angle) and feed mechanism (please see Figs. 8.7). As a result, the effective dimensions (a_e, d_e) become smaller than actual physical dimensions (a, d). Therefore, the resonant frequency must be computed using (a_e, d_e) instead of (a, d).

In practice, actual dimensions (a, d) are present. Therefore, conductor loss (P_c), dielectric loss (P_d), stored energy (W_t) etc must be computed using actual dimensions (a, d). But internal fields computed using (a_e, d_e) do not produce proper field patterns over the region bounded by (a, d). Typical results are shown in Fig. 8.9 for TM^z_{101} mode (please see Fig. 8.3 and 8.4 also). As the conductor (at $z = 0$ plane) and dielectric are present over actual physical dimensions (a, d), we have used (a, d) to compute P_c, P_d, W_t etc. Hence, resonant frequency (f_r), α_i, β_i $(i = 1,2,3)$ must be computed using (a, d) otherwise field distortion may occur as shown in Fig. 8.9.

Another issue is related to computation of input impedance (Z_{in}). During the evaluation of Z_{in}, we have to use actual dimensions (a, d) instead of (a_e, d_e). Because in some cases, probe position (x_o, y_o) may be outside the ETDRA considering (a_e, d_e). This condition will be more prominent in case of 30°–60°–90° and 45°–45°–90° TDRAs as shown in Chapter IX and X respectively where $a_e \cong 0.55 \times a$ for fundamental TM^z_{101} mode. Keeping these considerations in mind as mentioned above, the process by which resonant frequency, far-field

radiation patterns, different types of losses, Q-factors etc are calculated is shown below:

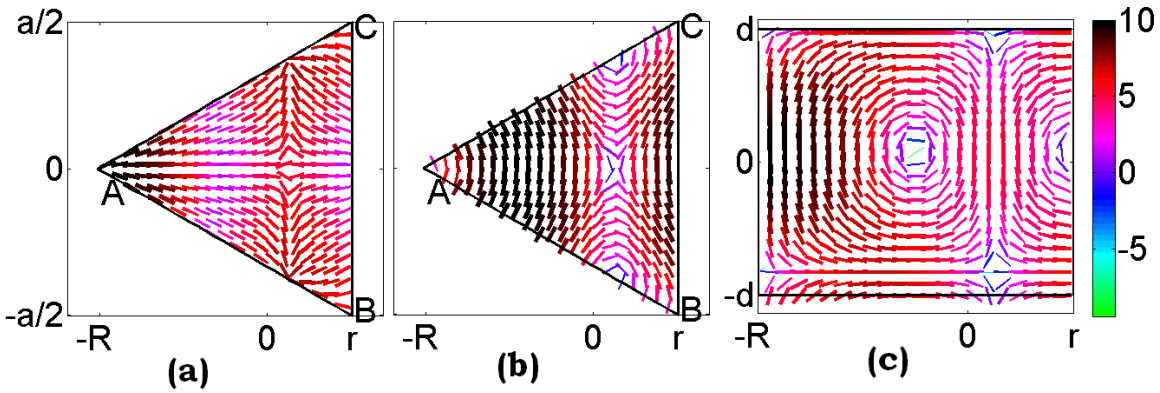

Fig. 8.9 Field plot over (a, d) region whereas fields are computed using (a_e, d_e)
(a) $\vec{E}$-field patterns at $z = d/2$ plane (b) $\vec{H}$-field patterns at $z = d/2$ plane
(c) $\vec{E}$field patterns at $y = 0$ plane

Followed Procedure

1. Computation of resonant frequency (f_r) only

- Use (a_e, d_e) to compute f_r

2. Computation of $P_r, P_c, P_d, Q_t, W_t, Z_{in}$ etc.

I. Compute $f_r,\ \alpha_i,\ \beta_i$ using (a, d)

II. Compute internal field distribution using (a, d)

III. Compute far-field patterns using (a, d)

IV. Compute $P_r, P_c, P_d, Q_t, W_t, Z_{in}$ etc using (a, d)

It should be pointed here that, in case of Microstrip Antennas (MA), say for example equilateral Triangular MA (TMA), computation of $P_r, P_c, P_d, Q_t, W_t, Z_{in}$, far-field patterns, etc. using either a (actual physical dimension) or a_e (effective dimension due to fringing) do not produce much difference as shown in Table 8.4. This is because the difference between a and a_e is small. Similar observation is also found in rectangular MA, 30°–60°–90° TMA etc.

Table 8.4

Characteristics of equilateral TMA computed using actual and effective length ($a = 100mm, d = 1.59mm, \varepsilon_r = 2.32, tan\delta = 0.0005$)

Sl No	Mode	Computed using a_e				Computed using a			
		f_r (GHz)	Q_r	Q_t	Gain (dB)	f_r (GHz)	Q_r	Q_t	Gain (dB)
1	TM^z_{10}	1.2928	163.97	128.95	6.0834	1.3125	161.51	127.57	6.1021
2	TM^z_{21}	3.4204	113.73	99.964	9.1152	3.4726	112.02	98.695	9.1254
3	TM^z_{43}	7.8638	77.103	71.744	10.945	7.9836	75.945	70.758	10.951

Coming back to our analysis on ETDRA, one antenna structure is fabricated having $a = 36mm, d = 21mm$ and $\varepsilon_r = 10$ as shown in Fig. 8.10. The ETDRA is excited using 50Ω coaxial probe. The probe is placed immediately outside the ETDRA at apex. The same antenna is also simulated using FEM based commercial numerical 3D EM simulator HFSS [9]. Some experimental results are also collected from published literature. It is found that theoretical results are in close agreement with experimental data and/or data obtained using EM simulator HFSS [9].

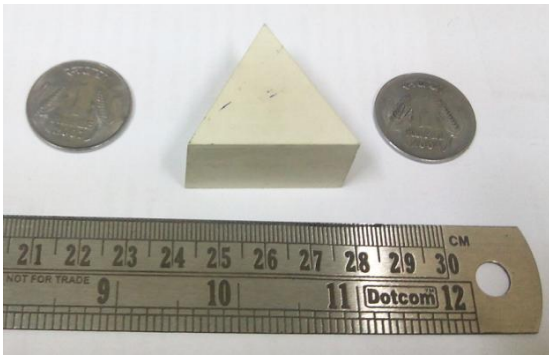

Fig. 8.10 Photograph of fabricated ETDRA

8.3.1 Resonant Frequency

The resonant frequencies are computed using the PMC model (equation (8.8)) and IPMC model (equation (8.19)) for different TM^z_{mnp} modes of the ETDRA as shown in Tables 8.5 and 8.6 respectively. In our experiment, we have successfully excited the pure TM^z_{101}, TM^z_{201} and TM^z_{221} modes. Other modes may be excited for different probe positions. The experimental resonant frequencies for these three modes are also shown. It is found that the expressions for effective dimensions (a_e, d_e) are in excellent agreement (4% error) with measured data. PMC model (equation (8.8)) also gives similar results as found

for IPMC model. But, in case of low profile ETDRA, PMC model is more accurate than IPMC model as shown Table 8.7. Therefore, it is concluded that the PMC model is more accurate than IPMC model.

The effect of excitation (and finite size of ground plane) on the resonant frequency of an ETDRA (i.e. same ETDRA but different feeding mechanism) can easily be found from samples 1 and 2 (and samples 3 and 4) in Table 8.7. This effect is not accounted for calculating effective dimensions (a_e, d_e). Due to this reason, a tradeoff is maintained for different feeding mechanisms in equations (8.24) and (8.25) which results in an error of 4% for computing resonant frequency.

Table 8.5

Comparison of resonant frequency for TM^z_{mnp} modes using PMC model

Mode	$a = 66mm, d = 24mm, \varepsilon_r = 12$ [112]			$a = 36mm, d = 21mm, \varepsilon_r = 10$ (our)		
	Reso. Freq. (GHz)		Error (%)	Reso. Freq. (GHz)		Error (%)
	equ. (8.8)	[112]		equ. (8.8)	Mea. (our)	
TM^z_{101}	1.528	1.5	-1.8	2.667	2.61	-2.2
TM^z_{201}	2.286	2.2	-3.9	4.340	4.20	-3.3
TM^z_{211}	2.732	2.8	2.4	5.282	5.17	-2.3
TM^z_{221}	3.355	3.3	-1.7			
TM^z_{311}	3.480	3.6	3.3			
TM^z_{411}	4.261	4.4	3.2			
TM^z_{421}	4.822	4.8	-0.5			

Table 8.6

Comparison of resonant frequency for TM^z_{mnp} modes using IPMC model

Mode	$a = 66mm, d = 24mm, \varepsilon_r = 12$ [112]			$a = 36mm, d = 21mm, \varepsilon_r = 10$ (our)		
	Reso. Freq. (GHz)		Error (%)	Reso. Freq. (GHz)		Error (%)
	equ. (8.19)	[112]		equ. (8.19)	Mea. (our)	
TM^z_{101}	1.499	1.5	0.1	2.647	2.61	-1.4
TM^z_{201}	2.275	2.2	-3.4	4.333	4.20	-3.2
TM^z_{211}	2.724	2.8	2.7	5.277	5.17	-2.2
TM^z_{221}	3.350	3.3	-1.5			
TM^z_{311}	3.476	3.6	3.4			
TM^z_{411}	4.258	4.4	3.2			
TM^z_{421}	4.820	4.8	-0.4			

Table 8.7

Computation of resonant frequency for TM^z_{101} mode ($\varepsilon_r = 82$)

Sl No.	Ref.	Dimension		Reso. Freq. (GHz)			Error (%)	
		a (mm)	d (mm)	PMC Model	IPMC Model	Mea.	PMC Model	IPMC Model
1	[107]	20	1.1	7.76	7.42	7.59	-2.24	2.28
2	[108]	20	1.1	7.76	7.42	7.9	1.77	6.12
3	[109]	20	0.98	8.68	8.22	8.8	1.38	6.55
4	[110]	20	0.98	8.68	8.22	8.91	2.60	7.70
5	[111]	20	1.06	8.04	7.69	8.09	0.58	5.22

8.3.2 Radiation Patterns

In this section, theoretical results on far-field radiation patterns are presented for various TM^z_{mnp} modes using 'PMC model'. Modes with even values of p will not be excited for an ETDRA placed on a metallic ground plane [5, 177] because these modes will be short circuited. Therefore, theoretical results are presented for odd values of p only. Far-field power are computed at $\varphi = 0^o$ (E-plane) and $\varphi = 90^o$ (H-plane) planes. Theoretical far-field power patterns are shown in Figs. 8.11 for first few modes of an ETDRA having $a = 66mm, d = 24mm, \varepsilon_r = 12$ and $tan\,\delta = 0.0005$.

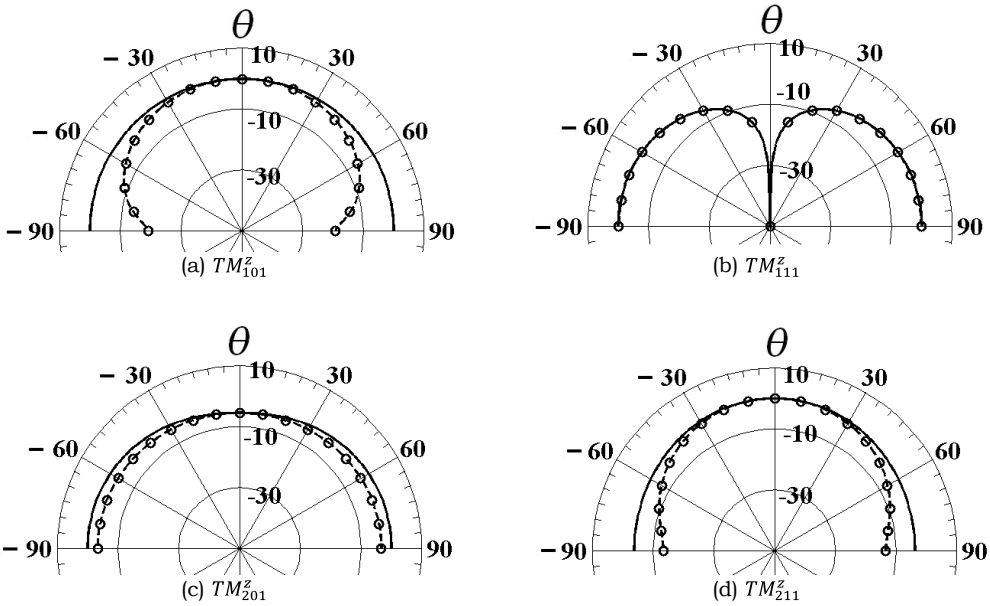

(a) TM^z_{101} (b) TM^z_{111}

(c) TM^z_{201} (d) TM^z_{211}

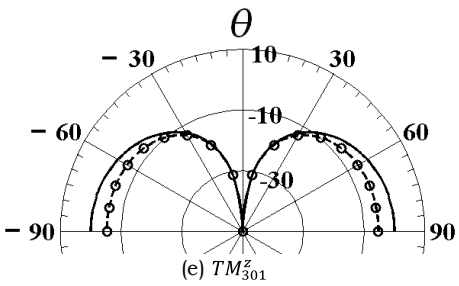

(e) TM^z_{301}

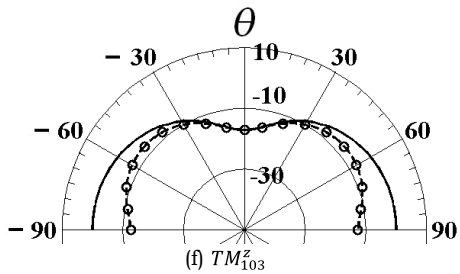

(f) TM^z_{103}

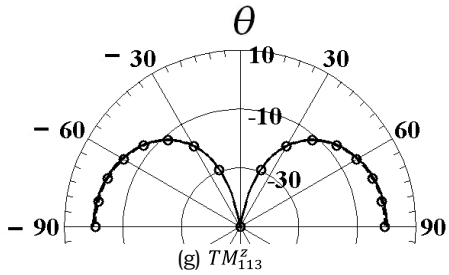

(g) TM^z_{113}

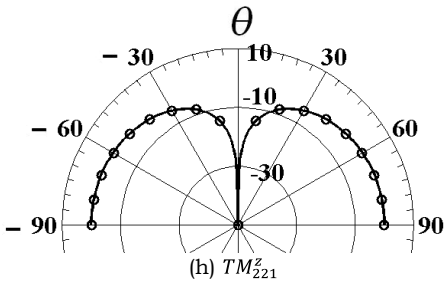

(h) TM^z_{221}

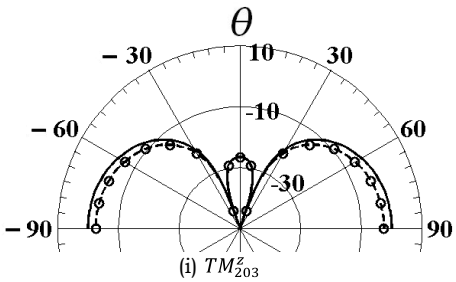

(i) TM^z_{203}

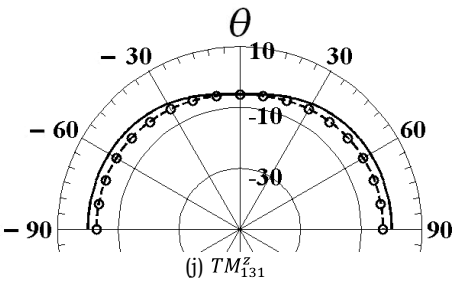

(j) TM^z_{131}

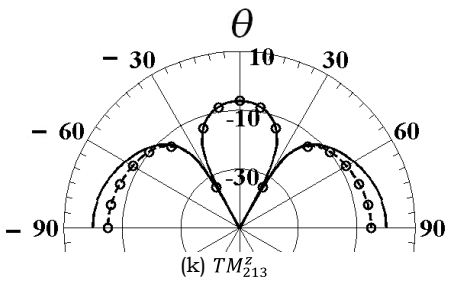

(k) TM^z_{213}

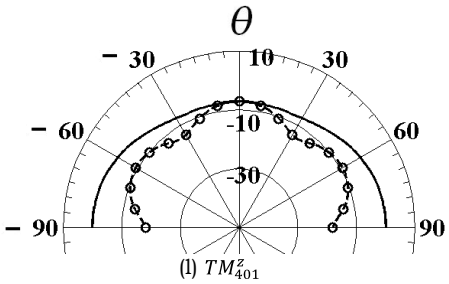

(l) TM^z_{401}

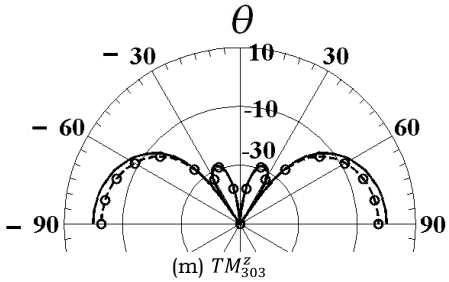

(m) TM^z_{303}

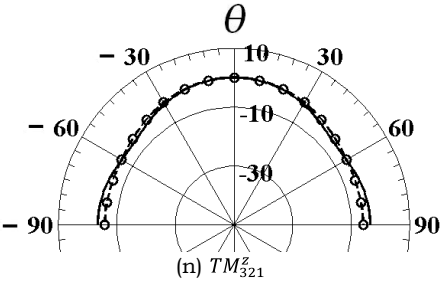

(n) TM^z_{321}

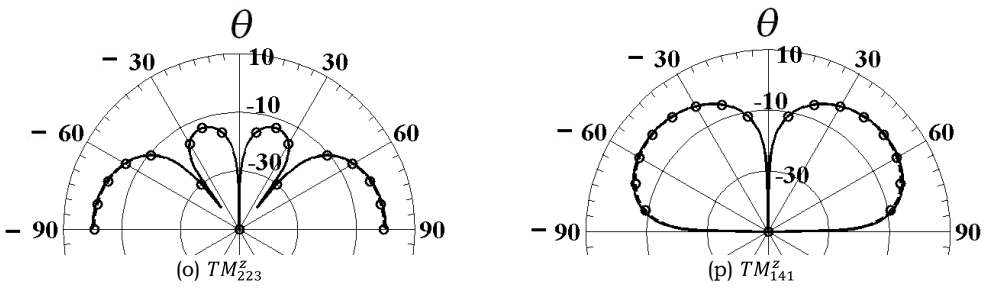

Fig. 8.11 Normalized far-zone E-plane (solid line) and H-plane (circle with dotted line) power patterns for various TM^z_{mnp} modes ($a = 66mm, d = 24mm, \varepsilon_r = 12, tan\,\delta = 0.0005$)

In [5], the radiation characteristics of Equilateral Triangular Microstrip Antenna (ETMA) have been reported. We have also noticed all those properties as shown in Chapter III. From Fig. 8.11, it is found that the radiation characteristics of an ETDRA for different combination of m and n are exactly same as found for ETMA. The electric fields of modes with even values of p will be short circuited for a DRA placed on a metallic ground plane [5, 174]. These modes are not shown here for brevity. On the other hand, modes with odd values of p (= 1, 3, 5, 7, 9 etc) have the similar property as found in rectangular DRA [172]. Therefore, a mode weather will produce a peak or null in the broadside direction is mainly controlled by the proper choice of m and n.

Further, it is found from Fig. 8.11 that the TM^z_{103} mode produces a large dip in the broadside direction. This is due to the improper choice of a, d and ε_r. An ETDRA having $a = 66mm, d = 24mm, \varepsilon_r = 50$ and $tan\,\delta = 0.0005$ does not show a dip in the broadside direction as shown in Fig. 8.12(a). Further, it is also found that some modes such as TM^z_{203} and TM^z_{213} also show beam splitting property. This is due to the improper choice of a, d and ε_r. For example, an ETDRA having $a = 66mm, d = 24mm, \varepsilon_r = 50$ and $tan\,\delta = 0.0005$ does not show beam splitting property and shows a peak in the broadside direction as shown in Fig. 8.12(b).

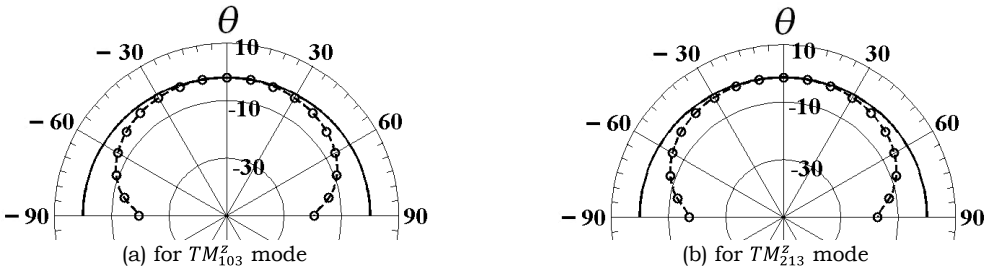

(a) for TM^z_{103} mode (b) for TM^z_{213} mode

Fig. 8.12 Improvement of radiation patterns (E-plane in solid line and H-plane in circle with dotted line) by selecting proper dimensions and ε_r for various TM^z_{mnp} modes ($a = 66mm, d = 24mm, \varepsilon_r = 50, tan\,\delta = 0.0005$)

Although we have computed the far-field patterns using actual physical dimensions (a, d) as described earlier, it should be pointed here that normalized E-plane ($\varphi = 0^o$ plane) and H-plane ($\varphi = 90^o$ plane) computed using (a, d) and (a_e, d_e) are same. Typical results are shown in Fig. 8.13 for TM^z_{101} and TM^z_{213} modes.

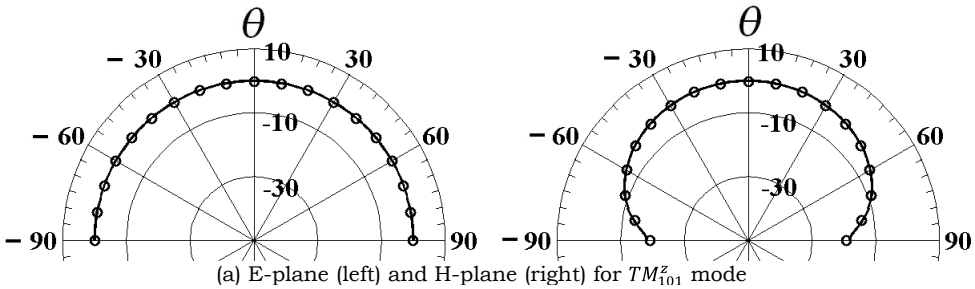

(a) E-plane (left) and H-plane (right) for TM^z_{101} mode

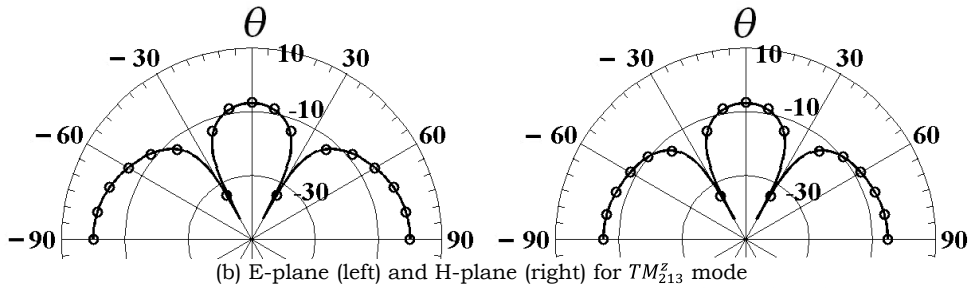

(b) E-plane (left) and H-plane (right) for TM^z_{213} mode

Fig. 8.13 Comparison far-zone power patterns computed using (a, d) and (a_e, d_e) for different mode ($a = 66mm, d = 24mm, \varepsilon_r = 50, tan\,\delta = 0.0005$) : solid line for (a, d) and circle for (a_e, d_e)

For experimental validation, our theoretical results on far-field radiation patterns (PMC and IPMC model) are compared with measured data as found in [110]. The measured data corresponding to 8.91GHz (resonant frequency) are extracted from [110] for theoretical validation. This is shown in Fig. 8.14(a). For

further verification, our own experimental results on (normalized) *E*-plane and *H*-plane power patterns of the fabricated antenna are compared with this theory as shown in Fig. 8.14(b). It is found that theoretical results are in close agreement with experimental data. Little discrepancy occurs in the E-plane. This may be due to the finite size of ground plane. It is found that PMC and IPMC both models give almost the same results for predicting far-field radiation patterns.

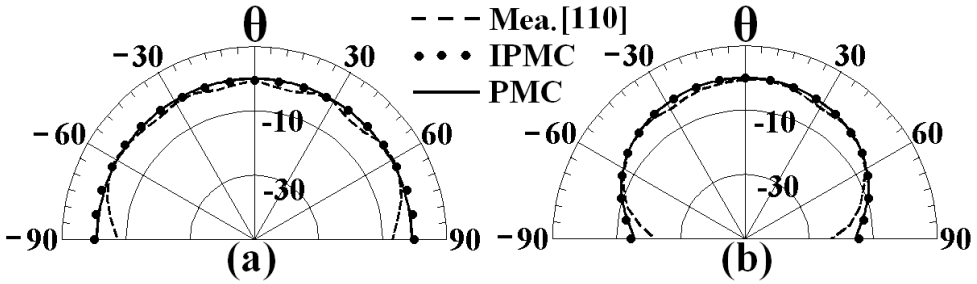

(i) for TM^z_{101} mode (a = 20mm, h = 0.98mm, ε_r = 82) [110]

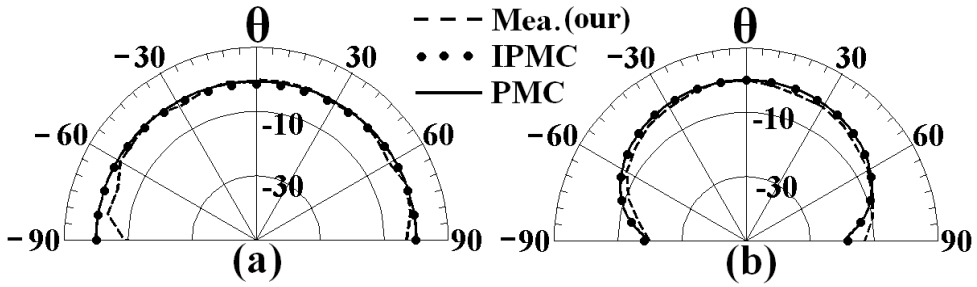

(ii) for TM^z_{101} mode (a = 36mm, h = 21mm, ε_r = 10) (our)

Fig. 8.14 Experimental validation of far-field patterns for TM^z_{101} mode: (a) E-plane (b) H-plane

Theoretical results on some higher order TM^z_{mnp} modes are compared with data obtained using 3D EM simulator HFSS. These are shown in Fig. 8.15.

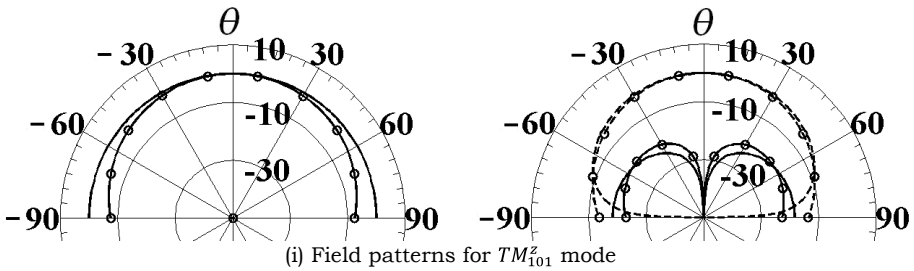

(i) Field patterns for TM^z_{101} mode

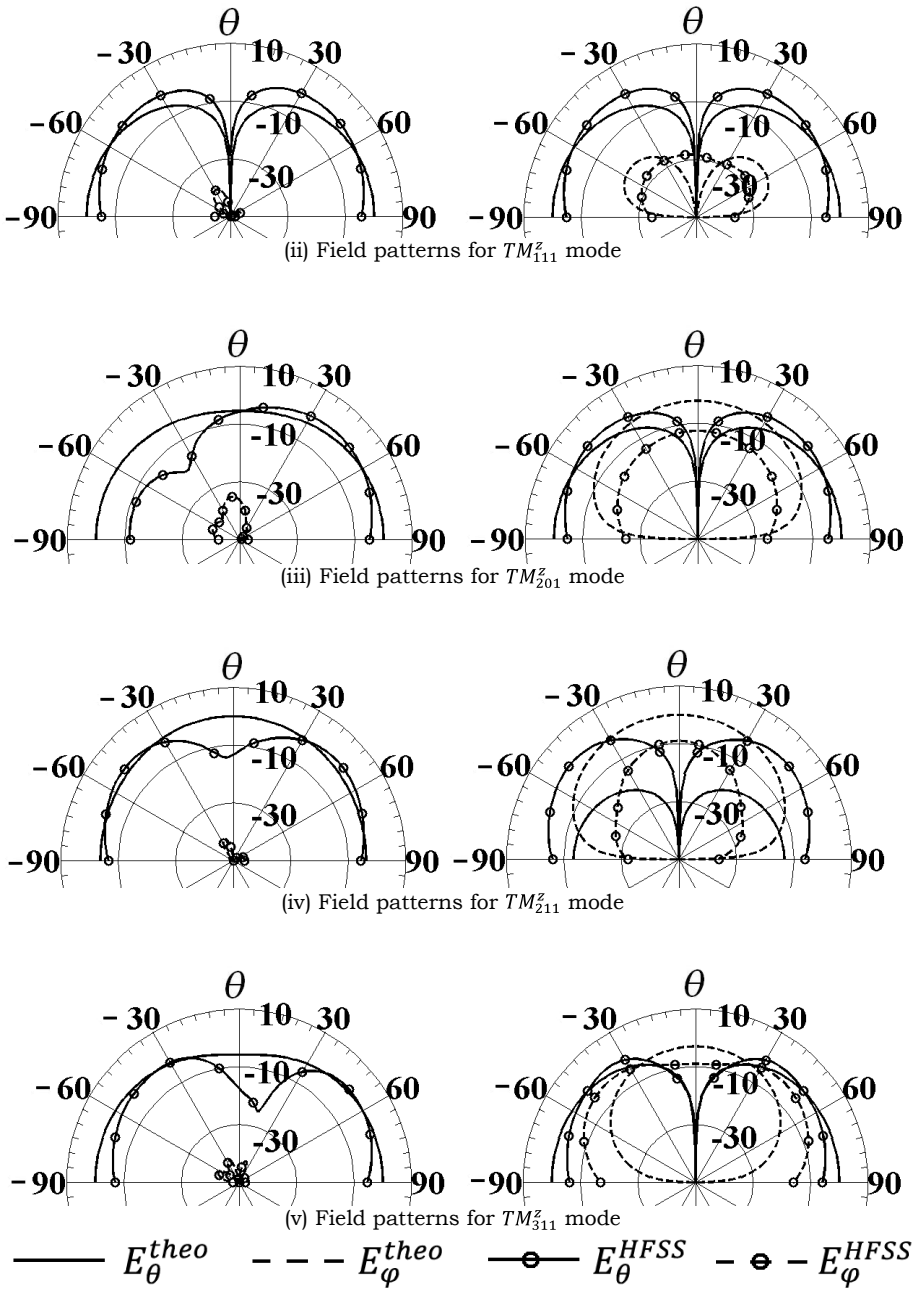

Fig. 8.15 Comparison of normalized far-field power patterns at $\varphi = 0^o$ (left) and $\varphi = 90^o$ (right) plane with data obtained using 3D EM simulator HFSS for different TM^z_{mnp} modes $(a = 66mm, d = 24mm, \varepsilon_r = 12)$[112 – 113]

It is clear from Fig. 8.15 that theoretical results are in good agreement with data obtained using 3D EM simulator HFSS [9]. Little discrepancy is found. This is due to the effect of excitation which is not included in our source free simple theory.

8.3.3 Radiated Power, Quality factor, Efficiency and Gain

In this analysis, the effect of feed mechanism is not considered. In [21], it is clearly mentioned that the natural resonant frequency and the Q-factors (radiation Q-factor (Q_r) and total Q-factor (Q_t)) are highly sensitive with feeding mechanism [21]. Proper source modeling is required to obtain accurate results. In Table 8.8, comparison between theoretical and measured total Q-factor (Q_t) is shown using PMC and IPMC models. In all cases, the loss-tangent ($tan\delta$) is assumed to be equal to 0.0005 for theoretical calculation. The discrepancy is due to non-consideration of feed and finite size of ground plane in our theory. Further, it is found that the IPMC model produces slight larger Q_t compared to the PMC model, but both models produce almost same Q_t.

Typical theoretical results on P_r (%), Q_r, Q_t, BW, G and e for various TM^z_{mnp} modes of an ETDRA having $a = 66mm, d = 24mm$ and $\varepsilon_r = 12$ are shown in Table 8.9 using the PMC model. From Table 8.9, it is found that the TM^z_{321} (or TM^z_{231}) mode can produce higher gain (8.1dB) compared to fundamental TM^z_{101} mode (4.7dB). Further, it is also shown in the previous section that, by selecting proper dimensions and relative permittivity of the ETDRA, one can control the far-field radiation patterns as found for rectangular DRA. Therefore, a higher order mode may be used to produce higher gain compared to fundamental mode by selecting proper dimensions and relative permittivity of an ETDRA.

Table 8.8

Comparison of total Q-factor using PMC model

Sl No	Ref	Mode	Dimension (mm)		ε_r	Mea. Q_t	Theoretical Q_t	
			a	d			PMC	IPMC
1	[112]	TM^z_{101}	66	24	12	11.21	25.564	29.322
2	our	TM^z_{101}	36	21	10	7.85	22.782	24.762
3	[113]	TM^z_{201}	66	24	12	14.667	48.207	50.213
4	[113]	TM^z_{211}	66	24	12	13.333	46.894	49.071

Table 8.9

Radiation characteristics of first few TM^z_{mnp} modes of an ETDRA

$(a = 66mm, d = 24mm, \varepsilon_r = 12, tan\delta = 0.0005)$

Sl No	Mode	f_r (GHz)	$P_r(\%)$	$e(\%)$	Q_r	Q_t	BW (%)	Gain (dB)
1	TM^z_{101}	1.256	24.21	98.52	25.95	25.56	2.766	4.73
2	TM^z_{111}	1.763	6.718	94.98	93.53	88.83	0.796	4.635
3	TM^z_{201}	1.968	12.68	97.29	49.55	48.21	1.467	6.257
4	TM^z_{211}	2.483	12.99	97.38	48.39	47.12	1.501	6.746
5	TM^z_{301}	2.774	1.555	81.76	404	330.3	0.2141	6.565
6	TM^z_{103}	2.843	11.73	97.13	53.55	52.01	1.359	7.264
7	TM^z_{113}	3.1	6.476	94.94	97.03	92.12	0.7676	8.702
8	TM^z_{221}	3.16	17.99	98.12	34.94	34.28	2.063	4.503
9	TM^z_{203}	3.221	5.914	94.49	106.2	100.4	0.7044	8.566
10	TM^z_{311}	3.279	16.39	97.94	38.33	37.54	1.884	5.971
11	TM^z_{123}	3.559	0.7897	69.71	795.6	554.6	0.1275	9.297
12	TM^z_{401}	3.612	2.041	85.61	307.9	263.6	0.2683	9.328
13	TM^z_{303}	3.768	0.962	73.75	653.1	481.7	0.1468	7.147
14	TM^z_{321}	3.917	8.233	96.01	76.32	73.28	0.965	7.937
15	TM^z_{223}	4.061	2.458	87.81	255.6	224.4	0.3151	6.582
16	TM^z_{411}	4.107	4.798	93.36	130.9	122.3	0.5784	5.942
17	TM^z_{313}	4.154	1.361	79.96	461.7	369.2	0.1915	7.942
18	TM^z_{403}	4.422	0.3701	52.1	1698	884.6	0.07993	9.928
19	TM^z_{501}	4.464	0.9396	73.43	668.7	491	0.144	6.683
20	TM^z_{105}	4.593	8.316	96.08	75.56	72.59	0.9741	9.854
21	TM^z_{331}	4.632	22.07	98.48	28.47	28.04	2.522	4.361
22	TM^z_{233}	4.674	1.241	78.52	506.4	397.6	0.1778	10.83
23	TM^z_{241}	4.714	11.89	97.22	52.86	51.39	1.376	5.803
24	TM^z_{115}	4.756	7.889	95.88	79.65	76.36	0.926	8.938
25	TM^z_{413}	4.835	0.7711	69.46	814.9	566	0.1249	6.308

For fixed value of (a/d) ratio, variations of $P_r(\%), Q_r, Q_t, BW, e$ and G with d are shown in Fig. 8.16 for first few modes. It is found that they are almost constant as found for rectangular DRA (please see Chapter VII). Numerical instability occurs at TM^z_{111} mode in the calculation of gain (G). To find such type of discrepancy, variations of $P_r(\%), Q_r, Q_t, BW, e$ and G with (a/d) ratio for a fixed value of a are calculated for first few modes as shown in Fig. 8.17. It is clear from Fig. 8.17 that $P_r(\%), Q_r, Q_t, BW, e$ and G take different values at

different modes.

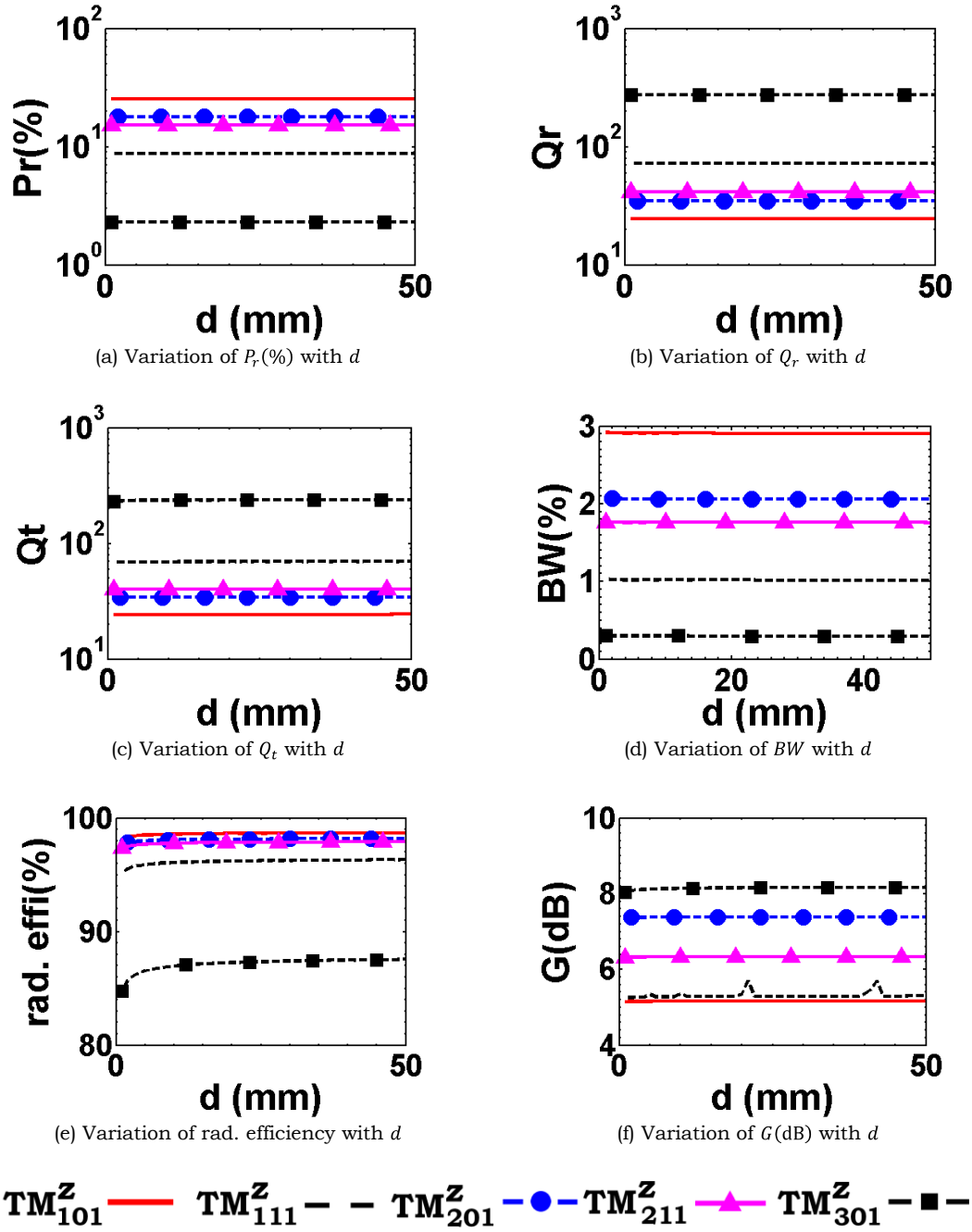

(a) Variation of $P_r(\%)$ with d

(b) Variation of Q_r with d

(c) Variation of Q_t with d

(d) Variation of BW with d

(e) Variation of rad. efficiency with d

(f) Variation of $G(\mathrm{dB})$ with d

Fig 8.16 Radiation characteristics of ETDRA for different TM^z_{mnp} modes for fixed a/d ratio ($a/d = 1,\ \varepsilon_r = 12, \tan\delta = 0.0005$)

From Fig. 8.17, it is found that for certain values (a/d) ratio, numerical instability occurs for TM^z_{111} mode. A further investigation reveals that U_{max} (=

$\frac{r^2}{2\eta_o} \times \left[|E_\theta|^2 + |E_\varphi|^2\right]_{max}\Big)$ occurs at different (θ, φ) point and U_{max} follows similar curve as found for gain (G). To calculate U_{max}, the θ and φ axis is divided with

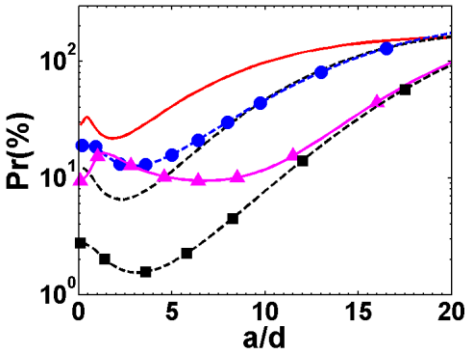

(a) Variation of $P_r(\%)$ with (a/d) ratio

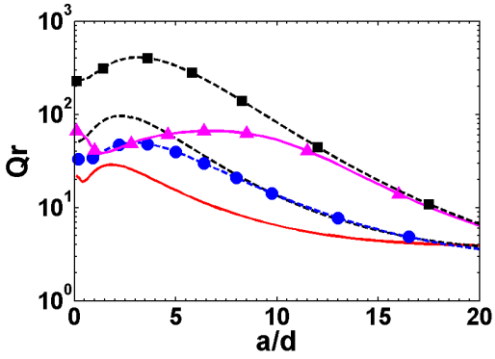

(b) Variation of Q_r with (a/d) ratio

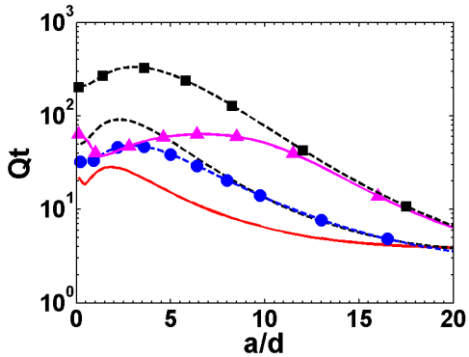

(c) Variation of Q_t with (a/d) ratio

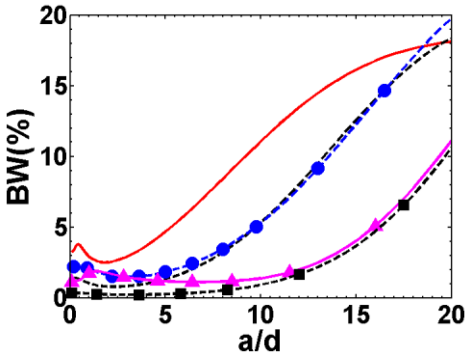

(d) Variation of BW with (a/d) ratio

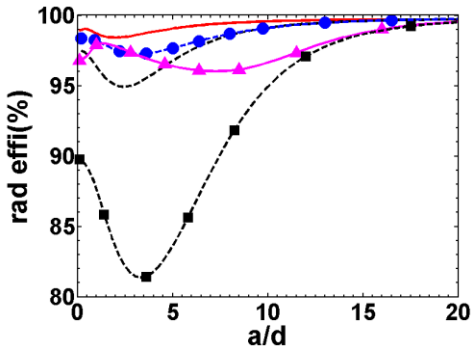

(e) Variation of rad. efficiency with (a/d) ratio

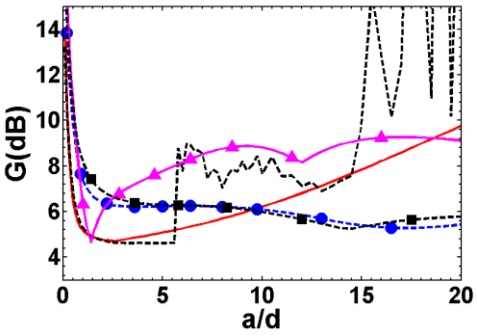

(f) Variation of $G(\mathrm{dB})$ with (a/d) ratio

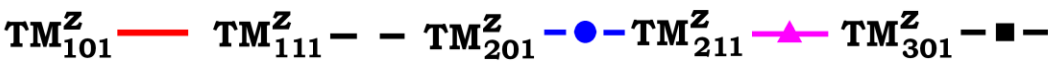

Fig 8.17 Radiation characteristics of ETDRA for different TM^z_{mnp} modes with (a/d) ratio $(a = 66mm, \varepsilon_r = 12, \tan\delta = 0.0005)$

a step size of 1°. A step size of less than 1° produces exactly the same results as found in step size of 1°. Such type of numerical instability is also observed

for $TM^z_{22p}, TM^z_{33p}, TM^z_{44p}$ etc. modes. This may be due to non-consideration of feed in our simple theory. IPMC model produces similar results and is not shown here for the sake of brevity. It should be pointed here that if we increase the step size from 1° to 5°, such type of numerical instability is not observed. In that case, the actual (θ, φ) point corresponding to U_{max} will be calculated wrongly.

8.3.4 Input Impedance

The concept of effective dimensions (a_e, d_e) is not suitable to predict the input impedance (Z_{in}). It is so since in certain cases, i.e. for certain combinations of 'a' and 'd', the probe position (x_o, y_o) would lie outside the triangle of side 'a_e'. Hence, the input impedance (Z_{in}) is calculated using (a, d).

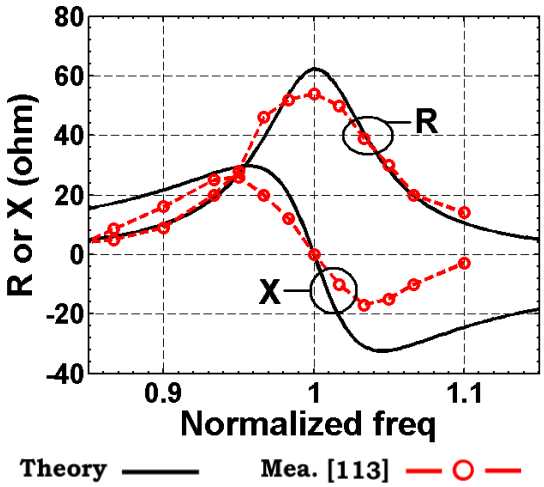

Fig 8.18 Comparison of input impedance with experimental data for TM^z_{101} mode ($a = 66mm,\ d = 24mm, \varepsilon_r = 12$)

Due to the use of (a, d), theoretical resonant frequency will be smaller than experimental data. Therefore the x-axis (frequency scale) is normalized with respect to resonant frequency as reported in [6]. In Fig. 8.18, theoretical input impedance is compared with experimental data [113] for fundamental TM^z_{101} mode. Measured Q_t is used for theoretical computation. It is found that our theoretical results are in good agreement with experimental data. It is found that our theory on Z_{in} is in good agreement with experimental data.

8.4 Conclusion

In this chapter, theoretical investigation on Equilateral Triangular Dielectric Resonator Antenna (ETDRA) is presented for various TM^z_{mnp} modes.

The ETDRA is modeled here as source free cavity. For theoretical investigation, the triangular surfaces on the top and bottom of the source free isolated ETDRA are modeled either as Perfect Magnetic Conductors (PMC) or Imperfect Magnetic Conductors (IPMC), whereas the side walls of rectangular cross-section are modeled as PMC only. These two models are termed as IPMC and PMC models respectively. Both cases are considered separately to investigate the ETDRA. Approximate solution for the eigenfunction is given here. Closed form analytic expressions are given here to predict the far-zone electric field for various TM^z_{mnp} modes. Radiated power $P_r(\%)$, radiation Q-factor (Q_r), total stored energy (W_t), bandwidth (BW), efficiency (e), gain (G) are also discussed here. From this theoretical investigation, it is found that:

- Radiation characteristics of an ETDRA for a TM^z_{mnp} modes are mainly controlled by the choice of m and n modal indices.
- Due to the existence of an imperfect wall at $z = \pm d$ in IMPC model, stored magnetic energy (W_m) and electric energy (W_e) are not equal.
- By selecting proper dimensions and relative permittivity of an ETDRA, higher order modes can produce higher gain compared to fundamental TM^z_{101} mode.
- Our theory does not account the effect of three corners on internal E-fields (please see Figs. 8.7-8.8) and feed mechanism. Further, ETDRA has sinusoidal variation along its height, whereas an equilateral Triangular Microstrip Antenna (TMA) has a constant variation due to thin substrate. Therefore, the effect of excitation on Q-factor is large compared to equilateral TMA.
- For a given mode, radiated power in percentage $P_r(\%)$, total Q-factor (Q_t) and gain (G) become almost same for fixed values of aspect ratio (a/d) and relative permittivity of an ETDRA as found for rectangular DRA.

Chapter IX

30°–60°–90° Triangular Dielectric Resonator Antenna

9.1 Introduction

Dielectric Resonator Antennas (DRAs) are very attractive over conventional shaped Microstrip Antennas (MA) due to their inherent wideband nature, high gain and high radiation efficiency. Literature survey shows that hemispherical, cylindrical and rectangular shaped DRAs have been reported so far [5, 174]. Some experimental investigations have also been reported on equilateral Triangular Dielectric Resonator Antenna (TDRA) [107-115]. On the other hand, 30°–60°–90° TDRA has not been reported so far. There is no work available, neither experimental nor theoretical on 30°–60°–90° TDRA.

In this chapter, theoretical investigations on 30°–60°–90° Triangular Dielectric Resonator Antenna (TDRA) is presented for arbitrary TM^{y}_{mnp} modes. The conventional waveguide model is used to investigate the performance of the 30°–60°–90° TDRA. For theoretical investigations, the surfaces of the 30°–60°–90° TDRA are modeled as Perfect Magnetic Conductors (PMC). Approximate solutions for the eigenfunctions and eigenvalues are given here. Simple curve fitted formula is given here to predict the resonant frequencies efficiently for different TM^{z}_{mnp} modes. A closed form analytical expressions are given for the first time to predict the far-field radiation patterns for different modes. Theoretical results are verified with experimental data and data obtained using 3D EM simulator HFSS [9].

9.2 Theory

In this section, theoretical investigations on source free 30°–60°–90°

TDRA having base a, height d and relative permittivity ε_r is presented. In Fig. 9.1, antenna geometry is shown in the standard Cartesian coordinate system. The antenna is placed on x-y plane and the height of the antenna is aligned along the z-axis. The 30°–60°–90° TDRA is placed on a metallic ground, whose size is sufficiently large compared to the 30°–60°–90° TDRA. Modal characteristics of 30°–60°–90° TDRA is presented here for arbitrary TM^z_{mnp} modes for the first time, hitherto unreported. Eigenfunctions, eigenvalues, far-field radiation patterns, radiated power, gain, Q-factor etc. are investigated. One antenna prototype is fabricated for experimental validation.

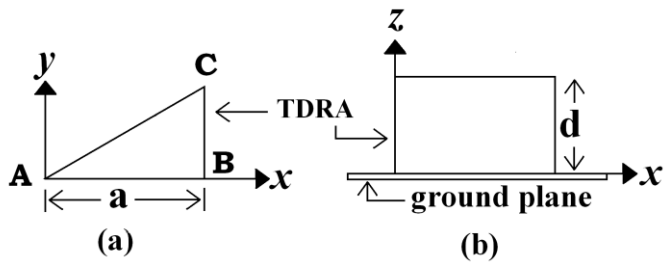

Fig. 9.1 Antenna configuration (a) top view (b) side view

9.2.1 Eigenfunctions

In Fig. 9.1, the antenna geometry of a 30°–60°–90° TDRA having base a, height d and relative permittivity ε_r is shown. The antenna is placed on a conducting ground plane at $z = 0$ surface. The origin is placed at the apex (A) of the triangular geometry. For theoretical investigations, the image theory is applied first to remove the ground plane and the process results a source free isolated 30°–60°–90° TDRA having base a, height h where $h = 2d$. Simple dielectric waveguide model is applied here to find the approximate solution of eigenfunctions ($\psi = F(x,y) \times H(z)$) for arbitrary TM^z_{mnp} modes. Here, $F(x,y)$ is the standing wave solution along the x-y direction, whereas $H(z)$ is the standing wave solution along the z-direction. For theoretical investigation, all surfaces of the 30°–60°–90° TDRA are modeled as Perfect Magnetic Conductors (PMC).

9.2.1.1 Evaluation of $F(x,y)$ Function

To evaluate the standing wave field variations along the *x-y* direction $F(x,y)$, duality property of the electromagnetic field is applied here. If a metallic 30°–60°–90° triangular waveguide is enclosed by metals along the *x-y* plane and is infinitely long along the *z*-direction, the eigenfunctions ($T(x,y)$) for TE^z and TM^z modes are given by [52, 134-135]:

$$T_{TE^z}(x,y) = cos\frac{\pi lx}{a}cos\left(\frac{\pi(m-n)}{\sqrt{3}a}y\right) + cos\frac{\pi mx}{a}cos\left(\frac{\pi(n-l)}{\sqrt{3}a}y\right) + cos\frac{\pi nx}{a}cos\left(\frac{\pi(l-m)}{\sqrt{3}a}y\right) \quad (9.1)$$

$$T_{TM^z}(x,y) = sin\frac{\pi lx}{a}sin\left(\frac{\pi(m-n)}{\sqrt{3}a}y\right) + sin\frac{\pi mx}{a}sin\left(\frac{\pi(n-l)}{\sqrt{3}a}y\right) + sin\frac{\pi nx}{a}sin\left(\frac{\pi(l-m)}{\sqrt{3}a}y\right) \quad (9.2)$$

where m,n,l are modal indices such that $l+m+n=0$. The procedure to use the 'duality property' in the prediction of characteristic function for dielectric waveguide from metallic waveguide is given in Chapter IV (30°–60°–90° Triangular Microstrip Antenna) and is not repeated here for brevity. The $F(x,y)$ function for TM^z_{mnp} mode of 30°–60°–90° TDRA (PMC boundary condition) is given by:

$$F(x,y) = cos\frac{\pi lx}{a}cos\left(\frac{\pi(m-n)}{\sqrt{3}a}y\right) + cos\frac{\pi mx}{a}cos\left(\frac{\pi(n-l)}{\sqrt{3}a}y\right) + cos\frac{\pi nx}{a}cos\left(\frac{\pi(l-m)}{\sqrt{3}a}y\right) \quad (9.3)$$

9.2.1.2 Evaluation of $H(z)$ Function

To evaluate the standing wave field solutions along the height of the 30°–60°–90° TDRA ($H(z)$ function), the top and bottom surfaces of the TDRA are

also modeled as PMC. Initially, the $H(z)$ function is assumed as:

$$H(z) = (E\,cos(k_z z) + F\,sin(k_z z)), \qquad |z| \le d$$

After applying the PMC boundary conditions at $z = \pm d$, we obtain:

$$H(z) = \left[\frac{E}{sin(k_z d)}\right] \times sin\big(k_z(d-z)\big); \quad k_z = p\pi/(2d)\ ;\ p = 1,2,3,4\ldots \tag{9.4}$$

The constant terms $E/sin(k_z d)$ can easily be clumped up with the modal amplitude.

Therefore, the approximate solution for the eigenfunctions $\big(\psi = F(x,y) \times H(z)\big)$ of an isolated source free 30°–60°–90° TDRA is:

$$\begin{aligned}\psi_{mnp} &= \left[cos\frac{\pi l x}{a}cos\left(\frac{\pi(m-n)}{\sqrt{3}a}y\right) + cos\frac{\pi m x}{a}cos\left(\frac{\pi(n-l)}{\sqrt{3}a}y\right)\right.\\ &\qquad \left. + cos\frac{\pi n x}{a}cos\left(\frac{\pi(l-m)}{\sqrt{3}a}y\right)\right] \times sin[k_z(d-z)]\\ &= \left(\sum_{i=1}^{3} cos(\alpha_i x)\,cos(\beta_i y)\right) \times sin[k_z(d-z)]\end{aligned} \tag{9.5}$$

where $\alpha_1 = \pi l/a\,, \alpha_2 = \pi m/a\,, \alpha_3 = \pi n/a\,, \beta_1 = \pi(m-n)/\sqrt{3}a\,,\ \beta_2 = \pi(n-l)/\sqrt{3}a\,, \beta_3 = \pi(l-m)/\sqrt{3}a$. Therefore, the internal electric and magnetic fields components can be expressed for TM^z_{mnp} modes as:

$$E_x = \left(\frac{-jA}{\omega\mu\varepsilon}\right)\left(\sum_{i=1}^{3} -\alpha_i \sin(\alpha_i x)\cos(\beta_i y)\right) \times (-k_z)\,cos[k_z(d-z)]$$

$$E_y = \left(\frac{-jA}{\omega\mu\varepsilon}\right)\left(\sum_{i=1}^{3} -\beta_i \cos(\alpha_i x)\sin(\beta_i y)\right) \times (-k_z)\,cos[k_z(d-z)]$$

$$E_z = \left(\frac{-jA}{\omega\mu\varepsilon}\right)(\chi^2)\left(\sum_{i=1}^{3} cos(\alpha_i x)\,cos(\beta_i y)\right) \times sin[k_z(d-z)]$$

$$H_x = \left(\frac{A}{\mu}\right)\left(\sum_{i=1}^{3} -\beta_i \cos(\alpha_i x)\sin(\beta_i y)\right) \times sin[k_z(d-z)]$$

$$H_y = \left(\frac{-A}{\mu}\right)\left(\sum_{i=1}^{3} -\alpha_i \sin(\alpha_i x)\cos(\beta_i y)\right) \times sin[k_z(d-z)]$$

$$H_z = 0 \tag{9.6}$$

where A is a constant and other notations are carrying their usual meaning. In Fig. 9.2, internal field distributions for some modes are shown.

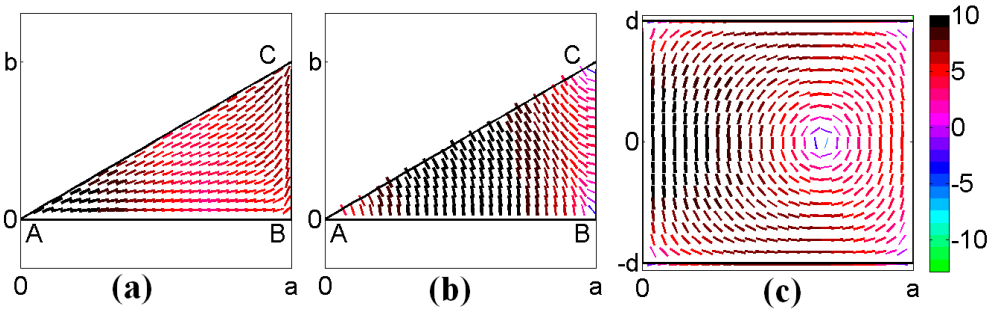

(i) Internal field distribution for TM^z_{101} mode (scale is in dB)

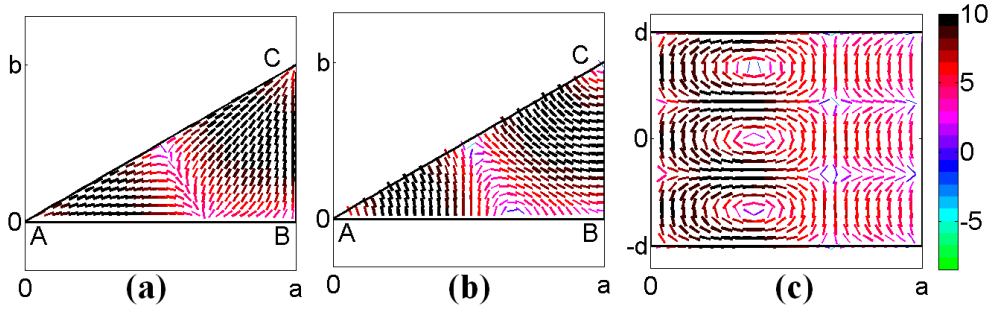

(ii) Internal field distribution for TM^z_{113} mode (scale is in dB)

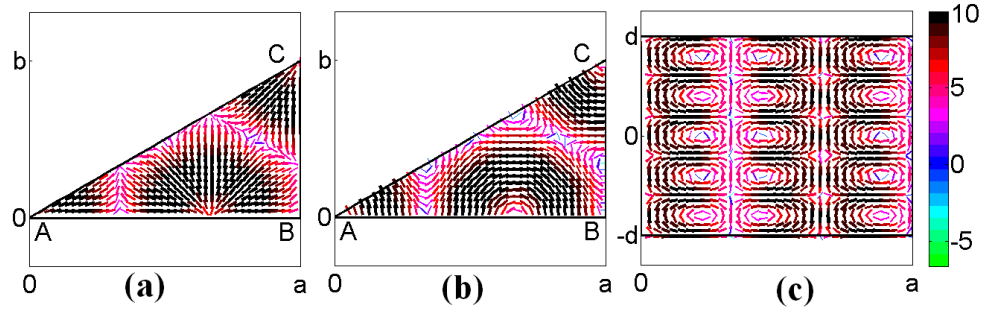

(iii) Internal field distribution for TM^z_{305} mode (scale is in dB)

Fig. 9.2 Internal electric and magnetic field distribution for different TM^z_{mnp} modes (a = 66mm, d = 24mm, ε_r = 12 (a) $\vec{E}$ field patterns at $z = d/4$ plane (b) $\vec{H}$ field patterns at $z = d/4$ plane (c) $\vec{E}$ field patterns at $y = 0$ plane

9.2.2 Resonant Frequency

The resonant frequency of an isolated source free 30°–60°–90° TDRA for arbitrary TM^z_{mnp} mode is evaluated using separation equation $\left(\chi^2 + k_z^2 = \varepsilon_r k_0^2 \text{ where } \chi = \left(2\pi/\sqrt{3}a\right)(m^2 + mn + n^2)^{1/2}\right)$ as:

$$f_r = \frac{c}{2\pi\sqrt{\varepsilon_r}} \times \left[\left(\frac{2\pi}{\sqrt{3}a}\right)^2 (m^2 + mn + n^2) + k_z^2\right]^{1/2} \tag{9.7}$$

where c is the velocity of light in free space. It is worth mentioning here that the fundamental mode occurs for $m = 1, n = 0$ and $p = 1$.

To have an idea on modal indices for different modes, the resonant frequencies are computed for first few modes as shown in Table 9.1. A closer look of the equation (9.7) reveals that m and n can be interchanged to produce same results. Therefore, mode degeneracy exists in 30°–60°–90° TDRA.

Table 9.1

Resonant frequencies for first few modes of a 30°–60°–90° TDRA

$(a = 66mm, d = 24mm, \varepsilon_r = 12)$

Sl No	Mode	Reso. Freq. (GHz)		Sl No	Mode	Reso. Freq. (GHz)
1	TM^z_{101}	1.1775		11	TM^z_{401}	3.1604
2	TM^z_{111}	1.5917		12	TM^z_{213}	3.3663
3	TM^z_{201}	1.7626		13	TM^z_{231}	3.4217
4	TM^z_{211}	2.1971		14	TM^z_{303}	3.5325
5	TM^z_{301}	2.4442		15	TM^z_{441}	3.5854
6	TM^z_{221}	2.7739		16	TM^z_{223}	3.7682
7	TM^z_{103}	2.8092		17	TM^z_{133}	3.8435
8	TM^z_{311}	2.8754		18	TM^z_{501}	3.8922
9	TM^z_{311}	3.0064		19	TM^z_{331}	4.0368
10	TM^z_{203}	3.1003		20	TM^z_{403}	4.0611

Theoretical results on resonant frequency are compared with data obtained using 3D EM simulator HFSS [9] as shown in Table 9.2. Large discrepancy is found between theoretical and simulated data. The error is maximum (27.76% aprox.) for the fundamental TM^z_{101} mode and the error is

decreasing for higher order modes. This is due to the avoidance of electric field lines in the corner for the TDRA bounded by PMC as explained in the case of the Equilateral TDRA (ETDRA) and is not repeated here for brevity.

Table 9.2

Comparison of resonant frequency with 3D simulator HFSS

($a = 66mm, d = 24mm, \varepsilon_r = 12$)

Mode	Resonant Frequency (GHz)		Error (%)
	Theoretical	HFSS[9]	
TM^z_{101}	1.1775	1.63	27.76
TM^z_{201}	1.7626	1.99	11.42
TM^z_{301}	2.4442	2.51	2.623
TM^z_{221}	2.7739	2.81	1.286

As the theoretical resonant frequency is smaller than the data obtained using the 3D EM simulator, the concept of decrease in effective size as described in case of ETDRA (please see Chapter VIII) is used to predict the effective dimensions of the 30°–60°–90° TDRA.

For a first order approximation, curve-fitted formula for computing the effective length (a_e) of 30°–60°–90° TDRA is defined for various TM^z_{mnp} modes as:

$$a_e = a \times (0.9918 \times e^{0.0004874t} - 1.214 \times e^{-0.7892t}) - 0.1 \times d \times \varepsilon_r^{-t} \quad (9.8)$$

Here, $t = |m| + |n|$. The effective height (d_e) of the 30°–60°–90° TDRA is expressed as [185]:

$$d_e = d \times (1 - 1.0 \times \varepsilon_r^{-1}) \quad (9.9)$$

9.2.3 Far-Field Radiation Patterns

We have reported the closed form analytical expressions for predicting the far-field radiation patterns of a 30°–60°–90° triangular microstrip antenna using conventional cavity model [165-166] where $\vec{E}_z$ component is used only,

because the tangential components $\vec{E}_x\ (\propto \partial/\partial z)$ and $\vec{E}_y\ (\propto \partial/\partial z)$ are equal to zero according to cavity model ($H(z)$ = constant) [6, 12-15]. In case of 30°–60°–90° TDRA, $\vec{E}_x$ and $\vec{E}_y$ components are not zero and their effects must be accounted for accurate prediction of the far-field radiation patterns as done for equilateral TDRA.

To predict the far field radiation patterns of a 30°–60°–90° TDRA for arbitrary TM^z_{mnp} modes, 'Equivalence Principle' [4, 16] is applied for the first time, hitherto unreported. All surfaces of the 30°–60°–90° TDRA are modeled as PMC for theoretical investigation. Therefore, the magnetic surface currents $\left(\vec{M}_s = \vec{E} \times \hat{n}\right)$ on each surface must be evaluated to find the far-zone electric field. Before starting any theoretical calculation, it is assumed that

$$f(x,y,z) = xk_o sin(\theta)\cos(\varphi) + yk_o sin(\theta)\sin(\varphi) + zk_o cos(\theta) = xV_1 + yV_2 + zV_3 \quad (9.10a)$$

where

$$V_1 = k_o sin(\theta)\cos(\varphi);\ V_2 = k_o sin(\theta)\sin(\varphi);\ V_3 = k_o cos(\theta) \quad (9.10b)$$

Surface Current along AC Surface

$$M_s^{AC} = \vec{E} \times \hat{n} = \left[E_x\hat{x} + E_y\hat{y} + E_z\hat{z}\right] \times \left(\hat{y}\, cos(\alpha) - \hat{x}\, sin(\alpha)\right);\quad \alpha = \pi/6$$
$$= \hat{z}E_x cos(\alpha) - \hat{x}E_z cos(\alpha) + \hat{z}E_y sin(\alpha) - \hat{y}E_z sin(\alpha)$$
$$= -\hat{x}E_z cos(\alpha) - \hat{y}E_z sin(\alpha) + \hat{z}\left(E_x cos(\alpha) + E_y sin(\alpha)\right) \quad (9.11)$$

Surface Current along AB Surface

$$M_s^{AB} = \vec{E} \times \hat{n} = \left[E_x\hat{x} + E_y\hat{y} + E_z\hat{z}\right] \times (-\hat{y});\quad \alpha = \pi/6$$
$$= -\hat{z}E_x + 0 + \hat{x}E_z = \hat{x}E_z - \hat{z}E_x \quad (9.12)$$

Surface Current along BC Surface

$$M_s^{BC} = \vec{E} \times \hat{n} = \left[E_x\hat{x} + E_y\hat{y} + E_z\hat{z}\right] \times \hat{x} = -\hat{z}E_y + \hat{y}E_z = \hat{y}E_z - \hat{z}E_y \quad (9.13)$$

Surface Current along TOP Surface ($z = +d$)

$$M_s^{Top} = \vec{E} \times \hat{n} = \left[E_x\hat{x} + E_y\hat{y} + E_z\hat{z}\right] \times (\hat{z}) = \left[-\hat{y}E_x + \hat{x}E_y\right] = \hat{x}E_y - \hat{y}E_x \quad (9.14)$$

Surface Current along BOTTOM Surface $(z = -d)$

$$M_s^{Bottom} = \vec{E} \times \hat{n} = \left[E_x\hat{x} + E_y\hat{y} + E_z\hat{z}\right] \times (-\hat{z}) = \left[\hat{y}E_x - \hat{x}E_y\right] = -\hat{x}E_y + \hat{y}E_x \qquad (9.15)$$

Evaluation of I_z for PMC Model

Closer look reveals that $H(z)$ function is same as derived for equilateral TDRA using the PMC model. Hence, the contribution along the height (I_z) on far-field radiation patterns will take same closed form relations as derived for equilateral TDRA using the PMC model. Therefore, the final results are summarized here as:

$$I_s^z = \int_{z=-d}^{d} \sin[k_z(d-z)] \times e^{jk_o z\cos(\theta)} dz \quad ; \; k_z = \frac{p\pi}{2d}$$

$$= \int_{z=-d}^{d} \sin[k_z(d-z)] \times e^{jzV_3} dz \quad ; \quad V_3 = k_o\cos(\theta)$$

$$= -j \times d \times \left[e^{jk_z d} \times sinc\big((v_3 - k_z)d\big) - e^{-jk_z d} \times sinc\big((v_3 + k_z)d\big)\right] \qquad (9.16)$$

and

$$I_c^z = \int_{z=-d}^{d} \cos[k_z(d-z)] \times e^{jk_o z\cos(\theta)} dz \quad ; \; k_z = \frac{p\pi}{2d}$$

$$= \int_{z=-d}^{d} \cos[k_z(d-z)] \times e^{jzV_3} dz \quad ; \quad V_3 = k_o\cos(\theta)$$

$$= d \times \left[e^{jk_z d} \times sinc\big((v_3 - k_z)d\big) + e^{-jk_z d} \times sinc\big((v_3 + k_z)d\big)\right] \qquad (9.17)$$

The contributions of the *x*-*y* coordinates on far-field radiation patterns are quite similar to 30°–60°–90° Triangular Microstrip Antenna (TMA). Therefore, the final results are given here.

Fields along AC Surface (PMC)

$$M_s^{AC} = -\hat{x}E_z\cos(\alpha) - \hat{y}E_z\sin(\alpha) + \hat{z}\left(E_x\cos(\alpha) + E_y\sin(\alpha)\right) \quad ; \; \alpha = \pi/6$$

- **$\hat{x}$-component $\vec{F}$ due to M_s^{AC} surface current**

$$M_s^{AC} = -\hat{x}E_z cos(\alpha) - \hat{y}E_z sin(\alpha) + \hat{z}\left(E_x cos(\alpha) + E_y sin(\alpha)\right)$$

$$F_x^{AC} = C_{xy} \times \int_l \int_{z=-d}^{d} [-E_z cos(\alpha)] \times e^{j\times f(x,y,z)} dl dz \quad at\ y = \eta x \quad ;\ \eta = 1/\sqrt{3}$$

$$= C_{xy} \times [-E_3] \times (\chi^2) \times I_{AC}^{x1} \times I_{zS}^{PMC} \tag{9.18}$$

where

$$I_z = \int_{z=-d}^{d} sin[k_z(d-z)] \times e^{jV_3 z} dz = I_{zS}^{PMC}$$

$$I_{AC}^{x1} = \int_{x=0}^{M} \left(\sum_{i=1}^{3} \cos(\alpha_i x)\cos(\beta_i y)\right) \times e^{j\times(xV_1 + yV_2)} dx \quad \text{at} \quad y = \eta x \ ; \ \ \chi_1 = V_1 + V_2/\sqrt{3}$$

$$= \frac{-j}{((n-l)^2 b^2 - \chi_1^2)} \times \left[e^{j\chi_1 a}\{jb(n-l)\sin(b(n-l)a) - \chi_1 \cos(b(n-l)a)\} + \chi_1\right]$$

$$+ \frac{-j}{((l-m)^2 b^2 - \chi_1^2)} \times \left[e^{j\chi_1 a}\{jb(l-m)\sin(b(l-m)a) - \chi_1 \cos(b(l-m)a)\} + \chi_1\right]$$

$$+ \frac{-j}{((m-n)^2 b^2 - \chi_1^2)} \times \left[e^{j\chi_1 a}\{jb(m-n)\sin(b(m-n)a) - \chi_1 \cos(b(m-n)a)\} + \chi_1\right]$$

where $b = 2\pi/3a$.

- **$\hat{y}$-component $\vec{F}$ due to M_s^{AC} surface current**

$$M_s^{AC} = -\hat{x}E_z cos(\alpha) - \hat{y}E_z sin(\alpha) + \hat{z}\left(E_x cos(\alpha) + E_y sin(\alpha)\right)$$

$$F_y^{AC} = C_{xy} \times \int_l \int_{z=-h}^{h} [-E_z sin(\alpha)] \times e^{j\times f(x,y,z)} dl dz \quad at\ x = \frac{y}{\eta} \quad ;\ \eta = 1/\sqrt{3}$$

$$= C_{xy} \times [-E_3] \times (\chi^2) \times I_{AC}^{y1} \times I_{zS}^{PMC} \tag{9.19}$$

where

$$I_{AC}^{y} = \int_{x=0}^{a/\sqrt{3}} \left(\sum_{i=1}^{3} \cos(\alpha_i x)\cos(\beta_i y)\right) \times e^{j\times(xV_1 + yV_2)} dy \quad at \quad x = y/\eta$$

$$= \frac{-j}{\sqrt{3}((n-l)^2 b^2 - \chi_1^2)} \times \left[e^{j\chi_1 a}\{jb(n-l)sin(b(n-l)a) - \chi_1 cos(b(n-l)a)\} + \chi_1\right]$$

$$+\frac{-j}{\sqrt{3}((l-m)^2b^2-\chi_1^2)}\times\left[e^{j\chi_1 a}\{jb(l-m)sin(b(l-m)a)-\chi_1 cos(b(l-m)a)\}+\chi_1\right]$$

$$+\frac{-j}{\sqrt{3}((m-n)^2b^2-\chi_1^2)}$$

$$\times\left[e^{j\chi_1 a}\{jb(m-n)sin(b(m-n)a)-\chi_1 cos(b(m-n)a)\}+\chi_1\right]$$

- **$\hat{z}$-component $\vec{F}$ due to M_s^{AC} surface current**

$$M_s^{AC}=-\hat{x}E_z cos(\alpha)-\hat{y}E_z sin(\alpha)+\hat{z}\left(E_x cos(\alpha)+E_y sin(\alpha)\right)$$

$$F_z^{AC}=C_{xy}\times\int_{l}\int_{z=-d}^{d}\left[E_x cos(\alpha)+E_y sin(\alpha)\right]\times e^{j\times f(x,y,z)}dldz \quad at\ y=\eta x\ ;\ \eta=1/\sqrt{3}$$

$$=C_{xy}\times\left[E_1\times I_{AC}^{zx1}+E_2\times\left(1/\sqrt{3}\right)\times I_{AC}^{zx2}\right]\times(-k_z)\times I_{zC}^{PMC} \tag{9.20}$$

where

$$I_z=\int_{z=-d}^{d}(-k_z)\,cos[k_z(d-z)]\times e^{jV_3 z}dz=(-k_z)\times I_{zC}^{PMC}$$

$$I_{AC}^{zx1}=\int_{x=0}^{a}\left(\sum_{i=1}^{3}-\alpha_i\sin(\alpha_i x)\cos(\beta_i y)\right)\times e^{j\times(xV_1+yV_2)}dx \qquad at\quad y=\eta x$$

$$=\frac{e(n-l)}{((n-l)^2b^2-\chi_1^2)}\times\left[e^{j\chi_1 a}\{b(n-l)\cos(b(n-l)a)-j\chi_1\sin(b(n-l)a)\}-b(n-l)\right]$$

$$+\frac{e(l-m)}{((l-m)^2b^2-\chi_1^2)}$$

$$\times\left[e^{j\chi_1 a}\{b(l-m)\cos(b(l-m)a)-j\chi_1\sin(b(l-m)a)\}-b(l-m)\right]$$

$$+\frac{e(m-n)}{((m-n)^2b^2-\chi_1^2)}$$

$$\times\left[e^{j\chi_1 a}\{b(m-n)\cos(b(m-n)a)-j\chi_1\sin(b(m-n)a)\}-b(m-n)\right]$$

where $b=2\pi/3a\,,e=\pi/2a$

and

$$I_{AC}^{zx2}=\int_{x=0}^{a}\left(\sum_{i=1}^{3}-\beta_i\cos(\alpha_i x)\sin(\beta_i y)\right)\times e^{j\times(xV_1+yV_2)}dx \qquad at\quad y=\eta x$$

$$= \frac{e(n-l)}{\sqrt{3}[(n-l)^2 b^2 - \chi_1^2]} \times \left[e^{j\chi_1 a}\{b(n-l)\cos(b(n-l)a) - j\chi_1 \sin(b(n-l)a)\} - b(n-l)\right]$$

$$+ \frac{e(l-m)}{\sqrt{3}[(l-m)^2 b^2 - \chi_1^2]} \times \left[e^{j\chi_1 a}\{b(l-m)\cos(b(l-m)a) - j\chi_1 \sin(b(l-m)a)\} - b(l-m)\right]$$

$$+ \frac{e(m-n)}{\sqrt{3}[(m-n)^2 b^2 - \chi_1^2]} \times \left[e^{j\chi_1 a}\{b(m-n)\cos(b(m-n)a) - j\chi_1 \sin(b(m-n)a)\} - b(m-n)\right]$$

$$= \frac{1}{\sqrt{3}} \times I_{AC}^{zx1}$$

Hence,

$$F_z^{AC} = C_{xy} \times [E_1 \times I_{AC}^{zx1} + E_2 \times (1/\sqrt{3}) \times I_{AC}^{zx2}] \times (-k_z) \times I_{zC}^{PMC}$$

$$= C_{xy} \times I_{AC}^{zx1} \times \left[E_1 + \frac{E_2}{3}\right] \times (-k_z) \times I_{zC}^{PMC} \quad (9.21)$$

Fields along AB Surface (PMC)

$M_s^{AB} = \hat{x}E_z - \hat{z}E_x$

- **$\hat{x}$-component $\vec{F}$ due to M_s^{AB} surface current**

$M_s^{AB} = \hat{x}E_z - \hat{z}E_x$

$$F_x^{AB} = C_{xy} \times \int_l \int_{z=-d}^{d} [E_z cos(\alpha)] \times e^{j \times f(x,y,z)} dl dz \quad \text{at } y = 0$$

$$= C_{xy} \times E_3 \times (\chi^2) \times I_{AB}^{x4} \times I_{zS}^{PMC} \quad (9.22)$$

where

$$I_{AB}^{x} = \int_{x=0}^{a} \left(\sum_{i=1}^{3} \cos(\alpha_i x)\right) \times e^{jxV_1} dx \quad ; \quad \chi_2 = k_o \sin(\theta)\cos(\Phi) = V_1$$

$$= \frac{ja\chi_2}{\pi[l^2 - \chi_2^2]} \times \left[e^{jV_1 a}\, cos(\pi l) - 1\right] + \frac{ja\chi_2}{\pi[m^2 - \chi_2^2]} \times \left[e^{jV_1 a}\, cos(\pi m) - 1\right]$$

$$+ \frac{ja\chi_2}{\pi[n^2 - \chi_2^2]} \times \left[e^{jV_1 a}\, cos(\pi n) - 1\right] \quad ; \quad \chi_2 = V_1 a/\pi$$

- **$\hat{z}$-component $\vec{F}$ due to M_s^{AB} surface current**

$$M_s^{AB} = \hat{x}E_z - \hat{z}E_x$$

$$F_z^{AB} = C_{xy} \times \int_l \int_{z=-d}^{d} [-E_x] \times e^{jf(x,y,z)} dldz \qquad at\ y = 0$$

$$= C_{xy} \times [-E_1] \times I_{AC}^{zx1} \times (-k_z) \times I_{zC}^{PMC} \tag{9.23}$$

where

$$I_{AC}^{zx1} = \int_{x=0}^{a} \left(\sum_{i=1}^{3} -\alpha_i \sin(\alpha_i x) \right) \times e^{jxV_1} dx \quad ; \quad V_1 = k_o \sin(\theta)\cos(\Phi)$$

$$= \frac{l^2}{l^2 - \chi_2^2} \times \left[e^{jV_1 a}\, cos(\pi l) - 1 \right] + \frac{m^2}{m^2 - \chi_2^2} \times \left[e^{jV_1 a}\, cos(\pi m) - 1 \right]$$

$$+ \frac{n^2}{n^2 - \chi_2^2} \times \left[e^{jV_1 a}\, cos(\pi n) - 1 \right] \qquad ; \quad \chi_2 = V_1 a/\pi$$

Fields along BC Surface (PMC)

$$M_s^{BC} = \hat{y}E_z - \hat{z}E_y$$

- **$\hat{y}$-component $\vec{F}$ due to M_s^{BC} surface current**

$$M_s^{BC} = \vec{E} \times \hat{n} = \left[E_x\hat{x} + E_y\hat{y} + E_z\hat{z} \right] \times \hat{x} = -\hat{z}E_y + \hat{y}E_z = \hat{y}E_z - \hat{z}E_y$$

$$F_y^{BC} = C_{xy} \times \int_{y=0}^{a/\sqrt{3}} \int_{z=-d}^{d} [E_z] \times e^{j \times f(x,y,z)} dldz \quad at\ x = a$$

$$= C_{xy} \times [E_3] \times (\chi^2) \times e^{jV_1 M} \times I_{BC}^{y1} \times I_{zS}^{PMC} \tag{9.24}$$

where

$$I_{BC}^{y} = \int_{y=0}^{a/\sqrt{3}} \left(\sum_{i=1}^{3} \cos(\alpha_i x)\cos(\beta_i y) \right) \times e^{j \times (yV_2)} dl \quad \text{at } x = a$$

$$= \frac{\sqrt{3}a\cos(l\pi)}{\pi[(m-n)^2 - v^2]} \times \left[e^{j\pi v/3} \times \left\{ (m-n) sin\left(\frac{\pi(m-n)}{3} \right) + jv \cos\left(\frac{\pi(m-n)}{3} \right) \right\} - jv \right]$$

$$+ \frac{\sqrt{3}a\cos(m\pi)}{\pi[(n-l)^2 - v^2]} \times \left[e^{j\pi v/3} \times \left\{ (n-l) sin\left(\frac{\pi(n-l)}{3} \right) + jv \cos\left(\frac{\pi(n-l)}{3} \right) \right\} - jv \right]$$

$$+\frac{\sqrt{3}a\cos(n\pi)}{\pi[(l-m)^2-v^2]}\times\left[e^{j\pi v/3}\times\left\{(l-m)sin\left(\frac{\pi(l-m)}{3}\right)+jv\cos\left(\frac{\pi(l-m)}{3}\right)\right\}-jv\right]$$

where

$$v=\frac{\sqrt{3}aV_2}{\pi}\quad,\quad\frac{V_2a}{\sqrt{3}}=\frac{\pi v}{3}$$

- **$\hat{z}$-component $\vec{F}$ due to M_s^{BC} surface current**

$$M_s^{BC}=\vec{E}\times\hat{n}=\left[E_x\hat{x}+E_y\hat{y}+E_z\hat{z}\right]\times\hat{x}=-\hat{z}E_y+\hat{y}E_z=\hat{y}E_z-\hat{z}E_y$$

$$F_z^{BC}=C_{xy}\times\int_{y=0}^{a/\sqrt{3}}\int_{z=-d}^{d}\left[-E_y\right]\times e^{j\times f(x,y,z)}dydz\quad\text{at } x=M=\frac{\sqrt{3}a}{2}$$

$$=C_{xy}\times[-E_2]\times e^{jV_1M}\times I_{BC}^{z1}\times(-k_z)\times I_{zC}^{PMC}\qquad(9.25)$$

where

$$I_{BC}^{z}=\int_{y=}^{a/\sqrt{3}}\left(\sum_{i=1}^{3}-\beta_i\cos(\alpha_ix)\sin(\beta_iy)\right)\times e^{j\times(yV_2)}dl\quad\text{at } x=a$$

$$=\frac{(m-n)\cos(\pi l)}{(m-n)^2-v^2}\times\left[e^{j\pi v/3}\times\left\{(m-n)cos\left(\frac{\pi(m-n)}{3}\right)-jv\sin\left(\frac{\pi(m-n)}{3}\right)\right\}-(m-n)\right]$$

$$+\frac{(n-l)\cos(\pi m)}{(n-l)^2-v^2}\times\left[e^{j\pi v/3}\times\left\{(n-l)cos\left(\frac{\pi(n-l)}{3}\right)-jv\sin\left(\frac{\pi(n-l)}{3}\right)\right\}-(n-l)\right]$$

$$+\frac{(l-m)\cos(\pi n)}{(l-m)^2-v^2}\times\left[e^{j\pi v/3}\times\left\{(l-m)cos\left(\frac{\pi(l-m)}{3}\right)-jv\sin\left(\frac{\pi(l-m)}{3}\right)\right\}-(l-m)\right]$$

Fields along TOP Surface ($z=+d$)

$$M_s^{Top}=\vec{E}\times\hat{n}=\left[E_x\hat{x}+E_y\hat{y}+E_z\hat{z}\right]\times(\hat{z})=\left[-\hat{y}E_x+\hat{x}E_y\right]=\hat{x}E_y-\hat{y}E_x$$

- **$\hat{x}$-component $\vec{F}$ due to M_s^{Top} surface current**

$$M_s^{Top}=\vec{E}\times\hat{n}=\left[E_x\hat{x}+E_y\hat{y}+E_z\hat{z}\right]\times(\hat{z})=\left[-\hat{y}E_x+\hat{x}E_y\right]=\hat{x}E_y-\hat{y}E_x$$

$$F_x^{Top}=C_{xy}\times\int_{x=0}^{a}\int_{y=0}^{\eta x}\left[E_y\right]\times e^{j\times f(x,y,z)}dxdy\quad at\ z=d$$

$$=C_{xy}\times[E_2]\times I_{cs}\times e^{jdV_3}\times(-k_z)\,cos[k_z(d-z)]\quad;\quad z=d\qquad(9.26)$$

where

$$I_{cs} = \int_{x=0}^{a}\int_{y=0}^{\eta x}\left(\sum_{i=1}^{3} -\beta_i \cos(\alpha_i x)\sin(\beta_i y)\right)\times e^{j\times(xV_1+yV_2)}dxdy \tag{9.27}$$

- **$\hat{y}$-component $\vec{F}$ due to M_s^{Top} surface current**

$$M_s^{Top} = \vec{E}\times\hat{n} = \left[E_x\hat{x}+E_y\hat{y}+E_z\hat{z}\right]\times(\hat{z}) = \left[-\hat{y}E_x+\hat{x}E_y\right] = \hat{x}E_y-\hat{y}E_x$$

$$F_y^{Top} = C_{xy}\times\int_{x=0}^{a}\int_{y=0}^{\eta x}[-E_x]\times e^{j\times f(x,y,z)}dxdy \quad at\ z=d$$

$$= C_{xy}\times[-E_1]\times I_{sc}\times e^{jdV_3}\times(-k_z)\cos[k_z(d-z)]\ \ ;\quad z=d \tag{9.28}$$

where

$$I_{sc} = \int_{x=0}^{a}\int_{y=0}^{\eta x}\left(\sum_{i=1}^{3} -\alpha_i \sin(\alpha_i x)\cos(\beta_i y)\right)\times e^{j\times(xV_1+yV_2)}dxdy \tag{9.29}$$

Fields along BOTTOM Surface ($z=-d$)

$$M_s^{Bottom} = -\hat{x}E_y+\hat{y}E_x$$

- **$\hat{x}$-component $\vec{F}$ due to M_s^{Bottom} surface current**

$$M_s^{Bottom} = \vec{E}\times\hat{n} = \left[E_x\hat{x}+E_y\hat{y}+E_z\hat{z}\right]\times(-\hat{z}) = \left[\hat{y}E_x-\hat{x}E_y\right] = -\hat{x}E_y+\hat{y}E_x$$

$$F_x^{Bottom} = C_{xy}\times\int_{x=0}^{a}\int_{y=0}^{\eta x}\left[-E_y\right]\times e^{j\times f(x,y,z)}dxdy \quad at\ z=-d$$

$$= C_{xy}\times[-E_2]\times I_{cs}\times e^{-jdV_3}\times(-k_z)\cos[k_z(d-z)]\ \ ;\ z=-d \tag{9.30}$$

- **$\hat{y}$-component $\vec{F}$ due to M_s^{Bottom} surface current**

$$M_s^{Bottom} = -\hat{x}E_y+\hat{y}E_x$$

$$F_y^{Bottom} = C_{xy}\times\int_{x=0}^{a}\int_{y=0}^{\eta x}[E_x]\times e^{j\times f(x,y,z)}dxdy \quad at\ z=-d$$

$$= C_{xy}\times[E_1]\times I_{sc}\times e^{-jdV_3}\times(-k_z)\cos[k_z(d-z)]\ \ ;\quad z=-d \tag{9.31}$$

Here, E_1, E_2, and E_3 are the field strength of E_x, E_y and E_z components

respectively, C_{xy} is constant and other terms are carrying their usual meaning. The total far-zone electric field at point $P(r,\theta,\varphi)$ is evaluated as [16]:

$$E_\theta = -\frac{jk_o \exp(-jk_o r)}{4\pi r} \times exp(-jV_1 R) \times \left[L_\varphi + \eta_0 N_\theta\right] \quad (9.32a)$$

$$E_\varphi = \frac{jk_o \exp(-jk_o r)}{4\pi r} \times exp(-jV_1 R) \times \left[L_\theta - \eta_0 N_\varphi\right] \quad (9.32b)$$

where,

$$N_\theta = A_x cos(\theta)cos(\varphi) + A_y cos(\theta)sin(\varphi) - A_z sin(\theta)$$
$$N_\varphi = -A_x sin(\varphi) + A_y cos(\varphi)$$

$$L_\theta = F_x cos(\theta)cos(\varphi) + F_y cos(\theta)sin(\varphi) - F_z sin(\theta)$$
$$L_\varphi = -F_x sin(\varphi) + F_y cos(\varphi) \quad (9.33)$$

$$F_x = F_x^{AC} + F_x^{AB} + F_x^{Top} + F_x^{Bottom}$$
$$F_y = F_y^{AC} + F_y^{AB} + F_y^{BC} + F_y^{Top} + F_y^{Bottom}$$
$$F_z = F_z^{AC} + F_z^{AB} + F_z^{BC}$$

$$A_x = A_y = A_z = 0 \quad (9.34)$$

Various constants as defined during the evaluation of far-field radiation patterns are summarized here for reference purpose.

$$V_1 = sin(\theta)\cos(\varphi) \quad ; \quad V_2 = sin(\theta)\sin(\varphi) \quad ; \quad V_3 = cos(\theta)$$
$$\chi_1 = (V_1 + \eta V_2) \quad ; \quad \chi_2 = V_1 a/\pi \quad ; \quad \eta = 1/\sqrt{3} \quad ; \quad e = \frac{\pi}{2a}$$
$$v = \frac{\sqrt{3}aV_2}{\pi} \quad ; \quad \frac{V_2 a}{\sqrt{3}} = \frac{\pi v}{3} \quad ; \quad b = \frac{2\pi}{3a} \quad (9.35)$$

9.2.4 Radiated Power, Quality factor, Efficiency and Gain

The Knowledge of radiated power in percentage which is calculated as [15] $P_r(\%) = (2\pi/Q_r) \times 100$ where Q_r is the radiation quality factor, bandwidth (BW), efficiency (e), gain (G) etc. is very important to choose a particular mode

for designing an antenna using 30°–60°–90° TDRA. These are evaluated using standard procedure as found in [12-16] or as calculated for Equilateral TDRA in Chapter VIII.

9.2.5 Input Impedance

The evaluation of input impedance (Z_{in}) is straight forward as done for rectangular and equilateral triangular shaped dielectric resonator antenna. The input impedance is evaluated as [4]:

$$Z_{in} = \frac{-j\omega(a_o/I_o)^2}{\omega^2 - \omega_o^2\left(1 + \frac{j}{Q_t}\right)} \tag{9.36}$$

where

$$a_o = \iiint \vec{E}_o . \vec{J}\, dv \tag{9.37}$$

Here, $\vec{J}$ is probe current density, I_o is the magnitude of current, ω is operating frequency, ω_o is resonant frequency, Q_t is total quality factor and $\vec{E}_o$ is the normalized electric field inside the 30°–60°–90° TDRA. For thin probe approximation, the probe current density ($\vec{J}$) is modeled here as one dimensional $\hat{z}$ directed current as [4]:

$$\vec{J} = \begin{cases} \hat{z} I_o \dfrac{\sin[k_d(l-z)]}{\sin(k_d l)} \delta(x-x_o)\delta(y-y_o), & z \le l \\ 0 \quad , & z > l \end{cases} \tag{9.38}$$

where $k_d = p\pi/(2l)$, l is probe length and (x_o, y_o) is probe location. This approximation is valid when $l/r \gg 1$ where r is the radius of the coaxial probe.

9.3 Results

In this section, theoretical results on resonant frequency, far-field patterns, Q-factor etc. are discussed. Radiation characteristics for various modes are discussed. Two 30°–60°–90° TDRAs are fabricated in our laboratory.

The TDRA is excited using 50Ω coaxial probe for measurement. The probe is placed just outside the TDRA grazing its surfaces. The probe is placed in different positions to excite different modes. Theoretical results are compared with experimental data and data obtained using an EM simulator to show the accuracy of our theory.

9.3.1 Resonant Frequency

In Table 9.3, comparison of theoretical resonant frequencies with experimental data is shown for different TM^z_{mnp} modes of the 30°–60°–90° TDRA. In our experiment, we have successfully excited the pure TM^z_{101}, TM^z_{111} TM^z_{211}, TM^z_{301} and TM^z_{221} modes. It is found that the expression for effective dimensions (a_e, d_e) are in excellent agreement (5% error) with measured data. This is due to non consideration of feed mechanism and finite size of ground plane in our theoretical calculation.

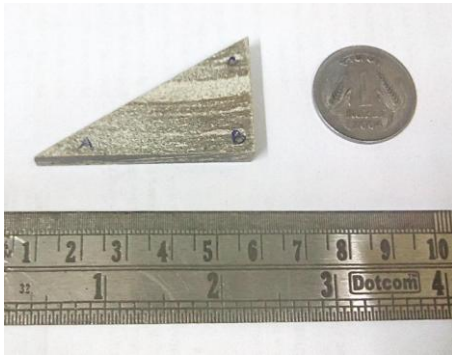

Fig. 9.3 Photograph of fabricated 30°–60°–90° TDRA

Table 9.3

Experimental validation of resonant frequency for TM^z_{mnp} modes

$(a = 48mm, d = 7.8mm, \varepsilon_r = 25)$

Mode	Resonant Frequency (GHz)		Error (%)
	Theoretical	Measured	
TM^z_{101}	2.5874	2.553	-1.3472
TM^z_{111}	2.6159	2.699	3.08
TM^z_{211}	2.9528	2.921	-1.0871
TM^z_{301}	3.1724	3.279	3.2502
TM^z_{221}	3.3235	3.421	2.8497

9.3.2 Radiation Patterns

In this section, we will first present the theoretical results on far-field radiation patterns for different TM^z_{mnp} modes. In Fig. 9.4, E-plane ($\varphi = 0^o$) and H-plane ($\varphi = 90^o$) power patterns are shown with absolute gain (in dB) for first few modes of a 30°–60°–90° TDRA having $a = 66mm, d = 24mm, \varepsilon_r = 12$ and $tan\,\delta = 0.0005$.

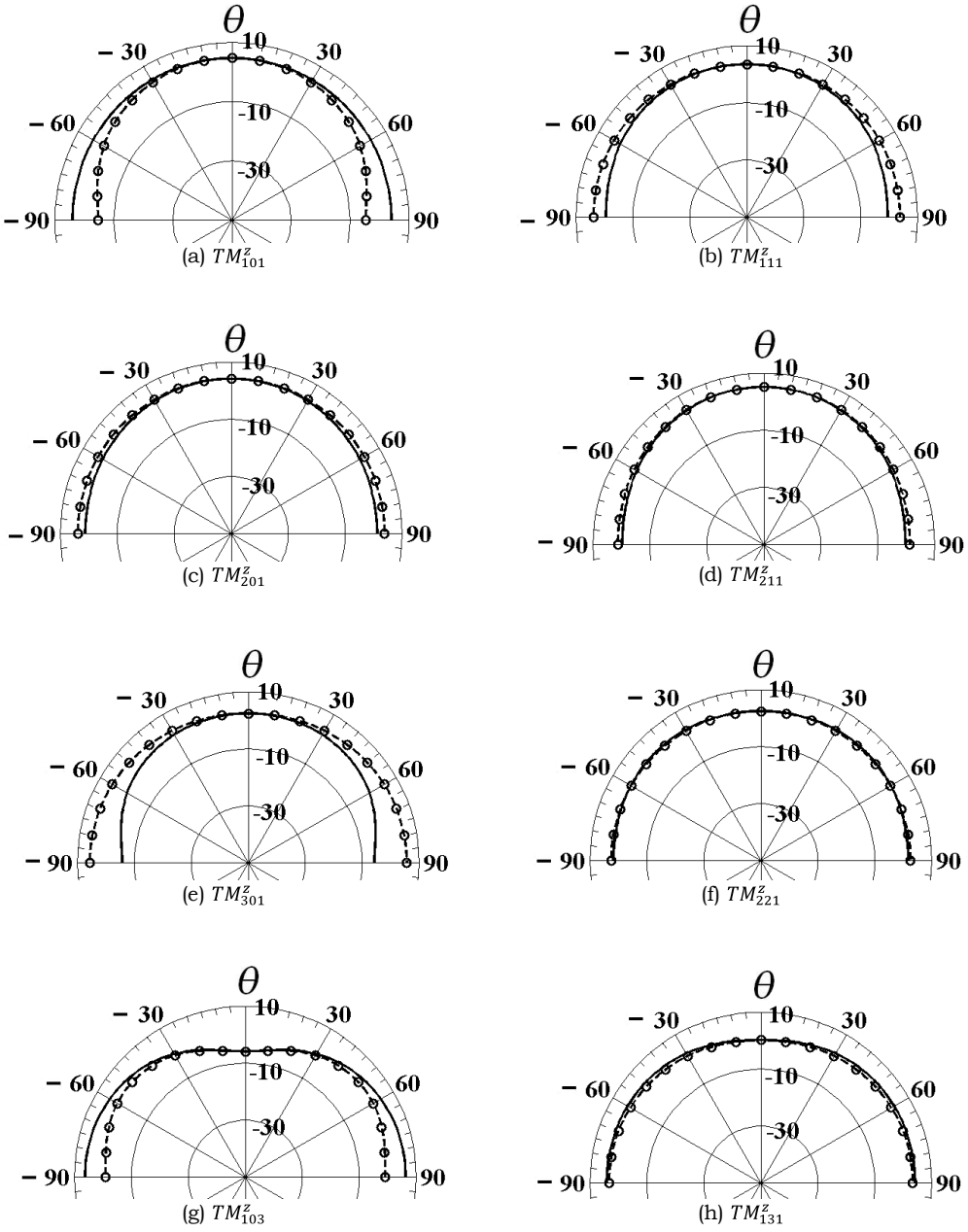

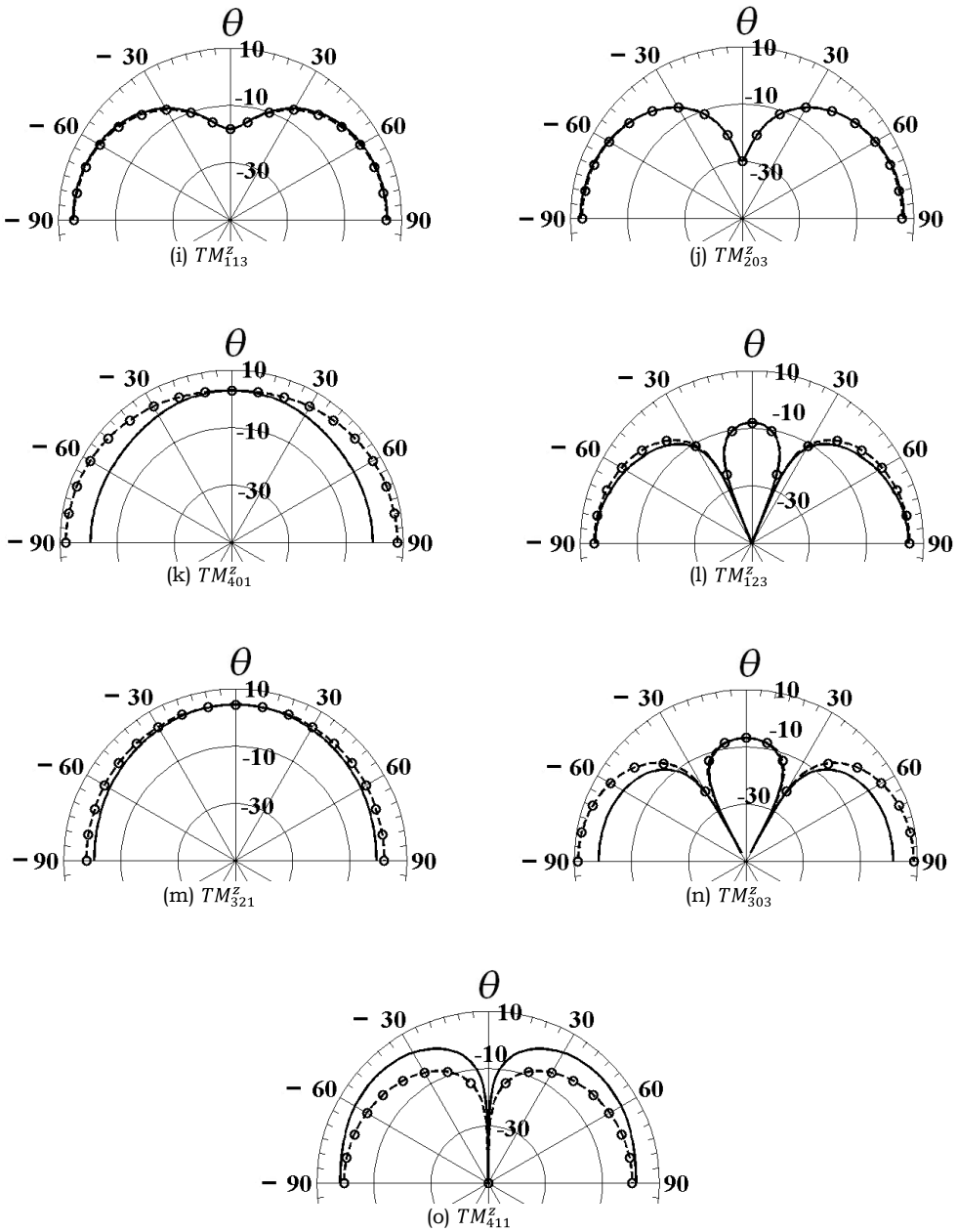

(i) TM^z_{113} (j) TM^z_{203}

(k) TM^z_{401} (l) TM^z_{123}

(m) TM^z_{321} (n) TM^z_{303}

(o) TM^z_{411}

Fig. 9.4 Far-zone E-plane (solid line) and H-plane (circle with dotted line) power patterns with absolute gain (in dB) of 30°–60°–90° TDRA for different TM^z_{mnp} modes ($a = 66mm, d = 24mm, \varepsilon_r = 12, tan\,\delta = 0.0005$)

From Fig. 9.4, it is found that a small dip in the broadside direction is produced for TM^z_{103} Mode. The magnitude of dip is large enough for TM^z_{113} and TM^z_{203} modes. By selecting proper dimensions and relative permittivity of the 30°–60°–90° TDRA, we can easily remove such dip from the radiation patterns

as shown in Fig. 9.5. Typical results are shown for TM^z_{203} mode in Fig. 9.5. In similar fashion, we can easily stop the beam splitting property for TM^z_{123} and TM^z_{303} modes. Typical results are shown for TM^z_{303} mode in Fig. 9.5. Further, it is found that TM^z_{411} mode is the first mode which produces a null in the broadside direction.

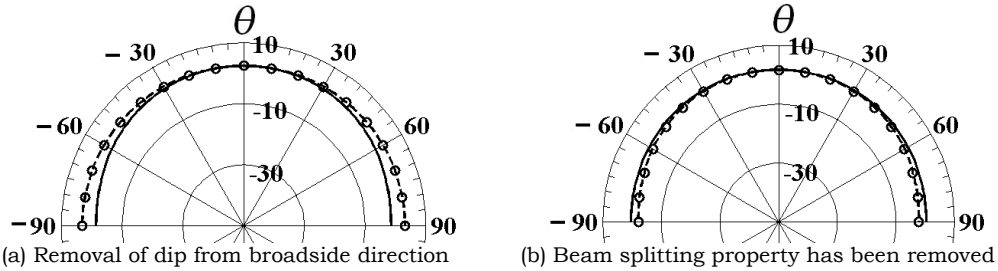

(a) Removal of dip from broadside direction for TM^z_{203} mode

(b) Beam splitting property has been removed for TM^z_{123} mode

Fig. 9.5 Improvement of far-zone E-plane (solid line) and H-plane (circle with dotted line) power patterns with absolute gain (in dB) of 30°–60°–90° TDRA ($a = 66mm, d = 24mm, \varepsilon_r = 82, tan\,\delta = 0.0005$)

For experimental validation, a 30°–60°–90° TDRA having $a = 66mm, d = 24mm, \varepsilon_r = 12$ and $tan\,\delta = 0.0005$ is fabricated at our laboratory. The antenna is excited using 50Ω coaxial probe. The probe has radius equal to 0.63mm. Far-field radiation patterns are measured for fundamental TM^z_{101} mode. The measured data are compared with theoretical results as shown in Fig. 9.6. It is found that our theoretical results are in good agreement with experimental data. Little discrepancy is found. This is due to the finite size of metallic ground plane.

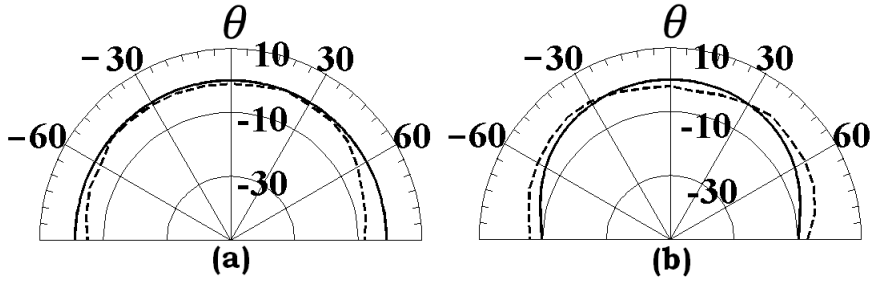

Fig. 9.6 Comparison of far-field radiation patterns between our theory (in solid) and experimental data (in dashed) for TM^z_{101} mode of 30°–60°–90° TDRA (a) E-plane (φ = 0°) (b) H-plane (φ = 90°) (a = 48mm, h = 7.8mm, ε_r = 25)

For further verification, theoretical results for different TM^z_{mnp} modes are compared with data obtained using 3D EM simulator HFSS [9] as shown in Fig. 9.7. It is clear from Fig. 9.7 that our theoretical results are in good agreement with data obtained using 3D EM simulator HFSS. Little discrepancy is found especially for TM^z_{221} mode. The size of the finite ground is taken sufficiently large. Therefore, the distortion in the far-field patterns is mainly due to the effect of excitation which is not used in our source free theory.

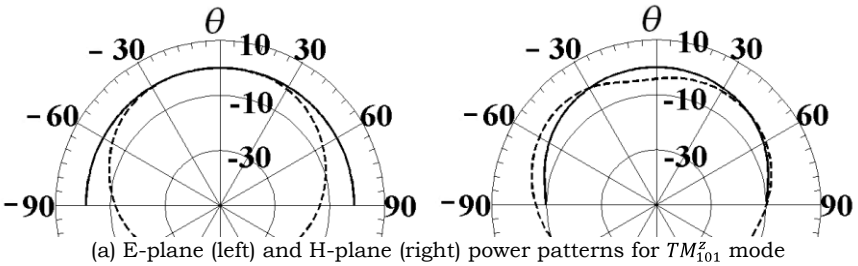

(a) E-plane (left) and H-plane (right) power patterns for TM^z_{101} mode

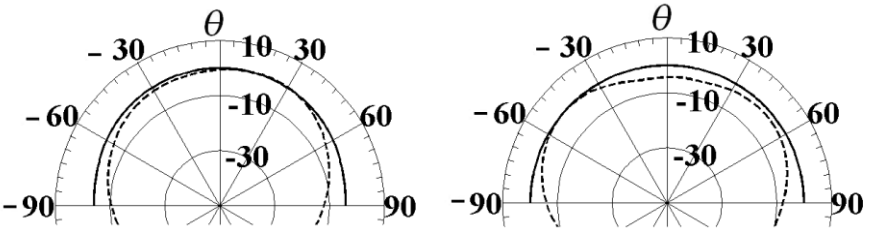

(b) E-plane (left) and H-plane (right) power patterns for TM^z_{111} mode

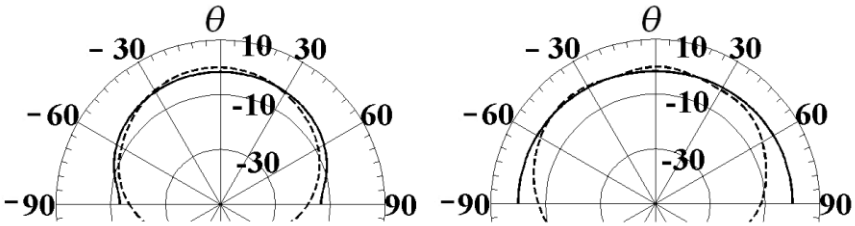

(c) E-plane (left) and H-plane (right) power patterns for TM^z_{301} mode

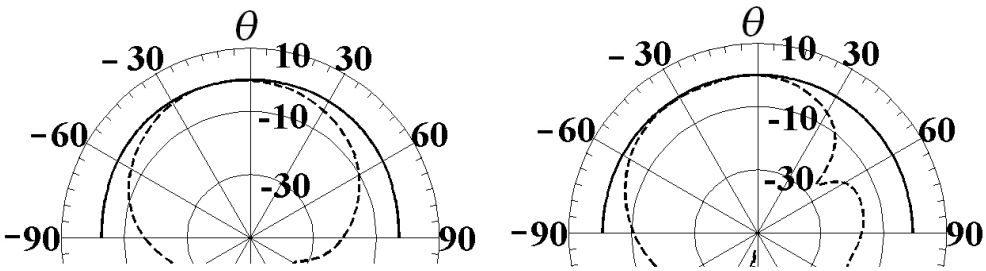

(d) E-plane (left) and H-plane (right) power patterns for TM^z_{221} mode

Fig. 9.7 Comparison between theoretical (in solid line) and simulated (in dotted line) normalized power patterns for different TM^z_{mnp} modes: ($a = 48mm, d = 7.8mm, \varepsilon_r = 25, tan\,\delta = 0.0005$)

9.3.3 Radiated Power, Quality factor, Efficiency and Gain

In this analysis, the effect of feed mechanism is not considered. Stored energy, different types of losses within the TDRA, radiated power in percentage $\left(P_r(\text{in }\%)\right)$ which is calculated in terms of radiation Q-factor (Q_r) [15] as $P_r(\text{in }\%) = 2\pi/Q_r \times 100\%$, total Q-factor (Q_t), bandwidth (BW), efficiency (e), gain (G) are calculated without considering the effect of excitation. A general MATLAB code is written to obtain various quantities for different TM^z_{mnp} modes. Typical theoretical results on P_r, Q_r, Q_t, BW, G and e for various modes of a source free 30°–60°–90° TDRA having $a = 66mm, d = 24mm$ and $\varepsilon_r = 12$ are shown in Table 9.4. From Table 9.4, it is found that higher order TM^z_{mnp} modes can produce more gain compared to fundamental TM^z_{101} mode. Therefore, by selecting the proper material and dimensions of 30°–60°–90° TDRA, a higher order mode may give an enhanced gain over TM^y_{101} mode.

Variation of $P_r(\%)$, Q_r, Q_t, e and G with resonant frequencies for fixed value of (a/d) ratio are shown in Fig. 9.8 for different TM^z_{mnp} modes. It is found that for a fixed value of aspect ratio (a/d), these quantities are almost constant except radiation efficiency (e) as found for rectangular DRA and equilateral TDRAs. In case of radiation efficiency (e), small variation is found for small size of 30°–60°–90° TDRA .

Variations of $P_r(\%), Q_r, Q_t, BW, e$ and G with (a/d) ratio for fixed value of a are shown in Fig. 9.9 for first few modes. Numerical instability occurs in the evaluation of G . This may be due to non-consideration of feed in our source free theory as explained in the case of the Equilateral TDRA (Chapter VIII) and is not repeated here for the sake of brevity.

Table 9.4

Radiation characteristics of various TM^z_{mnp} modes

($a = 66mm, d = 24mm, \varepsilon_r = 12, tan\delta = 0.0005$)

Sl No	Mode	f_r (GHz)	$P_r(\%)$	$e(\%)$	Q_r	Q_t	BW (%)	Gain (dB)
1	TM^z_{101}	1.178	15.02	97.63	41.84	40.85	1.731	4.715
2	TM^z_{111}	1.592	12.09	97.13	51.97	50.47	1.401	4.394
3	TM^z_{201}	1.763	20.52	98.3	30.62	30.1	2.349	4.522
4	TM^z_{211}	2.197	12.4	97.25	50.65	49.26	1.436	5.122
5	TM^z_{301}	2.444	15.59	97.81	40.3	39.42	1.794	6.445
6	TM^z_{221}	2.774	15.57	97.82	40.36	39.48	1.791	6.299
7	TM^z_{103}	2.809	8.269	96.71	75.98	73.48	0.9623	6.405
8	TM^z_{311}	2.875	11.14	96.99	56.38	54.68	1.293	5.204
9	TM^z_{113}	3.006	6.377	95.76	98.53	94.35	0.7494	13.36
10	TM^z_{203}	3.1	6.318	95.71	99.44	95.18	0.7429	7.58
11	TM^z_{401}	3.16	10.87	96.92	57.8	56.02	1.262	7.86
12	TM^z_{213}	3.366	2.31	89.04	272	242.2	0.2919	7.171
13	TM^z_{231}	3.422	13.38	97.5	46.96	45.78	1.545	5.213
14	TM^z_{303}	3.533	3.184	91.78	197.3	181.1	0.3904	9.574
15	TM^z_{411}	3.585	5.796	94.41	108.4	102.3	0.6909	8.377
16	TM^z_{223}	3.768	2.203	88.51	285.3	252.5	0.2801	10.27
17	TM^z_{133}	3.844	1.665	85.33	377.4	322	0.2196	8.757
18	TM^z_{501}	3.892	12.94	97.43	48.54	47.29	1.495	6.526
19	TM^z_{331}	4.037	15.49	97.84	40.56	39.69	1.782	7.803
20	TM^z_{403}	4.061	1.504	83.97	417.8	350.9	0.2015	10.73
21	TM^z_{241}	4.107	10	96.7	62.81	60.74	1.164	5.818
22	TM^z_{323}	4.268	1.375	82.7	456.8	377.8	0.1872	7.634
23	TM^z_{511}	4.312	9.474	96.53	66.32	64.02	1.105	6.91
24	TM^z_{143}	4.4	0.8194	73.99	766.8	567.4	0.1246	10.28
25	TM^z_{105}	4.572	5.586	94.27	112.5	106	0.6669	10.08

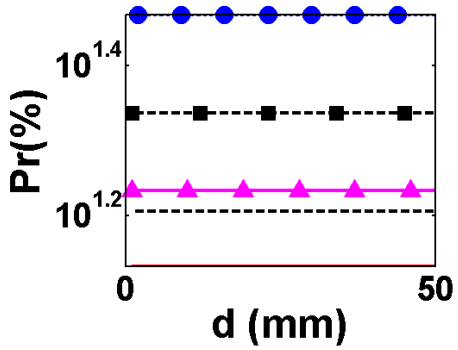

(a) Variation of $P_r(\%)$ with d

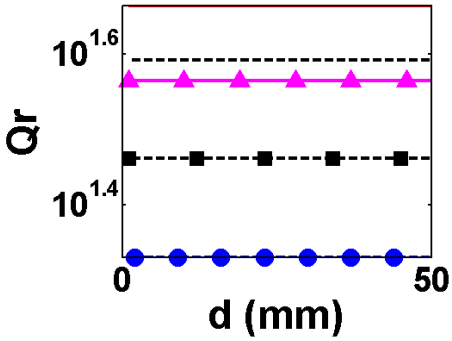

(b) Variation of Q_r with d

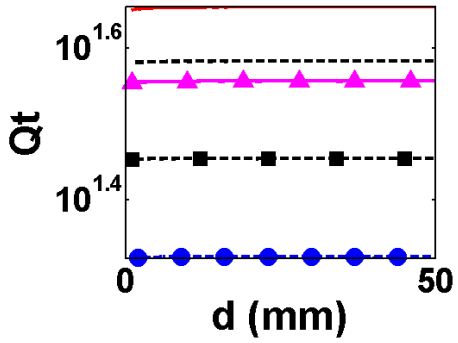

(c) Variation of Q_t with d

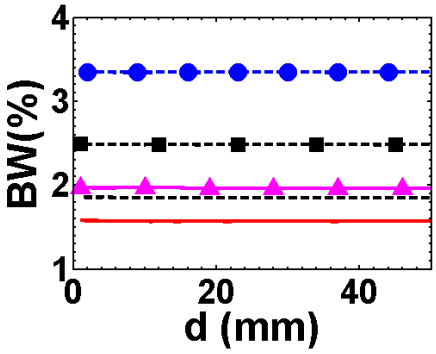

(d) Variation of BW with d

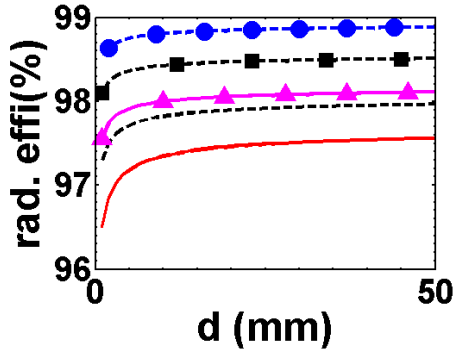

(e) Variation of rad. efficiency with d

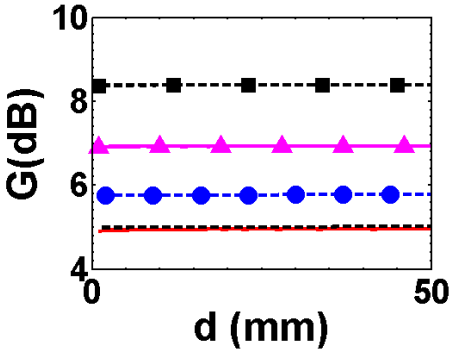

(f) Variation of $G(\mathrm{dB})$ with d

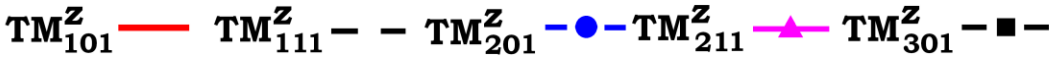

Fig 9.8 Radiation characteristics of 30°–60°–90° TDRA for fixed a/d ratio
($a/d = 1,\ \varepsilon_r = 12, \tan\delta = 0.0005$)

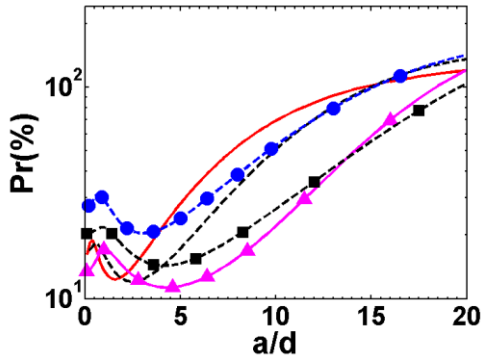

(a) Variation of $P_r(\%)$ with (a/d) ratio

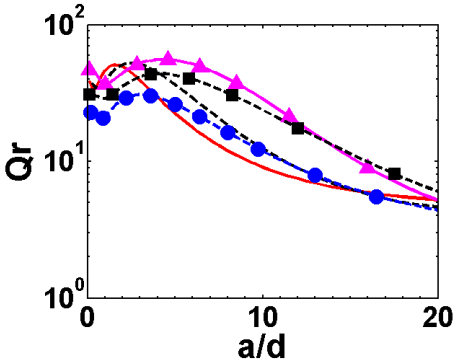

(b) Variation of Q_r with (a/d) ratio

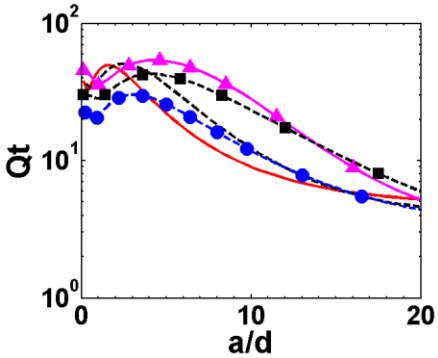

(c) Variation of Q_t with (a/d) ratio

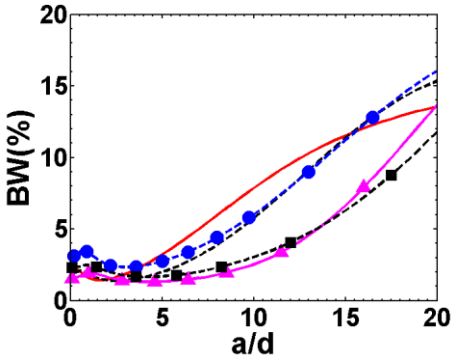

(d) Variation of BW with (a/d) ratio

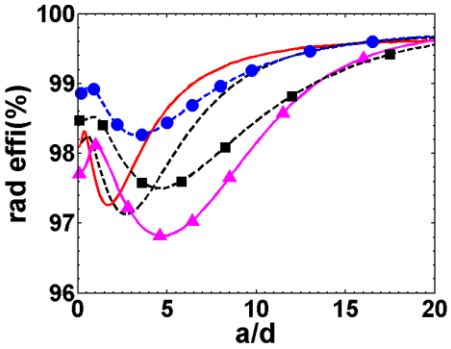

(e) Variation of rad. efficiency with (a/d) ratio

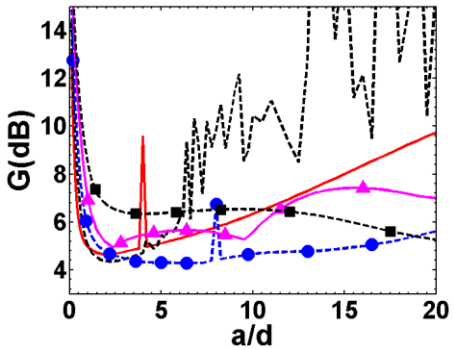

(f) Variation of $G(\mathrm{dB})$ with (a/d) ratio

TM^z_{101} TM^z_{111} TM^z_{201} TM^z_{211} TM^z_{301}

Fig 9.9 Radiation characteristics of 30°–60°–90° TDRA for different TM^z_{mnp} modes with (a/d) ratio: $(a = 66mm, \varepsilon_r = 12, \tan\delta = 0.0005)$

9.3.4 Input Impedance

Evaluation of input impedance (Z_{in}) using parameter (a, d) instead of (a_e, d_e) along with necessary explanation is discussed in detail for equilateral

TDRA in Chapter VIII. Similar phenomena is also found for 30°–60°–90° TDRA where effective length a_e at fundamental TM^z_{101} is almost nearly equal to $0.55 \times a$. Confinement of electric field in the middle portion of the 30°–60°–90° TDRA is shown in Fig. 9.10. Theoretical electric field distribution is shown in Fig. 9.11 for comparison purpose.

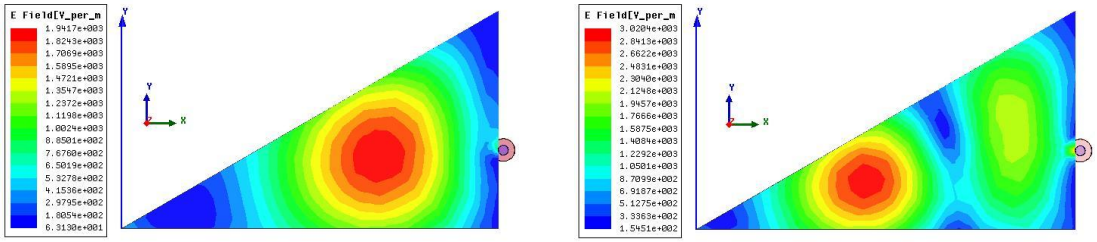

(a) TM^z_{101} mode (b) TM^z_{201} mode

Fig. 9.10 Confinement of $\vec{E}$-field which avoid the corners within the 30°–60°–90° TDRA bounded by PMC for different modes (a = 66mm, d = 24mm, ε_r = 12) (a) TM^z_{101} mode (b) TM^z_{201} mode

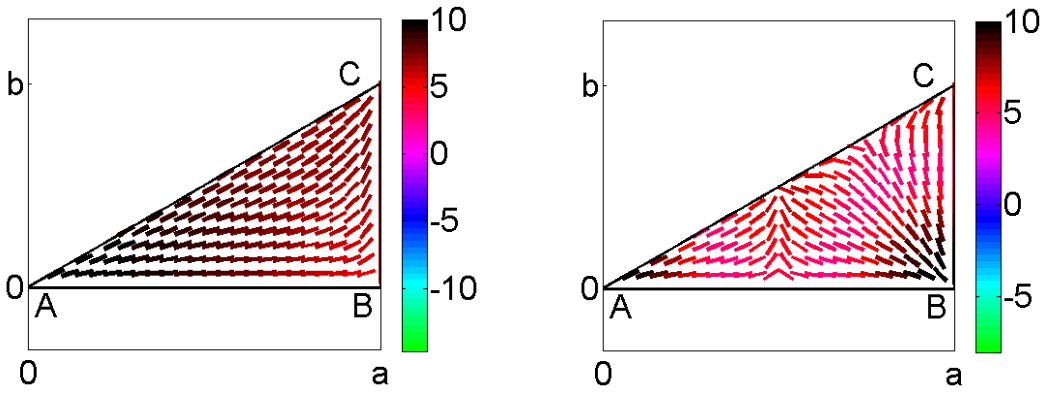

(a) TM^z_{101} mode (b) TM^z_{201} mode

Fig. 9.11 Theoretical (source free theory) $\vec{E}$-field distribution (in dB) within the 30°–60°–90° TDRA for different modes (a = 66mm, d = 24mm, ε_r = 12) (a) TM^z_{101} mode (b) TM^z_{201} mode

As our theory does not include the effect of excitation, in some cases, probe position (x_o, y_o) may eventually be outside the 30°–60°–90° TDRA (i.e. $|x_o| > |a_e|$). For example, we can easily excite the fundamental TM^z_{101} mode $(a = 66mm)$ by placing the probe inside the TDRA either near corner A (for example, $x_o = 15mm, y_o = 6mm$) or near corner C (for example, $x_o = 58mm, y_o = 32mm$). In the second case, we will face difficulty to compute Z_{in} using $a_e (\cong 0.55 \times a \cong 36.3mm)$ because $x_o > a_e$. Therefore, Z_{in} is computed considering the base of the triangle

at its actual value 'a' instead of the effective value 'a_e' and is plotted against normalized frequency. Theoretical input impedance is compared with experimental data for TM^z_{101} mode in Fig. 9.12 . Measured Q_t is used for theoretical computation. It is found that there is little discrepancy between our theory and experimental data and they are in good agreement. This small discrepancy is due to the air gap between the probe and TDRA. Hand-drill is used to make the hole inside the TDRA. The diameter of the hole is 1.8mm (approx.) whereas the diameter of the probe is 1.22mm. Further, the length of the hole (17mm approx.) is also slightly longer than the probe length ($PL = 16mm$). The effect of the resulting air gap is not included in our theory.

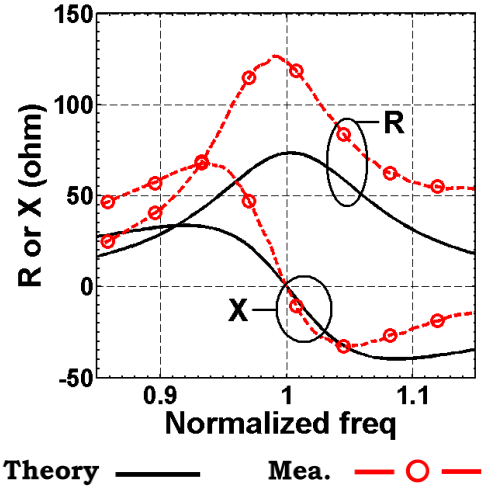

Fig 9.12 Comparison of input impedance with experimental data for TM^z_{101} mode of 30°–60°–90° TDRA ($a = 39mm,\ d = 25mm, \varepsilon_r = 10, x_o = 17mm, y_o = 5.2mm, PL = 16mm$)

9.4 Conclusion

In this chapter, theoretical investigation on 30°–60°–90° Triangular Dielectric Resonator Antenna (TDRA) is presented for TM^z_{mnp} modes for the first time. The 30°–60°–90° TDRA is modeled here as source free cavity enclosed by Perfect Magnetic Conductors (PMC) for theoretical investigations. Approximate solution for the eigenfunctions and eigenvalues are given here. Closed form analytic expressions to predict the far-zone electric field are also given here. Radiated power in percentage $P_r(\%)$, Radiation Q-factor (Q_r), total stored energy (W_t), bandwidth (BW), efficiency (e), gain (G) etc. are also discussed here. Theoretical results are compared with experimental data and data obtained using the 3D EM simulator to show the accuracy of our theory. From this theoretical investigation, it is found that:

- Radiation characteristics of a 30°–60°–90° TDRA for different TM^z_{mnp} modes are mainly controlled by the choice of modal indices m and n as found for equilateral TDRA.
- TM^z_{411} mode is the first mode which produces a null in the broadside direction.
- Higher order modes can produce higher gain compared to fundamental TM^z_{101} mode by selecting proper dimensions and relative permittivity of the 30°–60°–90° TDRA
- For a given mode, radiated power in percentage $P_r(\%)$, total Q-factor (Q_t), efficiency (e), gain (G) etc. are almost same for fixed values of aspect ratio (a/d) and relative permittivity of the 30°–60°–90° TDRA.

Chapter X

45°–45°–90° Triangular Dielectric Resonator Antenna

10.1 Introduction

In Chapters VIII and IX, theoretical investigations on equilateral and 30°–60°–90° shaped Triangular Dielectric Resonator Antennas (TDRAs) are presented respectively. In this chapter, we will present the theoretical investigations on isosceles 45°–45°–90° TDRA. The analysis on isosceles 45°–45°–90° TDRA made up with low loss dielectric material is very important in terms of size. It takes just half volume of a square shaped Dielectric Resonator Antenna (DRA) for a given frequency as shown in this chapter.

Literature survey shows that experimental investigations on prediction of resonant frequency for different TM^z_{mn} modes of an isosceles 45°–45°–90° Triangular Microstrip Antenna (TMA) have been reported only [149]. We have theoretically investigated the radiation characteristics of an isosceles 45°–45°–90° TMA as shown in Chapter V for the first time. On the other hand, isosceles 45°–45°–90° TDRA as yet not receive much attention. Experimental investigations on isosceles 45°–45°–90° TDRA has been reported by R. K. Mongia *et al* in 1994 [106]. Besides that, there is no other work on isosceles 45°–45°–90° TDRA. Detailed literature survey on 45°–45°–90° triangular shaped antennas including both microstrip antenna (MA) and DRA are presented in Chapter II.

In this chapter, theoretical investigations on isosceles 45°–45°–90° TDRA are presented for the first time. Simple dielectric waveguide model is used to investigate it. For theoretical investigation, all surfaces of the isosceles 45°–45°–90° TDRA are modeled as Perfect Magnetic Conductors (PMC). Approximate solution for the eigenfunctions (ψ) and eigenvalues of a source

free isosceles 45°–45°–90° TDRA are given here for TM^z modes. Approximate expression is also given here to predict the resonant frequency. Closed form expressions for far-field radiation patterns of arbitrary TM^z_{mnp} modes are given here using 'Equivalence Principle' [10] for the first time. Theoretical results are compared with experimental data and data obtained using 3D EM simulator HFSS to show the accuracy of our theory for different dimensions and relative permittivity of the antenna.

10.2 Theory

In this section, theoretical investigations on source free isosceles 45°–45°–90° TDRA having equal side length a, height d and relative permittivity ε_r as shown in Fig. 10.1 is presented. Standard Cartesian coordinate system is used to represent the antenna geometry. The antenna is placed on a metallic ground, whose size is sufficiently large compared to the largest dimension of isosceles 45°–45°–90° TDRA. It is found that the isosceles 45°–45°–90° TDRA supports TM^z mode. Therefore, TM^z mode of 45°–45°–90° TDRA is discussed here. Eigenfunctions, eigenvalues, resonant frequency (f_r), far-field radiation patterns, radiated power, gain, Q-factor, gain, bandwidth etc. are investigated.

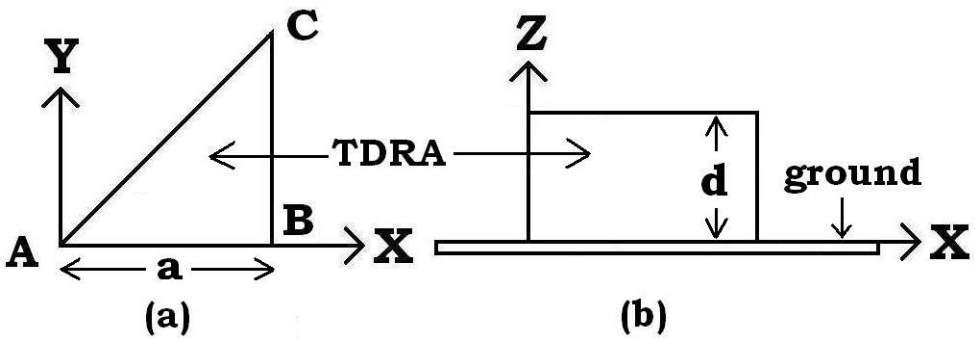

Fig. 10.1 Antenna configuration (a) top view (b) side view

10.2.1 Eigenfunctions

In Fig. 10.1, the antenna geometry is shown where the source free

isosceles 45°–45°–90° TDRA is placed on a ground plane at $z = 0$ surface. The origin is placed at the apex (point A) of the triangular geometry as shown in Fig. 10.1(a). To remove the effect of ground plane on the performance of the TDRA, image theory is applied and the process results an source free isolated isosceles 45°–45°–90° TDRA having equal side length a, height h where $h = 2d$. Simple magnetic wall dielectric waveguide model is applied here to find the approximate solution of eigenfunctions $\left(\psi(x,y,z)\right)$ for an arbitrary TM^z_{mnp} modes.

Due to the existence of one inclined plane AC side as shown in Fig. 10.1 in x-y plane, it is better to express the eigenfunctions $\left(\psi(x,y,z)\right)$ as $\psi(x,y,z) = F(x,y) \times H(z)$. Here, $F(x,y)$ is the standing wave solution along the x-y direction, whereas $H(z)$ is the standing wave solution along the z-direction. This simplifies the evaluation of the eigenfunctions in terms of $F(x,y)$ and $H(z)$ functions separately using method of separation.

The evaluation of $F(x,y)$ function is exactly same as derived for isosceles 45°–45°–90° Triangular Microstrip Antenna (TMA) and is not repeated here for brevity. Therefore, the solution for $F(x,y)$ function is:

$$F(x,y) = \left[cos\left(\frac{m\pi}{a}x\right)cos\left(\frac{n\pi}{a}y\right) + cos\left(\frac{n\pi}{a}x\right)cos\left(\frac{m\pi}{a}y\right)\right] \tag{10.1}$$

where m, n are modal indices. The evaluation of $H(z)$ function is quite similar to equilateral and 30°–60°–90° TDRAs. After applying Perfect Magnetic Conductors (PMC) at $z = \pm d$, $H(z)$ can be expressed for TM^z_{mnp} modes as:

$$H(z) = D \times sin\left(k_z(d-z)\right); \quad k_z = p\pi/(2d) \; ; \; p = 1,2,3,4 \ldots \tag{10.2}$$

Here, D is a constant. Therefore, the approximate solution of eigenfunctions for TM^z_{mnp} modes of a source free isosceles 45°–45°–90° TDRA is:

$$\psi = \left[cos\left(\frac{m\pi}{a}x\right)cos\left(\frac{n\pi}{a}y\right) + cos\left(\frac{n\pi}{a}x\right)cos\left(\frac{m\pi}{a}y\right)\right] \times sin[k_z(d-z)] \tag{10.3}$$

The complete electric and magnetic fields inside the isosceles 45°–45°–90°

TDRA can be expressed for TM^z_{mnp} modes as:

$$E_x = \left(\frac{-jA}{\omega\mu\varepsilon}\right)\left[-\frac{m\pi}{a}\sin\left(\frac{m\pi x}{a}\right)\cos\left(\frac{n\pi y}{a}\right) - \frac{n\pi}{a}\sin\left(\frac{n\pi x}{a}\right)\cos\left(\frac{m\pi y}{a}\right)\right](-k_z)\cos[k_z(d-z)]$$

$$E_y = \left(\frac{-jA}{\omega\mu\varepsilon}\right)\left[-\frac{n\pi}{a}\cos\left(\frac{m\pi x}{a}\right)\sin\left(\frac{n\pi y}{a}\right) - \frac{m\pi}{a}\cos\left(\frac{n\pi x}{a}\right)\sin\left(\frac{m\pi y}{a}\right)\right](-k_z)\cos[k_z(d-z)]$$

$$E_z = \left(\frac{-jA}{\omega\mu\varepsilon}\right)(\chi^2)\left[\cos\left(\frac{m\pi x}{a}\right)\cos\left(\frac{n\pi y}{a}\right) + \cos\left(\frac{n\pi x}{a}\right)\cos\left(\frac{m\pi y}{a}\right)\right]\sin[k_z(d-z)]$$

$$H_x = \left(\frac{A}{\mu}\right)\left[-\frac{n\pi}{a}\cos\left(\frac{m\pi x}{a}\right)\sin\left(\frac{n\pi y}{a}\right) - \frac{m\pi}{a}\cos\left(\frac{n\pi x}{a}\right)\sin\left(\frac{m\pi y}{a}\right)\right]\sin[k_z(d-z)]$$

$$H_y = \left(\frac{-A}{\mu}\right)\left[-\frac{m\pi}{a}\sin\left(\frac{m\pi x}{a}\right)\cos\left(\frac{n\pi y}{a}\right) - \frac{n\pi}{a}\sin\left(\frac{n\pi x}{a}\right)\cos\left(\frac{m\pi y}{a}\right)\right]\sin[k_z(d-z)]$$

$$H_z = 0 \qquad (10.4)$$

where A is a constant and other notations are carrying their usual meaning. It is important to have some knowledge on internal electric and magnetic field distribution for different modes in hand. It will help to identify modes without plotting any field. Typical results are shown in Figs. 10.2 - 10.4 for some modes.

10.2.2 Resonant Frequency

Resonant frequency can easily be evaluated using separation equation $\left(\chi^2 + k_z^2 = \varepsilon_r k_0^2 \text{ where } \chi = (\pi/a)(m^2+n^2)^{1/2}\right)$. Therefore, the resonant frequency of an isolated source free isosceles 45°–45°–90° TDRA for an arbitrary TM^z_{mnp} mode is evaluated as:

$$f_r = \frac{c}{2\pi\sqrt{\varepsilon_r}} \times \left[\left(\frac{\pi}{a}\right)^2 (m^2+n^2) + k_z^2\right]^{1/2} \qquad (10.5)$$

where c is the velocity of light in free space. Substituting $m = 1, n = 0$ and $p = 1$ in equation (10.5) for fundamental TM^z_{101} mode of operation, the resonant frequency (f_r) is evaluated as:

$$f_r = \frac{c}{2\pi\sqrt{\varepsilon_r}} \times \left[\left(\frac{\pi}{a}\right)^2 + \left(\frac{\pi}{2d}\right)^2\right]^{1/2} \tag{10.6}$$

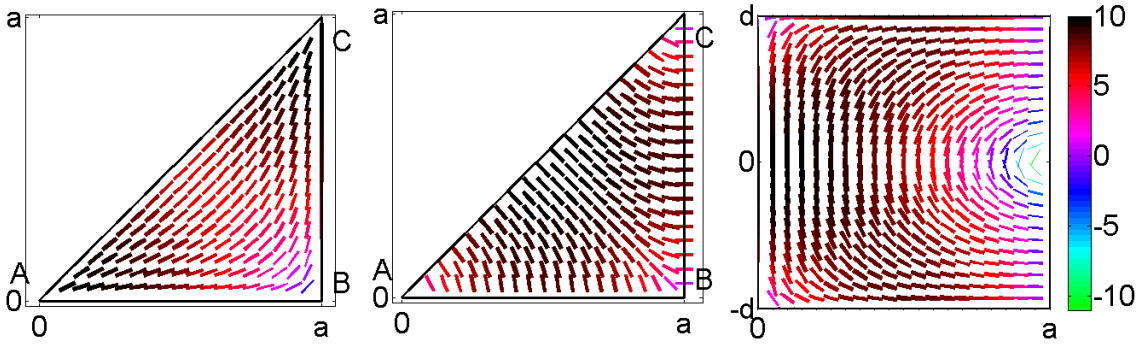

(a) (b) (c)

Fig. 10.2 Internal field distribution for TM^z_{101} mode (a = 66mm, d = 24mm, ε_r = 12)
(a) $\vec{E}$ field patterns at $z = d/2$ plane (b) $\vec{H}$ field patterns at $z = d/2$ plane (c) $\vec{E}$ field patterns at $y = 0$ plane

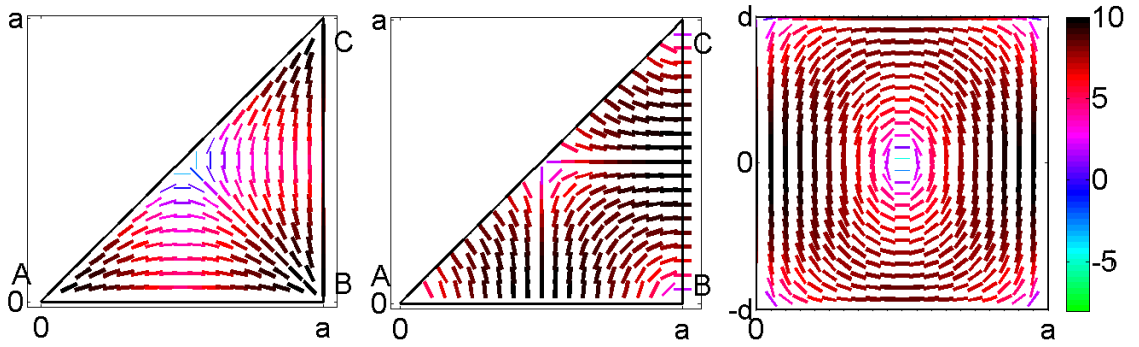

(a) (b) (c)

Fig. 10.3 Internal field distribution for TM^z_{111} mode (a = 66mm, d = 24mm, ε_r = 12)
(a) $\vec{E}$ field patterns at $z = d/2$ plane (b) $\vec{H}$ field patterns at $z = d/2$ plane (c) $\vec{E}$ field patterns at $y = 0$ plane

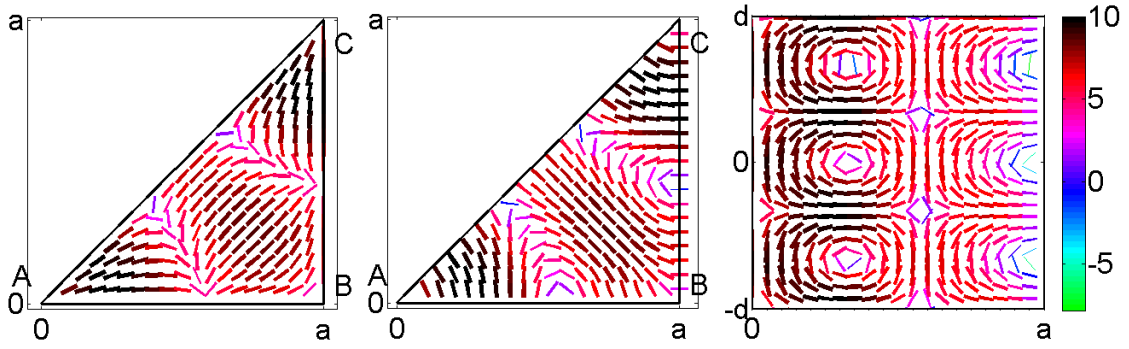

(a) (b) (c)

Fig. 10.4 Internal field distribution for TM^z_{213} mode (a = 66mm, d = 24mm, ε_r = 12)
(a) $\vec{E}$ field patterns at $z = d/2$ plane (b) $\vec{H}$ field patterns at $z = d/2$ plane (c) $\vec{E}$ field patterns at $y = 0$ plane

A close look on $\chi\left(=(\pi/a)(m^2+n^2)^{1/2}\right)$ reveals that a square DRA has the same value for χ according to magnetic wall model of DRA. Therefore, 45°–45°–90° TDRA will take just half volume compared to a square DRA having side a for same resonant frequency. Hence, the analysis on 45°–45°–90° TDRA is important in terms of space utilization.

To have an idea on different modes of a 45°–45°–90° TDRA, the resonant frequencies are computed for different TM^z_{mnp} modes as shown in Table 10.1.

Table 10.1

Resonant frequencies for first few modes of a 45°–45°–90° TDRA

$(a = 66mm, d = 24mm, \varepsilon_r = 12)$

Sl No	Mode	Resonant Frequency (GHz)		Sl No	Mode	Resonant Frequency (GHz)
1	TM^z_{101}	1.1150		11	TM^z_{411}	2.8503
2	TM^z_{111}	1.2935		12	TM^z_{113}	2.8597
3	TM^z_{201}	1.5917		13	TM^z_{331}	2.9248
4	TM^z_{211}	1.7215		14	TM^z_{203}	3.0064
5	TM^z_{221}	2.0624		15	TM^z_{421}	3.0683
6	TM^z_{301}	2.1642		16	TM^z_{213}	3.0771
7	TM^z_{311}	2.2614		17	TM^z_{223}	3.2800
8	TM^z_{321}	2.5306		18	TM^z_{303}	3.3449
9	TM^z_{401}	2.7739		19	TM^z_{501}	3.4007
10	TM^z_{103}	2.7835		20	TM^z_{313}	3.4086

Some isosceles 45°–45°–90° TDRAs are simulated using 3D EM simulator HFSS [9]. It is found that theoretical resonant frequencies are always smaller than the corresponding data obtained using the 3D EM simulator as shown in Table 10.2. This can easily be explained with respect to electric field lines which tend to avoid the corner for PMC boundary by applying the duality principle as explained by S. A. Schelkunoff in case of metallic waveguide for magnetic field lines [24]. This phenomenon is explained in detail for equilateral TDRA in Chapter VIII and is not repeated here for the sake of brevity. Similar observation is also found for 30°–60°–90° TDRAs as shown in Chapter IX. Accordingly, the effective length a_e of an isosceles 45°–45°–90° TDRA for

various TM^z_{mnp} modes is expressed as:

$$a_e = 1.901 \times 10^{-12}t - 4.022 \times 10^{-10}t + 3.584 \times 10^{-8}t - 1.755 \times 10^{-6}t + 5.169 \times 10^{-5}t - 0.0009408t + 0.01051t - 0.07023t + 0.2782t + 0.3333t \;;\; t = |m|^2 + |n|^2 \quad (10.7)$$

Table 10.2

Comparison of resonant frequencies with HFSS [9]

$(a = 30mm, d = 10mm, \varepsilon_r = 40)$

Mode	Resonant Frequency (GHz)		Error (%)
	Theoretical	HFSS [9]	
TM^z_{101}	1.4246	1.85	22.99
TM^z_{111}	1.6291	2.02	19.35
TM^z_{201}	1.9756	2.33	15.21

10.2.3 Far-Field Radiation Patterns

Literature survey shows that there is no theoretical work on isosceles 45°–45°–90° TDRA. Therefore, we take the opportunity to predict the far-field radiation patterns of an isosceles 45°–45°–90° TDRA for different TM^z_{mnp} modes for the first time. To find the far field radiation patterns for arbitrary TM^z_{mnp} modes of operation, 'Equivalence Principle' [4, 16] is applied. All surfaces of the isosceles 45°–45°–90° TDRA are modeled as Perfect Magnetic Conductors (PMC) for theoretical investigation. Thereafter, the magnetic surface currents on each surface are evaluated as $\vec{M}_s = \vec{E} \times \hat{n}$. The procedure for evaluating various components of far-zone electric field are similar to Equilateral TDRA (ETDRA) or 30°–60°–90° TDRA and are not repeated here for brevity. Therefore, the total far-zone electric field at point $P(r, \theta, \varphi)$ is evaluated as [16]:

$$E_\theta = -\frac{jk_o \exp(-jk_o r)}{4\pi r} \times \left[L_\varphi + \eta_0 N_\theta\right] \quad (10.8)$$

$$E_\varphi = \frac{jk_o \exp(-jk_o r)}{4\pi r} \times \left[L_\theta - \eta_0 N_\varphi\right] \quad (10.9)$$

where,

$$N_\theta = A_x cos(\theta)cos(\varphi) + A_y cos(\theta)sin(\varphi) - A_z sin(\theta)$$
$$N_\varphi = -A_x sin(\varphi) + A_y cos(\varphi)$$
$$L_\theta = F_x cos(\theta)cos(\varphi) + F_y cos(\theta)sin(\varphi) - F_z sin(\theta)$$
$$L_\varphi = -F_x sin(\varphi) + F_y cos(\varphi) \qquad (10.10)$$

$$F_x = F_x^{AC} + F_x^{AB} + F_x^{Top} + F_x^{Bottom}$$
$$F_y = F_y^{AC} + F_y^{BC} + F_y^{Top} + F_y^{Bottom}$$
$$F_z = F_z^{AC} + F_z^{AB} + F_z^{BC}$$
$$A_x = A_y = A_z = 0 \qquad (10.11)$$

$$F_x^{AC} = C_{xy} \times [-E_3] \times (\chi^2) \times I_{AC}^{x} \times I_{zS}^{PMC}$$
$$I_{AC}^{x} = \frac{j\chi_1}{((m+n)^2 b^2 - \chi_1^2)} \times \left[e^{j\chi_1 a} \times \cos\big((m+n)\pi\big) - 1\right]$$
$$+ \frac{j\chi_1}{((m-n)^2 b^2 - \chi_1^2)} \times \left[e^{j\chi_1 a} \times \cos\big((m-n)\pi\big) - 1\right] \quad ; \quad b = (\pi/a) \qquad (10.12)$$

$$F_y^{AC} = C_{xy} \times [-E_3] \times (\chi^2) \times I_{AC}^{y} \times I_{zS}^{PMC}$$
$$I_{AC}^{y} = \frac{j\chi_1}{((m+n)^2 b^2 - \chi_1^2)} \times \left[e^{j\chi_1 a} \times \cos\big((m+n)\pi\big) - 1\right]$$
$$+ \frac{j\chi_1}{((m+n)^2 b^2 - \chi_1^2)} \times \left[e^{j\chi_1 a} \times \cos\big((m-n)\pi\big) - 1\right] \qquad (10.13)$$

$$F_z^{AC} = C_{xy} \times [E_1 \times I_{AC}^{zx1} + E_2 \times I_{AC}^{zx2}] \times (-k_z) \times I_{zC}^{PMC}$$
$$I_{AC}^{zx1} = -\frac{\pi}{2a} \frac{b(m+n)^2}{\left[\big(b(m+n)\big)^2 - \chi_1^2\right]} \times \left[e^{j\chi_1 a} \cos\big((m+n)\pi\big) - 1\right]$$
$$-\frac{\pi}{2a} \frac{b(m-n)^2}{\left[\big(b(m-n)\big)^2 - \chi_1^2\right]} \times \left[e^{j\chi_1 a} \cos\big((m-n)\pi\big) - 1\right] \qquad (10.14)$$
$$I_{AC}^{zx2} = -\frac{\pi}{2a} \frac{b(m+n)^2}{\left[\big(b(m+n)\big)^2 - \chi_1^2\right]} \times \left[e^{j\chi_1 a} \cos\big((m+n)\pi\big) - 1\right]$$
$$+ \frac{\pi}{2a} \frac{b(m-n)^2}{\left[\big(b(m-n)\big)^2 - \chi_1^2\right]} \times \left[e^{j\chi_1 a} \cos\big((m-n)\pi\big) - 1\right] \qquad (10.15)$$

$$F_x^{AB} = C_{xy} \times E_3 \times (\chi^2) \times I_{AB}^x \times I_{zS}^{PMC}$$

$$I_{AB}^x = \frac{ja\chi_2}{\pi[m^2 - \chi_2^2]} \times \left[e^{jV_1 a}\, cos(\pi m) - 1\right] + \frac{ja\chi_2}{\pi[n^2 - \chi_2^2]} \times \left[e^{jV_1 a}\, cos(\pi n) - 1\right] \qquad (10.16)$$

$$F_z^{AB} = C_{xy} \times [-E_1] \times I_{AC}^{zx1} \times (-k_z) \times I_{zC}^{PMC}$$

$$I_{AC}^{zx1} = \frac{m^2}{m^2 - \chi_2^2} \times \left[e^{jV_1 a}\, cos(\pi m) - 1\right] + \frac{n^2}{n^2 - \chi_2^2} \times \left[e^{jV_1 a}\, cos(\pi n) - 1\right] \qquad (10.17)$$

$$F_y^{BC} = C_{xy} \times [E_3] \times (\chi^2) \times e^{jV_1 a} \times I_{BC}^y \times I_{zS}^{PMC}$$

$$I_{BC}^y = \cos(m\pi) \times \frac{jav}{\pi[n^2 - v^2]} \times \left[e^{jV_2 a} \times cos(n\pi) - 1\right]$$

$$+ \cos(n\pi) \times \frac{jav}{\pi[m^2 - v^2]} \times \left[e^{jV_2 a} \times cos(m\pi) - 1\right] \;\; ; \quad v = \frac{aV_2}{\pi} \qquad (10.18)$$

$$F_z^{BC} = C_{xy} \times [-E_2] \times e^{jV_1 a} \times I_{BC}^z \times (-k_z) \times I_{zC}^{PMC}$$

$$I_{BC}^z = \frac{n^2 \cos(m\pi)}{(n^2 - v^2)} \times \left[e^{jV_2 a} \times cos(n\pi) - 1\right] + \frac{m^2 \cos(n\pi)}{(m^2 - v^2)} \times \left[e^{jV_2 a} \times cos(m\pi) - 1\right] \qquad (10.19)$$

$$F_x^{Top} = C_{xy} \times [E_2] \times I_{cs} \times e^{jdV_3} \times (-k_z)\, cos[k_z(d - z)] \quad ; \; z = d$$

$$F_y^{Top} = C_{xy} \times [-E_1] \times I_{sc} \times e^{jdV_3} \times (-k_z)\, cos[k_z(d - z)] \quad ; \; z = d$$

$$F_x^{Bottom} = C_{xy} \times [-E_2] \times I_{cs} \times e^{-jdV_3} \times (-k_z)\, cos[k_z(d - z)] \quad ; \; z = -d$$

$$F_y^{Bottom} = C_{xy} \times [E_1] \times I_{sc} \times e^{-jdV_3} \times (-k_z)\, cos[k_z(d - z)] \quad ; \; z = -d \qquad (10.20)$$

$$I_{zS}^{PMC} = I_s^z = -j \times d \times \left[e^{jk_z d} \times sinc\big((v_3 - k_z)d\big) - e^{-jk_z d} \times sinc\big((v_3 + k_z)d\big)\right]$$

$$I_{zC}^{PMC} = I_c^z d \times \left[e^{jk_z d} \times sinc\big((v_3 - k_z)d\big) + e^{-jk_z d} \times sinc\big((v_3 + k_z)d\big)\right]$$

$$V_1 = sin(\theta)\cos(\varphi) \;\; ; \quad V_2 = sin(\theta)\sin(\varphi) \;\; ; \quad V_3 = cos(\theta)$$

$$\chi_1 = (V_1 + V_2) \quad ; \quad \chi_2 = aV_1/\pi \quad ; \quad v = aV_2/\pi \;\; ; \;\; b = \pi/a \qquad (10.21)$$

Here, E_1, E_2 and E_3 are the amplitudes of E_x, E_y and E_z components respectively, C_{xy} is constant and other terms are carrying their usual meaning.

10.2.4 Radiated Power, Quality factor, Efficiency and Gain

The total quality factor (Q_t) is evaluated as:

$$Q_t = \frac{\omega_r W_t}{P_c + P_d + P_r} \tag{10.22}$$

where ω_r is the resonant frequency, W_t is total stored energy, P_c is conductor loss, P_d is dielectric loss and P_r is radiation loss. These quantities are evaluated using standard procedure as presented in Chapter III.

10.3.5 Input Impedance

The computation of input impedance (Z_{in}) is similar process as demonstrate for rectangular DRA, equilateral TDRA and 30°–60°–90° TDRA in Chapters VII-IX as [4]:

$$Z_{in} = \frac{-j\omega(a_o/I_o)^2}{\omega^2 - \omega_o^2\left(1 + \frac{j}{Q_t}\right)} \tag{10.23}$$

where

$$a_o = \iiint \vec{E}_o . \vec{J}\, dv \tag{10.24}$$

Here, $\vec{E}_o$ is normalized electric field inside the 45°–45°–90° TDRA for a particular mode, $\vec{J}$ is probe current density and other terms carrying their meaning. Probe current density ($\vec{J}$) is modeled here as one dimensional $\hat{z}$ directed current as [4]:

$$\vec{J} = \begin{cases} \hat{z} I_o \dfrac{\sin[k_d(l-z)]}{\sin(k_d l)} \delta(x - x_o)\delta(y - y_o), & z \le l \\ 0 \quad , & z > l \end{cases} \tag{10.25}$$

where $k_d = p\pi/(2l)$, l is probe length and (x_o, y_o) is probe location.

10.3 Results

In this section, theoretical results on resonant frequency, far-field patterns, Q-factor etc. are discussed. Radiation characteristics for various TM^z_{mnp} modes are discussed. Two antenna prototypes are fabricated in our laboratory as shown in Fig. 10.5. Conventional 50Ω coaxial probe is used to excite the isosceles 45°–45°–90° TDRA. The same antenna is also simulated using FEM based commercial numerical 3D EM simulator HFSS [9].

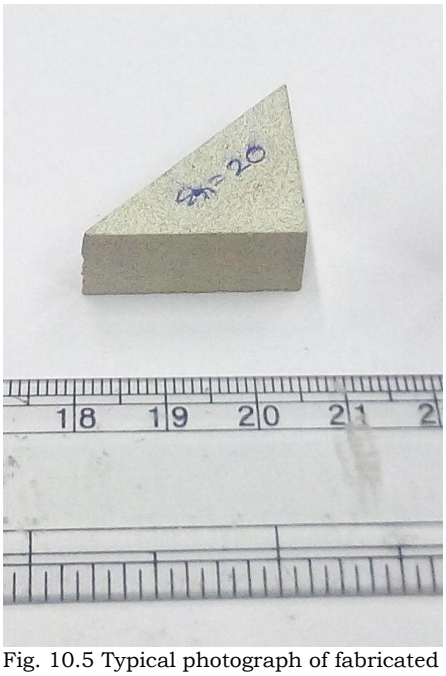

Fig. 10.5 Typical photograph of fabricated antenna

10.3.1 Resonant Frequency

In Table 10.3, theoretical results on resonant frequencies for different modes are compared with our experimental data. The isosceles 45°–45°–90° TDRA is excited using coaxial for experimental validation of our theory. The probe is placed immediately outside the TDRA to avoid the drilling problem. Different modes are identified from its internal field patterns. Experimental results are shown in Table 10.3. It is worth mentioning here that the excitation

of other higher order modes may be possible with other types of feeding mechanism.

Little discrepancy is found between our theory and experimental data as our theory does not account the effect of excitation and finite size of ground plane. In [21], it is clearly mentioned that the natural resonant frequency is highly sensitive to excitation [21]. Proper feed modeling is required to obtain accurate results.

Table 10.3

Comparison of resonant frequency with experimental data

($a = 25.4mm, d = 10mm, \varepsilon_r = 20$)

Mode	Reso. Freq. (GHz)		Error (%)
	Theoretical	Measured	
TM^z_{101}	2.9557	2.928	-0.94649
TM^z_{111}	3.2563	3.266	0.29594
TM^z_{201}	3.7465	3.716	-0.81951
TM^z_{211}	3.9787	4.068	2.1951
TM^z_{301}	4.7188	4.829	2.2818

10.3.2 Far-Field Radiation Patterns

In this section, theoretical results on far-field radiation patterns are presented for various TM^z_{mnp} modes. The modes with even values of p will not be excited for a DRA placed on a metallic ground plane [5, 177] as mentioned in Chapters VIII and IX. Therefore, theoretical results are presented for odd values of p only. Far-field power patterns are computed at conventional $\varphi = 0^o$ and $\varphi = 90^o$ planes. It is found that the results are exactly same as found in the case of 45°–45°–90° Triangular Microstrip Antenna (TMA) in Chapters VIII. Therefore, it is important to investigate the far-field radiation patterns at four planes i.e. $\varphi = 0^o, \varphi = 45^o, \varphi = 90^o$ and $\varphi = 135^o$ planes. Theoretical results are shown in Fig. 10.6 for first five modes.

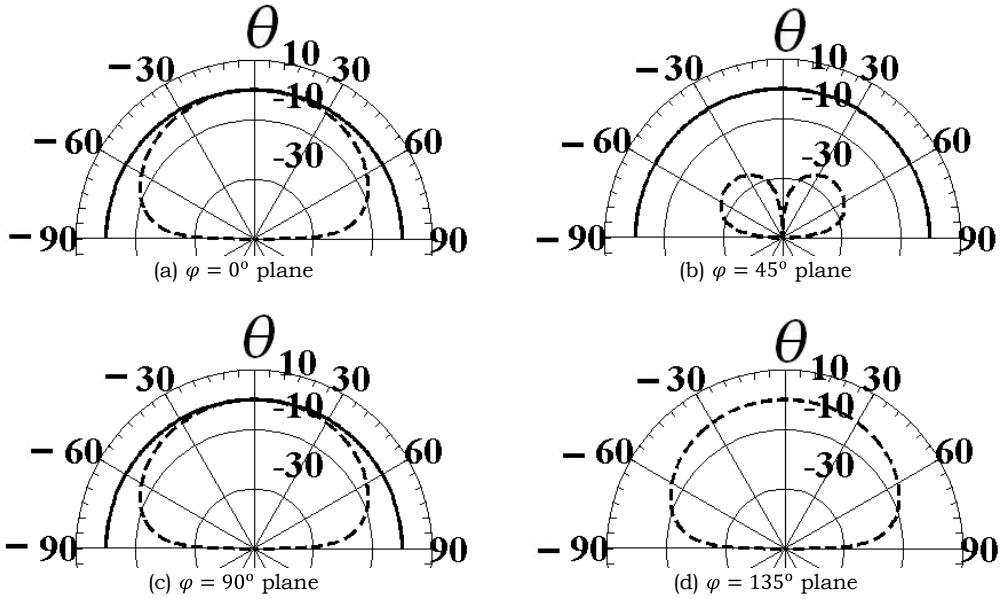

(a) $\varphi = 0^o$ plane (b) $\varphi = 45^o$ plane

(c) $\varphi = 90^o$ plane (d) $\varphi = 135^o$ plane

(i) Normalized far-zone E_θ (solid line) and E_φ (dotted line) for TM^z_{101} mode
($a = 66mm, d = 24mm, \varepsilon_r = 12, tan\,\delta = 0.0005$)

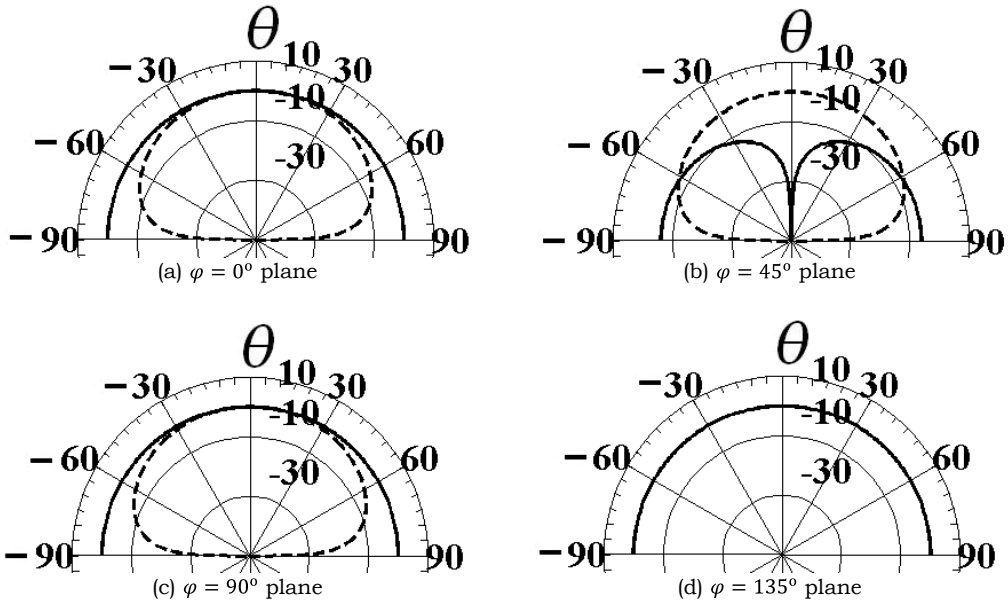

(a) $\varphi = 0^o$ plane (b) $\varphi = 45^o$ plane

(c) $\varphi = 90^o$ plane (d) $\varphi = 135^o$ plane

(ii) Normalized far-zone E_θ (solid line) and E_φ (dotted line) for TM^z_{111} mode
($a = 66mm, d = 24mm, \varepsilon_r = 12, tan\,\delta = 0.0005$)

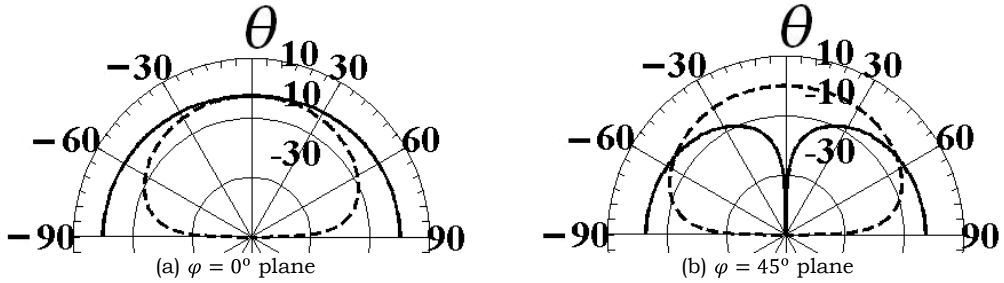

(a) φ = 0° plane (b) φ = 45° plane

(c) φ = 90° plane (d) φ = 135° plane

(iii) Normalized far-zone E_θ (solid line) and E_φ (dotted line) for TM^z_{201} mode
($a = 66mm, d = 24mm, \varepsilon_r = 12, tan\,\delta = 0.0005$)

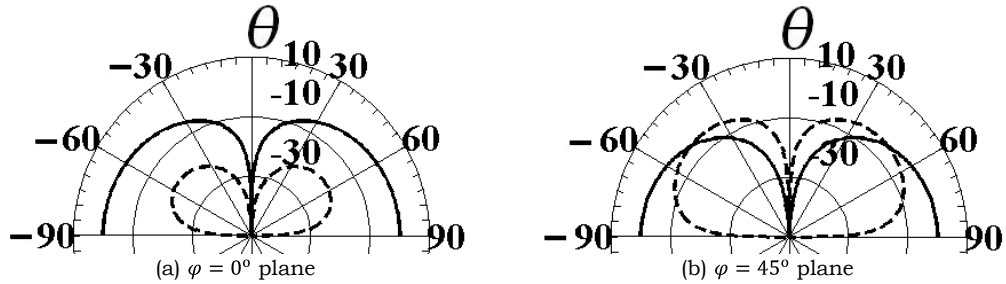

(a) φ = 0° plane (b) φ = 45° plane

(c) φ = 90° plane (d) φ = 135° plane

(iv) Normalized far-zone E_θ (solid line) and E_φ (dotted line) for TM^z_{211} mode
($a = 66mm, d = 24mm, \varepsilon_r = 12, tan\,\delta = 0.0005$)

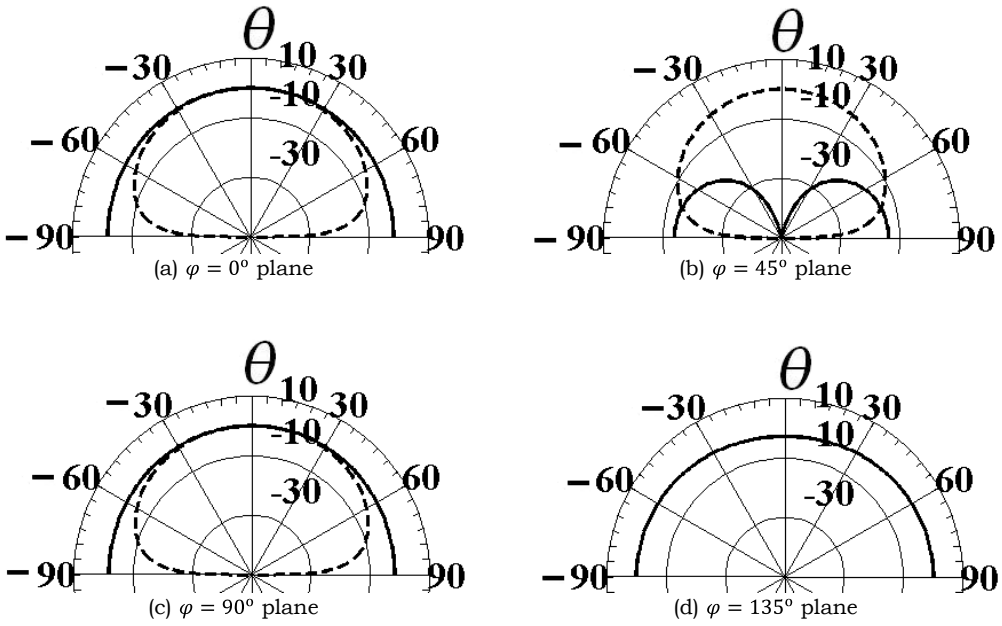

(a) $\varphi = 0^o$ plane (b) $\varphi = 45^o$ plane

(c) $\varphi = 90^o$ plane (d) $\varphi = 135^o$ plane

(v) Normalized far-zone E_θ (solid line) and E_φ (dotted line) for TM^z_{221} mode

Fig. 10.6 Theoretical far-zone electric field for different TM^z_{mnp} modes ($a = 66mm, d = 24mm, \varepsilon_r = 12, tan\,\delta = 0.0005$)

It is found from Fig. 10.6 that E_θ and E_φ both are present at $\varphi = 0^o, 45^o$ and 90^o planes for all modes whereas either E_θ or E_φ is present at $\varphi = 135^o$ plane. This observation is exactly same as found for isosceles 45°–45°–90° TMA. More precisely, the far-zone radiation patterns of an isosceles 45°–45°–90° TDRA for TM^z_{mnp} ($p = 1,3,5,7,9\ldots$) modes are exactly similar for TM^z_{mn} modes of an isosceles 45°–45°–90° TMA.

For further investigation, magnitude and angle of E_θ and E_φ components are calculated at $\theta = 0^o$ as shown in Table 10.4. The angular difference (D_θ) between E_θ and E_φ is either 0° or 180° at broadside direction. Similar observation is also found in other broadside radiating modes.

For experimental validation, our theoretical results on far-field radiation patterns are compared with our experimental data as shown in Fig. 10.7. It is found that theoretical results are in good agreement with experimental data. Little discrepancy is found as our source free theory does not include the effect of excitation and finite size of ground plane.

Table 10.4

Comparative study between E_θ or E_φ for TM^z_{mn} modes at $\theta = 0^o$

Mode	φ (degree)	E_{Total} (dB)	Magnitude (dB)		Angle (degree)		D_θ (degree)
			E_θ	E_φ	E_θ	E_φ	
TM^z_{101}	0	130.4	127.4	127.4	-65.5	-65.5	0
	45	130.4	130.4	-189.2	-65.5	114.5	-180
	90	130.4	127.4	127.4	-65.5	114.5	-180
	135	130.4	-189.2	130.4	114.5	114.5	0
TM^z_{223}	0	118.9	115.9	115.9	42.9	-137.1	180
	45	118.9	-203.9	118.9	42.9	-137.1	180
	90	118.9	115.9	115.9	-137.1	-137.1	0
	135	118.9	118.9	-203.9	-137.1	-137.1	0

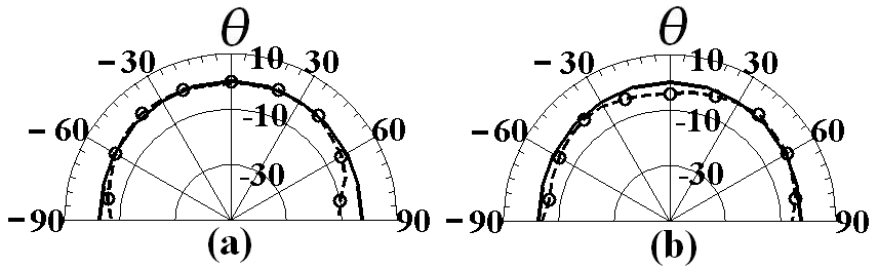

Fig. 10.7 Experimental validation of far-field radiation patterns for TM^z_{101} mode of 45°–45°–90° TDRA : theory (solid line) and experiment (dotted line with circle) (a) E-plane (b) H-plane ($a = 25\text{mm}, d = 10\text{mm}, \varepsilon_r = 25$)

Theoretical results on some higher order TM^z_{mnp} modes are compared with data obtained using 3D EM simulator HFSS as shown in Fig. 10.8. It is clear that theoretical results are in good agreement with experimental data or data obtained using a 3D EM simulator (HFSS). The small discrepancy is due to not a consideration of the effect of source and finite size of ground plane.

Theoretically, either E_θ or E_φ is present at $\varphi = 135^o$ plane with the orthogonal component negligible whereas both components are present in the 3D EM simulator HFSS output data. This may be due to our simple magnetic wall approximation. Apart from that, little discrepancy is found between theoretical results and data obtained using the 3D EM simulator. This may be due to non-consideration of feed and finite size of ground plane into our theory.

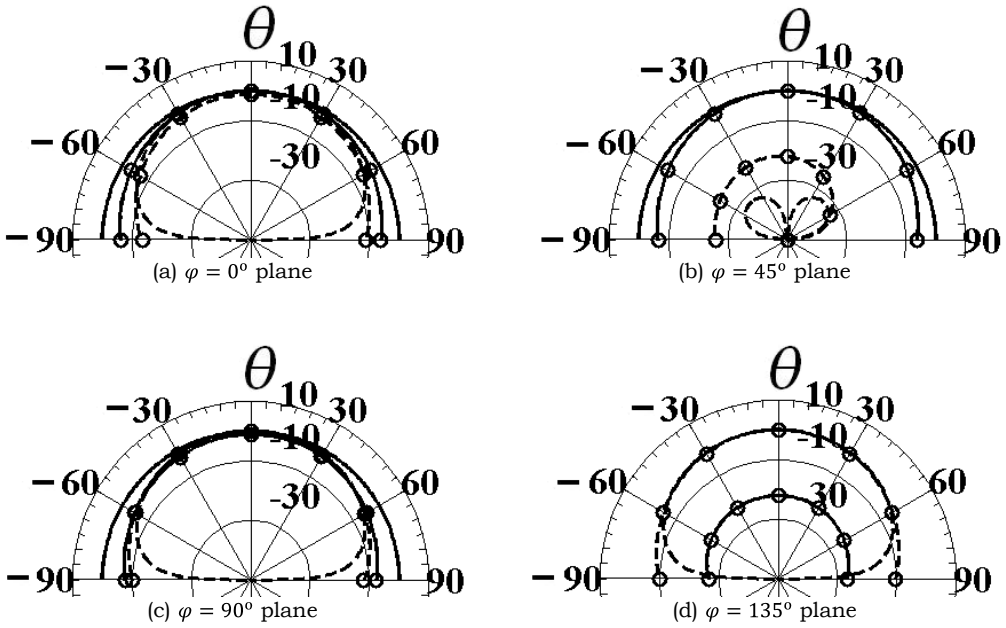

(a) $\varphi = 0^o$ plane (b) $\varphi = 45^o$ plane

(c) $\varphi = 90^o$ plane (d) $\varphi = 135^o$ plane

(i) Normalized far-zone E_θ (solid line) and E_φ (dotted line) for TM^z_{101} mode
($a = 30mm, d = 20mm, \varepsilon_r = 40, tan\,\delta = 0.0005$)

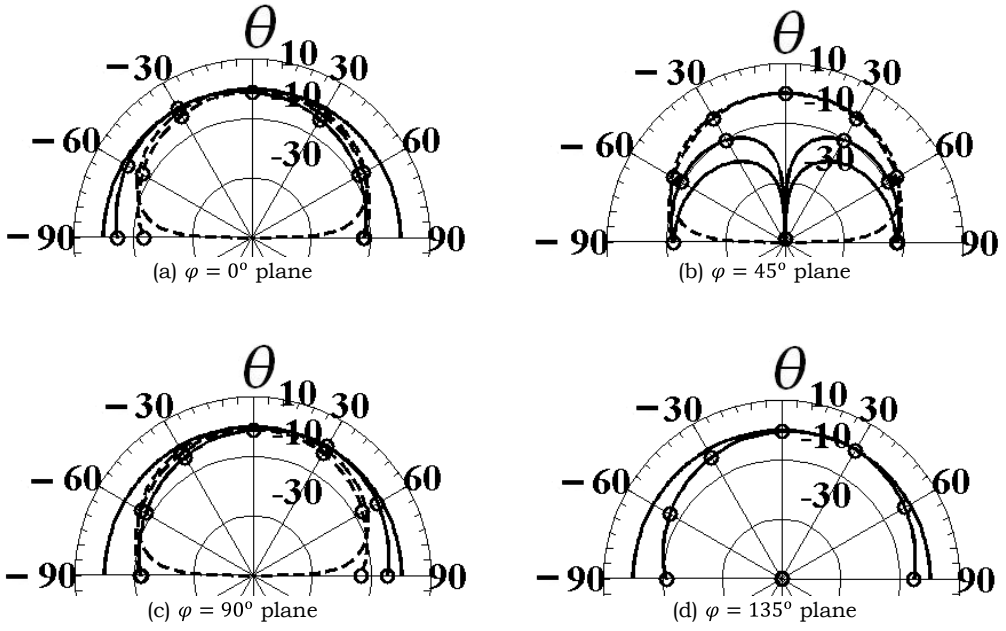

(a) $\varphi = 0^o$ plane (b) $\varphi = 45^o$ plane

(c) $\varphi = 90^o$ plane (d) $\varphi = 135^o$ plane

(ii) Normalized far-zone E_θ (solid line) and E_φ (dotted line) for TM^z_{111} mode
($a = 30mm, d = 20mm, \varepsilon_r = 40, tan\,\delta = 0.0005$)

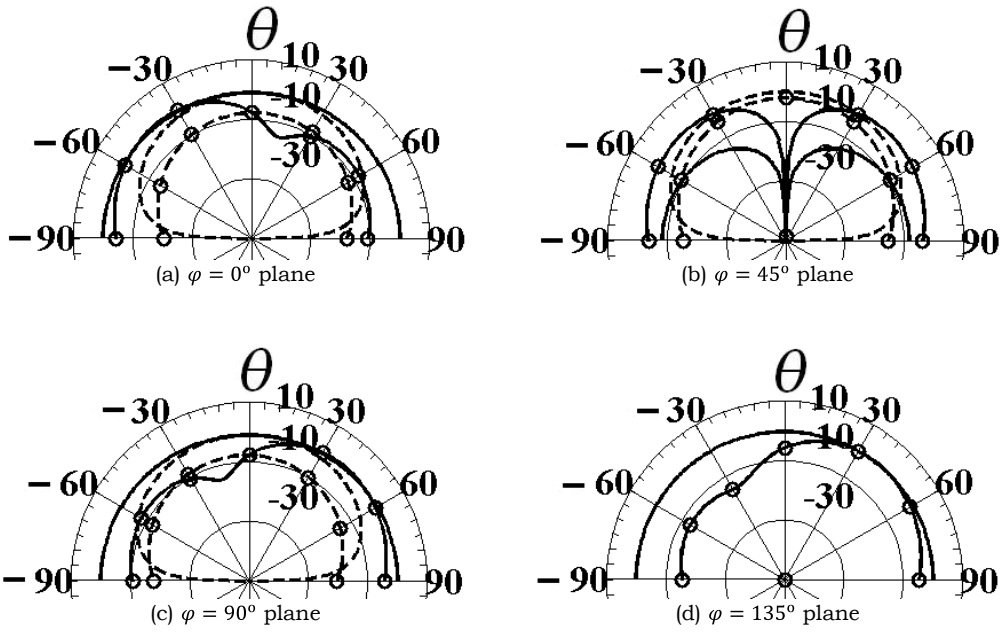

(a) φ = 0° plane (b) φ = 45° plane

(c) φ = 90° plane (d) φ = 135° plane

(iii) Normalized far-zone E_θ (solid line) and E_φ (dotted line) for TM^z_{201} mode

E_θ^{theo} E_φ^{theo} E_θ^{HFSS} E_φ^{HFSS}

Fig. 10.8 Comparison of far-zone electric field with simulated data for different TM^z_{mnp} modes ($a = 30mm, d = 20mm, \varepsilon_r = 40, tan\,\delta = 0.0005$)

10.3.3 Radiated Power, Quality factor, Gain and Bandwidth

Theoretical results on radiation Q-factor (Q_r), total Q-factor (Q_t), radiation power (P_r in %), gain (G), and BW for first few modes of an isosceles 45°–45°–90° TDRA having $a = 66mm, d = 24mm$ and $\varepsilon_r = 10$ are shown in Table 10.5. From Table 10.5, it is found that $TM^z_{103}, TM^z_{411}, TM^z_{203}, TM^z_{213}, TM^z_{223}, TM^z_{303}$ and TM^z_{313} modes can produce higher gain (21.61dB, 9.04dB, 10.34dB, 9.04dB, 10.92dB, 10.85dB and 9.4dB respectively) compared to the fundamental TM^z_{101} mode (7.72dB). Further, it is also found that one can control the far-field radiation patterns by selecting proper dimensions and relative permittivity as shown in previous chapters and is not repeated here for brevity.

Variation of $P_r(\%)$, Q_r, Q_t, e and G with resonant frequencies are shown in Fig. 10.9 for fixed value of aspect ratio (a/d). It is found from Fig. 10.9 that these quantities are almost constant as found for rectangular DRA, equilateral TDRA and 30°–60°–90° TDRA. In case of radiation efficiency (e), small variation

is found for small size of 45°–45°–90° TDRA. Numerical instability occurs in the evaluation of G for TM^z_{101} mode. To find such type of instability, $P_r(\%), Q_r, Q_t, BW, e$ and G are calculated for different values of (a/d) ratio for a fixed value of a are shown in Fig. 10.10 for first few modes. Numerical instability occurs in the evaluation of G for TM^z_{101} and TM^z_{201} modes. This may be due to non-consideration of feed in our source free theory as explained in detail in the case of the Equilateral TDRA (Chapter VIII) and is not repeated here for the sake of brevity.

Table 10.5

Radiation characteristics of first few TM^z_{mnp} modes

($a = 66mm, d = 24mm, \varepsilon_r = 12$ and $tan\delta = 0.0005$)

Sl No	Mode	f_r (GHz)	$P_r(\%)$	$e(\%)$	Q_r	Q_t	$BW(\%)$	Gain (dB)
1	TM^z_{101}	1.115	22.35	98.39	28.11	27.66	2.556	7.718
2	TM^z_{111}	1.294	18.77	98.11	33.47	32.84	2.153	4.504
3	TM^z_{201}	1.592	21.49	98.36	29.23	28.75	2.459	8.22
4	TM^z_{211}	1.721	3.451	90.65	182.1	165	0.4284	5.539
5	TM^z_{221}	2.062	17.56	98.03	35.78	35.08	2.016	7.004
6	TM^z_{301}	2.164	14.4	97.62	43.63	42.59	1.66	5.085
7	TM^z_{311}	2.261	4.219	92.33	148.9	137.5	0.5142	7.702
8	TM^z_{321}	2.531	5.867	94.39	107.1	101.1	0.6995	5.973
9	TM^z_{401}	2.774	20.83	98.36	30.16	29.67	2.383	4.293
10	TM^z_{103}	2.784	12.14	97.22	51.74	50.3	1.406	21.61
11	TM^z_{411}	2.85	4.422	92.73	142.1	131.8	0.5366	9.041
12	TM^z_{113}	2.86	10.91	96.92	57.59	55.82	1.267	6.545
13	TM^z_{331}	2.925	13.96	97.58	45.01	43.92	1.61	7.787
14	TM^z_{203}	3.006	11.07	96.97	56.77	55.05	1.284	10.34
15	TM^z_{421}	3.068	3.122	90.04	201.3	181.2	0.3902	6.801
16	TM^z_{213}	3.077	5.016	93.56	125.3	117.2	0.6033	9.041
17	TM^z_{223}	3.28	4.132	92.31	152.1	140.4	0.5038	10.92
18	TM^z_{303}	3.345	3.312	90.59	189.7	171.9	0.4114	10.85
19	TM^z_{501}	3.401	15.41	97.82	40.78	39.89	1.773	5.885
20	TM^z_{313}	3.409	1.94	84.95	323.8	275.1	0.2571	9.399

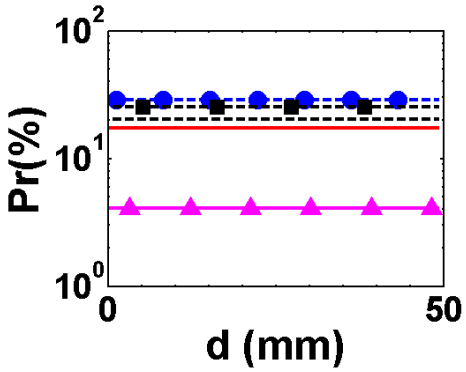

(a) Variation of $P_r(\%)$ with d

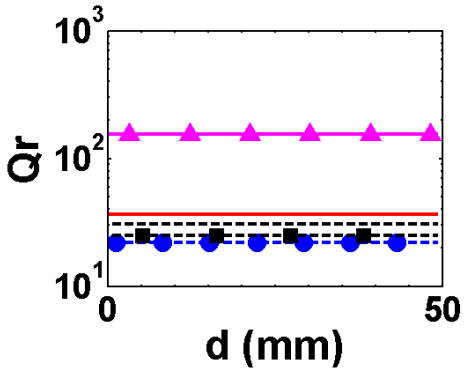

(b) Variation of Q_r with d

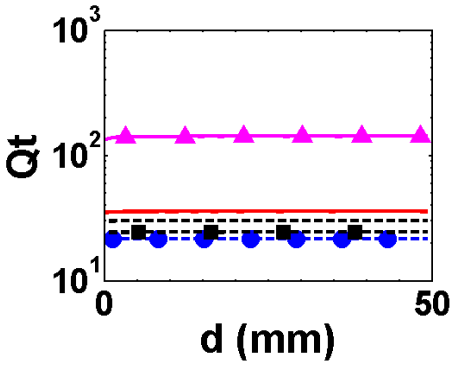

(c) Variation of Q_t with d

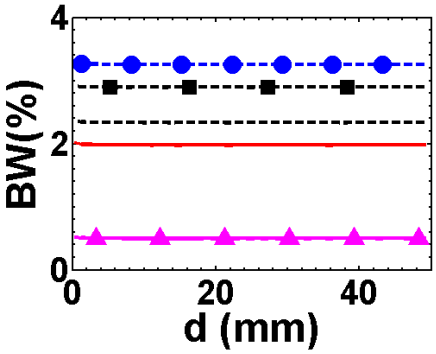

(d) Variation of BW with d

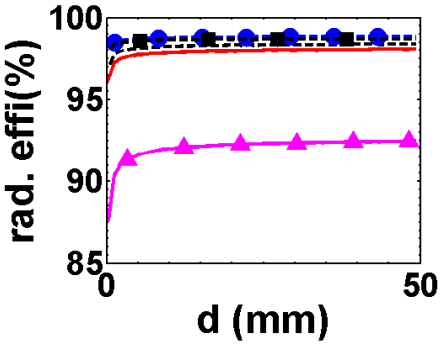

(e) Variation of rad. efficiency with d

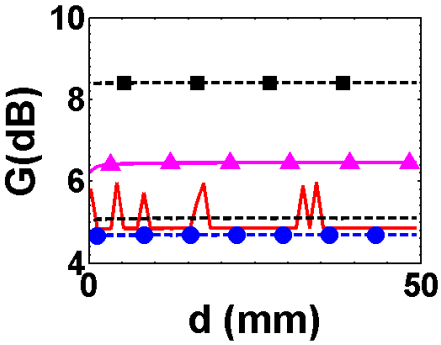

(f) Variation of $G(\mathrm{dB})$ with d

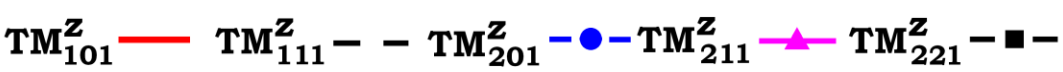

Fig 10.9 Radiation characteristics of 45°–45°–90° TDRA for fixed a/d ratio
($a/d = 1,\ \varepsilon_r = 12, \tan\delta = 0.0005$)

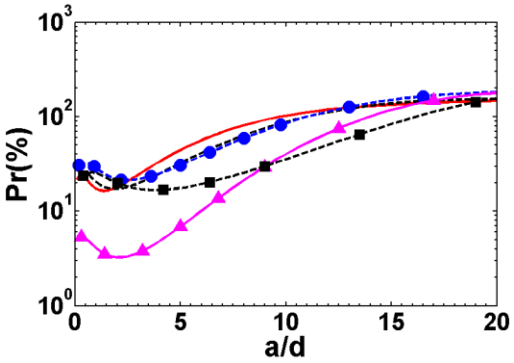

(a) Variation of $P_r(\%)$ with (a/d) ratio

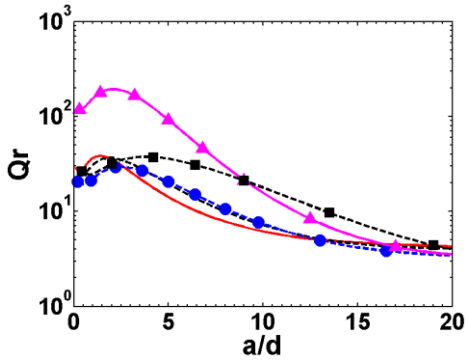

(b) Variation of Q_r with (a/d) ratio

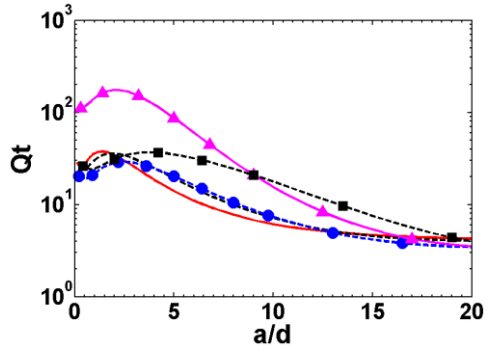

(c) Variation of Q_t with (a/d) ratio

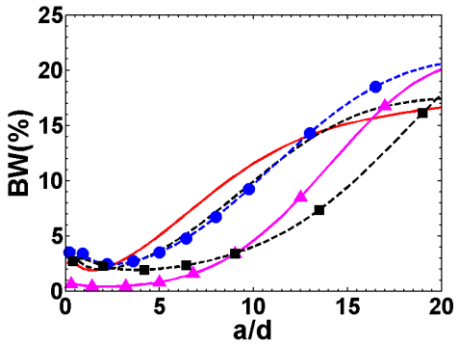

(d) Variation of BW with (a/d) ratio

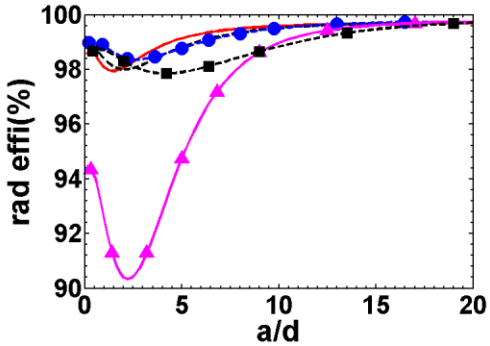

(e) Variation of rad. efficiency with (a/d) ratio

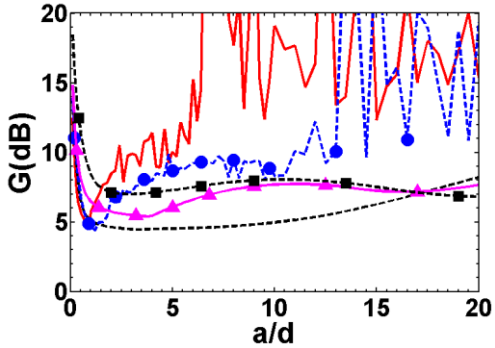

(f) Variation of G(dB) with (a/d) ratio

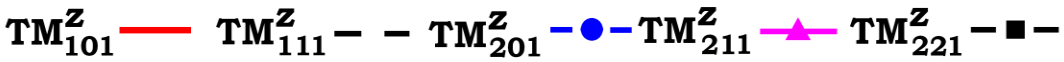

Fig 10.10 Radiation characteristics of 45°–45°–90° TDRA for different TM^z_{mnp} modes with (a/d) ratio: $(a = 66mm,\ \varepsilon_r = 12, \tan\delta = 0.0005)$

A closer observation between Figs. 10.9(f) and 10.10(f) reveals that numerical instability occurs due to improper choice of dimensions of TDRA. For example, TM^z_{201} mode does not show numerical instability for $(a/d) = 1$ (please

see Fig. 10.9(f)) whereas the same mode shows numerical instability for different values of (a/d) ratio (please see Fig. 10.10(f)). The same observation is also found for 30°–60°–90° TDRA also (please see Figs. 9.8(f) and 9.9(f) in Chapter IX).

10.3.4 Input Impedance

Evaluation of input impedance (Z_{in}) using (a, d) instead of (a_e, d_e) is already discussed in detail for equilateral TDRA and 30°–60°–90° TDRA in Chapters VIII-IX and is not repeated here for the sake of brevity. A similar phenomenon is also found for 45°–45°–90° TDRA. Therefore, Z_{in} is computed using (a, d) and is plotted against normalized frequency. Typical results are shown for TM^z_{111} mode in Fig. 10.11. Measured Q_t is used for theoretical computation. It is found that our theory is in good agreement with experimental data.

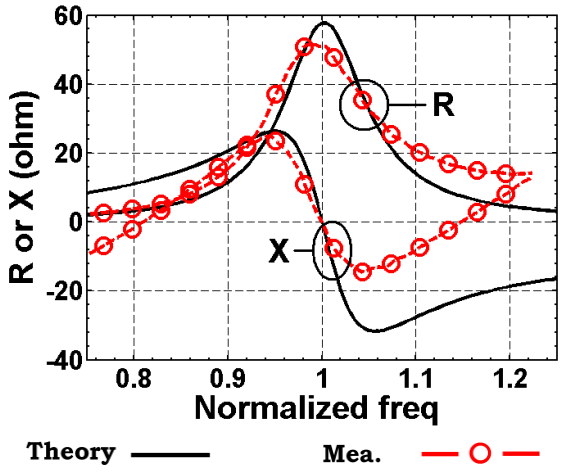

Fig 10.11 Comparison of input impedance with experimental data for TM^z_{111} mode ($a = 47mm,\ d = 26mm, \varepsilon_r = 10, x_o = 40mm, y_o = 7mm, PL = 12mm$)

10.4 Conclusion

In this chapter, theoretical investigation on isosceles 45°–45°–90° Triangular Dielectric Resonator Antenna (TDRA) is presented for TM^z_{mnp} modes for the first time. The isosceles 45°–45°–90° TDRA is modeled here as source free cavity, bounded by Perfect Magnetic Conductors (PMC). Approximate solution for the eigenfunctions and eigenvalues are given here. Approximate expression is also given here to predict the resonant frequency for different TM^z_{mnp} modes. Closed form analytic expressions are given here to predict the far-zone electric field for various TM^z_{mnp} modes. Radiation Q-factor (Q_r) ,

radiated power in percentage ($P_r(\%) = 2\pi/Q_r \times 100\%$), bandwidth ($BW$), efficiency ($e$), gain ($G$) etc. are also discussed. From this theoretical investigation, it is found that:

- Radiation characteristics of an isosceles 45°–45°–90° TDRA placed on a metallic ground plane are mainly controlled by the choice of modal indices m and n for a particular TM^z_{mnp} mode.
- Higher order modes can be used to produce higher gain compared to fundamental TM^z_{101} mode by selecting proper dimensions and permittivity of the TDRA.
- For a given mode, radiated power $P_r(\%)$, total Q-factor (Q_t) and gain (G) become almost same for fixed values of aspect ratios (a/d) and relative permittivity of the 45°–45°–90° TDRA as found for rectangular DRA, equilateral TDRA and 30°–60°–90° TDRA.

Chapter XI

Isosceles Triangular Dielectric Resonator Antenna

11.1 Introduction

In the last three Chapters, modal characteristics of equilateral, 30°–60°–90° and 45°–45°–90° shaped Triangular Dielectric Resonator Antennas (TDRAs) are presented. In this chapter, theoretical investigation on isosceles TDRA is presented. Literature survey shows that there is no work available neither theoretical nor experimental investigation on isosceles TDRA [5, 174]. In Chapter VI, we have presented approximate investigations on fundamental TM_{10}^{z} mode of an isosceles Triangular Microstrip Antenna (TMA). This theory is extended here to investigate an isosceles TDRA for the first time.

In this chapter, simple magnetic wall dielectric waveguide model is used to investigate the isosceles $\theta_i - \theta_i - \varphi_i$ TDRA. The surfaces of the TDRA are modeled as Perfect Magnetic Conductors (PMC) to find the approximate solution of eigenfunctions (ψ) and eigenvalues for TM_{mnp}^{z} modes. Approximate expression is given here to predict its resonant frequency. 'Equivalence Principle' [4, 16] is used to find the far-zone electric field. Theoretical results are compared with experimental data and data obtained using 3D EM simulator HFSS [9] to show the accuracy of our theory.

11.2 Theory

In Fig. 11.1, a source free isosceles $\theta_i - \theta_i - \varphi_i$ TDRA having equal side length a, height d and relative permittivity ε_r is shown in Cartesian coordinate system. For theoretical investigations, the isosceles TDRA is modeled here as a dielectric cavity bounded by PMC. Image theory is applied first to remove the

ground plane, which results an isosceles TDRA in free space having height $h = 2d$. TM^z mode of the isosceles TDRA is investigated here. Eigenfunctions, eigenvalues, resonant frequency (f_r), far-field radiation patterns, radiated power, gain, Q-factor, bandwidth are investigated.

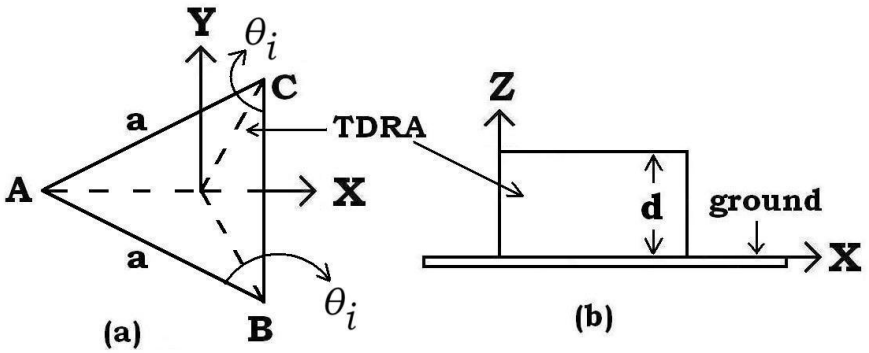

Fig. 11.1 Antenna configuration (a) top view (b) side view

11.2.1 Eigenfunctions

Due to the presence of inclined surfaces along AC and AB sides, the eigenfunctions is expressed as $\psi(x,y,z) = F(x,y) \times H(z)$. The evaluation of $F(x,y)$ is similar as shown in Chapter VI for isosceles $\theta_i - \theta_i - \varphi_i$ TMA using modified tri-linear transformation and can be expressed as:

$$F(x,y) = \sum_{i=1}^{3} \cos\left[\alpha_i\left(x + \frac{R}{T_1}\right)\right]\cos\left(\beta_i y\right) \tag{11.1}$$

$$\alpha_1 = \frac{\pi l T_1}{H}, \qquad \alpha_2 = \frac{\pi m T_1}{H}, \qquad \alpha_3 = \frac{\pi n T_1}{H} \tag{11.2}$$

$$\beta_1 = \frac{\pi}{2}\left[J(m-l) + \frac{(m+l)}{G}\right]T_2 \tag{11.3a}$$

$$\beta_2 = \frac{\pi}{2}\left[J(n-m) + \frac{(n+m)}{G}\right]T_2 \tag{11.3b}$$

$$\beta_3 = \frac{\pi}{2}\left[J(l-n) + \frac{(n+l)}{G}\right]T_2 \tag{11.3c}$$

$$\chi^2 = \frac{2}{3}\pi^2\left[\frac{S}{H^2} + \frac{Q}{4}\left(3J^2 + \frac{1}{G^2}\right)\right](m^2 + mn + n^2) \tag{11.4}$$

$$\alpha_i{}^2 + \beta_i{}^2 = \chi_{mn}^2 \tag{11.5}$$

$$l + m + n = 0 \quad ; \quad \{l, m, n\} = 0, \pm 1, \pm 2, \pm 3 \cdots \tag{11.6}$$

$$t = \sin\left(\frac{\varphi}{2}\right), \qquad G = (r + 2tR), \qquad H = (r + R), \qquad J = \frac{SG}{H^2 Q} \tag{11.7}$$

$$r = (b/2)\, tan(\theta/2) \; ; \; p = sin(\theta/2) \; ; \; q = cos(\theta/2) \; ; \; T_1 = 2p \; ; \; T_2 = 2q \tag{11.8}$$

Applying PMC at $z = \pm d$, the $H(z)$ function can be expressed as:

$$H(z) = sin\big(k_z(d - z)\big); \quad k_z = p\pi/(2d) \; ; \; p = 1,2,3,4 \ldots \tag{11.9}$$

Therefore, the eigenfunctions can be expressed as:

$$\psi = \left(\sum_{i=1}^{3} \cos\left[\alpha_i \left(x + \frac{R}{T_1}\right)\right] \cos[\beta_i y]\right) \times sin[k_z(d - z)] \tag{11.10}$$

Limitation

It is found that the solutions for eigenfunctions (ψ)and eigenvalues (k) of the isosceles $\theta_i - \theta_i - \varphi_i$ TDRA having $\theta_i \geq 60°$ are valid for TM_{mnp}^z ($m = 1, n = 0$ & $p = 1,2,3,4 \ldots$) modes only. The reason has already been explained in detail in Chapter VI for isosceles $\theta_i - \theta_i - \varphi_i$ TMA and is not repeated here for the sake of brevity. A similar phenomenon is also found for higher values of modal indices m and n. Therefore, we will only discuss the TM_{10p}^z ($p = 1,2,3,4 \ldots$) modes of the isosceles $\theta_i - \theta_i - \varphi_i$ TDRA having $\theta_i \geq 60°$.

In Fig. 11.2, internal field distributions are shown for an isosceles TDRA for TM_{101}^z and TM_{103}^z modes only. Three sides *AC*, *AB* and *BC* are also shown to define the triangular region. The field strength is normalized (in dB) to express the internal field distribution within the TDRA.

11.2.2 Resonant Frequency

To predict the resonant frequency, separation equation ($\chi^2 + k_z^2 = \varepsilon_r k_0^2$) is used. Resonant frequency of an isolated source free isosceles $\theta_i - \theta_i - \varphi_i$ TDRA

is evaluated as:

$$f_r = \frac{c}{2\pi\sqrt{\varepsilon_r}} \times [\chi^2 + k_z^2]^{1/2} \tag{11.11}$$

where c is the velocity of light in free space.

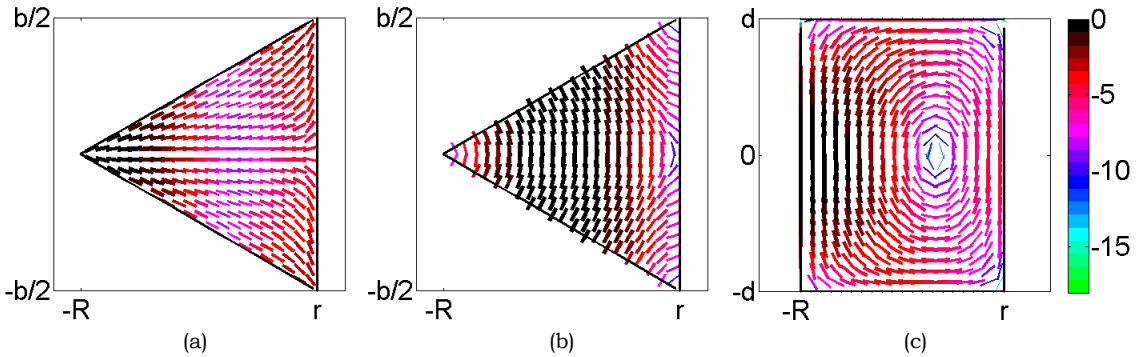

(a) (b) (c)

(i) Internal field distribution of 60°–60°–60° TDRA at TM_{101}^z mode

(a) $\vec{E}$ field patterns at $z = d/2$ plane (b) $\vec{H}$ field patterns at $z = d/2$ plane (c) $\vec{E}$ field patterns at $y = 0$ plane

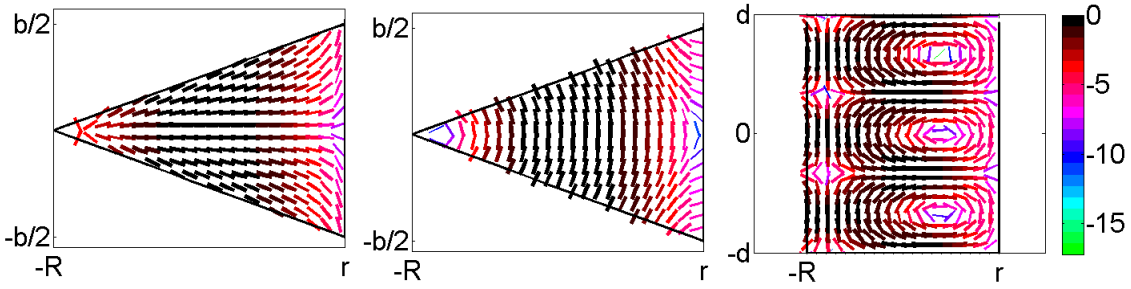

(a) (b) (c)

(ii) Internal field distribution 70°–70°–40° TDRA at TM_{103}^z mode

Fig. 11.2 Approximate internal field patterns for different isosceles TDRA at TM_{10p}^z modes (a) $\vec{E}$ field patterns at $z = d/2$ plane (b) $\vec{H}$ field patterns at $z = d/2$ plane (c) $\vec{E}$ field patterns at $y = 0$ plane (a = 66mm, d = 24mm, ε_r = 12)

It is found from rigorous 3D EM simulations using HFSS [9] that as the angle θ_i increases from 60° to 90°, resonant frequency also increases as expected. Typical results are shown in Fig. 11.3. It should be noted here that the resonant frequency decreases as the size of the $\theta_i - \theta_i - \varphi_i$ TMA decreases (i.e. θ_i increases from 60° to 90°) as explained in Chapter VI. This is because of the fact that the effective length of the isosceles TMA increases due to fringing as the size of the $\theta_i - \theta_i - \varphi_i$ TMA decreases (please see Fig. 6.4 in Chapter VI).

On the other hand, the fringing effect is not found in case of DRA due to high permittivity of the material. Further, electric fields avoid the corners of the TDRA as explained for other TDRAs in Chapters VIII-X. This reduces the effective area which results higher resonant frequency as the size of the TDRA decreases.

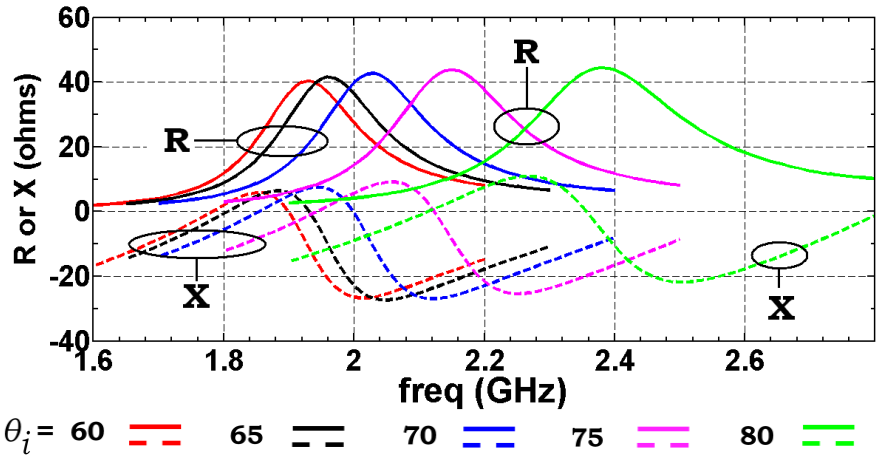

Fig. 11.3 Variation of simulated input impedance for different isosceles TDRAs ($a = 50mm, d = 20mm, \varepsilon_r = 12, tan\,\delta = 0.0005$)

For a first order approximation, based on data obtained from 3D EM simulator HFSS [9], the effective side length (a_e) of the isosceles $\theta_i - \theta_i - \varphi_i$ TDRA is expressed as:

$$a_e = 0.7362 - 0.003537 \times cos(0.2066\theta_i) - 0.08584 \times sin(0.2066\theta_i) + 0.01881 \times cos(0.4132\theta_i) - 0.004876 \times sin(0.4132\theta_i) \quad (11.12)$$

Here, the angle θ_i is in degrees.

11.2.3 Far-Field Radiation Patterns

'Equivalence Principle' [4, 16] is used to find the far zone electric field of an isosceles $\theta_i - \theta_i - \varphi_i$ TDRA. For theoretical investigation, the surfaces of the TDRA are modeled here as Perfect Magnetic Conductors (PMC). The magnetic surface currents $\left(\vec{M}_s = \vec{E} \times \hat{n}\right)$ are evaluated to find the far-field patterns which are similar to those for equilateral TDRA as shown in Chapter VIII and are not

repeated here for brevity. All surface integrals are evaluated using our singularity free, simple and novel technique as presented in Chapter XIII. The total far-zone electric field at point $P(r,\theta,\varphi)$ is evaluated as [16]:

$$E_\theta = -\frac{jk_o \exp(-jk_o r)}{4\pi r} \times exp(-jV_1 R) \times \left[L_\varphi\right] \quad (11.13a)$$

$$E_\varphi = \frac{jk_o \exp(-jk_o r)}{4\pi r} \times exp(-jV_1 R) \times [L_\theta] \quad (11.13b)$$

where,

$$L_\theta = F_x cos(\theta)cos(\varphi) + F_y cos(\theta)sin(\varphi) - F_z sin(\theta)$$

$$L_\varphi = -F_x sin(\varphi) + F_y cos(\varphi) \quad (11.14)$$

Here, all terms are carrying their usual meaning.

11.2.4 Radiated Power, Quality factor, Efficiency and Gain

The total quality factor (Q_t) is evaluated as:

$$Q_t = \frac{\omega_r W_t}{P_c + P_d + P_r} \quad (11.15)$$

where ω_r is the resonant frequency, W_t is total stored energy, P_c is conductor loss, P_d is dielectric loss and P_r is radiation loss. These quantities are evaluated using standard procedures as presented in Chapter III.

11.2.5 Input Impedance

Computation of input impedance (Z_{in}) is similar as demonstrated for rectangular DRA, equilateral TDRA, 30°–60°–90° TDRA and 45°–45°–90° TDRA in Chapters VII-X using the following relation [4]:

$$Z_{in} = \frac{-j\omega(a_o/I_o)^2}{\omega^2 - \omega_o^2\left(1 + \frac{j}{Q_t}\right)} \quad (11.16)$$

where all terms are defined earlier (Chapters VII-X) and are not repeated here for the sake of brevity. Probe current density $\vec{J}$ is modeled here as one dimensional $\hat{z}$ directed current as [4]:

$$\vec{J} = \begin{cases} \hat{z} I_o \dfrac{\sin[k_d(l-z)]}{\sin(k_d l)} \delta(x-x_o)\delta(y-y_o), & z \le l \\ 0 \quad , & z > l \end{cases} \tag{11.17}$$

where $k_d = p\pi/(2l)$, l is probe length and (x_o, y_o) is the probe location.

11.3 Results

In this section, theoretical results on resonant frequency, far-field patterns, Q-factor etc. are discussed. Three antennas are fabricated in our laboratory as shown in Fig. 11.4. Conventional 50Ω coaxial probe is used to excite those isosceles TDRAs. The same are also simulated using FEM based 3D EM simulator HFSS [9]. All measurements are performed using Agilent E-series VNA (Model No: E85071B, Frequency range: 300MHz to 8.5GHz).

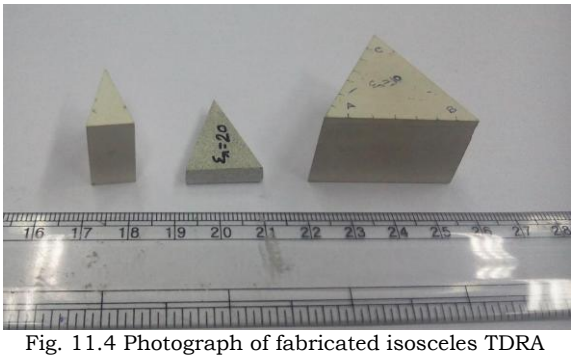

Fig. 11.4 Photograph of fabricated isosceles TDRA

11.3.1 Resonant Frequency

In Table 11.1, theoretical resonant frequencies are compared with experimental data and data obtained using 3D EM simulator HFSS [9]. It is found that our theory can predict the resonant frequency with an accuracy of 3.1%.

Table 11.1

Experimental verification of resonant frequency

θ_i (deg)	a (mm)	d (mm)	ε_r	Mode	Frequency (GHz)			Error (%)	
					HFSS	Theory	Mea.	HFSS	Theory
60	66	24	12	TM^z_{101}	1.501	1.454	1.5 [113]	-0.067	3.06
60	36	21	10	TM^z_{101}	2.55	2.5537	2.61	2.29	2.16
70	25	4.5	20	TM^z_{101}	4.79	4.7091	4.85	1.24	2.91
75	19.67	19	10	TM^z_{101}	4.76	4.9538	4.82	1.24	-2.78

11.3.2 Far-Field Radiation Patterns

In this section, theoretical results on far-field radiation patterns of different isosceles $\theta_i - \theta_i - \varphi_i$ TDRA are presented for various TM^y_{10p} modes. It is already mentioned in Chapters VIII - X that the modes with even values of p will not be excited for a DRA placed on a metallic ground plane [5, 177]. Therefore, theoretical results are presented here for odd values of p only. Normalized far-zone electric field strength at $\varphi = 0^o$ and $\varphi = 90^o$ plane are shown in Fig. 11.5 for some isosceles $\theta_i - \theta_i - \varphi_i$ TDRAs. It is found from Fig. 11.5 that TM^z_{10p} (p = 1,3,5 ...) modes produce a peak in the broadside direction. Due to the improper choice of dimensions and/and permittivity, slight dip may be observed (for example, 80°–80°–20° TDRA at TM^z_{103} mode in Fig. 11.5(d)).

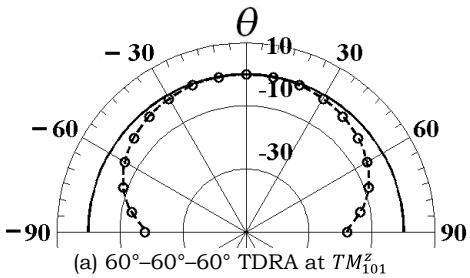

(a) 60°–60°–60° TDRA at TM^z_{101}

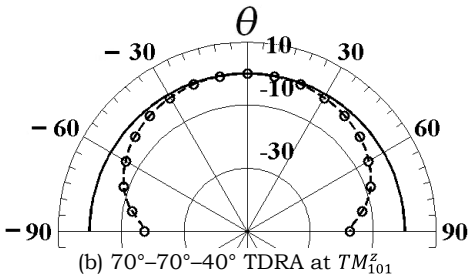

(b) 70°–70°–40° TDRA at TM^z_{101}

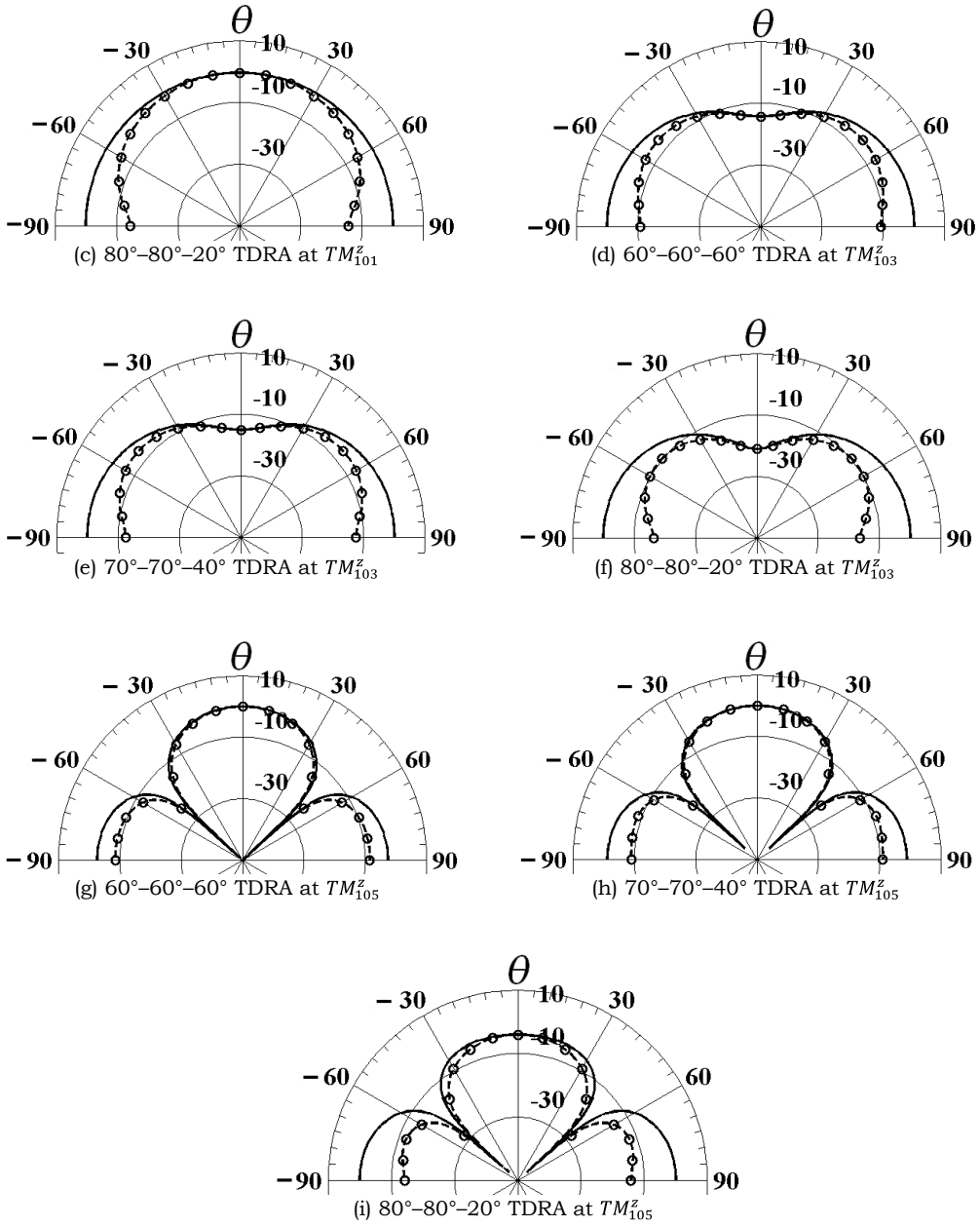

(c) 80°–80°–20° TDRA at TM^z_{101} (d) 60°–60°–60° TDRA at TM^z_{103}

(e) 70°–70°–40° TDRA at TM^z_{103} (f) 80°–80°–20° TDRA at TM^z_{103}

(g) 60°–60°–60° TDRA at TM^z_{105} (h) 70°–70°–40° TDRA at TM^z_{105}

(i) 80°–80°–20° TDRA at TM^z_{105}

Fig. 11.5 Normalized far-zone E-plane (solid line) and H-plane (circle with dotted line) power patterns of different isosceles TDRA at different TM^z_{10p} modes ($a = 66mm, d = 24mm, \varepsilon_r = 12, tan\,\delta = 0.0005$)

For experimental validation, our theoretical results on E-plane ($\varphi = 0^o$ plane) and H-plane ($\varphi = 90^o$ plane) are compared with experimental data for some isosceles $\theta_i - \theta_i - \varphi_i$ TDRAs having θ_i = 60°, 70° and 75° as shown in Figs. 11.6[(i)-(iii)]. It is found that our theory is in good agreement with

experimental data. Little discrepancy is found which is due to the finite size of ground plane.

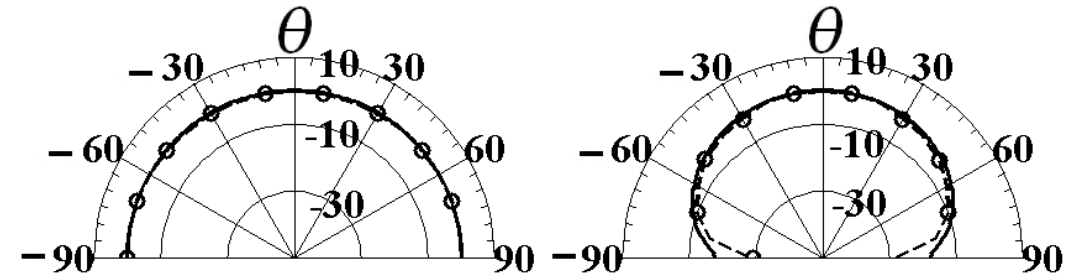

(a) E-plane (φ = 0°) (b) H-plane (φ = 90°)

(i) 60°–60°–60° TDRA at TM_{101}^{z} ($a = 66mm, d = 24mm, \varepsilon_r = 12$) [113]

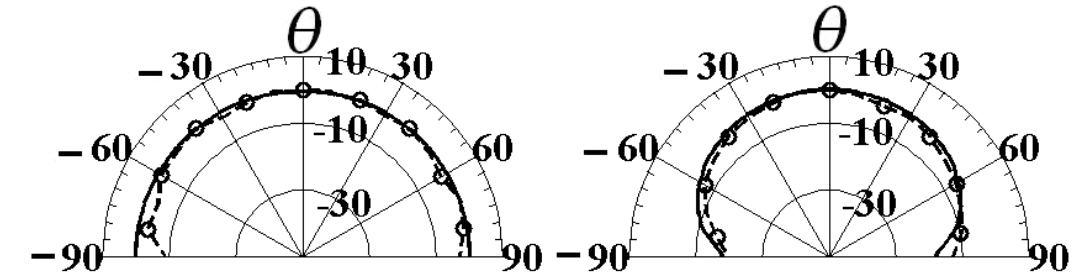

(a) E-plane (φ = 0°) (b) H-plane (φ = 90°)

(ii) 60°–60°–60° TDRA at TM_{101}^{z} ($a = 36mm, d = 21mm, \varepsilon_r = 10$)

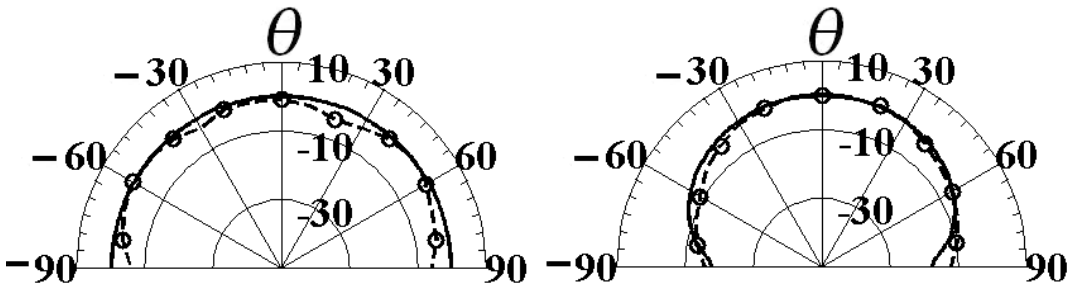

(a) E-plane (φ = 0°) (b) H-plane (φ = 90°)

(iii) 70°–70°–40° TDRA at TM_{101}^{z} ($a = 25mm, d = 4.5mm, \varepsilon_r = 20$)

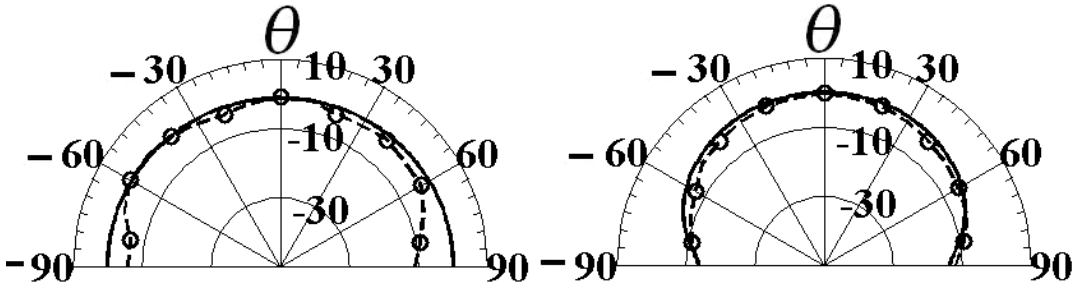

(a) E-plane (φ = 0°) (b) H-plane (φ = 90°)

(iv) 75°–75°–30° TDRA at TM_{101}^{z} ($a = 19.67mm, d = 19mm, \varepsilon_r = 10$)

Fig. 11.6 Comparison of theoretical (solid line) power patterns with experimental data (circle with dashed line) for different isosceles TDRAs

11.3.3 Radiated Power, Quality factor, Efficiency and Gain

In Table 11.2, theoretical radiation Q-factor (Q_r), total Q-factor (Q_t), radiation power in percentage (P_r in %) which is calculated as [15] $P_r = 2\pi/Q_r \times 100\%$, gain ($G$), BW and radiation efficiency $e(\%)$ for different isosceles $\theta_i - \theta_i - \varphi_i$ TDRAs are shown. From Table 11.2, it is found that as θ_i increases from 60° to 90°, f_r, Q_r and Q_t increase whereas $P_r(\text{in }\%), BW$ and $e(\%)$ decreases. Further, for a fixed isosceles $\theta_i - \theta_i - \varphi_i$ TDRA, higher order modes produce a higher gain compared to fundamental TM^z_{101} mode.

Table 11.2

Characteristics of different isosceles $\theta_i - \theta_i - \varphi_i$ TDRAs

($a = 66mm, d = 24mm, \varepsilon_r = 12$ and $tan\delta = 0.0005$)

Mode	θ_i (deg)	f_r (GHz)	$P_r(\%)$	$e(\%)$	Q_r	Q_t	BW (%)	Gain (dB)
TM^z_{101}	60	1.256	32.96	98.91	19.07	18.86	3.75	4.71
	65	1.261	17.36	97.93	36.2	35.45	1.995	4.67
	70	1.279	12.36	97.09	50.84	49.36	1.433	4.66
	75	1.321	7.519	95.24	83.57	79.59	0.8884	4.60
	80	1.431	3.585	90.26	175.3	158.2	0.447	4.65
	85	1.873	1.412	76.15	444.9	338.8	0.2087	5.89
TM^z_{103}	60	2.843	17.48	98.41	35.94	35.37	1.999	7.33
	65	2.845	9.52	97.12	66	64.1	1.103	7.23
	70	2.853	7.074	96.14	88.82	85.39	0.8281	7.35
	75	2.872	4.657	94.22	134.9	127.1	0.5562	7.74
	80	2.925	2.644	90.08	237.6	214	0.3304	8.41
	85	3.165	1.151	77.59	545.8	423.5	0.167	8.79
TM^z_{105}	60	4.593	12.5	97.35	50.28	48.95	1.444	9.87
	65	4.594	7.109	95.44	88.39	84.35	0.8383	9.52
	70	4.599	5.762	94.42	109	103	0.6868	8.87
	75	4.611	4.407	92.82	142.6	132.3	0.5343	8.35
	80	4.644	3.102	90.05	202.6	182.4	0.3877	9.13
	85	4.798	1.604	81.73	391.6	320.1	0.2209	9.14

In Fig. 11.7, variation of $P_r(\%)$, Q_r, Q_t, BW, e and G with height (d) are shown for different isosceles $\theta_i - \theta_i - \varphi_i$ TDRAs for TM^z_{101} mode for fixed aspect

ratio (a/d). It is found that $P_r(\%)$, Q_r, Q_t, BW and G are almost constant, whereas little variation is found in the case of radiation efficiency (e) as found for other triangular shaped DRAs.

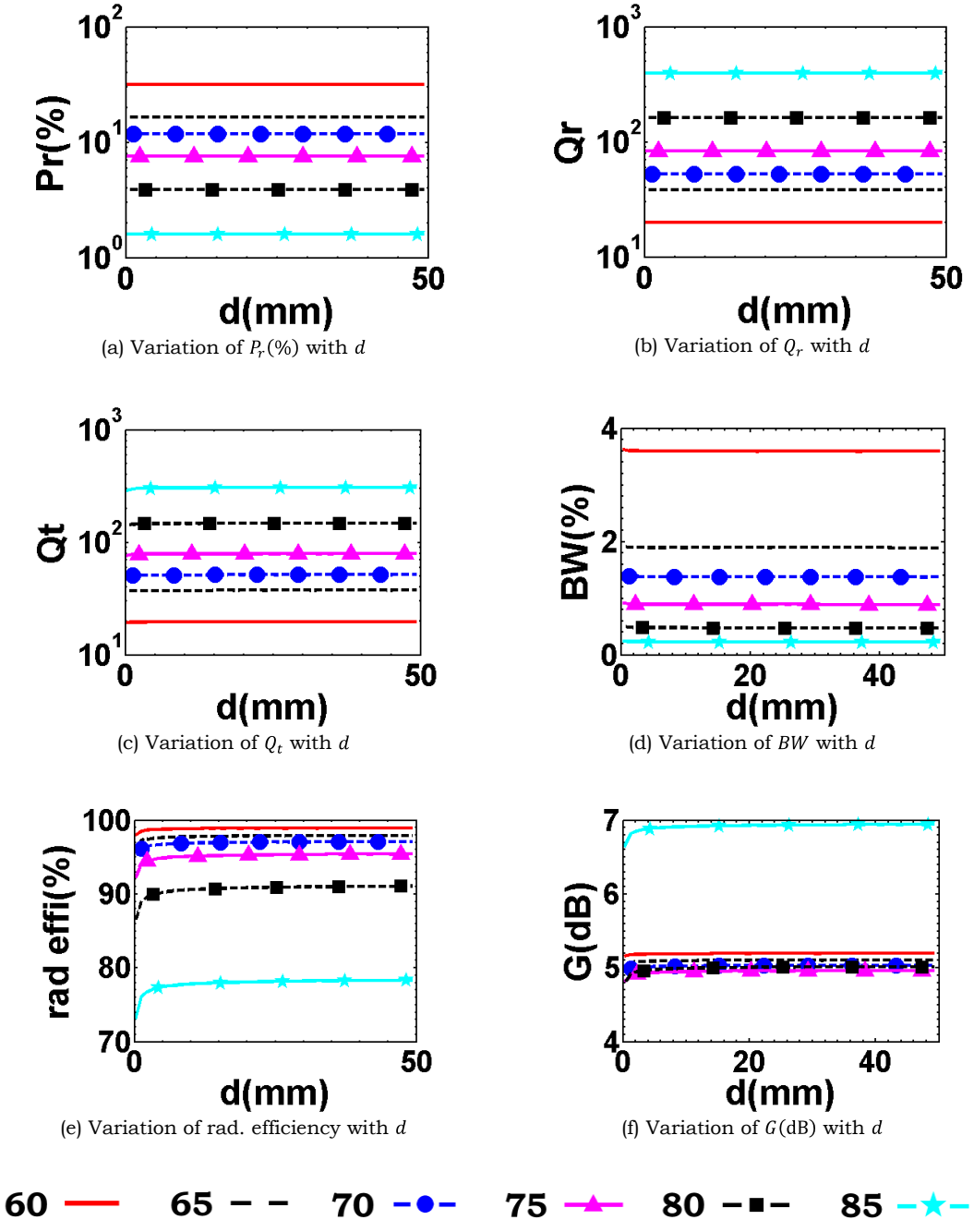

(a) Variation of $P_r(\%)$ with d

(b) Variation of Q_r with d

(c) Variation of Q_t with d

(d) Variation of BW with d

(e) Variation of rad. efficiency with d

(f) Variation of $G(\mathrm{dB})$ with d

Fig 11.7 Characteristics of different isosceles TDRAs at TM^z_{101} mode with height $(a/d = 1, \varepsilon_r = 12, \tan\delta = 0.0005)$

In Fig. 11.8, variation of $P_r(\%)$, Q_r, Q_t, BW, e and G with resonant frequency are shown for different isosceles $\theta_i - \theta_i - \varphi_i$ TDRAs for TM^z_{101} mode.

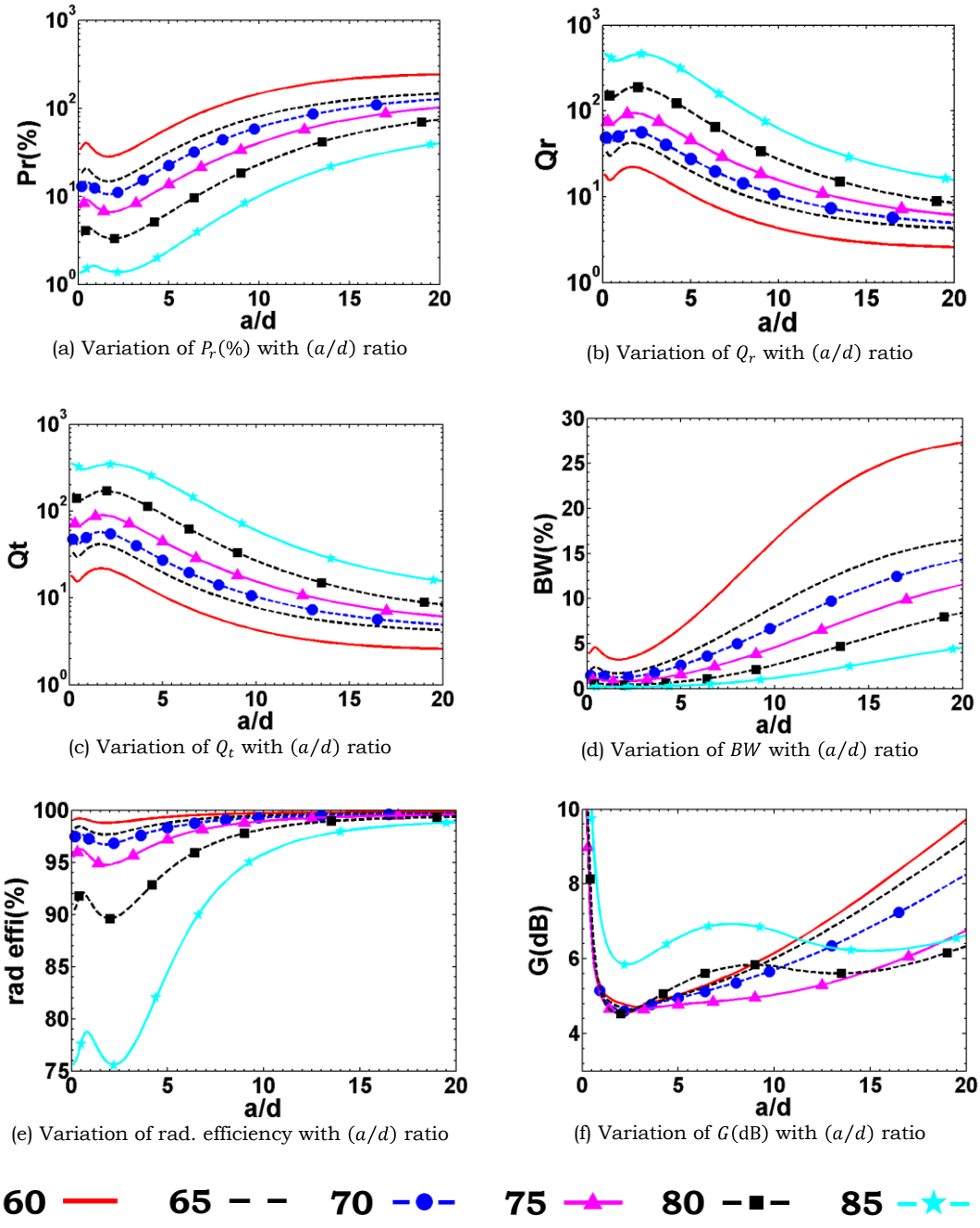

(a) Variation of $P_r(\%)$ with (a/d) ratio

(b) Variation of Q_r with (a/d) ratio

(c) Variation of Q_t with (a/d) ratio

(d) Variation of BW with (a/d) ratio

(e) Variation of rad. efficiency with (a/d) ratio

(f) Variation of G(dB) with (a/d) ratio

Fig 11.8 Characteristics of different isosceles TDRAs at TM^z_{101} mode with aspect ratio $(a = 66mm, \varepsilon_r = 12, \tan\delta = 0.0005)$

11.3.4 Input Impedance

Evaluation of input impedance (Z_{in}) using (a, d) instead of (a_e, d_e) is already discussed in detail for equilateral, 30°–60°–90° and 45°–45°–90° TDRAs in Chapters VIII-X and is not repeated here for the sake of brevity. A similar phenomenon is also found for isosceles TDRA. Theoretical results are compared with experimental data as shown in Fig. 11.9 for TM^z_{101} mode of an isosceles 67°–67°–46° TDRA where Z_{in} is computed using (a, d) and is plotted with normalized frequency. Little discrepancy is found between our theory and experimental data. This is due to the air gap between the probe and TDRA. Hand-drill is used to make the hole inside the TDRA. The diameter of the hole is 1.85mm (approx.) whereas the diameter of the probe is 1.22mm. Further, the length of the hole (19mm approx.) is also slightly longer than the probe length ($PL = 17mm$). The effect of the air gap is also not included in our theory.

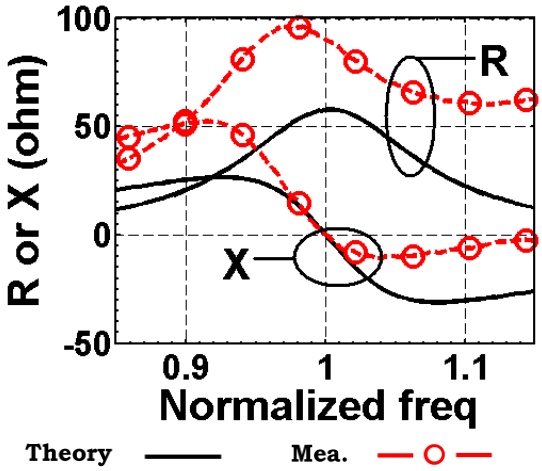

Fig 11.9 Comparison of input impedance with experimental data for TM^z_{101} mode ($\theta_i = 67^o,\ a = 39mm,\ d = 30.5mm, \varepsilon_r = 10, x_o = 16mm, y_o = 0mm, PL = 17mm$)

11.4 Conclusion

In this chapter, theoretical investigation on isosceles $\theta_i - \theta_i - \varphi_i$ Triangular Dielectric Resonator Antenna (TDRA) is presented for TM^z_{mnp} modes for the first time using simple magnetic wall dielectric waveguide model. Our theory is valid for TM^z_{10p} modes only as the tri-linear transformation is not applicable for arbitrary isosceles triangles. Approximate solutions for eigenfunctions and eigenvalues are derived. Approximate expression is also given here to predict the resonant frequency with an accuracy of 4%. Far-field

radiation patterns, radiation Q-factor (Q_r), radiated power in percentage $(P_r(\%) = 2\pi/Q_r \times 100\%)$, bandwidth (BW), efficiency (e), gain (G) are also discussed. From these theoretical investigations, it is found that:

- Resonant frequency for fundamental TM^z_{101} mode increases as the size of the isosceles $\theta_i - \theta_i - \varphi_i$ TDRA decreases (i.e. θ_i increases from 60° to 90°) whereas the same decreases for isosceles $\theta_i - \theta_i - \varphi_i$ TMA.
- All TM^z_{10p} $(p = 1,3,5 \ldots)$ modes produce a peak in the broadside direction.
- Higher order modes can be used to produce higher gain compared to fundamental TM^z_{101} mode by selecting proper dimensions and permittivity of the TDRA.

Part IV

Efficient Technique

Chapter

Chapter XII

Inhomogeneous Rectangular Dielectric Resonator Antenna

12.1 Introduction

Dielectric Resonator Antenna (DRA) has got various advantages like small size, low loss, inherent wideband nature and high radiation efficiency. Hemispherical, cylindrical and rectangular shaped DRAs have been analyzed widely [5, 174]. For a fixed relative permittivity (ε_r), Rectangular DRA (RDRA) having dimensions $a \times b \times d$ shows greater flexibility in terms of frequency selection over cylindrical and spherical DRAs due to its two aspect ratios. The flexibility can further be increased by introducing an additional segment having different relative permittivity (please see Fig. 12.1).

The basic structure of metallic waveguide and dielectric loaded partially filled waveguide are similar but partially filled waveguides have extra degrees of freedom. Hence it shows greater flexibility to tune its cutoff frequency, bandwidth, etc. [186-187]. Partially filled waveguides have been investigated using mode matching technique [186-187] and transmission line theory [188]. Similar analysis on aperture fed RDRA using mode matching technique is available in [23]. Hollow RDRA has also been analyzed using transmission line model [189].

The vertically stacked configuration of RDRA having two or more segments has been reported using dielectric waveguide model [190]. CAD model had also been reported by the subsequent researchers [191-192] to predict the resonant frequency of such stacked RDRA.

In this work, stacking of RDRA is done along the width (y-direction) of RDRA as shown in Fig. 12.1. The two segments have an identical cross-section along x-z direction ($a \times d$) but different width (b_1, b_2) along y-direction and have

different relative permittivity ($\varepsilon_{r1}, \varepsilon_{r2}$). Simple boundary conditions are applied as available for conventional RDRA [21]. Fundamental TE_{111}^{y} mode is investigated using mode matching technique. A closed form simple transcendental equation is given here for computing the wave-numbers along the y - direction inside the two parallel segments of RDRA. Theoretical results are verified with the 3D EM simulator for a wide range of dimensions and relative permittivity. One sample is also fabricated for theoretical validation. It is found that our theoretical results are in close agreement with measured data and data obtained using the 3D EM simulator. It is found that Horizontally Inhomogeneous RDRA (HIRDRA) gives broadside radiation patterns for TE_{111}^{y} mode and the patterns are almost symmetric.

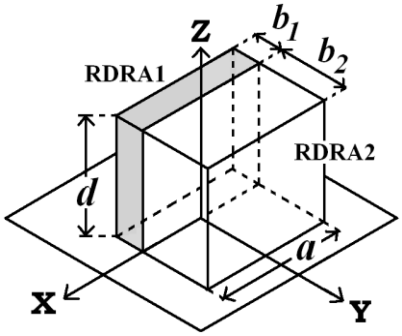

Fig. 12.1 Geometry of the antenna

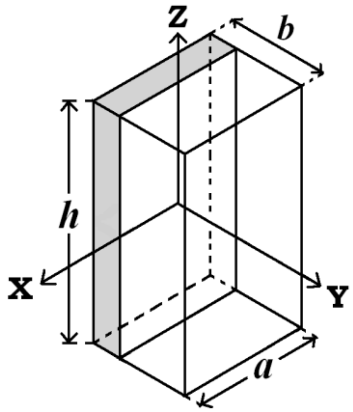

Fig. 12.2 Geometry of an isolated HIRDRA

12.2 Theory

Two RDRA segments, RDRA1 and RDRA2 having dimensions $a \times b_1 \times d$ and $a \times b_2 \times d$ and relative permittivity ε_{r1} and ε_{r2} respectively are stacked horizontally along the y-direction and placed over a common ground plane as shown in Fig. 12.1. The x-axis is placed along the interface between these two RDRAs and the origin is placed at the center of its side a. For theoretical analysis, ground plane is removed first by applying image theory and this process results in an isolated similar structure having dimensions $a \times b \times h$ where $h = 2d$ and $b = b_1 + b_2$ as shown in Fig. 12.2. Perfect Magnetic

Conductors (PMC) are considered at $x = \pm a/2$ and $z = \pm h/2$ and imperfect magnetic conductors are considered at $y = -b_1$ and $y = b_2$ [21].

12.2.1 Eigenfunctions

The structure of isolated horizontally inhomogeneous RDRA has a dielectric discontinuity along the y - direction only. We are interested to investigate the fundamental TE^{y}_{111} mode for theoretical simplicity. A suitable choice of wave variation along x and z-directions inside the two RDRA segments for pure TE^{y} mode can be expressed as:

$$f(x,z) = sin\left(\frac{m\pi}{a}\left(x+\frac{a}{2}\right)\right) sin\left(\frac{p\pi}{h}\left(z+\frac{h}{2}\right)\right) \tag{12.1}$$

Due to the existence of imperfect magnetic conductors, fields are exponentially decaying outside the resonator along the y-direction. Thus, following [175], the eigenfunctions (ψ_{mnp}) inside the two RDRA segments can be expressed as:

$$\psi = f(x,z) \times \begin{cases} A_3 e^{\gamma_y (y+b_1)}, & y \le -b_1 \\ \left[A_1\, cos\left(k_{y1}y\right) + B_1\, sin\left(k_{y1}y\right)\right], & -b_1 \le y \le 0 \\ \left[A_2\, cos\left(k_{y2}y\right) + B_2\, sin\left(k_{y2}y\right)\right], & 0 \le y \le b_2 \\ A_4 e^{-\gamma_y (y-b_2)}, & y \ge b_2 \end{cases} \tag{12.2}$$

where

$$k_{x1}^2 + k_{y1}^2 + k_{z1}^2 = \varepsilon_{r1} k_0^2 \tag{12.3}$$

$$k_{x2}^2 + k_{y2}^2 + k_{z2}^2 = \varepsilon_{r2} k_0^2 \tag{12.4}$$

$$k_{x1}^2 - \gamma_y^2 + k_{z1}^2 = k_0^2 \tag{12.5}$$

Here, k_0 is the free-space wave number,

$$k_{x1} = k_{x2} = k_x = m\,\pi/a \quad ; \quad m = 1,2,3,4\ldots. \tag{12.6}$$

$$k_{z1} = k_{z2} = k_z = p\,\pi/h \quad ; \quad p = 1,2,3,4\ldots. \tag{12.7}$$

and other terms are carrying usual meaning. It is worth mentioning that γ_y can be expressed from equations (12.3) – (12.5) as:

$$\gamma_y^2 = (\varepsilon_{r1} - 1)k_0^2 - k_{y1}^2 \tag{12.8}$$

$$\gamma_y^2 = (\varepsilon_{r2} - 1)k_0^2 - k_{y2}^2 \tag{12.9}$$

Computation Various Constant:

To evaluate the coefficients $A_1 - A_4$ and $B_1 - B_2$, tangential electric and magnetic fields are matched at $y = -b_1, 0$ and b_2.

Fields matching at $y = -b_1$

$$E_x, E_z \Rightarrow A_3 = \frac{1}{\varepsilon_{r1}} \times \left[A_1 \cos(-k_{y1}b_1) + B_1 \sin(-k_{y1}b_1)\right]$$

$$= \frac{1}{\varepsilon_{r1}} \times \left[A_1 \cos(k_{y1}b_1) - B_1 \sin(k_{y1}b_1)\right] \tag{12.9}$$

$$H_x, H_z \Rightarrow A_3(\gamma_y) = \frac{1}{\varepsilon_{r1}} \times (k_{y1})\left[-A_1 \sin(-k_{y1}b_1) + B_1 \cos(-k_{y1}b_1)\right]$$

$$= \frac{1}{\varepsilon_{r1}} \times (k_{y1})\left[A_1 \sin(k_{y1}b_1) + B_1 \cos(k_{y1}b_1)\right] \tag{12.10}$$

Dividing equation (12.9) by (12.10), we get:

$$\frac{A_3}{A_3(\gamma_y)} = \frac{\frac{1}{\varepsilon_{r1}} \times \left[A_1 \cos(k_{y1}b_1) - B_1 \sin(k_{y1}b_1)\right]}{\frac{1}{\varepsilon_{r1}} \times (k_{y1})\left[A_1 \sin(k_{y1}b_1) + B_1 \cos(k_{y1}b_1)\right]}$$

$$\Rightarrow \frac{A_1}{B_1} = \frac{-\left[R_1 + tan(k_{y1}b_1)\right]}{\left[R_1 \tan(k_{y1}b_1) - 1\right]} = \frac{\left[R_1 + tan(k_{y1}b_1)\right]}{\left[1 - R_1 \tan(k_{y1}b_1)\right]} \quad ; \quad R_1 = k_{y1}/\gamma_y \tag{12.11}$$

Fields matching at $y = b_2$

$$E_x, E_z \Rightarrow A_4 = \frac{1}{\varepsilon_{r2}} \times \left[A_2 \cos(k_{y2}b_2) + B_2 \sin(k_{y2}b_2)\right] \tag{12.12}$$

$$H_x, H_z \Rightarrow A_4(-\gamma_y) = \frac{1}{\varepsilon_{r2}} \times (k_{y2})\left[-A_2 \sin(k_{y2}b_2) + B_2 \cos(k_{y2}b_2)\right] \tag{12.13}$$

Dividing equation (12.12) by (12.13), we get:

$$\frac{A_4}{A_4(-\gamma_y)} = \frac{\frac{1}{\varepsilon_{r2}} \times \left[A_2\, cos(k_{y2}b_2) + B_2\, sin(k_{y2}b_2)\right]}{\frac{1}{\varepsilon_{r2}} \times (k_{y2})\left[-A_2\, sin(k_{y2}b_2) + B_2\, cos(k_{y2}b_2)\right]}$$

$$\Rightarrow \frac{A_2}{B_2} = \frac{\left[R_2 + tan(k_{y2}b_2)\right]}{\left[R_2\, tan(k_{y2}b_2) - 1\right]} \quad ; \quad R_2 = k_{y2}/\gamma_y \tag{12.14}$$

Fields matching at $y = 0$

$$E_x, E_z \Rightarrow \frac{1}{\varepsilon_{r1}} \times [A_1\, cos(0) + B_1\, sin(0)]$$

$$= \frac{1}{\varepsilon_{r2}} \times [A_2\, cos(0) + B_2\, sin(0)] \tag{12.15}$$

$$H_x, H_z \Rightarrow \frac{1}{\varepsilon_{r1}} \times (k_{y1})[-A_1\, sin(0) + B_1\, cos(0)]$$

$$= \frac{1}{\varepsilon_{r2}} \times (k_{y2})[-A_2\, sin(0) + B_2\, cos(0)] \tag{12.16}$$

Dividing equation (12.15) by (12.16), we get:

$$\frac{\frac{1}{\varepsilon_{r1}} \times [A_1\, cos(0) + B_1\, sin(0)]}{\frac{1}{\varepsilon_{r1}} \times (k_{y1})[-A_1\, sin(0) + B_1\, cos(0)]} = \frac{\frac{1}{\varepsilon_{r2}} \times [A_2\, cos(0) + B_2\, sin(0)]}{\frac{1}{\varepsilon_{r2}} \times (k_{y2})[-A_2\, sin(0) + B_2\, cos(0)]}$$

$$\Rightarrow \frac{A_1}{B_1} = \frac{k_{y1}}{k_{y2}} \times \frac{A_2}{B_2} \tag{12.17}$$

$$\Rightarrow \frac{\left[R_1 + tan(k_{y1}b_1)\right]}{\left[1 - R_1\, tan(k_{y1}b_1)\right]} = \frac{k_{y1}}{k_{y2}} \times \frac{\left[R_2 + tan(k_{y2}b_2)\right]}{\left[R_2\, tan(k_{y2}b_2) - 1\right]} \text{ ; from equ. (12.11)and (12.14)}$$

$$\Rightarrow k_{y2}\left[k_{y1} + \gamma_y\, tan(k_{y1}b_1)\right]\left[k_{y2}\, tan(k_{y2}b_2) - \gamma_y\right]$$

$$- k_{y1}\left[k_{y2} + \gamma_y\, tan(k_{y2}b_2)\right]\left[k_{y1}\, tan(k_{y1}b_1) - \gamma_y\right] = 0 \tag{12.18}$$

A close look at equations (12.3)-(12.4) reveal that k_{y1} and k_{y2} are the functions of free-space wave number k_0. Hence, equation (12.18) is a function of k_0 only for a given set of values of a, b_1, b_2, d, ε_{r1} and ε_{r2}. After solving equation (12.18) for k_0 , one can find the resonant frequency. After simple algebraic mathematical calculation, the eigenfunctions can be expressed as:

$$\psi = D \times sin\left(\frac{m\pi}{a}\left(x+\frac{a}{2}\right)\right) sin\left(\frac{p\pi}{h}\left(z+\frac{h}{2}\right)\right) \times \begin{cases} A\, sin\left(k_{y1}y+\alpha\right), & \text{in RDRA1} \\ B\, sin\left(k_{y2}y+\beta\right), & \text{in RDRA2} \end{cases} \quad (12.19)$$

where

$$A = T_3\sqrt{(T_1)^2+1} \quad ; \quad B = \sqrt{(T_2)^2+1} \quad ; \quad \alpha = tan^{-1}(T_1) \quad ; \quad \beta = tan^{-1}(T_2) \quad (12.20a)$$

$$T_1 = \frac{\left[k_{y1}+\gamma_y\, tan\left(k_{y1}b_1\right)\right]}{\left[\gamma_y - k_{y1}\, tan\left(k_{y1}b_1\right)\right]}, T_2 = \frac{\left[k_{y2}+\gamma_y\, tan\left(k_{y2}b_2\right)\right]}{\left[k_{y2}\, tan\left(k_{y2}b_2\right)-\gamma_y\right]}, T_3 = \left(\frac{\varepsilon_{r1}}{\varepsilon_{r2}}\right) \times \left(\frac{k_{y2}}{k_{y1}}\right) \quad (12.20b)$$

Here, D is a constant. It is worth mentioning here that k_{y1} and k_{y2} will be either real or pure imaginary for loss-less cases [4, 188] such that if k_{y1} is real, k_{y2} will be imaginary and vice versa. Further, α will be either pure imaginary or real for imaginary and real values of k_{y1} respectively. A similar phenomenon is also found for β.

12.2.2 Resonant Frequency

The transcendental equation (12.18) can be solved for free-space wave number k_0 which results the resonant frequency of the structure for TE^{y}_{111} mode. To evaluate the resonant frequency, bisection method is used. A solution is obtained if the relative absolute convergence between any two successive solutions is less than 10^{-12}.

12.2.3 Internal Field Components

Once the eigenfunctions of a cavity is found, it is quite simple to express all the internal field components using Maxwell's equations [4, 16]. The internal field components within these two RDRA segments can be written as:

Field components in RDRA1 $(|x| \le a/2\,, -b_1 \le y \le 0, |z| \le h/2)$

$$E_x = \frac{1}{\epsilon} \times (k_z) \times DA \times sin\left(k_x\left(x+\frac{a}{2}\right)\right) sin\left(k_{y1}y+\alpha\right) cos\left(k_z\left(x+\frac{h}{2}\right)\right)$$

$$E_y = 0$$

$$E_z = \frac{-1}{\epsilon} \times (k_x) \times DA \times cos\left(k_x\left(x+\frac{a}{2}\right)\right) sin(k_{y1}y+\alpha)\, sin\left(k_z\left(x+\frac{h}{2}\right)\right)$$

$$H_x = \frac{-j}{\omega\mu\epsilon} \times (k_x k_{y1}) \times DA \times cos\left(k_x\left(x+\frac{a}{2}\right)\right) cos(k_{y1}y+\alpha)\, sin\left(k_z\left(x+\frac{h}{2}\right)\right)$$

$$H_y = \frac{-j}{\omega\mu\epsilon} \times (k_x^2 + k_z^2) \times DA \times sin\left(k_x\left(x+\frac{a}{2}\right)\right) sin(k_{y1}y+\alpha)\, sin\left(k_z\left(x+\frac{h}{2}\right)\right)$$

$$H_z = \frac{-j}{\omega\mu\epsilon} \times (k_{y1}k_z) \times DA \times sin\left(k_x\left(x+\frac{a}{2}\right)\right) cos(k_{y1}y+\alpha)\, cos\left(k_z\left(x+\frac{h}{2}\right)\right) \qquad (12.21)$$

Field components in RDRA2 $|x| \le a/2,\ \ 0 \le y \le b_2,\ |z| \le h/2$)

$$E_x = \frac{1}{\epsilon} \times (k_z) \times DB \times sin\left(k_x\left(x+\frac{a}{2}\right)\right) sin(k_{y2}y+\beta)\, cos\left(k_z\left(x+\frac{h}{2}\right)\right)$$

$$E_y = 0$$

$$E_z = \frac{-1}{\epsilon} \times (k_x) \times DB \times cos\left(k_x\left(x+\frac{a}{2}\right)\right) sin(k_{y2}y+\beta)\, sin\left(k_z\left(x+\frac{h}{2}\right)\right)$$

$$H_x = \frac{-j}{\omega\mu\epsilon} \times (k_x k_{y2}) \times DB \times cos\left(k_x\left(x+\frac{a}{2}\right)\right) cos(k_{y2}y+\beta)\, sin\left(k_z\left(x+\frac{h}{2}\right)\right)$$

$$H_y = \frac{-j}{\omega\mu\epsilon} \times (k_x^2 + k_z^2) \times DB \times sin\left(k_x\left(x+\frac{a}{2}\right)\right) sin(k_{y2}y+\beta)\, sin\left(k_z\left(x+\frac{h}{2}\right)\right)$$

$$H_z = \frac{-j}{\omega\mu\epsilon} \times (k_{y2}k_z) \times DB \times sin\left(k_x\left(x+\frac{a}{2}\right)\right) cos(k_{y2}y+\beta)\, cos\left(k_z\left(x+\frac{h}{2}\right)\right) \qquad (12.22)$$

12.2.4 Far-Field Radiation Patterns

Far-field radiation patterns are computed using 'Equivalence Principle' [4, 16]. For theoretical investigations of fundamental TE_{111}^{y} mode of the HIRDRA, Perfect Magnetic Conductor (PMC) is applied at $x = \pm a/2$ and $z = \pm h/2$. Imperfect magnetic Conductor (IPMC) is applied at $y = -b_1$ and $y = b_2$. For theoretical computation, the top view of the HIDRA is shown in Fig. 12.3. Therefore the magnetic surface current $\vec{M}_s$ is evaluated at $x = \pm a/2$ and

$z = \pm h/2$ whereas the electric surface current $\vec{J}_s$ and $\vec{M}_s$ both are evaluated at $y = -b_1$ and $y = b_2$.

Fields along AB Surface $(x = a/2)$

$$M_s^{AB} = \vec{E} \times \hat{n} = [E_x\hat{x} + 0 + E_z\hat{z}] \times (\hat{x}) = [0 + 0 + E_z\hat{y}] \quad (12.23a)$$

Fields along FE Surface $(x = -a/2)$

$$M_s^{FE} = \vec{E} \times \hat{n} = [E_x\hat{x} + 0 + E_z\hat{z}] \times (-\hat{x}) = [0 + 0 - E_z\hat{y}] \quad (12.23b)$$

Fields along AF Surface $(y = -b_1)$

$$M_s^{AF} = \vec{E} \times \hat{n} = [E_x\hat{x} + 0 + E_z\hat{z}] \times (-\hat{y}) = [-E_x\hat{z} + E_z\hat{x}]$$

$$J_s^{AF} = \hat{n} \times \vec{H} = (-\hat{y}) \times \left[H_x\hat{x} + H_y\hat{y} + H_z\hat{z}\right] = [H_x\hat{z} - H_z\hat{x}] \quad (12.23c)$$

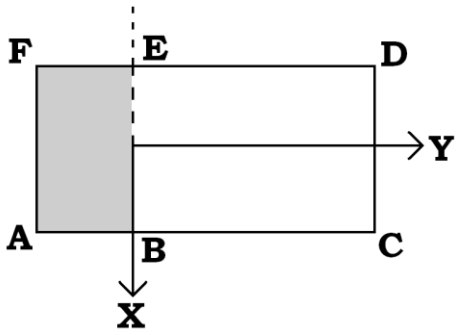

Fig. 12.3 Top view of HIRDRA for evaluating far-field

Fields along TOP Surface $(z = +h/2)$

$$M_s^{TOP1} = \vec{E} \times \hat{n} = [E_x\hat{x} + 0 + E_z\hat{z}] \times (\hat{z}) = [-E_x\hat{y}] \quad (12.23d)$$

Fields along BOTTOM Surface $(z = -h/2)$

$$M_s^{BOTTOM1} = \vec{E} \times \hat{n} = [E_x\hat{x} + 0 + E_z\hat{z}] \times (-\hat{z}) = [E_x\hat{y}] \quad (12.23e)$$

Before doing any calculations for radiated fields, let's first consider a simple integration defined for real U and V as:

$$I_x = \int_{x=t_1}^{t_2} \begin{bmatrix} sin(Ux+V) \\ cos(Ux+V) \end{bmatrix} \times e^{jWx} dx = I(P, Q, t_1, t_2, U, V, W) \quad (12.24a)$$

$$= \frac{e^{jV}}{Q} \times J(t_1, t_2, R = W + U) + \frac{P}{Q} \times e^{-jV} \times J(t_1, t_2, R = W - U) \qquad (12.24b)$$

where

$$J(t_1, t_2, R) = \int_{x=t_1}^{t_2} e^{jxR}\, dx = \begin{cases} \dfrac{e^{jRt_2} - e^{jRt_1}}{R}, & R \neq 0 \\ (t_2 - t_1), & R = 0 \end{cases} \qquad (12.24c)$$

Assuming that;

$\chi_1 = k_o sin(\theta) cos(\varphi) \quad ; \quad \chi_2 = k_o sin(\theta) sin(\varphi) \quad ; \quad \chi_3 = k_o cos(\theta)$

$$I_x^{sin} = \int_{x=t_1}^{t_2} sin(k_x(x + a/2)) \times e^{jWx} dx = \int_{x=t_1}^{t_2} sin(k_x x + k_x\, a/2) \times e^{jWx} dx$$
$$= I(P = -1, Q = 2j, t_1, t_2, U = k_x, V = k_x\, a/2\,, W = \chi_1) \qquad (12.25a)$$

$$I_x^{cos} = \int_{x=t_1}^{t_2} cos\big(k_x(x + a/2)\big) \times e^{jWx} dx$$
$$= I(P = 1, Q = 2, t_1, t_2, U = k_x, V = k_x\, a/2\,, W = \chi_1) \qquad (12.25b)$$

$$I_y^{sin} = \int_{x=t_1}^{t_2} sin\big(k_{y1} y + \alpha\big) \times e^{jWy} dy$$
$$= I(P = -1, Q = 2j, t_1, t_2, U = k_{y1}, V = \alpha, W = \chi_2) \qquad (12.25c)$$

$$I_y^{cos} = \int_{x=t_1}^{t_2} cos\big(k_{y1} y + \alpha\big) \times e^{jWy} dy$$
$$= I(P = 1, Q = 2, t_1, t_2, U = k_{y1}, V = \alpha, W = \chi_2) \qquad (12.25d)$$

$$I_z^{sin} = \int_{x=t_1}^{t_2} sin\big(k_z(z + h/2)\big) \times e^{jWz} dz$$
$$= I(P = -1, Q = 2j, t_1, t_2, U = k_z, V = k_z\, h/2\,, W = \chi_3) \qquad (12.25e)$$

$$I_z^{cos} = \int_{x=t_1}^{t_2} cos\big(k_z(z + h/2)\big) \times e^{jWz} dz$$
$$= I(P = 1, Q = 2, t_1, t_2, U = k_z, V = k_z\, h/2\,, W = \chi_3) \qquad (12.25f)$$

- **Radiated Field from RDRA1:**

Fields along AB Surface $(x = a/2)$

$$M_s^{AB} = \vec{E} \times \hat{n} = [E_x\hat{x} + 0 + E_z\hat{z}] \times (\hat{x}) = [0 + 0 + E_z\hat{y}]$$

$$E_z = \frac{-1}{\epsilon}\frac{\partial\psi}{\partial x} = \frac{-1}{\epsilon} \times (k_x) \times DA \times cos\left(k_x\left(x + \frac{a}{2}\right)\right) sin(k_{y1}y + \alpha)\, sin\left(k_z\left(x + \frac{h}{2}\right)\right)$$

$$F_y^{AB} = \frac{-1}{\epsilon} \times (k_x) \times DA \times cos(k_x a) \times I_y^{sin1} \times I_z^{sin1} \qquad (12.26)$$

Fields along FE Surface $(x = -a/2)$

$$M_s^{FE} = \vec{E} \times \hat{n} = [E_x\hat{x} + 0 + E_z\hat{z}] \times (-\hat{x}) = [0 + 0 - E_z\hat{y}]$$

$$E_z = \frac{-1}{\epsilon}\frac{\partial\psi}{\partial x} = \frac{-1}{\epsilon} \times (k_x) \times DA \times cos\left(k_x\left(x + \frac{a}{2}\right)\right) sin(k_{y1}y + \alpha)\, sin\left(k_z\left(x + \frac{h}{2}\right)\right)$$

$$F_y^{FE} = \frac{-1}{\epsilon} \times (-k_x) \times DA \times cos(0) \times I_y^{sin1} \times I_z^{sin1} \qquad (12.27)$$

Fields along AF Surface $(y = -b_1)$

$$M_s^{AF} = \vec{E} \times \hat{n} = [E_x\hat{x} + 0 + E_z\hat{z}] \times (-\hat{y}) = [-E_x\hat{z} + E_z\hat{x}]$$

$$J_s^{AF} = \hat{n} \times \vec{H} = (-\hat{y}) \times \left[H_x\hat{x} + H_y\hat{y} + H_z\hat{z}\right] = [H_x\hat{z} - H_z\hat{x}]$$

$$E_x = \frac{1}{\epsilon}\frac{\partial\psi}{\partial z} = \frac{1}{\epsilon} \times (k_z) \times DA \times sin\left(k_x\left(x + \frac{a}{2}\right)\right) sin(k_{y1}y + \alpha)\, cos\left(k_z\left(x + \frac{h}{2}\right)\right)$$

$$E_z = \frac{-1}{\epsilon}\frac{\partial\psi}{\partial x} = \frac{-1}{\epsilon} \times (k_x) \times DA \times cos\left(k_x\left(x + \frac{a}{2}\right)\right) sin(k_{y1}y + \alpha)\, sin\left(k_z\left(x + \frac{h}{2}\right)\right)$$

$$H_x = \frac{-j}{\omega\mu\epsilon}\frac{\partial^2\psi}{\partial x\partial y} = \frac{-j}{\omega\mu\epsilon} \times (k_x k_{y1}) \times DA \times cos\left(k_x\left(x + \frac{a}{2}\right)\right) cos(k_{y1}y + \alpha)\, sin\left(k_z\left(x + \frac{h}{2}\right)\right)$$

$$H_z = \frac{-j}{\omega\mu\epsilon}\frac{\partial^2\psi}{\partial y\partial z} = \frac{-j}{\omega\mu\epsilon} \times (k_{y1}k_z) \times DA \times sin\left(k_x\left(x + \frac{a}{2}\right)\right) cos(k_{y1}y + \alpha)\, cos\left(k_z\left(x + \frac{h}{2}\right)\right)$$

$$F_x^{AF} = \frac{-1}{\epsilon} \times (k_x) \times DA \times I_x^{cos1} \times sin(-k_{y1}b_1 + \alpha) \times I_z^{sin1}$$

$$F_z^{AF} = \frac{1}{\epsilon} \times (-k_z) \times DA \times I_x^{sin1} \times sin(-k_{y1}b_1 + \alpha) \times I_z^{cos1}$$

$$A_x^{AF} = \frac{-j}{\omega\mu\epsilon} \times (-k_{y1}k_z) \times DA \times I_x^{sin1} \times cos(-k_{y1}b_1 + \alpha) \times I_z^{cos1}$$

$$A_z^{AF} = \frac{-j}{\omega\mu\epsilon} \times (k_x k_{y1}) \times DA \times I_x^{cos1} \times cos\left(-k_{y1} b_1 + \alpha\right) \times I_z^{sin1} \tag{12.28}$$

Fields along TOP Surface $(z = +h/2)$

$$M_s^{TOP1} = \vec{E} \times \hat{n} = [E_x\hat{x} + 0 + E_z\hat{z}] \times (\hat{z}) = [-E_x\hat{y}]$$

$$E_x = \frac{1}{\epsilon}\frac{\partial\psi}{\partial z} = \frac{1}{\epsilon} \times (k_z) \times DA \times sin\left(k_x\left(x + \frac{a}{2}\right)\right) sin\left(k_{y1}y + \alpha\right) cos\left(k_z\left(x + \frac{h}{2}\right)\right)$$

$$F_y^{Top1} = \frac{1}{\epsilon} \times (-k_z) \times DA \times I_x^{sin1} \times I_y^{sin1} \times cos(k_z h) \tag{12.29}$$

Fields along BOTTOM Surface $(z = -h/2)$

$$M_s^{BOTTOM1} = \vec{E} \times \hat{n} = [E_x\hat{x} + 0 + E_z\hat{z}] \times (-\hat{z}) = [E_x\hat{y}]$$

$$E_x = \frac{1}{\epsilon}\frac{\partial\psi}{\partial z} = \frac{1}{\epsilon} \times (k_z) \times DA \times sin\left(k_x\left(x + \frac{a}{2}\right)\right) sin\left(k_{y1}y + \alpha\right) cos\left(k_z\left(x + \frac{h}{2}\right)\right)$$

$$F_y^{Bottom1} = \frac{1}{\epsilon} \times (k_z) \times DA \times I_x^{sin1} \times I_y^{sin1} \times cos(0h) \tag{12.30}$$

- **Radiated Field from RDRA2:**

Fields along BC Surface $(x = a/2)$

$$M_s^{AB} = \vec{E} \times \hat{n} = [E_x\hat{x} + 0 + E_z\hat{z}] \times (\hat{x}) = [0 + 0 + E_z\hat{y}]$$

$$E_z = \frac{-1}{\epsilon}\frac{\partial\psi}{\partial x} = \frac{-1}{\epsilon} \times (k_x) \times DB \times cos\left(k_x\left(x + \frac{a}{2}\right)\right) sin\left(k_{y2}y + \beta\right) sin\left(k_z\left(x + \frac{h}{2}\right)\right)$$

$$F_y^{BC} = \frac{-1}{\epsilon} \times (k_x) \times DB \times cos(k_x a) \times I_y^{sin2} \times I_z^{sin2} \tag{12.31}$$

Fields along ED Surface $(x = -a/2)$

$$M_s^{ED} = \vec{E} \times \hat{n} = [E_x\hat{x} + 0 + E_z\hat{z}] \times (-\hat{x}) = [0 + 0 - E_z\hat{y}]$$

$$E_z = \frac{-1}{\epsilon}\frac{\partial\psi}{\partial x} = \frac{-1}{\epsilon} \times (k_x) \times DB \times cos\left(k_x\left(x + \frac{a}{2}\right)\right) sin\left(k_{y2}y + \beta\right) sin\left(k_z\left(x + \frac{h}{2}\right)\right)$$

$$F_y^{ED} = \frac{-1}{\epsilon} \times (-k_x) \times DB \times cos(0) \times I_y^{sin2} \times I_z^{sin2} \tag{12.32}$$

Fields along CD Surface $(\boldsymbol{y = b_2})$

$$M_s^{CD} = \vec{E} \times \hat{n} = [E_x\hat{x} + 0 + E_z\hat{z}] \times (\hat{y}) = [E_x\hat{z} - E_z\hat{x}]$$

$$J_s^{CD} = \hat{n} \times \vec{H} = (\hat{y}) \times \left[H_x\hat{x} + H_y\hat{y} + H_z\hat{z}\right] = [-H_x\hat{z} + H_z\hat{x}]$$

$$E_x = \frac{1}{\epsilon}\frac{\partial\psi}{\partial z} = \frac{1}{\epsilon} \times (k_z) \times DB \times sin\left(k_x\left(x + \frac{a}{2}\right)\right) sin\left(k_{y2}y + \beta\right) cos\left(k_z\left(x + \frac{h}{2}\right)\right)$$

$$E_z = \frac{-1}{\epsilon}\frac{\partial\psi}{\partial x} = \frac{-1}{\epsilon} \times (k_x) \times DB \times cos\left(k_x\left(x + \frac{a}{2}\right)\right) sin\left(k_{y2}y + \beta\right) sin\left(k_z\left(x + \frac{h}{2}\right)\right)$$

$$H_x = \frac{-j}{\omega\mu\epsilon}\frac{\partial^2\psi}{\partial x\partial y} = \frac{-j}{\omega\mu\epsilon} \times (k_x k_{y2}) \times DB \times cos\left(k_x\left(x + \frac{a}{2}\right)\right) cos\left(k_{y2}y + \beta\right) sin\left(k_z\left(x + \frac{h}{2}\right)\right)$$

$$H_z = \frac{-j}{\omega\mu\epsilon}\frac{\partial^2\psi}{\partial y\partial z} = \frac{-j}{\omega\mu\epsilon} \times \left(k_{y2}k_z\right) \times DB \times sin\left(k_x\left(x + \frac{a}{2}\right)\right) cos\left(k_{y2}y + \beta\right) cos\left(k_z\left(x + \frac{h}{2}\right)\right)$$

$$F_x^{CD} = \frac{-1}{\epsilon} \times (-k_x) \times DB \times I_x^{cos2} \times sin\left(k_{y2}b_2 + \beta\right) \times I_z^{sin2}$$

$$F_z^{CD} = \frac{1}{\epsilon} \times (k_z) \times DB \times I_x^{sin2} \times sin\left(k_{y2}b_2 + \beta\right) \times I_z^{cos2}$$

$$A_x^{CD} = \frac{-j}{\omega\mu\epsilon} \times \left(k_{y2}k_z\right) \times DB \times I_x^{sin2} \times cos\left(k_{y2}b_2 + \beta\right) \times I_z^{cos2}$$

$$A_z^{CD} = \frac{-j}{\omega\mu\epsilon} \times (-k_x k_{y2}) \times DB \times I_x^{cos2} \times cos\left(k_{y2}b_2 + \beta\right) \times I_z^{sin2} \qquad (12.33)$$

Fields along Top2 Surface $(\boldsymbol{z = +h/2})$

$$M_s^{Top2} = \vec{E} \times \hat{n} = [E_x\hat{x} + 0 + E_z\hat{z}] \times (\hat{z}) = [-E_x\hat{y}]$$

$$E_x = \frac{1}{\epsilon}\frac{\partial\psi}{\partial z} = \frac{1}{\epsilon} \times (k_z) \times DB \times sin\left(k_x\left(x + \frac{a}{2}\right)\right) sin\left(k_{y2}y + \beta\right) cos\left(k_z\left(x + \frac{h}{2}\right)\right)$$

$$F_y^{Top2} = \frac{1}{\epsilon} \times (-k_z) \times DB \times I_x^{sin2} \times I_y^{sin2} \times cos(k_z h) \qquad (12.34)$$

Fields along Bottom2 Surface $(\boldsymbol{z = -h/2})$

$$M_s^{Bottom2} = \vec{E} \times \hat{n} = [E_x\hat{x} + 0 + E_z\hat{z}] \times (-\hat{z}) = [E_x\hat{y}]$$

$$E_x = \frac{1}{\epsilon}\frac{\partial\psi}{\partial z} = \frac{1}{\epsilon} \times (k_z) \times DB \times sin\left(k_x\left(x + \frac{a}{2}\right)\right) sin\left(k_{y2}y + \beta\right) cos\left(k_z\left(x + \frac{h}{2}\right)\right)$$

$$F_y^{Bottom2} = \frac{1}{\epsilon} \times (k_z) \times DB \times I_x^{sin2} \times I_y^{sin2} \times cos(0h) \qquad (12.35)$$

Therefore, the total far-zone electric field at point $P(r,\theta,\varphi)$ is evaluated as [16]:

$$E_\theta = -\frac{jk_o \exp(-jk_o r)}{4\pi r} \times \left[L_\varphi + \eta_0 N_\theta\right] \tag{12.26a}$$

$$E_\varphi = \frac{jk_o \exp(-jk_o r)}{4\pi r} \times \left[L_\theta - \eta_0 N_\varphi\right] \tag{12.26b}$$

where,

$$N_\theta = A_x cos(\theta)cos(\varphi) + A_y cos(\theta)sin(\varphi) - A_z sin(\theta)$$

$$N_\varphi = -A_x sin(\varphi) + A_y cos(\varphi)$$

$$L_\theta = F_x cos(\theta)cos(\varphi) + F_y cos(\theta)sin(\varphi) - F_z sin(\theta)$$

$$L_\varphi = -F_x sin(\varphi) + F_y cos(\varphi) \tag{12.27}$$

$$F_x = F_x^{AF} + F_x^{CD}$$

$$F_y = F_y^{AB} + F_y^{FE} + F_y^{BC} + F_y^{ED} + F_y^{Top1} + F_y^{Bottom1} + F_y^{Top2} + F_y^{Bottom2}$$

$$F_z = F_z^{AF} + F_z^{CD} \tag{12.28}$$

$$A_x = A_x^{AF} + A_x^{CD}$$

$$A_y = 0$$

$$A_z = A_z^{AF} + A_z^{CD} \tag{12.29}$$

Here, all terms are carrying their usual meaning.

12.3 Results

In this section, theoretical results on resonant frequency and far-field patterns are discussed. Four antennas are fabricated in our laboratory. Typical photograph of fabricated antenna is shown in Fig. 12.4. Dielectric bars are cut manually using hack saw. Different types of sand papers are used to make its surfaces smooth. It is obvious to have some roughness in the surfaces. It is found that these types of small roughness do not give much impact on its characteristics as shown in the next sub-section. Three antennas out of four

are excited using aperture on the ground plane. The last antenna does not cover the whole aperture. Therefore, it is excited using 50Ω coaxial probe.

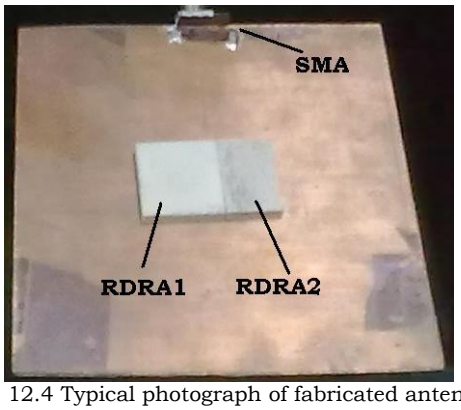

Fig. 12.4 Typical photograph of fabricated antenna

12.3.1 Resonant Frequency

Some samples are simulated using FEM based commercially available 3D numerical EM simulator HFSS [9]. Theoretical results on resonant frequencies are compared with data obtained using 3D EM simulator HFSS. In Table 12.1, total twelve samples are shown for comparison purpose. It is found that theoretical resonant frequencies ($\boldsymbol{f_r^T}$) are in good agreement with an accuracy between 1 - 9%. This is due to the effect of feed mechanism and finite size of ground plane, which are not included in our theory [21]. It is worth mentioning here that the analytical solution for the resonant frequency of conventional RDRA gives accuracy between 1-12% [21].

Due to large no of parameters ($\boldsymbol{a, b_1, b_2, d, \varepsilon_{r1}}$ **and** $\boldsymbol{\varepsilon_{r2}}$), it is very difficult to fit a curve for arbitrary dimensions and permittivity. Complex curve fitted CAD model as reported in [190-192] can be used to minimize the error in the prediction of resonant frequency. These can be done by defining effective dimensions and/or effective permittivity. For a first order approximation, the effective permittivity can be expressed as:

$$\varepsilon_{re1} = 0.88 \times \varepsilon_{r1} \qquad (12.30a)$$

$$\varepsilon_{re2} = 0.88 \times \varepsilon_{r2} \quad (12.30b)$$

where it is assumed that the effect of all dimensional parameters (a, b_1, b_2 and d) are included inherently. Effective permittivity ($\varepsilon_{re1}, \varepsilon_{re2}$) can be expressed using complex function of (a, b_1, b_2, d, ε_{r1} and ε_{r2}) to reduce the error in the prediction of resonant frequency. The same purpose is achieved with a simple curve fitted formula which is valid for arbitrary dimensions (a, b_1, b_2 and d) and relative permittivities of (ε_{r1} and ε_{r2}) as shown in Table 12.1. Equation (12.30) is much simpler than those reported in [190-192]. Further, this simple approximation can predict the resonant frequency within 3% error for a wide range of dimensions and relative permittivity of HIRDRA as shown in Table 12.1.

Table 12.1

Comparison of theoretical resonant frequency with 3D EM simulator HFSS

Sl No	Dimensions (mm)				ε_{r1}	ε_{r2}	Resonant Frequency (GHz)			Error (%)	
	a	d	b_1	b_2			Theory ($\varepsilon_{r1}, \varepsilon_{r2}$)	Theory ($\varepsilon_{re1}, \varepsilon_{re2}$)	HFSS [9]	(ε_{r1}, ε_{r2})	(ε_{re1}, ε_{re2})
1	10	8	5	5	10	25	4.565	4.865	4.737	-3.6	2.63
2	10	12	3	6	80	25	2.761	2.942	2.954	-6.5	-0.39
3	15	15	1	3	40	80	2.215	2.359	2.365	-6.3	-0.24
4	10	10	10	10	50	100	1.836	1.957	2.011	-9.5	-2.73
5	15	10	5	3	100	10	1.850	1.972	1.982	-6.7	-0.51
6	6	4	2	3	10	40	6.324	6.742	6.754	-6.4	-0.17
7	6	6	2	2	10	40	6.592	7.023	6.966	-5.4	0.82
8	6	6	3	3	30	100	3.707	3.952	3.977	-6.8	-0.63
9	12	2.5	1.5	1	100	40	4.988	5.316	5.436	-8.2	-2.26
10	12	2.5	3	2	25	80	5.121	5.458	5.526	-7.3	-1.24
11	5	6	4	5	40	80	4.000	4.264	4.353	-8.8	-2.08
12	5	6	1	4	40	80	4.193	4.469	4.590	-8.6	-2.68

In Table 12.2, theoretical results on resonant frequencies are compared with experimental data. It is found that theoretical results are in good agreement with measured data. Typical photograph of experimental result displaying on S_{11} (in dB) is shown in Figure 12.5.

It is worth mentioning that the interchange of the source free RDRA segments as shown in Figure. 12.1 does not change the resonant frequency of the entire antenna system; because it consists of only two segments and the antenna structure remains unaltered after applying the image theory. A typical result is shown in Table 12.2 (sample III and IV). A little discrepancy is found in the second decimal place of measured resonant frequency. This is due to positional displacement. Further, our theory does not account the effect of excitation (or feed mechanism) and the finite size of ground plane.

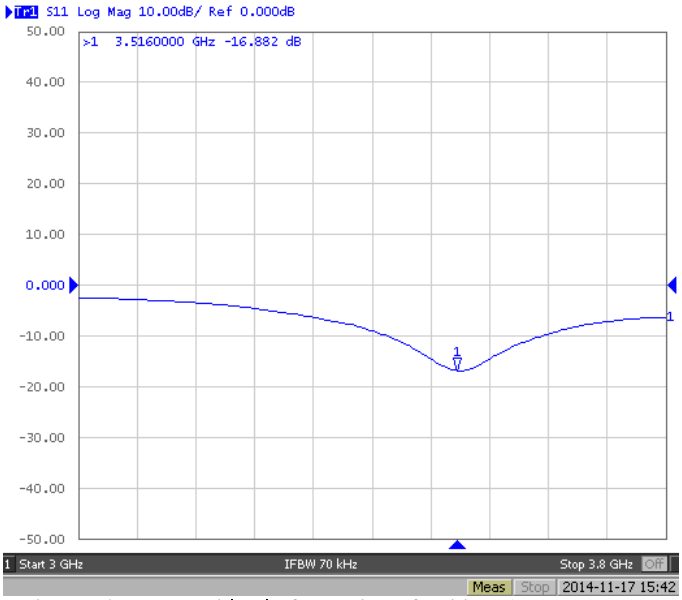

Fig. 12.5 Measured $|S_{11}|$ of sample I of Table II ($a = 25mm, d = 5mm, b_1 = 25mm, b_2 = 17mm, \varepsilon_{r1} = 10, \varepsilon_{r2} = 25$)

It should be noted here that the design of vertically stacked RDRA to achieve wide impedance bandwidth is mainly based on trial and error method and experience. The guidelines for vertically stacked RDRA as reported in [190-192] are limited to a range of thickness and permittivity of the inserted segment. Besides, the permittivity of the inserted segment (ε_i) must be higher than the permittivity of original RDRA (ε_r). But no such restriction is applicable to our case.

Our theory is further applied to compute the resonant frequency of sample no 4 in [193] which deals with full-wave numerical analysis of discontinuities within RDRA. A good agreement with full-wave 3D numerical technique is found. This is shown in Table 12.3.

Further, equations (12.3) – (12.8) as mentioned above give exact same resonant frequency as found for conventional single RDRA for $\varepsilon_{r1} = \varepsilon_{r2} = \varepsilon_r$

(say). Some typical results are shown in Table 12.4.

Table 12.2

Experimental validation of resonant frequency

Sample	Dimensions (mm)				ε_{r1}	ε_{r2}	Resonant Freq. (GHz)		Err (%)
	a	d	b_1	b_2			Theory	Mea. (our)	
I	25	5	25	17	10	25	3.569	3.52	1.37
II	25	25	5	3	10	25	2.757	2.68	2.79
III	25	5	25	5	10	25	4.511	4.42	2.02
IV	25	5	5	25	25	10	4.511	4.43	1.79

Table 12.3

Theoretical validation of resonant frequency with [193] *

Dimensions (mm)				ε_{r1}	ε_{r2}	Res. Freq. (GHz)		Error (%)
a	d	b_1	b_2			Theory	[193]	
7.45	3.725	1.49	1.49	85	75	4.627	4.627	0.0

*Sample No 4 of Table 3 in [193]

Table 12.4

Comparison of resonant frequency with conventional RDRA

for $\varepsilon_{r1} = \varepsilon_{r2} = \varepsilon_r$ and $b = b_1 + b_2$

Sl No	Dimensions (mm)				ε_r	Resonant Frequency (GHz)		Error (%)
	a	d	b_1	b_2		Theory	[21]	
1	15.24	7.62	1	2.1	10.8	6.95	6.95	0.0
2	10.16	7.11	5.16	5	20	4.63	4.63	0.0
3	9.31	9.31	2.3	2.3	37.84	4.00	4.00	0.0
4	8.77	3.51	4	4.77	37.84	4.89	4.89	0.0
5	12.7	6.35	3.35	3	79.46	2.40	2.40	0.0

12.3.2 Radiation Patterns

In this section, theoretical results on far-field radiation patterns are compared with experimental data. MATLAB code is written to compute the E-plane ($\varphi = 0^o$) and H-plane ($\varphi = 90^o$) power patterns. Theoretical far-zone power patterns are shown in Figs. 12.6 for TE^y_{111} mode. It is found that

theoretical results are in close agreement with experimental data. Little discrepancy occurs in the E-plane. This may be due to the finite size of ground plane.

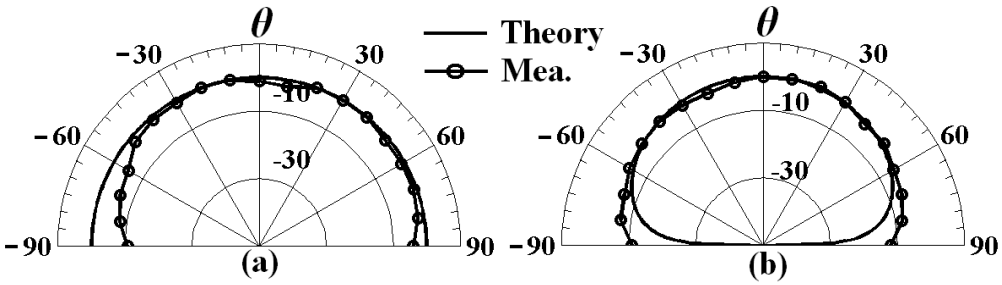

Fig. 12.6 Theoretical and measured far-field patterns of HIRDRA : (a) *E*-plane and (b) *H*-plane ($a = 25mm, d = 5mm, b_1 = 25mm, b_2 = 5mm, \varepsilon_{r1} = 10, \varepsilon_{r2} = 25$)

12.4 Advantages

Horizontally Inhomogeneous RDRA (HIRDRA) is formed here by adding two RDRA segments side by side. This type of structure gives two additional degrees of freedom (width ratio and relative permittivity) to the design of RDRA. These can be used to obtain a wider tuning range in terms of frequency. For example, a conventional probe fed RDRA having dimensions $9mm \times 4mm \times 8mm$ will show resonance at 5.091GHz and 8.087GHz for $\varepsilon_r = 30$ and 10 respectively. Therefore, HIRDRA can be designed to obtain any resonant frequency within 5-8 GHz such that $b_1 + b_2 = b$. This is shown in Fig. 12.7. Probe length can be adjusted to achieve the optimized result.

The second advantage is that the structure is very cost-effective and useful for practical realization. In the above example, the RDRA will show resonance at 5.8GHz for $\varepsilon_r = 21$ which is not readily available, whereas $\varepsilon_r = 20$ (readily available) will show resonance at 5.95GHz. HIRDRA having $b_1 = b_2 = 2mm$ using $\varepsilon_{r1} = 10$ and $\varepsilon_{r2} = 30$, both readily available is able to cover the entire 5.8GHz band (5.69GHz - 5.97GHz) as shown in Fig. 12.7. In this way, with proper tuning, the additional degrees of freedom can lead to an application specific design with any combination of materials available.

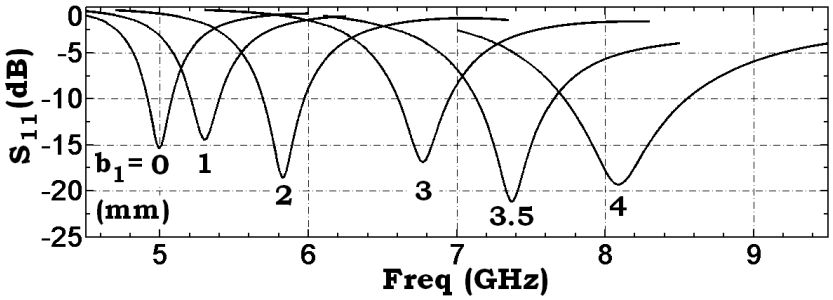

Fig. 12.7 Simulated S_{11} for different values of b_1 , showing the wide tuning range of HIRDRA *($a = 9mm, b = 4mm, d = 8mm, \varepsilon_{r1} = 10$, $b_2 = b - b_1$* and $\varepsilon_{r2} = 30$)

Further, this theory can easily be extended to investigate fractal shaped RDRAs, log-periodic antenna using RDRAs etc., which are not possible using the theory on vertically stacked RDRAs as reported in [190-192].

12.5 Conclusion

In this chapter, inhomogeneous RDRA is investigated analytically for the first time. Fundamental TE^{y}_{111} mode is investigated here for theoretical simplicity. One transcendental equation is given here using the mode matching technique to predict its resonant frequency. It is found that:

- Our theory can predict the resonant frequency with an accuracy of 3%.
- The fundamental TE^{y}_{111} mode produces a peak in the broadside direction.
- Our theory is valid for arbitrary dimensions and permittivity as shown in Table 12.1.

Chapter XIII

Singularity Free Expressions for Far-Field Radiation Patterns

13.1 Introduction

In this dissertation, different types of triangular shaped Microstrip Antennas (MA) and Dielectric Resonator Antennas (DRA) are investigated analytically. Closed form compact expressions for evaluating far-field radiation patterns (E_θ, E_φ) for different antennas are given here in the respective chapters. Analytical expressions for (E_θ, E_φ) are very important to design an antenna quickly for a given specification. Other characteristics such as radiated power (P_r), total Q-factor (Q_t), radiation Q-factor (Q_r), gain (G), directivity (D), bandwidth (BW) etc. are directly related to far-field radiation patterns [12-16, 162]. The input impedance of an antenna is highly dependent on the efficient evaluation of total Q-factor (Q_t) which is in turns a function of (E_θ, E_φ). To evaluate the total radiated power (P_r) over the hemisphere, we generally use numerical integration because of complicated non-separable complex expressions both for $E_\theta(\theta, \varphi)$ and $E_\varphi(\theta, \varphi)$. There is always a possibility to have $1/0$ or $0/0$ form due to singularities occurring for arbitrary dimensions and relative permittivity of an antenna. Therefore, it is important to evaluate the far-zone electric field (E_θ, E_φ) at point $P(r, \theta, \varphi)$ efficiently. Any singularity in the expressions on far-field radiation patterns must be handled efficiently to obtain accurate results quickly. It should be pointed here that MATLAB [164] can integrate a singular function, but it takes a long time. If all the non-singular integrations are solved numerically for a particular value of (θ, φ), it will be time consuming process to evaluate the P_r, Q_t, Q_r, G, D, BW etc.

Commercially available numerical EM simulators such as IE3D [8], HFSS

[9], CST [10] etc. use different numerical techniques to solve a particular boundary value problem (here, radiation from an antenna). Radiation characteristics of an antenna for different modes can easily be predicted using those EM simulators but the user does not get any physical insight. If any singularity occurs in the evaluation of far-field patterns, the EM simulator takes care of it inherently. The end user does not face any difficulty to obtain the end results. The time required to simulate an antenna using the EM simulator is shown in Table 13.1.

On the other hand, singularity free analytic solution of an antenna as presented in this chapter is able to predict the results with proper physical insight. Analytical solutions can give the results much faster than EM simulators. To show the difference, a personal computer having Core 2 duo Intel processor and 3GB RAM is used to simulate rectangular and equilateral triangular shaped microstrip antennas using IE3D, HFSS and CST. Far-field radiation patterns are observed for different modes. The same (far-field radiation patterns) are also evaluated using analytic solutions. A comparison of time is shown in Table 13.1. It is clear from Table 13.1 that analytical solution can predict the far-field radiation patterns of an antenna orders faster than numerical EM simulators.

Table 13.1

Comparison of time between analytical solution and EM simulators

Sl	Antenna	Mode	Time (seconds)			
			IE3D	HFSS	CST	Analytical
1	Rectangular MA	TM_{10}^{z}	218	297	310	2.82
		TM_{21}^{z}	254	305	344	3.12
2	Equilateral TMA	TM_{11}^{z}	241	388	371	3.08
		TM_{30}^{z}	278	391	447	3.11

To predict the far-field radiation patterns (E_θ, E_φ) for any antenna with rectilinear symmetry in Cartesian coordinate system, we generally come across expression of the form frequently as:

$$I_3 = \int \begin{Bmatrix} sin(ax) \\ cos(ax) \end{Bmatrix} exp^{(jbx)} dx \qquad (13.1a)$$

which is singular when $a^2 = b^2$ because I_3 can be expressed as:

$$I_3 = \frac{exp^{(jbx)}}{a^2 - b^2} \times \begin{Bmatrix} [jbsin(ax) - acos(jbx)] \\ [jbcos(ax) + asin(ax)] \end{Bmatrix} \qquad (13.1b)$$

If we do not have any prior knowledge about the original integral (here, expression (13.1a)), it will be a time consuming process to remove the singularity from equation (13.1b) when $a^2 = b^2$. A non-singular integral i.e. (13.1a) becomes singular for particular values of a^2 and b^2. Handling this type of singularity due to the occurrence of (13.1a) in case of rectangular shaped slot, horn, microstrip antenna etc is quite simple compared to the case of equilateral Triangular Microstrip Antenna (TMA). This is due to the complex expression for internal fields (and geometry) of an equilateral TMA. The final expressions of far-field radiation patterns are given by K. F. Lee *et al.* [6] without any explicit step for derivation. If we try to obtain the same expressions as given by K. F. Lee *et al.* in [6], we have to segregate $(m-n), (n-l)$ and $(l-m)$ terms from each line integration along the three sides of the equilateral TMA. This is a time consuming process compared to Rectangular Microstrip Antenna (RMA). Further, there is always a possibility to encounter a singularity at any mode for a particular choice of antenna parameters and/or modal indices. Because each term of equation (13)-(14) of [6] has $(A^2 - B^2)$ like terms in the denominator.

Further, we will encounter similar type of integrations in the evaluation of conductor loss (P_c), dielectric loss (P_d) etc. analytically. Most of the time, these are calculated numerically which is a time consuming process.

In this dissertation, closed form expressions to predict the far-field radiation patterns for different Microstrip Antenna (MA) and Dielectric Resonator Antenna (DRA) are derived analytically as given in the respective chapters. From these expressions, it is found that almost all terms have

$(A^2 - B^2)$ like terms in the denominator. Table 13.2 depicts the total number of singularities for different antennas in the expressions on far-zone electric field (E_θ, E_φ).

Table 13.2

No of singularity for different antennas

Sl No	Ref.	Antenna	Mode	No. of Singularity
1	[162]	Slot Aperture	TE_{10}^z	1
2	[14]	Rectangular MA	TM_{mn}^z	4
3	[6]	Equilateral TMA	TM_{mn}^z	15
4	Our	30°–60°–90° TMA	TM_{mn}^z	12
5	Our	45°–45°–90° TMA	TM_{mn}^z	6
6	Our	Isosceles TMA	TM_{10}^z	10
7	[170]	Rectangular DRA	TE_{111}^z	7
8	Our	Equilateral TDRA	TM_{mnp}^z	29*
9	Our	30°–60°–90° TDRA	TM_{mnp}^z	26*
10	Our	45°–45°–90° TDRA	TM_{mnp}^z	18*
11	Our	Isosceles TDRA	TM_{101}^z	29*

In case of Triangular DRA (TDRA) as marked by '*', the contribution from top and bottom surfaces on the far-field radiation patterns are not considered to give the total no of singularity because of complexity. Typical example of the 2D integration is shown by equation (13.2a) for Equilateral TDRA (ETDRA).

$$I_{cs} = \int_{x=0}^{M} \int_{y=-\eta x}^{\eta x} \left(\sum_{i=1}^{3} -\beta_i \cos(\alpha_i x) \sin(\beta_i y) \right) \times e^{jk_o f(x,y)} dxdy \quad ; \quad \eta = \frac{1}{\sqrt{3}} \tag{13.2a}$$

One will encounter two numbers of this type of integrals for ETDRA. Initially, we tried to solve these kind of integrals analytically. We faced several singularities for arbitrary choice of dimensions, permittivity and modal indices of the ETDRA. I_{cs} can be expressed as:

$$I_{cs} = \left[\frac{(-j\beta_1)}{2(\beta_1^2 - V_2^2)} \times \left(I_{A=(n-l)}^{\beta=\beta_1} + I_{A=(l-m)}^{\beta=\beta_1} \right) + \frac{(-j\beta_2)}{2(\beta_2^2 - V_2^2)} \times \left(I_{A=(l-m)}^{\beta=\beta_2} + I_{A=(m-n)}^{\beta=\beta_2} \right) + \frac{(-j\beta_3)}{2(\beta_3^2 - V_2^2)} \times \left(I_{A=(m-n)}^{\beta=\beta_3} + I_{A=(n-l)}^{\beta=\beta_3} \right) \right] \tag{13.2b}$$

where

$$I_A^{\beta} = \frac{V_2\left[bA \times \left\{e^{j\chi_1 M} \times cos(bAM) - 1\right\} - j\chi_1 \times e^{j\chi_1 M} \times sin(bAM)\right]}{[b^2A^2 - \chi_1^2]} + \frac{\beta\left[jbA \times e^{j\chi_1 M} \times sin(bAM) - \chi_1 \times (e^{j\chi_1 M} \times cos(bAM) - 1)\right]}{[b^2A^2 - \chi_1^2]} + \frac{V_2\left[bA \times \left\{e^{j\chi_2 M} \times cos(bAM) - 1\right\} - j\chi_2 \times e^{j\chi_2 M} \times sin(bAM)\right]}{[b^2A^2 - \chi_2^2]} - \frac{\beta\left[jbA \times e^{j\chi_2 M} \times sin(bAM) - \chi_2 \times (e^{j\chi_2 M} \times cos(bAM) - 1)\right]}{[b^2A^2 - \chi_2^2]} \quad (13.2c)$$

Here all terms are defined in Chapter VIII. The evaluation of I_A^{β} is much lengthier, complex and time consuming process than those presented on any antennas. It is very difficult to overcome those singularities during the evaluation of far-field radiation patterns ($\varphi = 0^o$ and $\varphi = 90^o$ plane) for arbitrary dimensions and permittivity of the equilateral TDRA. Considerable preprocessing effort is required to remove all singularities for efficient computation of I_{cs}. Similar type of difficulties (singularities) will be encountered during the evaluation of far-field patterns of other triangular shaped TDRAs. Therefore, it is important to have one method to produce singularity free expressions.

The L'Hôpital's rule is generally applied to find the value of a function at singularity. The derivation of far-zone electric field and the removal of the singularity may be simple as found (or identified) for rectangular slot aperture (one singularity for TE_{10} mode of operation) [162] or rectangular Microstrip Antenna (MA) (two singularities for TM_{mn}^z mode of operation) [14] but it is a time consuming process for equilateral Triangular MA (TMA) (15 number of singularities for TM_{mn}^z mode of operation) [6] or equilateral TDRA (29 number of singularities for TM_{mnp}^z mode of operation). Further, evaluation of E_θ and E_φ for an equilateral TMA (three modal indices: m, n, l) [6] are much more complex and lengthier than that for rectangular MA (two modal indices: m, n) [14]. An unequal p-sided ($p > 3$) polygonal antenna may have a complex characteristic

function having p number of modal indices and consequently will require a complex mathematical analysis for evaluating the far-field radiation patterns.

It should be pointed out here that the microstrip antennas are analyzed using Cavity Model where the transverse components of electric field i.e. E_x and E_y are set to zero for TM^z mode of operation [12-15]. In case of DRA, these two components (i.e. E_x and E_y) are not zero and we have to consider the contribution of all components of internal fields. Obviously, the analysis of the equilateral triangular DRA will be more complex than equilateral TMA due to the existence of E_x and E_y for TM^z mode of operation.

In this chapter, analytic evaluation of far-field radiation patterns for various antennas with rectilinear symmetry reported in the literature so far i.e. rectangular slot aperture [162], rectangular MA [14], rectangular DRA [170] and equilateral TMA [6] as shown in Fig. 13.1 are revisited. 30°–60°–90° TMA is also investigated here. A simple technique is demonstrated to construct the singularity free far-field radiation patterns of an antenna in Cartesian coordinate system. Various components of electric ($\vec{F}$) and magnetic ($\vec{A}$) potentials are evaluated either by line integration or surface integration depending on the antenna geometry [12-15]. A close look reveals that the radiating fields are combination of $sin(\ \ ) - cos(\ \ ) - exp(\ \ )$ terms. These terms are decomposed into a summation of single $exp(\ \ )$ terms and these $exp(\ \ )$ terms are integrated analytically by taking care of singularity as:

$$I(t_1, t_2, W) = \int_{x=t_1}^{t_2} exp^{(jWx)}\, dx = \begin{cases} (t_2 - t_1), & W = 0 \\ \left(\dfrac{e^{iWt_2} - e^{-iWt_1}}{iW}\right), & W \neq 0 \end{cases} \tag{13.3}$$

After that, all terms are added to get final expressions for far-field radiation patterns which do not suffer from singularity. This procedure is general and is able to handle both real as well as complex singularities (if any). To use this technique, all radiating field integrands are expressed as a summation of $I(W)$ function for various values of W. For example, second integral of I_3 in equation (13.1) can be expressed as:

$$I_4 = (1/2) \times [I(t_1, t_2, W = a + b) + I(t_1, t_2, W = -a + b)] \quad (13.4)$$

It should be pointed here that the complexity occurs after the first step (i.e. decomposition of $sin(\ ), cos(\ )$ and $exp(\ )$ terms into the summation of isolated $exp(\ )$ terms) in standard method. One can easily avoid the singularities in the expressions of far-field radiation patterns of an antenna using this technique and thus time consuming complex mathematical simplification process. This technique is applied to rectangular slot aperture [162], Rectangular MA (RMA) [14], Rectangular DRA (RDRA) [170], equilateral TMA [6] and 30°–60°–90° TMA as shown in Fig. 1 to show the correctness of our theory. This process may be applied to other coordinate systems if one can express the governing term(s) as a combination of *exp*() terms.

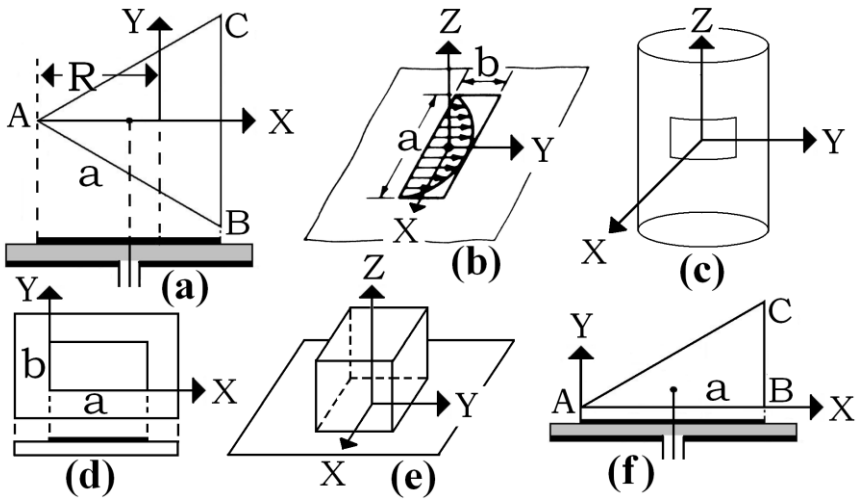

Fig. 13.1 Geometry of different antennas (a) equilateral TMA (b) slot aperture on waveguide (c) rectangular slot on cylindrical surface (d) rectangular MA (e) rectangular DRA (f) $30^o - 60^o - 90^o$ TMA

It should be noted here that the singularity in the spectral domain MoM analysis of an antenna is taken care of by either evaluating residue or by changing the contour of integral path. Analytic removal of singularity in spectral domain MoM analysis [194] is much more complex and much more time consuming than our technique.

Further, this novel technique is very efficient to compute certain type of

integrals to find stored energy within the antenna (or cavity) in a general form to reduce the number of integrands for a particular problem. For example, equations (13.1) can be expressed in a general way as:

$$I_3 = \frac{1}{q}[I(t_1, t_2, W = a + b) + pI(t_1, t_2, W = b - a)] \tag{13.5}$$

where p and q are constant depending on choice of function. Typical results are shown for equilateral TMA to show the effectiveness of our theory for computing stored energy of an antenna. Total 18 number of integrals are replaced by a single integration using this novel technique for equilateral TMA. In this way, one can save huge computational time as well as pen & pencil work.

Theoretical results on far-field radiation patterns are compared with measured data as found in the published literature [15, 21, 162, 165]. Analytic results for various integrals are compared with numerical integration using the inbuilt function of MATLAB® [164] to show the accuracy of our theory.

13.2 Source of Singularity

Before going into details, it is important to have knowledge about the sources of singularity in the evaluation of far-field radiation patterns from 'Equivalence Principle' [4, 16]. It is found that singularity may occur in two ways:

(i) Any intermediate step while evaluating radiation patterns may be singular. For example, consider the integral I_1 as defined by equation (13.6) which will occur if we try to find the radiation patterns of an equilateral Triangular Microstrip Antenna (TMA) whose equal side length is a from electric surface current. The antenna geometry for equilateral TMA is shown in Fig. 13.1(a).

$$I_1 = \int_{x=0}^{M=\sqrt{3}a/2} \sin(px) \int_{y=-x/\sqrt{3}}^{x/\sqrt{3}} \cos(qy)\, dxdy \tag{13.6}$$

Here, p and q are constant. The steps to solve equation (13.6) are given below:

$$\begin{aligned} I_1 &= \int_{x=0}^{M=\sqrt{3}a/2} sin(px) \int_{y=-x/\sqrt{3}}^{x/\sqrt{3}} cos(qy)\, dxdy \\ &= \int_{x=0}^{M} sin(px) \left[\frac{sin(qy)}{q}\right]_{y=-x/\sqrt{3}}^{x/\sqrt{3}} dx \\ &= \frac{1}{q}\int_{x=0}^{M} 2\, sin(px)\, sin\left(xq/\sqrt{3}\right) dx \\ &= \frac{1}{q}\int_{x=0}^{M} [cos\left(p + q/\sqrt{3}\right)x - cos\left(p - q/\sqrt{3}\right)x]\, dx \\ &= \frac{1}{q}\left[\frac{sin\left(p + q/\sqrt{3}\right)x}{(p + q/\sqrt{3})} - \frac{sin\left(p - q/\sqrt{3}\right)x}{(p - q/\sqrt{3})}\right]_{x=0}^{M} \\ &= \frac{1}{q}\left[sinc\left[\left(p + q/\sqrt{3}\right)M\right] - sinc\left[\left(p - q/\sqrt{3}\right)M\right]\right] \end{aligned} \tag{13.6a}$$

where

$$sinc(x) = \begin{cases} 1, & x = 0 \\ \sin(x)/x, & x \neq 0 \end{cases} \tag{13.6b}$$

Now, we can see that I_1 is singular when q is equal to zero. In that case ($q = 0$), I_1 takes different solution as given below:

$$\begin{aligned} I_1 &= \int_{x=0}^{M=\sqrt{3}a/2} sin(px) \int_{y=-x/\sqrt{3}}^{x/\sqrt{3}} cos(0)\, dxdy \\ &= \frac{2}{\sqrt{3}}\int_{x=0}^{M} x\, sin(px)\, dx \\ &= \frac{2}{\sqrt{3}}\left[-\frac{Mcos(pM)}{p} + \frac{sin(pM)}{p^2}\right] \end{aligned} \tag{13.6c}$$

Further, when p becomes equal to 0, I_1 will be singular. All types of

possibility must be considered to get accurate results. But in text books [12-15, 162] (and in the published articles), one single compact form for far-field radiation patterns is found and considerations of various factors to remove the singularity are not seen.

(ii) Singularity in the final expressions of far-field radiation patterns may occur due to simplification. For example, consider the radiation from the BC side of an equilateral TMA where one will encounter I_2 type integral as defined by equation (13.7):

$$I_2 = \int_{y=-a/2}^{a/2} \cos(\beta y) \times e^{jV_2 y}\, dy \tag{13.7}$$

where $V_2 = k_o\, sin(\theta)\, sin(\varphi)$. After some straight forward mathematical calculation, I_2 can be expressed as:

$$I_2 = \frac{2\sin\{(\beta + V_2)a/2\}}{(\beta + V_2)} - \frac{2\sin\{(-\beta + V_2)a/2\}}{(\beta - V_2)} \tag{13.7a}$$

$$= \frac{1}{(\beta^2 - V_2^2)}\left[\sin\{(\beta + V_2)a/2\}\,(\beta - V_2) + \sin\{(\beta - V_2)a/2\}\,(\beta + V_2)\right]$$

$$= \frac{1}{(\beta^2 - V_2^2)}\left[2\beta\, sin(\beta a/2)\, cos(V_2 a/2) - 2V_2\, cos(\beta a/2)\, sin(V_2 a/2)\right] \tag{13.7b}$$

The terms as derived in equation (13.7.b) are present in the equation (14) of [6]. This produces singularity ($\beta = 2\pi(m-n)/3a$ and V_2 become zero) for all $TM^z_{m,n=m}$ modes of equilateral TMA at $\varphi = 0^o$ plane. This singularity occurs due to mathematical simplification. It should be noted here that this singularity can easily be removed by expressing I_2 after the 1st step (i.e. equation (13.7a)) as:

$$I_2 = a[sinc\{(\beta + V_2)a/2\} + sinc\{(\beta - V_2)a/2\}] \tag{13.7c}$$

By applying our novel technique as presented the next section, one can easily evaluate the singularity free far-field expressions for any antenna with rectilinear symmetry. This technique can easily be applied to reduce the total number of integrals in a general sense by single integrals to evaluate other

important quantities such as electric stored energy (W_e), magnetic stored energy (W_m), conductor loss (P_c), dielectric loss (P_d) etc.

13.3 Theory

The main objective of this work is to establish this technique for different antennas in Cartesian coordinate system. The analysis of rectangular aperture (slot) antenna is inherently included in the Rectangular MA (RMA). Therefore, a detailed description of this technique is given for RMA. A similar process can be applied to other antennas. The far-zone electric field at a point $P(r,\theta,\varphi)$ [16] is evaluated as:

$$E_\theta = -\frac{jk_o \exp(-jk_o r)}{4\pi r} \times \left[L_\varphi + \eta_0 N_\theta\right] \tag{13.8}$$

$$E_\varphi = \frac{jk_o \exp(-jk_o r)}{4\pi r} \times \left[L_\theta - \eta_0 N_\varphi\right] \tag{13.9}$$

where

$$N_\theta = A_x cos(\theta)cos(\varphi) + A_y cos(\theta)sin(\varphi) - A_z sin(\theta) \tag{13.10}$$

$$N_\varphi = -A_x sin(\varphi) + A_y cos(\varphi) \tag{13.11}$$

$$L_\theta = F_x cos(\theta)cos(\varphi) + F_y cos(\theta)sin(\varphi) - F_z sin(\theta) \tag{13.12}$$

$$L_\varphi = -F_x sin(\varphi) + F_y cos(\varphi) \tag{13.13}$$

Here all notations are carrying usual meaning. If not mentioned otherwise, it is assumed that $V_1 = k_o\, sin(\theta)\, cos(\varphi)$, $V_2 = k_o\, sin(\theta)\, sin(\varphi)$ and $V_3 = k_o\, cos(\theta)$.

13.3.1 Radiating Slot Aperture

If a rectangular waveguide mounted on an infinite ground plane as shown in Fig. 13.1(b) is operating at fundamental TE_{10} mode, then electric field distribution on that rectangular aperture can be expressed as [162]:

$$\boldsymbol{E}_a = \hat{\boldsymbol{a}}_y E_o \cos(\pi x/a) \qquad \begin{cases} -a/2 \le x \le a/2 \\ -b/2 \le y \le b/2 \end{cases} \tag{13.14}$$

Here all terms are carrying their usual meaning. The compact expressions for far-field radiation patterns are given by C. A. Balanis [162]. It is clear from [162, Table 12.1, pp. 596] that the fields are singular for

$$(k_o a/2)\, sin(\theta)\, cos(\varphi) = \pm \pi/2 \tag{13.15}$$

To predict the far-field radiation patterns accurately, we have to consider the contribution of those singular points separately. This extra mathematical processing can easily be avoided using our technique. The far-field patterns from magnetic surface current (M_s) can be expressed as:

$$F_x = C_{xy} \int_{x=-a/2}^{a/2} \int_{y=-b/2}^{b/2} M_s \times exp^{j(V_1 x + V_2 y)}\, dxdy \tag{13.16}$$

$$= C_{xy} E_o \times \int_{x=-a/2}^{a/2} \left[\frac{exp^{j(V_1+\pi/a)x} + exp^{j(V_1-\pi/a)x}}{2}\right] dx \times \int_{y=-b/2}^{b/2} exp^{jV_2 y} dy$$

$$= \left(C_{xy} E_o/2\right) \times [I(t1 = -a/2\,, t2 = a/2\,, W = V_1 + \pi/a)$$

$$+ I(t1 = -a/2\,, t2 = a/2\,, W = V_1 - \pi/a)]$$

$$\times I(t1 = -b/2\,, t2 = b/2\,, W = V_2) \tag{13.17}$$

$$F_y = F_z = A_x = A_y = A_z = 0 \tag{13.18}$$

where $C_{xy} = 2$ and other terms are carrying their usual meaning. Equation (13.16) takes care all the singularities. In Fig. 13.2, real and imaginary parts of E_φ are plotted to show the effectiveness of our theory. It is clear from Fig. 13.2(a) that our theory is able to calculate the value of E_φ at $\varphi = 0^o$ and $\theta = 90^o$ which is a singular point ($E_\varphi = -\infty - i\infty$) according to [162].

13.3.2 Rectangular Slot on Cylindrical Surface

In a similar way, we can easily predict the far-field radiation patterns of a rectangular slot on a conducting cylindrical surface as shown in Fig. 13.1(c). The electric field in the aperture can be expressed as [195]:

$$E_\varphi(a,\varphi,z) = F_1(\varphi)G_1(z) \qquad (13.19a)$$

$$E_z(a,\varphi,z) = F_2(\varphi)G_2(z) \qquad (13.19b)$$

and for dominant TE_{10} mode of operation in the rectangular waveguide can be expressed as [195, pp. 574]:

$$F_1(\varphi) = G_1(z) = 0 \qquad (13.20)$$

$$F_2(\varphi) = \cos[\pi\varphi/(2\varphi_o)] \quad ; \quad |\varphi| \le \varphi_o \qquad (13.21)$$

$$G_2(z) = E_o \quad ; \quad |z| \le w \qquad (13.22)$$

For a specific value of φ_o $(= \pi/2n,\ n \text{ is integer})$, far-field radiation patterns may be singular. For example, singularity occurs for $\varphi_o = \pi/4$ and $n = 2$. To produce singularity free far-field radiation patterns, similar process can be used as given by equation (13.16) with simple modification due to coordinate system and is not repeated here for brevity.

The analysis of radiating fields from arbitrary mode of operation for rectangular aperture (or waveguide) can be performed as demonstrated for Rectangular Microstrip Antenna (RMA) below.

13.3.3 Rectangular Microstrip Antenna (RMA)

The antenna geometry of a Rectangular Microstrip Antenna (RMA) is shown in Fig. 13.1(d). The closed form compact expressions for predicting the far-field radiation patterns are given in [14, equation (4.13) and (4.14)] which are singular when

$$k_o\, sin(\theta)\, cos(\varphi) = \pm k_x \quad \text{and} \quad k_o\, sin(\theta)\, sin(\varphi) = \pm k_y \qquad (13.23)$$

where $k_x = m\pi/a$ and $k_y = n\pi/b$. To apply this technique, 'Equivalence Principle' [4, 14, 16] is used to find the magnetic surface currents along the four surfaces of the RMA. Radiation from each surface are then calculated individually using our novel technique as:

$$F_x = F_x^{OA} + F_x^{BC}$$
$$F_y = F_y^{OB} + F_y^{AC}$$
$$F_z = A_x = A_y = A_z = 0 \tag{13.24}$$

$$F_x^{OA} = C_{xy} \times E_3 \times cos(k_y 0) \times e^{jV_2 0} \times (1/2) \times [I(t1 = 0, t2 = a, W = k_x + V_1) + I(t1 = 0, t2 = a, W = -k_x + V_1,)] \tag{13.25}$$

$$F_y^{OB} = C_{xy} \times E_3 \times cos(k_x 0) \times e^{jV_1 0} \times (1/2) \times [I(t1 = 0, t2 = b, W = k_y + V_2) + I(t1 = 0, t2 = b, W = -k_y + V_2,)] \tag{13.26}$$

$$F_x^{BC} = -C_{xy} \times E_3 \times cos(k_y b) \times e^{jV_2 b} \times (1/2) \times [I(t1 = 0, t2 = a, W = k_x + V_1) + I(t1 = 0, t2 = a, W = -k_x + V_1,)] \tag{13.27}$$

$$F_y^{AC} = -C_{xy} \times E_3 \times cos(k_x a) \times e^{jV_1 a} \times (1/2) \times [I(t1 = 0, t2 = b, W = k_y + V_2) + I(t1 = 0, t2 = b, W = -k_y + V_2,)] \tag{13.28}$$

where $C_{xy} = 2d$, h is the thickness of the substrate and other terms are carrying their usual meaning. Now, E_φ (= NaN + NaNi) is singular at $\varphi = 0^o$ and $\theta = 57.6606^o$ for TM_{11}^z mode of operation according to [14] whereas our theory gives a finite value of E_φ ($= 0.1472 - 0.1009i$) as shown in Fig. 13.2(b).

13.3.4 Rectangular Dielectric Resonator Antenna (RDRA)

Rectangular DRA (RDRA) is a favorite candidate for modern communication system. The analytical expressions to predict the far-zone electric field (E_θ, E_φ) of a Rectangular DRA (RDRA) having $a \times b \times d$ dimensions and relative permittivity ε_r for the fundamental TE_{111}^y mode (please see Fig. 13.1(e)) are given in [170]. These expressions are singular when

$$V_1 = \pm k_x \quad ; \quad V_2 = \pm k_y \quad ; \quad V_3 = \pm k_z \tag{13.29}$$

Here, $V_1 = k_o\, sin(\theta)\, cos(\varphi)\,, V_2 = k_o\, sin(\theta)\, sin(\varphi)\,, V_3 = k_o\, cos(\theta)$ and k_x, k_y and k_z are as given below:

$$k_x = \frac{\pi}{a}, k_z = \frac{\pi}{2d}, k_y \tan\left(\frac{k_y b}{2}\right) = \sqrt{(\varepsilon_r - 1)k_o^2 - k_y^2} \tag{13.30}$$

To avoid those singularities, our theory is applied to calculate electric and magnetic potentials as given below:

$$F_x = -2j \times E_3\, cos\big(k_y b/2\big)\, sin(V_2\, b/2) \times f_{xs} \times f_{zc} \tag{13.31}$$

$$F_y = 2j \times f_{yc} \times [E_3 \times f_{zc} \times sin(V_1\, a/2) - E_1 \times f_{xc} \times sin(V_3\, h/2)] \tag{13.32}$$

$$F_z = 2j \times E_1\, cos\big(k_y b/2\big) \times f_{xc} \times f_{zs} \times sin(V_2\, b/2) \tag{13.33}$$

$$A_x = 2H_3 \times sin\big(k_y b/2\big) \times f_{xc} \times f_{zs} \times cos(V_2\, b/2) \tag{13.34}$$

$$A_y = 0 \tag{13.35}$$

$$A_z = -2H_1 \times sin\big(k_y b/2\big) \times f_{xs} \times f_{zc} \times cos(V_2\, b/2) \tag{13.36}$$

$$f_{xs} = f_x(t = a, A = -1, B = 2j, U = k_x, V = V_1) \tag{13.37}$$

$$f_{zc} = f_z(t = 2d, A = 1, B = 2, U = k_z, V = V_3) \tag{13.38}$$

$$f_{yc} = f_y\big(t = b, R = 1, S = 2, U = k_y, V = V_2\big) \tag{13.39}$$

$$f_{xc} = f_x(t = a, A = 1, B = 2, U = k_x, V = V_1) \tag{13.40}$$

$$f_{zs} = f_z(t = 2d, A = -1, B = 2j, U = k_z, V = V_3) \tag{13.41}$$

Here $E_1 = \left(\frac{D}{\varepsilon}\right)(-k_z)$, $E_3 = \left(\frac{-D}{\varepsilon}\right)(-k_x), H_1 = \left(\frac{-jD}{\omega\mu\varepsilon}\right)(k_x k_y)$ and $H_3 = \left(\frac{-jD}{\omega\mu\varepsilon}\right)(k_y k_z)$ are the field strength of E_x, E_z, H_x and H_z respectively, D is constant and *function* $f()$ is given by:

$$f(t, A, B, U, V) = \frac{1}{B}[I(t1 = -t/2\,, t2 = t/2\,, W = U + V) + AI(t1 = -t/2\,, t2 = t/2\,, W = V - U)] \tag{13.42}$$

By applying our theory, we can easily avoid the singularity of E_θ at $\theta = 39.7071^o$ (and φ = const.) due to $1/[V_3^2 - k_z^2]$ term for TE_{111}^y mode as shown in Fig. 13.2(c).

This technique can easily be extended to arbitrary TE_{mnp}^{y} mode of a RDRA just by making $k_x = m\pi/a$ and $k_y = n\pi/b$ as presented in Chapter VII.

13.3.5 Equilateral Triangular MA (ETMA)

The derivation of far-field radiation patterns of an equilateral TMA is given in detail in Chapter III. This is very time consuming. Mathematical complexity occurs after decomposition of all combined *sin*()/*cos*()-*exp*() terms into isolated *exp*() terms. If we stop our calculation at that stage and use equation (13.3), we can easily bypass those complex calculations and singularity. The final closed form expressions for far-field radiation patterns are:

$$F_x = \sum_{n=0}^{\infty}\sum_{m=n}^{\infty} C_{xy} \times [I_{\chi=\chi_1}^{x1} + I_{\chi=\chi_2}^{x2}]$$

$$F_y = \sum_{n=0}^{\infty}\sum_{m=n}^{\infty} C_{xy} \times [I_{\chi=\chi_1}^{y1} + I_{\chi=-\chi_2}^{y2} + e^{jV_1 M} \times I^{y3}]$$

$$F_z = A_x = A_y = A_z = 0 \qquad (13.43)$$

where

$$I_{\chi=\chi_1}^{x1} = \frac{-1}{4}\sum_{i=1}^{3}\int_{0}^{M}\left[e^{jC_i^{x1}x} + e^{jD_i^{x1}x} + e^{jE_i^{x1}x} + e^{jF_i^{x1}x}\right]dx$$

$$I_{\chi=\chi_1}^{y1} = \frac{-1}{4}\sum_{i=1}^{3}\int_{0}^{\frac{a}{2}}\left[e^{jC_i^{y1}y} + e^{jD_i^{y1}y} + e^{jE_i^{y1}y} + e^{jF_i^{y1}y}\right]dy$$

$$I_{\chi=\chi_2}^{x2} = \frac{1}{4}\sum_{i=1}^{3}\int_{0}^{M}\left[e^{jC_i^{x1}x} + e^{jD_i^{x1}x} + e^{jE_i^{x1}x} + e^{jF_i^{x1}x}\right]dx$$

$$I_{\chi=-\chi_2}^{y2} = \frac{-1}{4}\sum_{i=1}^{3}\int_{-\frac{a}{2}}^{0}\left[e^{jC_i^{y1}y} + e^{jD_i^{y1}y} + e^{jE_i^{y1}y} + e^{jF_i^{y1}y}\right]dy$$

$$I^{y3} = \sum_{i=1}^{3} \frac{\cos(\alpha_i M)}{2} \int_{y=-\frac{a}{2}}^{\frac{a}{2}} \left(e^{j(\beta_i+V_2)y} + e^{j(-\beta_i+V_2)y}\right) dy \tag{13.44}$$

$$\alpha_1 = \frac{2\pi l}{\sqrt{3}a}, \alpha_2 = \frac{2\pi m}{\sqrt{3}a}, \alpha_3 = \frac{2\pi n}{\sqrt{3}a}, M = \frac{\sqrt{3}a}{2}, R = \frac{a}{\sqrt{3}} \tag{13.45}$$

$$\beta_1 = \frac{2\pi(m-n)}{3a}, \beta_2 = \frac{2\pi(n-l)}{3a}, \beta_3 = \frac{2\pi(l-m)}{3a} \tag{13.46}$$

$$\chi_1 = V_1 + V_2/\sqrt{3} \quad ; \quad \chi_2 = V_1 - V_2/\sqrt{3} \quad ; \quad C_{xy} = C_{mn} \times 2h \times e^{-jV_1 R} \tag{13.47}$$

$$\begin{cases} C_i^{x1} = \alpha_i + \beta_i\eta + \chi; & D_i^{x1} = -\alpha_i + \beta_i\eta + \chi \\ E_i^{x1} = \alpha_i - \beta_i\eta + \chi; & F_i^{x1} = -\alpha_i - \beta_i\eta + \chi \end{cases} \quad ; \quad \eta = tan(\pi/6) \tag{13.48}$$

$$\begin{cases} C_i^{y1} = \alpha_i/\eta + \beta_i + \sqrt{3}\chi; & D_i^{y1} = -\alpha_i/\eta + \beta_i + \sqrt{3}\chi \\ E_i^{y1} = \alpha_i/\eta - \beta_i + \sqrt{3}\chi; & F_i^{y1} = -\alpha_i/\eta - \beta_i + \sqrt{3}\chi \end{cases} \tag{13.49}$$

All terms are evaluated using equation (13.3). According to K. F. Lee *et al.* [6], $\varphi = 17^o$ and $\theta = 51.4082^o$ point produces singularity ($E_\varphi = \text{NaN} + \text{NaNi}$) due to $1/[(n-l)^2b^2 - \chi_1^2]$ term for TM_{30}^z mode of an equilateral TMA having $a = 100mm, h = 1.59mm$ and $\varepsilon_r = 2.32$. One may encounter several singularities due to presence of total 15 number of $1/(A^2 - B^2)$ like terms in the far-field expressions [6, equation (13)-(14)] whereas our theory does not produce any singularity. A typical result is shown in Fig. 13.2(d) for TM_{30}^z mode. It should be pointed here that the obvious singularity for $TM_{m,n=m}^z$ modes at $\varphi = 0^o$ plane [6] is removed without any extra mathematical work. Hence, this theory is very time efficient from the mathematical handwork point.

13.3.6 30°–60°–90° TMA

We have investigated the characteristics of a 30°–60°–90° TMA in Chapter IV. We have also reported our work on 30°–60°–90° TMA [165-166]. The far-field radiation patterns for TM_{mn}^z mode of 30°–60°–90° TMA (see Fig. 13.1(e)) having base length (AB) equal to *a,* are singular due to the presence of

$1/(A^2 - B^2)$ terms. Therefore, it is important to have singularity free expressions for efficient evaluation of far-zone electric field. Our theory is applied to predict the singularity free far-field radiation patterns. Typical results are given here for TM_{10}^z mode as:

$$F_x = C_{xy} \times [I^{x1} + I^{x2}] \tag{13.50}$$

$$F_y = C_{xy} \times [I^{y1} + e^{jV_1 a} \times I^{y2}] \tag{13.51}$$

$$F_z = A_x = A_y = A_z = 0 \tag{13.52}$$

where

$$I^{x1} = -[T(t1 = 0, t2 = a, E = 2b, F = \chi_1) + 2 \times T(t1 = 0, t2 = a, E = b, F = \chi_1)] \tag{13.53a}$$

$$I^{y1} = -[T\left(t1 = 0, t2 = a/\sqrt{3}, E = 2b, F = \sqrt{3}\chi_1\right) + 2 \times T\left(t1 = 0, t2 = a/\sqrt{3}, E = b, F = \sqrt{3}\chi_1\right)] \tag{13.53b}$$

$$I^{x2} = [2 \times T(t1 = 0, t2 = a, E = d, F = V_1) + T(t1 = 0, t2 = a, E = 0, F = V_1)] \tag{13.53c}$$

$$I^{y2} = [T\left(t1 = 0, t2 = a/\sqrt{3}, E = 2f, F = V_2\right) - 2 \times T\left(t1 = 0, t2 = a/\sqrt{3}, E = f, F = V_2\right)] \tag{13.53d}$$

$$b = \frac{2\pi}{3a}\ ,\ g = \frac{2\pi}{\sqrt{3}a}\ ,\ d = \frac{\pi}{a}\ ,\ f = \frac{\pi}{\sqrt{3}a}\ ,\ C_{xy} = C_{mn} \times 2h \tag{13.54}$$

$$V_1 = k_o\, sin(\theta)\, cos(\varphi)\,, V_2 = k_o\, sin(\theta)\, sin(\varphi)\ ,\ \chi_1 = V_1 + V_2/\sqrt{3} \tag{13.56}$$

Here, C_{mn} is constant. Equation (13.53) is solved by equation (13.3) as:

$$T(t1, t2, E, F) = \int_{t1}^{t2} \cos(E)\, exp^{(jFx)}\, dx$$

$$= \frac{1}{2}[I(t1, t2, W = E + F) + I(t1, t2, W = F - E)] \tag{13.57}$$

The singularities [165-166] due to the existence of $1/(A^2 - B^2)$ terms are removed as already shown for rectangular aperture, rectangular MA,

rectangular DRA and equilateral TMA.

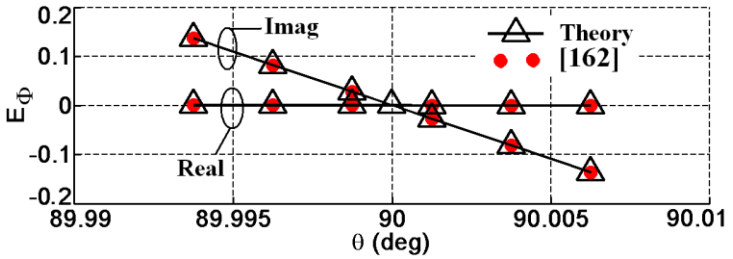

(a) TE_{10} mode of rectangular waveguide aperture [162]

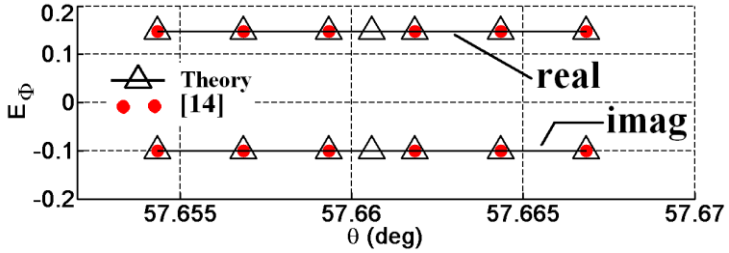

(b) TM_{11}^{z} mode of rectangular MA [14]

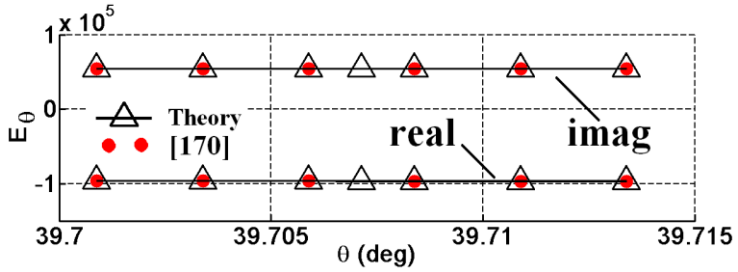

(c) TE_{111}^{y} mode of RDRA [170]

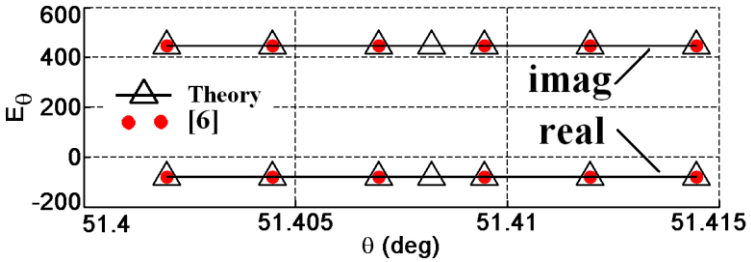

(d) TM_{30}^{z} mode of equilateral TMA [6]

Fig. 13.2 Removal of singularity from far-zone electric field
(a) E_φ at $\varphi = 0^o$ plane ($a = 100mm, a/b = 2$)
(b) E_φ at $\varphi = 0^o$ plane ($a = 100mm, a/b = 1.5, \varepsilon_r = 2.32$)
(c) E_θ at $\varphi =$ const. plane ($a = b = 15mm, d = 25mm, \varepsilon_r = 9.8$)
(d) E_θ at $\varphi = 17^o$ ($a = 100mm, h = 1.59mm, \varepsilon_r = 2.32$)

13.4 Results

In this section, our theoretical results are compared with measured data

as found in literature for fundamental modes of RMA [162], RDRA [170], equilateral TMA [15] and 30°–60°–90° TMA [165-166]. These are shown in Figs. 13.3 - 13.6 respectively. Fig. 13.3 is normalized with respect to -40dB as found in [162] and Figs. 13.4 - 13.6 are normalized with respect to -50dB as found in the literature [15, 21, 165-166]. It is found that our singularity free expressions are in excellent agreement with measured data as found in literature. Little discrepancy is observed in E-plane power patterns. This may be due to the finite size of ground plane.

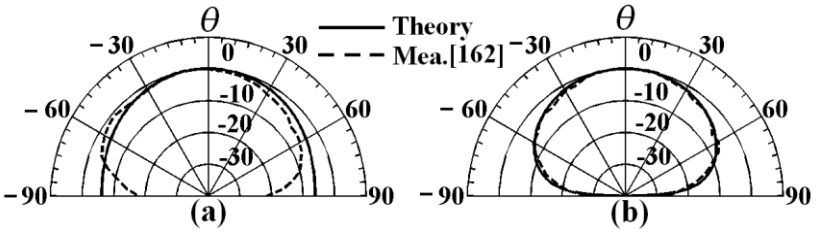

Fig. 13.3 Comparison between theoretical and experimental far-field radiation patterns of RMA at TM_{10}^{z} mode (a) E-plane (b) H-plane ($a = 11.86mm, b = 9.06mm, h = 1.588mm, \varepsilon_r = 2.2$) [162]

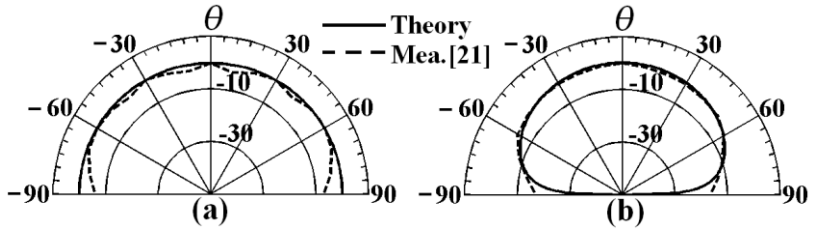

Fig. 13.4 Comparison between theoretical and experimental far-field radiation patterns of RDRA at TE_{111}^{y} mode (a) E-plane (b) H-plane ($a = d = 9.31mm, b = 4.6mm, \varepsilon_r = 37.84$) [21]

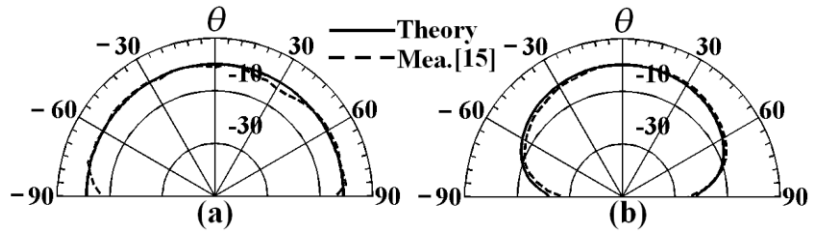

Fig. 13.5 Comparison between theoretical and experimental far-field radiation patterns of equilateral TMA at TM_{10}^{z} mode (a) E-plane (b) H-plane ($f_r = 10\text{GHz}, h = 1.27mm, \varepsilon_r = 10$) [15]

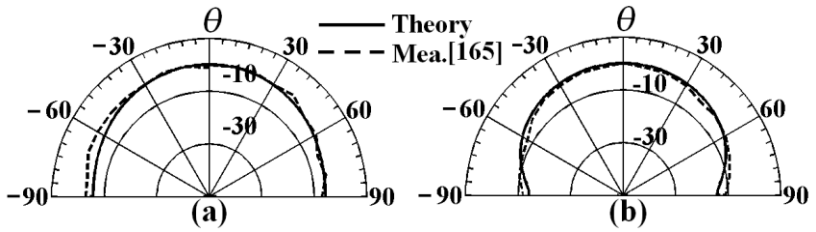

Fig. 13.6 Comparison between theoretical and experimental far-field radiation patterns of 30°–30°–90° TMA at TM_{10}^{z} mode (a) E-plane (b) H-plane ($a = 100mm, h = 0.762mm, \varepsilon_r = 2.5$) [165]

13.5 Other Application

This technique can easily be extended here to evaluate total Q-factor (Q_t), different types of losses, stored energy, etc. Typical example is shown here with respect to stored energy. If the stored electrical and magnetic energy are W_e and W_m respectively then

$$W_t = W_e + W_m \tag{13.58a}$$

where

$$W_e = \frac{\varepsilon_o \varepsilon_r}{4} \iiint_v |E|^2 \, dv \qquad \text{and} \qquad W_m = \frac{\mu_o}{4} \iiint_v |H|^2 \, dv \tag{13.58b}$$

Evaluation of W_e and W_m are quite simple for rectangular shaped antenna/cavity as the all functions are separable. In case of triangular microstrip antenna, the eigenfunctions are non-separable with respect to x-y coordinate as shown in the respective chapters. Therefore, a typical example is shown here for equilateral TMA to justify the advantages of our novel technique. To evaluate W_e and W_m of an equilateral TMA, we have to perform three equations as given below:

$$I_x = \int_{x=0}^{M} \int_{y=-\eta x}^{\eta x} \left| \left(\sum_{i=1}^{3} -\alpha_i \sin(\alpha_i x) \cos(\beta_i y) \right) \right|^2 dxdy \tag{13.59}$$

$$I_y = \int_{x=0}^{M} \int_{y=-\eta x}^{\eta x} \left| \left(\sum_{i=1}^{3} -\beta_i \cos(\alpha_i x) \sin(\beta_i y) \right) \right|^2 dxdy \tag{13.60}$$

$$I_z = \int_{x=0}^{M} \int_{y=-\eta x}^{\eta x} \left| \left(\sum_{i=1}^{3} \cos(\alpha_i x) \cos(\beta_i y) \right) \right|^2 dxdy \tag{13.61}$$

It should be pointed here that one has to deal with equations (13.59) - (13.61) to calculate conduction loss (P_c), dielectric loss (P_d) for an equilateral triangular shaped metallic cavity, waveguide and microstrip antenna.

If we expand equations (13.59) - (13.61), we get 6 integrals from each

equation. Further, these integrals (total $3 \times 6 = 18$ numbers) are similar in nature where the integrands are combination of *sin*()/*cos*() functions. Each integral may produce a singularity for a particular choice of antenna dimensions and operating mode. For example, consider the integral I_5 as shown below:

$$I_5 = \int_{x=0}^{M(=\sqrt{3}a/2)} \int_{y=-\eta x}^{\eta x} \sin(\alpha_1 x)\cos(\beta_1 y) \times \sin(\alpha_2 x)\cos(\beta_2 y)\, dxdy\,; \quad \eta = 1/\sqrt{3} \qquad (13.62)$$

$$= \int_{x=0}^{M} sin(\alpha_1 x)\, sin(\alpha_2 x)\, dx \times \int_{y=0}^{\eta x} [cos((\beta_1+\beta_2)y) + cos((\beta_1-\beta_2)y)]\, dy$$

$$= \frac{1}{2}\int_{x=0}^{M} \left[cos\big((\alpha_1-\alpha_2)x\big) - cos\big((\alpha_1+\alpha_2)x\big)\right]$$

$$\times \left[\frac{sin((\beta_1+\beta_2)\eta x)}{(\beta_1+\beta_2)} + \frac{sin((\beta_1-\beta_2)\eta x)}{(\beta_1-\beta_2)}\right] dx$$

For exact evaluation of I_5, we have to consider all possible cases for $(\beta_1 \pm \beta_2) = 0$ and $(\alpha_1 \pm \alpha_2) \pm (\beta_1 \pm \beta_2)\eta = 0$. Obviously, due to consideration of several factors, the final result for I_5 will be bigger. In this way, total 18 integrals have to be solved to find the values of I_x, I_y and I_z. Singularities may also appear therein under certain conditions.

Our theory is applied in a general sense where one integration is solved and this integral is able to find the results of equations (13.59)-(13.61) without any singularity. Equations (13.59)-(13.61) can be expressed in general form as:

$$I_{4sc} = \int_{x=0}^{M} \int_{y=-\eta x}^{\eta x} \left\{\frac{e^{ik_{x1}x} + Ae^{-ik_{x1}x}}{B}\right\}\left\{\frac{e^{ik_{x2}x} + Ce^{-ik_{x2}x}}{D}\right\}$$

$$\times \left\{\frac{e^{ik_{y1}y} + Ee^{-ik_{y1}y}}{F}\right\}\left\{\frac{e^{ik_{y2}y} + Ge^{-ik_{y2}y}}{H}\right\} dxdy \qquad (13.63)$$

where *A, B, C, D, E, F, G* and *H* are constant and are used to choose *sin*()-*cos*() functions. After some simple mathematical manipulation, we can write:

$$I_{4sc} = \left(\frac{1}{BDFH}\right) \times [I_1 + C \times I_2 + A \times I_3 + AC \times I_4] \tag{13.64}$$

where

$$\begin{aligned} I_1 &= IJ(t_1, t_2, R_1 = (k_{x1} + k_{x2}), S_1, S_2, S_3, S_4, \eta) \\ I_2 &= IJ(t_1, t_2, R_2 = (k_{x1} - k_{x2}), S_1, S_2, S_3, S_4, \eta) \\ I_3 &= IJ(t_1, t_2, R_3 = -(k_{x1} - k_{x2}), S_1, S_2, S_3, S_4, \eta) \\ I_4 &= IJ(t_1, t_2, R_4 = -(k_{x1} + k_{x2}), S_1, S_2, S_3, S_4, \eta) \end{aligned} \tag{13.65}$$

$$\begin{aligned} IJ = \quad & J(t_1, t_2, R, S_1 = (k_{y1} + k_{y2}), \eta) \\ + \ & G \times J(t_1, t_2, R, S_2 = (k_{y1} - k_{y2}), \eta) \\ + \ & E \times J(t_1, t_2, R, S_3 = -(k_{y1} - k_{y2}), \eta) \\ & + EG \times J(t_1, t_2, R, S_4 = -(k_{y1} + k_{y2}), \eta) \end{aligned} \tag{13.65}$$

$$J(t_1, t_2, R, S, \eta) = \int_{x=t_1}^{t_2} e^{iRx} dx \times \int_{y=-\eta x}^{\eta x} e^{iSy}\, dy$$

$$= \frac{1}{iS}[I(t_1, t_2, W = R + S\eta) - I(t_1, t_2, W = R - S\eta)] \tag{13.66}$$

By defining $A - H, k_{x1}, k_{x2}, k_{y1}$ and k_{y2}, we can easily evaluate $I_{4sc}(\quad)$. The final expressions for I_x, I_y and I_z are:

$$\begin{aligned} I_x = {} & \alpha_1^2 \times I_{4sc}(sin(\alpha_1 x)\, sin(\alpha_1 x)\, cos(\beta_1 y)\, cos(\beta_1 y)) \\ & + \alpha_2^2 \times I_{4sc}(sin(\alpha_2 x)\, sin(\alpha_2 x)\, cos(\beta_2 y)\, cos(\beta_2 y)) \\ & + \alpha_3^2 \times I_{4sc}(sin(\alpha_3 x)\, sin(\alpha_3 x)\, cos(\beta_3 y)\, cos(\beta_3 y)) \\ & + 2\alpha_1\alpha_2 \times I_{4sc}(sin(\alpha_1 x)\, sin(\alpha_2 x)\, cos(\beta_1 y)\, cos(\beta_2 y)) \\ & + 2\alpha_2\alpha_3 \times I_{4sc}(sin(\alpha_2 x)\, sin(\alpha_3 x)\, cos(\beta_2 y)\, cos(\beta_3 y)) \\ & + 2\alpha_3\alpha_1 \times I_{4sc}(sin(\alpha_3 x)\, sin(\alpha_1 x)\, cos(\beta_3 y)\, cos(\beta_1 y)) \end{aligned} \tag{13.67}$$

$$\begin{aligned} I_y = {} & \beta_1^2 \times I_{4sc}(cos(\alpha_1 x)\, cos(\alpha_1 x)\, sin(\beta_1 y)\, sin(\beta_1 y)) \\ & + \beta_2^2 \times I_{4sc}(cos(\alpha_2 x)\, cos(\alpha_2 x)\, sin(\beta_2 y)\, sin(\beta_2 y)) \\ & + \beta_3^2 \times I_{4sc}(cos(\alpha_3 x)\, cos(\alpha_3 x)\, sin(\beta_3 y)\, sin(\beta_3 y)) \\ & + 2\beta_1\beta_2 \times I_{4sc}(cos(\alpha_1 x)\, cos(\alpha_2 x)\, sin(\beta_1 y)\, sin(\beta_2 y)) \end{aligned}$$

$$+2\beta_2\beta_3 \times I_{4sc}(cos(\alpha_2 x)\, cos(\alpha_3 x)\, sin(\beta_2 y)\, sin(\beta_3 y))$$
$$+2\beta_3\beta_1 \times I_{4sc}(cos(\alpha_3 x)\, cos(\alpha_1 x)\, sin(\beta_3 y)\, sin(\beta_1 y)) \quad (13.68)$$

$$I_z = I_{4sc}(cos(\alpha_1 x)\, cos(\alpha_1 x)\, cos(\beta_1 y)\, cos(\beta_1 y))$$
$$+I_{4sc}(cos(\alpha_2 x)\, cos(\alpha_2 x)\, cos(\beta_2 y)\, cos(\beta_2 y))$$
$$+I_{4sc}(cos(\alpha_3 x)\, cos(\alpha_3 x)\, cos(\beta_3 y)\, cos(\beta_3 y))$$
$$+2 \times I_{4sc}(cos(\alpha_1 x)\, cos(\alpha_2 x)\, cos(\beta_1 y)\, cos(\beta_2 y))$$
$$+2 \times I_{4sc}(cos(\alpha_2 x)\, cos(\alpha_3 x)\, cos(\beta_2 y)\, cos(\beta_3 y))$$
$$+2 \times I_{4sc}(cos(\alpha_3 x)\, cos(\alpha_1 x)\, cos(\beta_3 y)\, cos(\beta_1 y)) \quad (13.69)$$

To verify our analytical solution for $I_{4sc}(\ )$ function, Numerical Integration (NI) using the inbuilt functions (*syms, matlabFunction, quad2d* etc.) of MATLAB [164] are used. A personal computer having having Core 2 duo Intel processor and 3GB RAM is used for all types of computation. Typical results are shown in Table 13.3 for TM_{21} mode. In Table 13.4, comparison between our theory and NI to evaluate I_x, I_y and I_z are shown for various modes.

Table 13.3

Accuracy of $I_{4sc}(\ \ )$ function for TM_{21} Mode (a = 100mm)

Sl No	Function $I_{4sc}(\ \ )$	Theory	NI
1	$sin(\alpha_2 x)\, sin(\alpha_2 x)\, cos(\beta_2 y)\, cos(\beta_2 y)$	0.0012	0.0012
2	$cos(\alpha_1 x)\, cos(\alpha_2 x)\, sin(\beta_1 y)\, sin(\beta_2 y)$	-1.7028e-4	-1.7028e-4
3	$cos(\alpha_1 x)\, cos(\alpha_3 x)\, cos(\beta_1 y)\, cos(\beta_3 y)$	-1.7121e-4	-1.7121e-4

Table 13.4

Accuracy of $I_x(\ \ ), I_y(\ \ )$ and $I_z(\ \ )$ functions (a = 100mm)

Mode (m, n)	$I_x(\ \ )$		$I_y(\ \ )$		$I_z(\ \ )$	
	Theory	NI	Theory	NI	Theory	NI
1,0	10.0825	10.0825	1.3140	1.3140	0.0065	0.0065
1,1	17.0947	17.0947	17.0947	17.0947	0.0065	0.0065
2,1	29.6549	29.6549	10.2326	10.2326	0.0032	0.0032
4,3	144.3159	144.3159	66.5182	66.5182	0.0032	0.0032

13.6 Advantages of the proposed technique

There are several advantages of the use of our proposed technique. The advantages of our proposed simple techniques are:

- It is simple and easy to understand.
- We do not have to have any prior knowledge on singular point. Our proposed technique takes care all singularities (if any) analytically.
- Decomposition of combined $sin(\ ) - cos(\ ) - exp(\ )$ terms as a summation of single $exp(\ )$ terms is the first step to find the far-field radiation patterns. Complexity occurs after this step. We can easily avoid those complex calculations after the first step. In this way, we can easily save huge time (approximately 90-95%).
- Due to simplification of an expression, there is a possibility to get extra singularities as shown in this chapter. In case of our method, there is no chance to generate extra singularity
- Our analytic solution gives results much faster than the 3D EM simulator or inbuilt functions on numerical integration of MATLAB
- Similar types of integration can easily be expressed in a general form.

In summary, we can calculate singularity free closed form analytic expressions for far-field radiation patterns (E_θ, E_φ), electric stored energy (W_e), magnetic stored energy (W_m), conduction loss (P_c), dielectric loss (P_d) for any antenna (or cavity resonator, waveguide etc.) with rectilinear symmetry quickly.

13.7 Conclusion

Theoretical investigations on far-field radiation patterns of different antennas are presented in Cartesian coordinate system. A time efficient two steps simple procedure is presented to evaluate singularity free far-zone electric field as:

- Decompose all the combined $sin(\ ) - cos(\ ) - exp(\ )$ terms as a summation of $exp(\ )$ terms
- Integrate each $exp(\ )$ terms analytically using equation (13.3)
- 2D/3D integration can easily be integrated in a similar way.

This theory is applied to different antennas in rectangular coordinate system for computing far-field patterns. Theoretical results are compared with measured data as found in the open literature to show the accuracy of our theory. This process is also applied to evaluate certain types of integrals which occur to evaluate stored energy or losses of an antenna (or waveguide) by single integration. Theoretical results are compared with numerical integration using the inbuilt function of MATLAB® to show the accuracy of our theory. Therefore, it is concluded that this novel technique can efficiently be utilized

i) to give singularity free expressions for far-zone electric fields
ii) to reduce unnecessary time consuming mathematical processing
iii) to provide a much more efficient analysis than these offered by the numerical simulator.

It should be pointed here that the analytical results of all type of integrations as presented in respective chapters are always verified with this singularity free procedure.

Part V

Conclusion

Chapter

14. Conclusion and Scope of Future Work

Chapter XIV

Conclusion and Scope of Future Work

14.1 Introduction

A study of theoretical investigations on radiation characteristics of different triangular shaped radiators is presented in this dissertation. Equilateral, 45°–45°–90°, 30°–60°–90° and isosceles triangular shaped Microstrip Antennas (MAs) and Dielectric Resonator Antennas (DRAs) both are investigated. Eigenfunction (ψ), eigenvalue, resonant frequency (f_r), input impedance (Z_{in}), quality factor (Q_t), gain (G), bandwidth (BW) etc are investigated. The topics on Rectangular DRA (RDRA) hitherto left untouched by researchers are also studied here. Theoretical results are verified with experimental data and data obtained using 3D EM simulator HFSS [9]. At the end of each chapter, we have already summarized the characteristics of the investigated antenna.

14.2 Principal Contributions

Literature survey shows that modal investigations had been presented on equilateral Triangular Microstrip Antenna (TMA) only by K. F. Lee *et al* in 1988 [6]. Resonant frequency of 45°–45°–90° TMA [149], 30°–60°–90° TMA [155] and equilateral Triangular DRA (TDRA) [107, 112] for different TM modes has been reported only. Input impedance of 45°–45°–90° TMA [145] and 30°–60°–90° TMA [152] has also been reported for TM_{10}^{z} mode only. The theory as presented in Chapters IV to Chapters XIII, which is valid for different TM_{mnp}^{z} modes is our main and totally novel contributions. In summary, we may write:

1. Radiation characteristics (i.e. resonant frequency, far-field patterns, input impedance, Q-factor, etc.) of 30°–60°–90° (Chapters IV) and 45°–45°–90° (Chapters V) TMAs are presented for different TM^z_{mn} modes.
2. Theoretical investigations on probe fed isosceles $\theta_i - \theta_i - \varphi_i$ TMA is presented here. This theory is valid at fundamental TM^z_{10} mode of isosceles $\theta_i - \theta_i - \varphi_i$ TMA having $\theta_i \geq 60°$ (Chapters VI).
3. Eigenfunction, far-field radiation patterns, Q-factors, bandwidth, gain, etc. are investigated for arbitrary TE^y_{mnp} mode of rectangular DRA (Chapters VII).
4. Radiation characteristics of an equilateral Triangular DRA (TDRA) are presented for different TM^z_{mnp} modes (Chapters VIII).
5. 30°–60°–90° TDRA is investigated in Chapters IX for different TM^z_{mnp} modes.
6. Characteristics of an isosceles 45°–45°–90° TDRA for different TM^z_{mnp} modes is presented in Chapters X.
7. Isosceles $\theta_i - \theta_i - \varphi_i$ TDRA is also investigated here (Chapters XI). This theory is valid for $TM^z_{m=1,n=0,p}$ modes of the isosceles $\theta_i - \theta_i - \varphi_i$ TDRA having $\theta_i \geq 60°$.
8. Horizontally Inhomogeneous Rectangular DRA (HIRDRA) is also investigated at fundamental TE^y_{111} mode (Chapters XII).
9. A time efficient, simple and novel technique is demonstrated to evaluate singularity free closed form expressions of far-field radiation patterns, stored energy, different type of losses etc. of any antenna with rectilinear symmetry for any arbitrary chosen mode (Chapters XIII).

It is found that our theory can predict the results much faster than commercially available numerical EM simulators (IE3D [8], HFSS [9] and CST [10]) as shown in Chapter I.

14.3 Scope of Future Work

Although equilateral, 45°–45°–90°, 30°–60°–90° and isosceles shaped TMAs and TDRAs are investigated analytically in this dissertation, a significant amount of work remains to be done on triangular geometry. In the near future, the unsolved areas may be focused on as an extension of this work. The scope of future work may be summarized as:

1. General solution of arbitrary shaped isosceles $\theta_i - \theta_i - \varphi_i$ TMA and TDRA may be studied for different TM_{mn}^{z} modes.
2. The eigenfunction of an arbitrary shaped scalene triangular radiator may be evaluated for different TE and TM modes.
3. More rigorous analysis of any triangular shaped antenna may be studied using Imperfect Magnetic Conductor (IPMC) boundary condition.
4. TDRAs have been investigated here without considering the effect of feed mechanism. The effects of excitation on resonant frequency, far-field patterns, Q-factors etc. may be studied analytically.
5. Stacked configuration of the antenna using equilateral, 45°–45°–90°, 30°–60°–90° and isosceles shaped TMAs and TDRAs geometry may be studied. This study may be extended for an arbitrary shaped scalene TMA and TDRA.
6. The analysis of triangular shaped radiations may be extended to other rectilinear shaped radiators such as parallelogram, pentagon, hexagon etc for different TE/TM modes analytically.

References

[1] S. A. Long, M. McAllister and L. Shen, "The resonant cylindrical dielectric cavity antenna," *IEEE Transactions on Antennas and Propagation*, vol. 31, no. 3, pp. 406-412, 1983

[2] H. Lenzing, "Higher order modes in large-aperture receiving antennas," *IEEE Transactions on Communication Technology*, vol. 18, no. 1, pp. 83-84, 1970

[3] J. A. Stratton, *Electromagnetic Theory*, McGraw-Hill Book Company, Inc, USA, 1941

[4] R. F. Harrington, *Time harmonic Electromagnetic Fields*, McGraw-Hill, Inc, USA, 1961

[5] A. Petosa, *Dielectric Resonator Antenna Handbook*, Artech House, Norwood, MA, 2007

[6] K. F. Lee, K. M. Luk and J. S. Dahele, "Characteristics of the equilateral triangular patch antenna," *IEEE Transactions on Antennas and Propagation*, vol. 36, no. 11, pp. 1510-1518, 1988

[7] A. V. Oppenheim, A. S. Willsky and S. H. Nawab, *Signals and Systems*, 2nd edition, Phi Learning Private Limited, New Delhi, 1986

[8] IE3D v. 2005, user manual

[9] HFSS v. 13.0, user manual

[10] CST v. 2006

[11] Y. T. Lo, D. Solomon and W. Richards, "Theory and experiment on microstrip antennas," *IEEE Transactions on Antennas and Propagation*, vol. 27, no. 2, pp. 137-145, 1979

[12] J. R. James and P. S. Hall, *Hand Book of Microstrip Antennas*, Peter Peregrinus Ltd., London, United Kingdom, 1989

[13] R. Garg, P. Bhartia, I. Bahl and A. Ittipiboon, *Microstrip Antenna Design Handbook*, Artech House, Boston, London, 2001

[14] K. M. Lee and K. M. Luk, *Microstrip Patch Antennas*, Imperial College Press, London, 2011

[15] I. J. Bahl and P. Bhartia, *Microstrip Antennas*, Artech House, Inc, Massachusetts, USA, 1980

[16] C. A. Balanis, *Advanced Engineering Electromagnetics*, John Wiley & Sons, Inc, USA, 1989

[17] S. A. Long and M. W. McAllister, "The input impedance of the dielectric resonator antenna, " *International Journal of infrared and mm waves*, vol. 7, no. 4, pp. 555-570, 1986

[18] M. W. McAllister and S. A. Long, "Resonant hemispherical dielectric antenna," Electronics Letters, vol. 20, no. 16, pp. 657 – 659, 1984

[19] M. W. McAllister, S. A. Long, G. L. Conway, *"Rectangular Dielectric Resonator Antenna," Electronics Letters*, vol. 19, pp. 218 – 219, 1983

[20] R. K. Mongia, "Theoretical and experimental resonant frequencies of rectangular dielectric resonators," *IEE Proceedings H on Microwaves, Antennas and Propagation*, vol. 139, no.1, pp. 98-104,1992

[21] R. K. Mongia and A. Ittipiboon, *"*Theoretical and experimental investigations on rectangular dielectric resonator antennas*," IEEE Transactions Antennas and Propagation*, vol. 45, pp. 1348 - 1356, 1997

[22] J. S. Row and Kin-Lu Wong, "Resonance in a superstrate-loaded rectangular microstrip structure," *IEEE Transactions on Microwave Theory and Techniques*, vol. 41, no. 8, pp. 1349-1355, 1993

[23] Y. M. M. Antar and Z. Fan, "Theoretical investigation of aperture-coupled rectangular dielectric resonator antenna," *IEEE Transactions on Antennas and Propagation*, 1996

[24] S. A. Schelkunoff, *Electromagnetic Waves*, Princeton, D. Van Nostrand Company, inc, 1957

[25] A. Yoshihiko, "Operation modes of a waveguide Y circulator," *IEEE Transactions on Microwave Theory and Techniques*, vol. 22, no. 11, pp. 954-960, 1974

[26] A. Yoshihiko, "Mode Classification of a triangular ferrite post for Y-circulator operation," *IEEE Transactions on Microwave Theory and Techniques*, vol. 25, no. 1, pp. 59-61, 1977

[27] J. Helszajn and D. S. James, "Planar triangular resonators with magnetic walls," *IEEE Transactions on Microwave Theory and Techniques*, vol. 26, no. 2, pp. 95-100, 1978

[28] J. Helszajn, D. S. James and W. T. Nisbet, "Circulators using planar triangular resonators," *IEEE Transactions on Microwave Theory and Techniques*, vol. 27, no. 2, pp. 188-193, 1979

[29] J. Helszajn, "Contour-integral equation formulation of complex gyrator admittance of junction circulators using triangular resonators," *IEE Proceedings H on Microwaves, Antennas and Propagation*, vol. 132, no. 4, pp. 255-260, 1985

[30] M. Caplin, W. D'Orazio and J. Helszajn, "First circulation condition of E-plane circulator using single-prism resonator," *IEEE Microwave and Guided Wave Letters*, vol. 9, no. 3, pp. 99-101, 1999

[31] J. Helszajn, R. D. Baars and W. T. Nisbet, "Characteristics of circulators using planar triangular and disk resonators symmetrically loaded with magnetic ridges," *IEEE Transactions on Microwave Theory and Techniques*, vol. 28, no. 6, pp. 616-621, 1980

[32] J. Helszajn, *The Stripline Circulator: Theory and Practice*, John Wiley & Sons, Inc, Canada, 2008

[33] T. Miyoshi, S. Yamaguchi and S. Goto, "Ferrite planar circuits in microwave integrated circuits," *IEEE Transactions on Microwave Theory and Techniques*, vol. 25, no. 7, pp. 593-600, 1977

[34] J. Helszajn, "Synthesis of UHF circulators using quarter-wave coupled triangular resonators on a single substrate above the uniform line," *IET Microwaves, Antennas & Propagation,* vol. 3, no. 3, pp. 536-545, 2009

[35] M. Cuhaci and D. S. James, "Radiation from triangular and circular resonators in microstrip," IEEE MTT-S International Microwave Symposium Digest-1977, pp. 438-441, 1977

[36] M. Cuhaci, Study of microstrip triangular resonators, MA Sc. thesis, Dept. of Electrical Engineering, University of Ottawa, Ottawa, Canada, 1979

[37] W. T. Nisbet and J. Helszajn, "Mode charts for microstrip resonators on dielectric and magnetic substrates using a transverse-resonance method," *IEE Journal on Microwaves, Optics and Acoustics*, vol. 3, no. 2, pp. 69-77, 1979

[38] T. Okoshi, Y. Uehara and T. Takeuchi, "The segmentation method - an approach to the analysis of microwave planar circuits (short papers)," *IEEE Transactions on Microwave Theory and Techniques*, vol. 24, no. 10, pp. 662-668, 1976

[39] T. Okoshi, *Planar Circuits for Microwaves and Lightwaves*, Springer-Verlag, Heidelberg, 1985

[40] R. Chadha and K. C. Gupta, "Green's functions for triangular segments in planar microwave circuits," *IEEE Transactions on Microwave Theory and*

Techniques, vol. 28, no. 10, pp. 1139-1143, 1980

[41] H. D. Frary, "The Green's Function for a Plane Contour," *American Journal of Mathematics*, vol. 42, no. 1, pp. 11-25, 1920

[42] Michelle E. Johnston, Jan C. Myland, Keith B. Oldham, "A Green function for the equilateral triangle," *Zeitschrift für angewandte Mathematik und Physik ZAMP*, vol. 56, no. 1 , pp. 31-44, 2005

[43] A. K. Sharma and B. Bhat, "Analysis of triangular microstrip resonators," *IEEE Transactions on Microwave Theory and Techniques*, vol. 30, no. 11, pp. 2029-2031, 1982

[44] W. Chen, K. F. Lee and J. S. Dahele, "Theoretical and experimental studies of the resonant frequencies of the equilateral triangular microstrip antenna," *IEEE Transactions on Antennas and Propagation*, vol. 40, no. 10, pp. 1253-1256, 1992

[45] H. Shinonaga, "Y Dielectric Waveguide for Millimeter- and Submillimeter-Wave," *IEEE Transactions on Microwave Theory and Techniques*, vol. 29, no. 6, pp. 542-546, 1981

[46] A. M. Khilla and I. Wolff, "Field theory treatment of H-plane waveguide junction with triangular ferrite post," *IEEE Transactions on Microwave Theory and Techniques*, vol. 26, no. 4, pp. 279-287, 1978

[47] E. F. Keuster and D. C. Chang, "A geometrical theory for the resonant frequencies and Q factors of some triangular microstrip patch antennas," *IEEE Transactions on Antennas and Propagation*, vol. 31, no. 1, pp. 27-34, 1983.

[48] Y. Tu, A Study of Triangular Microstrip Antennas, MS thesis, Dept. of Electrical and Computer Engg, Electromagnetics Laboratory, University of Colorado, Colorado, 1983

[49] E. L. Ginzton, *Microwave Measurements*, McGraw Hill, New York, USA, 1957

[50] D. White, P. L. Overfelt and G. E. Everett, "Guided wave propagation by the superposition of plane waves in triangular waveguides with perfectly conducting walls," *Antennas and Propagation Society International Symposium*, 1983 , vol. 21, pp. 664-666, 1983

[51] P. L. Overfelt and D. J. White, "TE and TM modes of some triangular cross-section waveguides using superposition of plane waves (Short Paper)," *IEEE Transactions on Microwave Theory and Techniques*, vol. 34, no.1, pp. 161-167, 1986

[52] Chapter 3, Electromagnetic Waveguides by F. E. Borgnis and C. H. Papas, in *Elektrische Felder und Wellen / Electric Fields and Waves (Handbuch der Physik Encyclopedia of Physics)* by G. Wendt, R.W.P. King, F.E. Borgnis, C.H. Papas and H. Bremmer, Springer, 1958

[53] B. J. McCartin, "Eigenstructure of the equilateral triangle, Part II: The Neumann problem," *Mathematical Problems in Engineering*, vol. 8, no. 6, pp. 517-539, 2002

[54] B. J. McCartin, "Eigenstructure of the equilateral triangle, part I: The Dirichlet problem," *SIAM Review*, vol. 45, no. 2, pp. 267–287, 2003

[55] B. J. McCartin, "Eigenstructure of the equilateral triangle. Part III. The Robin problem," *International Journal of Mathematics and Mathematical Sciences*, vol. 2004, no. 16, pp. 807–825, 2004

[56] B. J. McCartin, "Eigenstructure of the discrete Laplacian on the equilateral triangle: The Dirichlet & Neumann problems," *Applied Mathematical Sciences*, vol. 4, no. 53-56, pp. 2633–2646, 2010

[57] B. J. McCartin, *Laplacian eigenstructure of the equilateral triangle* – Hikari Ltd,

2011
[58] J. S. Dahele and K. F. Lee, "Experimental study of the triangular microstrip antenna," *IEEE AP/S Int. Symp. Dig.*, pp. 283-286, 1984
[59] J. S. Dahele and K. F. Lee, "On the resonant frequencies of the triangular patch antenna," *IEEE Transactions on Antennas and Propagation*, vol. 35, no. 1, pp. 100-101, 1987
[60] R. Garg and S. A. Long, "An improved formula for the resonant frequencies of the triangular microstrip patch antenna," *IEEE Transactions on Antennas and Propagation*, vol. 36, no. 4, pp 570-, 1988
[61] W. Chen, K. F. Lee and J. S. Dahele, "Resonant frequencies of the equilateral triangular patch antenna," *IEEE Antennas and Propagation Society International Symposium, 1992. AP-S. 1992 Digest. Held in Conjuction with: URSI Radio Science Meeting and Nuclear EMP Meeting.*, vol. 3, pp. 1431-1434, 1992
[62] K. Güney, "Resonant frequency of a triangular microstrip antenna," *Microwave and Optical Technology Letters*, vol. 6, no. 9, pp. 555–557, 1993
[63] N. Kumprasert and W. Kiranon, "Simple and Accurate Formula for the Resonant Frequency of the Equilateral Triangular Microstrip Patch Antenna," *IEEE Transactions on Antennas and Propagation*, vol. 42, no. 8, pp. 1178-1179, 1994
[64] D. Karaboga, K. Guney, N. Karaboga and A. Kaplan, "Simple and accurate effective side length expression obtained by using a modified genetic algorithm for the resonant frequency of an equilateral triangular microstrip antenna," *International Journal of Electronics*, vol. 83, no. 1, pp. 99-108, 1997
[65] P. Mythili and A. Das, "Simple approach to determine resonant frequencies of microstrip antennas," *IEE Proceedings Microwaves, Antennas and Propagation*, vol. 145, no. 2, pp. 159-162, 1998
[66] K. P. Ray and G. Kumar, "Determination of the resonant frequency of microstrip antennas," *Microwave and Optical Technology Letters*, vol. 23, no. 2, pp. 114–117, 1999
[67] C. S. Gurel and E. Yazgan, "New computation of the resonant frequency of a tunable equilateral triangular microstrip patch," *IEEE Transactions on Microwave Theory and Techniques*, vol. 48, no. 3, pp. 334-338, 2000
[68] Nasimuddin Nasimuddin and A. K. Verma, "Fast and accurate model for analysis of equilateral triangular patch antenna," *Journal of Microwaves and Optoelectronics*, vol. 3, no. 4, pp. 99-110, 2004
[69] D. Guha and J. Y. Siddiqui, "Resonant frequency of equilateral triangular microstrip patch antenna with and without air gaps," *IEEE Transactions on Antennas and Propagation*, vol. 52, no. 8, pp. 2174 - 2177, 2004.
[70] Nasimuddin, K. Esselle, and A. K. Verma, "Resonant frequency of an equilateral triangular microstrip antenna," *Microwave and Optical Technology*, vol. 47, no. 5, pp. 485–489, 2005.
[71] M. Biswas and A. Mandal, "Cad model to compute the input impedance of an equilateral triangular microstrip patch antenna with radome," *Progress In Electromagnetics Research* M, vol. 12, pp. 247-257, 2010.
[72] E. Aydin and S. Can, "Modified resonant frequency computation for tunable equilateral triangular microstrip patch," *IEICE Electronics Express*, vol. 7, no. 7, pp. 500-505, 2010.
[73] M. Dam and M. Biswas, "Fast and accurate model to compute the resonant frequency of triangular patch antenna on suspended and composite substrates," *2012 International Conference on Communications, Devices and*

Intelligent Systems (CODIS), pp. 220-223, 2012

[74] M. Biswas and M. Dam, "Fast and accurate model of equilateral triangular patch antennas with and without suspended substrates," *Microwave and Optical Technology*, vol. 54, no. 11, pp. 2663–2668, 2012

[75] K. Guney and E. Kurt, "Effective side length formula for resonant frequency of equilateral triangular microstrip antenna," *International Journal of Electronics*, vol. 103, no. 2, pp. 261-268, 2016

[76] K. Guney and N. Sarikaya, "Computation of resonant frequency for equilateral triangular microstrip antennas using the adaptive neuro-fuzzy inference system," *International Journal of RF and Microwave Computer-Aided Engineering*, vol. 14, no. 2, pp. 134–143, 2004

[77] S. Sagiroglu and K. Guney, "Calculation of resonant frequency for an equilateral triangular microstrip antenna with the use of artificial neural networks," *Microwave and Optical Technology*, vol. 14, no. 2, pp. 89-93, 1997

[78] S. Sagiroglu and A. Kalinli, "Determining resonant frequencies of various microstrip antennas within a single neural model trained using parallel Tabu search algorithm," *Electromagnetics*, vol. 25, no. 6, pp. 551–565, 2005

[79] C. L. Mak, K. M. Luk and K. F. Lee, "Wideband triangular patch antenna," *IEE Proceedings Microwaves, Antennas and Propagation*, vol. 146, no. 2, pp. 167 – 168, 1999.

[80] M. C. Pan and Kin-Lu Wong, "A broadband active equilateral-triangular microstrip antenna," *Microwave and Optical Technology*, vol. 22, no. 6, pp. 387–389, 1999

[81] L. Yuan, R. Chair, K. M. Luk and K. F. Lee, "Broadband triangular patch antenna with a folded shorting wall," *IEEE Antennas and Wireless Propagation Letters,* vol. 3, no. 1, pp. 189-192, 2004

[82] J. S. Row, "Broadband short-circuited triangular patch antenna," *IEEE Transactions on Antennas and Propagation*, vol. 54, no. 7, pp. 2137-2141, 2006

[83] Y. X.Guo, K. M. Luk and K. F. Lee, "Small wideband triangular patch antenna with an *L*-probe feeding," *Microwave and Optical Technology*, vol. 30, no. 3, pp. 218–220, 2001

[84] L. Yuan, K. M. Luk, R. Chair and K. F. Lee, "A wideband triangular shaped patch antenna with folded shorting wall," *IEEE Antennas and Propagation Society International Symposium, 2004*, vol. 4, pp. 3517-3520, 2004

[85] A. C. Lepage, X. Begaud, G. Le Ray and A. Sharaiha, "UWB directive triangular patch antenna," *International Journal of Antennas and Propagation*, vol. 2008, Article ID 410786, pp. 1-7, 2008

[86] S. T. Choi, K. Hamaguchi and R. Kohno, "A novel microstrip-fed ultrawideband triangular monopole antenna with wide stubs," *Microwave and Optical Technology Letters*, vol. 51, no. 1, pp. 263–266, 2009

[87] V. T. Bhat and K. J. Vinoy, "Studies on ultra wideband triangular patch antennas for imaging applications," *IEEE Asia-Pacific Conference on Antennas and Propagation (APCAP), 2012*, pp. 253-254, 2012

[88] R. D. Wasesa, B. S. Nugroho and Y. Wahyu, "Ultra wideband planar triangular patch antenna with slit ridged ground plane," *2013 International Conference of Information and Communication Technology (ICoICT)*, pp. 332-335, 2013

[89] J. HanLu, C. L. Tang and K. L. Wong, "Circular polarisation design of a single-feed equilateral-triangular microstrip antenna," *Electronics Letters*, vol. 34, no. 4, pp. 319 – 321, 1998

[90] C. L. Tang and K. L. Wong, "A modified equilateral-triangular-ring microstrip

antenna for circular polarization," *Microwave and Optical Technology Letters*, vol. 23, no. 2, pp. 123–126, 1999.

[91] J. H. Lu, C. L. Tang and K. L. Wong, "Single-feed slotted equilateral-triangular microstrip antenna for circular polarization," *IEEE Transactions on Antennas and Propagation*, vol. 47, no. 7, pp. 1174 - 1178, 1999

[92] S. T. Fang and K. L. Wong, "A dual-frequency equilateral-triangular microstrip antenna with a pair of narrow slots," *Microwave and Optical Technology*, vol. 23, no. 2, pp. 82–84, 1999

[93] K. M. Lee, Y. J. Sung, J. W. Baik and Y. S. Kim, "A tunable triangular microstrip patch antenna for multiband applications," *Microwave and Optical Technology Letters*, vol. 51, no. 7, pp. 1788–1790, 2009

[94] E. T. Rahardjo, K. Oka Saputra, M. Asvial and D. Hartanto, "Radiation characteristics of cross slot triangular microstrip antenna and its array to enhance circularly polarization bandwidth," *2007 IEEE Antennas and Propagation Society International Symposium,* pp.729-732, 2007

[95] H. Errifi, A. Baghdad, A. Badri and A. Sahel, "Radiation characteristics enhancement of microstrip triangular patch antenna using several array structures," *I. J. Wireless and Microwave Technologies*, vol. 5, no. 3, pp. 1-17, 2015

[96] J. S. Hong and S. Li, "Theory and experiment of dual-mode microstrip triangular patch resonators and filters," *IEEE Transactions on Microwave Theory and Techniques*, vol. 52, no. 4, pp. 1237-1243, 2004

[97] W. Hu, Z. Ma, Y. Kobayash, T. Anada and G. Hagiwara, "Dual-mode bandpass filters using microstrip slotted equilateral triangular patch resonators," *IEICE Transactions on Electronics*, vol. E89-C, no. 4, pp. 503-508, 2006

[98] J. K. Xiao, X. P. Zu, H. F. Huang and W. L. Dai, "Multi-mode bandstop filter using defected equilateral triangular patch resonator," *2010 9th International Symposium on Antennas Propagation and EM Theory (ISAPE),* pp. 1252-1255, 2010

[99] L. Wang, L. L. Wang, Y. P. Zeng and D. Xiang, "A triangular shaped channel MIM waveguide filter," *Journal of Modern Optics*, vol. 59, no. 19, pp. 1686-1689, 2012

[100] C. Zheng and F. Xu, "Compact bandpass filter based on one-third equilateral triangular resonator of substrate integrated waveguide," *Electronics Letters* , vol. 51, no. 19, pp. 1505-1507, 2015

[101] L. Fu, J. Ren, Y. Yin, J, Lei and R. Lian, "Design of wideband triangular patch antenna with modified ground plane," *2013 International Workshop on Microwave and Millimeter Wave Circuits and System Technology (MMWCST),* pp. 123-126, 2013

[102] C. H. Lee and C. C. Huang, "A new compact microstrip bandpass filter using triangular open-loop resonators and folded-line DGS," *Microwave and Optical Technology Letters*, vol. 48, no. 1, pp. 43–47, 2006

[103] D. Guha, S. Biswas and C. Kumar, "Printed antenna designs using defected ground structures: a review of fundamentals and state-of-the-art developments," *Forum for Electromagnetic Research Methods and Application Technologies (FERMAT)*, vol. 2, pp. 1-13, 2014.

[104] S. H. Chiou, and J. H. Lu, "Cross-polarization level reduction of broadband triangular patch antenna with dual L-strip lines," *Microwave and Optical Technology*, vol. 33, no. 3, 300–303, 2002

[105] A. C. Lepage and X. Begaud, "A compact ultrawideband triangular patch

antenna," *Microwave and Optical Technology Letters*, vol. 40, no. 4, pp. 287–289, 2004

[106] A. Ittipiboon, R. K. Mongia, Y. M. M. Antar, P. Bhartia and M. Cuhaci, "Aperture fed rectangular and triangular dielectric resonators for use as magnetic dipole antennas," *Electronics Letters*, vol. 29, no. 23, pp. 2001-2002, 1993

[107] H. Y. Lo, K. W. Leung, K. M. Luk and E. K. N. Yung, "Low profile equilateral-triangular dielectric resonator antenna of very high permittivity," *Electronics Letters*, vol. 35, no. 25, pp. 2164 - 2166, 1999

[108] H. Y. Lo, K. W. Leung and K. M. Luk, "Slot-line-excited equilateral-triangular dielectric resonator antenna of very high permittivity," *Microwave and Optical Technology Letters*, vol. 29, no. 4, pp. 230–231, 2001

[109] H. Y. Lo and K. W. Leung, "Excitation of low-profile equilateral-triangular dielectric resonator antenna using a conducting conformal strip," *Microwave and Optical Technology*, vol. 29, no. 5, pp. 317–319, 2001

[110] K. W. Leung, H. Y. Lo, K. K. So and K. M. Luk, "High-permittivity dielectric resonator antenna excited by a rectangular waveguide," *Microwave and Optical Technology Letters*, vol. 34, no. 3, pp. 157–158, 2002

[111] K. W. Leung, K. M. Chow and K. M. Luk, "Low-profile high-permittivity dielectric resonator antenna excited by a disk-loaded coaxial aperture," *IEEE Antennas and Wireless Propagation Letters*, vol. 2, no. 1, pp. 212-214, 2003

[112] A. A. Kishk, "A triangular dielectric resonator antenna excited by a coaxial probe," *Microwave and Optical Technology Letters*, vol. 30, no. 5, pp. 340 – 341, 2001

[113] A. A. Kishk, "Wide-Band Truncated Tetrahedron Dielectric Resonator Antenna Excited by a Coaxial Probe," *IEEE Transactions on Antennas and Propagation*, vol. 51, no. 10, pp. 2913–2917, 2003

[114] A. Gupta, R. K. Gangwar, and S. P. Singh, "Three element dual segment triangular dielectric resonator antenna for *x*-band applications," *Progress In Electromagnetics Research* C, vol. 34, pp. 139-150, 2013

[115] R. Kumari, K. Parmar and S. K. Behera, "Conformal Patch Fed Stacked Triangular Dielectric Resonator Antenna for WLAN Applications," International Conference on Emerging Trends in Robotics and Communication Technologies (INTERACT), Chennai, pp. 104-107, 2010

[116] A. Petosa and A. Ittipiboon, "Dielectric Resonator Antennas: A Historical Review and the Current State of the Art," *IEEE Antennas and Propagation Magazine*, vol. 52, no. 5, pp. 91-116, 2010

[117] M. Sancho, "Integral formulation of the boundary value problem in waveguides," *American Journal of Physics*, vol. 48, no. 12, pp. 1083-1087, 1980

[118] J. Mazumder, "A method for the study of TE and TM modes in waveguides of very general cross section," *IEEE Transactions on Microwave Theory and Techniques*, vol. 28, no. 9, pp. 991-995, 1980

[119] B. S. Rodrigueza, B. Sensalea and V. Leitão, "Determination of the TE and TM modes in arbitrary shaped waveguides using hypersingular boundary element method," *AEU - International Journal of Electronics and Communications*, vol. 62, no. 8, pp. 576-581, 2008

[120] L. F. Wang, "Convex meshfree solutions for arbitrary waveguide analysis in electromagnetic problems," *Progress In Electromagnetics Research B*, vol. 48, pp. 131-149, 2013

[121] M. Swaminathan, E. Arvas, T. K. Sarkar and A. R. Djordjevic, "Computation of cutoff wavenumbers of TE and TM modes in waveguides of arbitrary cross

sections using a surface integral formulation," IEEE Transactions on Microwave Theory and Techniques, vol. 38, no. 2, pp. 154-159, 1990.
[122] M. F. Iskander, Iterative solutions of finite wedge structures, Ph.D. dissertation, Electrical Engineering Dept., University of Manitoba, Canada, 1975
[123] M. D. Deshpande, D. G. Shively and C. R. Cockrell, Resonant Frequencies of Irregularly Shaped Microstrip Antennas Using Method of Moments, NASA Technical Paper 3386, CECOM Technical Report 93-E-1, 1993
[124] H. R. Hassani and D. Mirshekar-Syahkal, "Analysis of triangular patch antennas including radome effects," *IEE Proceedings H Microwaves, Antennas and Propagation*, vol. 139, no. 3, pp. 251-256, 1992
[125] M. Simeoni and M. Jofre, "Equilateral triangular waveguide antenna - a spectral domain analysis," *IET Microwaves, Antennas and Propagation*, vol. 4, no. 3, pp. 296-304, 2010
[126] Y. Chen and C. F. Wang, *Characteristic Modes: Theory and Applications in Antenna Engineering*, John Wiley & Sons, Inc., Hoboken, New Jersey, 2015
[127] T. Dissanayake, K. Esselle and Y. Ge, "A printed triangular-ring antenna with a 2:1 bandwidth," *Microwave and Optical Technology Letters*, vol. 44, no. 1, pp. 51–53, 2005
[128] C. M. Wu, "Wideband dual-frequency CPW-fed triangular monopole antenna for DCS/WLAN application," *AEU - International Journal of Electronics and Communications*, vol. 61, no. 9, pp. 563–567, 2007
[129] J. J. Wanga, Y. Z. Yinb and X. W. Daic, "A novel fractal triangular monopole antenna with notched and truncated ground for UWB application," *Journal of Electromagnetic Waves and Applications*, vol. 23, no. 10, pp. 1313-1321, 2009
[130] X. Mu, S. X. Gong and T. Hong, "A planar triangular monopole antenna with modified ground for UWB application," *Microwave and Optical Technology Letters*, vol. 53, no. 8, pp. 1818–1820, 2011
[131] A. Panahi, X. L. Bao, G. Ruvio and M. J. Ammann, "A printed triangular monopole with wideband circular polarization," *IEEE Transactions on Antennas and Propagation*, vol. 63, no. 1, pp. 415 - 418, 2014
[132] Y. D. Yang, Y. Z. Huang and S. J. Wang, "Mode analysis for equilateral-Triangle-resonator microlasers with metal confinement layers," *IEEE Journal of Quantum Electronics*, vol. 45, no. 12, pp. 1529-1536, 2009
[133] Y. Z. Huang, W. H. Guo and Q. M. Wang, "Analysis and numerical simulation of eigenmode characteristics for semiconductor lasers with an equilateral triangle micro-resonator," *IEEE Journal of Quantum Electronics*, vol. 37, no. 1, pp. 100-107, 2001
[134] H. C. Chang, G. Kioseoglou, E. H. Lee, J. Haetty, M. H. Na, Y. Xuan, H. Luo, A. Petrou, and A. N. Cartwright, "Lasing modes in equilateral-triangular laser cavities," *Phys. Rev. A*, vol. 62, 013816, pp. 1-6, 2000
[135] R. H. Heald and L. M. Sargent, "An investigation of the aerodynamic characteristics of rotating circular and triangular cylinders," Technical Report, Project Number CP8-405-6468, U. S. Department of Commerce of National Bureau of Standards, 1959
[136] I. S. Sokolnikoff, *Mathematical Theory of Elasticity*, McGraw-Hill Book Company, Inc., USA, 1946
[137] E. M. Sparrow, "Laminar Flow in Isosceles Triangular Ducts," *AIChE Journal*, vol. 8, no. 5, pp. 599-604, 1962
[138] S. T. McComas, "Hydrodynamic Entrance Lengths for Ducts of Arbitrary Cross Section," *ASME. J. Basic Eng*, vol. 89, no. 4, pp. 847-850,1967

[139] J. A. Keiffer Jr., Pressure drop and velocity distribution in the laminar entrance region of a triangular duct, Master of Science dissertation, Naval Postgraduate School, USA, 1968

[140] P. C. Lu and R. W. Miller, "Some Heat Transfer Problems Inside an Equilateral Triangular Region," American Society of Mechanical Engineers, New York, 1967

[141] M. A. Bijlani, Vibration of Triangular Plates, Master of Applied Science dissertation, University of Ottawa, Ottawa, Canada, 1982

[142] I. J. Bahl and P. Bhartia, *Microwave Solid State Circuit Design*, John Wiley & Sons, Inc., Hoboken, New Jersey, 2003

[143] F. L. Ng, "Tabulation of Methods for the Numerical Solution of the Hollow Waveguide Problem," *IEEE Transactions on Microwave Theory and Techniques*, vol. 22, no. 3, pp. 322-329, 1974

[144] P. M. Morse and H. Feshbach, *Methods of Theoretical Physics*, vol. 1, McGraw-Hill, USA, 1953

[145] G. A. Kyriacou and J. N. Sahalos, "The geometrical theory for the input impedance of the isosceles orthogonal triangular microstrip patch antenna," *Archiv für Elektrotechnik*, vol. 73, no. 5, pp. 365-371, 1990

[146] E. G. Lim, E. Korolkiewicz, S. Scott, A. Sambell and B. Aljibouri, "An efficient formula for the input impedance of a microstrip right-angled isosceles triangular patch antenna," *IEEE Antennas and Wireless Propagation Letters*, vol. 1, no. 1, pp. 18-21, 2002

[147] S. K. Lee, S. F. Ooi, E. G. Lim, E. Korolkiewicz and A. Sambell, "Efficient Coupling Impedance Formulas for the Right-angled Isosceles Triangular Patch for Use in Segmentation Analysis," *36th European Microwave Conference,* pp. 241-244, 2006

[148] E. G. Lim, *Circular polarised microstrip antenna design using segmental methods*, Doctoral thesis, Northumbria University. 2002

[149] V. Sharma, S. Shekhawat, V. K. Saxena, J. S. Saini, K. B. Sharma, B. Soni and D. Bhatnagar, "Right isosceles triangular microstrip antenna with narrow L-shaped slot," *Microwave and Optical Technology Letters*, vol. 51, no. 12, pp. 3006–3010, 2009

[150] P. L. Overfelt, Analysis of Three- and Four-Sided Uniform Waveguides With Unusual Cross-Section/Boundary Conditions, technical report, Report no. NWC TP 6989, Naval Weapons Center, NWC TP 6989, 1989

[151] G. Kumar and K. P. Ray, *Broadband Microstrip Antennas*, Artech House, Norwood, MA, 2003

[152] G. A. Kyriacou and J. N. Sahalos, "Input impedance of a 30^o -60^o -90^o triangular patch antenna," *Canadian Journal of Physics*, vol. 67, no. 11, pp. 1044-1048, 1989

[153] Zhang J, Fu J, "Comments on 'TE and TM modes of some triangular cross-section waveguides using superposition of plane waves'," *IEEE Transactions on Microwave Theory and Techniques*, vol. 34, no. 1, pp. 612 – 613, 1991

[154] W. Lin, *Microwave Theory and Techniques*, Science Press, Beijing, 1979 (in Chinese).

[155] M. M. Olaimat and N. Dib, "Improved formulae for the resonant frequencies of triangular microstrip patch antennas," *International Journal of Electronics*, vol. 98, no. 3, pp. 407-424, 2011

[156] M. M. Olaimat and N. Dib, "A Study of 15°–75°–90° degrees Angles Triangular Patch Antenna," *Progress In Electromagnetics Research Letters*, vol. 21, pp. 1-9, 2011

[157] E. P. Ogherohwo, A. O. Adeniran and O. Olabisi, "A study of 30°–60°–90° scalene triangular patch antenna (TPA) at 900MHz," *International Journal of Research and Reviews in Applied Sciences*, vol. 13, no. 2, pp. 658-664, 2012
[158] K. Kathiravan and A. K. Bhattacharyya, "Analysis of Triangular Patch Antenna," *Electromagnetics*, vol. 9, no. 4, pp. 427-438, 1989
[159] A. C. Lepage, X. Begaud, G. Le Ray and A. Sharaiha, "F-probe fed broadband triangular patch antennas mounted on a finite ground plane," *IEEE Antennas and Propagation Society International Symposium*, 2004, vol. 4, pp. 4296-4299 2004
[160] A. C. Lepage, X. Begaud, G. Le Ray, and A. Sharaiha, "UWB Directive Triangular Patch Antenna," *International Journal of Antennas and Propagation*, vol. 2008, Article ID 410786, pp. 1-7, 2008
[161] S. M. Dawso, Design and analysis of an electrically small inductively loaded sector antenna for frequency reconfiguration using varactor diodes, Master of Science, Electrical and Computer Engineering Dept., the Graduate College of the University of Illinois at Urbana-Champaign, 2011
[162] C. A. Balanis, *Antenna Theory Analysis and Design*, 3rd ed, John Wiley & Sons, Inc., Hoboken, New Jersey, 2005
[163] D. M. Pozar, *Microwave Engineering*, 4th ed, John Wiley & Sons, Inc., USA, 2012
[164] MATLAB v. 2010a
[165] S. Maity and and B. Gupta, "Simplified analysis for 30°–60°–90° triangular microstrip antenna," *Journal of Electromagnetic Waves and Applications*, vol. 28, no. 1, pp. 91-101, Nov. 2013
[166] S. Maity and B. Gupta, "Cavity model analysis of 30°–60°–90° triangular microstrip antenna," *International Journal of Electronics and Communications (AEÜ)*, vol. 69, pp. 923-932, 2015
[167] V. K. Tiwari, D. Bhatnagar, J. S. Saini and P Kumar, "Investigation of radiation properties of a right isosceles triangular microstrip antenna," *Indian Journal of Radio & Space Physics*, vol. 34, pp. 353-356, 2005
[168] W. R. Smythe, *Static and dynamic electricity*, McGraw-Hill Book Company, Inc., USA, 1939
[169] A. Damle and G. C. Peterson, "Understanding the eigenstructure of various triangles," SIAM Undergraduate Research Online, vol. 3, no. 1, pp. 187-208, 2010 (https://www.siam.org/students/siuro/vol3/S01061.pdf")
[170] A. S. Zoubi, *Rectangular Dielectric Resonator Antennas Fed by Dielectric Image Guide*, Ph.D. dissertation, The University of Mississippi, USA, 2008.
[171] A. Petosa and S. Thirakoune, "Rectangular Dielectric Resonator Antennas with Enhanced Gain," *IEEE Transactions on Antennas and Propagation*, vol. 59, no. 4, pp. 1385 - 1389, 2011
[172] S. Maity and B. Gupta, "Closed form expressions to find radiation patterns of rectangular dielectric resonator antennas for Various Modes," *IEEE Transactions on Antennas and Propagation*, vol. 62, no. 12, pp. 6524-6527, 2014
[173] S. Maity and B. Gupta, "Input impedance of probe fed rectangular dielectric resonator antenna," *URSI Regional Conference in Radio Science (RCRS) 2014*, Pune, India, Jan 2014
[174] K. M. Luk and K. W. Leung, *Dielectric Resonator Antennas*, Research Studies Press Ltd, Baldock, UK, 2003
[175] E. A. J. Marcatili, 'Dielectric rectangular waveguide and directional coupler for integrated optics', Bell Syst. Tech. J. , vol. 48, pp. 2071-2102, 1969

[176] X. S. Fang and K. W. Leung, "Designs of single-, dual-, wide-band rectangular dielectric resonator antennas," *IEEE Transactions on Antennas and Propagation*, vol. 59, pp. 2409 - 2414, 2011
[177] 130_Y. M. Pan, K. W. Leung and K. M. Luk, "Design of the Millimeter-wave Rectangular Dielectric Resonator Antenna Using a Higher-Order Mode", *IEEE Transactions on Antennas and Propagation*, vol. 59, no. 8, pp. 2780–2788, 2001
[178] J. L. Volakis and K. Sertel, *Integral Equation Methods for Electromagnetics*, SciTech Publishing, Inc., USA, 2012
[179] S. A. Long and E. M. O'Connor, "The history of the development of the Dielectric resonator antenna," *International Conference on Electromagnetics in Advanced Applications (ICEAA)* – 2007, pp. 872-875, 2007
[180] 180_W. C. W. Trueman, S. R. Mishra, C. L. Larose and R. K. Mongia, "Resonant frequencies and Q-factors of dielectric parallelepipeds," *IEEE Transactions Instrumentation and Measurement*, vol. 44, pp. 322-325, 1995
[181] S. Dhar, R. Ghatak, B. Gupta and D. R. Poddar, "A wideband minkowski fractal dielectric resonator antenna," *IEEE Transactions on Antennas and Propagation*, vol. 61, no. 6, pp. 2895 - 2903, 2013
[182] M. Zahn, *Electromagnetic Field Theory*, John Wiley & Sons, Inc, USA, 1979
[183] S. Maity and B. Gupta, "Comments on "A triangular dielectric resonator antenna excited by a coaxial probe"," *Microwave and Optical Technology Letters*, vol. 54, no. 6, pp. 1548, 2012
[184] D. Kajfez and P. Guillon, Dielectric Resonators, Noble Publishing Corporation, USA, 1986
[185] Y. M. M. Antar, D. Cheng, G. Seguin, B. Henry and M. G. Keller, "Modified waveguide model (MWGM) for rectangular dielectric resonator antenna (DRA)" , *Microwave and Optical Technology Letters*, vol. 19, no. 2, pp. 158–160, 1998
[186] L. Pincherle, "Electromagnetic waves in metal tubes filled longitudinally with two dielectrics," *Phys. Rev.* vol. 66, pp. 118-130, 1944
[187] P. H. Vartanian, W. H. Ayres and A. L. Helgesson, "Propagation in dielectric slab loaded rectangular waveguide," *IRE Transactions on Microwave Theory and Techniques*, vol. 6, no. 2, pp. 215-222, 1958
[188] W. L. Weeks, *Electromagnetic Theory for Engineering Applications*, John Wiley & Sons, Inc, 1964
[189] K. Lu, K. W. Leung and Y. M. Pan, "Theory and experiment of the hollow rectangular dielectric resonator antenna," *IEEE Antennas and Wireless Propagation Letters*, vol. 10, pp. 631-634, 2011
[190] A. Petosa, N. Simons, R. Siushansian, A. Ittipiboon, and M. Cuhaci, "Design and analysis of multisegment dielectric resonator antennas," *IEEE Transactions on Antennas and Propagation*, vol. 48, no. 5, pp. 738-742, 2000
[191] A. Rashidian, K. Forooraghi and M. T. Aligodarz, "Investigations on two-segment dielectric resonator antennas," *Microwave and Optical Technology Letters,* vol. 45, no. 6, pp. 533–537, 2005
[192] Ç. S. Gürela, H. Coşarb and Ö. Akalınc, "Accurate resonant frequency computation of multisegment rectangular dielectric resonator antennas," *Journal of Electromagnetic Waves and Applications*, vol. 24, no. 5-6, pp. 839-847, 2010
[193] K. A. Walters and G. W. Hanson, "Resonant frequency calculation for inhomogeneous dielectric resonators using volume integral equations and face-centered node points," *Microwave and Optical Technology Letters,* vol. 32, no. 5, pp. 356–359, 2002

[194] S. O. Park and C. A. Balanis, "Analytical technique to evaluate the asymptotic part of the impedance matrix of Sommerfeld-type integrals," *IEEE Transactions on Antennas and Propagation*, vol. 45, no. 5, pp. 798-805, 1997

[195] R. E. Collin and F. J. Zucker, *Antenna Theory*, Part I, McGraw-Hill, Inc, USA, 1969

Signature of the candidate
[SUDIPTA MAITY]